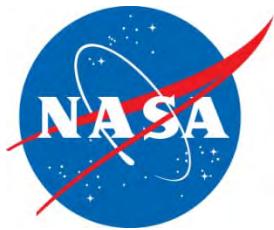
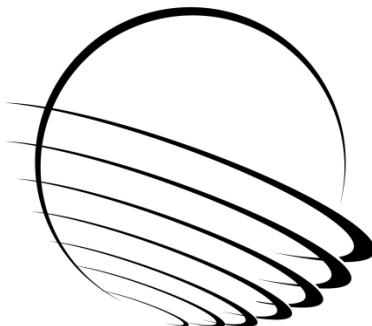


NASA/CP-2012-217653



41st Aerospace Mechanisms Symposium

Compiled/Edited by: Edward A. Boesiger



Proceedings of a symposium held at
Hilton Pasadena, CA
Hosted by the Jet Propulsion Laboratory and
Lockheed Martin Space Systems Company
Organized by the Mechanisms Education Association

May 16-18, 2012

May 2012

NASA STI Program ... in Profile

Since its founding, NASA has been dedicated to the advancement of aeronautics and space science. The NASA scientific and technical information (STI) program plays a key part in helping NASA maintain this important role.

The NASA STI program operates under the auspices of the Agency Chief Information Officer. It collects, organizes, provides for archiving, and disseminates NASA's STI. The NASA STI program provides access to the NASA Aeronautics and Space Database and its public interface, the NASA Technical Report Server, thus providing one of the largest collections of aeronautical and space science STI in the world. Results are published in both non-NASA channels and by NASA in the NASA STI Report Series, which includes the following report types:

- **TECHNICAL PUBLICATION.** Reports of completed research or a major significant phase of research that present the results of NASA Programs and include extensive data or theoretical analysis. Includes compilations of significant scientific and technical data and information deemed to be of continuing reference value. NASA counterpart of peer-reviewed formal professional papers but has less stringent limitations on manuscript length and extent of graphic presentations.
- **TECHNICAL MEMORANDUM.** Scientific and technical findings that are preliminary or of specialized interest, e.g., quick release reports, working papers, and bibliographies that contain minimal annotation. Does not contain extensive analysis.
- **CONTRACTOR REPORT.** Scientific and technical findings by NASA-sponsored contractors and grantees.

- **CONFERENCE PUBLICATION.** Collected papers from scientific and technical conferences, symposia, seminars, or other meetings sponsored or co-sponsored by NASA.

- **SPECIAL PUBLICATION.** Scientific, technical, or historical information from NASA programs, projects, and missions, often concerned with subjects having substantial public interest.

- **TECHNICAL TRANSLATION.** English-language translations of foreign scientific and technical material pertinent to NASA's mission.

Specialized services also include organizing and publishing research results, distributing specialized research announcements and feeds, providing help desk and personal search support, and enabling data exchange services.

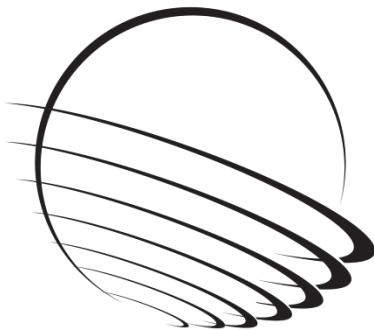
For more information about the NASA STI program, see the following:

- Access the NASA STI program home page at <http://www.sti.nasa.gov>
- E-mail your question via the Internet to help@sti.nasa.gov
- Fax your question to the NASA STI Help Desk at 443-757-5803
- Phone the NASA STI Help Desk at 443-757-5802
- Write to:
NASA STI Help Desk
NASA Center for AeroSpace Information
7115 Standard Drive
Hanover, MD 21076-1320



41st Aerospace Mechanisms Symposium

Compiled/Edited by: Edward A. Boesiger



Proceedings of a symposium held at
Hilton Pasadena, CA
Hosted by the Jet Propulsion Laboratory and
Lockheed Martin Space Systems Company
Organized by the Mechanisms Education Association

May 16-18, 2012

May 2012

Acknowledgement

The high quality of this symposium is the result of the work of many people, and their efforts are gratefully acknowledged. This extends to voluntary members of the Aerospace Mechanisms Organizing Committee representing the eight participating NASA Centers, co-sponsor Lockheed Martin Space Systems Corporation, and the European Space Agency. Appreciation is also extended to the session chairs, the authors, and particularly the personnel at the Jet Propulsion Laboratory responsible for the symposium arrangements and publication of these proceedings. A sincere thank you is well deserved by the Mechanisms Education Association officers, particularly Ed Boesiger, who are responsible for the year-to-year management of the AMS including editing of the papers and production of the program.

Special thanks to:

Donald Sevilla, JPL Host Chairman
Louise Jandura, JPL Co-Host Chairman

Stuart Lowenthal, MEA General Chairman, Lockheed Martin SS
Edward Boesiger, MEA Operations Chairman, Lockheed Martin SS

Monica King, JPL Symposium Organization Support
Kris Katagiri, JPL Symposium Organization Support
Ken Gowey, JPL Graphics Services, Technical Information Section

Available from:

NASA Center for AeroSpace Information
7115 Standard Drive
Hanover, MD 21076-1320
443-757-5802

This report is also available in electronic form at <http://www.sti.nasa.gov/> and
<http://ntrs.nasa.gov/>

PREFACE

The Aerospace Mechanisms Symposium (AMS) provides a unique forum for those active in the design, production and use of aerospace mechanisms. A major focus is the reporting of problems and solutions associated with the development and flight certification of new mechanisms. Organized by the Mechanisms Education Association, responsibility for hosting the AMS is shared by the National Aeronautics and Space Administration and Lockheed Martin Space Systems Company (LMSSC). Now in its 41st symposium, the AMS continues to be well attended, attracting participants from both the U.S. and abroad.

The 41st AMS, hosted by the Jet Propulsion Laboratory (JPL) in Pasadena, California, was held May 16, 17 and 18, 2012. During these three days, 38 papers were presented. Topics included gimbals and positioning mechanisms, components such as hinges and motors, CubeSats, tribology, and Mars Science Laboratory mechanisms. Hardware displays during the supplier exhibit gave attendees an opportunity to meet with developers of current and future mechanism components.

This publication was prepared by the Jet Propulsion Laboratory, California Institute of Technology, under a contract with the National Aeronautics and Space Administration.

A portion of this work was prepared outside NASA, JPL, and California Institute of Technology. Any views and opinions expressed in this outside work do not necessarily state or reflect those of NASA, JPL, or the California Institute of Technology.

Reference herein to any specific commercial product, process, or service by trade name, trademark, manufacturer, or otherwise, does not constitute or imply its endorsement by the United States Government or the Jet Propulsion Laboratory, California Institute of Technology.

© 2012. All rights reserved.

CONTENTS

Symposium Schedule	viii
Symposium Organizing and Advisory Committees	xii
Development of Brushed and Brushless DC Motors for use in the ExoMars Drilling and Sampling Mechanism	1
Robin Phillips, Massimo Palladino & Camille Courtois	
Rotary Percussive Sample Acquisition Tool (SAT): Hardware Development and Testing	17
Kerry Klein, Mircea Badescu, Nicolas Haddad, Lori Shiraishi & Phillip Walkemeyer	
Lock & Release Mechanism for the CHOMIK Penetrator Device and its Tribological Properties	29
Marcin Dobrowolski & Jerzy Grygorczuk	
Harmonic Drive™ Gear Material Selection and Life Testing.....	39
Jeffrey Mobley & Jonathan Parker	
New Supplier – Hardware Duplication – Some Pitfalls	53
Edwin Joscelyn	
Development of the Vibration Isolation System for the Advanced Resistive Exercise Device	67
Jason Niebuhr & Richard Hagen	
Passive Thrust Oscillation Mitigation for the CEV Crew Pallet System	81
Matthew Sammons, Cory Powell, Joe Pellicciotti, Ralph Buehrle & Keith Johnson	
The Damper Spring Unit of the Sentinel 1 Solar Array	97
Frans Doejaaren & Marcel Ellenbroek	
Ultra-low-weight Rotary Actuator for Operation on Mars and Pin Puller Mechanism Based on a Novel Shape Memory Alloy Technology.....	111
Nestor Nava, Marcelo Collado, Francisco Alvarez, Ramiro Cabás, Jose San Juan, Sandro Patti & Jean-Michel Lautier	
Design and Performance of the Telescopic Tubular Mast	127
Mehran Mobrem & Chris Spier	
Development of Variable Reluctance Resolver for Position Feedback.....	141
Gregory Leibovich & Sara Senanian	
FeF ₃ Catalytic Influence on PFPE Lubricants Lifetime under Loaded Conditions	147
Lionel Gaillard, Antoine Mariot, Catalin Fotea & Roland Holzbauer	
Trade Studies for a High Torque Density Planetary Gearbox.....	155
Jeffrey Mobley	
Single Motion Actuated Shape Memory Alloy Coupling.....	161
Alberto Perez, J. Newman & M. Romano	
Development and Testing of a High Compact Stepper Motor Mechanism	167
Jörg Schmidt & Greg Wright	

Cryogenic Temperature Testing of NEA Fuse Wire Mechanism	175
Edwin Vega & Geoff Kaczynski	
Developmental Testing of Electric Thrust Vector Control Systems for Manned Launch Vehicle Applications	181
Lisa Bates & David Young	
Development of High Temperature High Current Contact Technology in Slipring Assemblies for the BepiColombo MPO & MTM Spacecrafts	195
Fabrice Rottmeier, Mikaël Krummen & Mickaël Miler	
Lessons Learned to Avoid Coax Cable Failure in Moving Mechanical Mechanisms.....	211
Sheah Pirnack	
DLR's Dynamic Actuator Modules for Robotic Space Applications	223
Armin Wedler, M. Chalon, K. Landzettel, M. Görner, E. Krämer, R. Gruber, A. Beyer, H-J. Sedlmayr, B. Willberg, W. Bertleff, J. Reill, M. Grebenstein, M. Schedl, A. Albu-Schäffer & G. Hirzinger	
Mars Science Laboratory Rover Integrated Pump Assembly Bellows Jamming Failure	239
Michael Johnson, Joel Johnson, Gajana Birur, Pradeep Bhandari & Paul Karlmann	
Development of the Descent Brake Mechanism for the Mars Science Laboratory	253
David Dowen, Jeff Moser & Jeff Mobley	
Mars Science Laboratory Differential Restraint: The Devil is in the Details.....	263
Elizabeth Jordan	
Mars Science Laboratory's Dust Removal Tool	279
Kiel Davis, Jason Herman, Mike MakSYMuk, Jack Wilson, Philip Chu, Kevin Burke, Louise Jandura & Kyle Brown	
A Zoom Lens for the MSL Mast Cameras: Mechanical Design and Development.....	293
Daniel DiBiase, Jason Bardis & Rius Billing	
Wet Chemistry Automated Sample Processing System (WASP)	311
Juancarlos Soto, James Lasnik & Shane Roark & Luther Beegle	
Refinement of a Low-Shock Separation System.....	329
Chuck Lazansky	
Ares I Linear Mate Umbilical Plate and Collet.....	345
William Manley, Gabor Tamasy & Patrick Maloney	
GMI Spin Mechanism Assembly Design, Development, and Test Results.....	359
Scott Woolaway, Mike Kubitscheck, Barry Berdanier, David Newell, Chris Dayton & Joseph Pellicciotti	
Lessons Learned from the TIRS Instrument Mechanisms Development.....	373
Jason Budinoff, Richard Barclay, James Basl, Konrad Bergandy, Thomas Capon, Bart Drake, Michael Hersh, Chris Hormann, Edwin Lee, Adam Matuszeski, Armani Nerses, Kenneth Pellak, Kermit Pope, Joseph Schepis & Ted Sholar	

Resolution for Fretting Wear Contamination on Cryogenic Mechanism	399
Charles Clark	
Design and Manufacturing Considerations for Shockproof and Corrosion-Immune Superelastic Nickel-Titanium Bearings for a Space Station Application	407
Christopher DellaCorte & Walter Wozniak	
Wear of Steel Ti6Al4V in Vacuum	424
Timothy Krantz & Iqbal Shareef	
Angular Runout Test Setup for High-Precision Ball Bearings	439
Scott Miller, Jonathan Wood & Stuart Loewenthal	
LightSail-1 Solar Sail Design and Qualification	451
Chris Biddy & Tomas Svitek	
A Novel Release Mechanism Employing the Principle of Differential Coefficients of Thermal Expansion.....	465
Clint Apland, David Persons, David Weir & Michael Marley	
A Nichrome Burn Wire Release Mechanism for CubeSats.....	479
Adam Thurn, Steve Huynh, Steve Koss, Paul Oppenheimer & Sam Butcher, Jordan Schlater, Peter Hagan	
Antenna Deployment Mechanism for the Cubesat Xatcobeo. Lessons, Evolution and Final Design....	489
Jose Antonio Vilán Vilán, Miguel López Estévez & Fernando Aguado Agelet	

SYMPOSIUM SCHEDULE

WEDNESDAY, 16 MAY 2012

- 7:30 Wednesday Presenters' Breakfast - San Marino Room, Hilton Pasadena
- 8:00 **CHECK-IN AND REFRESHMENTS** - Skylight Arcade, Hilton Pasadena
- 8:30 **INTRODUCTORY REMARKS** - International Ballroom, Hilton Pasadena
Don Sevilla, Host Chairman, Jet Propulsion Laboratory, Pasadena, CA
Stuart Loewenthal, General Chairman, Lockheed Martin Space Systems, Sunnyvale, CA
Dr. Charles Elachi, Director, Jet Propulsion Laboratory, Pasadena, CA
- 9:00 **SESSION I – ACTUATOR COMPONENTS AND THEIR USE IN DRILLS**
Lionel Gaillard, Session Chair
ESA/ESTeC, Noordwijk, The Netherlands
- Development of Brushed and Brushless DC Motors for use in the ExoMars Drilling and Sampling Mechanism
Robin Phillips, Maxon Motor AG, Sachseln, Switzerland, et al
 - Rotary Percussive Sample Acquisition Tool (SAT): Hardware Development and Testing
Kerry Klein, Jet Propulsion Laboratory, Pasadena, CA, et al
 - Lock & Release Mechanism for the CHOMIK Penetrator Device and its Tribological Properties
Marcin Dobrowolski, Space Research Centre of the Polish Academy of Sciences, Warsaw, Poland, et al
 - Harmonic Drive™ Gear Material Selection and Life Testing
Jeffrey Mobley, Sierra Nevada Corporation, Durham, NC, et al
 - New Supplier – Hardware Duplication – Some Pitfalls
Edwin Joscelyn, Aeroflex, Hauppauge, NY
- 11:30 **LUNCH**
Lunch for AMS Attendees in the California Ballroom, Hilton Pasadena
- 12:30 **SESSION II – HINGES & DAMPERS**
Michael Kubitschek, Session Chair
Ball Aerospace & Technologies Corp., Boulder, CO
- Development of the Vibration Isolation System for the Advanced Resistive Exercise Device
Jason Niebuhr, Apogee Engineering, Colorado Springs, CO; et al
 - Passive Thrust Oscillation Mitigation for the CEV Crew Pallet System
Matthew Sammons, ATK Aerospace Systems, Beltsville, MD; et al
 - The Damper Spring Unit of the Sentinel 1 Solar Array
Frans Doejaaren, Dutch Space B.V., Leiden, The Netherlands; et al
- 2:00 **BREAK**
- 2:15 **SESSION III – DEPLOY, THEN A POTPOURRI OF POSTERS**
Colin Francis, Session Chair
Space Systems/Loral, Palo Alto, CA
- Ultra-low-weight Rotary Actuator for Operation on Mars and Pin Puller Mechanism Based on a Novel Shape Memory Alloy Technology
Nestor Nava, Arquimia Ingenieria, S.L., Leganés, Spain; et al
 - Design and Performance of the Telescopic Tubular Mast
Mehran Mobrem, Astro Aerospace - Northrop Grumman Aerospace Systems, Carpinteria, CA; et al

- Development of Variable Reluctance Resolver for Position Feedback
Gregory Leibovich, Ducommun LaBarge Technologies, Carson, CA; et al
- FeF₃ Catalytic Influence on PFPE Lubricants Lifetime under Loaded Conditions
Lionel Gaillard, European Space Agency, Noordwijk, The Netherlands; et al
- Trade Studies for a High Torque Density Planetary Gearbox
Jeffrey Mobley, Sierra Nevada Corporation, Durham, NC
- Single Motion Actuated Shape Memory Alloy Coupling
Alberto Perez, Naval Postgraduate School, Monterey, CA; et al
- Development and Testing of a High Compact Stepper Motor Mechanism
Jörg Schmidt, Phytron Elektronik GmbH, Grabenzell, Germany; et al
- Cryogenic Temperature Testing of NEA Fuse Wire Mechanism
Edwin Vega, NEA Electronics, Inc., Moorpark, CA; et al

6:00 -10:00 **RECEPTION** - California Ballroom, Hilton Pasadena

Invited component suppliers display current products and provide tutorials. Local high school FIRST Robotics Team demonstrations, and a light buffet meal.

THURSDAY, 17 MAY 2012

7:00 Thursday Presenters' Breakfast - San Marino Room, Hilton Pasadena

8:00 SESSION IV – ROCKETS TO ROBOTS

Brett Kennedy, Session Chair

Jet Propulsion Laboratory, Pasadena, CA

- Developmental Testing of Electric Thrust Vector Control Systems for Manned Launch Vehicle Applications
Lisa Bates, NASA Marshall Space Flight Center, Huntsville, AL; David Young, Raytheon – Jacobs ESTS Group / NASA MSFC, Huntsville, AL
- Development of High Temperature High Current Contact Technology in Slipring Assemblies for the BepiColombo MPO & MTM Spacecrafts
Fabrice Rottmeier, RUAG Space Switzerland, Nyon, Switzerland, et al
- Lessons Learned to Avoid Coax Cable Failure in Moving Mechanical Mechanisms
Sheah Pirnack, Lockheed Martin Space Systems, Denver, CO
- DLR's Dynamic Actuator Modules for Robotic Space Applications
Armin Wedler, German Aerospace Center (DLR), Wessling, Germany; et al

10:00 **BREAK**

10:15 SESSION V – MARS SCIENCE LABORATORY

Ruben Nalbandian, Session Chair

Moog, Inc., Chatsworth, CA

- Mars Science Laboratory Rover Integrated Pump Assembly Bellows Jamming Failure
Michael Johnson, Jet Propulsion Laboratory, Pasadena, CA, et al
- Development of the Descent Brake Mechanism for the Mars Science Laboratory
David Dowen, Sierra Nevada Corp., Louisville, CO; et al
- Mars Science Laboratory Differential Restraint: The Devil is in the Details
Elizabeth Jordan, Jet Propulsion Laboratory, Pasadena, CA
- Mars Science Laboratory's Dust Removal Tool
Kiel Davis, Honeybee Robotics Spacecraft Mechanisms Corp., New York, NY; et al

12:15 **LUNCH**

Lunch for AMS Attendees in the California Ballroom, Hilton Pasadena

1:15 SESSION VI – MORE MSL, INSTRUMENTS & SEPARATION

Doug Packard, Session Chair

NEA Electronics, Inc / Rocketstar Robotics, Inc, Moorpark, CA

- A Zoom Lens for the MSL Mast Cameras: Mechanical Design and Development
Daniel DiBiase, MDA Information Systems, Inc. – Space Division, Pasadena, CA, et al
- Wet Chemistry Automated Sample Processing System (WASP)
Juancarlos Soto, Ball Aerospace & Technologies Corp., Boulder, CO; et al
- Refinement of a Low-Shock Separation System
Chuck Lazansky, Sierra Nevada Corporation, Louisville, CO
- Ares I Linear Mate Umbilical Plate and Collet
William Manley, NASA Kennedy Space Center, FL; et al

3:15 BREAK

3:30 SESSION VII – INSTRUMENTS

Charlie Hodges, Session Chair

Sierra Nevada Corporation, Durham, NC

- GMI Spin Mechanism Assembly Design, Development, and Test Results
Scott Woolaway, Ball Aerospace & Technologies Corp., Boulder, CO; et al
- Lessons Learned from the TIRS Instrument Mechanisms Development
Jason Budinoff, NASA Goddard Space Flight Center, Greenbelt, MD; et al
- Resolution for Fretting Wear Contamination on Cryogenic Mechanism
Charles Clark, Lockheed Martin Space Systems, Palo Alto, CA

6:30-10:00 BANQUET – Pasadena Conference Center

6:30 – 8:30 Social Hour, Dinner and Live Jazz Band

8:30 – 10:00 Entertainment and Show

FRIDAY, 18 MAY 2012

7:00 Friday Presenters' Breakfast - San Marino Room, Hilton Pasadena

8:00 SESSION VIII – TRIBOLOGY/BEARINGS

Terri Taylor, Session Chair

Honeywell International, Glendale, AZ

- Design and Manufacturing Considerations for Shockproof and Corrosion-Immune Superelastic Nickel-Titanium Bearings for a Space Station Application
Christopher DellaCorte, NASA Glenn Research Center, Cleveland, OH; et al
- Wear of Steel Ti6Al4V in Vacuum
Timothy Krantz, NASA Glenn Research Center, Cleveland, OH; et al
- Angular Runout Test Setup for High-Precision Ball Bearings
Scott Miller, Lockheed Martin Space Systems, Palo Alto, CA; et al

9:30 BREAK

9:45 SESSION IX – SMALL SESSION ON SMALL SATELLITES

Scotty Allen, Session Chair

ATK Space Systems, Goleta, CA

- LightSail-1 Solar Sail Design and Qualification
Chris Biddy, Stellar Exploration, San Luis Obispo, CA; et al
- A Novel Release Mechanism Employing the Principle of Differential Coefficients of Thermal Expansion
Clint Apland, Johns Hopkins University / Applied Physics Laboratory, Laurel, MD; et al
- A Nichrome Burn Wire Release Mechanism for CubeSats
Adam Thurn, Naval Research Laboratory, Washington, D.C.; et al
- Antenna Deployment Mechanism for the Cubesat Xatcobeo. Lessons, Evolution and Final Design
Jose Antonio Vilán Vilán, Universidad de Vigo, Vigo, Spain; et al

11:45 SPECIAL PRESENTATION

Development of the Mars Science Laboratory Rover “Curiosity”, from Concept to Launch

12:15 TECHNICAL SESSIONS CONCLUSION

Edward Boesiger, Operations Chairman, Lockheed Martin Space Systems, Sunnyvale, CA

- Herzl Award Presentation
- Closing Remarks

12:30 LUNCH

Lunch for AMS Attendees in the California Ballroom, Hilton Pasadena

1:30 – 4:30 JPL TOUR

1:30 Buses depart hotel for JPL

2:00-4:00 Facility tour at JPL

4:30 Buses return to hotel

SYMPOSIUM ORGANIZING COMMITTEE

**Donald R. Sevilla, Host Chairman, JPL
Louise Jandura, Co-Host Chair, JPL**

**Stuart H. Loewenthal, General Chairman, Lockheed Martin
Edward A. Boesiger, Operations Chairman, Lockheed Martin**

**Steven W. Bauman, NASA GRC
William Caldwell, NASA Ames
Jared Dervan, NASA MSFC
Carlton F. Foster, NASA MSFC (retired)
Clae F. Hakun, NASA GSFC
Christopher P. Hansen, NASA JSC
Wayne Jermstad, NASA JSC
Alan C. Littlefield, NASA KSC
Ronald E. Mancini, NASA Ames (retired)
Fred G. Martwick, NASA ARC
Donald H. McQueen, Jr., NASA MSFC
Gérard Migliorero, ESA/ESTeC
Robert P. Mueller, NASA KSC
Fred B. Oswald, NASA GRC
Minh Phan, NASA GSFC
Joseph P. Schepis, NASA GSFC
Mark F. Turner, NASA ARC
Robin Tutterow, NASA LaRC
James E. Wells, NASA LaRC**

Development of Brushed and Brushless DC Motors for use in the ExoMars Drilling and Sampling Mechanism

Robin Phillips^{*}, Massimo Palladino^{**} and Camille Courtois⁺

Abstract

This paper presents a summary of work performed to qualify two COTS (Commercial Off The Shelf) motor types (one Ø13 mm brushed and one Ø22 mm brushless) for operation in a Martian atmosphere for the ExoMars Drilling and Sampling Mechanism. We present all the major steps in this process, which included an analysis of features that needed changing from the standard industrial motor design, a development program that was undertaken to select an appropriate design, and a qualification campaign that was then applied to the modified motors.

Introduction

Maxon motor is well known for having built all the drive and steering motors for JPL's Mars Pathfinder (Sojourner) and MER (Spirit & Opportunity) rovers where the soundness of the basic design has been demonstrated over the 7+ years that Opportunity has now spent roving on the Martian surface.

Maxon was also selected by ESA to develop motors for its ExoMars rover mission. However, the significant differences in requirements for the Drilling and Sampling mechanism did not allow the selection of the same type of motors as MER used. Specifically, the specified lifetime and power output for the main drill drive motor required the use of a brushless motor since the expected lifetime of a brushed motor was not sufficient for this application. Additionally, space restrictions inside the drill required the use of a smaller brushed motor (Ø13 mm) than had been used in either of the previous JPL missions.

As with the JPL RE25 development, the aim was to adapt industrial standard motors (i.e., a so called "Commercial Off The Shelf" or COTS design) rather than to develop a custom solution in order to lower development costs. The process followed in the development program included three main steps:

1. A detailed analysis of the standard industrial motor design to identify features that were unlikely to work correctly when exposed to the environmental conditions and duty cycles requirements of the ExoMars mission.
2. Research into possible solutions to the identified design problems and then an appropriate redesign of the motors.
3. Manufacture and qualification testing to simulate all relevant aspects of the ExoMars mission on the new design.

Mars Rover Electric Motors Background

Successful operation of electric motors on the Martian surface was initiated by the Viking project which put two landers on Mars in 1976. The Viking landers used numerous motors in the twin cameras (e.g., for rotating the camera housing and moving the scanning mirror) as well as for the sampling boom and communications antenna pointing. That electric motors have a history of causing technical difficulties for

^{*} maxon motor ag, Sachseln, Switzerland

^{**} ESA, ESTEC, Noordwijk, The Netherlands

⁺ RUAG Space, Nyon, Switzerland

Martian applications is revealed by the appearance of the “Surface-sampler boom motor” in the list of “Top Ten Problems” for the Viking development program between Feb 1973 and Sept 1974 (Ezell and Ezell 1984, p. 253).

After Viking there was a long pause until the Mars Pathfinder landed with the small Sojourner rover in 1997 which contained 11 maxon RE16 brushed motors. The Sojourner rover covered about 100 m before the lander communication link failed, thereby ending the mission after nearly 3 months. In covering the 100 m in just under 3 hours of driving time the drive motors rotated approximately 0.5 million times (with another 0.5 million during Earth based testing) with no indication of motor problems (Braun 1998).

Following the success of the Mars Pathfinder mission, two larger and much more capable rovers were flown on the Mars Exploration Rover (MER) missions that landed the rovers Spirit and Opportunity on Mars in 2003. Each rover contained 39 maxon motors for drive and steering functions, solar array deployment, camera mast actuators and the actuators for the science arm joints. Two different motor types were used, a modified RE25 as can be found in maxon’s standard program and a RE20 that was specially developed for the MER program. The success of these missions is well known and as of January 2012 Opportunity was still active and had driven nearly 35 km over the previous 8 years.

For the follow on MSL mission (launched in 2011), due to the increased distances the rover was expected to cover, brushless motors were selected. The development of these motors and associated gearboxes proved much more complex than expected and, as has been well documented in the press, ultimately led to a two year delay in the launch, emphasizing again the complexity involved in specialist motor design.

Selection of Motor Types for the ExoMars Application

The ExoMars program (as originally conceived by ESA) envisaged many motors of numerous types being used for various different functions on the rover, a summary of which is shown in Table 1. For the purposes of the development program being reported on here, the requirements for the Drilling and Sampling mechanism, hereafter “Drill”, were considered. Where possible the RE20 and RE25 brushed motors that were used on the MER missions were used in the original design. However, three applications in the drill required new motor sizes or types. These were the Drill mandrel clamp which has to fit within the diameter of the drill bit (see Figure 1) and hence is limited to Ø13 mm, the main drill drive

Table 1: List of motor applications on the ExoMars rover

Function	Motor type	Quantity on rover	Function	Motor type	Quantity on rover
Wheel Drive	RE 20-25	6	SPDS CSTM	RE 20-25	1
Steering Drive	RE 20-25	6	SPDS BSD	RE 20-25	1
Deployment Drive	RE 20-25	6	SPDS Jaw actuation	EC22	1
Camera Mast Pan Axis	RE 20-25	1	SPDS De-block actuation	RE 20-25	1
Camera Mast Tilt Axis	RE 20-25	1	SPDS Position/Rotary Motion	RE 20-25	1
Drill Positioner Translation	RE 20-25	1	SPDS Dosing Mechanism	RE 20-25	2
Drill Positioner Rotation	RE 20-25	1	SPDS Carousel	RE 20-25	1
Drill Positioner Jettison	RE 20-25	1	Solar Array Deployment	RE 20-25	1
Drill Translation	EC22long	1	Battery Isolation Switch	RE13?	2
Drill Rod Mag Rotation	RE 20-25	1	Life Marker Chip (LMC) Instrument Inlet Valve	EC14fl	4
Drill Rod Mag Clamp	RE 20-25	1	LMC Bellows pump	EC8	4
Drill Rod Lower Clamp	RE 20-25	1	LMC Rotary Valve	RE13	4
Drill Mandrel (main drive)	EC40	1	Mars Organic Molecule Analysis (MOMA) Instrument	RE10	2
Drill Mandrel Clamp	RE13	1			
Drill Tool	RE13	1			
SPDS=Sample Preparation & Distribution System					

motor which due to the required lifetime and power requirements need to be a Ø40-mm brushless motor and the drill translation unit which due to power requirements was best achieved with a Ø22-mm brushless motor.

In order to avoid the motor problems that plagued the MSL development, a program was started to design and qualify both of these two new motor types. This program also had the express goal of making sure that the technology needed for making such motors was available outside of the USA so as to be free of ITAR restrictions. The first stage of this program was to analyze the existing commercial motor designs for features that were unlikely to be compatible with the ExoMars environmental and operating specifications.



Figure 1: The ExoMars drill box breadboard (left) and drill mandrel EM (right)

Specifications Summary

Although much of the specification for the motors is similar to that for a terrestrial application, there are a few key areas that are significantly outside of the normal application regime that a COTS motor would be expected to be designed for, these are summarized in Table 2.

Table 2: Summary of ExoMars specification that is significantly different to an industrial standard application

Non-operating temperature range	-120 °C to 125 °C
Operating temperature range	-55 °C to 30 °C
Operating atmospheric conditions	1 bar, Earth standard 5-10 mbar CO ₂ (Martian atmosphere)
Vibration environment	Sine 100 Hz, 33 g Random 20-2000 Hz, 17.2 g _{rms}
Shock loading	100 Hz: 25 g , 300 Hz: 400 g 2 kHz – 10 kHz: 1500 g

Several features of both motors that were incompatible with these specifications had common solutions, such as modifying the bearing grease to Braycote 601EF for the low temperature pressure environment and changing the wiring to a type compatible with standard ESA wiring specifications. Various materials in the standard motor designs were modified, such as the aluminium housing and front flange of the EC22 which were changed to titanium, in order to avoid problems with differential expansion (aluminium bearing seat to stainless steel bearing race for example) or to reduce the mass. Other features, however, were specific to each motor type and are described in more detail in the next two sections.

Key Problems for Brushed Motors

Derating factor

The RE13 standard motor has a specification sheet defining the maximum mechanical output power (i.e., torque and speed) allowed. The extremes of the continuous operating regime are determined by the maximum allowed winding temperatures (125 °C in the case of the RE13). Normally the winding will cool via a mixture of conduction (via the shaft), convection (via the air surrounding the winding) and radiation. A reduction of atmospheric pressure will cause a corresponding reduction in the convection component of this cooling and hence in the available performance from the motor.

In order to quantify the size of this effect, a simple test was conducted with an RE13 motor in a vacuum chamber. The resultant measured thermal resistances (Table 3) could then be programmed into maxon's standard motor simulation software and new maximum continuous torque calculated. As can be seen from Table 3, the presence of even a small atmosphere causes a dramatic improvement in thermal conductivity.

Table 3: Measured winding to housing thermal resistance and corresponding maximum continuous torques for RE13

Atmospheric pressure (all with Earth standard composition)	Thermal Resistance (Winding->Housing) [K/W]	Maximum continuous torque [mN-m]
1 bar	7	2.39
7±1 mbar	9	1.85
<1x10 ⁻³ mbar	50	0.811

Vibration and Shock Considerations for Brushed Motors

For the RE13 motor, there was concern that during shock and vibrations (mainly from launch and landing) there is no contact between the motor winding and the housing. This is particularly of concern since the RE13 motor winding is a cantilever (Figure 2) and the gap between the winding and housing can in the worst case tolerances be only 170 µm, as shown in (Figure 3).



Figure 2: RE13 rotor showing bell shaped winding attached to shaft

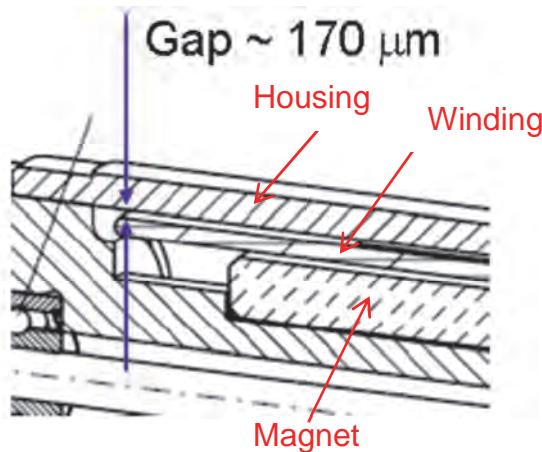


Figure 3: Detail of gap between RE13 winding and housing

Based on a resonance search performed on the rotor by itself (see Figure 4), the winding fundamental frequency and the associated amplification factor were found to be 529 Hz and 3.5 respectively. Considering the random vibration requirement, by using the Miles equation for displacements, the winding displacement is given by:

$$dispRMS = \sqrt{\frac{PSD(fres)Q}{32\pi^3 f^{res}^3}}$$

where f_{res} is the motor winding fundamental frequency, Q is the amplification factor at resonance, PSD(f_{res}) is the specified power spectral density of acceleration at frequency f and $dispRMS$ is the RMS displacement. The motor winding RMS displacement during random vibration was found to be 25 μm with a 3 sigma peak of 75 μm . Therefore, any contact between the motor winding and the housing is excluded, even at 3 sigma (since the gap is no less than 170 μm). A random vibration test was performed on the fully assembled RE13 as part of the qualification testing and no signs of contact between winding and housing were seen after the test.

A shock analysis was performed to assess the behavior of the RE13 motor winding, considering the required shock response spectrum. A half-sine shock of 1500 g amplitude and 0.5 ms was applied. Figure 5 shows that the shock generated (in red) envelopes the required shock response spectrum (in dotted blue).



Figure 4: Test setup for the random vibration test conducted on the RE13 winding

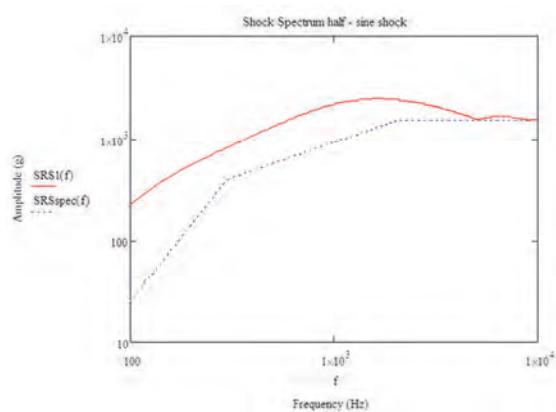


Figure 5: Shock response spectrum applied on the motors

The displacement of the motor winding during shock, evaluated by analysis, is about 1 mm. This shows that the contact is likely. However, the shock will only create a contact between the motor winding and the housing during a very short period of time. This is considered acceptable (the time is short enough to avoid any damage). The shock test performed on the assembled RE13 motor showed that indeed no effects from such contact were observable.

Brush material

Although brushed motors have the advantage of not needing complex commutation electronics, they determine the lifetime of the motors and cause the life to be much lower than for an equivalent brushless motor. Unfortunately the most common brush materials for high current applications used in industrial motors (copper or silver graphite mixtures) require the presence of water vapor and oxygen to build up a hardened patina on the wear surface of the brush. If the water vapor is not present, then extremely rapid wear can occur.

The situation with no water vapor applies on Mars and was noticed during qualification testing for the Viking lander camera scan mirror motors in the mid 1970's (Mutch 1978, p. 17). Twenty years later for the Sojourner rover the problem was circumvented by the use of precious metal brushes without lubrication in otherwise nearly standard RE-16 motors. This is a simple solution for situations where required torques are low and only limited lifetimes are required. Testing for Sojourner showed that under load and start-stop conditions motor failure occurred after about 30-40 million revolutions (Braun 1998) which was more than sufficient for the planned mission.

For the MER mission a more extensive testing program was undertaken to test various different brush materials. Some of the early testing has been described in detail in (D. E. Noon 1999) and (Reid, Braun and Noon 1999), and it consisted of testing motors from various manufacturers with brushes made of mixtures of copper or silver graphite with impregnation with various different lubricants. For the flight models, the RE20 was flown with a copper graphite brush with 8% MoS₂ content (from Le Carbone) whereas the RE25 was flown with silver graphite brushes and 5% MoS₂ content (from Shunk). The success of these rovers (and by implication the motor and brush choice) has been well documented in the general press. Although the motors have not been completely trouble free (e.g., one failed drive motor on Spirit and one drive motor with periodic increased current draw on Opportunity), they have worked well enough to allow, in particular the Opportunity mission to significantly surpass the expected distance covered. The ~35 km driven by Jan 2012 represents ~65 million motor revolutions. This is well within the estimated lifetimes of several hundred million revolutions obtained from testing – although it is worth noting that the testing demonstrated a very large scatter with the (D. Noon 2001) report stating that the life could be as low as 10 million revolutions, which was indeed the case for Spirit's failed motor.

It is clear from the published reports that the selection of the correct brush material is critical to obtaining good lifetimes. Unfortunately explanations as to why significantly different brush mixtures were chosen for the RE20 than for the RE25 motors are not available in the published literature. What has been published shows a wide variation in the performance of similar brush materials with differing motor loads. Given that insufficient understanding of these issues was available either within maxon or ESA, it was decided to undertake a new test program for the RE13 motors.

Table 4: Brush breakage test results showing values (in newtons) where the brushes failed. It is coincidence that types 1-3 have exactly the same mean and standard deviation.

No.	Type 1	Type 2	Type 3	Type 4	Type 5	Type 6	Type 7
Mean	9.5	9.5	9.5	10.8	9.1	7.2	5.9
SD	1.0	1.0	1.0	1.1	0.6	0.8	1.3

For the test, 24 RE13 motors based on type 118626 were used. Differences to the standard motor were the inclusion of Braycote 601EF lubricated bearings, a fiberglass re-enforced winding, an extended length shaft, and the various brush materials to be tested. The brush materials shown in Table 5 were tested, in each case three motors were built

It is of course not only important that the brushes have a long lifetime in use, but that they also are structurally strong enough to withstand launch vibrations and shocks. A simple mechanical strength test was undertaken using a standard maxon procedure that is used to quality control standard brush lots. The brush is attached to a holder through its normal mounting hole, a rod is placed into the brush hook and force applied to pull on the brush arm. The force needed to break the arm off is shown in Table 5 where it can be seen that for the copper-based brushes there is no difference in strength. For silver-based brushes, increasing amounts of MoS₂ weaken the brush. However, the effect is probably not large enough to cause a problem; for comparison the maxon standard material (type 8 in Table 5) is specified to withstand a force of 8 N, other standard materials have specified values as low as 4 N.

The brushes were constructed using the same mold as for the standard RE13, with a contact cross sectional area of 2.4 mm². Standard springs were also used that yield a contact force of 12.5 N·cm⁻² with new brushes (as the brushes wear, the force reduces as the spring uncoils).

The motors for the ExoMars application are required to operate for testing and qualification on Earth in a standard Earth atmosphere as well as for short periods in vacuum while travelling to Mars and of course extended operation on Mars in a 5-10 mbar CO₂ atmosphere. Hence the test program was specified with the segments as shown in Table 6. The motors were to be operated at the maximum working point defined by the specifications of 2.3 mNm load at a rotation speed of 8000 rpm.

Table 5: Brush material types tested. Motor group number is used elsewhere in this report to refer to a particular brush material type. Group 7 with a very high silver content was an attempt to produce a brush that was optimized for vacuum operation.

Motor Group	Brush Material
1	50% Cu 45% C 5% MoS ₂
2	50% Cu 40% C 10% MoS ₂
3	50% Cu 35% C 15% MoS ₂
4	50% Ag 45% C 5% MoS ₂
5	50% Ag 40% C 10% MoS ₂
6	50% Ag 35% C 15% MoS ₂
7	85% Ag 3% C 12% MoS ₂
8	50% Cu 50% C

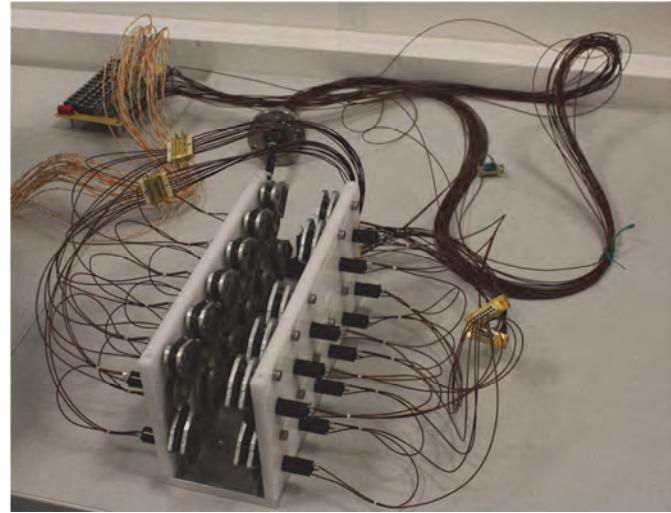
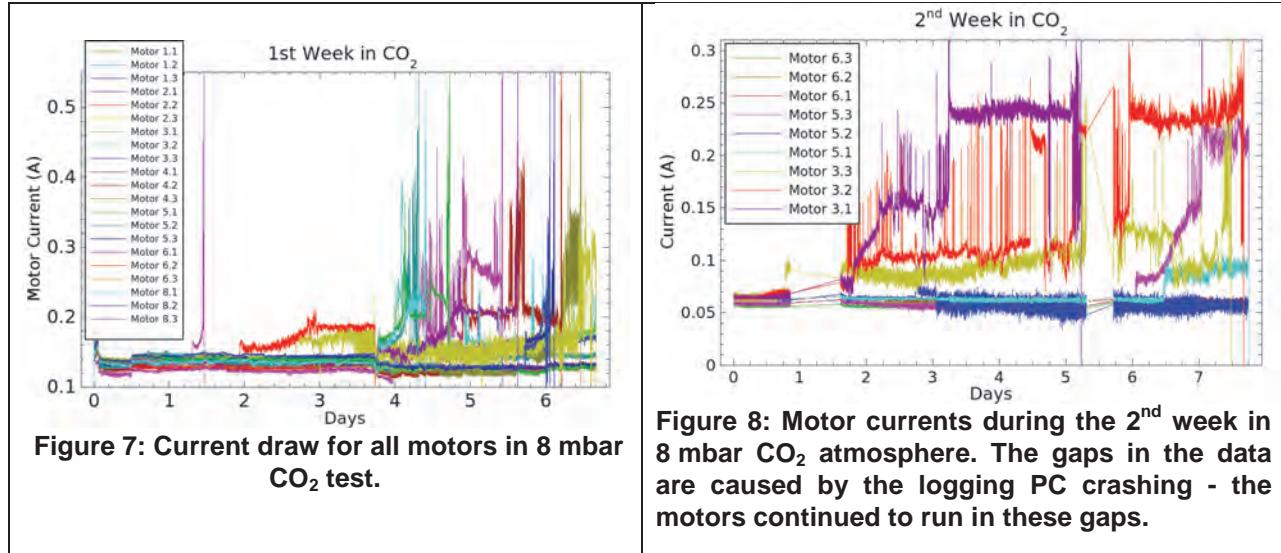


Figure 6: Motor holder setup. The eddy current brake magnets are visible on the inside.

Table 6: The test sequence followed. The motor revolutions column shows the approximate number of revolutions the motors made during each test phase (based on actual number of hours run and the approximate speed settings).

Period	Gas	Pressure	No. of motor revolutions
3 days	78% N ₂ , 21% O ₂ + other traces	~1000mbar	30 million
2 weeks	CO ₂	5-10mbar	165 million
1 week	none	<10 ⁻⁶ mbar	60 million



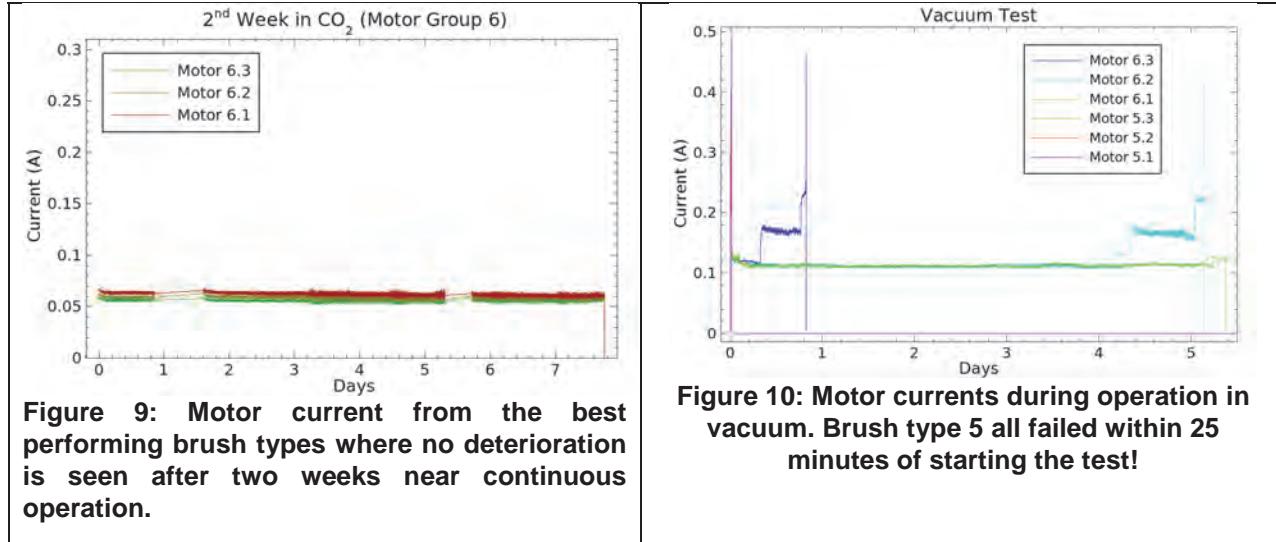


Figure 9: Motor current from the best performing brush types where no deterioration is seen after two weeks near continuous operation.

Figure 10: Motor currents during operation in vacuum. Brush type 5 all failed within 25 minutes of starting the test!

In order to simulate a near worst-case thermal situation, the motors were mounted in a plastic Polyoxymethylene (POM) holder (see Figure 6) so there would be minimal thermal conductivity. Eddy-current brake disks were used to provide the required load. Each motor was individually monitored and its current draw logged.

At the end of each test phase, 2 of the 3 motors with a particular brush type were opened up and pictures of the brushes and collectors taken under a microscope. The 3rd motors of each brush type were not opened so as to retain the worn material inside the motors. The motors that were opened had all loose brush material vacuumed out before re-assembly. Other than vacuuming, no attempt to clean them was made; in particular the collector slots were not cleaned (other than vacuuming).

The initial 2.5-day run under normal Earth atmospheric conditions produced the main result that the group 7 motors all failed within the first 14 hours. Inspection of these brushes showed that the cause of failure was the complete wear of the brushes. Thus these brushes are shown to be unsuitable. The following one week of operation in an 8 mbar CO₂ atmosphere was performed with the motors operating with loads of between 1.65 mN-m and 2.05 mN-m and speeds of between 8500 rpm and 9200 rpm. The differences were caused by a mixture of motor manufacturing tolerances (all motors shared the same power supply) and variations in how the eddy current brakes responded variably to running in a vacuum after being set under atmospheric conditions (brake adjustment after being placed in the vacuum chamber was not possible).

The first week of operation in an 8 mbar CO₂ atmosphere also produced a number of failed motors. The first motor (equipped with maxon standard brushes) failed after 1.5 days followed a few days later by additional motors. By day 6, all group 8 motors (standard brushes), all group 1 motors, all group 2 motors, and 2 of 3 group 4 motors had failed. These were the groups with lower MoS₂ content. Additionally, all group 3 (Cu 15% MoS₂ brushes) showed increase current draw. We therefore decided to interrupt the test and open all failed motors to inspect the brushes.

It immediately became clear upon inspecting the brushes that the motors were failing due to the complete wear of the brushes. As the brushes come to the end of their life, the section in contact with the collectors becomes wider causing several collectors to be in contact with the brush at the same time. This leads to winding segments being short circuited and hence a higher current draw.

One problem that had not been anticipated was that as the motors start to fail they dramatically heat up. In the case of motor 8.2, which had a temperature sensor on it, the housing reached over 180°C (implying

a winding temperature of $>200^{\circ}\text{C}!$). This caused the POM support structure to melt and hence their brake disks to contact the brake magnets. Thus no significance can be attributed to the presence or variation of spikes and other features in the current curves once the motors start to fail.

The major results of this first week of testing are that copper-based brushes do not work as well as silver-based brushes for high load situations like this, and that in both material types more MoS₂ results in slower wear rates.

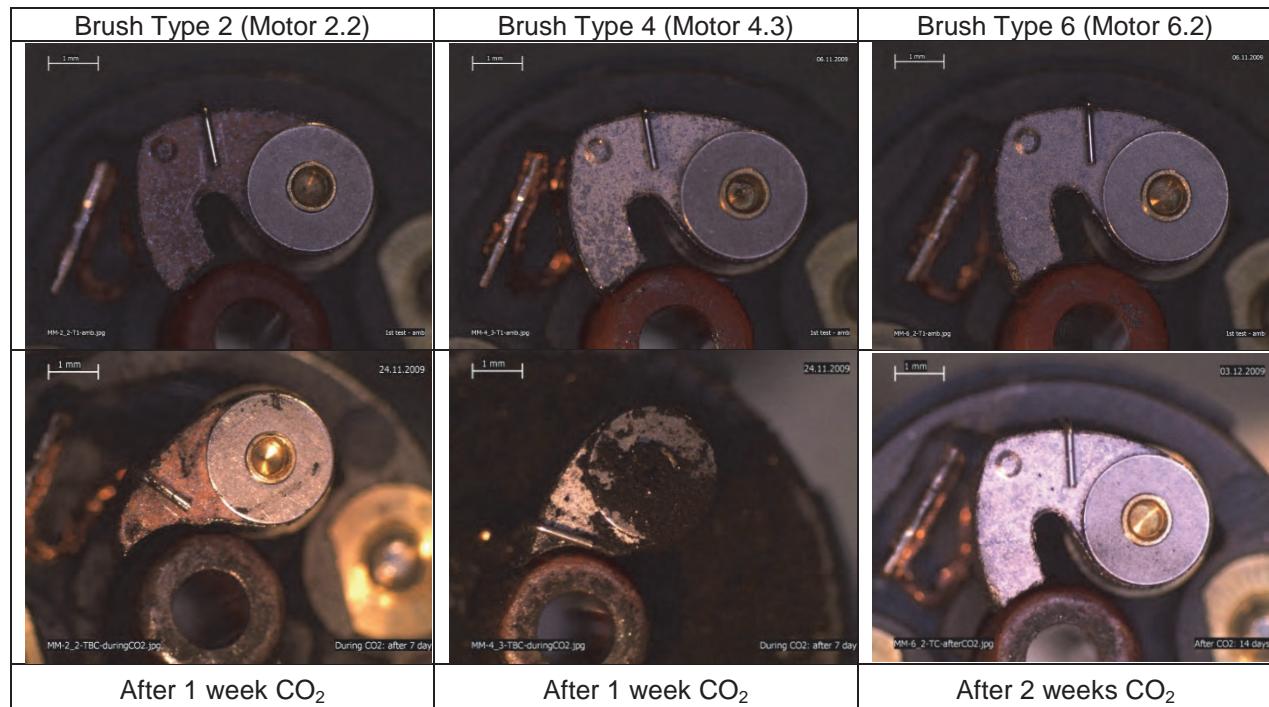


Figure 11: Pictures of the RE13 brushes after 1 week operation in Earth atmospheric conditions (top row) and 1 week operation (2 weeks for type 6) in an 8 mbar CO₂ atmosphere (bottom row).

Since the results from the first week of tests were now understood, we decided to run the second half of the CO₂ test at a lower voltage to test a different working point. The eddy current brakes were set to a value corresponding to a load of 0.65-0.8 mN-m at 8000 rpm. Since the ExoMars specification of 2.3 mN-m includes all possible margins, actual operation would be expected at a lower power setting so it is also important to test at these lower current settings.

The results from the second week of CO₂ testing clearly re-enforce the results of the first week. The silver-based brushes work considerably better than the copper-based brushes and the higher the quantity of MoS₂, the longer the brush lasts. No significant wear is present in group 6 brushes, even after 2 weeks of operation (see Figure 9). It seems likely that some significance can be attributed to the result that both motors 3.3 and 5.3 (i.e. those which were not opened and hence retained the worn brush dust) started to fail before those motors which were opened and cleaned, however the effect is not large.

The results from the vacuum testing were consistent with what was been reported by (D. E. Noon 1999) in that failure is extremely rapid and is caused by brush wear residue accumulating between the collector bars and causing partial shorts. Type 5 motors were already starting to wear out at the end of the CO₂ testing as they were showing increased current draw. Despite this, we were surprised at how fast they failed; after less than half an hour of running in vacuum all three group 5 motors had failed.

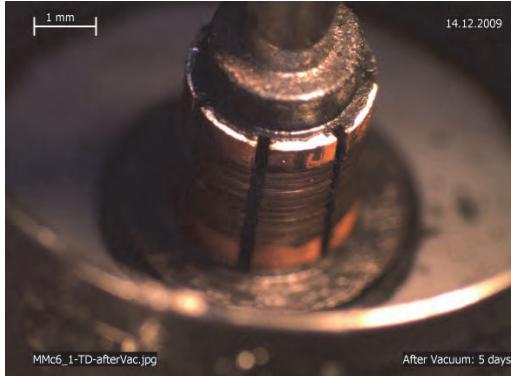


Figure 12: Type 6 collector after the final vacuum test - wear levels are very low, however the collector bars are partly shorted together by material stuck between them.

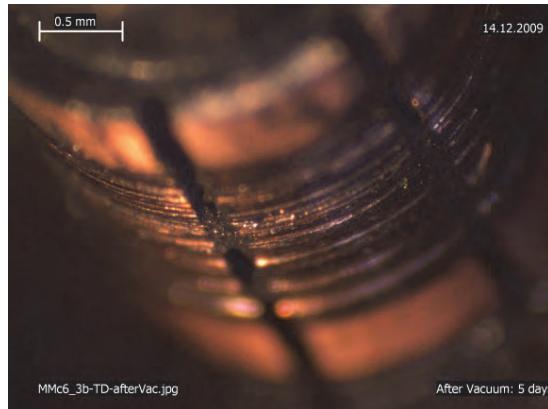


Figure 13: Example from type 5 brush where material can be seen shorting the collector bars.

Key Problems for Brushless Motors

For the BrushLess DC (BLDC) motors, the brush wear problem of course is not present. However, commutation for a BLDC motor needs a feedback device to tell the control electronics when to commutate (sensorless operation using back-EMF rather than a physical feedback device is not suitable for start stop operation or where high loads can be expected on startup). The most common way of performing this feedback is using hall sensors; however these are vulnerable to radiation damage. The ExoMars mission specifies a total dose threshold of 10 krad, defined as the end of life dose deposited under 2 mm of Al-eq solid sphere shielding with a safety factor of 2. In order to provide additional safety margins, the motor is specified with redundant hall sensors, each set being capable of operating the motor alone. Although a number of radiation hard hall sensors are available, these suffer from the major problem that they are US sourced and hence covered by ITAR. Additionally the sensors that we were aware of are all larger than ideal for a Ø22-mm motor. We therefore decided to test several non-US sourced sensors that maxon uses in various motor lines to see if a standard type could be used.

Figure 14 shows the test setup where 3 examples of each type of hall sensor to be tested, mounted on a PCB, were placed in front of a rotating permanent magnet. During the test, the sensors were in continuous operation. The permanent magnets were rotated using standard RE13 and RE25 motors, thereby simultaneously confirming that the radiation caused no problems for the two main types of brushed motors to be used (no effects were expected and none were seen). The radiation dose was delivered over a period of 90 hours at a rate of 0.079 Gy/min, yielding a total dose of 38 krad (Si). The sensors were additionally retested after an annealing period of 100 hours (at 25°C) to confirm no further changes.

Table 7 shows that only the Infineon TLE4945 sensor passed the test with no measurable degradation of the switching level. This result is not unexpected since the Infineon sensor is of bipolar design whereas the others are CMOS which is known to be more sensitive to radiation. Subsequent low temperature testing of the Infineon sensors was undertaken to ensure their operation at -55°C (the manufacturer only rates them to -40°C). With the successful passing of this test, these sensors were selected for design into the EC22 motors.

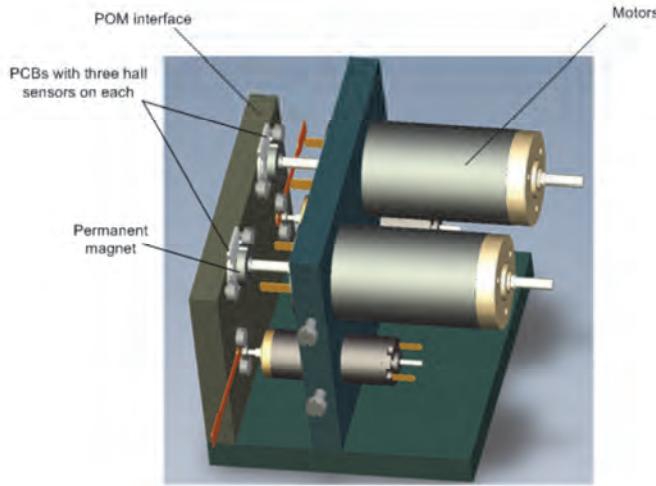


Figure 14: Test setup for hall sensor irradiation with test configuration of 4 PCBs, each with 3 hall sensors of one type, mounted in front of four motors with permanent magnets attached to their output shafts.

Table 7: Results of Hall sensor irradiation

Sensor type	Behavior during irradiation	Switching level after annealing
Melexis US3881LSE	Output voltage started dropping after ~20 krad	2.2 V
Melexis US4881LUC	Output voltage started dropping after ~20 krad	0 V
Infineon TLE4945	No change observed	5 V
Allegro A3230	No change observed	0 V

Qualification Testing

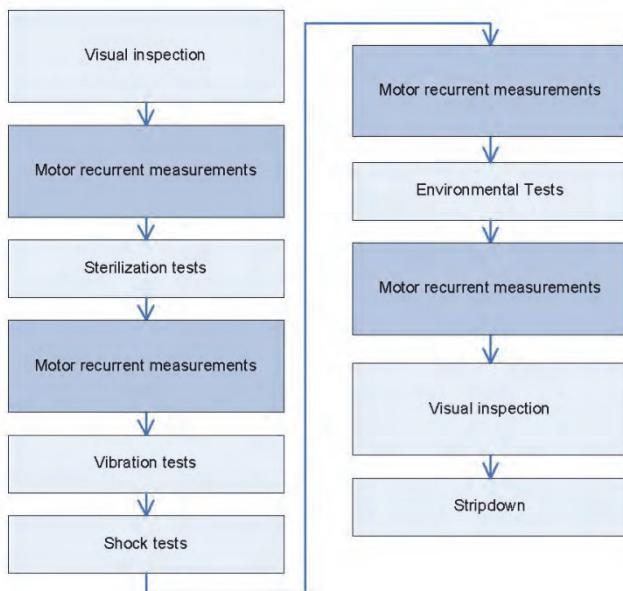


Figure 15: Motor qualification test sequence

In order to qualify the motors for operation on Mars, a test sequence was established to fully test all phases of a motor's life, including ground testing, launch, travel to Mars and of course operation on the Martian surface. The major steps of the test sequence are shown in Figure 15.

Table 8: Shock requirements for ExoMars mission

	Shock Response (Q=10)	
Frequency	Launch from Earth	Landing on Mars
100 Hz	25 g	10 g
300 Hz	400 g	30 g
2,000 Hz	1500 g	30 g
10,000 Hz	1500 g	30 g

The "motor recurrent measurements" shown in Figure 15 was a defined sequence of measurements, including winding resistance, dielectric strength and inductance, housing capacitance and motor torque constant that was repeated after every major test step.

Sterilization tests

The ExoMars program has established a document describing the planetary protection requirements that applies to "all ExoMars spacecraft elements" (Kminek 2007). For the purposes of this qualification, a simple test consisting of 60 hours at 125°C in a dry N₂ atmosphere was considered adequate.

Shock Tests

The requirements for launch and landing shocks are given in Table 8. Only the launch levels were tested as shown in Figure 16.

Vibration Tests

An initial resonance search was performed consisting of a sine sweep with frequency 5-2000 Hz, sweep rate of $2 \text{ oct}/\text{min} \pm 5\%$ with an amplitude of 0.5 g. Next, a sine sweep at the specified rate ($2 \text{ oct}/\text{min} \pm 5\%$) and at the amplitude shown in Table 9 was performed for 2 minutes for each of the three axes. The motors were not operated during this test (reflecting the launch conditions). Finally, a random vibration test was run, also for 2 minutes per axis for all three axes.

Table 9: Vibration parameters for both RE13 and EC22 motor tests

Sine vibration		Random Vibration		
Input Freq.(Hz)	Amplitude	Input Freq. (Hz)	Amplitude	
0-20	15.5 mm peak	20-100	+6 [dB/oct.]	
20-100	27.2 g	100-400	0.45 [g^2/Hz]	
		400-2000	-6 [dB/oct.]	

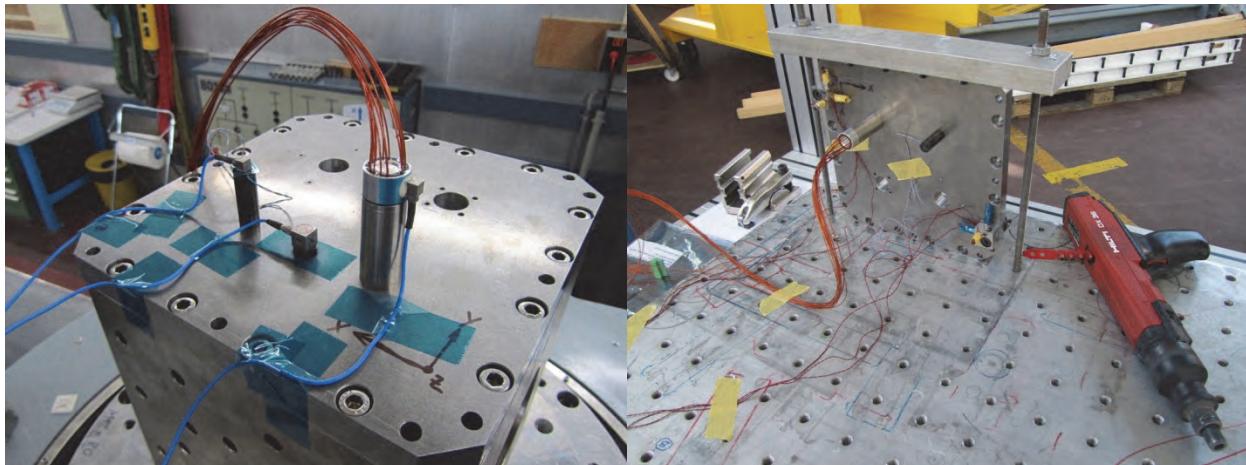


Figure 16: Picture of RE13 & EC22 test motors attached to a stiff mounting cube (note the feedback accelerometers attached to both motors in the left picture) on the shaker (left) and on a plate for the shock test (right). The powder actuated nail gun used to impart the shock gun is visible at the right.

Operating Cycles

The central part of the qualification tests for both motor types were low temperature, 8 mbar CO₂ and vacuum lifetime tests with representative loads were performed as shown in Table 11. In each case, the test setup consisted of a brake motor (whose braking load could be adjusted via a variable resistor across the windings) and the motor being tested as shown in Figure 17. A bearingless torque sensor was used to couple the two motors together and provide a reading of the actual braking force being applied. The speeds and loads used during the lifetime tests were the reference “worst case” loads given in the ExoMars specifications.

Table 10: CVCM per item

Temperature	RE13	EC22
-25°C	0.22 mg	0.57 mg
-50°C	0.37 mg	0.86 mg
-75°C	0.42 mg	0.92 mg

Table 11: Low temperature, CO₂ & vacuum tests

Motor	Test step	Temperature range	Load torque & rpm	No. of cycles	Approx. no. of motor revs.
EC22 RE13	Low temp. cycles	-120°C to +25°C	none	10 non-operating	0
EC22	Operating cycles	-55°C to 40°C	25Nm@12,000rpm	10x as in Figure 19	7.2 million
EC22	Lifetime test (8 mbar CO ₂)		25Nm@12,000rpm	500x as in Figure 19	360 million
EC22	Vacuum test		25Nm@12,000rpm	10x as in Figure 19	7.2 million
RE13	Operating cycles		2.3mNm@8,000rpm	10x as in Figure 19	4.8 million
RE13	Lifetime test (8 mbar CO ₂)		2.3mNm@8,000rpm	150+200 as in Figure 18	22.4 million
RE13	Vacuum test		2.3mNm@8,000rpm	3x as in Figure 19	1.4 million

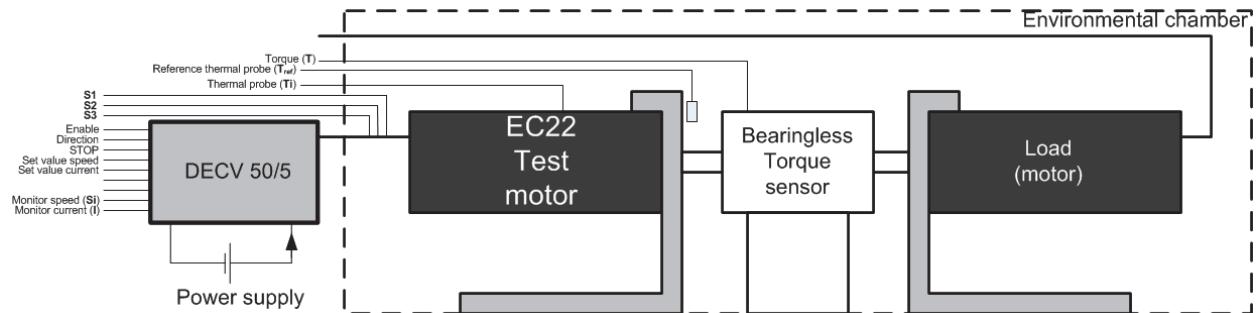


Figure 17: Test configuration for the EC22 (a similar configuration was used for the RE13)

Outgassing performance

To get a good performance from the motors in terms of particulates contamination and outgassing, which is essential for a mission like ExoMars that is searching for traces of life, the motors were baked out at 125°C for five days (the maximum allowable temperature of the windings). Following the qualification tests described above, the motors underwent outgassing tests at the ESA/ESTEC materials laboratory. The tests consisted of raising the temperature from 25°C to 125°C in steps of 25°C every 24 hours in a pressure of 10⁻⁷ mbar. The Collected Volatile Condensable Material (CVCM) and the Total Mass Loss (TML) were measured by using four Quartz Crystal Microbalance (QCM) plates at various temperatures as shown in Table 10.

Particulates emission from the brushes was a major concern for the RE13 motor since these are carbon based so several design features were added to make the exit path for wear particles from the motor as long as possible but to simultaneously ensure the minimum amount of material vents through the bearings during launch. However, the outgassing test results showed that there was negligible emission of particles from the brushes. The overall TML and CVCM levels were found to be very low.

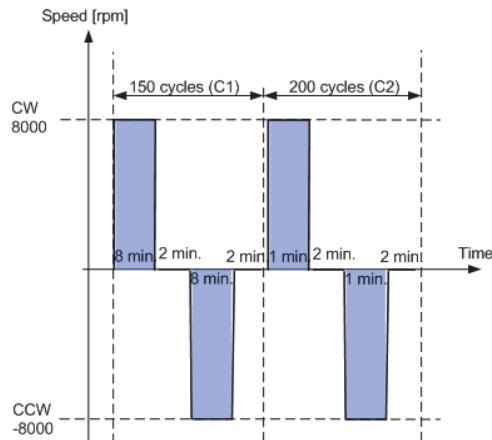


Figure 18: Reference cycle for RE13

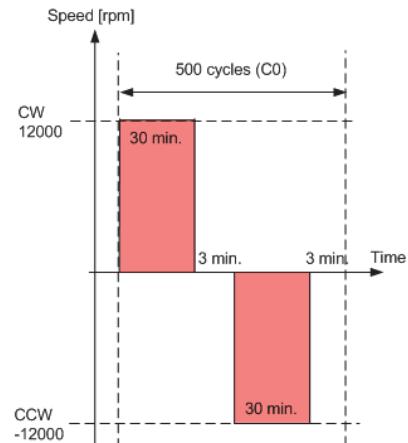


Figure 19: Reference cycle for EC22 (and certain RE13 tests)

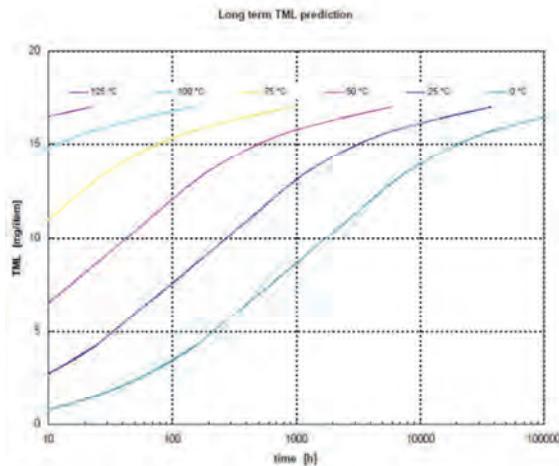


Figure 20: TML for RE13

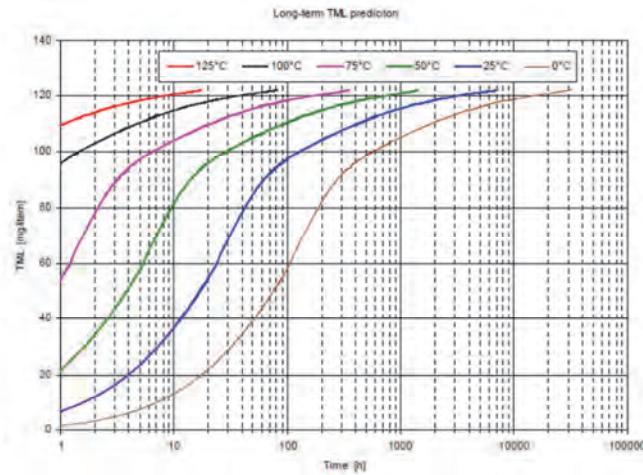


Figure 21: TML for EC22

For the RE13 and the EC22, the TML, measured at 125°C, is 17 mg/item and 122 mg/item, respectively. Figures 20 and 21 show the TML extrapolated to different temperatures to predict more realistic operating scenarios. For the EC22, there was some concern related to an aromatic amine and a plasticizer. The TML and CVCM results showed that the aromatic amine and the plasticizer have been clearly removed by the bake-out. The low TML and CVCM levels measured for the RE13 and EC22 during the outgassing tests have resulted in a discussion within the ExoMars project as to whether the current requirement to encapsulate the motors can be dropped. This would save a significant amount of mass on the ExoMars mission, due to the considerable number of motors involved in the mission.

Qualification Results

Both motors passed the sterilization, vibration and shock tests with no noticeable problems (as determined by the recurrent measurements taken after each test step).

The RE13 performed without problems through the life test in CO₂. However, during the vacuum test, after just 2 cycles (representing just 2 hours operation), increasing current draw was observed and after the 3rd cycle the test was aborted to prevent damaging the motor and destroying any evidence of the cause of the problem. Upon strip down of the motor, it was clear that the cause of the problem was as

had been seen in the previous brush wear tests and was caused by worn brush/collector material sticking between the collector bars and partially shorting the windings. No other major problems were seen during the strip down.

Although the EC22 completed all the life tests, including the vacuum part of the test sequence, two major problems were encountered. Most serious was the failure of two hall sensors after the "operating cycles" test listed in Table 11. In order to allow the sequence to proceed, the rest of the testing (including the main lifetime in CO₂ test) was performed using a sensorless controller (i.e., one that relies on back EMF to commutate). All the remaining hall sensors were still operational at the end of the test sequence. Upon strip down it was also noticed that the rear flange had worked loose (by about 0.5 mm) and had resulted in the partial failure of both bearings (due to extra forces on them since the rotor was no longer perfectly aligned to the stator. It is unlikely that the motor would have run for much longer in this condition.

Planned Future Work

Current work is concentrating on understanding the cause of the rear flange movement (for which a fairly simple mechanical design improvement is expected to provide a solution) and the more complex issue of why the hall sensors failed. So far, considerably more extreme temperature cycling on several additional PCBs has failed to reproduce the problem.

The next stage of the development program, which is expected to be performed during 2012, is to develop motor gearbox combinations using the motors described in this paper as well as the missing types listed in Table 1 that have not yet been qualified. This will also be an opportunity to confirm the effectiveness of the design changes to the EC22 to remove the two identified weaknesses.

Summary

The work presented here has shown that, with appropriate modifications, the COTS motors RE13 and EC22 are capable of standing up to the launch vibration and shock and a landing on Mars and then functioning for the full planned ExoMars mission in the environmental conditions found on Mars.

The necessity of a qualification campaign as described here is made clear by the failures that were encountered in the hall sensors and the weakness in the rear flange design of the EC22. With suitable modifications in these areas, we expect a trouble-free qualification of these motors when attached to the gearboxes for the next stage of development.

Acknowledgements

This work was performed in collaboration between maxon motor, RUAG Space and Selex-Galileo and was funded by an ESA development contract.

References

- Braun, David and Noon, Don. "Long Life" DC brush motor for use on the Mars Surveyor Program. 32nd Aerospace Mechanisms Symposium, 1998.
- Ezell, Edward C., and Linda N. Ezell. *On Mars: Exploration of the Red Planet 1958-1978*. Vols. SP-4212. NASA, 1984.
- Kminek, G. *Planetary Protection Requirements*. ESA Doc. EXM-MS-RS-ESA-00005 Iss.3 Rev.1, 2007.
- Kminek, G. *Planetary Protection Requirements*. ESA Doc. EXM-MS-RS-ESA-00005 Iss.3 Rev.1, 2007.
- Mutch, Thomas A. *The Martian Landscape*. Vols. SP-425. NASA, 1978.
- Noon, Don E. "Motor Brush Testing for Mars and Vacuum" 33^d Aerospace Mechanisms Symposium 1999
- Noon, Don. *Motor Brush Development Testing Results*. Unpublished, 2001.
- Reid, Lisa K., David F. Braun, and Don E. Noon. "Robotic Arm and Rover Actuator Systems for Mars Exploration." *New Perspectives in Mechatronics Systems*. Winterthur, 1999.

Rotary Percussive Sample Acquisition Tool (SAT): Hardware Development and Testing

Kerry Klein*, Mircea Badescu*, Nicolas Haddad*, Lori Shiraishi* and Phillip Walkemeyer*

Abstract

In support of a potential Mars Sample Return mission, an Integrated Mars Sample Acquisition and Handling (IMSAH) architecture has been proposed to provide a means for Rover-based end-to-end sample capture and caching. A key enabling feature of the architecture is the use of a low mass Sample Acquisition Tool (SAT) that is capable of drilling and capturing rock cores directly within a sample tube in order to maintain sample integrity and prevent contamination across the sample chain. As such, this paper will describe the development and testing of a low mass rotary percussive SAT that has been shown to provide a means for core generation, fracture, and capture.

Introduction

As part of a potential Mars Sample Return campaign NASA and the European Space Agency are mutually working on a Mars 2018 Joint Rover Mission to potentially send a rover to Mars in order to perform in-situ investigations as well as collection of Martian samples for a return to Earth upon a subsequent mission. As such, it is foreseen that a key NASA payload contribution is the development of a Sample Acquisition and Caching subsystem capable of acquiring Martian rock cores and soil samples that could be cached within a return canister. Once the samples have been successfully cached within the return canister, the canister would be placed on the Martian surface. A follow-on mission element would then utilize a fetch rover to pick up the return canister and place it within a Mars Ascent Vehicle which would be capable of inserting the canister into a passive orbit around Mars. A third and final element of the campaign would then rendezvous with the return canister and return it to Earth [1], [2], [3].



Figure 1. Integrated sample acquisition and caching prototype subsystem.

In support of the development of the Sample Acquisition and Caching subsystem, the Integrated Mars Sample Acquisition and Handling (IMSAH) architecture was developed in order to advance the key

* Jet Propulsion Laboratory, Pasadena, CA

elements necessary for end-to-end sample generation and containerization. The IMSAH architecture has been presented in depth in previous publications [4], [5], [6], [7], and is characterized by three major sub-elements as shown in Figure 1:

1. Tool Deployment Device (TDD)
2. Sample Acquisition Tool (SAT)
3. Sample Handling Encapsulation and Containerization (SHEC).

The corresponding operational process of the specified hardware as it pertains to the IMSAH architecture is depicted in Figures 2 and 3 and defined by the following operational needs [4] [7]:

- Sample transfer between the coring tool (SAT) and the caching mechanism (SHEC) is to occur by means of bit change-out
- Acquire samples into individual sample tubes in order to preserve sample integrity and minimize the risk associated with handling cores of unknown geometry.
- Utilize a rotary percussion mechanism for the Sample Acquisition Tool in order to reduce subsystem mass and maximize efficiency. The use of a rotary percussive coring tool allows for successful coring at a reduced weight on bit (i.e., lower arm preload), minimizes bit walk due to spindle rotation, and allows for robust hole start when compared with rotary only alternatives.
- The coring tool deployment, alignment, preload, and feed would be performed using a five degree-of-freedom (DOF) robotic arm. By using the specified deployment arm the system has enough DOFs to provide tool alignment and accommodate modest rover slip.

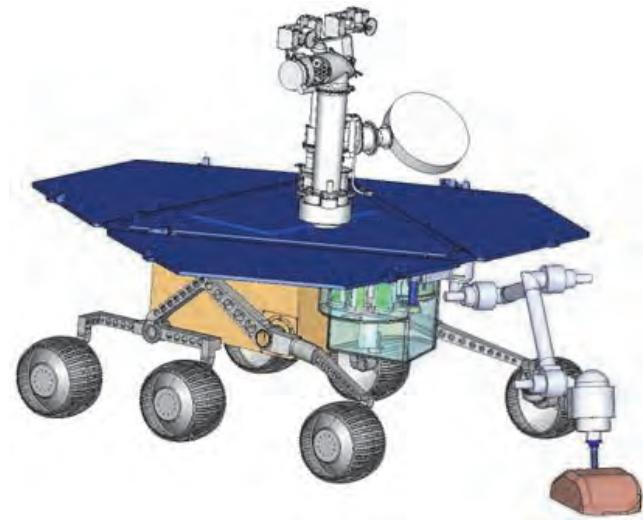


Figure 2. IMSAH coring tool deployment

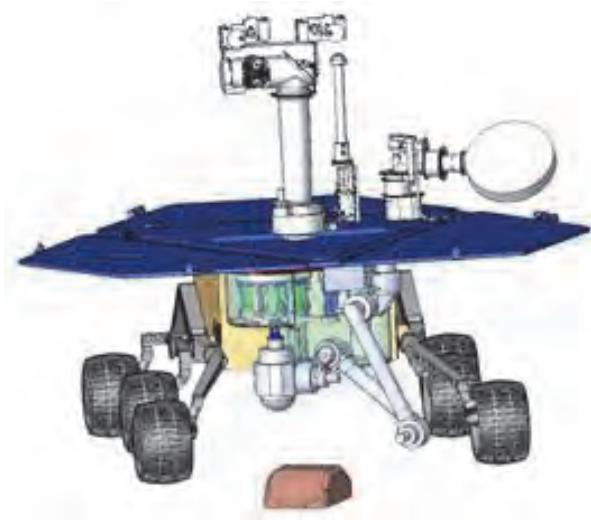


Figure 3. Bit change-out and sample transfer configuration

Of the three IMSAH sub-elements, this paper will focus on the development of the rotary percussive Sample Acquisition Tool (SAT) with an emphasis on the tool's mechanism designs, testing challenges, and lessons learned.

Sample Acquisition Tool Description & Requirements

The proposed IMSAH architecture allows for a less complex tool to be developed than what has previously been investigated or developed as it allows for the use of the TDD for both tool deployment, alignment, preload, and feed. These previous tools required stability tines due to the use of an integral 1-DOF linear feed mechanism which in turn results in the need for greater drilling preload and therefore greater demands on the tool deployment system. Furthermore, the use of the TDD as the linear feed allows for the employment of a sprung linear compliance stage between the turret and the coring tool to provide for both dynamic isolation of linear motion as well as extended linear range of motion during operation under light arm preloads.

In order to satisfy the IMSAH operational needs, as described in the previous section, the SAT was designed to provide for autonomous core generation, core fracture/retention, and bit change-out. The resulting functions necessary to perform these operations have been identified and listed as requirements as follows:

1. Acquire rock cores with approximately 1 cm in diameter by 5 cm in length.
2. Acquire at least 20 rock cores for return.
3. Acquire samples from Kaolinite, Santa Barbara Limestone, Siltstone, Saddleback Basalt, and Volcanic Breccia.
4. Be able to eject a bit that is inadvertently stuck in a rock
5. Be robust to anomalous cores that may be broken in the bit and/or at the bit opening.
6. Account for catastrophic slip conditions where it is presumed the rover experiences a significant shift in position while the SAT tool is in the ground.
7. Cores need to be of appropriate quality and suitable for caching

It is important to note that during the development effort the determination of the tool's performance as it pertains to core quality was a qualitative assessment that binned the generated cores into three categories as described below and represented in Figure 4:

- Good – full length cores or in a few segments
- Acceptable – mostly segments, discs, and/or pucks
- Bad – Powder and/or small chunks, stratigraphy not maintained

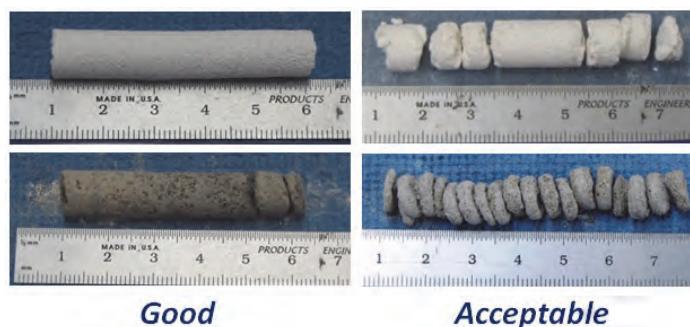


Figure 4. Assessment of core quality based on qualitative parameters.

The subsequent sections will provide detailed information associated with the development and testing of the tool as well as resultant lessons learned. The sections are arranged to give a general overview of the SAT followed by greater detail of the four SAT subassemblies/mechanisms.

Sample Acquisition Tool (SAT) Design & Testing

SAT Assembly Overview

Figure 5 provides a general overview of the completed sampling tool. The developed SAT is a rotary percussive coring tool comprised of four mechanical subassemblies – the Spindle Percussion Assembly (SPA), the Core Breakoff Assembly (CBO), the Magnetic Chuck Assembly (MCA), and the Core Bit Assembly (CBA). The mechanisms are driven by a total of three dc brushless motors mated to gear heads which provide the necessary actuation to complete the critical functions for core generation, fracture, and capture.



Figure 5. Rotary Percussive Sample Acquisition Tool (SAT)



Figure 6. Core Quality Results

In order to validate the tool's unit level functionality a series of verification and validation tests have been performed using a rock test suite that encompasses a variety of rock types that are analogous to Martian rocks (as specified in the requirements) and have been used in the past to qualify Martian surface sampling hardware. The results of the testing have shown the tool can successfully generate, fracture, and capture rock cores within a sample tube for all of the rocks within the test suite while maintaining an appropriate level of core quality, see Figure 6.

SAT General Hardware Development Lessons Learned

Early on in the tool's development it became apparent, as with most R&D efforts, that schedule and resources were going to be severely limited. As such, it was assessed that the tool design should be somewhat modular, and implement mechanisms and corresponding subassembly interfaces such that each mechanism could be tested and operated independently of the others. Doing so provided for several advantages:

- Mechanisms could be developed relatively independently of the others as long as interfaces were maintained and negotiated.
- Mechanisms could be tested at a subassembly level allowing for early performance/capability investigations prior to tool integration.
- Resultant modularity allows for relatively easy assembly/disassembly of tool during anomalous behavior investigations and allows for the isolation of possible suspect mechanism behavior.

Spindle Percussion Assembly (SPA) Design & Development

SPA Overview

Figures 7 and 8 provide an overview of the Spindle Percussion Assembly (SPA) within the SAT. The SPA is a linked spindle/percussion mechanism that provides the rotational DOF necessary to drive the Core Bit Assembly through the spindle drivetrain. In turn, the rotational DOF is translated to axial motion through the use of a cam and lever which drives a striker mass and provides the necessary impact energy to facilitate rock fracture. Since the tool development was intended to be a single point design, a linked spindle percussion mechanism was chosen early in the development life cycle because it allowed for a reduction in the number of required actuators and a lower tool mass.

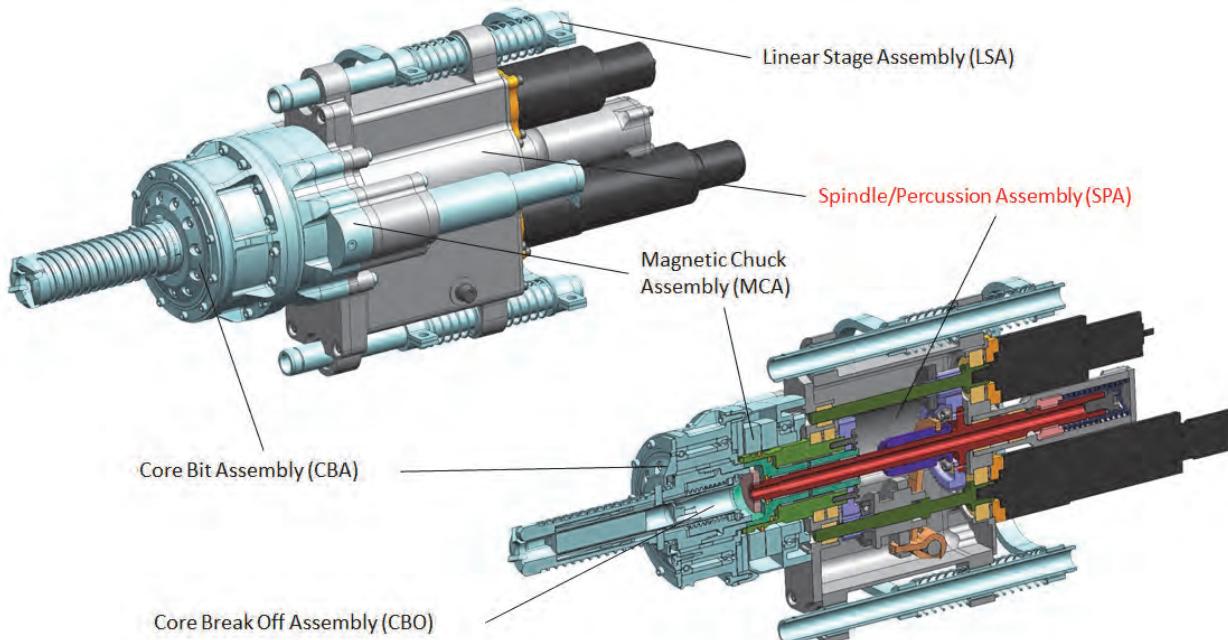


Figure 7. General overview of SPA within the SAT

In order to verify the SPA's ability to generate the necessary impact energy, a standalone test was devised using high-speed video to monitor the striker velocity upon contact with the anvil for a given spindle speed (see Figure 9). Due to the linked spindle/percussion mechanism, the impact energy is presented as a function of spindle speed.

The initial SPA design implemented a striker mass of approximately 51 g based on preliminary percussion development tests. However, due to a design error in the lever stroke length the resultant impact energy was approximately 20% less than the intended design point resulting in the need to increase the striker mass to approximately 61 g. However, during additional testing it also became apparent that the losses downstream of where impact energy was being measured were greater than

initially expected. As resources were not available to fully investigate the system losses, a final striker mass of 121 g (approximately 2x the 61 g striker mass and the largest striker than could be implemented within the assembly constraints) was selected in order to ensure that an appropriate level of margin could be maintained during drill operations in the harder rocks of the proposed test suite.

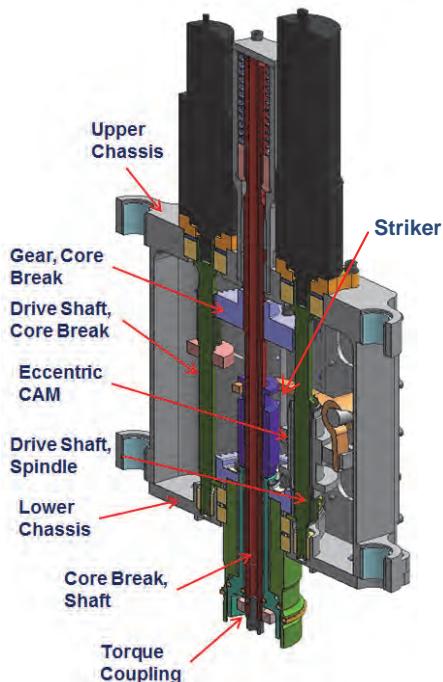


Figure 8. General schematic of SPA



Figure 9. Impact energy at a range of spindle speeds for a variety of striker masses.

SPA Lessons Learned

Several design choices were selected early in the development life cycle because they allowed for either a reduction in the number of actuators or resulted in a lower tool mass. In addition, a fair amount of effort was spent on trying to provide an optimized system in terms of generated impact energy vs. performance. However, in retrospect several noticeable drawbacks cropped up by pursuing these routes:

- Linked mechanisms provide for reduced flexibility in terms of which “knobs” can be turned when investigating tool performance and capability. If the required mechanism capability is clearly defined (i.e., flight like requirements are already known) this may be less of an issue. However, during early development efforts this is not necessarily the case and can actually limit one’s ability to investigate anomalous behavior due to either ill-defined requirements or test parameters.
- Due to the overall complexity of the mechanism, trying to provide an optimized system is very challenging especially due to the number of variables that can affect performance. During early development efforts greater emphasis should be placed on ensuring a high degree of capability rather than optimization as the tool will be utilized extensively to derive “flight” capability requirements. The optimization could then more successfully be implemented during the flight development effort. This is especially true for sampling mechanisms.

Magnetic Chuck Assembly (MCA) Design & Testing

MCA Overview

Figures 10 and 11 provide an overview of the Magnetic Chuck Assembly (MCA). The main design driver for the MCA was associated with the desire to allow for a passive breakaway of the Core Bit Assembly under a rover slip condition during drilling. The implementation of a passive release also required that a low-profile separation interface be maintained to prevent an off-nominal loading condition in the event of a hardware hangup or snag occurring during interface separation. As such, the MCA design utilizes two permanent magnets (one fixed and one with a rotational degree of freedom) to create a magnetic interface that can be turned on (engaged) or turned off (disengaged) while maintaining a very low-profile separation interface.

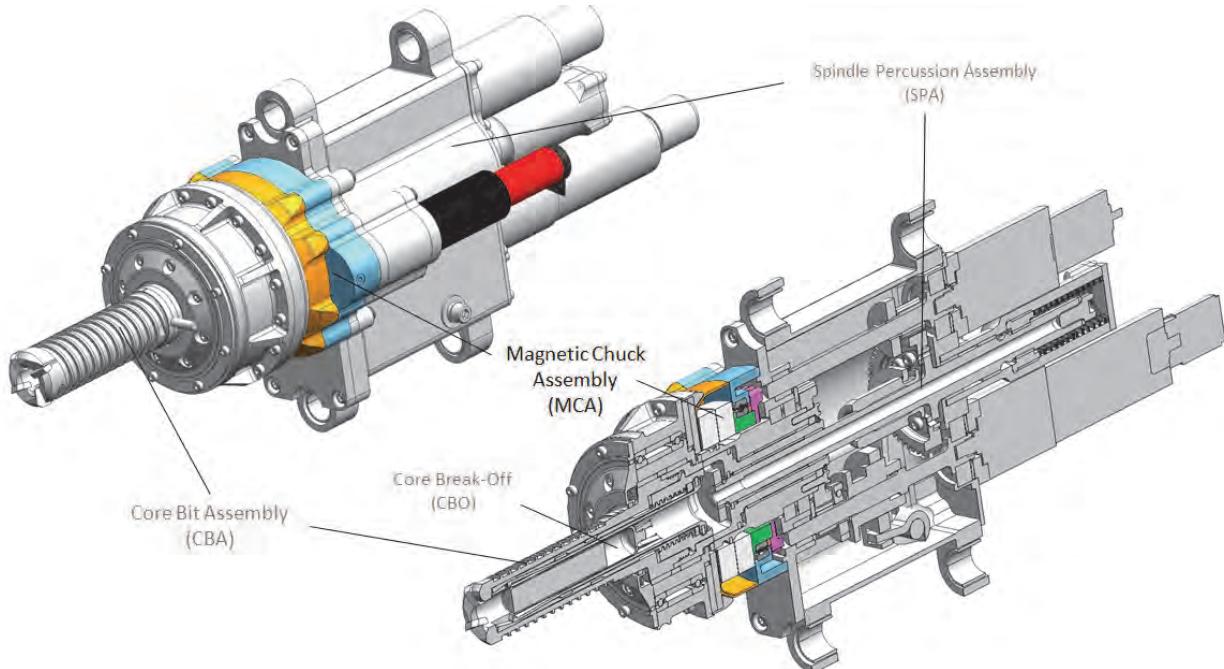


Figure 10. General overview of MCA within SAT

Upon testing, the MCA was shown to function as intended and the bit could be passively released under a given separation load of 100 N at the bit tip. In order to utilize the magnetic chuck approach, several compromises were required in terms of material selection. In order to prevent unwanted interactions between the MCA and adjacent mechanisms, several torque coupling interfaces and drive shafts were machined from non-magnetic A286 which could not be hardened as much as desired. In anticipation of the accelerated wear that would occur on these compromised interfaces, additional material was provided to allow for increased torque coupling wear during operation while preserving the tool's functional lifetime. As expected, accelerated wear was noticed during testing at the specified torque coupling interfaces (see Figure 12).

MCA Lessons Learned

In order to employ a new and novel approach for bit retention it became apparent that several common mechanism design issues would need to be considered:

- More often than not some type of compromise (e.g. accelerated wear of low hardness materials at torque interfaces due to material selection constraints) often results that may not present itself until the hardware is well into its verification and validation testing. As such, recognizing this

compromise early in the design processes may allow for a better anticipation of the actual hardware performance and possible mitigation paths.

- This also clearly highlights the need to address hardware durability early in the design lifecycle as well as providing a means for graceful degradation.

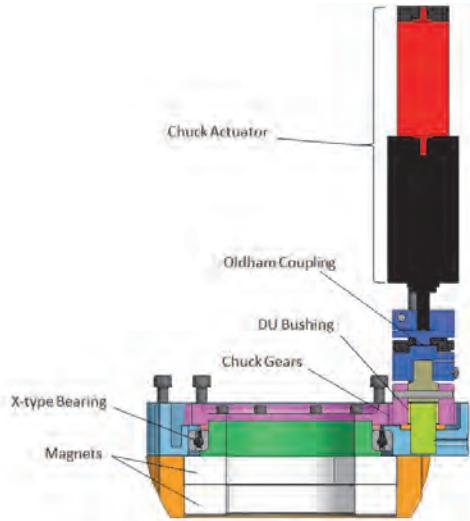


Figure 11. General schematic of MCA



Figure 12. Accelerated wear at torque couplings

Core Bit Assembly (CBA) Design & Testing

CBA Overview

Figures 13 and 14 provide an overview of the Core Bit Assembly (CBA). The CBA is used to provide the mechanical constraints for the Core Break-Off Mechanism and to accept the impact energy and the rotational input from the Spindle Percussion Assembly. The main component of the CBA is the custom drill bit which is supported by a duplex bearing pair and is free to translate axially within a sleeved bushing to allow maximum transmission of the applied impact energy to the rock. The drill bit is based on a COTS coring bit tooth configuration with two external helical flutes for cuttings removal.

Due to the choice of implementing a magnetic chuck, a large overall chuck interface was required for the CBA. This in turn resulted in a large bit housing which inadvertently reduced the tool's capability to accommodate large surface irregularities in the rock as well drilling full-depth holes at off-normal angles (see Figure 15). Furthermore, the large diameter has downstream impacts to the overall IMSAH architecture volume and mass as the SHEC houses the spare bits.

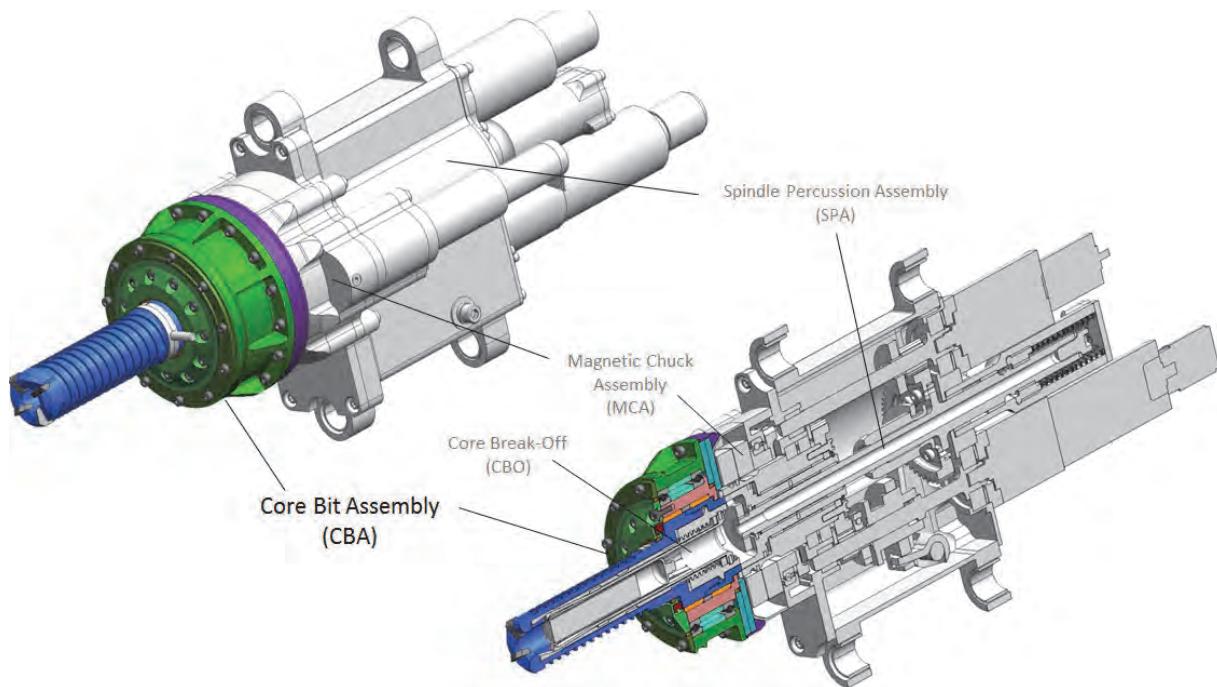


Figure 13. General overview of CBA within SAT

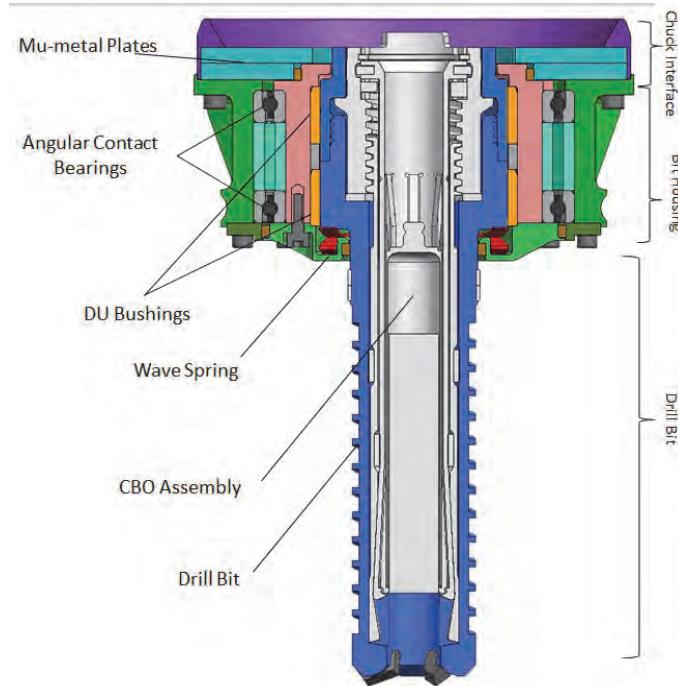


Figure 14. General schematic of the CBA



Figure 15. Tool cannot accommodate large surface irregularities or drilling at off-normal angles due to minimal clearance between bit housing and rock.

During the tool development it was presumed that the amount of rock that needs to be removed as well as bit tooth wear play a significant factor in the tool's rate of penetration performance. Since the ID of the bit is based on a desired core size of 9.9 mm (0.39 inch), the amount of material that is removed during drilling (and the corresponding bit face surface area) is driven by the coring bits outer diameter. Furthermore, because the coring bit houses the Core Break-Off mechanism understanding the tool's sensitivity to bit diameter would be useful for follow on development efforts. Although resources were not available to fully investigate the sensitivity of the tool to bit diameter, two bounding cases were developed:

1. Min Bit OD – 22.6 mm (0.89 inch)
2. Max Bit OD – 24.4 mm (0.96 inch)

It is clear from the test data shown in Table 1 that there appears to in fact be a significant improvement in rate of penetration even with a minor reduction in the bit face surface area of only 16%. For the purpose of this investigation relatively unworn bits were used during the rate of penetration investigation in order to limit the amount of test variables.

Table 1. Rate of penetration of coring tool utilizing 121g striker at 500 rpm

	Avg Drilling Rate [mm/min]	
	22.6 mm (0.96") Bit	24.4 mm (0.89") Bit
Limestone	26.2	59.6
Kaolinite	49.3	162
Siltstone	6.3	27.9
Saddleback Basalt	2.4	7.9
Volcanic Breccia	1.3	2.7

CBA Lessons Learned

During the CBA design effort, the modularity of the tool's sub-elements allowed for a relatively independent development from its mating hardware; however, it also resulted in a failure to check the implications of an increase of the mating chuck interface at the tool's assembly level resulting in a significant reduction in capability to drill holes that are off normal from the rock surface.

- As such, remember the big picture – resultant interface growth that is satisfied at the mechanism level, i.e. black box interfaces to black box as intended, might still allow proper mechanism function, but upset higher level functionality

In addition, it was recognized that since this was an early development effort with a low maturity level, a significant portion of the verification and validation effort should focus on understanding the tool's performance and capability sensitivity as it relates to bit diameter.

- Therefore, during early development efforts with hardware that has a low maturity level, significant emphasis should be placed on the desire to understand the hardware's performance sensitivity to varying requirements, especially if the results may be used as inputs on subsequent higher fidelity tools.

Core Break-Off (CBO) Mechanism Design & Testing

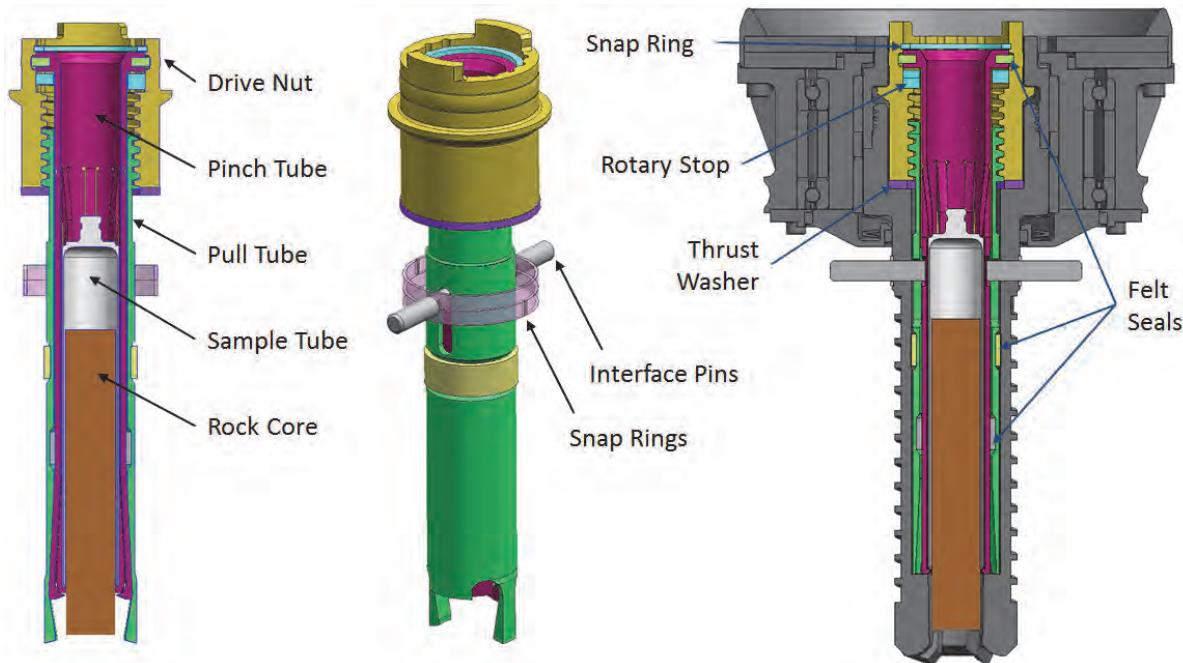


Figure 16. General schematic of CBO

CBO Overview

Figure 17 provides an overview of the Core Break-Off (CBO) Mechanism. The core break-off device is a pinching/cleaving mechanism that uses two opposing 45° wedges that are symmetrically split about the cleaving plane. The mechanism is actuated through the CBO drivetrain located within the SPA and is designed to fracture cores that range in diameter from 9 mm to 10 mm.

As alluded to above, the need to fracture the generated core close to the parent rock required the CBO to be nested within the ID of the drill bit. As such, during nominal drilling operations the CBO is disengaged from the CBO drivetrain in order to allow for unobstructed operation of the Core Bit Assembly. Once the desired core is generated, the CBO drivetrain interfaces to the CBO mechanism thru a novel axially compliant lead screw that translates axially to interface with the CBO torque interface as well as provide the rotational input to fracture the core. During testing, the CBO was able to fracture all generated cores as intended.

However, a significant problem did present itself during testing. In addition to providing a means for core fracture and capture, the CBO also provides a method for retaining the sample tube within the pinch tube by way of flexure retention fingers. During testing, these retention features began to fail at high stress concentration regions located at the base of the flexures. This failure method was initially missed during the design phase as the flexures were only analyzed under a low static load which showed significant margin. However, this load case did not appropriately account for the repeated cyclical loading generated by the SPA and the resultant failure of the flexure by fatigue.

CBO Lessons Learned

As previously mentioned, due to the vibratory environment generated by the percussive mechanism several retention features ended up failing to retain the sample tube. Therefore:

- In a vibratory environment, stress concentration regions should be analyzed for fatigue failure even if the resultant cyclical load is small and static results show high margin.

Conclusion

In support of the development of the Integrated Mars Sample Acquisition and Handling (IMSAH) architecture, a low-mass Sample Acquisition Tool (SAT) has been developed. As with most R&D efforts, the project's schedule and resources were limited so a modular approach to the tool's development was implemented such that individual subassemblies/mechanisms could be independently developed and tested from the others prior to integration. In addition, these same schedule constraints resulted in early design choices that limited the tool's flexibility to investigate some anomalous behavior due to several linked mechanisms as well as a premature attempt at performance optimization. As such, during early development efforts with low maturity levels, it became readily apparent that greater emphasis should be placed on the desire to understand the hardware's performance sensitivity to varying requirements. In doing so, more useful feedback can be provided to allow for better informed decisions on subsequent higher fidelity developments efforts. With that said, the developed SAT has demonstrated the necessary capability to autonomously generate, fracture, and capture rocks cores as necessitated by the proposed sampling architecture.

Acknowledgements

The research described in this publication was carried out at the Jet Propulsion Laboratory of California Institute of Technology under contract from the National Aeronautics and Space Administration (NASA).

References

- [1] R. Mattingly, S. Matousek, and F. Jordan, "Continuing Evolution of Mars Sample Return," IEEE Aerospace Conference, paper #1238, March 2004
- [2] R. Mattingly and L. May, "Mars Sample Return as a Campaign", IEEE Aerospace Conference, paper #1805, March 2011
- [3] P. Backes, J. Aldrich, D. Zarzhitsky, K. Klein, and P. Younse "Demonstration of Autonomous Coring and Caching for a Mars Sample Return Campaign Concept", IEEE Aerospace Conference, March 2012
- [4] P. Backes, R. Lindemann, C. Collins, and P. Younse, "An Integrated Coring and Caching Concept," IEEE Aerospace Conference, paper #1675, March 2010
- [5] P. Younse, C. Collins, and P. Backes, "A Sample Handling, Encapsulation, and Containerization Subsystem Concept for Mars Sample Caching Mission," International Planetary Probe Workshop (IPPW-7), June 2010
- [6] N. Hudson, P. Backes, M. DiCicco, and M. Bajracharya, "Estimation and Control for Autonomous Coring from a Rover Manipulator," IEEE Aerospace Conference, March 2010
- [7] P. Backes, P. Younse, M. DiCicco, N. Hudson, C. Collins, A. Allwood, R. Paolini, C. Male, J. Ma, A. Steele, P. Conrad, "Experimental Results of Rover-Based Coring and Caching," IEEE Aerospace Conference, March 2011
- [8] H. Price, K. Cramer, S. Doudrick, W. Lee, J. Matijevic, S. Weinstein, T. Lam-Trong, O. Marsal, and R. Mitcheltree, "Mars Sample Return Spacecraft Systems Architecture," IEEE Aerospace Conference, March 2000
- [9] A. Okon, "Mars Science Laboratory Drill, "40th Aerospace Mechanisms Symposium, Cocoa Beach Florida, May 2010

Lock & Release Mechanism for the CHOMIK Penetrating Device and its Tribological Properties

Marcin Dobrowolski* and Jerzy Grygorczuk*

Abstract

A unique geological low velocity penetrator CHOMIK for the Russian Phobos Sample Return mission has been developed at Space Research Centre PAS (SRC PAS). One of the most important goals of the mission is to collect a soil sample from Phobos and deliver it to the Earth. The sample will be collected from the surface layers of the Mars' satellite by the penetrator and deposited in a container that is going to land in 2014 in Kazakhstan, encased in the Russian re-entry capsule. Apart from sampling, CHOMIK will perform thermal and mechanical measurements of Phobos' regolith. The penetrator itself is an improved version of the MUPUS instrument for the ESA's Rosetta mission. A new lock and release (L&R) mechanism for the instrument has been developed to meet the Phobos lander requirements. The penetrator is held in place by a multi-arms mechanism and released using Dyneema string melting system. This actuation method provides reliable operation with negligible shock and no special handling requirements.

Introduction

The Space Research Centre PAS has been involved in the development of low-speed, hammer-driven penetrators since 1996. It was strictly involved with the MUPUS project for the Rosetta mission to the 67P/Churyumov–Gerasimenko comet. Rosetta spacecraft was launched in March 2004 and will reach the comet in 2014. Recently, in 2010 SRC was invited to take part in the Phobos Sample Return mission and develop a penetration system capable of collecting a sample of the Mars' satellite soil. Such a device has been delivered to Russia in April 2011 and the Phobos-Grunt spacecraft has been launched in November 2011.

One of the most important parts of the hammer-driven penetrator is its insertion device, which constitutes about 90% of the mass allocated for the whole penetrator. The insertion device consists of free suspended elements in one degree of freedom; e.g., hammer or counter-mass that is accelerated in opposite directions during operation in microgravity environment (law of conservation of momentum). The launch of the rocket and landing operations are dangerous for a delicate counter-mass suspension and, therefore, it was locked in the stowed configuration by a specially dedicated L&R mechanism. Such a unit has to hold the device steadily and to move the penetrator head in a predicted direction after release. The operating conditions of the system are about -160°C for MUPUS and about -100°C for CHOMIK in high vacuum environment. For a long time, from launch to landing which might take up to ten years, all components have to keep stable parameters of work. L&R mechanism is an extra element of the penetrator so it needs to minimize its mass and power consumption. Based on the abovementioned requirements, a method of holding and releasing of the penetrators was developed based on the Dyneema string melting system.

The Dyneema fiber (SK65) is a multi-filament fiber produced from UHMW-PE with the following main characteristics: high strength, low density, low elongation at break and negative coefficient of expansion during heating up. Table 1 shows main Dyneema fiber properties compared to steel.

* Space Research Centre of the Polish Academy of Sciences, Warsaw, Poland

For long duration exposure, Dyneema fiber can be used from cryogenic conditions up to a temperature of 70°C. A not very high melting temperature (~150°C) of the fiber makes it possible to cut the Dyneema string using a heating element operated by a small amount of electric power. Preliminary investigations have shown that good results can be achieved using a small resistor as a heating element and a 60° string angle of contact. Tests have shown that Dyneema string shrinks during the warming up process providing better contact to the resistor. The actuation time depends mainly on the local temperature. High reliability and repeatability ratio was observed in the presented actuation method.

Table 1. Comparison of the Dyneema fiber and steel selected properties

Material	Density kg/m ³	Tensile strength GPa	Young's modulus GPa	Elongation at break %	Melting temperature °C
DYNEEMA®SK65	970	3	95	3.6	149
Steel 316L	8000	0.6	200	45	1370

The general rule in our designs is using Dyneema string only as an actuator element not as a main holder element. For a string of 0.5-mm diameter, the tensile load capability is about 350 N but we reduce the cord's intensity of stress using leverage to eliminate the necessity of using very tough heating elements. A simple way of putting into use the listed principles is shown on the Figure 1 in MUPUS lock and release mechanism pictorial drawing.

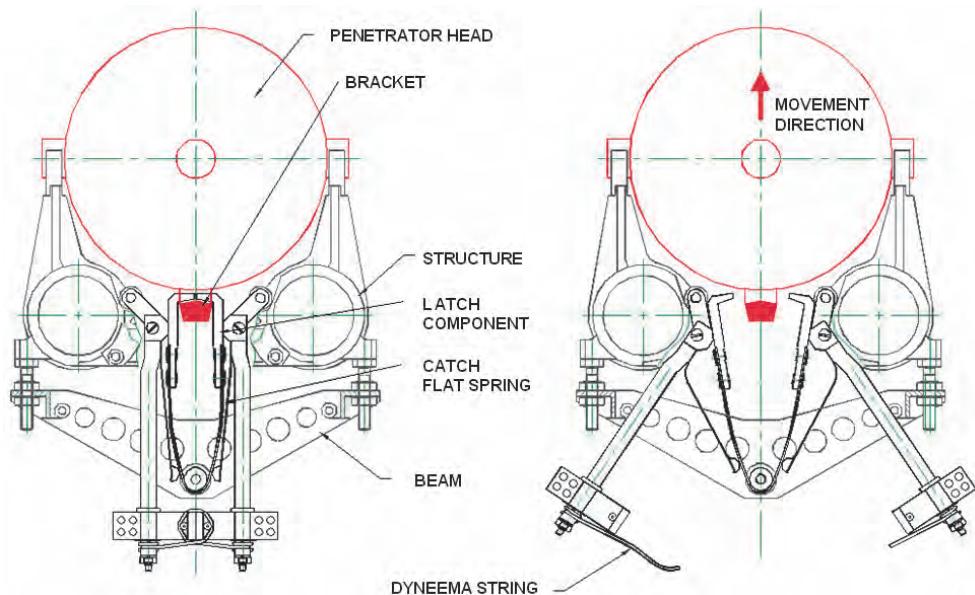


Figure 1. MUPUS penetrator head lock & release mechanism principle of operation

The MUPUS penetrator head, being a part of the counter-mass, has three cylindrical appendages that are placed in three bearings of the structure. The bearings are crossed to provide a zero degrees of freedom grip. When stowed, the penetrator head is held by the clamping of the latch component into its bracket. The proper tension between the cylindrical appendages and bearings is provided by an elastic flat spring and adjusting the gap between beam and structure. Melting of the Dyneema string releases the opening of the latch component and the unlocked bracket allows the motion of the penetrator head in the deployment direction, as it is indicated in Figure 1 by the red arrow.

CHOMIK lock & release mechanism description

CHOMIK L&R mechanism is modified and improved compared to MUPUS'. First of all, it has been designed for different dynamic loads during launch, able to withstand 10g of vibration acceleration and 40g shocks. Such loads result in a relatively high penetrator holding force, which in this case was about 400N. General requirements also influenced the instrument structure that has to contain electronics boards, penetrator guide, and the lock and release unit as a compatible part. The movement direction of the penetrator head after releasing also underwent changes. In MUPUS, the penetrator head has to retreat from the locked elements. In CHOMIK, the penetrator head has to operate inside its holding elements. The instruments with the penetrator head's movement directions pointed out and their lock & release mechanisms are shown in Figure 2 and Figure 3.

The selection of the melting elements determined the parameters of Dyneema string: 0.5-mm diameter with 10-15 N tension force safe loading. Such a system required 1:40 leverage to withstand the penetrator's head holding force. Figure 4 illustrates a kinematic diagram of the developed symmetric multi-arms system. The penetrator holding force is transmitted through the crank arms to a slider by the binary links. An angular shaped slider has a sliding joint with a possible displacement of 18 mm. It is blocked by the holders in the stowed position. During release, initially connected by Dyneema string, holders rotate, setting the slider free. The slider's linear movement cause the crank arms' rotation. Three pairs of adjustable holding pins separate from the penetrator's sockets creating 10-mm gaps between the lock and the penetrator.

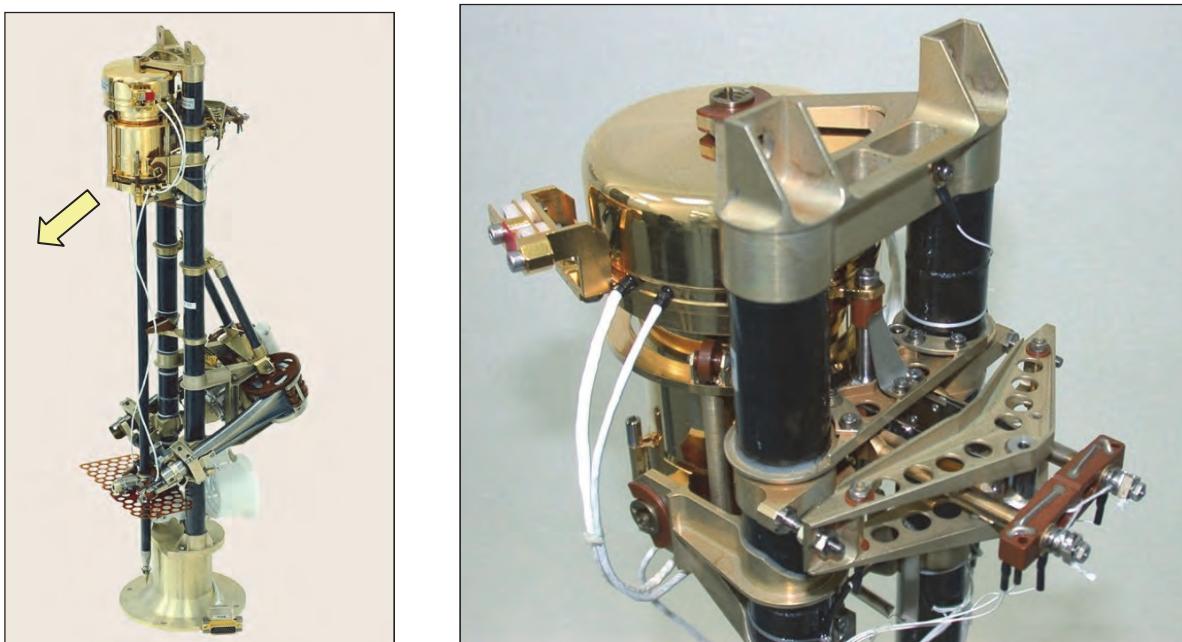


Figure 2. MUPUS penetrator with deployment system (left) and its lock and release mechanism in the stowed position (right)

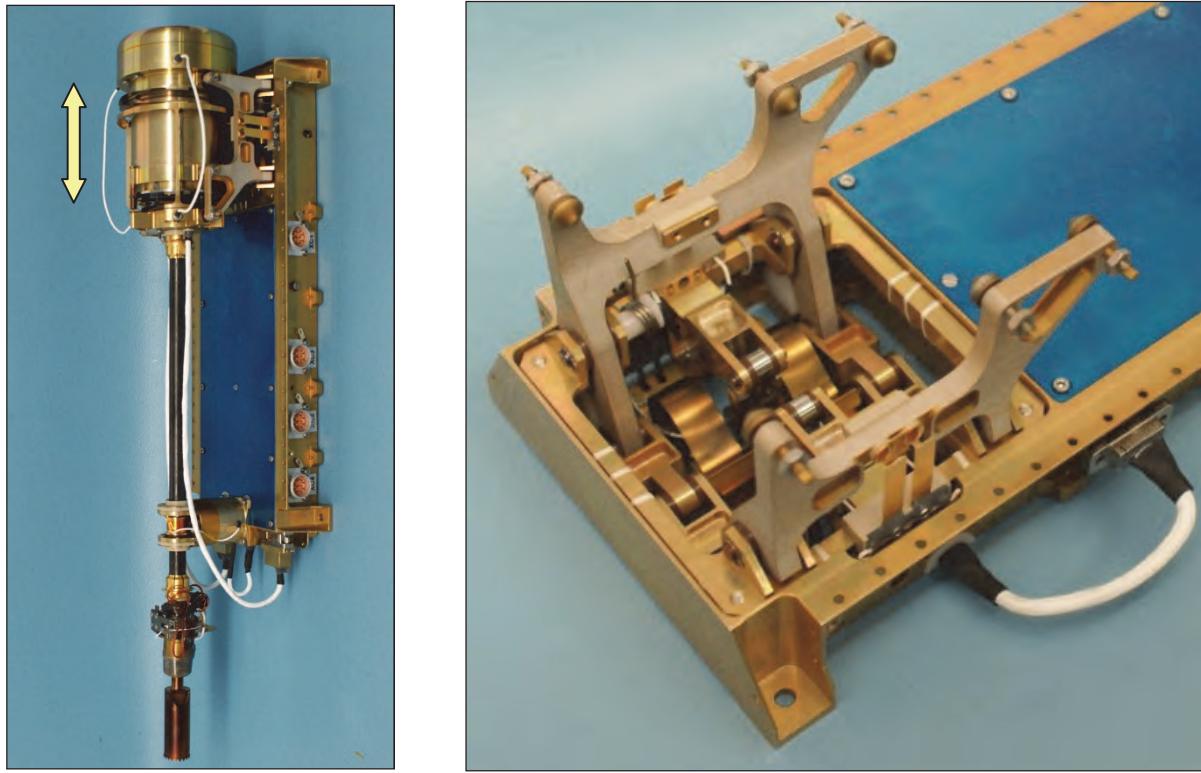


Figure 3. CHOMIK penetrator with electronic box (left) and its lock and release mechanism in the stowed position (right) – penetrator is removed

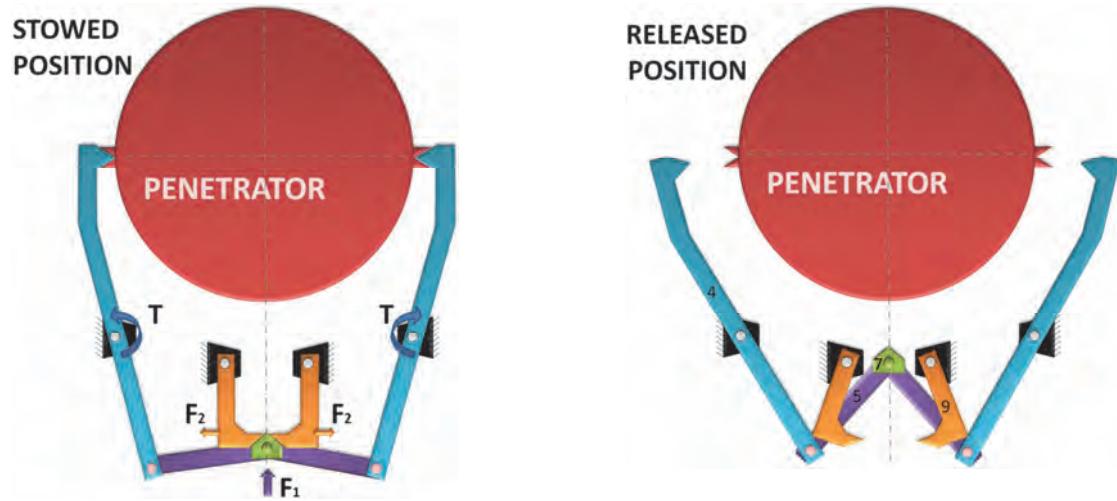


Figure 4. A planar kinematic diagram of the lock and release mechanism

There are three types of springs responsible for the mechanism release: (I) torsion springs generate torque T to the crank arms rotating them by 18° , (II) flat C-shaped springs guide and produce a pushing force F_1 to a slider, (III) flat springs, which are integrated with holders and execute two functions: kick-off and Dyneema string tensioning with F_2 force.

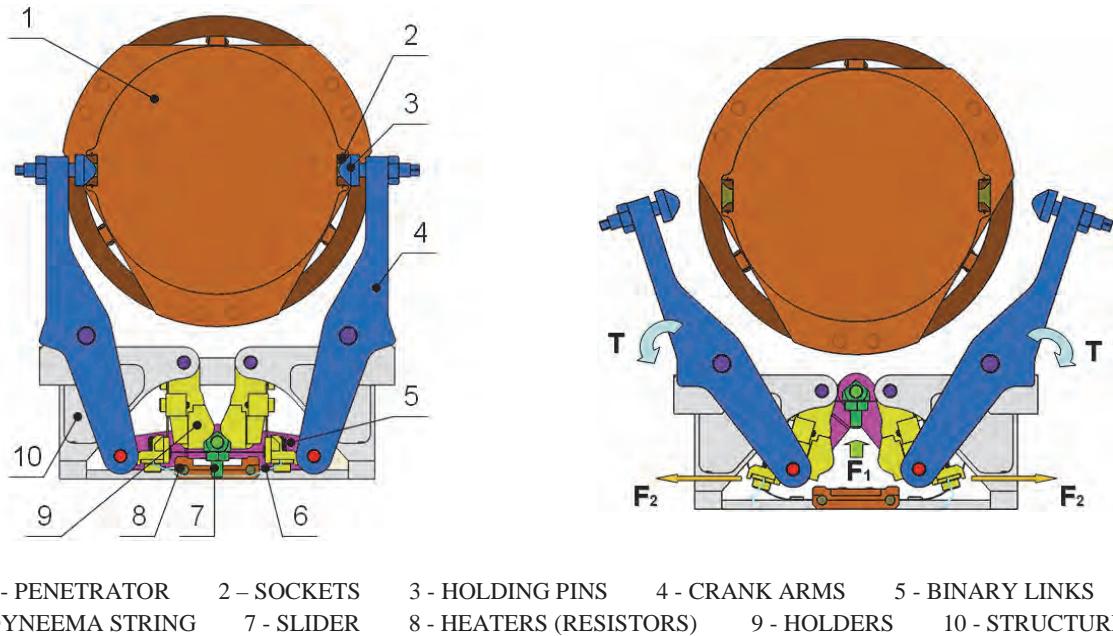


Figure 5. Practical realization of the mechanism

The tight string protects the holders after their displacement caused by the Dyneema cord elongation of about 3.5%. The design of the mechanism is shown in Figure 5. The complete lock and release mechanism weighs 150 grams and occupies a volume of 81x82x36 mm. Two redundant melting elements have $110\ \Omega$ of resistance and the actuation power voltage is 28V. Two connectors provide confirmation of the holding arms release.

The main challenge during the mechanism development was the elimination of the self-locking effect. To avoid such a situation, the design process was preceded by detailed kinematic studies, and then a structural-thermal model was assembled and tested. The investigation showed some problems with slider elements that potentially could produce a non-symmetric release. This issue has been solved by blocking one of the kick-off spring's motions and implemented in the qualification model.

Tests also showed that it is very important to place all moving arms in their suitable positions during the arming process. Figure 6 presents the mechanism's arming equipment which is helpful to provide symmetric arms' settings and to generate the preliminary tension making it possible to install the Dyneema string.

The mechanism successfully passed the vibration resistance test, shock test and linear overload test. A functional test has been carried out in the vacuum-thermal chamber. The temperature on the instrument structure was about -150°C and vacuum of about $10^{-6}\ \text{Pa}$. The Dyneema string application needs 6 seconds for release in those simulating Phobos environmental conditions, compared to less than 1 second at room temperature (laboratory air). Shock generated during release is very low compared to those created by a pyrotechnic actuator.

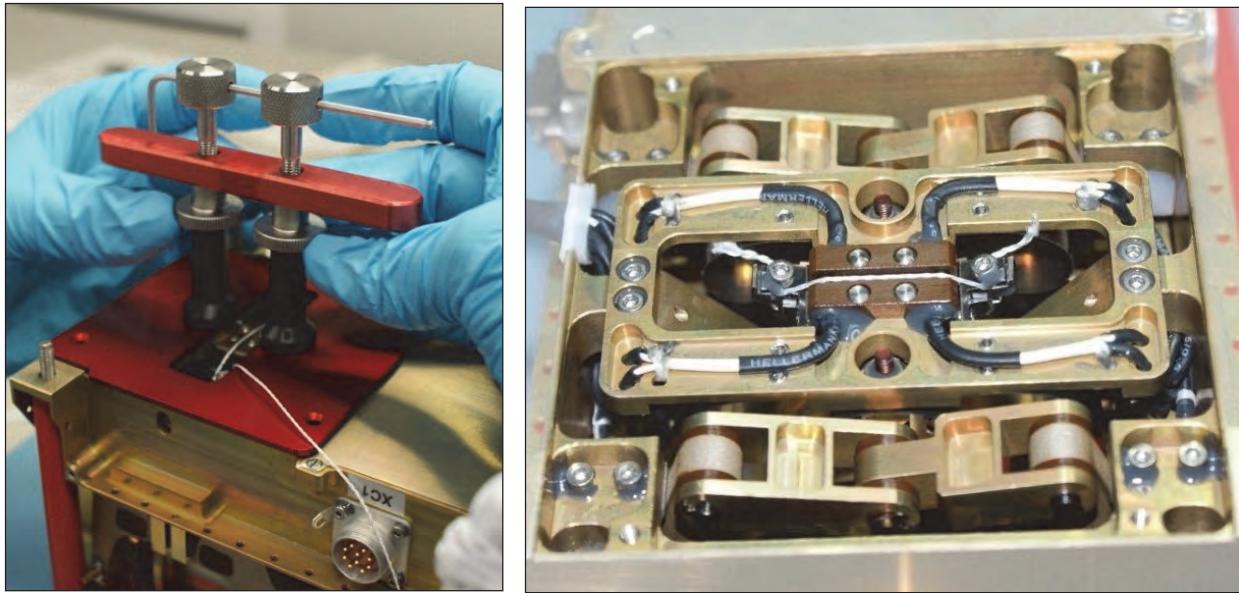


Figure 6. Mechanism arming equipment (left) and L&R mechanism with Dyneema string installed (right)

High-speed camera record has shown that the maximum speed of the holding pins is about 4 m/s during releasing (at room temperature). The time period, from Dyneema string melt to the crank arm full rotation, is about 5 milliseconds; then the crank arms rebound several times dissipating energy, and stop after about 52 milliseconds. As it is shown in Figure 7, the first crank arms movement is very equal, which is the result of accurate positioning of the mechanism element during Dyneema string installation using the arming equipment. Figure 8 shows selected moments of the mechanism action. Frame A shows the locked mechanism. In Frame B, the Dyneema string is melted but holders still occupy the slider lateral surface. In Frame C, the slider is shifting resulting in the binary links pull and that makes the crank arms rotation possible. Frame D shows a mechanism in the fully released position. The moments captured on the presented frames has been marked in Figure 7.

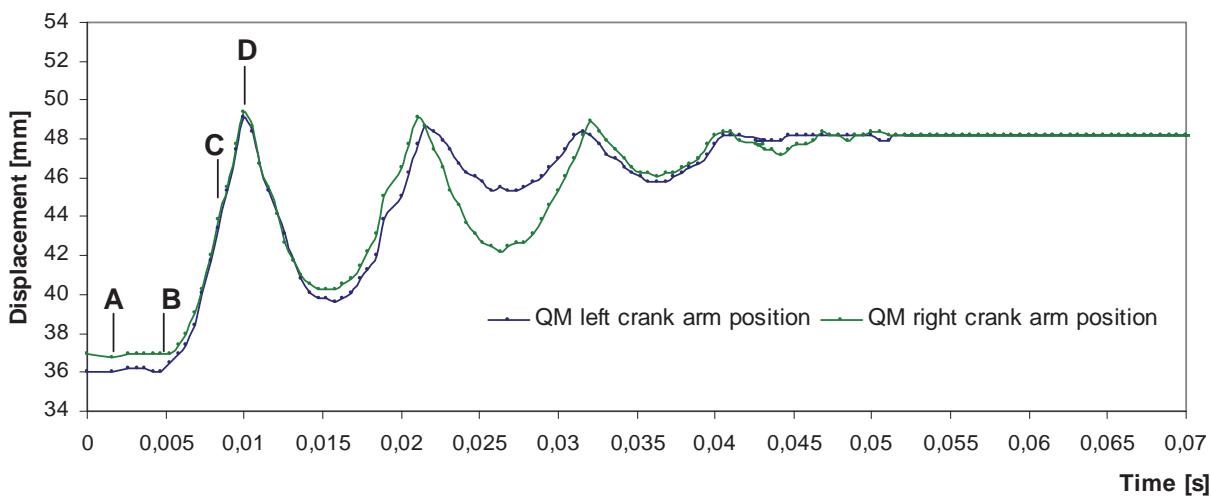


Figure 7. Holding pins displacement during mechanism release

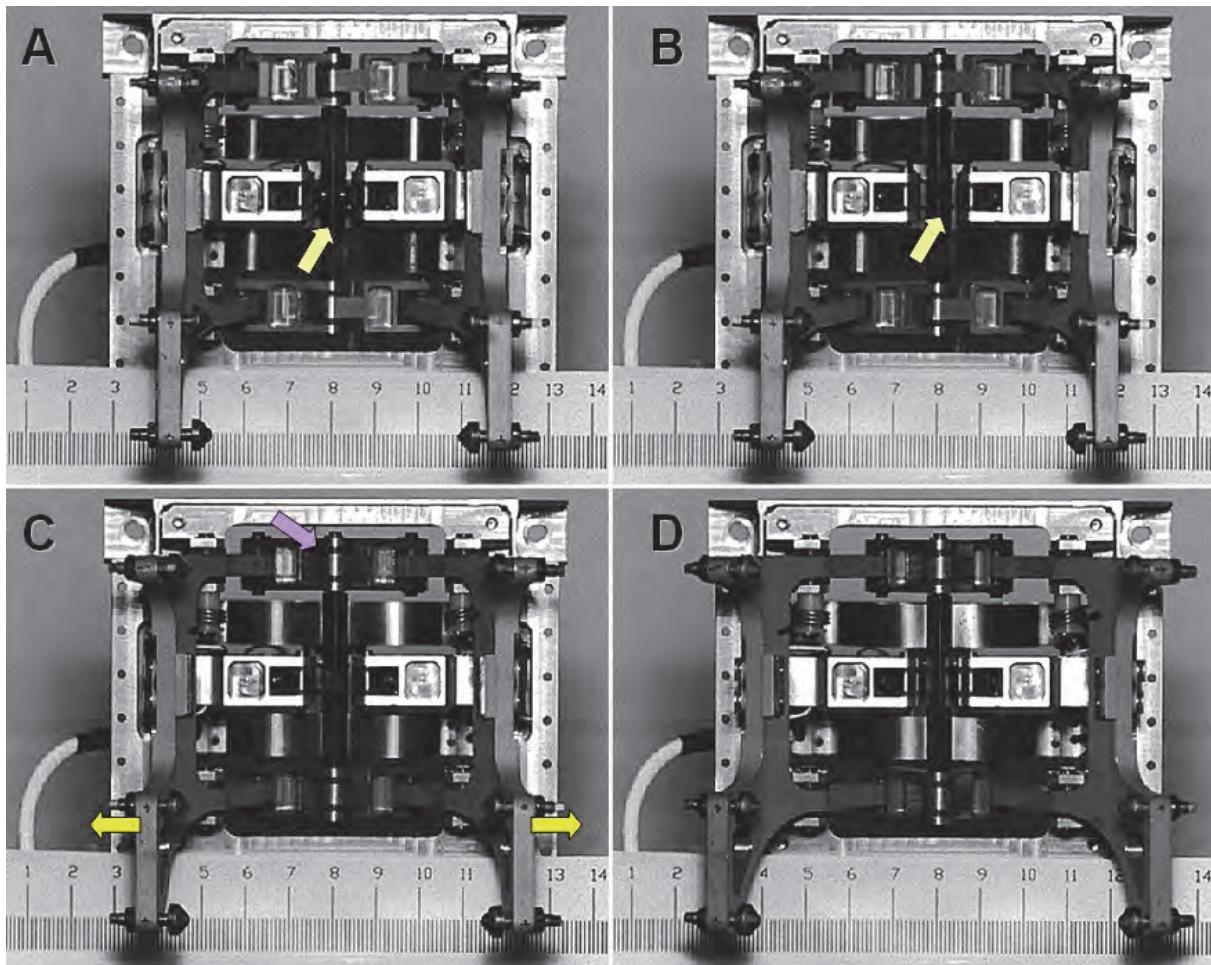


Figure 8. Lock & release mechanism action - penetrator is removed

Tribological tests

All rotating and sliding joints in the mechanism (Figure 9) have to work in very low temperatures and vacuum, with a small movement range and with only one, short time actuation. This influenced the slide bearings selection. Titanium alloy with titanium nitride layer and polyimide-based plastic Vespel SP1 were chosen as mating parts materials. Tribo-components made of Ti6Al4V alloy (shafts, pins, latches) with Vespel SP1 (bushings, sliders, guides) have been used in many SRC PAS mechanisms, including the CHOMIK device. This selection was based on our experience, previous material properties tests, and the ability to manufacture good quality layers on parts with a complicated shape by our partners.

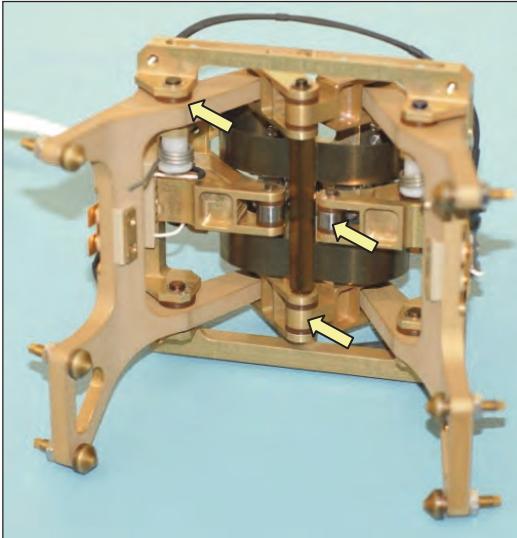


Figure 9. L&R mechanism with its exemplary plastic-metal slide components



Figure 10. Pin-on-Disk tribometer mounted in the SRC thermal-vacuum chamber

To develop a unit without a self-locking effect, a coefficient of friction for selected mating plastic-metal parts had to be known. Another unknown was a repeatability of the mechanism behavior during room and low temperature operation. Adequate tests were conducted in a newly built vacuum pin-on-disc tribometer (Figure 10). Ti6Al4V alloy with titanium nitride layer as a pin while Vespel SP1 as a disk were used.

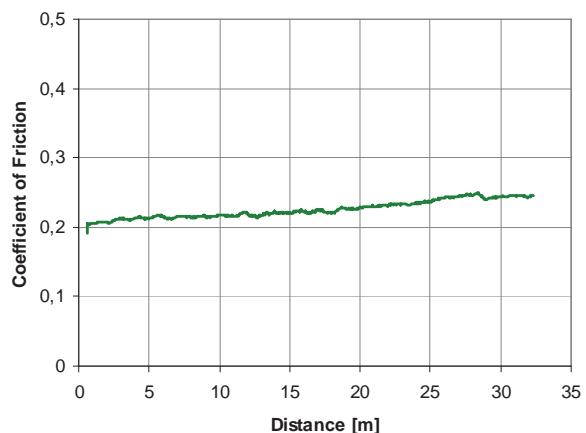
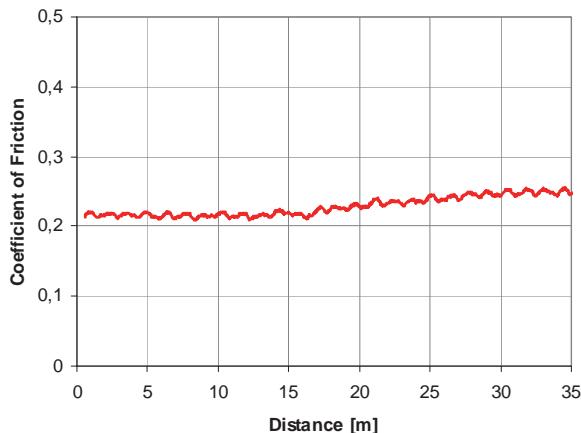


Figure 11. Coefficient of friction versus sliding distance for Ti6Al4V pin with TiN layer and Vespel SP1 disk for vacuum environment: room temperature (left), very low temperature (right)

The tests were conducted in the following conditions: (1) pressure: 0.01-0.04 Pa, (2) load: 50N, (3) sliding speed: 0.1 m/s , (4) contact area: 10 mm^2 . Figure 11 (left) shows coefficient of friction versus sliding distance at room temperature, whereas Figure 11 (right) is a diagram of coefficient of friction for -80°C . Tribological tests in the Phobos-simulated environment showed that the coefficient of friction for Vespel SP1 and Titanium alloy with titanium nitride layer is low, about 0.22. Moreover, friction properties are stable and on the same level, both at room or low temperature.

Conclusions

Development of the CHOMIK L&R mechanism provided successive arguments that thin Dyneema string melting method can be applied for releasing medium-high loaded space devices. The alike systems are developed at SRC PAS taking into account the superior reliability of the melting process. Medium-higher loads need a high leverage mechanism, which is the main subject of the presented paper. The conducted tests proved it. One of the lessons learned is that in case of the high leverage mechanism, additional springs counteracting the self-locking of the mechanism must be applied. Usage of a system that counteracts the cord elongation is also recommended. The investigations that have been made confirm that the Dyneema string melting actuation method is very reliable and Vespel SP1 and titanium alloy with titanium nitride layer are suitable mating materials for low temperature applications.

References

1. Grygorczuk J., Dobrowolski M., Wisniewski L., Banaszkiewicz M., Ciesielska M., Kedziora B., Seweryn K., Wawrzaszek R., Wierzchon T., Trzaska M., Ossowski M. "Advance mechanisms and tribological tests of the hammering sampling device CHOMIK. *"The Proceedings of ESMATS"* (September 2011).
2. Grygorczuk, J., Banaszkiewicz, M., Seweryn, K., Spohn, T. (2007). MUPUS Insertion device for the Rosetta mission. *Journal of Telecommunications and Information Technology* (1/2007), pp50-53.
3. Grygorczuk, J., Banaszkiewicz, M., Kargl, G., Kömle, N., Ball, A.J., Seweryn, K. (2009). Use of hammering to determine cometary nucleus mechanical properties. *Penetrometry in the Solar System II* (Eds: Günter Kargl, Norbert I. Kömle, Andrew J. Ball, Ralph Lorenz), *Proceedings of the 2nd International Workshop on Penetrometry in the Solar System*, Graz, 25th-28th September, 2006, Austrian Academy of Sciences Press, pp93-107.

The paper is supported by the Polish national grant project 791/N-ROSJA/2010/0 and ESA PECS project No. 98 105

Harmonic Drive™ Gear Material Selection and Life Testing

Jeffrey Mobley* and Jonathan Parker*

Abstract

Sierra Nevada Corporation (SNC), along with NASA Goddard Space Flight Center (GSFC), tested several Harmonic Drive gears for their longevity and performance to determine the best material combinations for a mission, requiring an actuator life nearly ten times previously qualified. Accelerated life testing in both ambient and vacuum environments revealed two suitable candidates for the flight build. The combination of a Nitronic 60 circular spline and 15-5PH H1075 flexible spline was ultimately chosen. It was surprising though, that 15-5PH H1075 on both circular and flexible splines outperformed the heritage material combination (Melonited Flex Spline against a 15-5PH Circular Spline) and also could have been used in the flight build.

Introduction

The NASA Global Precipitation Measurement (GPM) mission required actuators for its High Gain Antenna System (HGAS) and Solar Array Drive Assembly (SADA) with a life significantly higher than the required life of heritage actuators previously qualified by SNC for the Lunar Reconnaissance Orbiter (LRO) mission and the Solar Dynamics Observatory (SDO) mission as shown in Table 1. One of the life-limiting components in the actuator design is the Harmonic Drive gear. Wear was observed in the circular spline teeth during the post-life test teardown inspection on the SDO and LRO actuators. This wear was determined to be acceptable for those missions, but when extrapolated out to the life requirements of the GPM mission, the effect of tooth wear on performance became uncertain. The heritage LRO and SDO actuators used T-Cup Harmonic Drive gears manufactured by Harmonic Drive LLC in Peabody, MA in order to provide a large through hole in the actuator. The drives had a 200:1 gear ratio and utilized a combination of a Melonite™ treated Flex Spline and 15-5PH Circular Spline. This particular material combination had not been life tested by either SNC or Harmonic Drive LLC for the number of cycles required for the GPM mission.

Table 1: Required Life Comparison

Application	Cycle	# of Cycles (for 1X Life)	Total Degrees
SDO	360° (continuous)	2,500	900,000°
LRO	180° CW, 180° CCW	5,700	2,052,000°
GPM SADA	250°CW, 250° CCW	17,500	8,750,000°
GPM HGAS	190° CW, 190° CCW	48,600	18,468,000°

Harmonic Drive™ is a registered trade mark of Harmonic Drive LLC

* Sierra Nevada Corporation, Durham, NC

Hardware Configurations

Based on discussions between Harmonic Drive LLC and SNC, the following material combinations were selected for comparative life testing, with the goal of extending the life of the Harmonic Drive gear in order to meet the GPM HGAS requirement:

- 15-5PH H1075 Circular Spline against Melonited 15-5PH H1100 Flex Spline
 - Most similar to heritage
 - Removed weight reduction cuts for more repeatable performance
 - Reduced the size of the pre-melonite grit blast media for better surface finish
 - Increased the circular spline hardness from H1150 to H1075 for better wear resistance
- Nitronic 60 Circular Spline against Melonited Flex Spline
 - Same as above except for Circular Spline material
 - Nitronic 60 recommended by Harmonic Drive LLC based upon testing reported in Reference 1
- Nitronic 60 Circular Spline against 15-5PH H1075 Flex Spline
 - Same as above except for flex spline material
 - Melonite removed to result in less abrasive flex spline
 - Flex Spline hardness increased to H1075 for better wear resistance
- 15-5PH H1075 Circular Spline against 15-5PH H1075 Flex Spline
 - Chosen for test because the components were available from the other combinations
 - Low expectations due to potential for galling/cold welding from identical materials in contact

All Harmonic Drive gear configurations were customized HDT-25, 200:1, T-cup component sets manufactured in Peabody MA by Harmonic Drive LLC and all were of the same dimensional design. All combinations used the same wave-generator bearing material and design, and each was identically lubricated with Pennzane 2001-3PbNp oil and Rheolube 2004 grease per standard procedures. Table 2 summarizes the tested configurations with assigned part numbers.

Table 2: Material Combinations

<i>Part #</i>	<i>Circular Spline Material</i>	<i>Flexible Spline Material</i>
36638-1	15-5PH H1075	15-5PH H1100 w/ Melonite
36638-2	15-5PH H1075	15-5PH H1075
36638-3	Nitronic 60 Annealed	15-5PH H1100 w/ Melonite
36638-4	Nitronic 60 Annealed	15-5PH H1075

Ambient Life Test Plan

The Life Test plan is shown in Figure 1. A standard run-in was performed by Harmonic Drive LLC on each Harmonic Drive component prior to the start of any testing. Following run-in, each Harmonic Drive gear was characterized by measuring starting torque and torsional stiffness. The starting torque of the Wave Generator input was measured in six equidistant positions with the Circular Spline fixed and no load applied to the Flex Spline output. Torsional stiffness was measured in six equidistant locations at the Flex Spline output with the Circular Spline and Wave Generator input held stationary. Once each Harmonic Drive gear was assembled into its life test fixture, the torsional stiffness test was repeated at 25 equidistant locations to characterize the baseline assembled condition. The ambient life test was conducted to simulate 2X the required mission life and was conducted in air at room temperature. The Harmonic Drive gear input was driven at a nominal input speed of 52.36 rad/s (500 rpm). The Harmonic Drive gear output was loaded to 2.93 N·m (26 in-lb) with a friction brake (see Figure 2) to simulate the application frictional load plus the load required to accelerate the specified inertia. The life test was run alternating between clockwise and counter-clockwise directions for approximately 24 hours at a time. At the conclusion of the life test, the Harmonic Drive gear had completed over 51,300 output revolutions in each direction (39,936,000° of total travel). Following the ambient life test, the units were again tested for torsional stiffness while assembled in the test fixture. The units were then disassembled, inspected, cleaned, and inspected further with findings documented below.

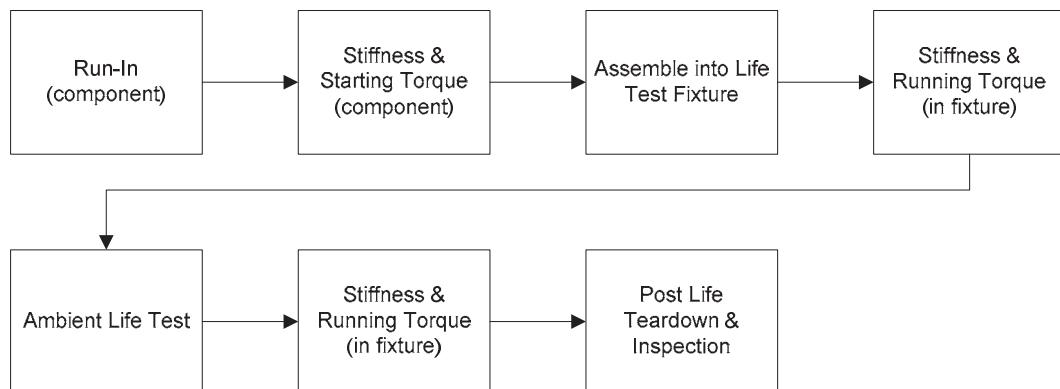


Figure 1: Test Flow

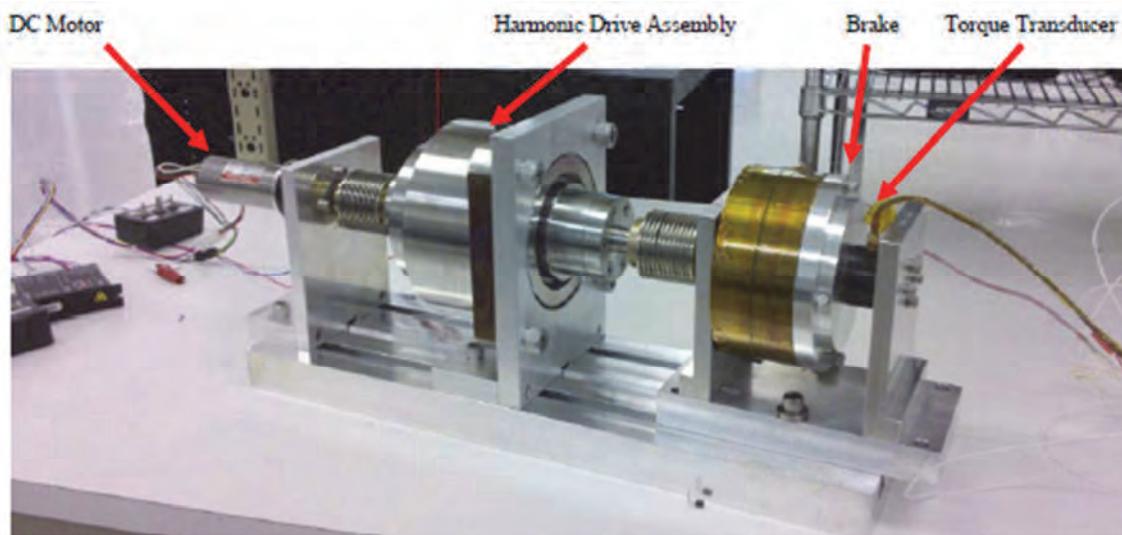


Figure 2: Ambient Life Test Setup

Ambient Life Test Results

Torsional Stiffness

As shown in Figure 3, the Harmonic Drive gears with a Melonite Flex Spline (36638-1 & 36638-3) showed a decrease in torsional stiffness (5 to 8%) compared to the 15-5PH Flex Splines which showed a slight increase (1% to 5%). As shown in Figure 4 and Figure 5, the shape of the post-life stiffness curves for the Harmonic Drive gears with the 15-5PH Flex Splines were very comparable to the pre-life stiffness curves. However, the shape of the post-life stiffness curves for the Harmonic Drive gears with the Melonite Flex Splines showed a significant reduction in low torque stiffness when compared to the pre-life stiffness curves. The reduction in stiffness on the Harmonic Drive gears with the Melonited Flex Splines was an early indication of increased wear in those drives.

Teardown Inspection

Each Harmonic Drive gear was disassembled to examine its components for wear and debris generation.

Circular Splines

Figure 6 illustrates the differences between the Circular Splines at the end of the life test. Configurations with the Melonite Flex Splines (36638-1 & 36638-3) contained metallic particles packed into the roots of the Circular Spline teeth. Numerous small fragments of metal were found in the roots of 36638-1 but were not as prevalent in 36638-3 even though the amount of wear was similar. The metal fragments were found to be fine metallic wear debris that had packed into the roots of the teeth and been formed into slivers as seen in the photo of the 36638-1 Circular Spline. Additionally there was a noticeable wear step on the 36638-1 & 36638-3 Circular Splines. The non-Melonite Harmonic Drive gears (36638-2 & 36638-4) showed only a slight wear step at the gear mesh and had no accumulation of metallic debris in the roots of the gear teeth. The lubricant color was darker than seen on the 36638-2 & 36638-4 flexible splines, further indicating an increased presence of wear debris.

Flex Splines

Figure 7 and Figure 8 illustrate the differences between the teeth and ID of the Flex Splines at the end of the life test. Configurations with the Melonite Flex Splines (36638-1 & 36638-3) showed very little difference between pre and post- life for both the teeth and the ID. The non-Melonite Flex Splines (36638-2 & 36638-4) teeth were visually worn in the area of highest contact, but the wear was comparable to that seen on their respective Circular Splines and not nearly as significant as seen on the 36638-1 & 36638-3 Circular Splines. The ID of the non-Melonite Flex Splines (36638-2 & 36638-4) were visually worn in the area of contact with the wave generator OD, but there were no signs of galling and the amount of wear was acceptable for a 2X life condition.

Wave Generator

Figure 9 and Figure 10 illustrate the differences between the OD and balls of the Wave Generators at the end of the life test. All Wave Generators showed some polishing on the OD from contact with the Flex Splines. The Melonited Flex Splines in 36638-1 and 36638-3 showed a higher level of polishing but not enough to cause any concern. The wave generator lubricant was lighter in the non-Melonite drives (36638-2 & 36638-4) indicating less wear particles present.

Harmonic Drive LLC Inspection

The Harmonic Drive gears were thoroughly cleaned and sent back to the manufacturer to measure the tooth profiles. A total of four teeth were measured on each flexible and circular spline and compared to the theoretically perfect tooth. The Harmonic Drive gears using the Melonite Flex Spline (36638-1 & 36638-3) showed much more deviation from the theoretical tooth profile than the non-melonite flexible splines. The teeth on the non-Melonite drives (36638-2 & 36638-4) were still generally within the acceptable manufacturing standard tolerance range, with 36638-2 (15-5/15-5) showing the least amount of deviation.

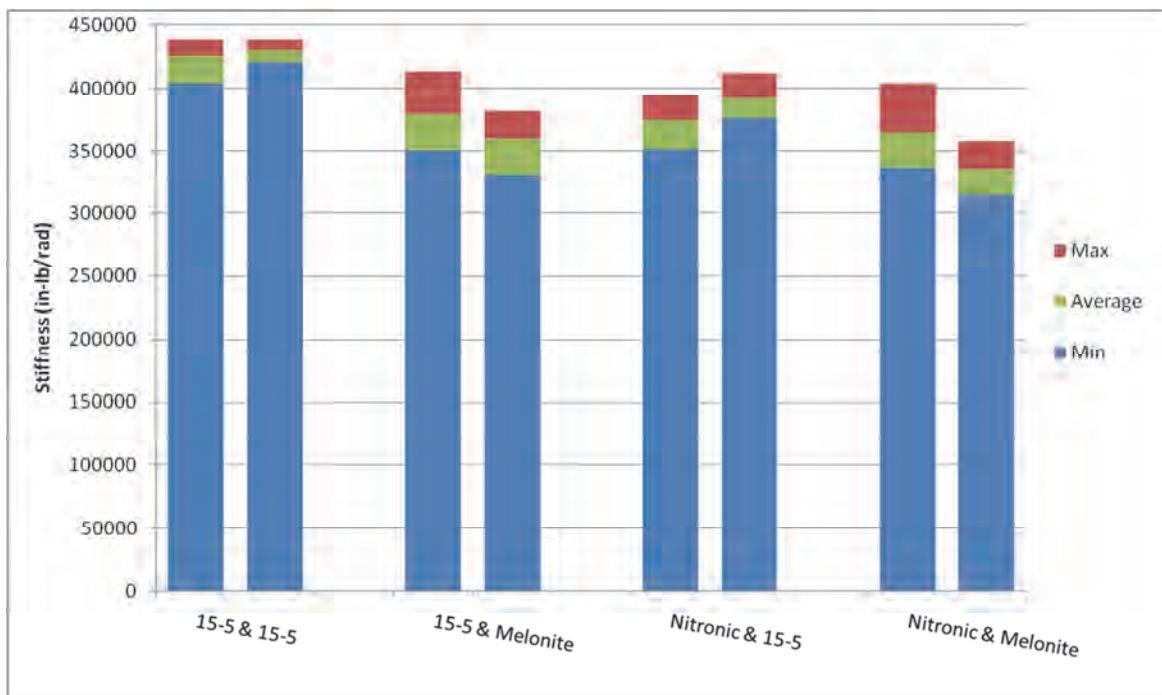


Figure 3: Pre and Post Ambient Life Stiffness

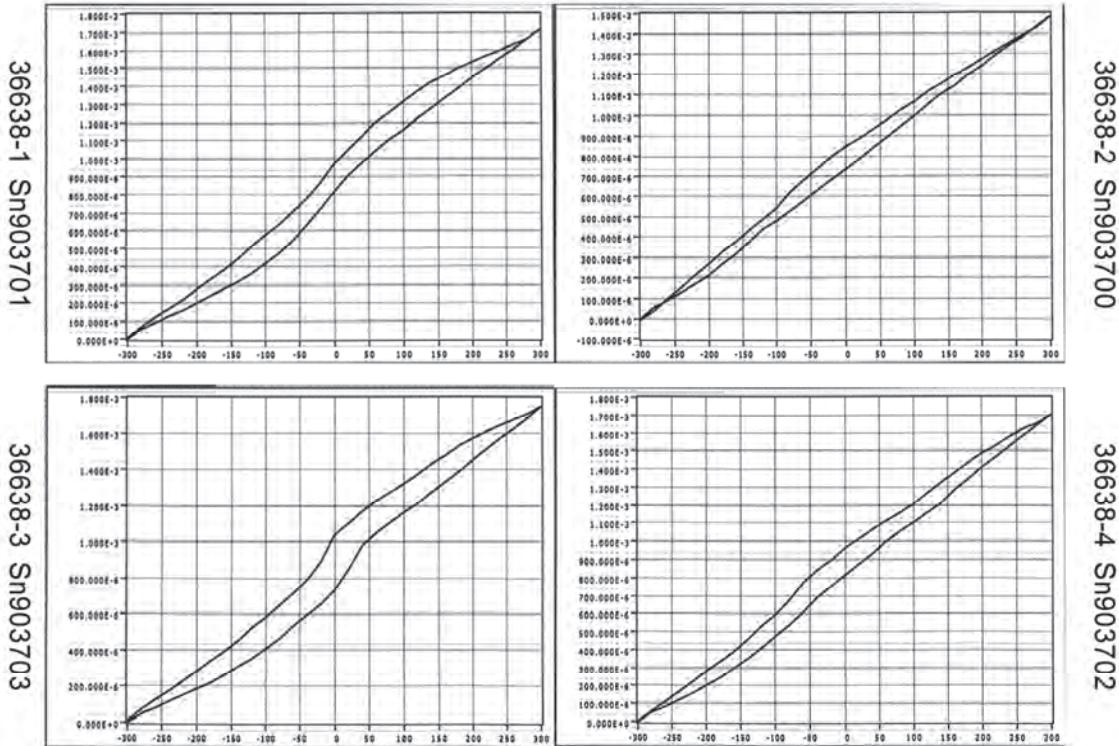


Figure 4: Pre- Life Minimum Stiffness Curves (Radians vs. In-Lb)

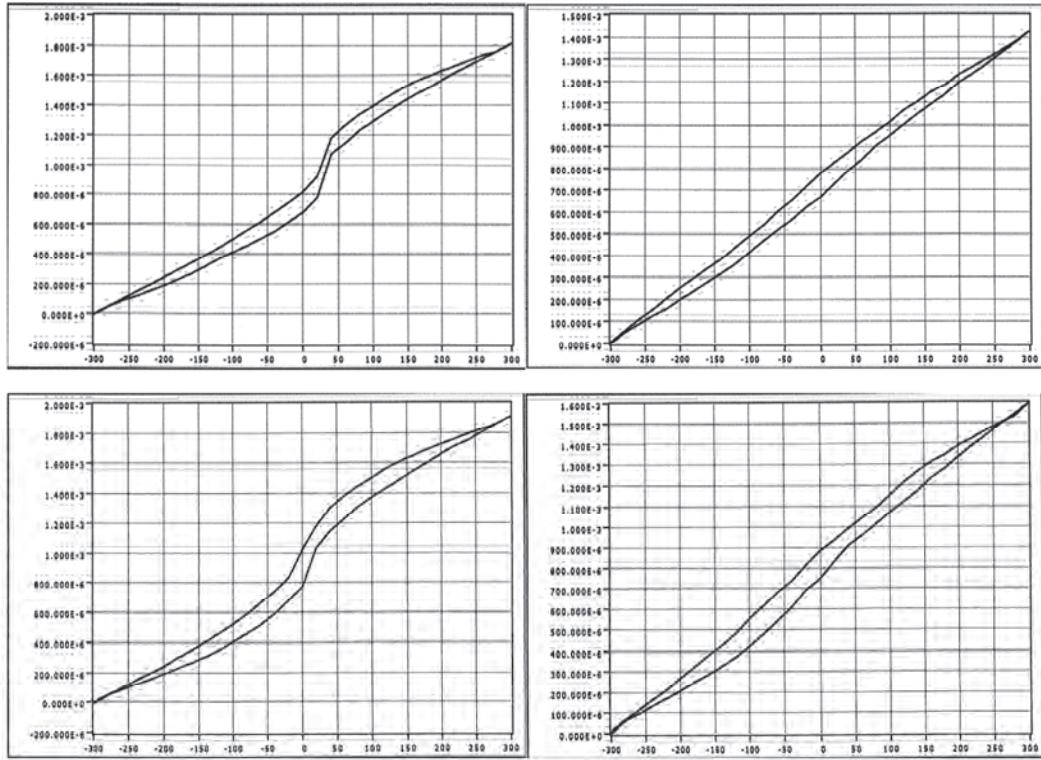


Figure 5: Post- Life Minimum Stiffness Curves (Radians vs. In-Lb)

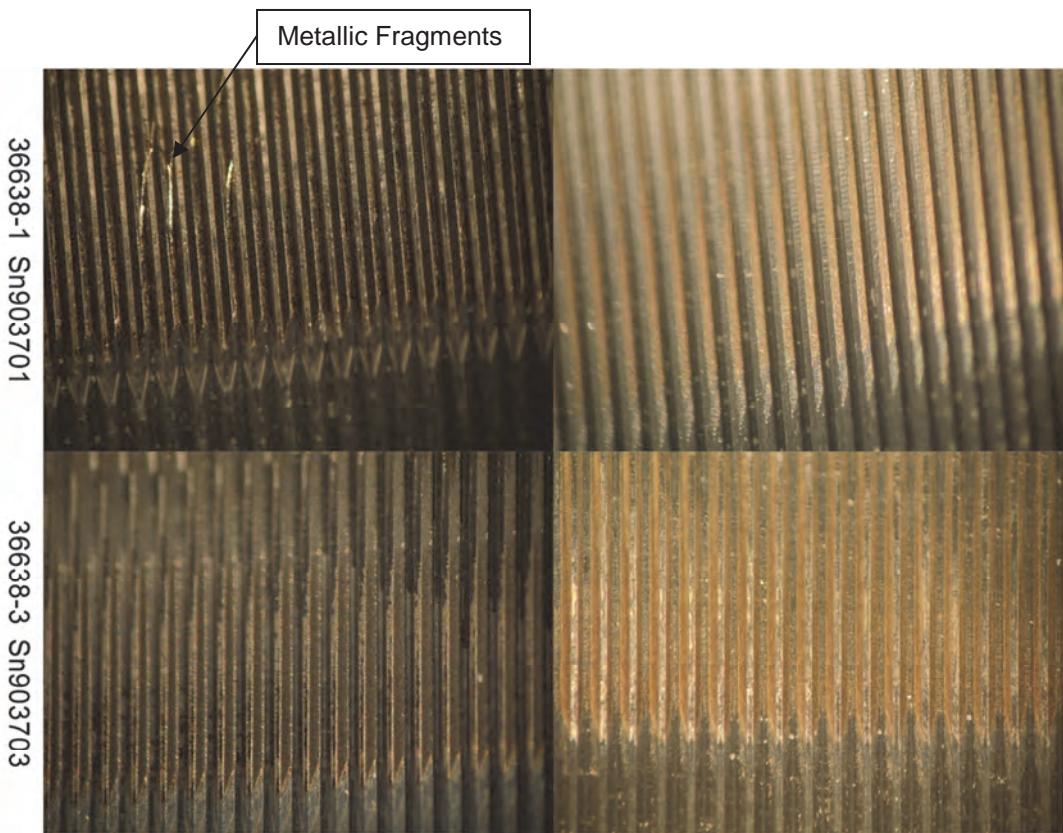


Figure 6: Circular Spline Teeth, Post Ambient Life

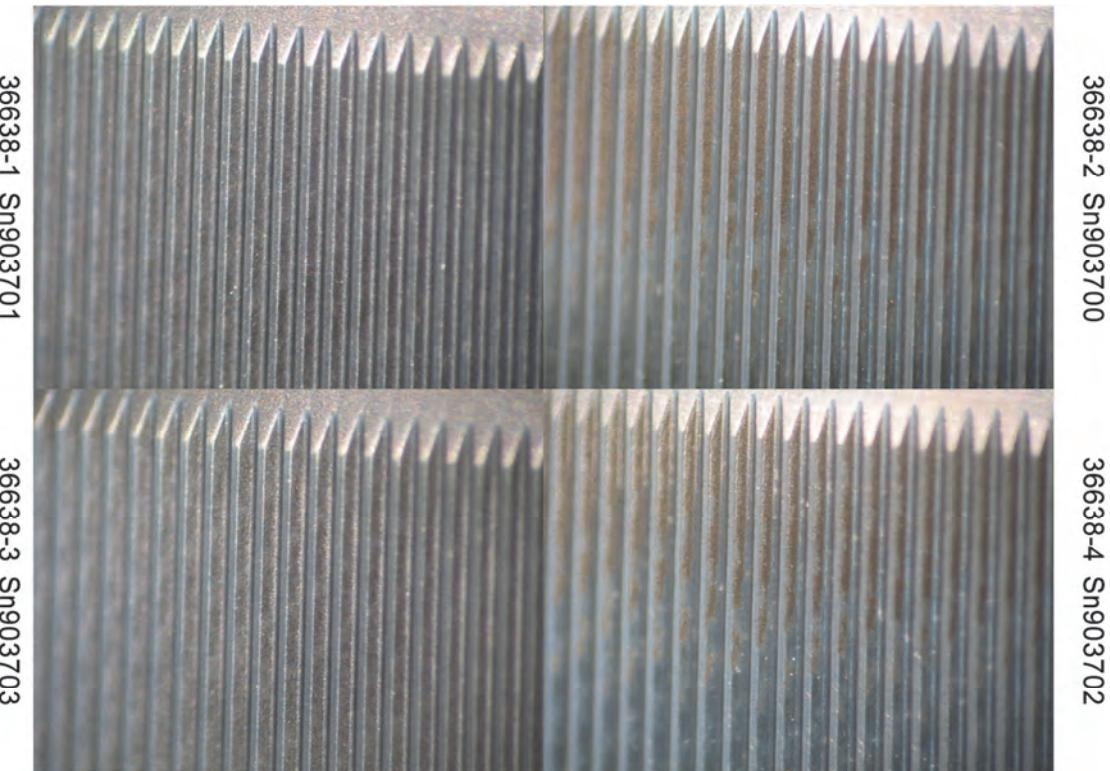


Figure 7: Flex Spline Teeth, Post Ambient Life

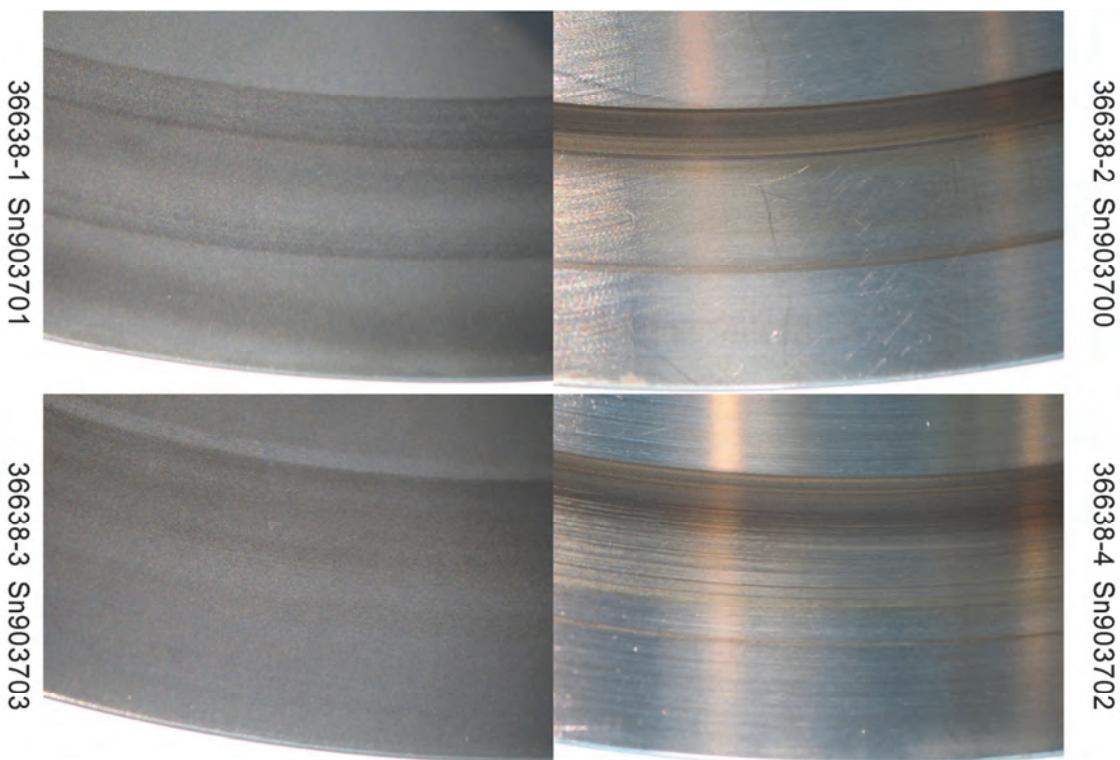


Figure 8: Flex Spline ID, Post Ambient Life

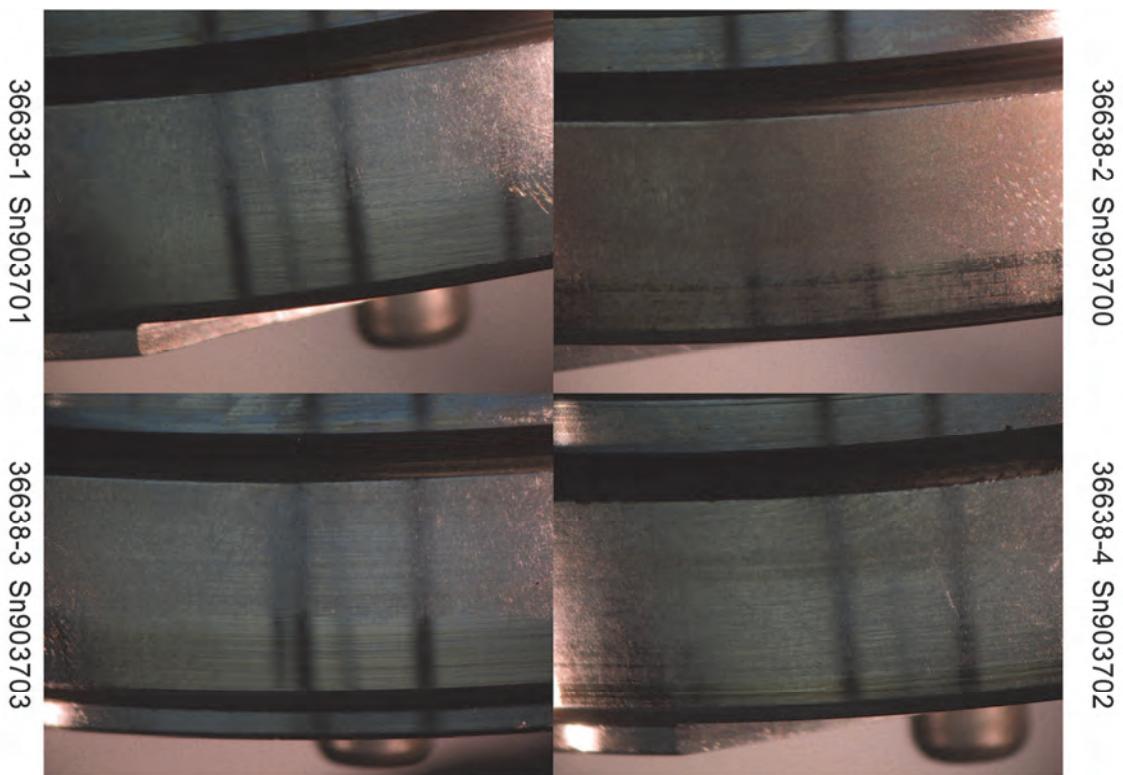


Figure 9: Wave Generator OD, Post Ambient Life



Figure 10: Wave Generator Balls, Post Ambient Life

Ambient Life Test Results Summary

The two Melonite Harmonic Drive gears (36638-1 and 36638-3) were eliminated from contention due to the reduction in torsional stiffness at the end of life and the presence of relatively large particles of metallic debris in the gear mesh. The two non-Melonite Harmonic Drive gears (36638-2 & 36638-4) were relatively comparable. 36638-2 visually looked slightly better, (primarily with regard to the circular spline teeth and gear lubricant) but the 36638-4 was nonetheless acceptable. The concern over how 15-5PH against 15-5PH would perform during vibration and in a vacuum environment, resulted in the 36638-4 configuration (15-5/Nitronic) being chosen as the least risky path forward for the flight build. A qualitative assessment of the key parameters of the post-life inspection is shown in Table 3. In parallel with building flight hardware with the chosen configuration, the program decided to further this study by performing a vacuum life test comparison between the non-Melonite drive configurations (36638-2 & 36638-4).

Table 3: Qualitative Summary of Ambient Life Test Results

	36638-1	36638-2	36638-3	36638-4
	15-5/Melonite	15-5/15-5	Nitronic/Melonite	Nitronic/15-5
Stiffness Change	Poor	Good	Poor	Good
Circular Spline Tooth Wear	Poor	Average	Poor	Average
Flex Spline Tooth Wear	Good	Average	Good	Average
Flex Spline Cup	Good	Average	Good	Average
Wave Generator OD	Average	Average	Average	Average
Gear Teeth Lube	Poor	Average	Poor	Average
Wave Generator Lube	Good	Average	Good	Average

Vacuum Life Test Plan

Based on the ambient life test results and concerns regarding the validity of a life test in ambient air, a second round of testing was conducted in a vacuum. The testing was repeated on new Harmonic Drive gears with the best performing configurations from the ambient test, 36638-2 and 36638-4, in a vacuum environment combined with thermal cycling.

Testing was performed per the same flow shown in Figure 1 except as noted below. Baseline torsional stiffness testing was performed on the vacuum test Harmonic Drive gears prior to life testing as previously done with the ambient test to characterize the pre-life performance. The vacuum life test consisted of 100,000 cycles of reversing 180° output revolutions in a $<5.0 \times 10^{-5}$ Torr vacuum environment, cycling between 0 and 40°C. The input to the Harmonic Drive gear was set to 52.36 rad/s (500 rpm). A magnetic particle brake was used to apply a constant 2.93 N·m (26 in-lb) friction load to the output for the duration of the test. Following the ambient life test, the units were again tested for torsional stiffness while assembled in the test fixture. The units were then disassembled, inspected, cleaned, and inspected further with findings documented below.

Vacuum Life Test Results

Torsional Stiffness

As shown in Figure 11, there was very little difference between the post-life torsional stiffness of the two configurations. The 36638-4 saw a 5% reduction in torsional stiffness while the 36638-2 saw a 9% reduction in torsional stiffness, but based on the stiffness plots seen in Figure 12, neither drive saw a significant reduction in low torque torsional stiffness that was seen on the Melonited drives during the ambient life test.

Teardown Inspection

Each Harmonic Drive gear was disassembled to examine its components for wear and debris generation.

Circular Splines

Figure 13 illustrates the differences between the Circular Splines at the end of the life test. The Nitronic 60 Circular Spline (36638-4) only showed a change in surface finish at the edge of flex spline contact, whereas the 15-5PH Circular Spline (36638-2) showed a slight wear step. Neither drive displayed significant generation of metallic debris or any buildup of debris in the roots. The gear mesh lubricant was lighter than seen after the ambient life test most likely due to reduced oxidation in vacuum.

Flex Splines

Figure 14 and Figure 15 show the teeth and ID of the Flex Splines at the end of the life test. The Flex Spline teeth of both drives were minimally worn in the area of highest tooth contact. There was no sign of galling or cold welding in the 36638-2 configuration (15-5PH against 15-5PH). The ID of the Flex Splines were visually worn in the area of contact with the wave generator OD, but there were no signs of galling and the amount of wear was acceptable for a 2X life condition and comparable to the ambient life test.

Wave Generator

Figure 16 and Figure 17 show the OD and balls of the Wave Generators at the end of the life test. Both Wave Generators showed some polishing on the OD from contact with the Flex Splines, but results were comparable to the ambient life test and to be expected for 2X life. Again, the wave generator lubricant was slightly lighter than seen in the ambient life test (less oxidation) and the 36638-4 configuration was slightly darker than the 36638-2 configuration.

GSFC Material Analysis

Very slight wear was observed on the flex spline teeth of both assemblies which appeared to be slight burnishing of the tooth surface. No pitting or scoring was visible. Grease from both assemblies exhibited evidence of metallic wear. Infrared spectroscopic analysis of the grease was inconclusive in determining a 'winner'. In all the samples, a weak intensity carbonyl band was detected, indicating very little grease/oil degradation. The greater amount of metallic wear debris in the flex spline-circular spline contact of the 15-5PH & 15-5PH combination suggests the 15-5PH & Nitronic 60 is a slightly better configuration

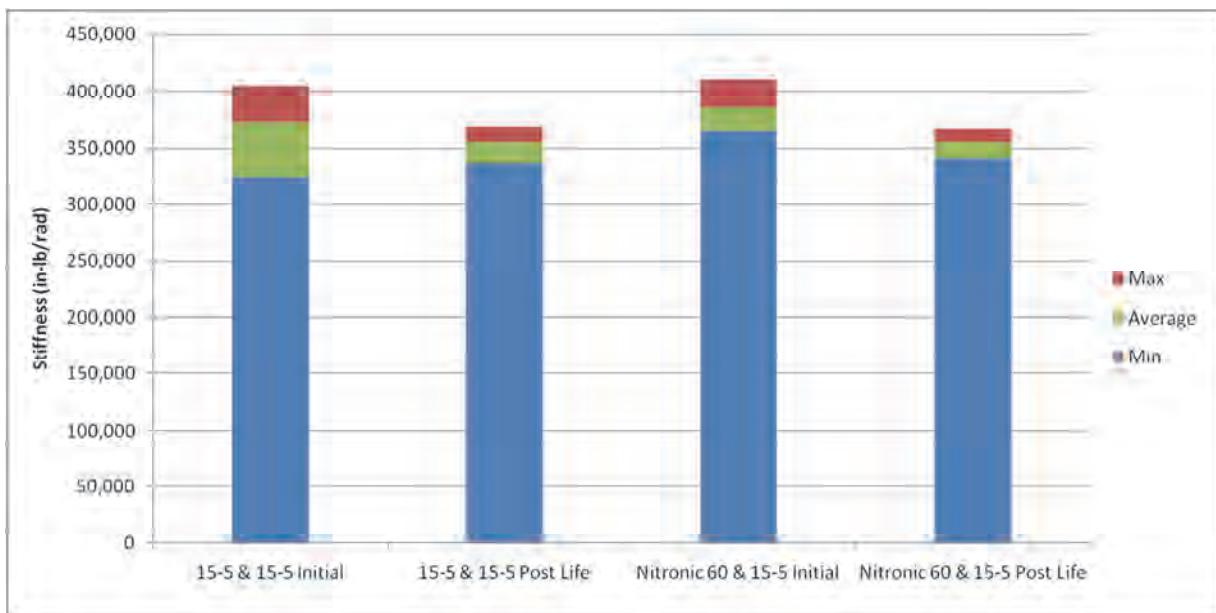


Figure 11: Pre and Post Vacuum Life Stiffness

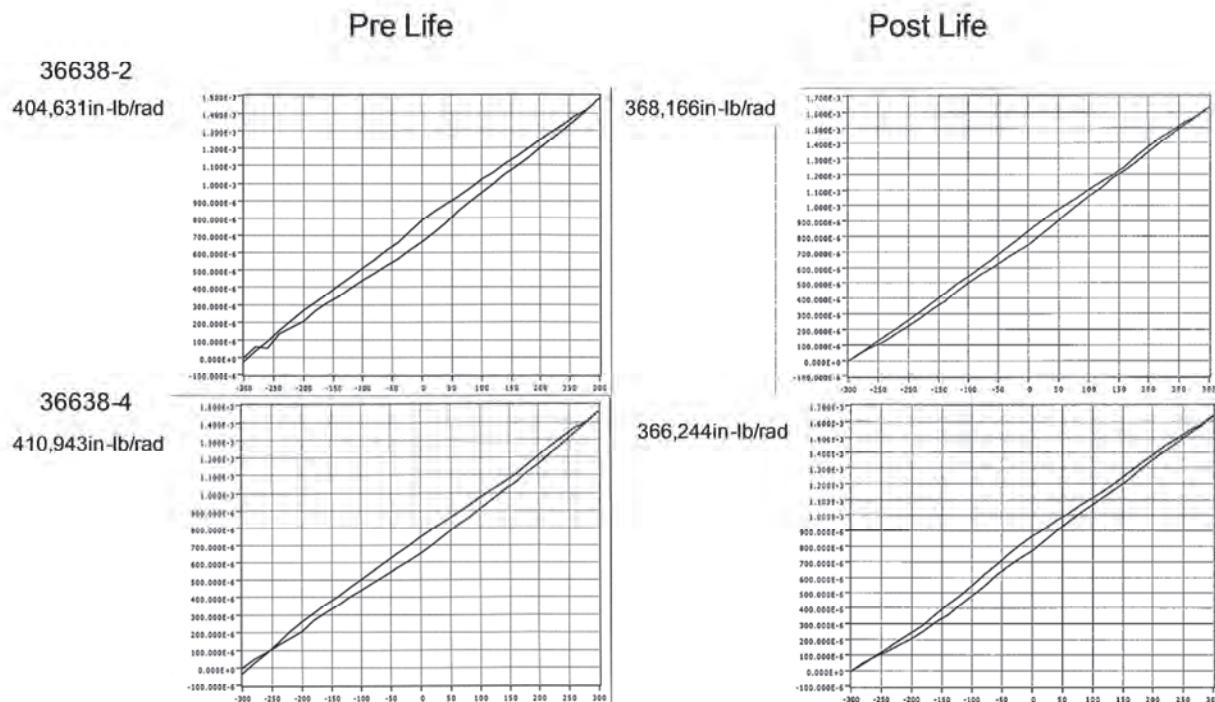
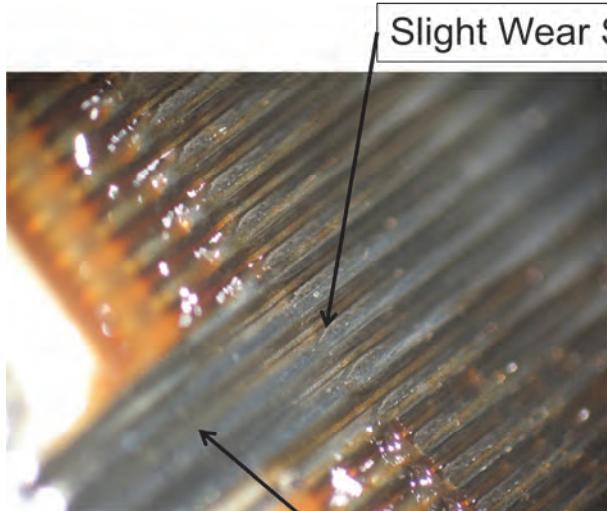


Figure 12: Pre and Post Life Torsional Stiffness Plots

36638-2, 15-5 & 15-5



36638-4, Nitronic 60 & 15-5

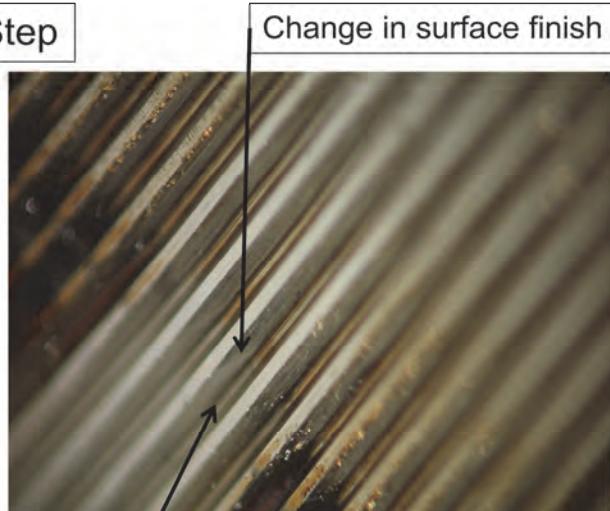
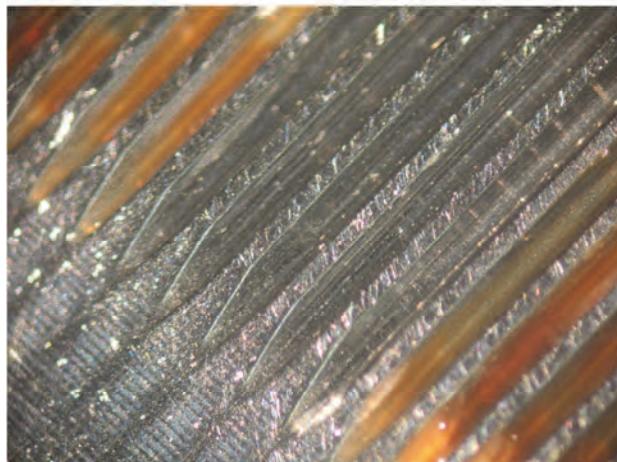


Figure 13 – Circular Spline Teeth, Post Vacuum Life

36638-2, 15-5 & 15-5



36638-4, Nitronic 60 & 15-5

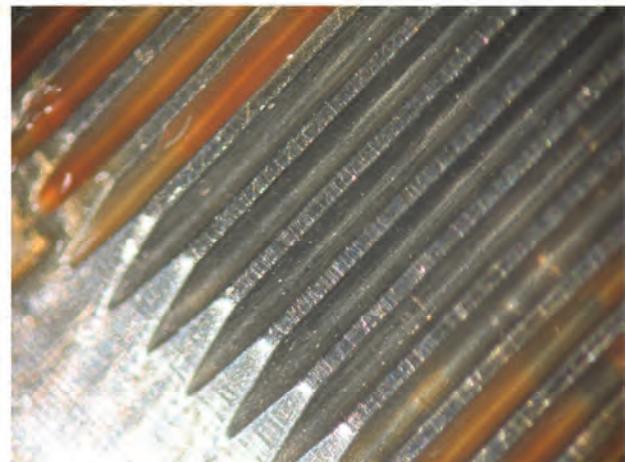
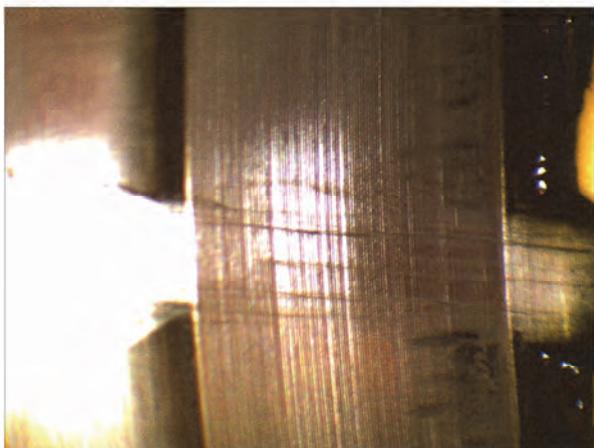


Figure 14 – Flex Spline Teeth, Post Vacuum Life

36638-2, 15-5 & 15-5



36638-4, Nitronic 60 & 15-5

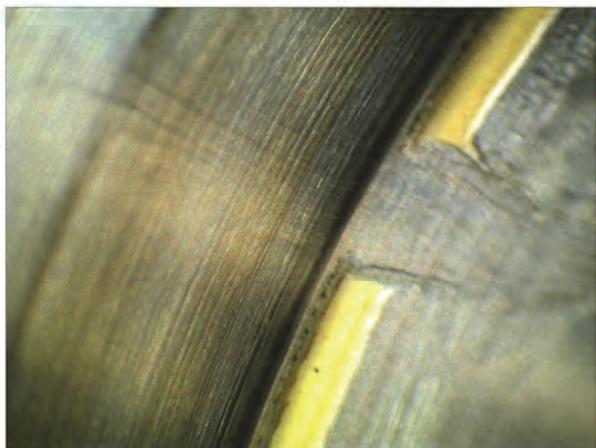


Figure 15: Flex Spline ID, Post Vacuum life

36638-2, 15-5 & 15-5



36638-4, Nitronic 60 & 15-5

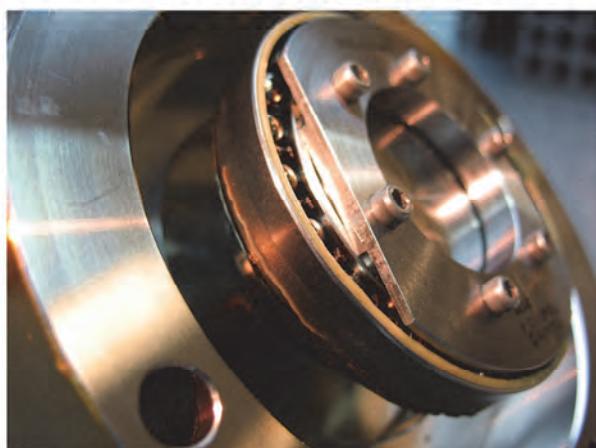


Figure 16: Wave Generator OD, Post Vacuum Life

36638-2, 15-5 & 15-5



36638-4, Nitronic 60 & 15-5



Figure 17: Wave Generator Balls, Post Vacuum Life

Vacuum Life Test Results Summary

The vacuum environment had little to no effect on the wear rate of the two Harmonic Drive gears tested. The slight differences in wear between the two configurations are not significant, and changes in wear between vacuum and ambient tests can be attributed to normal variation from unit to unit. The results of the vacuum life test supported the decision by the program to use the 15-5PH against Nitronic 60 Harmonic Drive gear configuration (36638-4) for the GPM program. Surprisingly, the 15-5PH against 15-5PH configuration (36638-2) would have also been an acceptable choice. A qualitative assessment of the key parameters of the post life inspection is shown in Table 4.

Table 4: Qualitative Summary of Vacuum Life Test Results

	36638-2	36638-4
	15-5PH / 15-5PH	Nitronic / 15-5PH
Stiffness Change	Good+	Good-
Circular Spline Tooth Wear	Good-	Good+
Flex Spline Tooth Wear	Good	Good
Flex Spline Cup	Average	Average
Wave Generator OD	Average	Average
Gear Teeth Lube	Average	Average
Wave Generator Lube	Average	Average

Conclusion

Accelerated Harmonic Drive gear life testing validated the concern that the heritage material combination of a Melonite Flex Spline running against a 15-5PH Circular Spline was not optimal for an extended life requirement of nearly ten times previously qualified. An alternate combination of a Melonite Flex Spline against a Nitronic 60 Circular Spline was also ruled out based upon test results. After completion of both Ambient and Vacuum accelerated life tests, two material combinations displayed test results indicating a high level of confidence in passing the increased life requirement. After joint deliberation between SNC and NASA GSFC, the combination of a 15-5PH H1075 Flex Spline and a Nitronic 60 Circular Spline was chosen for incorporation into the GPM HGAS and SADA actuators. Despite industry concerns over identical stainless steels operating in contact, the material combination of 15-5PH H1075 against 15-5PH 1075 performed nearly identically to the combination selected and would have been a high confidence selection as well.

References

1. Johnson, Michael R., Russ Gehling, and Ray Head "Life Test Failure of Harmonic Gears in a Two-Axis Gimbal for the Mars Reconnaissance Orbiter Spacecraft." *Proceedings of the 38th Aerospace Mechanisms Symposium*. May, 2006.

New Supplier - Hardware Duplication – Some Pitfalls

Edwin Joscelyn*

Abstract

Companies, for many reasons, often need to task a new supplier to duplicate the design and manufacture of a product that has already been qualified and flown on one of their earlier systems. This paper deals with such a situation. The conflicts that arise when required to include characteristics other than those defining the specific performance and dimensional requirements of the product is explored. While this paper uses the “reverse engineering” of a motor as the means to describe some of these problems, the basic conflicts and conditions can apply to other areas and products.

Introduction

The task was to duplicate the design of 3 different motor configurations. Although the performance specifications were clear and well written, there were no other mechanical design details provided other than the outline dimensions, winding location, and weight. The real challenge came from additional non-performance requirements that were specified. These requirements stemmed from the fact that these motors pre-existed from an earlier build cycle and the program was extremely sensitive to anything which differed from this earlier build in the new design. Winding profile, material, torque constants, resistance, inductance, harmonic distortion, detent torque, and drag torque parameters could not differ from the earlier designs. In addition some of the dimensions had tight tolerances on the OD and ID of the designs (e.g. 13 μm / 0.0005 inch). While these conditions alone might not seem to be in themselves presenting that difficult a design situation certain underlying factors proved otherwise.

In many cases, the task of “reverse engineering” is greatly simplified when there is a unit available which allows for physical inspection and disassembly of the product and the ability to make performance parameter measurements. This was not the case for this exercise.

Designing a duplicate and identical motor under these conditions is daunting at best. Attempting to get all of the performance parameters within specification is problematical. For example, one generally does not design a motor for a specific inductance. Inductance generally falls out as a by-product of the size of the motor, number of winding turns, laminations, etc. The motor’s torque constant K_t ($\text{N}\cdot\text{m}/\text{amp}$) is generally determined by the motor’s dimensions, materials, air gap and winding turns. The K_t is directly proportional to the number of turns while the inductance is determined by the number of turns squared. So, one can see the dilemma of attempting to converge these two parameters. This was only one of the issues...getting a pure sinusoidal BEMF waveform (< 2% harmonic distortion for the 3, 5th and 7th) was another of the major difficulties to solve.

We will attempt to walk through the iterative and somewhat frustrating process of arriving at a successful series of motors. This paper is not intended as a design review but rather as lessons learned when unrelated design restrictions are added to the design process. The work began in May 2008 and was completed in January 2010.

* Aeroflex, Hauppauge, NY

Description of motors

Let's call the 3 motor configurations T, G and H to depict the three different motor types. Within each configuration there were minor design changes for various applications. Every motor was to be redundant.

T – This motor configuration was a traditional design with the rotor on the inside and the stator on the outside. The design required a 0.75 slot per pole configuration, i.e. being an 18-slot, 24-pole, 3-phase, redundant machine. This configuration was necessary to meet a requirement that the phases were to be separated by 120 degrees mechanical and the primary and redundant phases to be separated by 60 degrees mechanical. The stator O.D. was given as 9.1427 to 9.1440 cm (3.5995 to 3.6000 inches) and the rotor I.D. was 4.8 cm (1.9 inches). Two different stack lengths were required for two designs within this configuration. The motors were to be sinusoidally commutated using resolver and drive electronics which were not part of the task at hand.

G - This configuration was an “inside-out” design, the rotor was on the outside and the stator was on the inside. The configuration for all 3 variations of the G motor design was as above, 24 pole, 18 slot, 3 phase, and redundant. The rotor specified O.D. was 12.6 cm (4.98 inches) and the stator I.D., which mounted to the program’s equipment, was given as 6.6040 to 6.6053 cm (2.6000 to 2.6005 inches). The different variations for this configuration were, again, in the stack length and motor performance parameters.

H – These motors were also of an “inside-out” configuration with the same slot design as in the G motor. The primary difference was size and performance parameters. The required rotor O.D. was 15.51 cm (6.105 in) and the specified stator I.D. was between 11.430 to 11.431 cm (4.5000 to 4.5005 inches).

Initial Major Design Restrictions and Design Concerns

Restrictions: The restrictions listed below are not necessarily required by a designer to comply with the performance parameters, and were partly responsible for some of the difficulties encountered during the design process. It was assed that these restrictions were a mandatory requirement of the customer for achieving an “identical” motor.

- 1 - Magnet material must be Samarium Cobalt
- 2 - Lamination material must be Carpenter 49 (High Nickel Steel)
- 3 - Primary and Redundant windings must be spaced at 120 degree intervals for each of the three phases alternating every 60 degree increment
- 4 - Stators were not to have a skew
- 5 - 0.75 slot per pole configuration with 18 slots and 24 poles was required.

Had these restrictions not been applied, several design techniques, such as 2.25 slot per pole design (24 poles 54 slots) without the angular separations, which were a more standard configuration for us, might have been used. Another familiar configuration, like a 72 slot (3 slots/pole) with a skew, might have also been employed. Given some degree of dimensional freedom, the Aeroflex zero-cog approach might also have been used thereby guaranteeing a low distortion sinusoidal BEMF waveform with very low drag and detent results. In other words, allowing a manufacturer to use more familiar designs, techniques, and materials while meeting the specific performance and environmental conditions can often lessen problem areas encountered than with the requirement to match exactly the mechanical and material design details as manufactured by another company.

Initial Concerns

1 - In many new design cases, existing laminations and their characteristics can be referred to laminations that have already been established and proven in previous designs. In this case the lamination designs needed to be designed from scratch. The task of deriving the exact geometry of the lamination, so important to duplication, was doubtful. The 0.75 slot/pole format would require investigating the magnetic flux details of the laminations using magnetic FEA analysis tools, which unfortunately is not always that precise. How close would we come?

2 – How would the resistance vs. inductance winding parameters balance against each other, both a function of the motor geometry as well as the copper windings?

3 - What is the BEMF waveform for the specified winding profile? Will it meet the 2% distortion requirement?

Major Parameters for T Motor

The development of the T motor was moderately painless and is illustrated to show how the T motors development was hoped to have also proceeded with the G and H configurations. It was considered painless because the performance parameters were more easily obtained without major modifications to any of the restrictions outlined above. Also, the T motor being the smallest of the 3 configurations made tooling for test easier to handle than the larger motors. Anyone having the experience of mounting rotors and stator with high energy magnets has sooner or later gotten his fingers bitten during the insertion of the rotor into the stator process if the proper tooling was not available. Special tooling "jacks" needed to be designed to allow the assembly into the test fixtures. The basic performance for one of the T motors is listed below:

* $K_t > 35 \text{ N-cm/amp}$ (49 in-oz/amp)

* $R = 2.6 \text{ ohms}$ within 10%, $L = 8 \text{ mH}$ within 25%

* Friction torque $< 1.8 \text{ N-cm}$ (2.5 in-oz) at 10 RPM

* Detent torque $< 3.5 \text{ N-cm}$ (5 in-oz)

A view of this motor is shown in Figure 1.

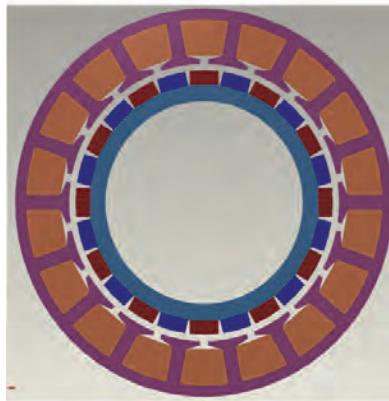


Figure 1. T Motor

A significant obstacle to the development and delivery effort was that Carpenter 49 lamination material was not available in the sheet stock we needed which required a special order with a long delivery schedule. It was decided to make the early prototypes using M-15 lamination material, which was

available and whose characteristics were well known to us. The plan was to learn as much as possible before the Carpenter material was received.

The usual manufacturing procedure to make a lamination stack is to stack and bond a number of 0.18 or 0.36-mm (0.007 or 0.014-inch) thick laminations, previously punched to shape, to make the desired stack height required. Since these laminations were of a new design, the technique used for these unique shaped laminations was to bond square sheets of 0.18-mm (0.007-inch) lamination stock to produce the height needed and cut the proper shape with an electrical discharge wire machine (EDM). The sheets are welded on the edges to make the electrical contact needed for the process. The non-recast EDM process produces a lamination stack with very well defined and smooth edges to the dimensions required. Some follow up machining, is required to obtain the 13 μm (0.0005 inch) tolerances required.

As a conservative strategy the thought was to start with a projected high Kt and a high detent prediction as a conservative approach to become familiar with the 0.75 slot per pole configuration. Using the measured data from a prototype M-15 lamination motor, we would then modify the air gap and turns to bring both parameters into specification. The FEA Kt and detent predictions as well as their ultimate measured parameters are shown in Figures 2 and 3.

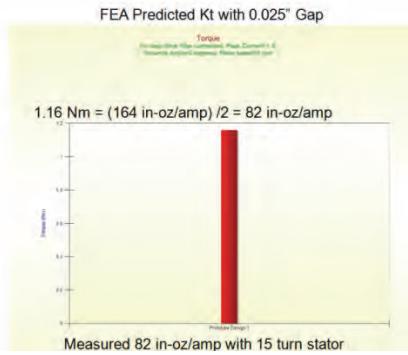


Figure 2. T Motor FEA Kt Prediction

Initial T motor Kt analysis and measurement data (Note: the program does not allow for separate primary and secondary windings so the $116 \frac{\text{N}\cdot\text{cm}}{\text{amp}}$ ($164 \frac{\text{in-oz}}{\text{amp}}$) value is for both primary and secondary energized).

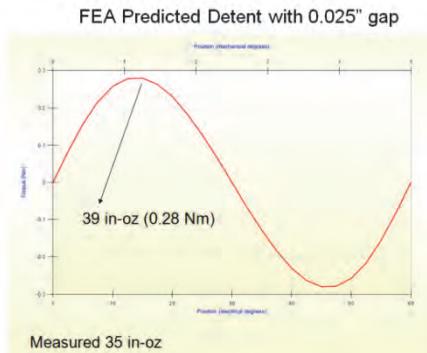


Figure 3. Initial T Motor Detent Analysis and Measurement

As can be seen the detent prediction was 28 N-cm (39 in-oz) and the measured detent on the prototype was 25 N-cm (35 in-oz). The Kt prediction and the measure Kt were spot on with $58 \frac{\text{N}\cdot\text{cm}}{\text{amp}}$ ($82 \frac{\text{in-oz}}{\text{amp}}$). Both of these were very high as expected compared with the required values of 3.5 N-cm (5 in-oz) and $35 \frac{\text{N}\cdot\text{cm}}{\text{amp}}$ ($49 \frac{\text{in-oz}}{\text{amp}}$). With these actual values increasing the air gap from 0.635 to 1.52 mm (0.025 to

0.060 inch) was predicted to achieve the detent and Kt parameters needed. The Carpenter material was now on hand and with the following air gap modification the results in Figures 4 were obtained with no surprises and were very close to the required values.

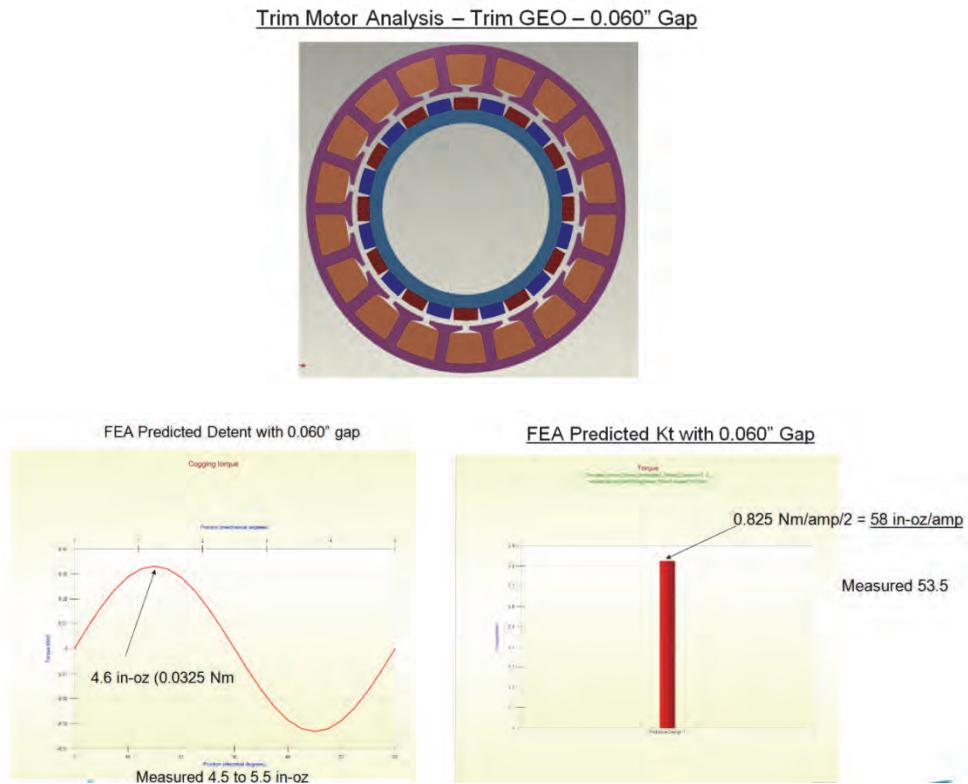


Figure 4. T motor Kt and detent with 1.52-mm (0.060-inch) magnetic air gap

To get some perspective on the windings, in order to achieve the required 2.6-ohm resistance it was necessary to use a winding of 5 wires of #29AWG and 3 of 28AWG for a total of 8 strands per coil. The inductance was fortunately within the range required (8 mH). It did, however, take several iterations of the winding turns to arrive at the final values of the design. So far so good!

The T motor BEMF curves are shown in Figure 5. The harmonic content was measured using the FFT functions of the scope (not shown).

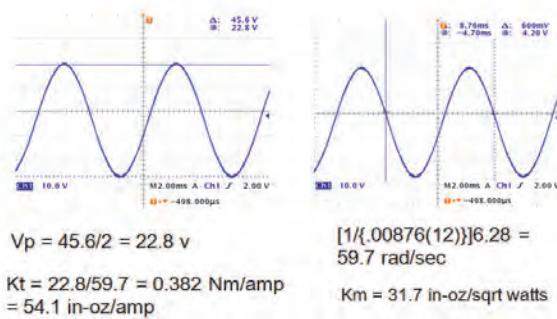


Figure 5. BEMF waveforms with 1.52-mm (0.060-inch) magnetic air gap

The spectrum analysis showed the harmonics to be less than the 2% limit. This motor performed as expected and promised similar expectations that the G and H motors would be equally accommodating...so it was hoped.

Major Motor Parameters for G Motor

The G and H motors were of an inside out design (rotor on the outside). This was not considered as an obstacle for obtaining the same results as was obtained for the T motors. The form factor for the G motors is illustrated in Figure 6.

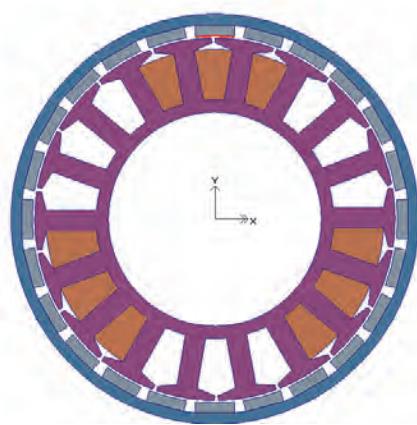


Figure 6. G motor

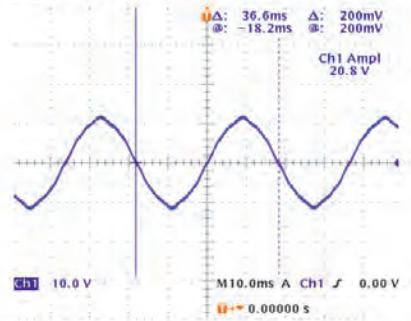
Major Specification Parameters

- * $K_t > 61 \text{ N-cm/amp}$ (87 in-oz/amp)
- * $R = 1.17 \text{ ohms}$ within 10%, $L = 3.58 \text{ mH}$ within 30%
- * Friction torque $< 11 \text{ N-cm/amp}$ (15 in-oz/amp) at 105 RPM
- * Detent torque $< 19 \text{ N-cm}$ (27 in-oz)
- * % Harmonic Distortion $< 2\%$

The initial lamination stack was already made with M-15 material and was not used since the Carpenter material had now arrived. (This becomes significant later on.)

The G motor, as with the T motor, began with a known smaller than expected air gap of 0.635 mm (0.025 inch). The FEA K_t was predicted to be 79.44 N-cm/amp (112.5 in-oz/amp) and the measured was 80.36 N-cm/amp (113.8 in-oz/amp) on this first prototype. The detent was predicted as 65 N-cm (92 in-oz), and the detent was measured at 64 N-cm (90 in-oz). The wave form, however, was not looking too good as seen in Figure 7:

GEO Main (EI) BEMF – Speed – 0.025" gap



Speed = 0.0366 (12 pole pairs) = 0.439 sec; $1/0.439(6.28) = 14.3$ rad/sec

$$23 \text{ v}/2 = 11.5/14.3 = 0.804 \text{ Nm/amp} = 113.8 \text{ oz-in/amp}$$

Figure 7. G motor BEMF waveform

The shape of the BEMF wave looked less like a perfect sine wave and harmonic distortion was viewed as a potential problem. The gap was then opened to 1.27 mm (0.050 inch) to lower the detent as well as the Kt with the hope this would also improve the distortion issue. The results were as follows:

Kt dropped 80.36 N-cm/amp (113.8 in-oz/amp) to 65.2 N-cm/amp (92.4 in-oz/amp)

Detent dropped from 69 N-cm (98 in-oz) to approximately 18 – 20 N-cm (25 – 28 in-oz)

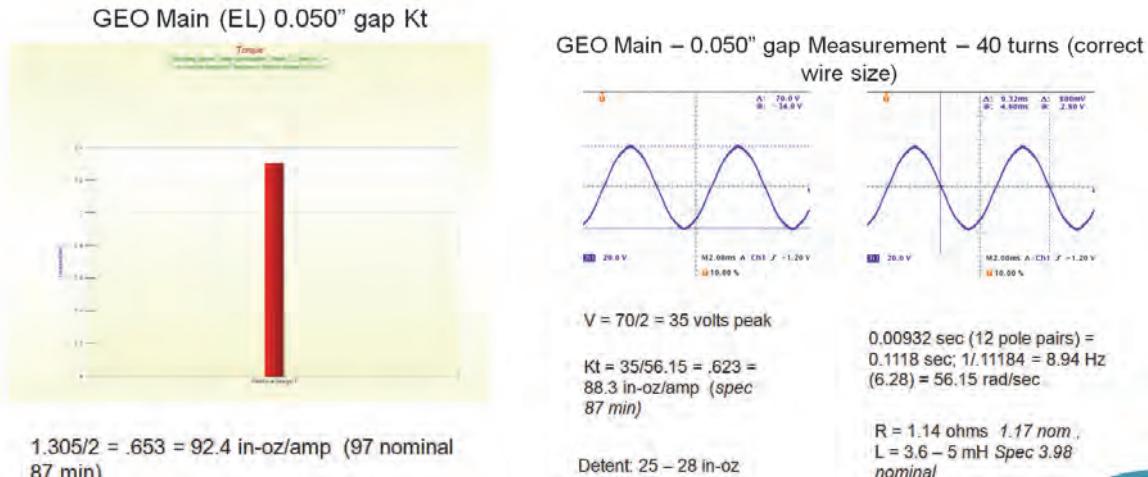


Figure 8. Motor with 1.27-mm (0.050-inch) air gap

The waveform became a little less peaked but nevertheless was still apparently distorted and a concern. This was caused by the 5th harmonic and was above the 2% spec and was unacceptable.

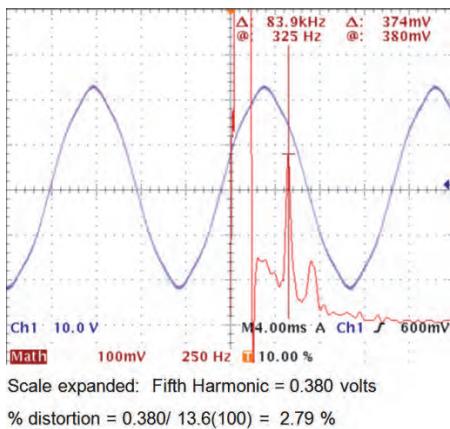


Figure 9. G motor Harmonic distortion

It was postulated that the lamination shape was perhaps deficient and that also shaping of the rotor magnets would perhaps contribute to improving the harmonic distortion. Inspection of the FEA analysis (Figure 10) did not show magnetic saturation in any part of the lamination material.

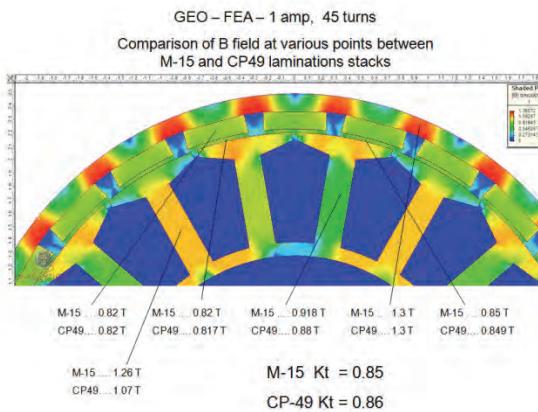


Figure 10. Flux Density Comparison of Lamination Materials

There were several other issues other than the distortion to address such as inductance and detent. It was hoped that correcting these deficiencies would help correct the distortion issues. A brief description of the inductance and detent improvement efforts are summarized in bullet form:

- The inductance was too high so the turns were reduced from 45 to 38 (inductance is a function of the turns squared). To compensate for the loss of Kt due to the turns reduction, decrease the air gap. This worked as intended for the inductance and Kt, but the detent was now 3 times higher than required due to the air gap reduction.
- A small skew was introduced into the lamination structure which reduces detent. The detent was now OK but the Kt dropped below the desired level due to the skew.
- Used higher energy product Neodymium magnets instead of samarium cobalt. Kt improved but still too low
- Bring coils to 40 turns to improve Kt with inductance still OK; attempt to go back to Samarium Cobalt magnets...Kt just $0.7 \text{ N-cm}/\text{amp}$ ($1 \text{ in-oz}/\text{amp}$) below the minimum; inductance marginal....parameters too marginal to attempt production. Went back to 180 C Neodymium, ultimately used for production.
- Back to distortion issue, solving may resolve the Kt, detent and inductance issues.

- Distortion remained above the 2% level for all of the above modifications

Some of the lamination styles that were tried to reduce the harmonic distortion are shown in Figure 11. Recognize that this is a time consuming process to build the stacks, EDM the laminations, machine, and coat with an insulator as well as wind and insert the coils.

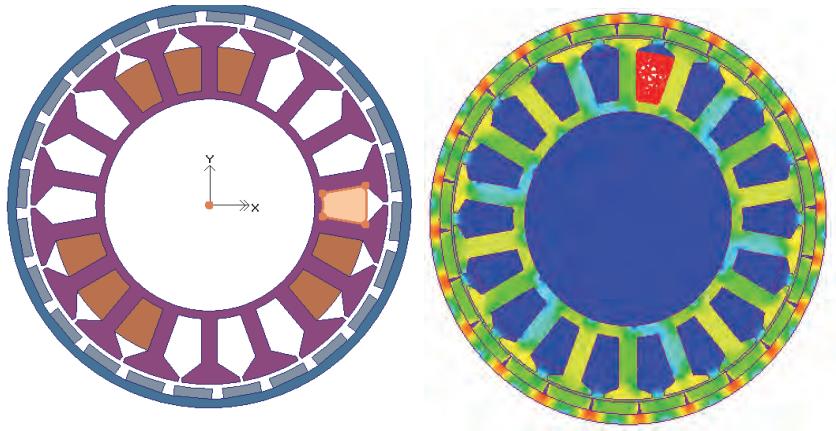


Figure 11. Pole shoe shaping, tooth gap, and magnetic span variations were tried.

FEA analysis alone was not considered a viable approach alone in that the difference of distortion was only about 1%. Shapes tried were: wide boot height to narrow boot height, wider tooth widths, wide tooth to tooth gap to narrow tooth to tooth gap, wide magnet to magnet spacing to narrow magnet to magnet spacing - all provided no change in harmonic distortion to bring values below the 2% limit. There were also models made with the edges of the magnets rounded.

At some point defeat must be acknowledged and a call for help initiated, be it self imposed or externally suggested. The suggestion was to call in help from an recommended and established consultant. This was accomplished and was followed by an impressive 14-page report from the consultant. The report offered a solution. The proposed solution was so deceptively simple that it was welcomed with great enthusiasm. At the same time, the report gratifyingly duplicated the non-sinusoidal BEMF results we were observing, as well as duplicating other motor parameters, so high expectations were anticipated.

The solution based on a detailed FEA analysis (using a different analysis tool than the ones we were using) was to make the magnets as flat rectangles rather than the having the normal surface curvature mirroring the stator curvature as in traditional designs.

A test motor was then wound, magnets purchased, and tested with the wonderful results that all of the parameters, including harmonic distortion were now within specification. A bonus feature was the detent was reduced from 18 to 9 N-cm (25 to 13 in-oz) giving a good margin.

What then followed was the production manufacture and testing of the modified rotor design. *Total disbelief....*the motor performed as poorly as it had before the rotor magnet change. What had happened? Our thoughts went back to the CP49 and the M-15 materials. We always felt (just experience), despite the FEA analysis showing the reasonable flux paths within the two materials (Figure 10) that the M-15 was the proper way to go given past experience with the CP49 Hi nickel materials annealing variations.

What had happened is that the flat magnets were mistakenly tested with the original M-15 stator that, as you recall, was originally made but never used. The M-15 lamination stack had gotten mixed up with the CP49 lamination stack. To prove that the model that was successful with the flat magnets was using M-15, a known M-15 stator stack was then wound and tested. Back to the good results tested!

Tests with older curved rotors using the M-15 stator also showed the same excellent results indicating that the issue was with the CP49 material and not anything else. The lesson learned here is that FEA analysis is a path towards good designs but is not the end all. Practical machines with practical materials must ultimately be the final say. We stayed with the flat magnets because we had purchased the entire programs supply. In retrospect, had we had been able to have gone with the M-15 material (usually our preferred material for this type of motor) most of these delays and perturbations relative to the harmonics would not have occurred or been necessary. A photo of the G motor is shown in Figure 13.

The data in Figure 12 shows the distortion improvement with the M-15 material from 2.79% to 1.57%.

Fundamental 18.4 volts; 5th Harmonic at 0.26 volts

$$\text{Harmonic distortion} = 0.260/18.4 = 0.0157 = 1.57\%$$

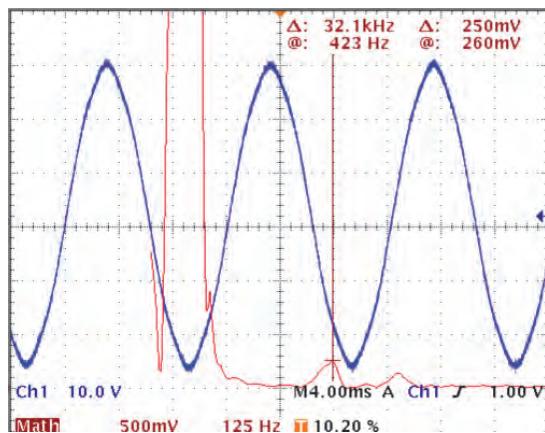


Figure 12. M-15 Harmonic Distortion Data for the M-15 Material



Figure 13. Photo of the G Motor - Rotor is encapsulated in titanium ring

Major Motor Parameters for H Motor

The H motor, also an inside out design, presented with a whole different set of issues. The initial design using CP49 and Samarium Cobalt magnets resulted so enormous a difference between performance and requirements that an initial drastic step needed to be taken before any iteration would be possible.

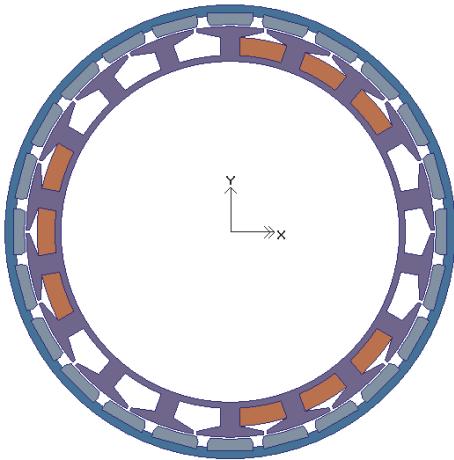


Figure 14. Geometry of the H motor

The K_t , detent and distortion below represent the performance requirements:

- * $K_t > 56 \text{ N-cm/amp}$ (80 in-oz/amp)
- * $R = 0.84 \text{ ohms}$ within 7%, $L = 2.28 \text{ mH}$ within 30%
- * Friction torque < 19 N-cm (27 in-oz) at 272 RPM
- * Detent torque < 15 N-cm (21 in-oz)
- * % Harmonic Distortion < 8%

The initial lamination stack was made with CP49 material. The waveform and detent were much worse than seen of the G motor and the decision to use M-15 at the outset was immediately made. The result for the first CP49 H motor is shown in Figure 15.

The K_t was measured at 183 N-cm/amp (259 in-oz/amp) and the detent was over 141 N-cm (200 in-oz).

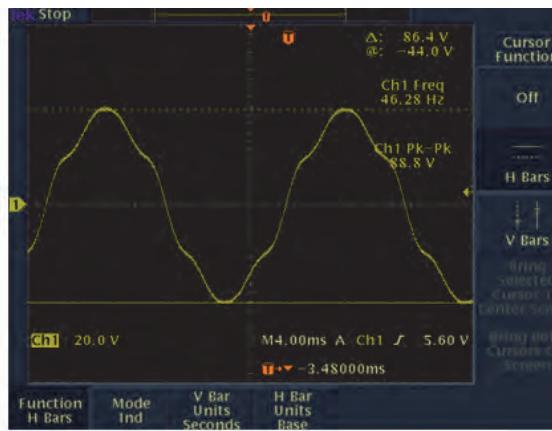


Figure 15. BEMF Curve with CP 49 and 0.635-mm (0.025-inch) air gap

The first attempt using M-15 material resulted in a K_t of about 79.8 N-cm/amp (113 in-oz/amp) with the detent being approximately 64 N-cm (91 in-oz). The decision to skew the stator was made to reduce the detent and smooth the waveform with the results shown in Figure 16.

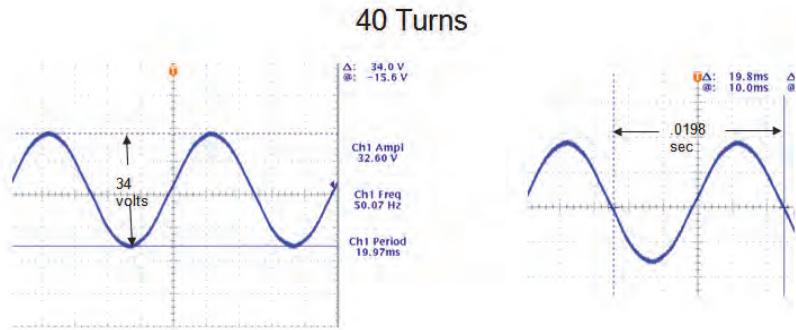


Figure 16. BEMF for H motor with M-15 Material

Again, exploring the flux density differences between the FEA analyses of the materials (Figure 17), there again did not seem to be much difference to cause this great disparity of performance for the H motor due to material as seen between Figures 15 and 16.

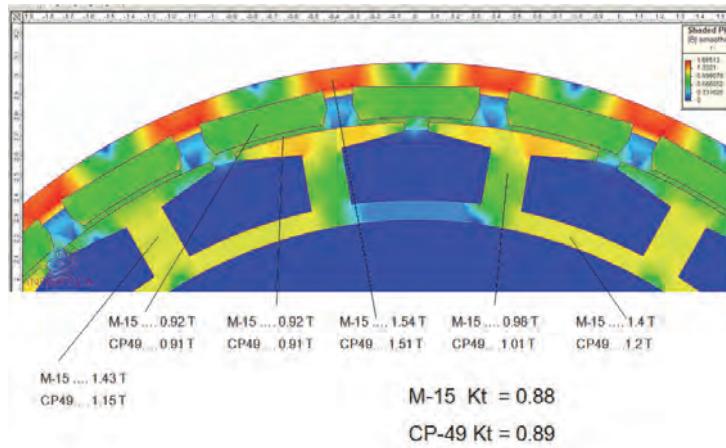


Figure 17. Comparison of lamination material for the H motor

This motor was most critical in terms of balancing the flux carrying capability of the laminations with the amount of copper area available affecting K_t , inductance and resistance. The motor needed a full complement of 40 turns (6 of #28 and 2 of #29 AWG wire) to conform to the specification requirements (K_t , resistance and inductance). A bonus of the skew was that the detent torque was reduced to about $\frac{1}{3}$ of specified allowable which was well received.

The wire would not fit within the area needed for the lamination design. (Several tooth widths were tried to arrive at the final configuration). Not a quick task when the programming, EDM process, lamination coating and winding time factors are considered. As a result, the motor could not be wound and inserted in the normal production manner. Normally, a string of coils per phase is wound on a mandrel, loosely tied to hold each coil of 40 turns together and then inserted into the stator as whole coils placed wire by wire into each stator slot. In this case the slot fill factor is so high that this would not allow the coil bundles to fit into the slots, just missing by a few percent. The stator needed to be hand wound, turn by turn, into the slots allowing each turn to be tightly fit into the slot maximizing the space available with just the right length of wire to make the resistance specified. Under these conditions it is necessary to have a very patient and amiable technician in your employ!



Figure 18. Photograph of the H motor with the lamination skew

Summary

With the above trades and compromises, all of the motors styles ultimately made their way into successful production cycles.

In summary, what was needed to be changed from the 5 initial restrictions (which were not specific to the performance requirements) in order to meet the performance criteria is as follows:

1 - Magnet material must be Samarium Cobalt - In one case (G motor) higher energy product Neodymium magnets needed to be substituted.

2 - Lamination material must be Carpenter 49 (High Nickel Steel) – In two cases silicon steel was needed to replace the high nickel steel.

3 - Primary and Redundant windings to be mechanically spaced at 120 degree intervals for each of the three phases alternating every 60 degree increment - Preserved

4 - Stators were not to have a skew – In one case (H motor) a partial skew was required for detent and waveform conformance.

5 - Parameters must meet the tight specification values – In one case some relief was required for the inductance values

6 - 0.75 slot per pole configuration with 18 slots and 24 poles was required. - Preserved

The major lesson learned from this project is to have give and take discussions between parties to determine which of the specification requirements are truly pertinent to the performance as opposed to those which would be nice to have based on existing hardware.

Development of the Vibration Isolation System for the Advanced Resistive Exercise Device

Jason H. Niebuhr^{*} and Richard A. Hagen^{**}

Abstract

This paper describes the development of the Vibration Isolation System for the Advanced Resistive Exercise Device from conceptual design to lessons learned. Maintaining a micro-g environment on the International Space Station requires that experiment racks and major vibration sources be isolated. The challenge in characterizing exercise loads and testing in the presence of gravity led to a decision to qualify the system by analysis. Available data suggests that the system is successful in attenuating loads, yet there has been a major component failure and several procedural issues during its 3 years of operational use.

Introduction

Resistive exercise (weightlifting) is prescribed for crew of the International Space Station (ISS) to maintain muscular strength and bone density during long duration space flight. However, the repetitive nature of exercise induces vibratory loads that can degrade the sensitive ISS micro-g environment and reduce its structural fatigue life. The Interim Resistive Exercise Device (iRED) was flown aboard the ISS from 2002 through 2008 as the primary means for resistive exercise. Ongoing maintenance issues, increased performance requirements, and the need for a Vibration Isolation System (VIS) eventually drove the need for a new clean-sheet exercise machine, called the Advanced Resistive Exercise Device (ARED) [1]. ARED creates resistance with a pair of vacuum cylinders that are connected through a variable length lever to an adjustable height bar as shown in Figure 1. The exerciser can stand, sit, or lie on the platform or bench (not shown) to perform a variety of exercises.

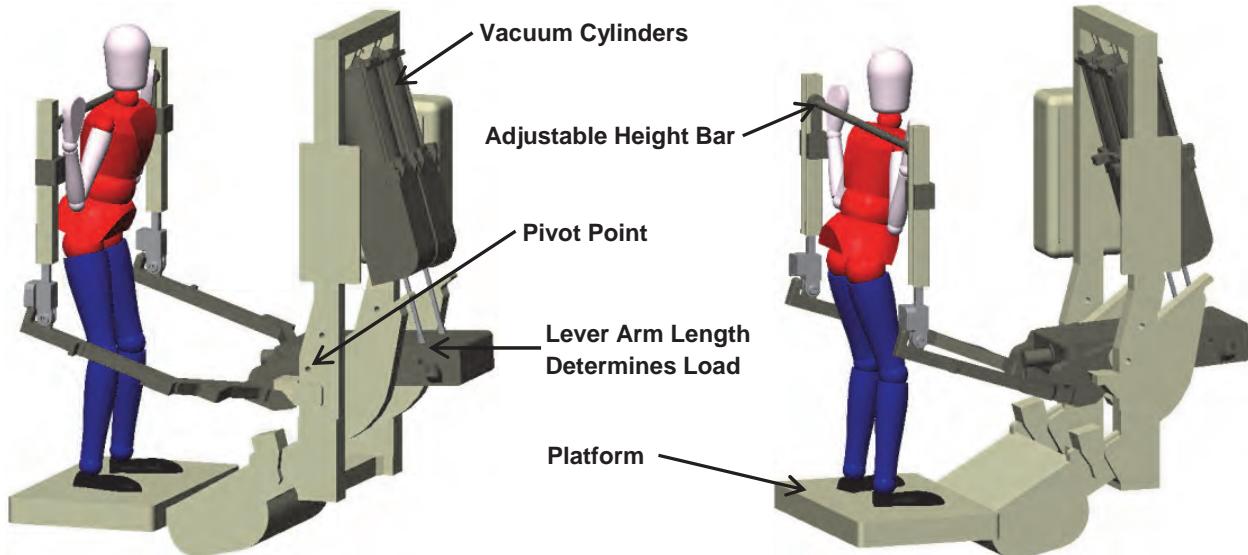


Figure 1. The Advanced Resistive Exercise Device

* Formerly with NASA JSC, now with Apogee Engineering at the US Air Force Academy, Colo. Spgs., CO

** NASA Johnson Space Center, Houston, TX

The primary micro-g requirement is a frequency-dependent acceleration limit at the US Lab and Columbus module rack interfaces. Structural dynamics transfer functions are available to quantify the acceleration at those racks as a function of input load at the ARED location within the ISS. With the assumption of equal loading in all axes, the acceleration limit and transfer functions can be taken together to consider the requirement in terms of allowable load. A similar frequency-dependent load limit is required to preserve ISS fatigue life. The composite allowable load enveloping both micro-g and structural fatigue requirements is shown in Figure 2. This is a simplified and conservative view of the requirements,

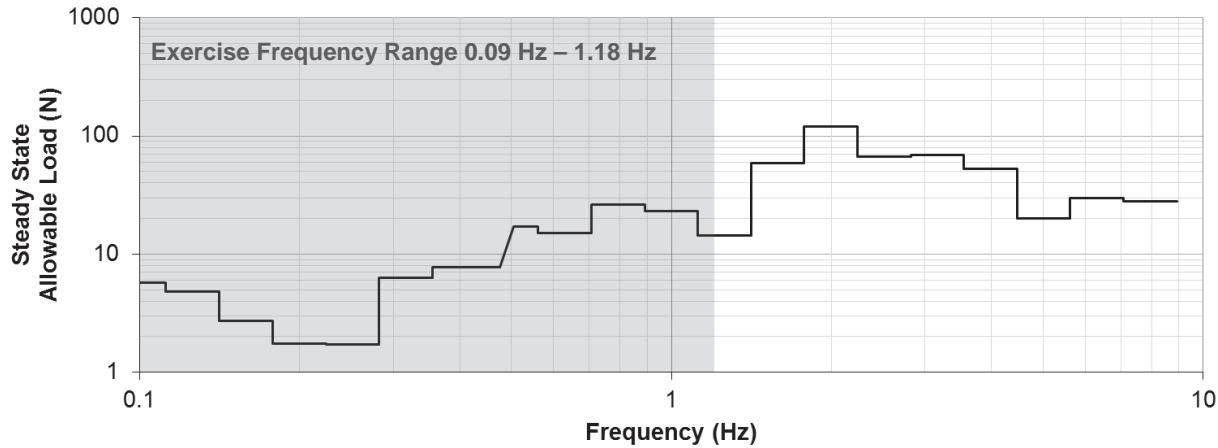


Figure 2. Allowable Loads Requirement and Exercise Frequency Range

yet highly insightful. The graph highlights the most significant challenge to the design; a major ISS structural mode exists near 0.24 Hz which can be seen as a steady state allowable load of only 1.7 N (0.4 lbf) between 0.18 Hz and 0.28 Hz. As shown by the shaded area of the graph, this is well within the 0.09 Hz – 1.18 Hz range of exercise frequencies recorded during the ARED man-in-the-loop test (MILT) [2]. Analysis of the ARED in a non-isolated configuration suggests that exercise loads can be as high as 67 N (15 lbf) at 0.24 Hz, requiring attenuation by more than an order of magnitude.

Analytical Approach

A rigid body dynamic model was created in the motion analysis software visualNastran 4D from MSC.Software Corporation. This software was chosen over general numerical computing codes for its native 3D visualization capabilities and ease of use. This made it possible to examine many different design concepts and better understand how they worked. Though somewhat controversial, it was felt that the cost and complexity of an actively-controlled isolation system wasn't justified. Being able to visually simulate system dynamics was essential in convincing both technical and non-technical stakeholders alike that a passive isolation system would be sufficient. Model development focused on three distinct elements: a geometrical and mass model of the ARED, a geometrical and mass model of the exercising crew member, and a mathematical model of the VIS.

Development of the ARED model was straightforward as solid geometry was imported from computer-aided design (CAD) software after being simplified into 12 major subcomponents by suppressing details like fasteners, fillets, and lightening pockets. Detailed mass properties of the subcomponents were retained from the original CAD model. Appropriate constraints were applied to the model to simulate fixed, rotational, and sliding joints. Capturing this level of detail kept the computing requirements manageable.

The exercise model consists of a CAD model human constrained to simulate exercise motion when driven by displacement. Figure 3 illustrates how the human model and subcomponents of a non-isolated ARED



Figure 3. Non-Isolated ARED and Human Model Motion During Squat Exercise

both move throughout the stroke of a squat exercise. The y-axis is parallel with the long axis of ARED, the z-axis positive toward the exerciser, and the x-axis completes the right-handed Cartesian system. Exercise variables include type, stroke, crew size, and frequency. The exercise types and stroke lengths range from a squat moving nearly 90% of the body's mass through 0.70 m (27.5 in) of stroke to a neck flexion that moves less than 6% of the body's mass through less than 0.23 m (9 in) of stroke [3]. However, the squat, dead lift, straight leg dead lift, and heel raise are worst-case and envelope all other exercises in the analysis because they move the most amount of body mass over the greatest distance. The 95th percentile American male represents the heaviest crew analyzed while the 5th percentile Japanese female is the lightest [4]. Data from the ARED MILT defines exercise stroke profiles and statistically quantifies exercise frequency. Figure 4 shows a box plot of the exercise frequencies for 3 of the worst-case exercises. The middle dash represents the average frequency, the box envelopes ± 1 standard deviation, and the whiskers represent the extreme value recorded. Either idealized sinusoidal

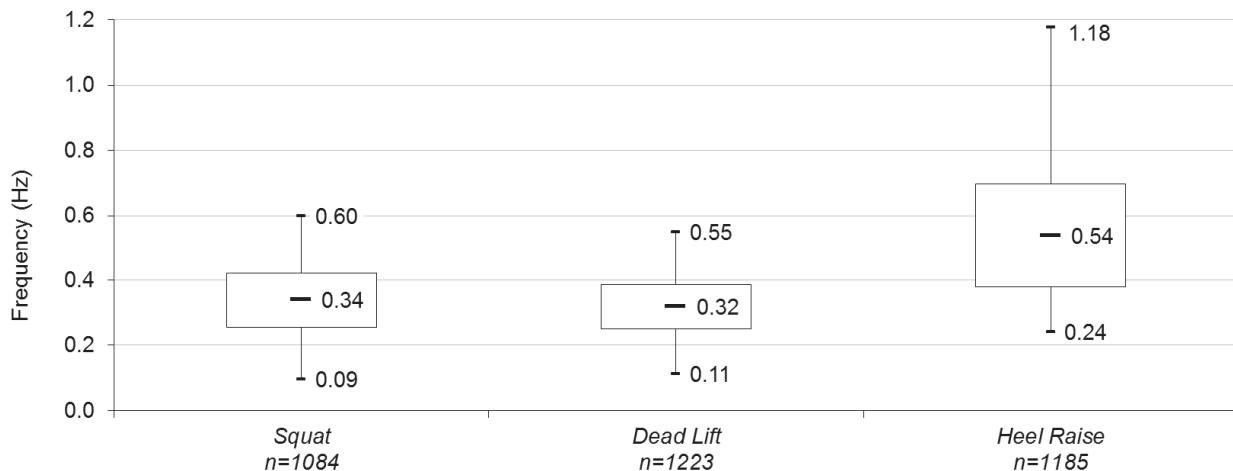


Figure 4. Box Plot of Frequency Statistics for 3 Exercises

or real stroke profile data derived from testing can be used to drive the human exercise model. Use of idealized sinusoidal data tends to be more severe because spectral energy is focused into a singular frequency, whereas real stroke profiles capture the inherent variability in human exercise. The idealized sinusoidal approximation becomes worse at lower exercise frequencies that are typically distinguished by longer pauses between exercise cycles.

The VIS model consists of mathematical definitions of spring and damping rates. Many different concepts were examined and several lessons learned:

- 1) The enveloping exercises only excited the system in 3 degrees of freedom (DOF) planar motion: Translation along the y- and z- axes, and rotation about the x-axis. Trading mounting rigidity for

isolation by reducing stiffness in only these 3 DOF is both sufficient and provides a certain level of safety when suspending nearly 567 kg (1250 lbm) in a micro-g environment.

- 2) Each enveloping exercise excites the 3 DOF differently. Squats and heel raises primarily excite the y-axis and rotation about the x-axis. Dead lifts, particularly the straight leg variant, tend to excite all 3 axes.
- 3) Decoupling the VIS DOF by lining them up with the ISS axes made the design of the system much easier. Changes to spring or damping rates in one axis only affect that axis.
- 4) Analysis lessons learned 2 and 3 combined with the knowledge that structural dynamics transfer function response varied in each axis allowed the stiffness and damping of the system to be optimized against the micro-g and structural fatigue requirements.

A key principle in vibration isolation is choosing isolator properties such that the natural frequency of the system is below the forcing frequency. In this case the forcing frequency is the aforementioned exercise frequency range from 0.09 Hz to 1.18 Hz. The natural frequency, f_n , is given by:

$$f_n = \frac{1}{2\pi} \sqrt{\frac{k}{m}} \text{ (Hz)}$$

Where k is the spring rate and m is the mass. Additional damping was added to more quickly dissipate energy in the system. Transmissibility, T , is a measure of the amplification of the isolation system or ratio of output to input. It is given by:

$$T = \frac{\sqrt{1 + \left(2 \cdot \frac{f}{f_n} \cdot \zeta\right)^2}}{\sqrt{\left(2 \cdot \frac{f}{f_n} \cdot \zeta\right)^2 + \left(1 - \left(\frac{f}{f_n}\right)^2\right)^2}}$$

Where f is the forcing frequency and ζ is the ratio of damping to critical damping. Values of $T > 1$ signify an amplification of input load, whereas values of $T < 1$ signify an attenuation of input load. The chosen spring rates, percent damping, resultant natural frequencies, and amplification at various frequencies are shown in Table 1 for each of the 3 DOF.

Table 1. VIS Properties and Isolation Qualities

Axis	Spring Rate	Damping	Natural Frequency	Amplification, T (0.09 Hz)	Amplification, T (0.24 Hz)	Amplification, T (1.18 Hz)
Y	70 N/m (0.4 lbf/in)	11%	0.06 Hz	0.7	0.08	0.01
Z	175 N/m (1 lbf/in)	10%	0.09 Hz	1.9*	0.19	0.02
X (rotation)	0.6 N•m/deg (5.2 in•lbf/deg)	17%	0.05 Hz	0.4	0.08	0.01

* Amplification based on 0.11 Hz minimum deadlift exercise frequency since the squat exercise creates minimal excitation in z-axis

The spring rates, particularly in the y-axis, had to be extremely low to keep the natural frequency of the system from overlapping the exercise frequency range and to meet the micro-g and fatigue requirements. The z-axis motion is generally only a fraction of what is seen in either of the other two axes which is why the spring rate and the resultant natural frequency was increased to nearly encroach upon resonance in a worst-case scenario. This was necessary to minimize the motion envelope; one of several other issues that developed as a result of the low spring rates. Inertial accelerations applied to ARED and friction forces also became issues. While ARED is allowed to move in response to exercise, the inside of the ISS is a relatively limited space and there was a possibility that a crew member could hit their head while exercising. Travel limits were setup to prevent this from occurring. Another consideration was the effect of inertial accelerations applied to the ARED system as a result of events like reboost and docking. These events are enveloped by a 0.4 g load factor applied in any direction and cause the ARED to move across the motion envelope and collide with the end of travel limits. This potentially overloads the interface and exceeds a transient acceleration micro-g requirement. Much larger dampers, called snubbers, were sized and located at the travel limits to attenuate those loads. They were selected by calculating the velocity of ARED due to the inertial acceleration and sizing them to efficiently dissipate the energy. Friction had to be considered because, if too high, it had the effect of causing the entire system to "inch-worm" until it reached one end of the motion envelope, potentially reacting repeatedly against the end of travel limits and not re-centering. A special effort was made during the mechanical design phase to select components with low friction as well as to include its effects within the analytical simulation.

Mechanical Design

To stay within cost and schedule constraints many commercial off-the-shelf (COTS) components are used in the design of the VIS. It is a nearly symmetrical assembly composed of 2 plate assemblies connected by a beam as shown in Figure 5.

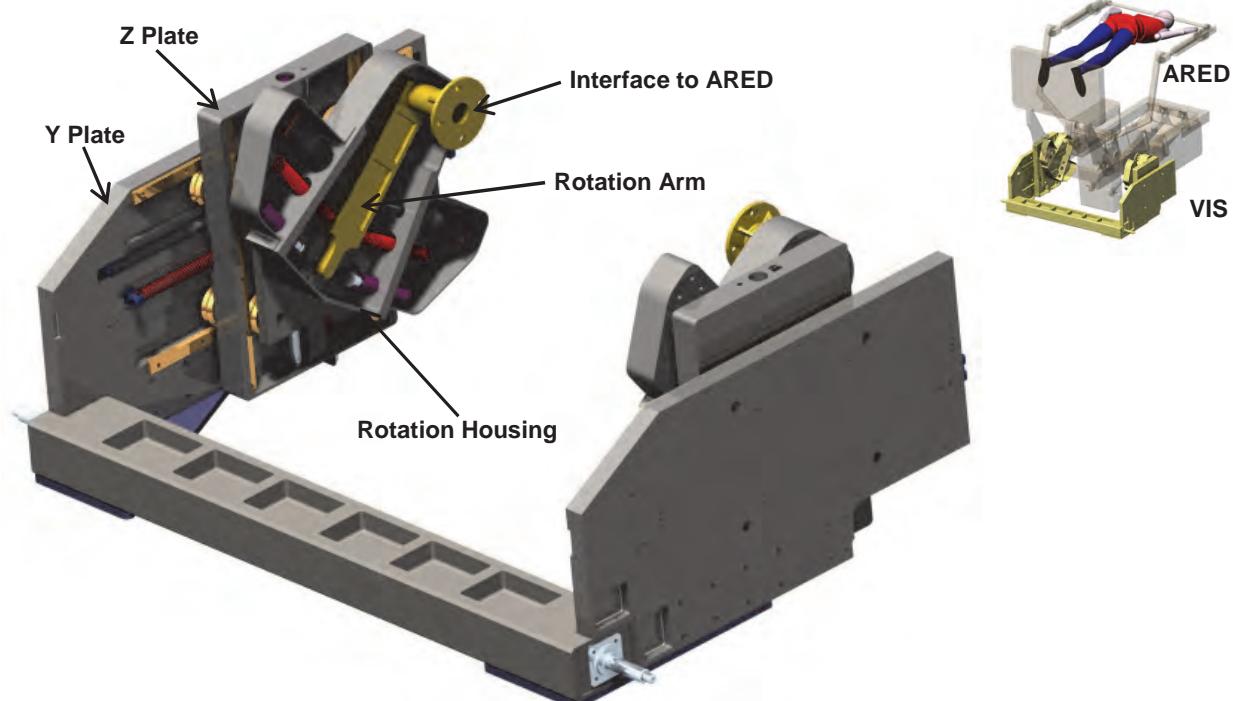


Figure 5. The Vibration Isolation System

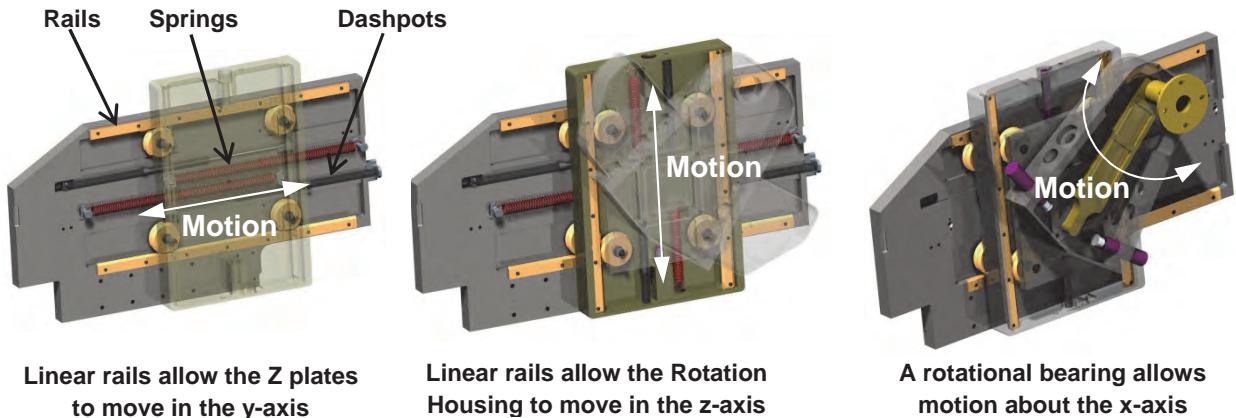


Figure 6. The Left Plate of the Vibration Isolation System

Each side has half of the linear and rotational bearings that constrain motion to 3 DOF and the isolation components that attenuate exercise loads. Figure 6 shows that the Y Plate contains linear rails, springs, and dashpots that connect to the Z Plate, allowing motion in the y-axis. The Z Plate has the same components that allow the Rotation Housing to move in the z-axis. Lastly the Rotation Housing has a bearing to allow rotational motion and an arm to convert linear spring and damper forces into torque about the x-axis. The allowable deflection between the left and right plates was specified as ± 0.051 mm (± 0.002 in) to reduce the possibility of the VIS binding under load. This placed a burden on manufacturing since interface joints and bearing rail surfaces were held to extremely tight tolerances. To minimize misalignment due to accumulated tolerances, there are only 11 VIS structural components from one side of ARED to the other. The VIS was assembled in a fixture to verify alignment and set the spacing of the two halves.

The linear bearings that constrain motion were chosen from amongst several candidates. The DualVee guide wheel design exhibited low friction, robustness, and ease of maintenance. Rails are made from 420C stainless steel while the bearings are made from 440C stainless steel, simplifying the material certification process. The low bearing friction is achieved by using a bearing with shields instead of seals, high quality Rheolube 2000 grease, and just enough bearing preload to maintain linear rigidity. The preload in the bearings is adjusted until the maximum load needed to move a given plate is 1.3 N (0.3 lbf). The double row angular contact design of the DualVee provides a robust bearing that can handle large static loads. Finally, by separating the bearing elements from the track as shown in Figure 7, maintenance is significantly reduced since dirt and debris attracted to the rails does not come in contact with the ball bearings. They also have a better tolerance for bearing misalignment than other linear bearing systems tested.

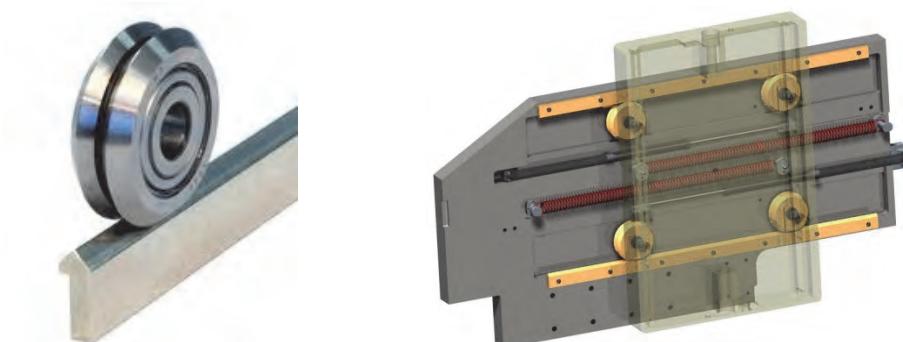


Figure 7. DualVee Bearing and Rail

Rotational motion of the VIS is constrained with a SKF double row angular contact bearing that also uses shields instead of seals and is lubricated with Rheolube 2000.

Low rate springs attenuate exercise loads in all axes. 17-7 PH stainless steel extension springs are preloaded against one another to maintain a constant spring rate across the motion envelope and keep ARED centered. Compression springs were not favored because the combination of length and low spring rate would have required a support to prevent buckling. It was felt that the resultant friction would have reduced spring life, increased load variability, and perhaps resulted in a noise problem.

The dashpots act to dissipate energy in the system by reacting to motion with a force proportional to velocity. Airpot dashpots were chosen for their simple design, use of an inert working fluid (air), adjustability, and advertised long life. A similar component is successfully used in the Active Rack Isolation System that protects ISS experiment racks from vibration. The dashpots consist of a carbon-graphite piston in a borosilicate glass cylinder with Rulon-lined ball joints at each end of the piston rod to allow for misalignment as shown in Figure 8. An adjustable screw orifice with a check valve adjusts the damping rate in the pull direction. The dashpots are wrapped with Kapton tape to contain debris in the event of breakage.

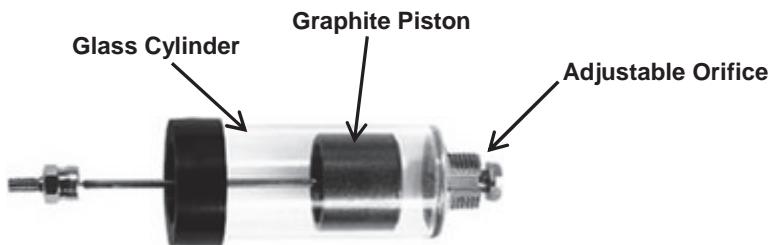


Figure 8. Airpot Dashpot

The snubbers that attenuate impact loads from reboost and docking events are located to engage at the end of the motion envelope. Oil-filled models from ACE Controls were chosen because of their compact size and adjustability. The rotation axis snubbers are shown in Figure 9.

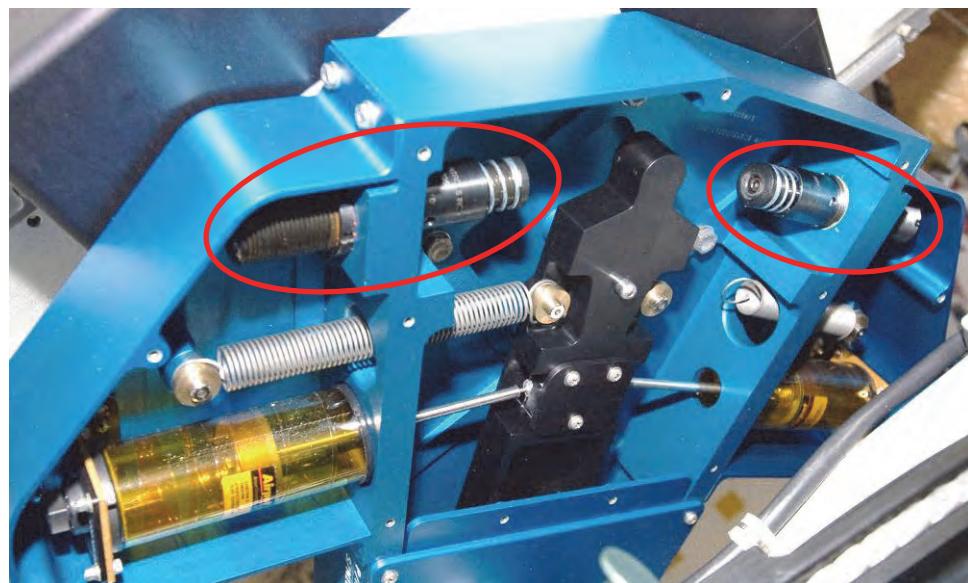


Figure 9. Snubbers Mounted in the Rotation Housing

A lock-out pin inserted by the crew passes through the rotation arm and both plates, anchoring the VIS in the centered position to protect it from damage when not in use. In addition to creating simple crew interfaces, significant effort was expended in designing the VIS to be easy to inspect, repair, or even upgrade if needed. All of the isolation components are accessible by removing covers and serviceable using standard ISS tools. Individual components are replaceable instead of requiring large subassemblies to be kept as spares.

The VIS attachment to the seat track in ISS is designed to accommodate misalignment due to initial tolerance variations or changes over time due to temperature or pressure fluctuations. This is accomplished by attaching at 3 points with sliding trunnions through spherical bearings as shown in Figure 10.

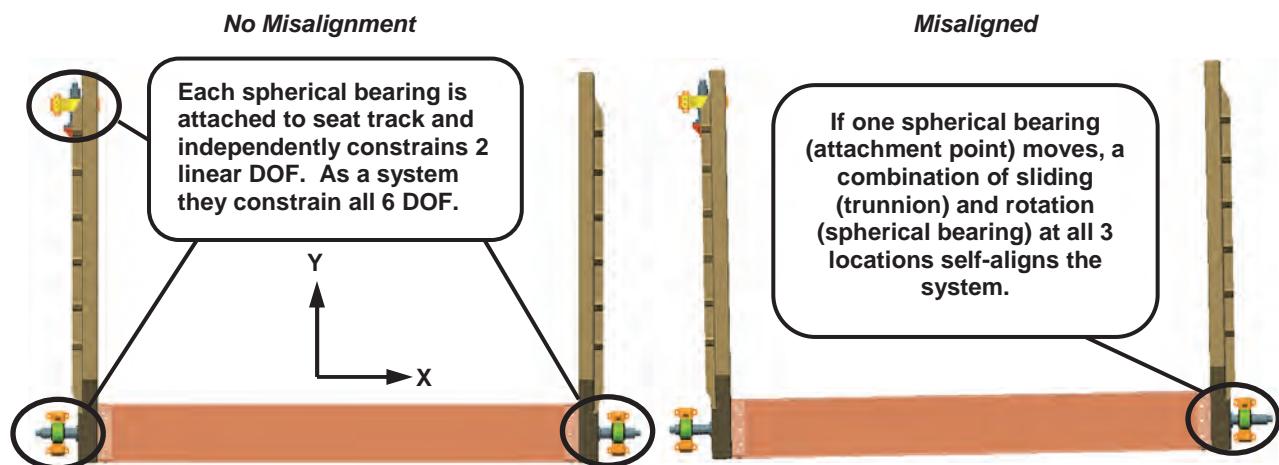


Figure 10. VIS Attachment to ISS Seat Track

This statically determinant mounting method does not transfer torque to the relatively torque-intolerant seat track. Installation was greatly simplified and crew can remove and replace the entire ARED and VIS system easily for relocation, emergencies, or storage access.

Test and Qualification Approach

Testing VIS performance is difficult in the presence of gravity. An earlier development program attempting to isolate the iRED tested the system lying sideways on an air bearing floor. The human subject was also supported sideways to perform exercises, which was very difficult and cast doubts on the validity of the results. A parabolic flight pattern on a reduced gravity aircraft provides a more realistic environment to perform exercises, but the window of weightlessness is too short and given the extremely low spring rates, there is significant risk of hardware damage during the pull-out phase of flight. Even testing on-orbit may not capture worst-case exercise scenarios due to natural human variability. While a test of system level performance was impractical, a test program was developed to:

- 1) Verify that components meet performance requirements and adjust those with variable settings
- 2) Life cycle test the system to identify and resolve potential issues
- 3) Gather component performance data for the system level qualification analysis model

The test stand consists of a Motion Science MS700 electromechanical actuator (EMA), Sensotec Model 31 load cell, and a string potentiometer all mounted on a t-slot table as illustrated in Figure 11.

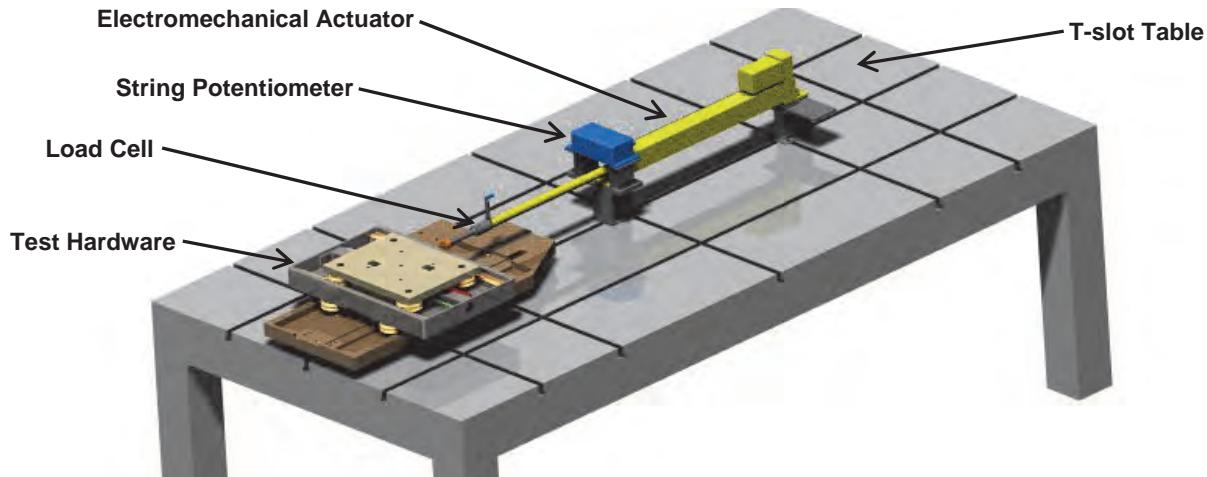


Figure 11. Vibration Isolation System Test Stand

Component level tests primarily involved the rails, dashpots, and snubbers. Several styles of rails were tested to find which provided the lowest friction. The rail bearings in the VIS are mounted on eccentric bushings to provide preload adjustment and tuned to provide rigidity while minimizing friction. The dashpot testing focused on finding the right setting to meet the target damping rate. Each model was cycled through 7 discrete constant velocities at each setting. The average force was recorded for each constant velocity, plotted, and fit to calculate the damping rate as shown in Figure 12. The dashpot behavior fit well to the expected characterization of force being linearly proportional to velocity.

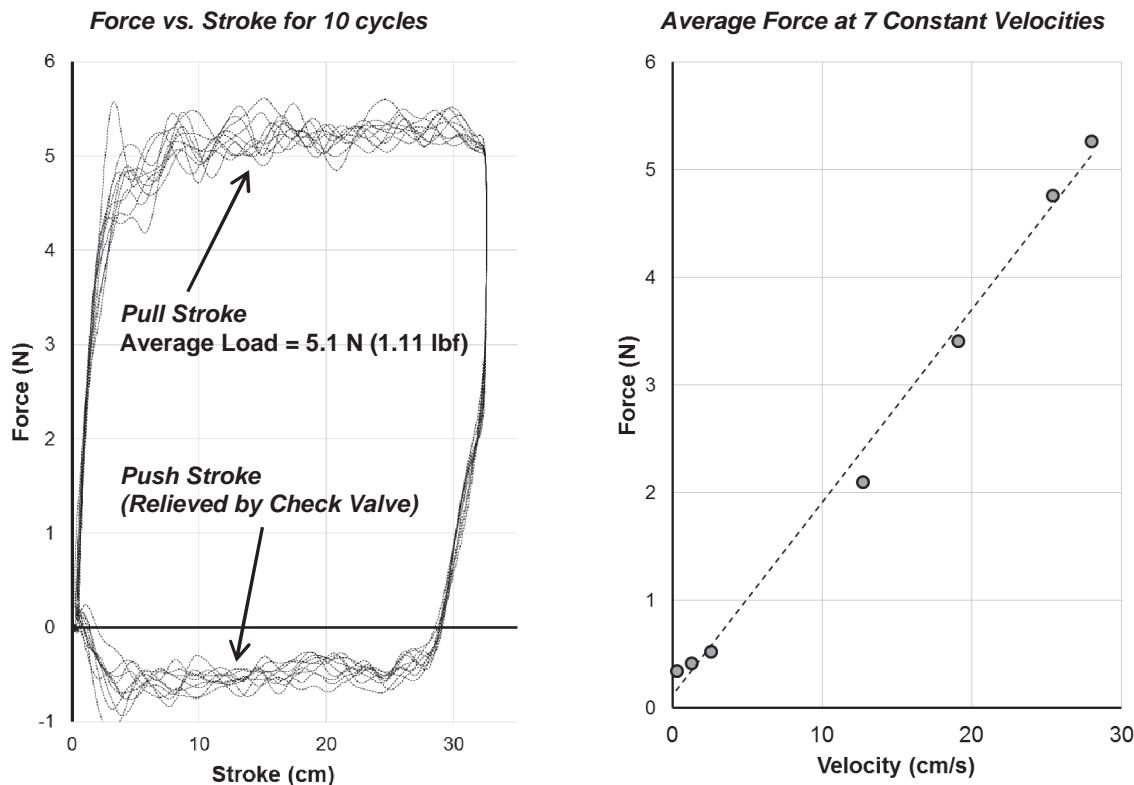


Figure 12. Component Test Results: Force vs. Stroke at 27.9 cm/s (11 in/s) and Average Force vs. Velocity with Linear Fit for Y Dashpot

Snubber testing revealed a shortcoming of the EMA test stand in that it wasn't able to supply a sufficient force at high velocities to characterize the snubbers. A simple pendulum-based test stand was developed as shown in Figure 13. It was easy to design, manufacture, and adjust to deliver the correct mass and impact velocity. Testing revealed that the snubbers are capable of dissipating the resultant energy from ISS reboost and docking events without overloading the ISS seat track interface.

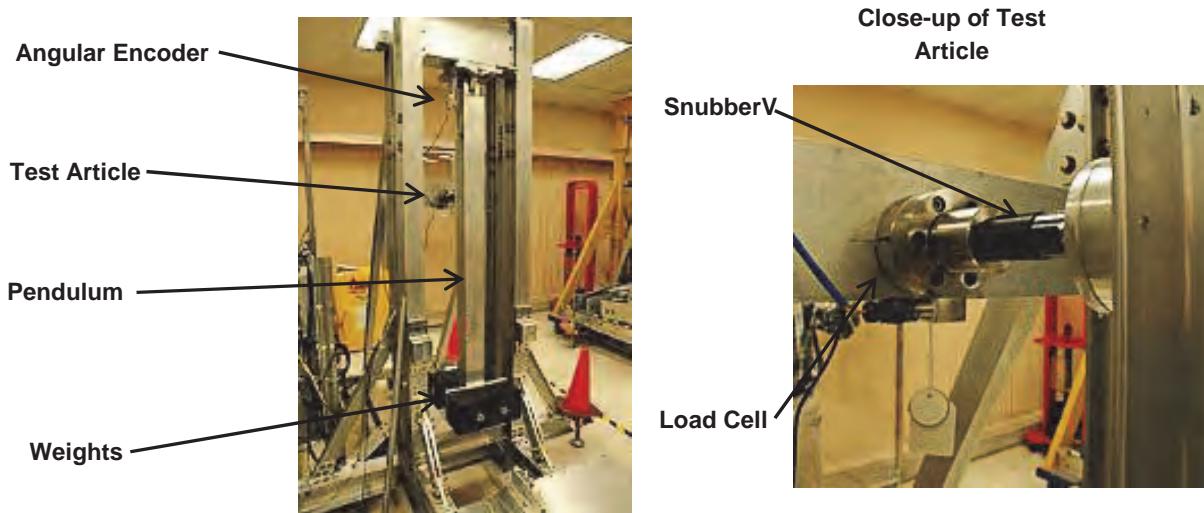


Figure 13. Pendulum Test Stand for VIS Snubbers

"Lead the fleet" life cycle testing is still underway with the EMA test setup. Each axis of the VIS is cycled through 300,000 cycles per year. Several observations have been noted to date:

- 1) The linear rails (of 420 stainless steel) have developed surface corrosion during life cycle testing after grease wore away. This may be an issue of test conditions being worse than service conditions as the test cycles start and stop in the same place, pushing the grease away at the cycle peaks. Regardless, the planned rail maintenance intervals were changed from once per year to 6 times per year as a measure of caution.
- 2) Graphite deposits were found on the cylinder walls after 100,000 cycles on the rotation axis dashpots. The manufacturer had seen this in other applications and there was no change in performance, so testing continued.
- 3) During testing of the rotation axis, debris was noticed on the rotation arm at the ball joint attachment. No changes in performance were apparent, so testing continued.

The component test data was used to update the damping properties of the dashpots and friction properties of the rails within the analytical model. As the VIS design matured, its own mass properties were added to the model as well. A case matrix was developed to include runs with both sinusoidal and real stroke profiles, exercise frequencies at the minimums, maximums, averages, and ISS structural mode frequencies for all 4 of the major exercises for a total of 51 cases. The load and torque time histories from this for each case were sent to Boeing for a coupled loads analysis within the ISS structural dynamics finite element model.

The results predicted successful performance of the VIS in both Node 1 and Node 3 of the ISS as shown in Figure 14 and the VIS achieved flight qualification.

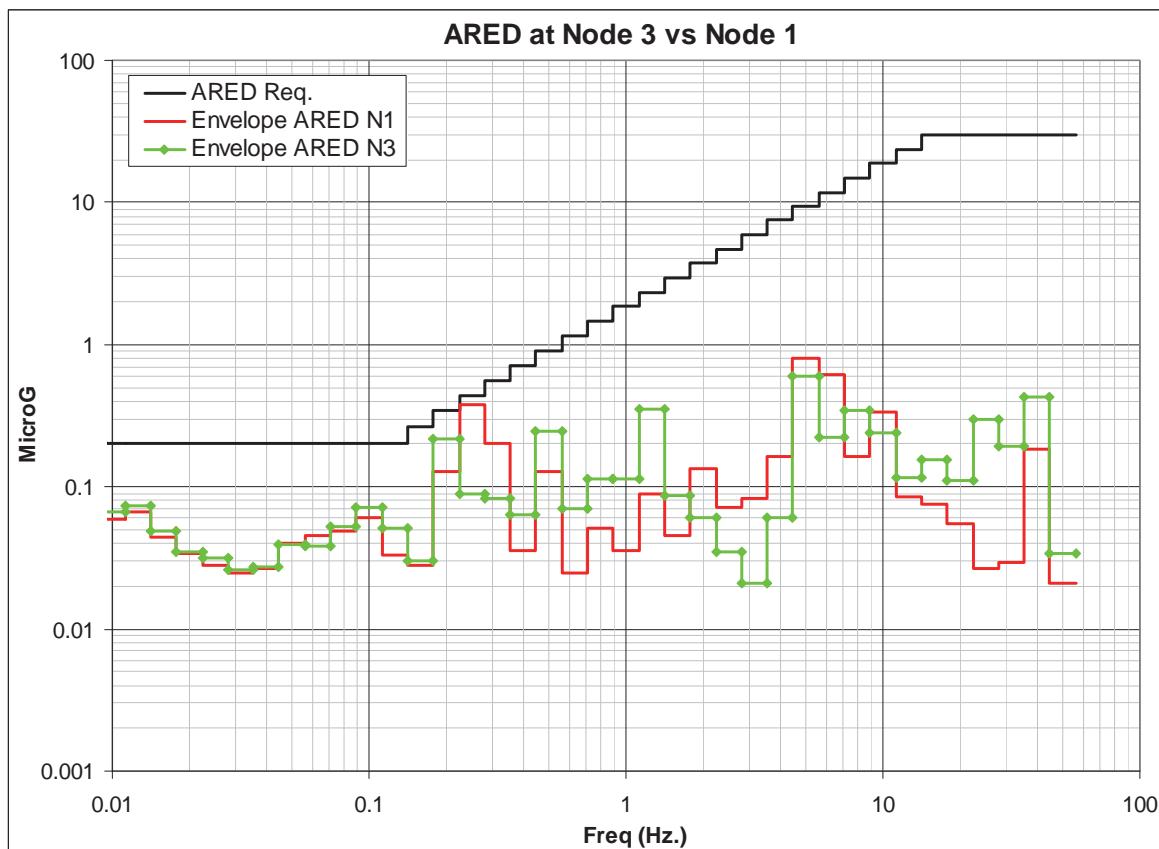


Figure 14. Results of Coupled Loads Analysis for 51 Exercise Load Cases [5]

Operational Performance

The ARED and VIS were flown to the ISS aboard STS-126 (ULF2) in November 2008. Assembly occurred during ISS Expedition 18 over 4 days in late 2009, with checkouts following. Figure 15 shows the ARED and VIS installed in Node 1 of the ISS with NASA Astronaut T.J. Creamer performing a dead lift exercise.

On-orbit accelerometers have shown that the VIS is meeting its micro-g and loads requirements, though no localized vibration surveys have been done to validate analytical predictions.

After 2 years of operational experience with no corrosion, the planned rail maintenance interval was changed from 6 times per year to 4 times per year. After additional evaluation the time interval between rail cleaning may be increased even more.

While the VIS has performed very well overall, it has not been free of problems. A major mechanical problem and two procedural issues have been identified:

Problem 1:

After just 6 months of operation, a rotation axis dashpot failed at the swaged connection between the stainless steel connecting rod and aluminum rod end ball bearing. When the failure wasn't immediately



Figure 15. NASA Astronaut T.J. Creamer Exercises on ARED (Image Courtesy of NASA)

noticed, subsequent ARED use resulted in breakage of the dashpot's glass cylinder as shown in Figure 16. The Kapton tape overwrap contained most of the debris. ARED was inoperable for a month until spares arrived. Since then, the swaged connection of the rotation axis dashpot has failed on 3 separate instances. However with spares available, downtime has been no more than a day. The failure appears to be most likely caused by several deficiencies in the dashpot design combined with the misalignment between the connecting rod ends as the rotation arm sweeps through its range of motion. A root cause analysis was undertaken to identify weaknesses in the design [6]. While the design does not have the robustness desired it was concluded that the dashpot has not been used in a manner that exceeded its specifications. Several design improvements for the rotation axis dashpot have been developed and approved for implementation:

- 1) Piston height has been increased to reduce binding that can cause excessive wear, generate debris, and increase friction. A groove around the piston has also been added to capture any debris that is generated.
- 2) The connecting rod ends have been redesigned to increase strength and wear resistance. In-house testing revealed several swages that tested at lower static loads than expected (but not below the design limit load.) Swaged connections are eliminated in favor of a stainless steel ball end threaded into the shaft. The ball ends will fit into a two-piece Vespel socket for durability.

This failure was not observed during life cycle testing although a clue in debris generation at the ball joint was noticed as previously discussed. The life cycle test profile velocities and ranges are based on

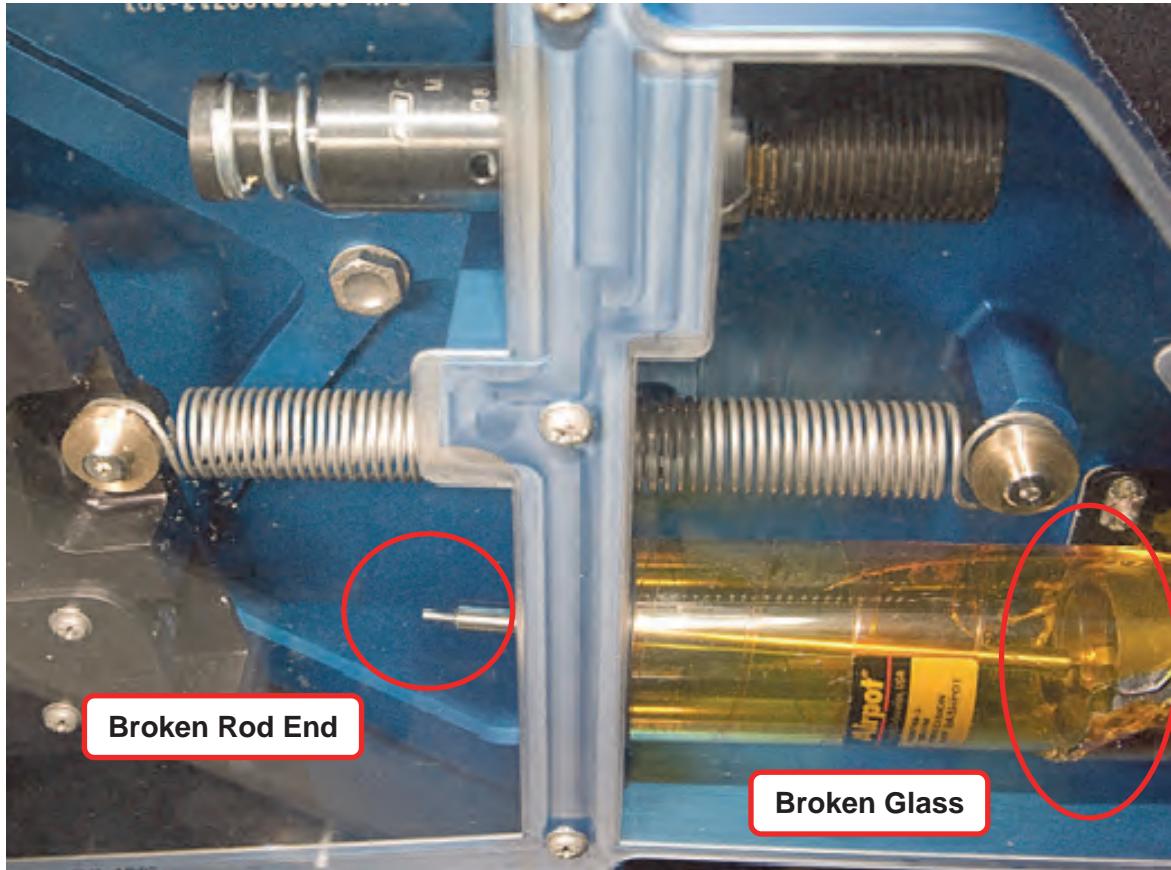


Figure 16. Broken Rotation Axis Dashpot (Image Courtesy of NASA)

averages and do not capture peak velocities and hence the peak dashpot loads seen during operation on the ISS.

Problem 2:

Procedural lapses have resulted in the VIS being locked during exercise which is clearly detected by ISS accelerometers and violates micro-g requirements. This seems to happen mostly with new crew unfamiliar with ARED operation. New labels and training procedures have so far addressed these issues.

Problem 3:

Incorrect installation of the lock-out pin dislodged one of the rotation axis springs, but this was easily fixed by the crew. New labels and training procedures have so far addressed these issues.

Lessons Learned

Lesson 1:

The use of motion simulation software was not only technically sufficient, but the visualization capabilities proved to be instrumental in bolstering confidence in a novel design.

Lesson 2:

Qualification by analysis can be a viable alternative if physical testing cannot provide a clear assessment of performance. However, careful attention must be given to risk mitigation.

Lesson 3:

Designing for ease of repair has been critical in addressing unforeseen issues. The rotation axis dashpots have proven to be easy to replace on orbit allowing for quick recovery from failures. This not only results in less time spent by crews on orbit, but by ground support crews as well since fewer procedures need to be developed.

Lesson 4:

Despite training and consideration of designing for humans, hardware may still be misused. Assume hardware will require on-orbit repair and design accordingly.

Lesson 5:

“Lead the fleet” life cycle testing should only be considered when the design is flexible enough that problems can be easily diagnosed when they arise and can also be easily fixed on-orbit.

Lesson 6:

Carefully consider life cycle test design for hardware used by humans. The profile used in testing the VIS revealed a corrosion issue that hasn’t developed on-orbit, but didn’t predict a hardware failure that happened after only 6 months of use. The profile is conservative in the number of cycles but doesn’t capture peak dashpot loads.

Conclusions

Despite several on-orbit problems, there have been numerous successes. A comparatively simple passive isolation system relying on COTS components was qualified by analysis and has demonstrated effectiveness saving untold development and sustaining engineering costs. Thorough characterization of load cases and attention to design for repair significantly mitigated risk and this has paid its dividends in reducing down-time while recovering from on-orbit failures.

References

1. Lamoreaux, Christopher D., and Mark E. Landdeck. "Mechanism Development, Testing, and Lessons Learned for the Advanced Resistive Exercise Device." *Proceedings of the 38th Aerospace Mechanisms Symposium*, (May 17-29, 2006), pp. 317-330
2. Bentley, Jason R., et al. "Advanced Resistive Exercise Device (ARED) Man-In-The-Loop Test (MILT)." NASA TP-2006-213717, May 2006.
3. Guilliams, Mark, Mike Rapley, and Nahom Beyene. "Resistive Exercise Description Document." JSC 29558, January 2002.
4. National Aeronautics and Space Administration, International Space Station Flight Crew Integration Standard, SSP 50005C, December 1999, pp. 3-45
5. Laible, Michael. "ARED Microgravity Assessment in Node 3 at Node 1 Port." Boeing EID684-13762, November 2009.
6. Zamaitis, J.A. and G. Szymczak. "ARED X-Dashpot Performance Report." EM-ARED-066, November 2011.

Passive Thrust Oscillation Mitigation for the CEV Crew Pallet System

Matthew Sammons*, Cory Powell**, Joe Pellicciotti†, Ralph Buehrle†† and Keith Johnson††

Abstract

The Crew Exploration Vehicle (CEV) was intended to be the next-generation human spacecraft for the Constellation Program. The CEV Isolator Strut mechanism was designed to mitigate loads imparted to the CEV crew caused by the Thrust Oscillation (TO) phenomenon of the proposed Ares I Launch Vehicle (LV). The Isolator Strut was also designed to be compatible with Launch Abort (LA) contingencies and landing scenarios. Prototype struts were designed, built, and tested in component, sub-system, and system-level testing. The design of the strut, the results of the tests, and the conclusions and lessons learned from the program will be explored in this paper.

Introduction

The Constellation Program aimed to send human explorers back to the Moon and beyond as part of the Vision for Space Exploration. The CEV, also called Orion, was the proposed human spacecraft capsule for the program. The launch environment of the proposed mission included the TO phenomenon described below. It had been determined that the effects of the TO event must be mitigated for crew safety and operational reasons.

CEV Background

Originally conceptualized as a six-man vehicle, the CEV was ultimately designed to support a four-man crew on trips to the Moon, Mars, and other destinations in the solar system as part of the Constellation Program. The interior of the Crew Module (CM) portion of the CEV contains a floating crew pallet structure supported by eight struts upon which the crew seats are installed. See Figure 1 for an image of CM interior design and crew seat pallet with struts. The goal of the NASA Engineering and Safety Center (NESC) team was to develop a Crew Impact Attenuation System (CIAS) to mitigate the TO effects on the crew.

TO Description

Like all launch vehicles, the launch vehicle dynamic environment is a significant input to the overall payload launch loads. The Ares I First Stage has a small oscillation in thrust at a frequency band centered at approximately $12 \text{ Hz} \pm 2.5 \text{ Hz}$, for about 10 seconds late in booster burn. Since the overall launch vehicle resonated with the input frequency of the boosters, the crew pallet struts had an additional requirement to mitigate the thrust oscillation resulting from the vehicle resonance.

* ATK Aerospace Systems, Beltsville, MD

** NASA Goddard Space Flight Center, Greenbelt, MD

† NASA NESC (Goddard Space Flight Center), Greenbelt, MD

†† NASA Langley Research Center, Hampton, VA

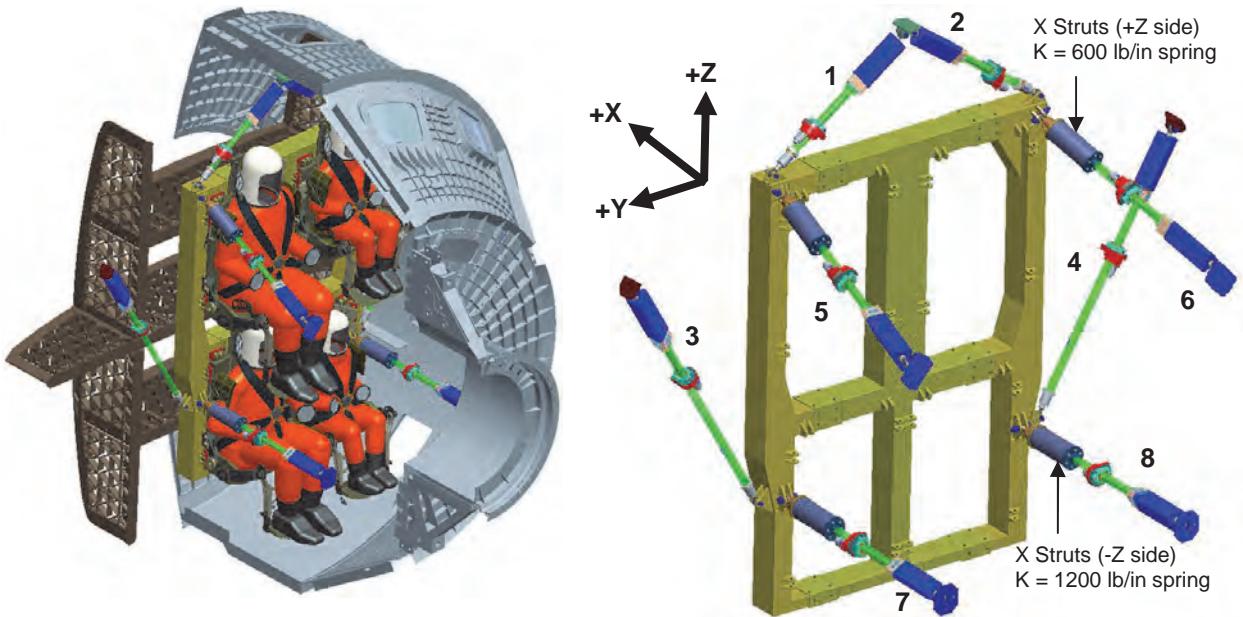


Figure 1. CEV CM with Crew (left); Crew Pallet with Struts (right)

Requirements

The TO isolation solution was driven by the requirements and constraints imposed on it derived from evaluations of a spring-based isolation system's impact on the crew in a TO event, LA scenario, and landing scenario. In addition, volumetric constraints and project constraints (resources, time) led to the design solution. This section will detail the results of the TO event, landing scenario, and LA evaluations.

CM Interior Environment

There are eight struts total: four in the X direction, launch axis, and two each in Z and Y directions. The CM baseline strut was modeled and tested using wire bender struts that absorb landing loads by dissipating energy through plastic deformation of steel wires – they have a one-time stroke during landing. As a pallet-based isolation system was selected (as opposed to seat-based), it was determined that the struts would need to be in series with the wire bender struts. Analyses showed that TO Isolators only needed to be present in the four X struts.

Crew Impact from TO Event

A requirement resulting from an investigation by the TO Focus Team and imposed by the Crew Office was to reduce crew response acceleration levels during the TO event to 0.25 g maximum at 12 Hz. This became the primary design driver for the isolation system.

The NESC team used the Brinkley Dynamic Response model to assess the likelihood of injury to the crew in both the landing and LA scenarios. For more information regarding the Brinkley injury risk criteria, see Reference 1.

Isolation Frequency

Knowing the TO frequency band of 12 ± 2.5 Hz, a NASTRAN® coupled loads model was used to evaluate the effectiveness in g-reduction at different isolation frequencies. Following the theory of load transmissibility, if the pallet system frequency is greater than that of the input, dynamic amplification will occur. By dropping the pallet system frequency below that of the input, dynamic amplification can be eliminated and transmissibility can be less than 1.0.

It was concluded that an isolation frequency of 5 Hz or less is required to reduce the crew acceleration responses to 0.25 g. A 4.5 Hz isolation frequency was selected as optimal, as it represents a good balance between deflection and transmitted dynamic load. This isolation frequency of the pallet is achieved by placing linear springs in series with the 4 X-axis struts.

Strut Deflection

During the TO event and while isolated at 4.5 Hz, the pallet will translate between 0.5 cm – 1 cm (0.2 in – 0.4 in). Therefore, the TO Isolator stroke was designed to allow for slightly more than the predicted max of 1 cm before hitting a hard stop. In order to eliminate Isolator deflection during ground operations, the mechanism was designed to be preloaded through launch until the TO event occurs between 3.25 g's to 4.5 g's quasi-static load.

Volumetric Constraints

Volumetric constraints were imposed by the available strut length and the crew size. It was determined that, being in-line with the CM struts, a maximum length of 39.4 cm (15.5 in) was not used for the landing event and allowable for the TO Isolator design. The cylindrical diametric size had to be kept to a minimum to ensure that it did not contact a crew member's shoulder. Computer Aided Design models proved this to be less than 11.4 cm (4.5 in).

Isolator Impact on Landing Loads

LS-DYNA®, kinematic analysis software, was used to investigate the effect from the TO Isolator on landing loads experienced by the crew and compared to the baseline.

The initial model consisted of CM struts in series with an isolation spring; subsequent models included a damper to address potential issues with LA. With a 30g input, it was found that introduction of the TO isolation springs does not significantly or detrimentally affect accelerations transmitted to the pallet. However, the isolation springs have a detrimental effect on the stroking of the baseline struts, which ideally should be held to a minimum. Preliminary analyses showed that the Isolators need to be locked out during a landing event to minimize CM strut stroke while keeping the Brinkley model's injury risk probability to an acceptable level.

Isolator Impact on LA Loads

Although other launch analyses were done using NASTRAN®, the effect of the Isolators on crew loads in the contingency case of a LA were evaluated with LS-DYNA® software.

This was done so that crew response of the abort event could be determined while keeping the Isolator kinematic motion in the model. Without damping, the seat accelerations were found to be unstable and grew without bounds. With just 44.5 N (10 lbf) of Coulomb friction in parallel with the Isolator, the accelerations were sufficiently attenuated and decayed once the abort loadings ended. Since actual damping levels throughout the crew module are unknown and difficult to determine it was not useful to attempt a detailed damping study for the isolation springs. Instead, it was decided to utilize a small amount of Coulomb damping in the model and then insure that the design of the isolation spring had a mechanism for providing a deterministic level of damping.

TO Isolator Strut Design

Design Overview

The TO Isolator strut was designed as a passive spring and damper system that would be active during ascent and locked out during landing. It is mounted in-line with the X-axis CM struts. For hardware testing, the Isolator was mounted to the wire bender via a 1.905 cm – 16 (.750"-16) threaded interface, see Figure 2.

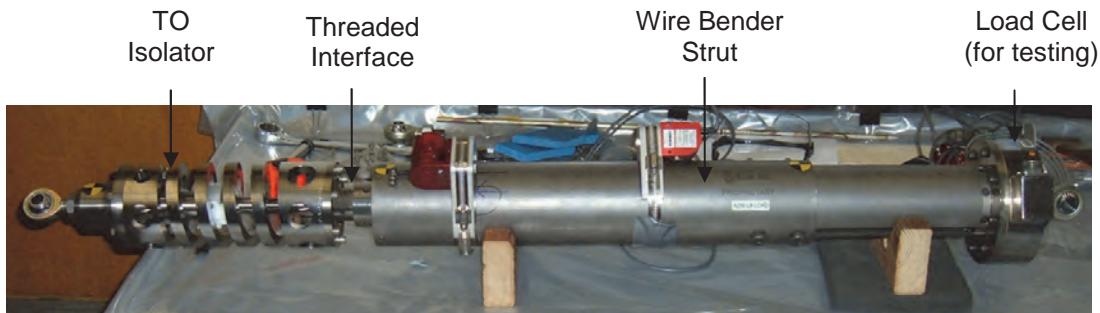


Figure 2. TO Isolator Strut In-line with Wire Bender Strut

The principal details of the TO isolation design are:

- Two 105 kN/m (600 lbf/in) springs (+Z) and two 210.2 kN/m (1200 lbf/in) springs (-Z) were required to achieve a balanced 4.5 Hz pallet system frequency.
- Springs are extended 4.123 cm (1.625 in), preloading the Center Rod in compression, so that the Isolator does not unseat prior to the TO event. During launch, the rod will not unseat from the housing thereby keeping the springs out of the load path until just before the TO event's quasi-static load is reached. The pallet then floats at 4.5 Hz for the range of 3.25 to 4.5 g's.
- During the TO event, cyclical motion of the Isolator will occur in the range of 0.5 cm – 1 cm (0.2 in – 0.4 in). The design allows for motion up to 1.59 cm (0.625 in).
- In the preloaded condition, the Isolator design does not affect the baseline strut stiffness.

Design Detail

The overall Isolator architecture is a large machined spring housed between two hubs. Threaded into and protruding from the exterior of the Front Hub is a threaded rod end with a spherical ball joint at its end. The interior of the Front Hub has a large counter-bore upon which a Delrin® pad sits, providing a contact surface for the Center Rod, which is preloaded against the pad. The Center Rod passes through the center of the spring and screws into the Back Hub which also provides a threaded interface to the wire bender strut. The concentric alignment of the entire Isolator assembly is controlled by a Flanged Sleeve which is pinned to the Front Hub at assembly and bolted between the front hub and the machined spring. Inside the flanged sleeve are some tight tolerance Delrin® tube bushings which provide a slip fit guide for the Center Rod. Refer to Figure 3 for a cross-section view of the Isolator assembly.

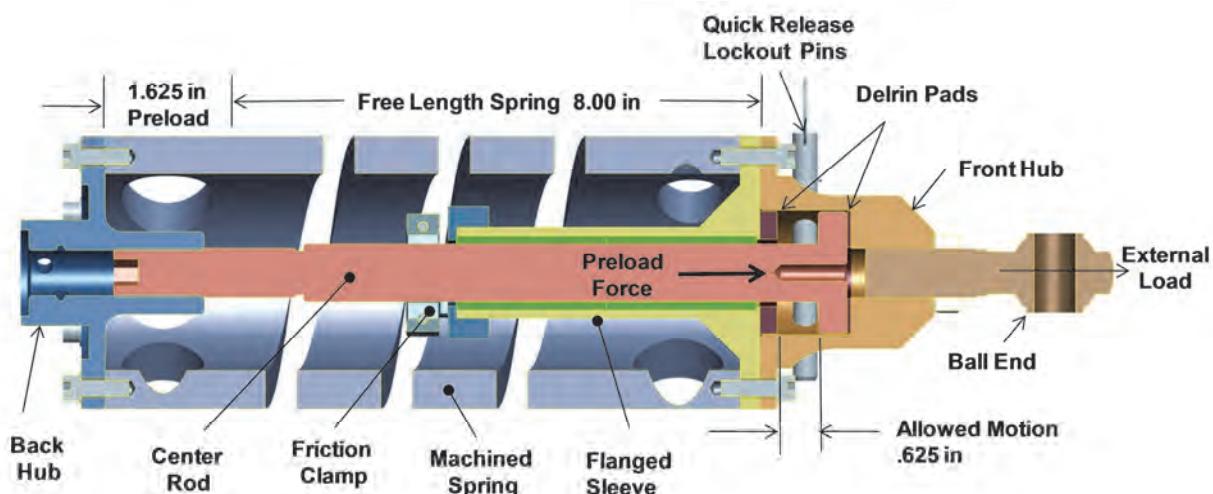


Figure 3. TO Isolator Strut Cross-Sectional View

During assembly, each spring is pulled back 4.123 cm (1.625 in) from its free length. The reactive force of this tensile load on the spring compresses the Center Rod onto the front Delrin® pad and preloads the assembly. During launch, when a large enough tension load is applied to overcome the preload, the center rod will unseat. After unseating as the spring extends further under still higher tensile launch loads, the relative motion of the Center Rod may travel 1.59 cm (0.625 in) until it hits another Delrin® pad stop on the Flanged Sleeve. The Delrin® pads were used so that titanium-on-titanium contact would not occur during impacts, preventing galling of the contacting parts. The expanded diameter head on the front end of the Center Rod limits its motion to this 1.59 cm (0.625 in) travel space. The Ares first stage forcing function has been computed to apply tensile loads resulting in head travel within this 1.59 cm (0.625 in) range, effectively isolating the pallet from the rest of the crew module in the X direction.

All of the load bearing machined parts and the machined spring are made out of titanium to reduce the weight of the assemblies. Each of the machined springs were machined from a single piece of titanium and have identical bolted interfaces on both ends. Due to the method of construction and the bolted interfaces, the springs can react both compressive and tensile loads. The 105 kN/m (600 lbf/in) Isolator spring assemblies each have a mass of 5.08 kg (11.2 lbm) and the 210.2 kN/m (1200 lbf/in) Isolator spring assemblies each have a mass of 6.21 kg (13.7 lbm). The total mass for all four Isolator spring assemblies is 22.6 kg (49.8 lbm) which does not include the existing CM portion of each strut.

Damping

To provide for the low-level damping required to maintain stability in a LA scenario, the motion of the Isolator requires a damping component. Due to the late addition into the design, a passive, friction-based damping system was devised. Two Delrin® components clamp on the Center Rod; fasteners squeeze the components together, providing a friction force against the Center Rod that can be controlled based on the fastener torque. They are designed to provide between 111 – 156 N (25 – 35 lbf) of frictional force.

Lockout Mechanism

In order to satisfy the locking requirement for landing loads, a feature was added to prevent any stroking of the Isolators. For ease of prototype testing and assembly, quick release (insertion) pins were inserted behind the head of the Center Rod preventing it from moving and creating a rigid load path that bypasses the machined spring.

For flight, a quick-reacting lock out mechanism would be required during landing. A concept for a Non-Explosive Actuator (NEA) driven blade was added to the design. The concept uses an NEA to hold a spring-loaded Plunger that is threaded into the NEA nut; when actuated by a 4-amp electrical signal, the NEA releases the Plunger which wedges behind the Center Rod, securing the Rod in place and creating

a single shear load path that bypasses the spring creating a strut stiffness equal to that of the CM baseline strut. A second blade 180° from the first would be needed for redundancy. The concept used for testing incorporated an NEA mockup on one of the four Isolators to characterize its static performance. Refer to Figures 4 and 5 for images of the Isolator and NEA Lockout Mechanism.

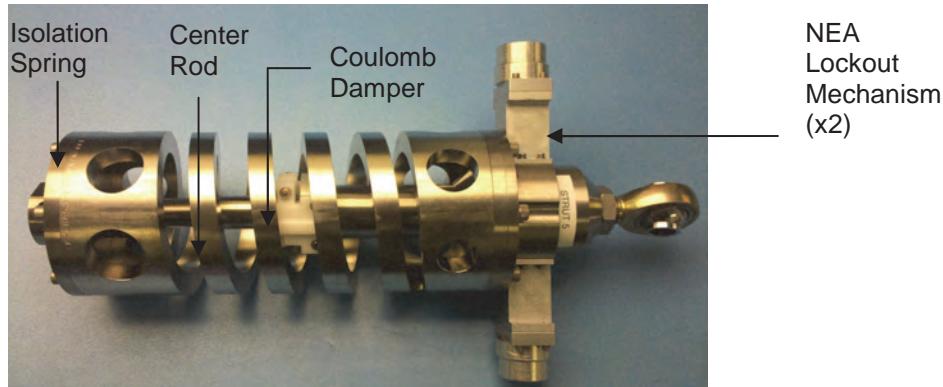


Figure 4. TO Isolator Strut with NEA Lockout Mechanism

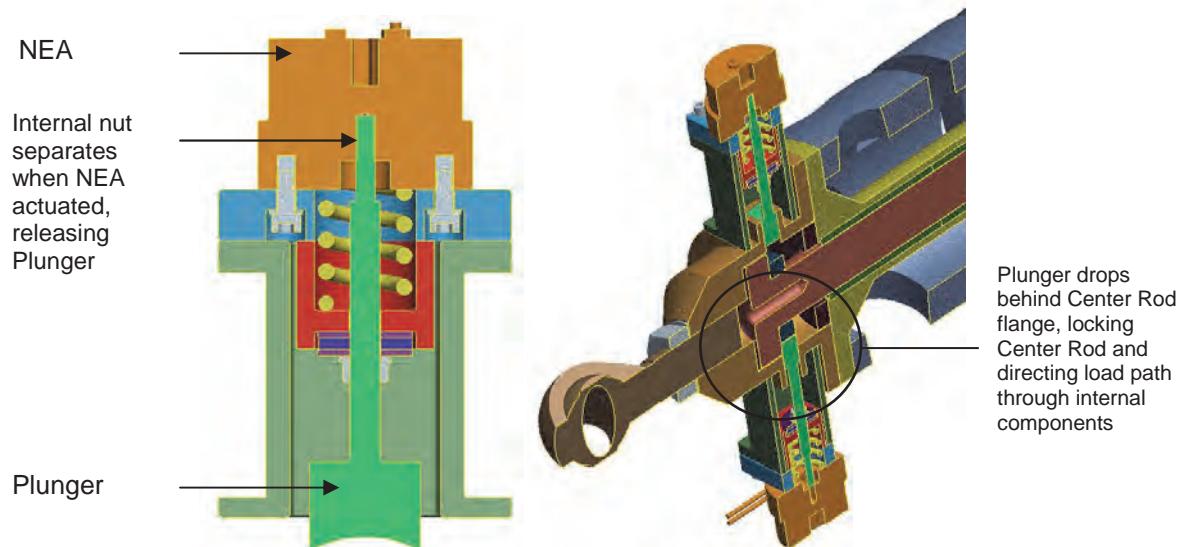


Figure 5. NEA Lockout Mechanism Cross-Sectional View

Test and Evaluation Program

The test and evaluation program aimed to characterize the effectiveness of the Isolation springs in attenuating the launch dynamic accelerations and loads imparted to the crew pallet. In addition, the test program aimed to understand the effect the Isolators had on the wire bender stroke during landing impact and better understand the correlation of model predictions to test results.

The test program included: Isolator Proof Testing, Isolator Stiffness and Damping Characteristics, Strut Impact Testing, System Drop Testing, Modal Testing of the launch configuration, and Vibration Testing to characterize performance.

TO Isolator Proof Testing / Stiffness and Damping Characteristics

Each Isolator assembly was tested in tension (locked and unlocked) and in compression to prove strength margins and verify spring stiffnesses. Maximum loading expected on the strut occurs during drop testing and is 4.448 kN (10,000 lbf). A test factor of 1.25 was included in proof tests leading to testing in compression and tension at 5.560 kN (12,500 lbf). All proof tests were performed successfully with no signs of failure or yielding. Spring stiffnesses and friction forces were found to be in acceptable ranges.

Strut Sub-System Impact Testing

Impact testing aimed to characterize TO vibration isolation springs in a dynamic environment and assess their effect on the behavior of the wire bender landing attenuation struts. In addition, an accurate LS-DYNA® model of the vibration isolation spring and attenuation strut was desired so that a reliable analytical model is available for subsequent landing simulations performed with the Orion vehicle under simulated landing conditions.

The tests were conducted using the 711th Human Performance Wing's Vertical Deceleration Tower (VDT) at Wright Patterson Air Force Base in Dayton, Ohio. The VDT consists of an 18 m (60 ft) vertical steel tower that allows a carriage to enter a free-fall state (guided by rails) from a pre-determined drop height. The plunger mounted on the rear of the carriage is guided into the hydraulic deceleration device (cylinder filled with water located at the base and between the vertical rails), producing an impact deceleration pulse, see Figure 6.

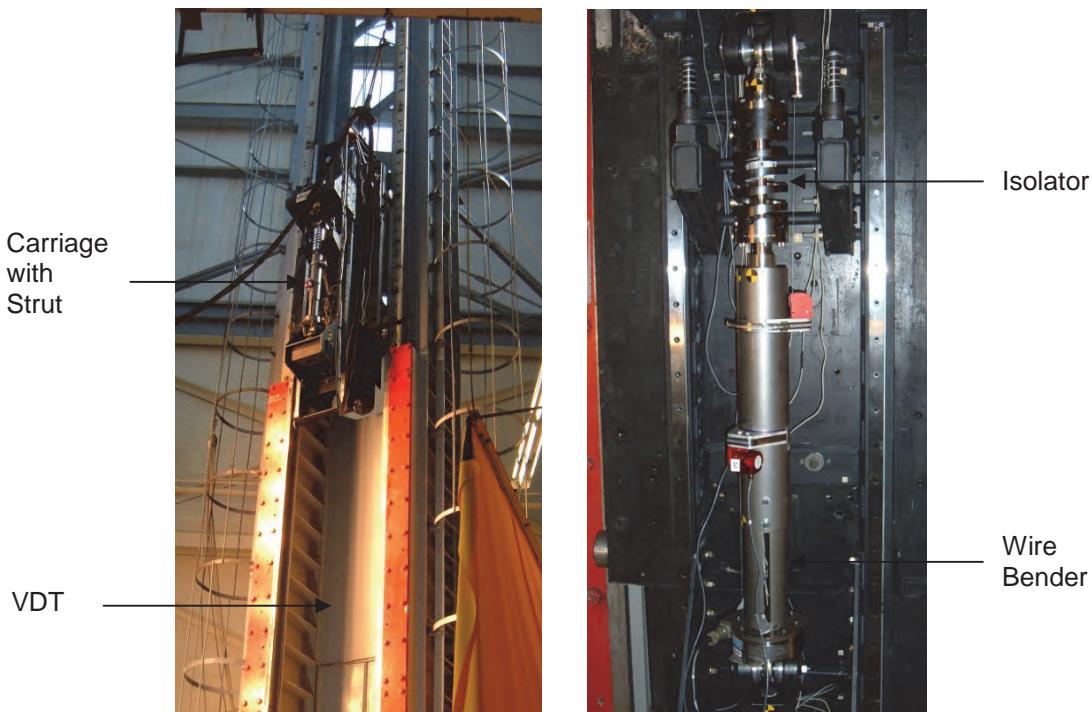


Figure 6. Attenuation Struts in VDT Setup

The testing showed that the transmitted acceleration peaks are similar regardless of the presence of the isolation spring. Testing and simulations for the strut with both the TO vibration isolation spring and the wire bender incorporated into the strut showed that the isolation spring has the effect of reducing the Brinkley injury criteria at the expense of increasing the strut stroke.

System Drop Testing

Orion CIAS impact tests were performed at the NASA Langley Landing and Impact Dynamic Research Facility to provide a demonstration of strut system performance, evaluate the performance differences

between the locked and unlocked condition of the TO Isolators during the landing impacts and assess LS-DYNA® modeling techniques and predictive capability. The test configuration had a crew pallet-mockup (green, Figure 7) suspended from a cage (yellow, Figure 7) via the eight struts simulating the Orion CM interior. The cage was housed in a ring base/support structure to provide adjustment for various landing parachute pitch angles. Vertical drop tests were conducted by releasing the test fixture from a crane hook at a height calculated to produce the desired impact velocity. Tapered stacks of paper honeycomb at the four corners of the test fixture base were used to produce impact pulses approximating Orion water landings (see Figure 7). Measurements recorded during the tests include TO Isolator displacements, forces and accelerations as well as pallet and cage accelerations. High-speed cameras and photogrammetry were used to verify impact conditions and observe TO behavior.

Eleven CIAS system drop tests were performed, which successfully demonstrated the performance of the system of struts and provided data for evaluation of the effect of the locked/unlocked condition. The accuracy of the LS-DYNA® model was also assessed. The tests featured impact velocities ranging from 3.05 - 10.7 m/s (10 - 35 ft/s) with the crew pallet locked at a 28° pitch angle. The findings from this test and simulation effort are as follows:

1. Strut force and pallet acceleration time histories can be predicted via LS-DYNA® simulations with a high degree of accuracy and are relatively insensitive to expected variations in strut parameters such as strut load limit levels, initial stiffness, and dead zones (initial slack). The load limit in the struts determines the peak acceleration of the pallet. The expected range of the strut force limits will result in a relatively minor variation in the strut forces and pallet accelerations.
2. The strut stroke is the most important parameter to consider for evaluation of the system response. It is also the most difficult output to predict, due to its high sensitivity to most input variables. Comparisons of test data with the LS-DYNA® simulation results for tests 3 through 11 had an average prediction error in the strut displacements of ±0.66 cm (0.26 in). The largest observed strut displacement error between a test and simulation was 3.8 cm (1.5 in). The overall average error was 20%. Accurate prediction of the strut strokes requires a high level of fidelity in the modeling of the structure to capture the flexural response of the crew pallet and the structure supporting the outboard ends of the struts, as well as very accurate modeling of the energy-absorbing wire bender strut force versus displacement curve.
3. Depending on the ratio of the load limit magnitude of the wire bender struts and the stiffness of the TO Isolator, there can be an amplification of the wire bender strut strokes for the unlocked condition. The testing revealed that there are combinations of wire bender struts and Isolator struts where the unlocked condition of the Isolator struts does not result in amplification of the wire bender strokes, and other combinations that can amplify the wire bender strokes by a factor of 2.5 to 3.0. These results confirmed the LS-DYNA® predictions that the Isolator needed to be in a locked configuration during landing.
4. The LS-DYNA® model is accurate enough to be used as an effective design tool for further CIAS studies. The design uncertainty on the pallet acceleration environment will reflect the expected variation in the strut yield force and is expected to be limited to 10% provided that the struts do not exceed their stroke limits. For the strut strokes, a design margin of 20% should be used.



Figure 7. Attenuation Strut in Assembly (Left); Drop-Test Fixture (Right)

System Modal Testing

As part of the pre-test planning for the base-drive vibration testing of the CIAS isolation system, a series of modal tests were performed at NASA Langley to assess the pre-test finite element model (FEM) predictions. The objectives of the modal test were: (1) to investigate potential fixture modes in the frequency range of the vibration test (0 - 20 Hz); and (2) to verify FEM predicted modes for the isolated crew pallet.

Two Isolator test configurations were evaluated: (1) locked and (2) unlocked. In the locked configuration, the isolated struts perform like rigid elements. For the unlocked configuration, the Isolators were shimmed to position with the Isolators in their active stroke range. Accelerometers measured the Frequency Response Functions (FRFs), calculated as the ratio of the acceleration response to the input force. Modal parameters (natural frequencies, damping factors, and mode shapes) were then estimated from the FRFs. Base-drive data acquired during the vibration testing was also used to obtain modal estimates with and without the friction dampers, see Figure 8.

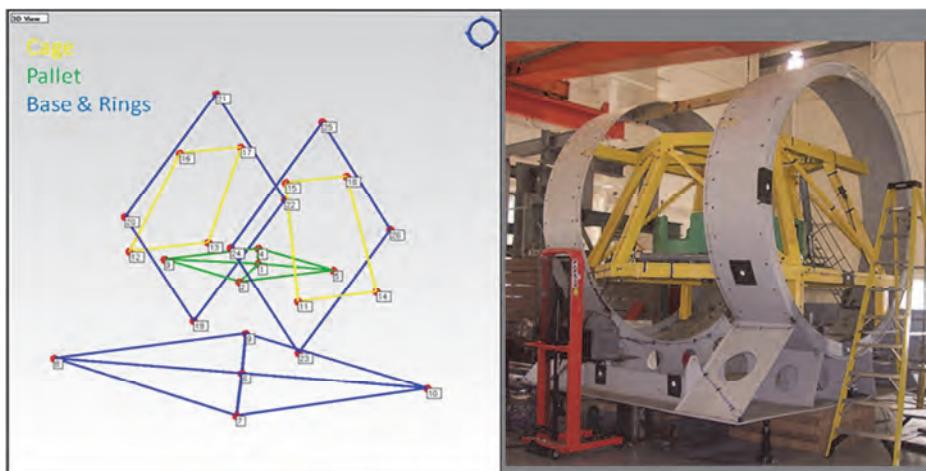


Figure 8. LS-DYNA® Model (Left); System-Level CM Mockup (Right)

Due to low-level inputs, at certain times it was difficult to overcome the friction in the damper, which created difficulties in test execution and data collection. Eventually the friction dampers were removed, allowing for more ideal performance of the Isolators; as a result all three pallet modes were identified.

There is good agreement between the measured frequency estimates and FEM predictions with the largest frequency difference at 8% for the first mode. Modal results are presented in Table 1.

Table 1. Modal Estimates for the CIAS Pallet Modes

Mode	Predicted (Hz)	Modal with friction dampers		Base-Drive with friction dampers		Base-Drive without friction dampers	
		Freq (Hz)	Damp (%)	Freq (Hz)	Damp (%)	Freq (Hz)	Damp (%)
Rocking-Y:+Z struts	3.77	4.1	8.8	-	-	4.1	3.2
Twist about X	4.37	-	-	4.5	7.9	4.7	4.1
Rocking-Y: -Z struts	5.35	5.3	6.0	5.3	7.1	5.4	3.5

System Vibration

The objective of the system-level vibration test was to demonstrate the effectiveness of the pallet-to-strut isolation springs for reducing crew loads during a TO event occurring at approximately 12 Hz. The Orion wire bender Vibration Testing Unit (VTU) was subjected to dwell tests at frequencies of 10 and 12 Hz with varying amplitudes to represent a range of possible launch oscillation loads. Testing occurred at the Naval Surface Warfare Center (NSWC) Dahlgren Division Vibration Test Facility. See Figure 9 for a picture of the test setup.

The test consisted of three configurations:

- Test Sequence 1: rigid, Isolators locked out
- Test Sequence 2: Isolators released, friction dampers installed
- Test Sequence 3: Isolators released, friction dampers removed

Each configuration was subjected to three sine sweeps at varying input levels to test linearity. After the sine sweeps, each configuration underwent dwell testing at the TO frequencies with three different input levels: 0.2, 0.35, 0.5g.

Conducting the signature sine sweeps verified the linearity of the system for Test Sequences 1 and 2. Because dampers were removed for Test Sequence 3, acceleration limits were reached as the pallet isolation frequency coupled with the input. As a result, only one successful sine sweep at 0.025g was completed over the range 2 – 8 Hz for Test Sequence 3. The test was modified to only sweep across 8 – 20Hz for levels higher than 0.025g (0.075 and 0.1g) which verified the linearity of the system over the range 8 – 20 Hz. However, the linearity of Test Sequence 3 over the range 2-8 Hz cannot be verified. Any slight deviation from linearity in Test Sequence 1, Test Sequence 2, and Test Sequence 3 (8-20 Hz only) can be attributed to the noise introduced by the hydraulic shakers.

Figures 10 and 11 display the reduction in accelerations attributed to the Isolators at the 10 Hz dwell and 12 Hz dwell. Tables 2 and 3 display the reduction in acceleration for the 10 Hz and 12 Hz dwells (note that a negative reduction indicates an increase in acceleration).



Figure 9. Orion VTU Mounted on Hydraulic Shakers in the NSWC Vibration Facility

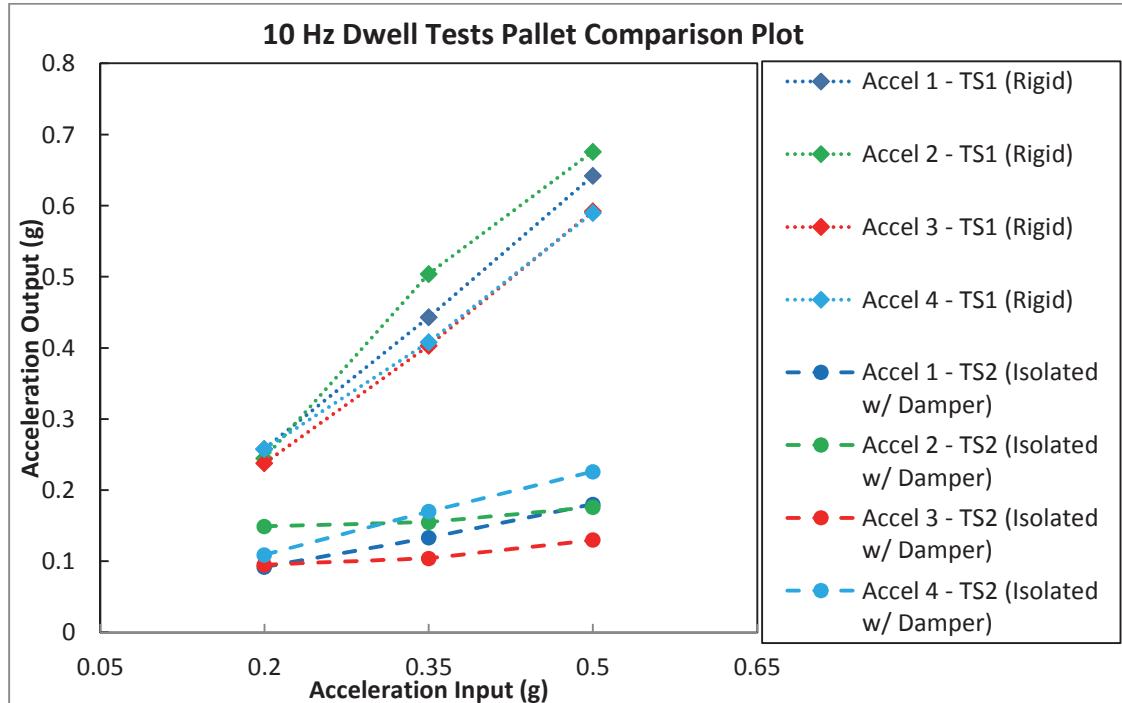


Figure 10. Comparison of Pallet 10 Hz Dwell Test Results for Each Test Configuration

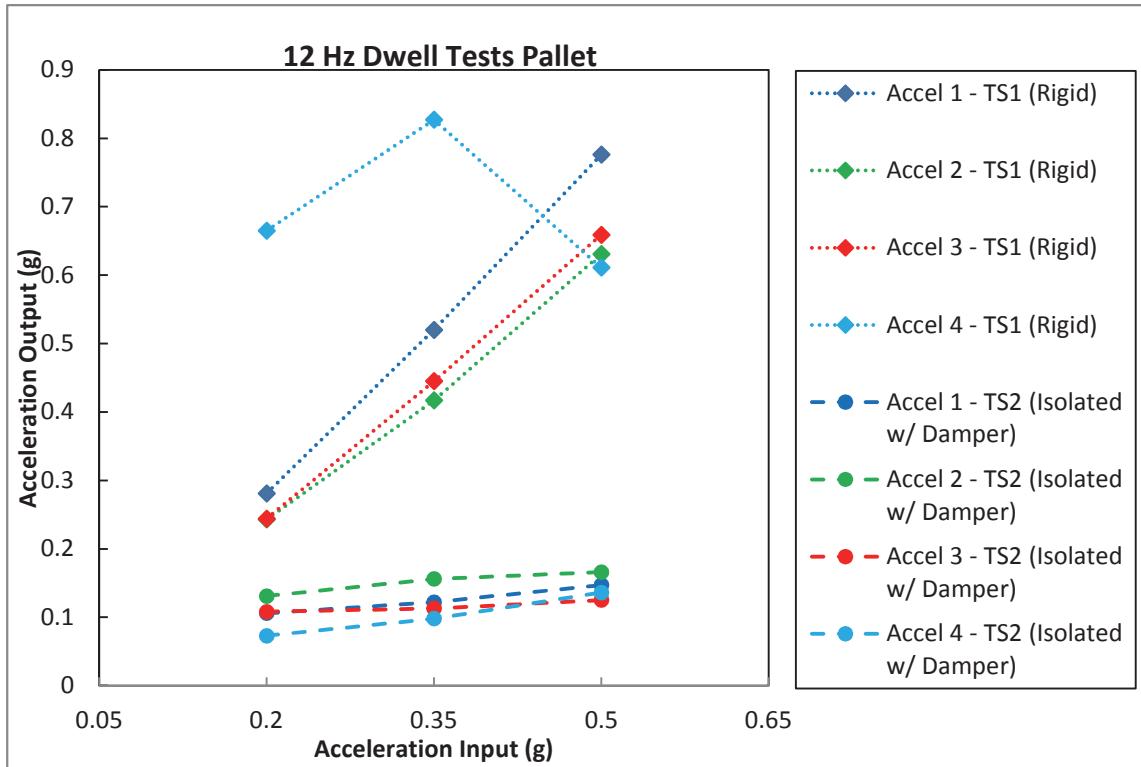


Figure 11. Comparison of Pallet 12 Hz Dwell Test Results for Each Test Configuration

Table 2. Average Pallet Accelerations for 10 Hz Dwell Tests

G Input	Test Sequence	Input as Measured (g)	Average Pallet Response (g)	Average Pallet Transmissibility	Average Pallet % Reduction Compared to Input*	Average Pallet % Reduction Compared to TS1 (Rigid)
0.2	TS1	0.203	0.258	1.27	-27.09	N/A
	TS2	0.2	0.092	0.46	54.00	64.34
	TS3	0.198	0.06	0.30	69.70	76.74
0.35	TS1	0.348	0.443	1.27	-27.30	N/A
	TS2	0.347	0.133	0.38	61.67	69.98
	TS3	0.355	0.112	0.32	68.45	74.72
0.5	TS1	0.501	0.642	1.28	-28.14	N/A
	TS2	0.506	0.18	0.36	64.43	71.96
	TS3	0.497	0.154	0.31	69.01	76.01

*Note: Negative reduction values indicate increase in input.

Table 3. Average Pallet Accelerations for 12 Hz Dwell Tests

G input	Test Sequence	Input as Measured (g)	Average Pallet Response (g)	Average Pallet Transmissibility	Average Pallet % Reduction Compared to Input*	Average Pallet % Reduction Compared to TS1 (Rigid)
0.2	TS1	0.198	0.281	1.42	-41.92	N/A
	TS2	0.197	0.106	0.54	46.19	62.28
	TS3	0.199	0.042	0.21	78.89	85.05
0.35	TS1	0.347	0.52	1.50	-49.86	N/A
	TS2	0.35	0.122	0.35	65.14	76.54
	TS3	0.344	0.073	0.21	78.78	85.96
0.5	TS1	0.507	0.776	1.53	-53.06	N/A
	TS2	0.5	0.147	0.29	70.60	81.06
	TS3	0.492	0.105	0.21	78.66	86.47

*Note: Negative reduction values indicate increase in input.

During Test Sequence 3, the average reduction in acceleration or loading remains relatively constant over all the input levels tests. Test Sequence 2 on the other hand seems to experience a greater percent reduction as the input level is increased. After the completion of Test Sequence 2, the Isolators were removed and the friction damper force was tested. The friction dampers for Isolators 7 and 8 were within the 111 – 156 N (25 – 35 lbf) target range while struts 5 and 6 had static/kinetic friction values of 267 N (60 lbf) and 67 N (15 lbf), respectively. During low level dwell and sine sweeps of Test Sequence 2, strut 5 was not fully released which resulted in a shift in the system dynamics.

The test demonstrated that the TO Isolators do an effective job at mitigating loads due to a TO event, reducing pallet accelerations to 20 - 40% of that of the input. The Delrin® friction dampers however, are overly sensitive and altered the dynamics of the system making correlation of pre-test analyses with the dampers difficult. This prototype damping system should be replaced with a more reproducible, controllable damper for a flight system.

Lessons Learned

Passive Friction Damping

The Isolator design solution utilized a passive, friction-based damping scheme. The inclusion of damping into the Isolator was not introduced until after fabrication of the Isolator parts, which partially drove the solution. Friction, by nature, is difficult to control and get repeatable results. The end result of this is that the friction force applied to the Center Rod, and therefore the damping coefficient of the Isolator, changes slightly from test to test. In addition, the Center Rod was turned down on a lathe, leaving a concentricity and roundness tolerance greater than desired. This caused variations in friction clamping force throughout Center Rod travel, which was observed in Isolator friction testing. A more appropriate finish on the Center Rod for a passive friction damping system would be to centerless grind the shaft, which would result in less surface variations and more consistent friction forces.

Structural Adhesive under Impact Loads

At both the forward and aft hard stop of Center Rod travel, a Delrin® piece would contact the Center Rod to prevent like-material contact. Hysol® EA 9394 structural adhesive epoxy was used to adhere the Delrin® to the substrate metal. This was selected due to the fact that it would require minimal modification to the components, ease of assembly, low-profile installation, and common usage in space industry. The

forward Delrin® pad was bonded to the inner counter-bore on the Front Hub. The aft Delrin® pad was bonded to the rear of Center Rod head.

The Delrin® pads did not dislodge or displace during proof testing. In the dynamic tests (such as Strut Impact Testing, System Drop Testing, and System Vibration) it was observed after certain test runs that the Delrin® would no longer be bonded to its substrate metal. The high impact loads would break the bond causing the Delrin® component to be loose within the cavity. Therefore it has been observed that structural adhesives are likely not appropriate for dynamic impact loading. If it were to be re-designed, the Delrin® pads would be hard mounted with small flat head screws slightly recessed below the impact surface.

Displacement Data Capture in Dynamic Environment

As a critical parameter used for performance and model correlation, the testing program required displacement measurements to be captured during an impact. String-potentiometers were installed in parallel to the struts to record the motion of the impact attenuation wire benders with very good performance. But when installed to measure isolator displacements during single strut/isolator impact tests, the string pots demonstrated greater error band than expected; often giving measurement readings that were much higher than theoretical maximums. From examining high speed camera video, the string pots appeared to have insufficient response during impact onset resulting in over deployment during initial extension and out-of-axis string movement during retraction. The exact cause of this is indeterminate; suspected causes are inertial affects within the device making it inadequate for isolator dynamics during impact or lack of stiffness in the string-pot mounting brackets. Linear Variable Differential Transformers (LVDTs) using rigid plunger shafts were implemented for system drop and vibration tests and were found to perform well with reliable isolation deflection data.

Data Acquisition System Updating

Data from the Orion vibration test was captured using two data acquisition systems (DASs) with different capabilities. The Modal DAS was used to acquire the acceleration measurements on the test article. This DAS was specifically designed to capture and process data for near real-time viewing during the test. For the strut load cell and LVDT data acquisition an EME Corporation Model 3200L DAS was utilized. The EME DAS was designed to capture time data only and did not have any processing capability. The EME Corporation Model 3200L DAS could only be set to acquire data based on a fixed time interval. If a test ran longer than expected, the EME DAS time may expire requiring a re-test. As a result, the EME DAS was set to have a time approximately 5 minutes longer than the estimated testing time. The problem is, once the EME DAS starts, it cannot be stopped until the fixed time expires. This led to gaps between tests and acquiring data past the test's completion. It is recommended that an updated DAS be used for future tests, which do not rely on user defined data acquisition time frame, to save time between tests and to eliminate the acquisition of data past the test's completion.

Conclusions

The TO study confirmed the optimal crew isolation frequency of 4.5 Hz and testing established the system performance and damping mechanism value. From a load mitigation perspective, it was found that the pallet isolation approach was very appealing. Results indicated that the isolation system provided a reduction of dynamic load to about 20% - 40% of the input and that Brinkley levels were met at a mass penalty of less than 5.9 kg (13 lbm) per strut.

The results of this test program illustrate the feasibility and benefits of implementing a pallet isolation system for the Orion CEV CM. The design and test data included herein are directly applicable to the Orion vehicle, but could be adapted to other designs with similar dynamic load issues. Isolation for load reduction is a flight proven technology utilized on several robotic spacecraft in addition to Space Transportation System payloads. Its low mass penalty is relatively insignificant when compared to the hardware benefits and the potential mass increases if this option is not exercised.

Acknowledgements

The authors would like to thank Chuck Lawrence, Greg Walsh, Steve Mark, Steve Hendricks, Justin Templeton, and Don Jarosz for their work and support on this project and acknowledge the invaluable contributions from the test teams at Wright Patterson AFB Impact Test facility, Dahlgren Naval Facility, as well as NASA Langley's Landing and Impact Research Facility and Vibration/Modal Laboratory. Their support during this project was essential to its success.

References

1. Lawrence, Charles et al. NASA/TM-2008 215198. The Use of a Vehicle Acceleration Exposure Limit Model and a Finite Element Crash Test Dummy Model to Evaluate the Risk of Injuries During Orion Crew Module Landings. April 2008.

The Damper Spring Unit of the Sentinel 1 Solar Array

Frans Doejaaren* and Marcel Ellenbroek*

Abstract

The Damper Spring Unit (DSU, see Figure 1) has been designed to provide the damping required to control the deployment speed of the spring driven solar array deployment in an ARA Mk3 or FRED based Solar Array in situations where the standard application of a damper at the root-hinge is not feasible. The unit consists of four major parts: a main bracket, an eddy current damper, a spring unit, an actuation pulley which is coupled via Kevlar cables to a synchro-pulley of a hinge. The damper slows down the deployment speed and prevents deployment shocks at deployment completion. The spring unit includes 4 springs which overcome the resistances of the damper and the specific DSU control cable loop. This means it can be added to any spring driven deployment system without major modifications of that system. Engineering models of the Sentinel 1 solar array wing have been built to identify the deployment behavior, and to help to determine the optimal pulley ratios of the solar array and to finalize the DSU design. During the functional tests, the behavior proved to be very sensitive for the alignment of the DSU. This was therefore monitored carefully during the qualification program, especially prior to the TV cold testing. During TV "Cold" testing the measured retarding torque exceeded the max. required value: 284 N-mm versus the required 247 N-mm. Although this requirement was not met, the torque balance analysis shows that the 284 N-mm can be accepted, because the spring unit can provide 1.5 times more torque than required. Some functional tests of the DSU have been performed without the eddy current damper attached. It provided input data for the ADAMS solar array wing model. Simulation of the Sentinel-1 deployment (including DSU) in ADAMS allowed the actual wing deployment tests to be limited in both complexity and number of tests. The DSU for the Sentinel-1 solar array was successfully qualified and the flight models are in production.

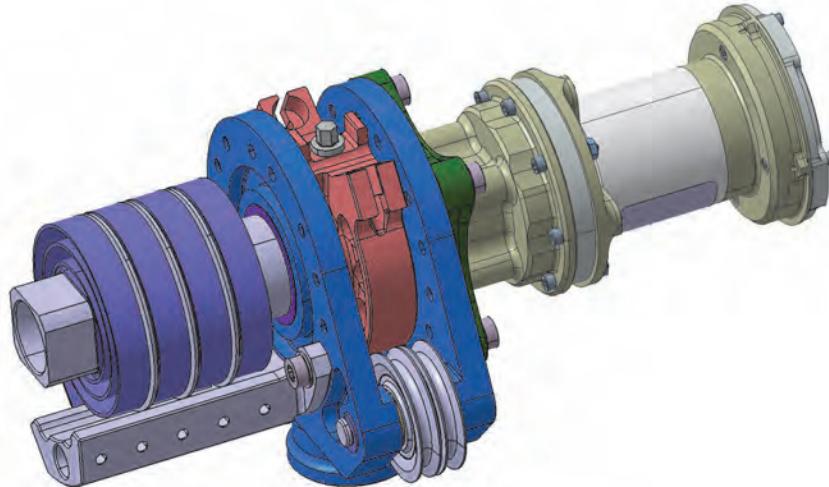


Figure 1: Damper Spring Unit.

* Dutch Space BV, Leiden, The Netherlands

Introduction

The Damper Spring Unit (DSU) is part of the deployment system of the Sentinel 1 Solar Array (SA), an ARA Mk3 product family solar array from Dutch Space. Sentinel-1 is an imaging radar satellite aimed at providing continuous all-weather, day-and-night imagery for monitoring sea ice zones and the arctic environment, surveillance of marine environment and monitoring land surface motion risks, mapping of land surfaces: forest, water and soil, and provide mapping in support of humanitarian aid in crisis situations. The function of the deployment system is to deploy the Sentinel 1 SA wing from the folded panel stack (stowed configuration) mounted on the S/C side wall to the deployed configuration (see Figure 2). The DSU is designed to provide the damping required to control the deployment speed of the spring driven solar array in situations where the standard application of a damper at the root-hinge is not feasible. The large number of power harness cables of the Sentinel 1 SA prevents the location of the damper at the root hinge. This paper gives a description of the damper spring unit and its functioning in the Sentinel 1 deployment system. The qualification program of the DSU is discussed, the torque balance analysis and deployment analysis in ADAMS, which is required to qualify the use of the DSU in the Sentinel 1 deployment system.

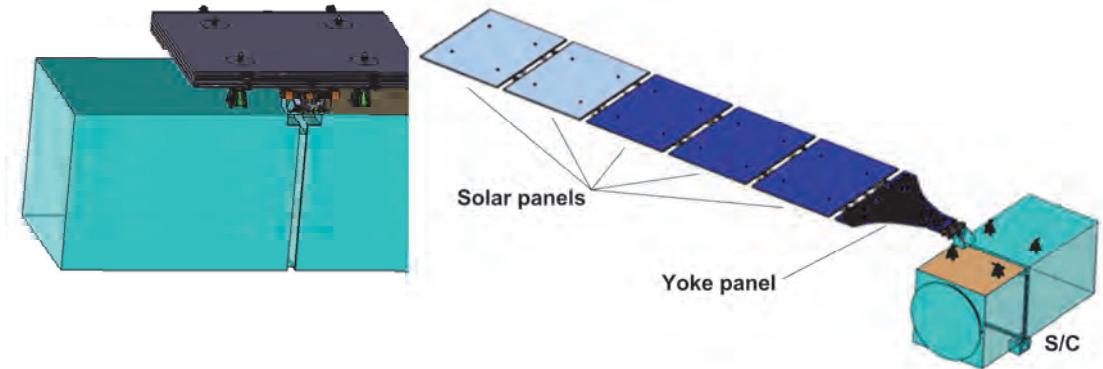


Figure 2: Sentinel 1 solar array wing (stowed and deployed configuration).

Sentinel 1

The DSU will be first applied in the Sentinel 1 solar array wing. The wing consists of 6 panels; 5 solar panels and a yoke panel. It is fixed to the spacecraft via 4 hold down stacks, each containing 2 Thermal Knives to cut the hold down cable inside the hold down stack (see Figure 2 and Figure 3). The deployment system of the Sentinel 1 SA consists of:

- Twelve (12) panel hinges per wing (i.e. two hinges per hinge line). Each hinge has a pre-tensioned spring to deliver the hinge line torque for deployment and a locking device.
- A deployment synchronization system which consists of pulleys, guide-blocks and cables to control the deployment. A system of Kevlar synchronization cables are connected via pulleys to the panel hinge assemblies. These cables synchronize the panel motion between all panels.
- The damper-spring-unit, mounted on the yoke panel front side (at sun side in deployed condition and between yoke panel and spacecraft side wall in stowed condition) and coupled via Kevlar cables to the synchro-pulley of a dedicated DSU hinge at hingeline 2 (see Figure 4).
- Kick-off-spring-unit attached on the yoke panel and connected with the root hinge synchronization pulley to support a compact first stage 90° deployment.

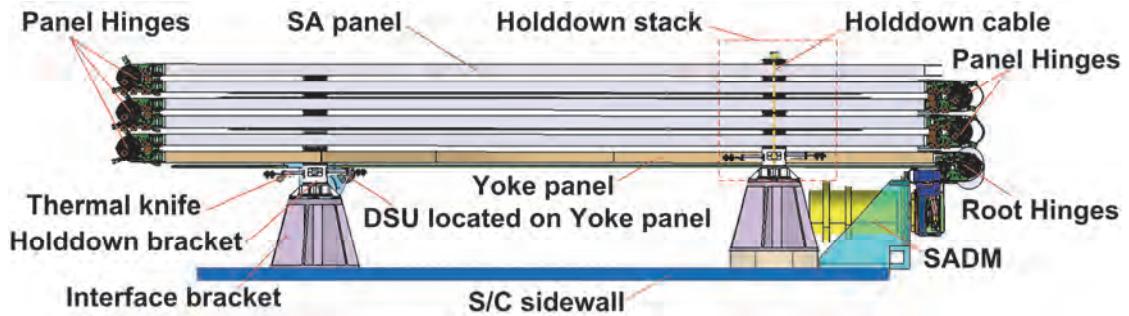


Figure 3: Sentinel 1 stowed solar array wing (side view).

The Sentinel 1 solar array deviates slightly from standard ARA Mk3 solar array designs mainly in respect with the deployment movement from stowed to the deployed configuration. The root hinge must deploy over 180 degrees, but more important, the trajectories of the C.O.G.'s of all panels have to be confined to a limited area which requires a two stage deployment movement of the panels which is shown in Figure 5. The synchronization system controls these 2 phases in a continuous way avoiding interference with S/C structure. The Sentinel 1 deployment design is a passive system as the traditional deployment system with the same design of hinges, motoring springs, synchro-cables and eddy-current deployment damper. The root hinges pulleys are, however, specifically designed eccentric and the routing of the cables is adapted. The deployment of the panels starts immediately after the last hold down cable has been cut. The deployment motion is driven by the kick-off spring on the yoke panel and the deployment springs mounted at the root hinge and at the panel hinges. The eccentric roll-on / roll-off pulleys on the root hinges realize a gradually increasing synchro-cable movement. The cable payout up to 90 degrees hinge line rotation is small, thus the panels will stay approximately stacked up to about 90° opening of the root hinge line (phase 1). In phase 2 the root hinge opens from about 90 to 180 degrees, while all other hinges open in a synchronized manner up to deployment completion (from about 5 to 180 degrees). This sequence ensures that the CoG travel and Mol shift – and therefore the disturbances on the spacecraft's attitude - are minimized. At the end of the deployment each individual hinge will latch to assure a stiff deployed configuration.

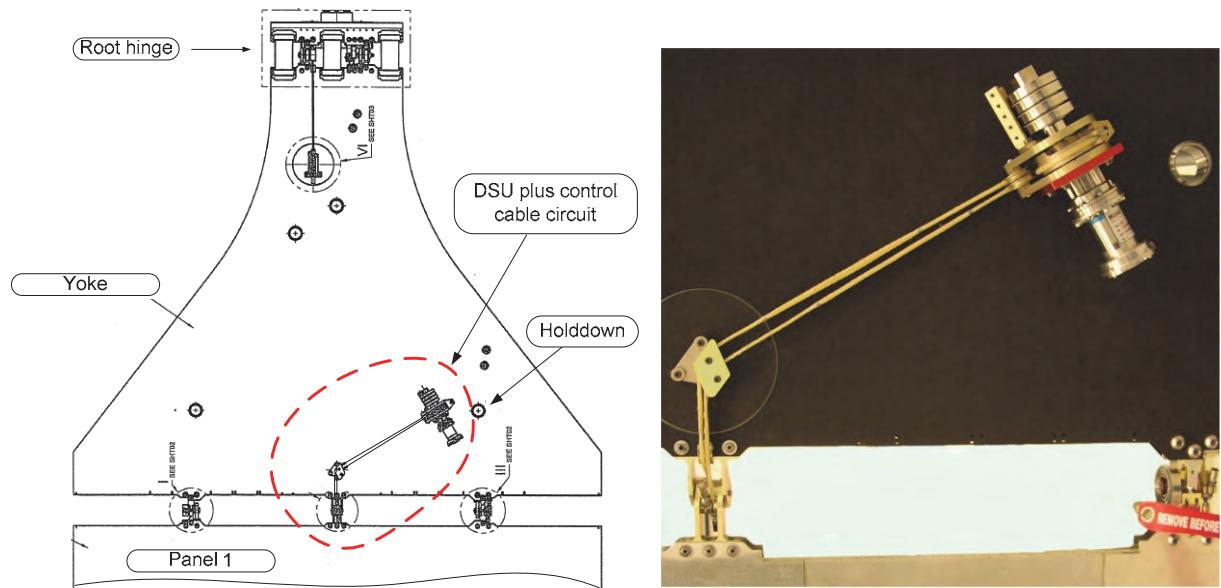


Figure 4: The DSU position at the Sentinel 1 solar array.

Sentinel 1 Engineering Model

Using engineering models helped us to identify the behavior of the two stage deployment system and how the DSU functions within this system (see Figure 5). Due to the severe thermal environment, some flexibility of the synchronization system is required. This flexibility also introduces unwanted non-synchrony. Design modifications are introduced to minimize these effects. As the DSU is not directly integrated in the synchronization system, its pulley can be increased or reduced in diameter. This change can introduce a more favorable ratio between the various pulleys and thus limit the non-synchrony effects of the flexibility. Unfortunately these effects cannot be eliminated completely, which means it has to be accounted for in the deployment analysis of the system. After the final pulley ratio was identified, the DSU design could be finalized.

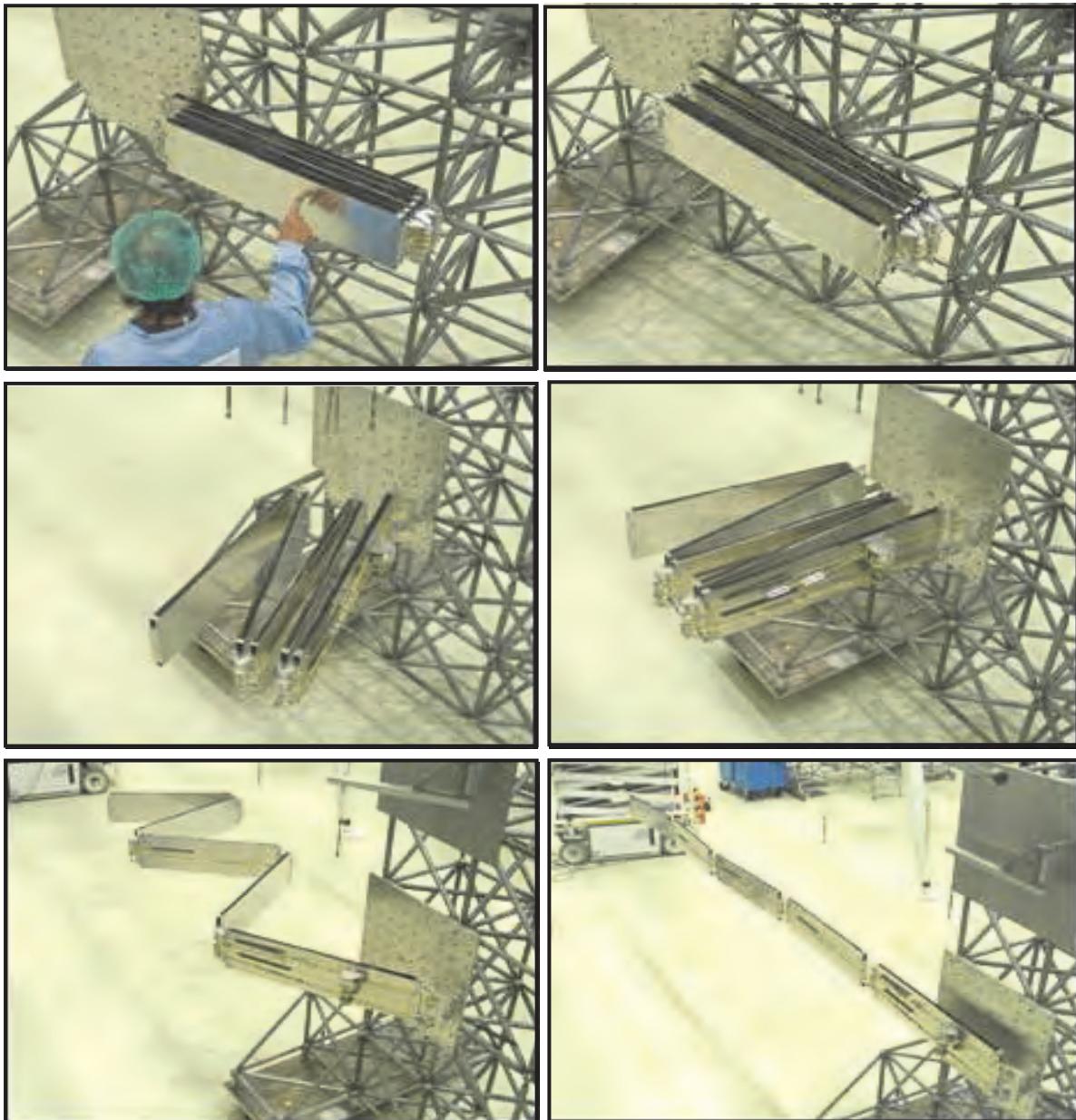


Figure 5: The deployment of the Sentinel 1 engineering model.

Damper Spring Unit description

The Damper Spring Unit consists of 4 major parts (see Figure 6):

- The main bracket, which supports all other parts of the DSU and allows fixation to the Solar Array. The main bracket interface with the solar array is dedicated per project. The Sentinel 1 DSU is fixed with a M4 into a blind insert and a M8 bolt which is interfaces with an adapted cup-cone bracket, see Figure 7.
- The spring unit, which includes 4 standard ARA Mk3 root hinge actuation springs, to counter the retarding torque of the specific DSU control cable loop and the eddy current damper start-up torque with sufficient factor of safety.
- The actuation pulley, which is coupled via Kevlar cables to a synchro-pulley of a hinge of the solar array (see Figure 9).
- The damper is an eddy current damper supplied by RUAG Space AG, Zurich, Switzerland. The damper consists of three basic modules:
 - A high efficiency damper unit which is a self-contained module with its own shaft supported by its own set of bearings. The damping is generated with a high purity copper disc rotating within a highly concentrated magnetic field. The field is provided by 12 pairs of samarium-cobalt magnets. The damping rate can be varied. The different damping rate levels depend on the relative orientation of the magnet pairs which can easily be set by rotating the ECD end cover.
 - An intermediate gear-head is employed based on a standard planetary unit. This unit provides the first stage of torque amplification.
 - The input stage is the second torque amplification stage and provides a further amplification ratio. This stage is designed to accommodate high torque levels (up to 100Nm).

The damper is currently qualified to provide a damping rate between 500 and 1700 $\frac{\text{N}\cdot\text{m}\cdot\text{s}}{\text{rad}}$ at operational temperatures of -55 to +100°C. A dedicated attachment plate is required to attach the damper to the main bracket.

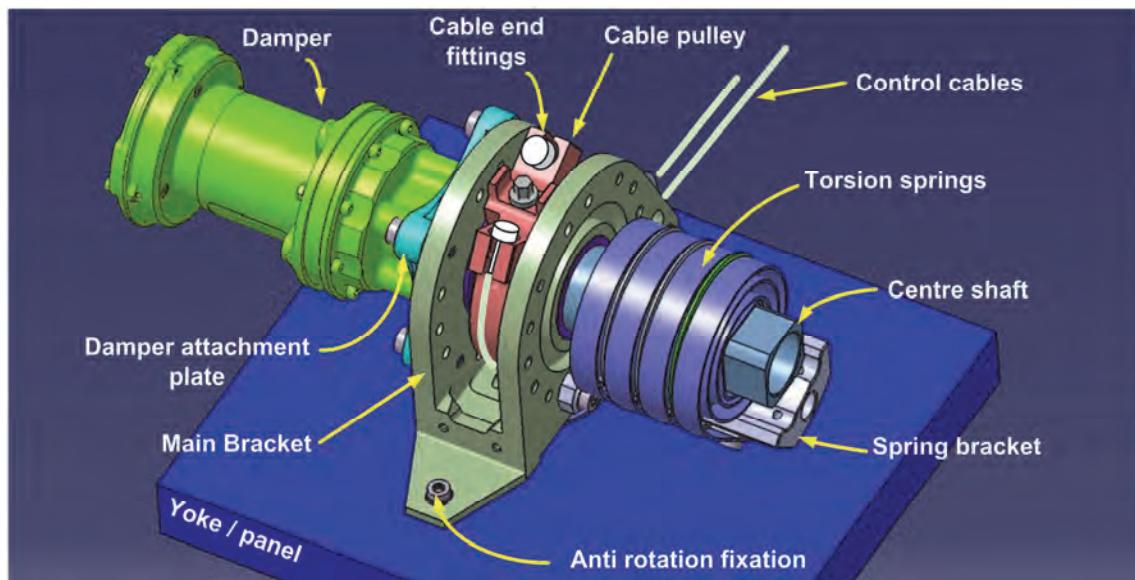


Figure 6: Damper Spring Unit parts.

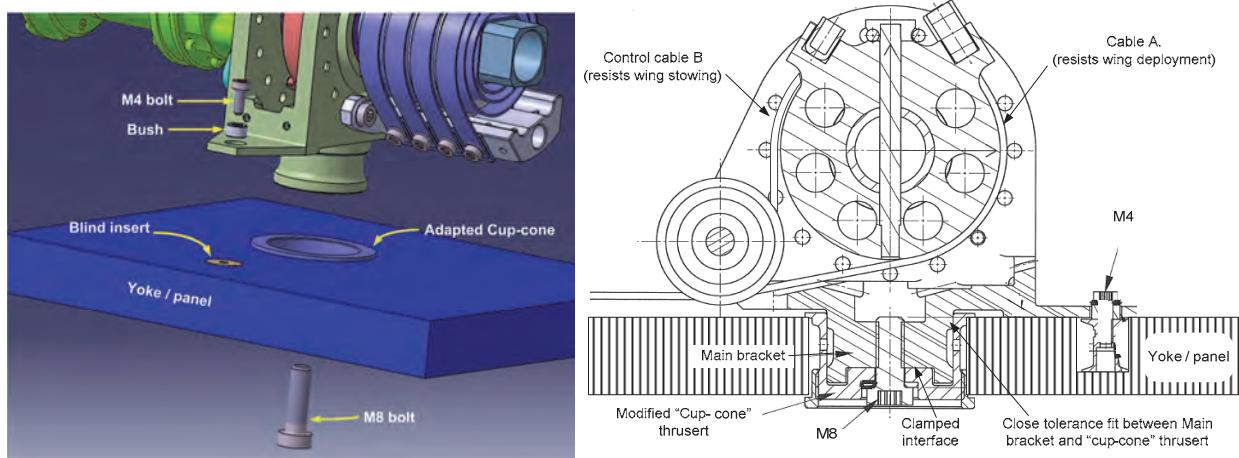


Figure 7: Damper Spring Unit interface.

Due to the heavy cable loads typical for a DSU application a new cable end fitting has been designed and qualified. The Kevlar cable is a standard ARAMk3 / FRED cable type of which the fitting is changed from a single knot in a cylindrical bush into a spike in a conical receptacle (see Figure 8). Both DSU cables contain a preload spring. The design of the preload spring depends on the routing of the synchro-cable. For the Sentinel 1 DSU cable route a preload spring with a preload of 5N has been adopted. This value is an important aspect in the torque balance of the unit as a whole and should be analyzed carefully. The torque balance analysis is described later in this paper. Figure 9 shows the interfaces of the DSU cables.

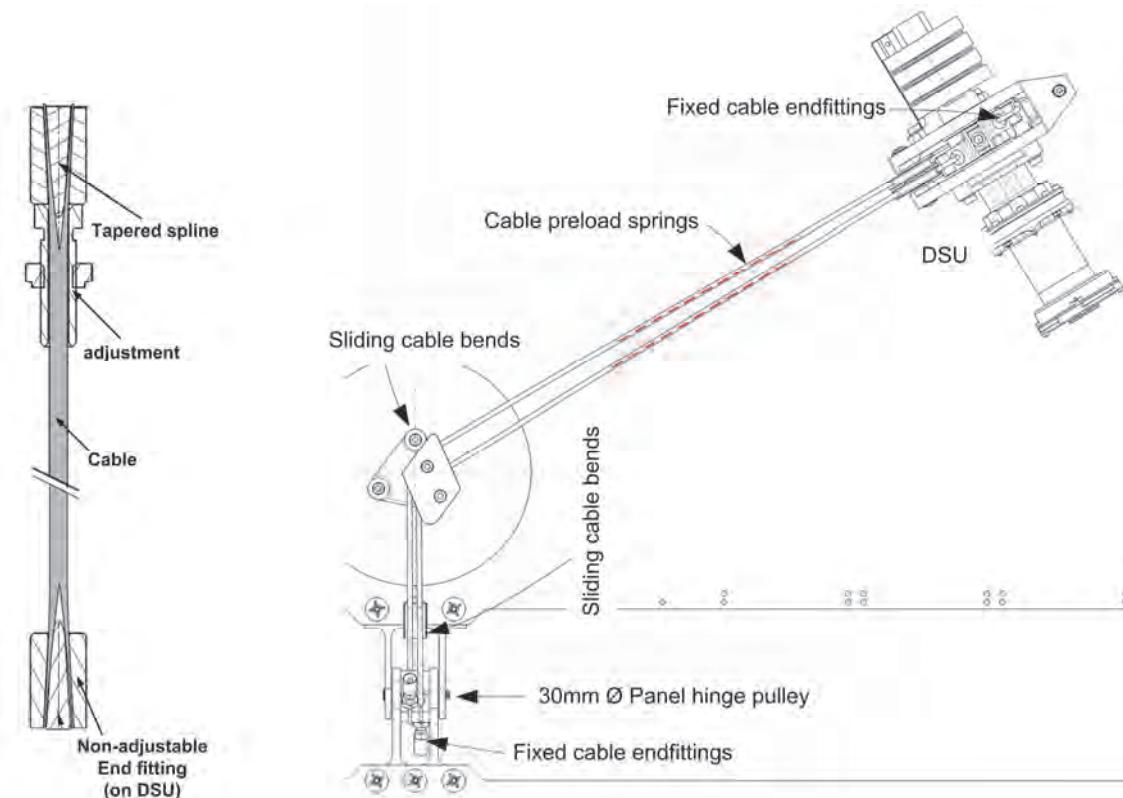


Figure 8: DSU control cable design.

Figure 9: DSU control cable interfaces.

The Center shaft design is less straightforward as one would expect due to the thermal environment requirements and the variation in thermal coefficient of the damper stainless steel input shaft and the aluminum 7075 Center shaft. The damper has a steel input shaft unlike the Center shaft, the main bracket and the cable pulley, which are of aluminum. An additional stainless steel shaft, the damper engagement shaft is introduced to interface with the damper input shaft and the Center shaft. The damper engagement shaft is coupled with the Center shaft by the lock bolt shown in Figure 10.

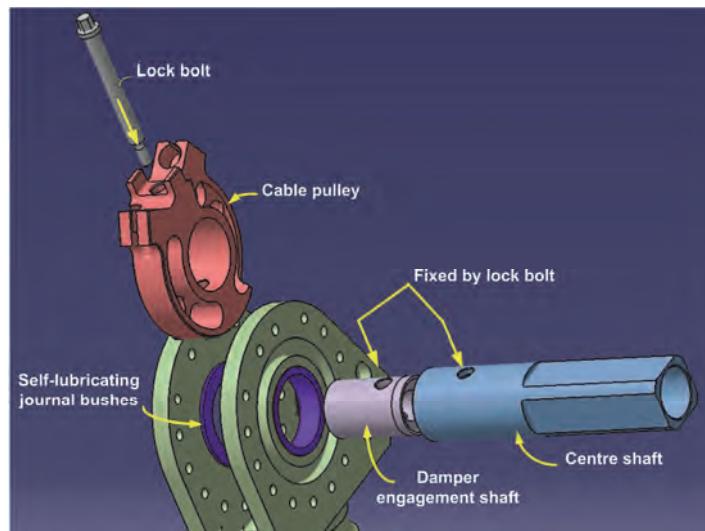


Figure 10: Damper Spring Unit shaft design.

Qualification program

The qualification program consisted of various functional tests at ambient and at the extreme temperatures (-115°C / +115°C), static load tests, random- and sine-vibration tests and a life test. As the damper has been qualified by RUAG, not all tests are performed with the damper attached to the main bracket. This allows a full characterization of the DSU, which is required to create the ADAMS model. Figure 11 gives the test sequence of the DSU, which indicates when the damper was not used.

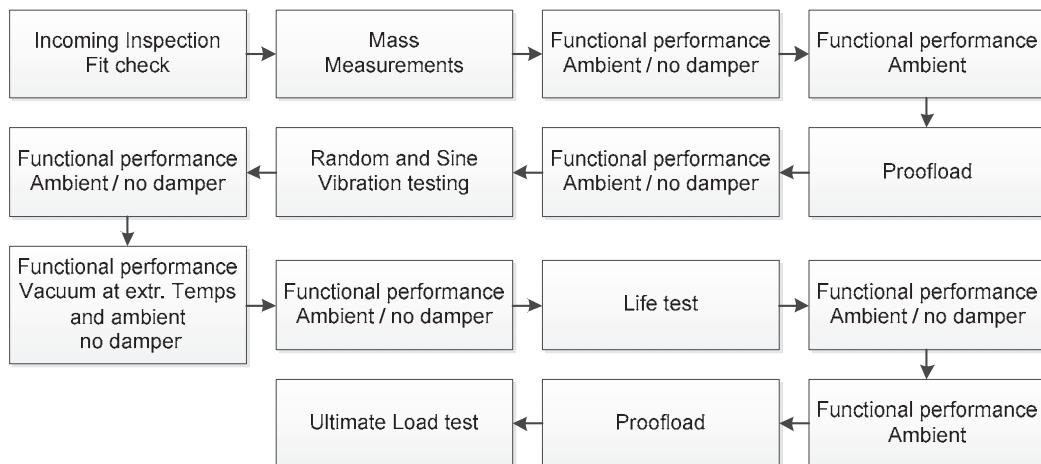


Figure 11: DSU qualification test sequence.

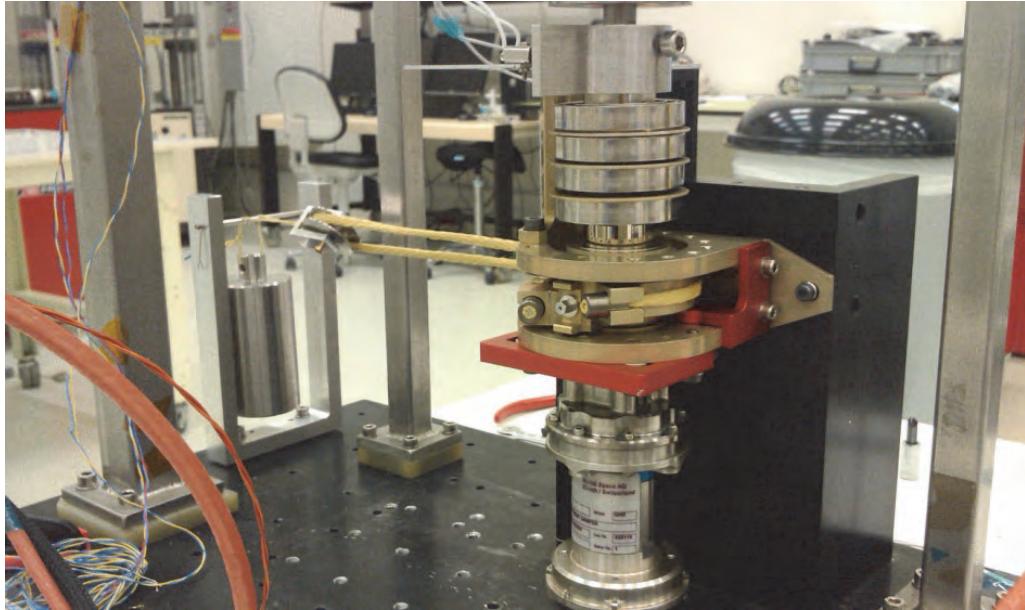


Figure 12: Functional test of the DSU qualification model (ambient).

Random vibration tests have been done and the test requirements of Table 1 and 2 have been met.

Table 1: Random Vibration Test requirements (all 3 axes)

Frequency Range [Hz]	PSD Qualification
10 – 80	+ 6 dB/oct until 0.6 g ² /Hz
80 – 400	0.6 g ² /Hz
400 – 2000	- 6 dB/oct
Overall random vibration level [G _{RMS}]	20
Duration [seconds]	120

Table 2: Sine Vibration Test requirements (all 3 axes)

Frequency Range [Hz]	g-level
5– 22	Maximum shaker amplitude
22 – 100	30

During the functional tests, the behavior proved to be very sensitive for the alignment of the DSU. This was therefore monitored carefully during the qualification program, especially prior to the TV cold testing. During TV “Cold” testing the retarding torque exceeded the max. required value: 284 N-mm versus the required 247 N-mm. This requirement had been set conservative and fortunately the torque balance analysis shows that the 284 N-mm is acceptable. Because this Non Conformance has been resolved and all other pass/fail criteria are met, like the ultimate load of cable A of 3360 N, the DSU qualification test program has been successful and the DSU design is qualified for use within the specified environment (temperatures, forces and number of on ground cycles).

Torque Balance Analysis

The torque balance analysis presented here shows the torque balance for the critical situation of the deployed position during cold deployment. In the cold condition the friction coefficients and the damper retarding torque are at their highest, and the deployed position has the lowest available DSU drive spring torque. Figure 13 shows the torque balance calculation flow and Figure 14 shows which cable forces and deflection angles are taken into account. The torque balance budget for the DSU and its control cables, given in Table 3, shows that the DSU motoring torque is a factor 3.3 higher than the worst case retarding torque. A motoring factor (torque margin) >3 is required, so this requirement is met. The DSU spring unit can provide up to 7400 N-m, consequently a higher motoring factor can be achieved if so desired.

ACTUATION TORQUE:

$$M_a = \text{DSU clock spring driving torque at deployed configuration}$$

$$\text{MOTARISATION FACTOR: } MF = M_a / M_r$$

RETARDING TORQUE:

$$M_r = \text{Summed retarding torque}$$

DSU cable induced friction torque calculation

Cable loads at the two DSU drum cables resulting from the cable preload springs.

Calculated including effects of :

- Pulley bearing frictions
- Guide block sliding frictions
- Friction at the panel hingeline induced by the cable forces

Calculation of DSU cable drum Torque to overcome:

- The difference between the two cable loads
- The drum hingeline friction due to the two cable loads

Figure 13: Torque balance calculation flow.

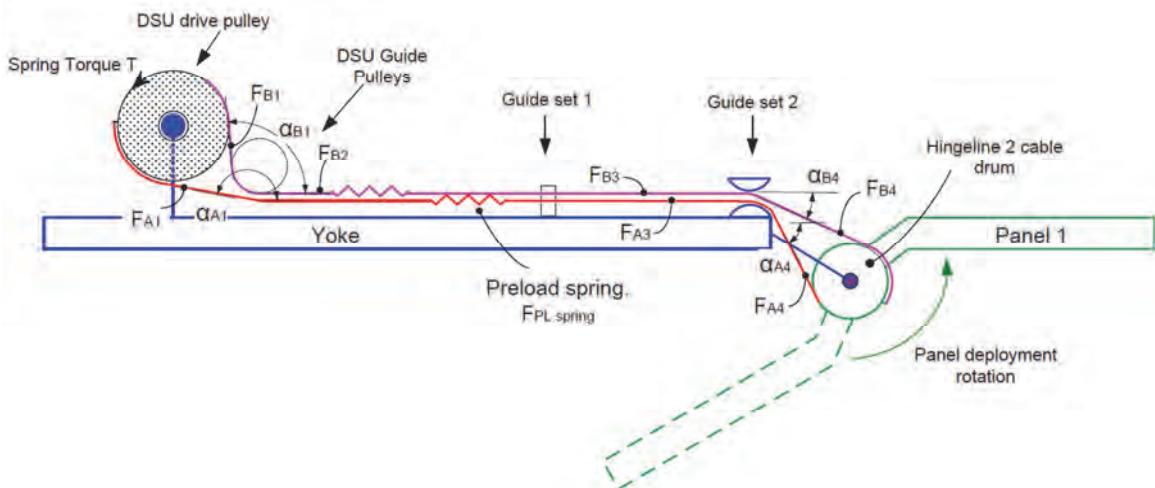


Figure 14: DSU cable forces and deflection angle definitions.

Table 3: The DSU system torque balance budget.

	COLD CASE DEPLOYMENT		
	Torque [Nmm]	Safety factor [-]	Factored torque [Nmm]
RETARDING TORQUE DSU	DEPLOYED		
damper start torque	-1240	3	-3720
Resistive torque of the DSU shaft + pulleys	-284	3	-852
TOTAL retarding	-1524	3	-4572
TOTAL motoring torque DSU springs	5100	1	5100
Motorization factor		3.3	

Sentinel 1 Deployment Simulation in Adams

The deployment of the Sentinel-1 solar array is studied with the commercial multi-body package ADAMS which is part of the mechanical engineering software of MSC. In ADAMS, a model of a solar array wing is characterized by Parts, Joints and Loads. The ADAMS Sentinel 1 model is shown in Figure 15.

The parts in the model description are:

- Panels: the yoke panel and the solar panels.
- Synchronization system: pulleys, guide-blocks and begin and end parts of the synchronization cable.
- The damper unit

The constraints in a solar array wing model define:

- revolute joints (or hinges) between the panels
- Constraints relating two markers that together define a marker for the (virtual) synchro-cable (The contributing load is implemented and a graphical element. No actual body is representing the cable)
-

The loads in the model are:

- Deployment torques, consisting of
 - Torques to deploy the stack of panels
 - Kick-off spring which pushes the complete stack during the first 60 degrees of the root hinge
- Non-linear loads to prevent that the hinges between the panels rotate beyond the structural boundaries (The panels are not able to cross each other)
- Linear loads activated when the hinge locks (=at the end of the hinge deployment)
- The damper load applied by the damper
- The loads in the synchronization cables

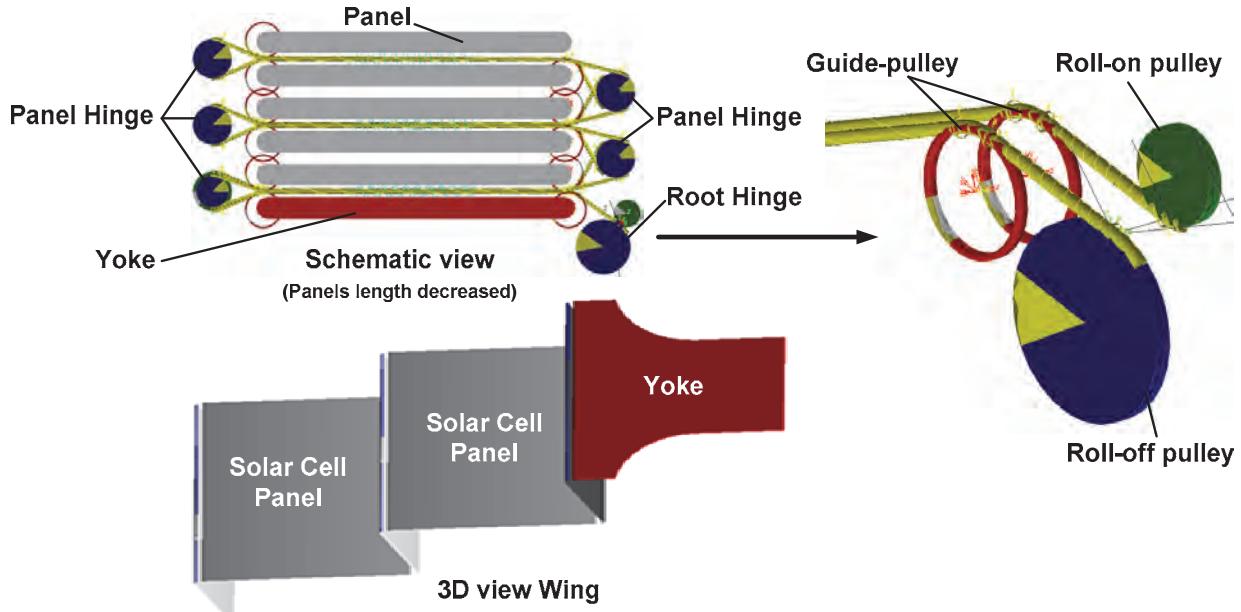


Figure 15: The Sentinel 1 SA wing representation in ADAMS.

The functional components are modeled in ADAMS as User Defined Entities (UDE's). Since the functional components are fully parameterized the UDE's can be re-used in a very efficient way. The actuation springs are straightforwardly represented by moments in the hinges. The characteristic moment – angle behavior is introduced as a prescribed curve. Unfortunately, in ADAMS cables and pulleys are not standardly available and therefore a toolbox developed by Sayfield International has been used. With this toolbox the synchronization system has also been modeled as a UDE with help of sub-models of the pulleys, slip-rings and cables from the toolbox. In these sub-models, the cables are not physically introduced but as forces. The spring damper unit is also modeled with the cable toolbox. Figure 16 shows the complete DSU system: the damper disk, where the damping load is applied, the outer disk, the cables and the pulley. Only the spring unit of the DSU is not shown. The spring is modeled by a moment as a function of the rotation angle of the outer disk.

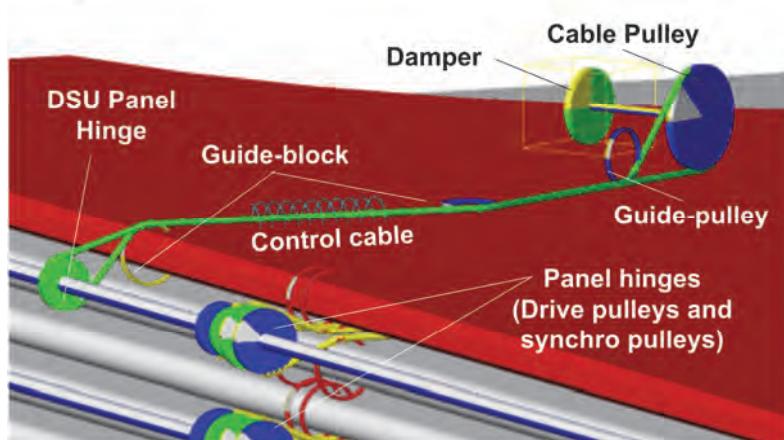


Figure 16: The DSU representation in ADAMS.

The two stage deployment of Sentinel 1 is shown in Figure 17. Such a trajectory is achieved by placing the pulleys off centered and using different sizes for the pulley radii. This adapted design changes the roll-on and roll off characteristics of the cables such that the wing opens approximately as required. This pulley configuration is shown in Figure 18.

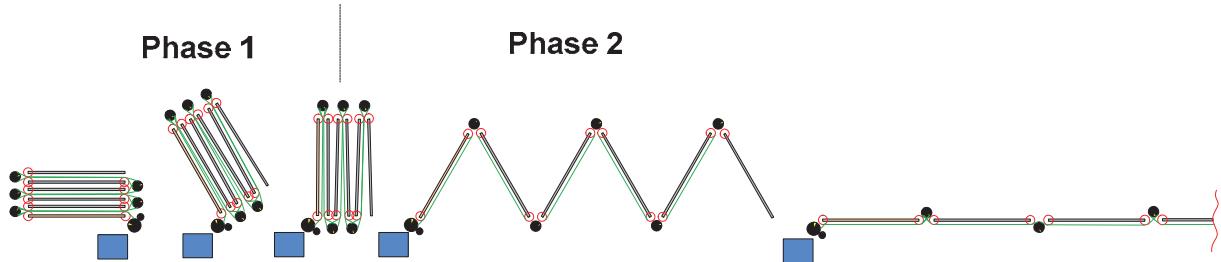


Figure 17: The two stage deployment.

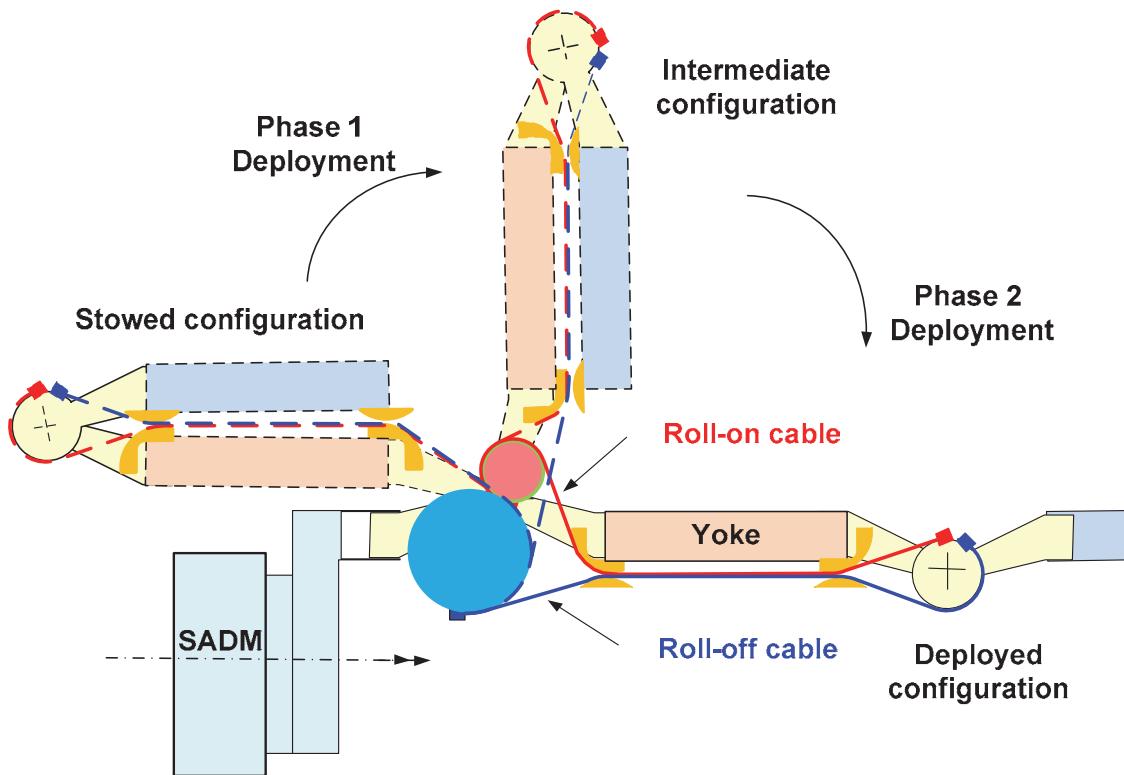


Figure 18: The Root Hinge Roll-off and Roll-on pulley configuration

Figure 19 shows the ideal roll-on and roll off characteristic and the realized characteristic as a function of the root angle. The root hinge pulleys do not display any significant roll-on and roll-off in the first 90 degrees. Because there is no roll-on and roll-off, the next hinge lines are not able to open. The stack opens as a complete package. After about 90 degrees the length of the cables starts to change with the root hinge angle forcing the next hinge lines to follow.

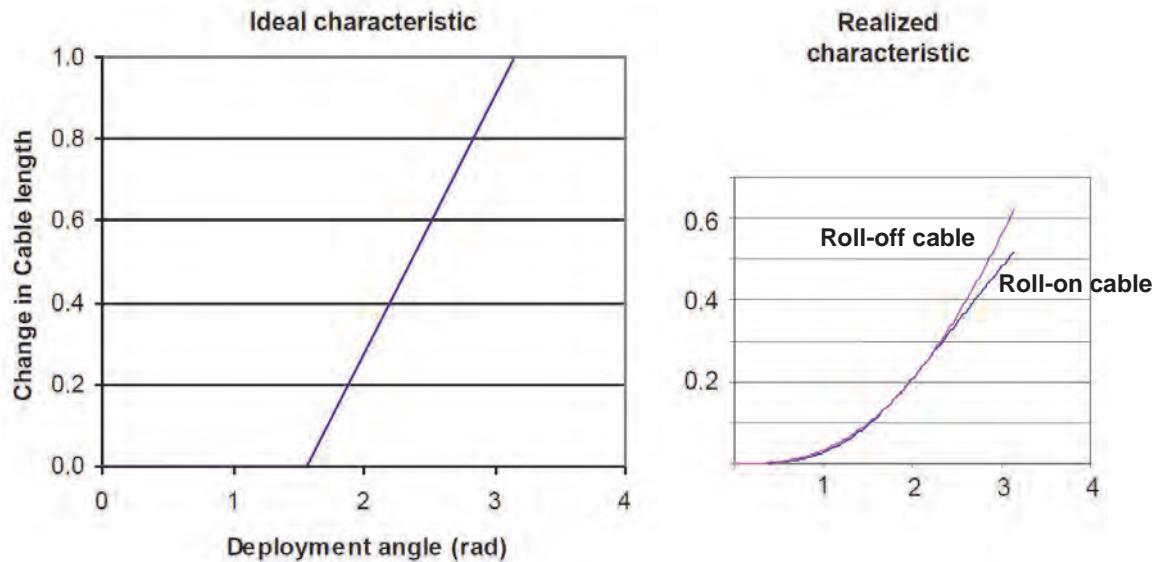


Figure 19: The roll-on / roll-off characteristic.

The parameters in the ADAMS model are now tuned to the baseline Sentinel 1 design including the flexibility of the synchronization system. The model is used to predict the deployment characteristics under various thermal conditions and provides the following output: forces in the synchro-cables and control cables of the DSU, the torque provided by the DSU, shocks in the hinges when they lock, deployment time and path of the wing and the loads at the satellite interface. The ADAMS model is validated with the deployment test results of all relevant units and consequently the ADAMS results could be used to qualify the use of the DSU within the Sentinel-1 solar array (verification of the occurring loads). It showed that the loads and shocks were within specification, the deployment time is within 88 and 284 seconds and deployment path of the Solar Array stays within the allowed deployment volume. Figure 20 shows the panel positions of the SA wing during deployment case 2, which provides maximum forces in the synchronization system.

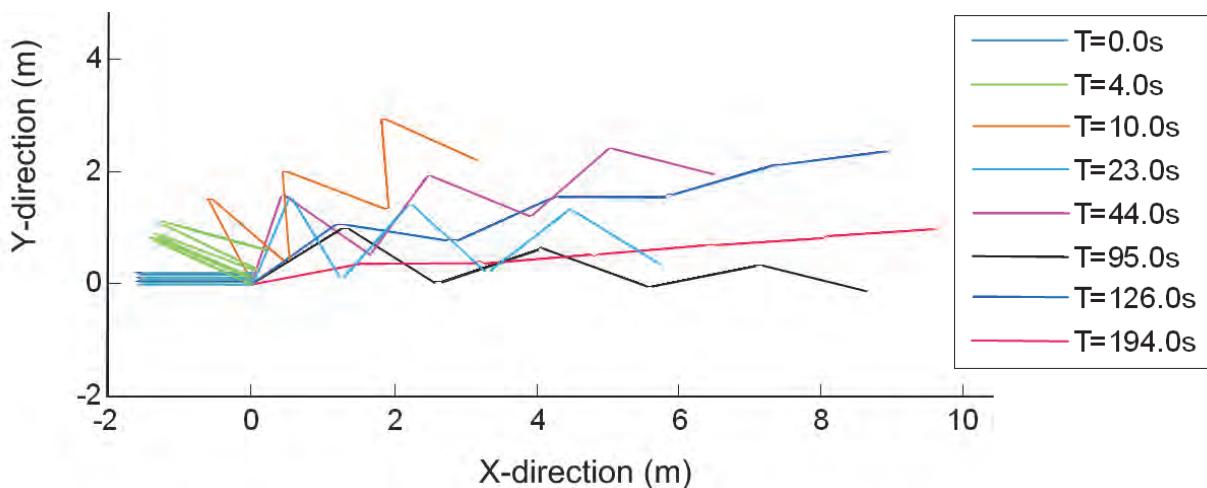


Figure 20: The deployment path of Sentinel 1.

Conclusion

The DSU for the Sentinel-1 solar array was successfully qualified and the flight models are produced (see Figure 21). Using engineering models proved to be essential to identify the deployment behavior of the Sentinel 1 wing and the required pulley diameter of the DSU. The qualification program showed that the alignment of the DSU needs to be controlled carefully to limit the friction of the control cables. The spring unit of the DSU design is over dimensioned for the Sentinel 1 SA; it can provide 1.5 times more torque than required, allowing application of the DSU in less favorable conditions / deployment systems. Representation of the Sentinel-1 deployment system (including DSU) in ADAMS allowed the actual wing deployment tests to be limited in both complexity and number of tests.

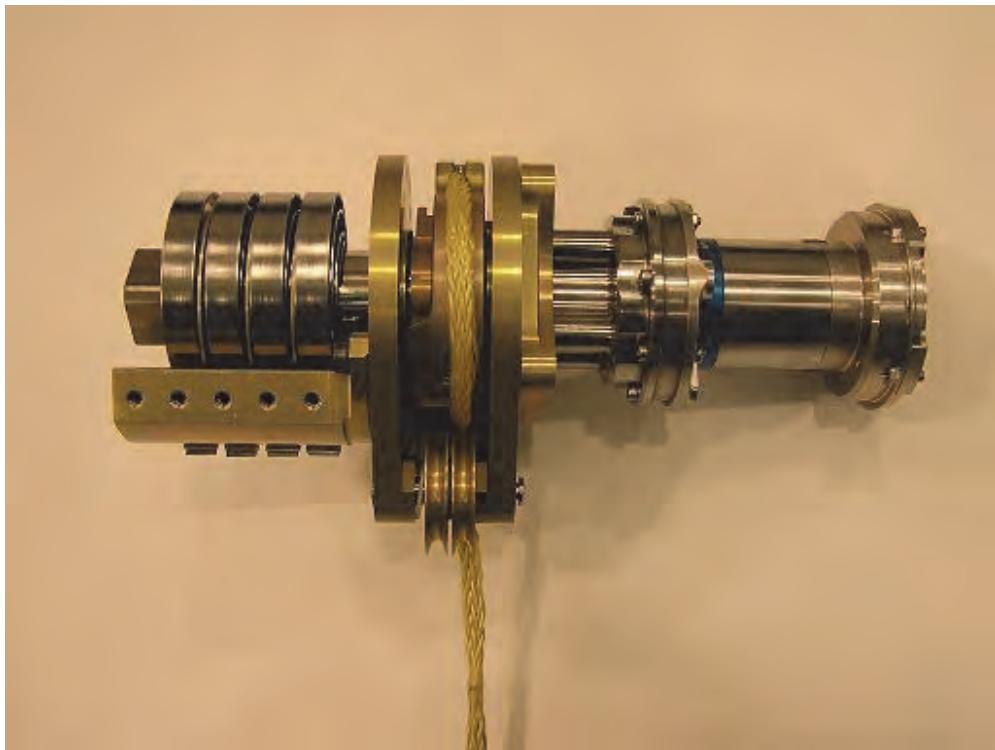


Figure 21: The DSU flight model.

Acknowledgements

The presented work has been carried out at Dutch Space B.V. The authors would like to thank Mr. B. Busz, Mr. J. Cremers, Mr. P. Duyster and Mr. T. Konink of Dutch Space B.V. and Chris Verheul of Sayfield for providing data and support.

References

1. ESA Requirements and Standards Division."Space engineering mechanisms." ECSS-E-ST-33-01C, March 2009.
2. Ruag Space AG. "Datasheet Eddy Current Damper." RUAG Space AG, Schaffhauserstrasse 580, CH-8052, Zurich, Switzerland.

Ultra-low-weight Rotary Actuator for Operation on Mars and Pin Puller Mechanism Based on a Novel Shape Memory Alloy Technology

Nestor Nava*, Marcelo Collado*, Francisco Alvarez*, Ramiro Cabás*, Jose San Juan**,
Sandro Patti*** and Jean-Michel Lautier***

Abstract

A novel Shape Memory Alloy (SMA) has been developed as an alternative to currently available alloys. This material, called SMARQ, shows a higher working range of temperatures with respect to the SMA materials used until now. This temperature restriction is one of the most critical limitations of the current SMA devices for their use in space and other applications. A full characterization test campaign has been completed in order to obtain the main material properties and check its suitability for usage as an active material in space actuators. Results of this characterization test campaign have been presented in this work. This new alloy has been proposed for its use as actuators for space mechanisms. One application of SMA technology is an ultra-low-weight rotary actuator that has been developed for operation on Mars. The aim of this actuator is to provide an in-flight calibration system for the Dust Sensor instrument of the MEIGA-MetNet Mission that will perform airborne dust opacity measurements on the Mars surface. The total mass of the actuator is less than 9 grams (without control FPGA). A Qualification Model (QM) and a Flight Model (FM) will be presented in this work. The actuator presented is designed and qualified to withstand an impact inertia up to 2000 g and work at low temperatures (-90°C) under vacuum conditions. Similarly, two versions of a Pin Puller mechanism working in the temperature range -30°C to +125°C have been designed and analyzed. Operative breadboard models of both devices were built and tested. The main characteristics of these devices as well as preliminary operating results will be shown in this work. The use of Shape Memory Alloys on the proposed actuators presents several advantages of lightweight, high force-to-weight ratio, and low volume.

Introduction

Shape Memory Alloys (SMA) can be defined as metals which, after an apparent plastic deformation in the martensitic phase, undergo a thermoelastic change in crystal structure when heated above its transformation temperature range, resulting in a recovery of the deformation that can be used to drive mechanisms [1]. SMA exhibit two properties, different than any other group of materials: the superelastic or pseudo-elastic effect and the shape memory effect [2]. When the material is at its high temperature phase, it can undergo large deformations by the action of an external stress and then instantly revert back to its original shape once the stress is removed. This behavior is known as pseudo-elasticity and it is due to the formation of stress-induced martensite. This martensite can withstand large deformations that can be completely recovered once the stress is removed [2]. When temperature is reduced, the material is transformed into twinned martensite, although if a mechanical stress is applied, the martensite structure is reoriented, producing a macroscopic deformation, apparently plastic. Nevertheless, when the material is heated, it changes to austenite, recovering its initial shape, as shown in Figure 1(a). The strain capabilities of this mechanism are usually limited to 7-8%. The martensitic transformation takes place in a temperature range that is one of the main parameters for the SMA alloys, and is called *transition temperatures*, as shown in Figure 1(b). The transformation occurs in the range defined by Ms (Martensite Start Temperature) and Mf (Martensite Finish Temperature). The reverse transformation (austenitic

* Arquimea Ingeniería, S.L., Leganés, Spain

** Dpto. Física de la Materia Condensada, Universidad del País Vasco, Bilbao, Spain

*** ESA ESTeC, Noordwijk, The Netherlands

transformation) takes place in the range between A_s (Austenite Start Temperature) and A_f (Austenite Finish Temperature). Both effects are related to the thermoelastic martensitic transformation, which is a diffusionless reversible phase change characterized by a change in the crystal structure [3]. Thus, these characteristics allow SMA to be applicable for force and strain generation, in the case of shape memory, and for mechanical energy storage, in the case of pseudo-elasticity.

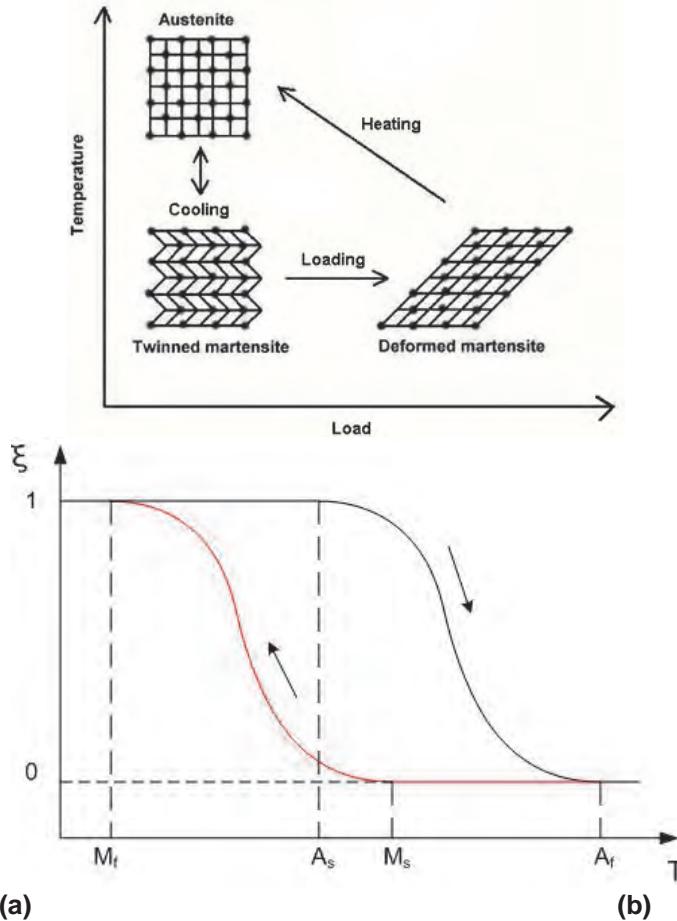


Figure 1. SMA characteristics: (a) microscopic diagram of shape memory effects; (b) martensite variation with temperature.

The main advantage of the SMA technology for its use in actuators is its great strength in relation to its ultra-low weight, optimizing the mechanical work performed by the device with a minimum mass. Furthermore, this technology has the advantage of being immune to electromagnetic interference, its noiseless actuation, and that it does not require lubrication to work.

The alloys currently available in the market, mainly NiTi based alloy, are limited in their operating temperatures. Arquimea suggests using a new SMA with further capabilities to overcome these temperature limitations. SMARQ material, a novel proprietary Shape Memory Alloy, is able to work in an extended temperature range, with transformation temperatures, tuneable during the manufacturing process, up to +180 °C. We present in this work the results obtained from the SMA characterization. In order to perform the complete characterisation of the SMA material for its use as actuators in space environment, this document explains the way the tests have been carried out by considering the SMA material as the key element of a SMA actuator. This approach requires the space characterization of the complete actuator element in order to identify the performance of the different elements in the space environment. The main objective of these tests is to obtain technical information about the actuator performances. Special attention will be paid to the main advantage of the Arquimea's SMA (SMARQ): its

higher working range of temperatures with respect to the SMA materials used until now. This temperature restriction is one of the most critical limitations of the current SMA devices for their application in space missions and other markets. The present project is expected to demonstrate the capabilities of SMARQ to overcome this limitation.

As above-mentioned, in order to perform the complete characterisation of the SMA material for its use in space environment, this document proposes to perform this characterization by considering the SMA material as the key element of a SMA actuator. A block diagram with all the constituent parts of a typical SMA device is shown in Figure 2. It must be taken into account that some of the blocks are basic blocks that must be part of any SMA device and others are optional, being or not a part of the device depending on the application requirements. The tests carried out as part of this work have been focused on the basic configuration of the SMA device, this is, the combination of the SMA Material and the mechanical and electrical interfaces. The characterization of the rest of the elements in space environment can be performed as independent blocks. The performance of the SMA material and the mechanical and electrical interfaces has been tested during the current work, in order to detect possible incompatibilities of the materials involved or mechanical limitations in the SMA actuators in space environment as well as to obtain information about the SMA actuator main parameters and working behavior.

As an application of SMA technology, a Dust Sensor (DS) instrument will be presented in this work. The Dust Sensor instrument of the MEIGA MetNet Mission will perform airborne dust opacity measurements on the Mars surface. The Dust Sensor is designed as a lightweight device (41 g) that performs an active measurement, using back scattering to estimate the concentration of particles in the airborne dust. The unit integrates an infrared (IR) optical active detector (there is an IR emitter and an IR detector) for a spectrographic (discrimination in wavelength) measurement of dust in suspension.

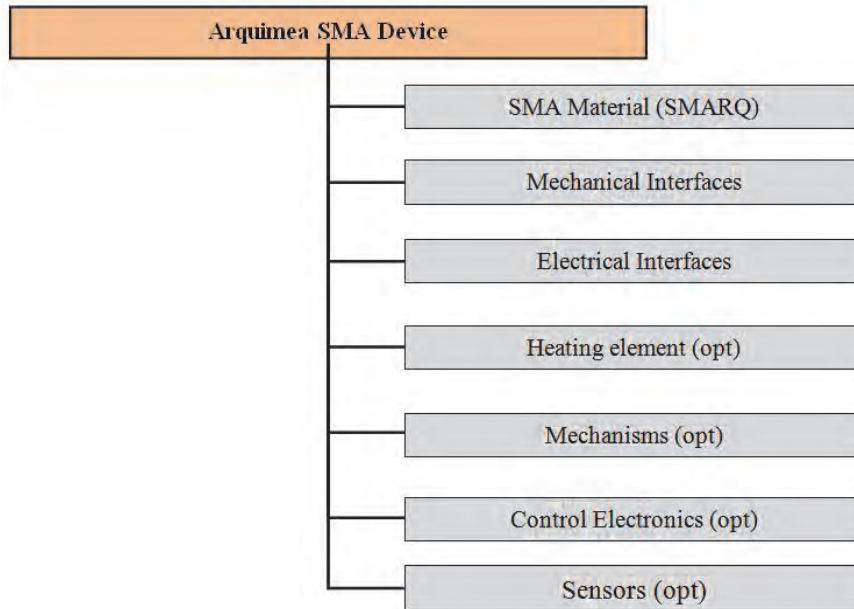


Figure 2. Block diagram of Arquimea SMA Device.



Figure 3. Qualification Model of the Dust Sensor

The emitter points to the airborne dust and the detector collects the scattering signal produced by the emitter light when interacting with particles similar in size to the light wavelength. Figure 3 shows the qualification model of the Dust Sensor device. The DS includes an in-flight calibration system based on a reflector stick that allows directing the emitter optical signal directly to the detector. The reflector stick is inserted in the optical path, when the actuator system is commanded to do so, by means of an actuator based on a Shape Memory Alloy. This in-flight calibration system is used to compensate the error in the entire DS acquisition chain. There is a weight budget of 40 grams for the Dust Sensor instrument, due to the small weight budget of the full MEIGA mission. This has greatly affected design decisions such as the lack of an enclosure, reduced support structures, limitation to the number and size of electronic components, and mainly in the actuator design. The mass budget for the actuator was less than 10 grams, which implied a challenge in design. The Dust Sensor device is controlled by the onboard computer of the MetNet Lander. Periodically, according to a preprogrammed schedule, the Dust Sensor device is powered on and a sequence of instructions is executed. Table 1 summarizes the main characteristics of the Dust Sensor device.

A novel Pin Puller mechanism based on SMA technology will be presented. A Pin Puller is a mechanical device in which a pressure cartridge causes a pin or piston to retract inside the structure frame, usually against a side load. In the extended position, the pin or output shaft can be seen to be loaded by a compression spring.

Table 1. Dust Sensor main characteristics.

Characteristic	Value	Notes
Mass	41.2 grams	
Main dimensions	85x65x20 mm	
Power consumption	360 mW nominal	2250 mW peak consumption during 750 ms max.
Voltage operation	5 V	
Communications	422 serial comms	Command oriented instrument.
Temperature accuracy	$\pm 1.5^\circ\text{C}$	
Reflector position accuracy	$\pm 7.5^\circ$	
Operational temperature range	-90 °C to +25 °C	Also in vacuum

The pin remains firmly locked in this position due to mechanical components that block the stroke. Once actuated, however, the actuator drives specific mechanical components releasing the stroke and allowing the pin to retract under the force of the drive spring. The Pin Puller is reset by manually moving the pin back into the extended position. This is done by either pulling it out from the top or pushing it from the bottom. The Pin Puller acts as a trigger for deployment mechanisms. The inertia force of the Solar Array

panels, antennas, booms, aperture door covers, etc. will be reacted through the release mechanism – through the Pin Puller in the shear direction across the pin and the housing to the structure. Pin pullers are normally used in pairs for redundancy. Applications include “Hold Down and Release” of numerous satellite deployable including solar panels, communication antennas, instrument cover doors, radiators, heat shields, tether experiments, and isolation systems. SMA Pin Pullers provide a number of advantages compared to traditional pyro devices:

- (1) There is no (or minimum) shock associated with SMA devices (note that there have been reported instances when pyro pullers have tripped relays when fired).
- (2) The number of safety personnel providing oversight during the installation of SMA devices would be greatly reduced.
- (3) Deployment tests can be performed repeatedly without having to remove/reinstall Pin Pullers.

The product tree for the SMA Pin Puller mechanism, including its classification by trigger mechanism is shown in Figure 4.

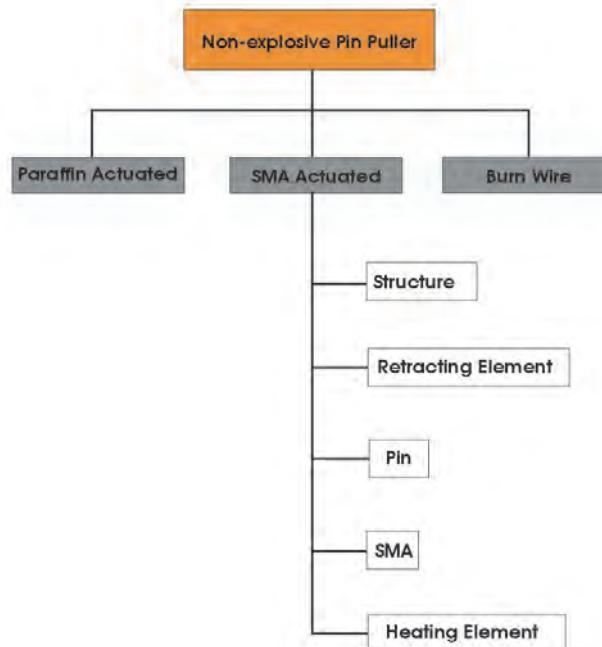


Figure 4. Product tree for the SMA Pin Puller mechanism.

A novel Shape Memory Alloy

SMARQ is a fully European material technology and production processes, based on a low cost production procedure, which allows the manufacture of high quality products. Both material and production processes are currently being evaluated for use in space applications. In order to perform the complete characterization of the SMA material for its use in space environment, the SMA material (SMARQ) has been considered as the key element of a basic SMA actuator, consisting in the SMA material and the mechanical and electrical interfaces (Figure 2). The tests carried out as part of this work have been dedicated to the basic configuration of the SMA device. The tests have been focused on the actuator behavior when heated by means of an electrical current. The characterization of the rest of the elements – such as external heater elements, mechanisms, sensors or control electronics – in a space environment can be performed as independent blocks. A transition temperature (A_s) of +145°C has been selected for the test samples in order to satisfy the initial environment requirements of operation temperatures between -70°C and +125°C.

SMARQ Characterization Test

A complete characterization test campaign for Arquimea's SMA material (SMARQ) was planned and completed. This test campaign included several tests in order to demonstrate the material capabilities to be used as the trigger element in space mechanisms. The following blocks of tests were carried out:

- Strength characterization tests.
 - Maximum Strength Test
 - Reconditioning Force Test
 - Superelastic Test
 - Pull Force Performance Test
- Transition temperatures tests.
- Electrical activation tests.
 - Electrical activation at 22°C.
 - Electrical activation at +125°C.
 - Electrical activation at -70°C.
- Lifetime tests at extreme thermal conditions.
 - Lifetime at +125°C.
 - Lifetime at -70°C.
- Material behavior tests in vacuum conditions.
- Assessment of material compatibility in space environment.

Strength characterization tests

The scope of these tests is to obtain information about the force capabilities of the SMA actuator. A maximum strength test was carried out to determine the maximum applied stress the material can withstand without failure. A reconditioning force test has been performed in order to obtain information about the stress necessary to deform the SMA at its martensite phase and its behavior at different temperatures. An additional test, consisting of completing several load/unload cycles at different temperatures over the Austenite Finish Temperature (A_f), in order to obtain the superelastic behavior of the material has been completed. Finally, a test was included to obtain information about the pull force performance (maximum force) of the material, by blocking the actuator movement during the phase transformation and measuring the generated force. A Tensile Test machine with oven has been used for the strength characterization. The equipment is able to perform universal tension tests at a controlled temperature, in the range between ambient and 200°C.

Transition temperatures test

This test has been carried out to obtain data about the material transition temperatures (A_s , A_f , M_s and M_f) for different samples. The non-operation temperature and the relationship between the strain and the temperature during transformation were obtained with this test. Arquimea's Actuators Test Bench was used to complete this test, as shown in Figure 5(a). The equipment is specifically designed to test smart materials and actuators, allowing the execution of complete thermo-electro-mechanical characterization of both, in its actual working configuration. The bench can also control the actuation of the device using an electronic driver and it has an oven that allows heating the sample to a specific temperature.

Electrical activation tests

An activation test has been performed at different temperatures in the working range (-70°C, +125°C). The material was loaded and externally activated by an electrical current. Measurements on strain, force, power consumption and generated force have been carried out for several samples, providing information to estimate the power consumption and the heating and cooling times. Arquimea Actuators Test Bench of Figure 4(a) was used to complete this test at temperatures between ambient and +125°C.

For the cryogenic tests (-70°C), a new test bench has been developed, as shown in Figure 4(b). A thermostatic bath was used to control the environment temperature of the sample at cryogenic temperatures down to -70°C. The bench used a vertical measurement approach in order to allow the

sample immersion in the thermal bath. Special attention was paid to the sample thermal isolation, in order to avoid the direct contact of the SMA with the thermostatic liquid, which would produce an important change in the convection conditions and therefore in the actuator behavior.

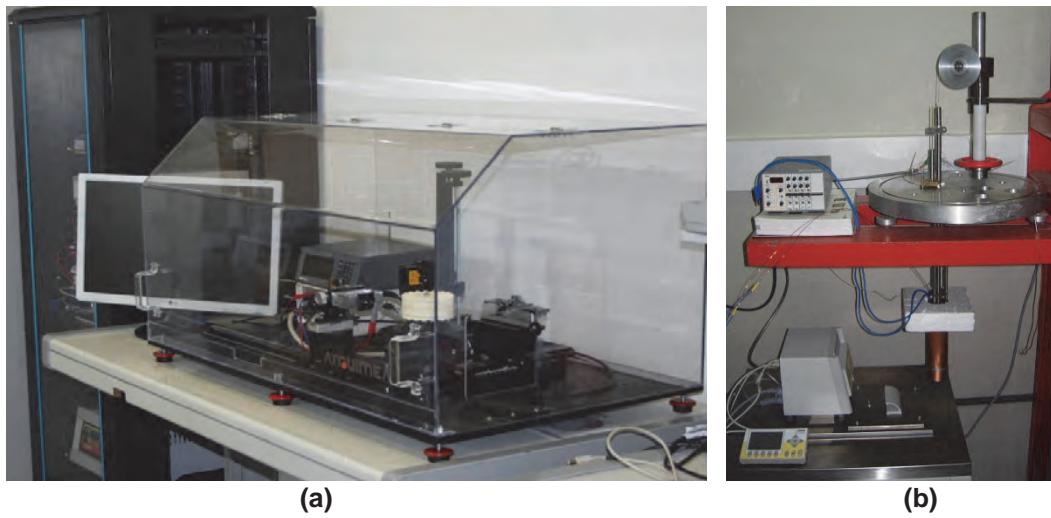


Figure 4. Devices used in the characterization campaign of SMAR: (a) Arquimea Actuators test bench; (b) test bench for cryogenic test.

Lifetime tests

The scope of this test is to obtain an initial approach to the lifetime capabilities of the material. The tests have been limited to probe that the material is able to complete 100 cycles at the worst case temperatures (-70°C and +125°C) without degradation of its performance. A lifetime of 100 cycles is a typical requirement for one-use space actuators, such as release and deployment actuators. The test bench of Figure 4(a) was used for the lifetime test at +125°C, while the test bench of Figure 4(b) was used for -70°C.

Vacuum tests

Due to the importance of the changes in power consumption and response times under vacuum conditions, a vacuum test was included in the SMA characterization test campaign. The objective of this test is to obtain technical information about the behavior of the SMARQ actuator in vacuum conditions at ambient temperature. A specific test bench has been developed for the vacuum tests. The equipment allows the strain and force measurement as well as the actuator electrical activation in vacuum conditions under constant loads. The test has been done controlling the pressure inside the vacuum chamber ($\sim 5 \cdot 10^{-3}$ mbar) and at ambient temperature (22°C).

Test Results

Strength characterization tests

The Maximum Strength Test was successfully completed. The material has shown its capabilities to withstand high loads, both in martensite and austenite phases. The material fractures at 500 MPa in its martensite state, showing an elongation over 12%. In the case of the test at higher temperatures, a stress of 400 MPa was applied without fracture of the sample.

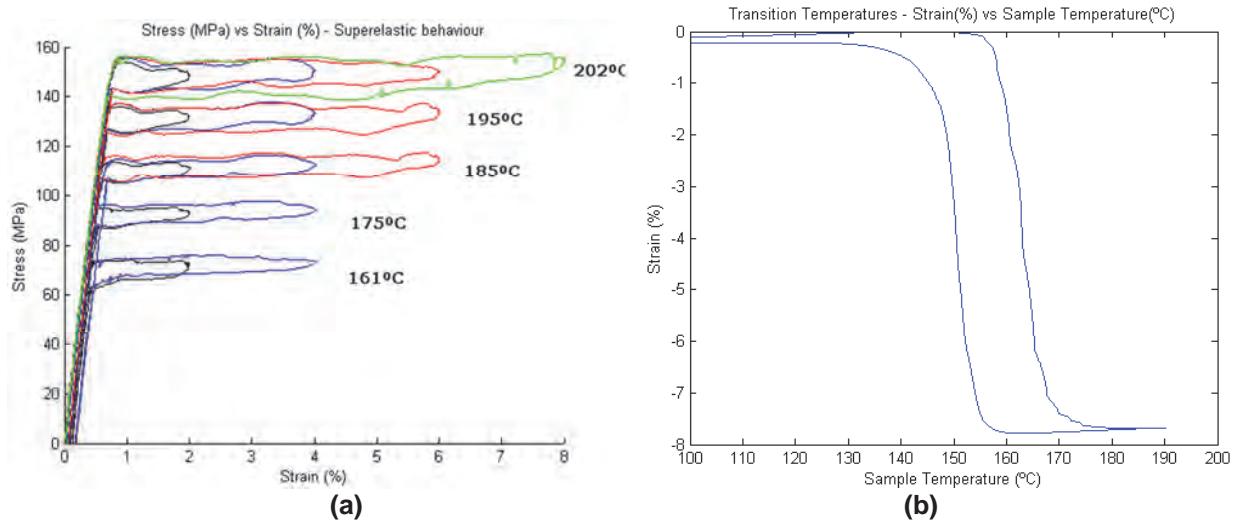


Figure 5. Results of strength characterization and transition temperature test: (a) reconditioning force – superelastic behavior; (b) SMARQ Transition Temperatures - Strain vs. Temperature. Actuation above 125°C is shown.

These stress levels are far beyond the elongation and loads used in the actuators, so the material shows good properties for its application in terms of strength. The results show that a maximum superelastic strain around 10% would be feasible. During the Reconditioning Force Test, important information was collected about the force required to deform the material at different temperatures. The Superelastic Effect test has shown the typical behavior of superelasticity, Figure 5(a), with the existence of upper and lower load plateaus at different temperatures, where the deformation takes place with approximately constant stress. A maximum deformation of at least 8% could be achieved during superelastic cycles. Information about the Clausius-Clayperon curves was also obtained after this test. The Pull Force Performance Test has successfully been completed. The transformation has been observed and the stress levels obtained are high. The material output force capabilities are shown to be over 120MPa.

Transition temperatures test

The test results of Figure 5(b) show that the material is able to work at environment temperatures over 125°C, since the austenitic transformation starts, under the applied load conditions, around 145-155°C. Besides, the material shows a martensitic transformation which finishes over 135°C, so the material would be completely in martensite state along the whole environment temperature range (-70°C, +125°C). A thermal hysteresis of 15°C has been obtained during the transformation and an 8% strain has been recovered.

Electrical activation tests

The test has shown the capabilities of the material to be electrically activated in the extreme temperatures in the working range, as well as in ambient temperature. This test shows that the material is able to work perfectly at these temperatures. The main differences between the tested temperatures are the energy necessary to complete the actuation, in terms of power and time, due to the higher difference between environment and transition temperatures. Information about the maximum non-firing current, activation currents, response times, and power consumption at each temperature have been obtained. The behavior of the wire during the electrical actuation was similar to the one produced with the oven in previous tests (transition temperatures test). A good stability and repeatability has been obtained along the cycles. Information about the wire resistance and its relationship with strain has been obtained. Moreover, an estimation of its relationship with the temperature has been carried out.

Lifetime tests

All the samples have successfully completed this test at both extreme temperatures. The values obtained during the 100 actuation cycles at each temperature for strain, stress, resistance and times show a high stability in the actuator behavior along its lifetime at the highest and lowest temperature in the working range.

This shows that the present actuator technology is mature to be used in applications with these environment and lifetime conditions. The test has shown the material capabilities to satisfy the lifetime requirements in the current application. It should be taken into account that the samples have suffered a larger amount of cycles during the whole test campaign, so the actual lifetime obtained is >200 cycles. Figure 6(a) shows the high stability in the strain behavior along the cycles in the lifetime test at +125°C. A comparative view for some of the cycles is shown in Figure 6(b). Future test will be conducted to verify the full capabilities of the technology in terms of lifetime. Tests will be completed in order to obtain the real lifetime limit for a 3.5% strain. Furthermore, other lifetime tests will be performed with different strain levels.

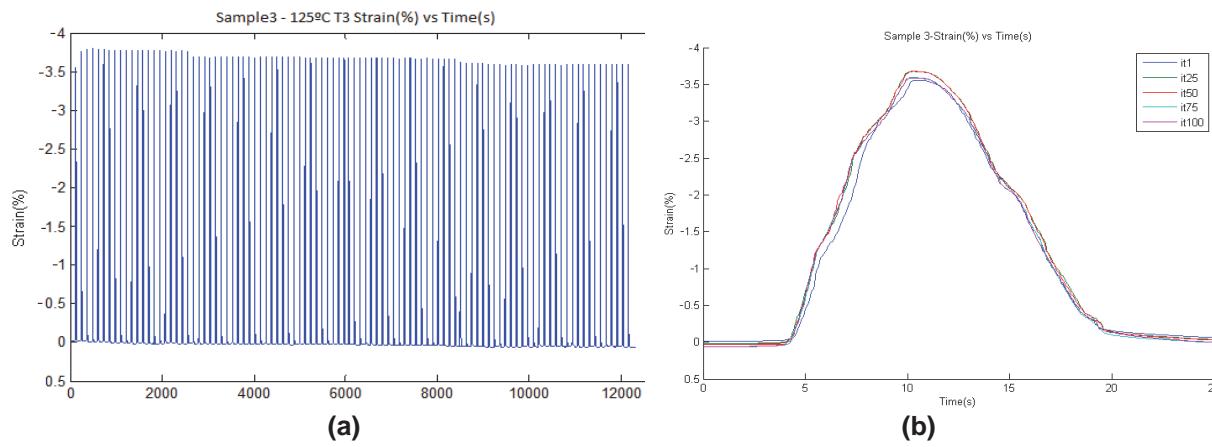


Figure 6. Results of lifetime tests: (a) Lifetime (+125°C) – Strain (%) vs. Time (s) (b) Detailed cycles: 1, 25, 50, 75 and 100.

Vacuum test

The cycles were successfully completed during this test. Complete actuations were achieved by using a power less than 1 W. The minimum required power to complete the actuation and the response time, are lower than the obtained in air, as could be expected. Finally, the material has not shown any problem related to the vacuum level during the test. More tests at higher vacuum levels will be done in the future in order to ensure the material works in a space environment. The main results obtained by SMARQ during the characterization test campaign in comparison to NiTi alloys are shown in Table 2.

An excellent behavior in terms of operating temperatures was shown, with capabilities to operate over the limits of current SMA technologies. Good results in terms of reliability and lifetime were also obtained during this work. Successful results were also found during the vacuum tests. Further work is being carried out in order to obtain extra information about the material, especially related to lifetime and vacuum behavior. Research work for the material resistivity optimization are on course and based on the SMARQ heritage, a new generation of mechanisms based on this technology will be developed in the near future.

Table 2. SMARQ Performances.

Property	Units	SMARQ	NiTi
Transformation Temperature (A_f)	°C	> 150 (173°C)	Max. 100
Non-actuating Temperature	°C	> 125 (As=152°C)	Max. 80
Difference ($A_s - A_f$)	°C	21	20 – 30
Thermal hysteresis	°C	15	30
Max. Strain recovery (One way memory)	%	~ 8	6 – 8
Maximum Strain (Superelasticity)	%	> 8	8
Recovery Stress (Martensite to Austenite)	MPa	~120	300 – 600 (Max)
Maximum Strength (Martensite)	MPa	~500	800 – 1000
Elongation at Failure	%	12	10 – 15
Stress Rate	MPa/°C	2	4 – 20
Electrical Resistivity (Martensite)	$10^{-6} \Omega \cdot m$	0.1	0.5 – 1
Power Consumption	$10^{-6} W \cdot m^2/m$	24.2 (min @ -70°C, air convection)	< 60
Response time	s	4.5 s (Tested geom. @-70°C, 4.5W, $A_f=173°C$) (*)	4.3 s (Test geom. @- 70°C, 4.5W, $A_f=90°C$)
Lifetime	Cycles	Tested > 100 (3.5%) (*)	100 (6%) 10^5 (2%) 10^7 (0.5%)

(*) No complete tests were performed to establish these parameters. Partial tests were carried out as a first approach. Nevertheless, the values are expected to be competitive with respect to NiTi.

Table 3. Rotary actuator main characteristics.

Characteristic	Value	Notes
Mass	< 9 grams	without control FPGA
Power consumption	2250 mW during 0.75 ms	
Voltage operation	5 V	
Torque	15.75 N/mm	
Rotary movement	40°	
Life	>700 cycles	
Operational temperature range	-90 °C to +25 °C	
Survival temperature range	-90°C to +70°C	
Operation time in vacuum	<750 ms	750 ms correspond to the worst case. This value depends on the initial temperature of the actuator.

A Rotary Actuator for Dust Sensor

One application of SMA based actuators is the presented, which comprises a rotary mechanism actuated by a SMA Fiber, a position sensor, an electronic driver and a control algorithm. Table 3 presents main technical details of the rotary actuator integrated in the Dust Sensor device. The actuator integrated in the Dust Sensor is an ultra-light weight rotary actuator based on a Shape Memory Alloy (SMA) fiber. The SMA fiber contracts when heated beyond the characteristic transition temperature of the material. This contraction is used for generating a rotary movement of a stick reflector. The stand-by or relaxed position is reached thanks to a return spring. The actuator has an integrated rotary position sensor for control and characterization of the actuator movement. This rotary sensor is a double capacitance detector which gives a rough position value of the reflector. The consumption of this sensor is negligible and its weight is very low since part of the sensor is integrated in the PCB of the Dust Sensor. A limit switch (end of stroke) is included as a redundant element to switch off the activation of the DS. This switch will detect that the reflector stick has reached its final position, the signal will be interpreted by the FPGA and immediately the actuator will be powered off. The actuator hardware includes an electronic driver that provides the SMA fiber a power line of +5V, ~500 mA. For reliability reasons, the driver is commanded using a signal above 1 KHz from the control FPGA, neither a 5 V DC nor 0 V DC signal will activate the SMA. A control algorithm completes the actuator system.

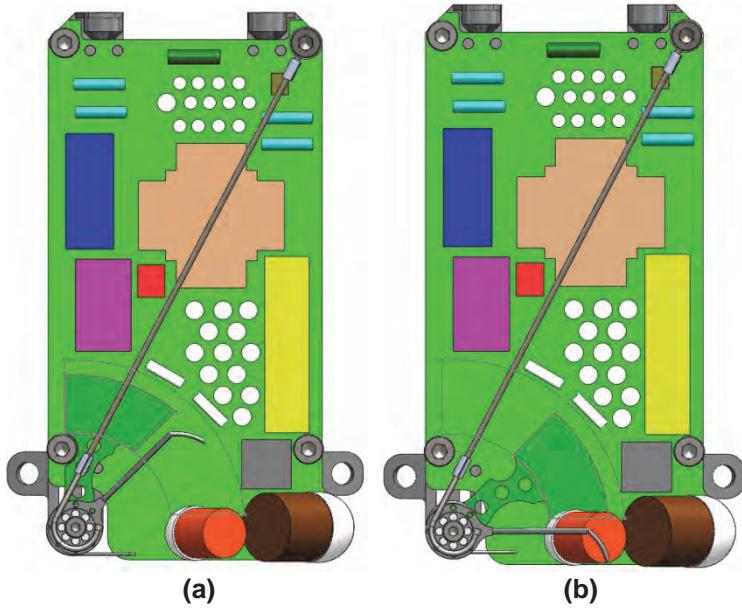


Figure 7. Initial (a) and further (b) position of the reflector stick.

The algorithm running on the Dust Sensor FPGA commands the actuation receives information of temperature, rotary position and limits switch sensors and sends a feedback to the electronic driver. Figure 7 shows the initial and further position of the stick reflector during an actuation

Qualification Campaign of Dust Sensor

Qualification objective is to demonstrate that the Dust Sensor conforms to the requirements of the mission including margins. The following tests have been applied to the Qualification Model of the Dust Sensor:

- Thermal cycling and vacuum test from -90°C to 70 °C, 6 cycles.
- Vibration. QM DS was subjected to qualification levels of sinusoidal and random vibration.
- Bioburden reduction. Due to planetary protection requirements, a bioburden reduction process shall be applied to the DS unit.
- Humidity low-temperature verification test. A low-temperature verification test in a humidity atmosphere was carried out.

- Shock. QM of the DS was subjected to three different shock tests in each of the three axes. Qualification levels of the test are as following:
 - Axis X and Z: 500g in the form of sinusoidal half-wave with a duration of 2 ms.
 - Axis Y: 2000g in the form of sinusoidal half-wave with a duration of 15-20 ms.

Test results

The following qualification tests results are presented:

- Vibration. After vibration tests, a visual inspection, physic properties verification and several functional tests were carried out with the result of no anomalies or deviations detected. Consequently, the rotary actuator can survive the vibrations expected from travel, landing and take-off without any expected problem.
- Shock. Figure 8(a) shows the accelerations obtained during the shock test in X axis using the free fall machine. Similar results were obtained in Z axis. Figure 8(b) shows the accelerations obtained during the shock test in the Y axis using the pneumatic cannon. After the shock test, no anomalies were detected in the Dust Sensor, nor in the actuator subsystem. The levels in the Y axis during the shock test are slightly below 2000g. In the initial calibration tests using a mechanical dummy model, the values obtained arrived at 2000g. Unfortunately in the QM test this value was not reached due to the variability of the method applied. As seen in Figure 8(b), the levels reached have several peaks during approximately 17 ms of duration, which is more restrictive than the single sinusoidal half-wave requested. Even though the values obtained demonstrate that the DS can support shock values near 2000g: no damage or defects were observed in the mechanical dummy model (that reached 2000g), neither in the QM of the DS.
- Thermal cycling and vacuum test. Thermal vacuum cycling is a critical test for the rotary actuator subsystem due to the complex thermal processes that take place during the huge thermal variation in vacuum (from -90°C to +70°C). During the test, several data from the sensors of the DS were logged. Also, more than 100 actuations over all the temperature range were logged. Figure 9 presents an actuation capture during the TVAC test at -90°C. As it can be seen, due to the absence of thermal convection losses, the SMA fiber heats very fast (less than 300 ms) and takes more time during the cold down (~1.25 s).

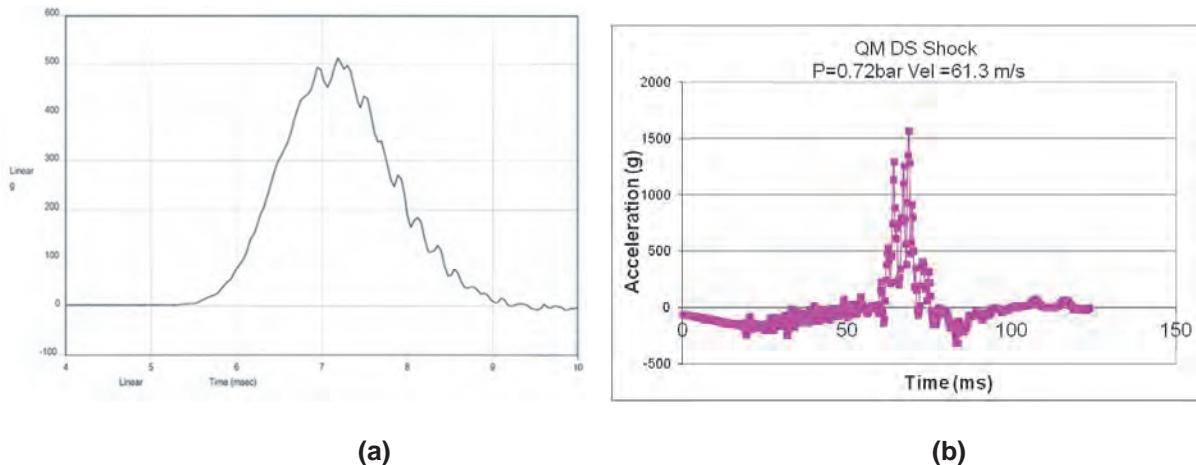


Figure 8. Results of shock test: (a) acceleration Vs Time obtained during the 500g shock test of the DS; (b) acceleration Vs Time obtained during the 2000g shock test of the DS.

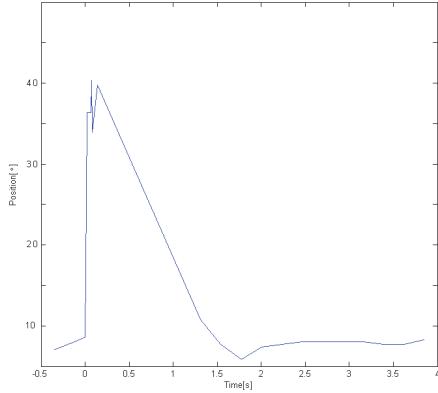


Figure 9. Position sensor output Vs time during an actuation at -90°C.

- Bioburden reduction. Bioburden reduction test verified that the actuator was not damaged after 50 hours at 111°C. No anomalies or deviations were detected. The SMA fiber was not damaged and the rotary actuator worked perfectly.
- Humidity low-temperature verification test. During the verification test, inside the thermal chamber, the rotary actuator was completely operational. At low temperatures, convection losses were high enough to increase the actuation time to values as high as 3 seconds. Convection losses made the fiber not to contract completely and, as a consequence, perform a partial actuation (limited angle movement) at temperatures below -30 °C. It must be noted that the rotary actuator is intended to be used in nearly vacuum atmosphere, with negligible thermal convection losses. As an additional test, in open atmosphere (49% of relative humidity) the critical parts of the rotary actuator were superficially completely frozen at -50°C. Ice appeared all over the mechanism. Several actuations were performed in these conditions. The Dust Sensor rotary actuator was able to actuate in an atmosphere with vapor water within the temperature range without being blocked.

The main lesson learned is that the complex thermal processes that take place along the whole temperature range of the mission are critical for a reliable and proper performance of this type of actuator. Here, the position sensor and end of stroke sensor included in the design play an important role for proper performance, and have allowed the completion of more than 700 cycles without failure during the qualification process. Future work includes the FM development and implementation in the MetNet platform.

A Pin Puller Mechanism

A Pin Puller is another application for SMA-based actuators. Two different versions of the pin puller were designed during this activity. Figure 10(a) shows a CAD model of the first design of the *Pin Puller V.1*. This design has been conceived to have a cylindrical shape in which length and diameter present similar dimensions, such as 80.0 mm of external diameter and 71.5 mm of length in un-actuated position (pin deployed). The mechanical parts have been designed to be made of an aluminum alloy. The commercial components have been modelled assuming their mechanical characteristics from the data sheets. The estimated weight of the whole structure, including commercial components and mechanical parts is 248.0 g. The Pin Puller mechanism is activated by a SMA actuator. Spheres support the pin at the initial position and a compression spring is loaded to perform the driving force once the release takes place. When the SMA actuates, a crown rotates allowing the spheres displacement, and thus the pin release and its movement to the actuated position (pin retracted). The mechanical design has been conceived in order to optimize the device's weight, reduce the parts complexity, and achieve a suitable stiffness. The assembly ensures the alignment of components and compactness of the design. Note a M4 drill on the pin tip that allows installing a threaded tool that can be used to pull for the device reset. Flat surfaces both in the pin shaft and in the frame do not allow the undesired rotation of pin, preventing the mechanism to be released by an external force.

Figure 10(b) shows an overview of the second design of Arquimea Pin Puller, named *Pin Puller V.2*. This design has been conceived in order to obtain a flat model structure. The device external diameter is 100.0 mm, the length is 50.9 mm with the pin retracted, and its estimated weight is 250 g. The *Pin Puller V.2* presents a mechanism similar to the *Pin Puller V.1*. Nevertheless, the V.2 pin is supported by rigid bars that keep it deployed during the un-actuated position. When a crown rotates by a SMA operation, the bars move, allowing the pin stroke by means of a compression spring. *Pin Puller V.2* has also been conceived in order to have a low weight structure, no complex features, and a suitable stiffness. The reset is also planned to be done by pulling a M4 threaded tool located in the pin tip. The components alignment is also ensured in this Pin Puller, as result of the accurate design process, by using an internal ring that also ensures the design compactness, locating the supporting spheres. Note that *Pin Puller V.2* has been designed to avoid any rotation of the pin.

Mechanical and Thermal Analyses

The 3D-CAD models of both versions of the Arquimea Pin Puller have been used to develop finite element analyses (FEA) of the structures. The goal of this analysis was to check the feasibility of the design as well as the components and assembly resistance. Two cases have been studied during the FEA, axial load condition and shear load condition. In particular, the axial load condition has been assumed as 180 N applied on the pin tip plus 1264 N applied by the stroke spring. The shear load condition has been assumed as 1000 N applied along a transversal axis of the pin. A factor of safety (FOS) of 1.25 has been suitably assumed both for incrementing the applied forces and for the numerical results in order to obtain a conservative design.

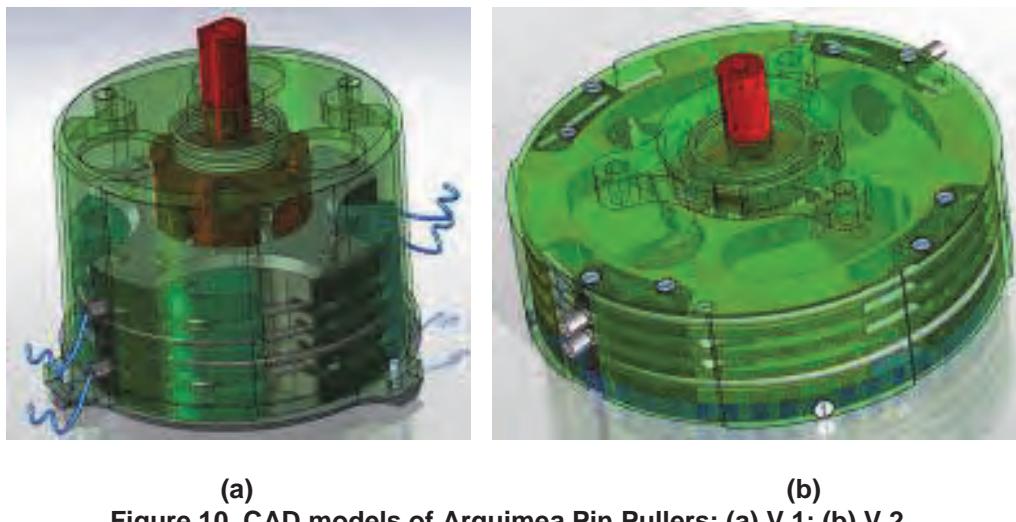


Figure 10. CAD models of Arquimea Pin Pullers: (a) V.1; (b) V.2.

Figure 11(a) shows the results of the Von Misses stress from the FEA of *Pin Puller V.1* structure for the second case of study (shear load). 450 N/mm^2 has been computed as the maximum value (lower than the yield limit of the selected aluminum alloy). Figure 11(b) shows the stress results of the *Pin Puller V.2* FEA. The maximum stress result has been computed as 290 N/mm^2 (lower than the yield limit of the selected aluminum alloy too) during the second case of study (shear load). Successful results have also been obtained during the vibration analysis of both Pin Puller structures. The same set-ups used for the above-mentioned FEAs have been used for computing the limits of resonance, obtaining 2128.6 Hz for version 1 and 2350.4 Hz for version 2. These limits are above the expected operating frequency for both devices.

Since mechanisms present difficulties during vacuum and extreme temperature conditions, tribology and thermal assessments have been done for both Pin Puller operations. Critical contact zones have been recognized in order to avoid high friction and adhesion. Certain solutions are proposed to resolve the problems, such as application of solid lubricant coating (MoS_2) on moving parts and designing the mechanical parts assuming specific features that reduce contact among components up to contact lines

even contact points. Similarly, suitable tolerances have been assigned to moving part features in order to avoid any jamming produced by the material expansion or contraction at extreme temperatures.

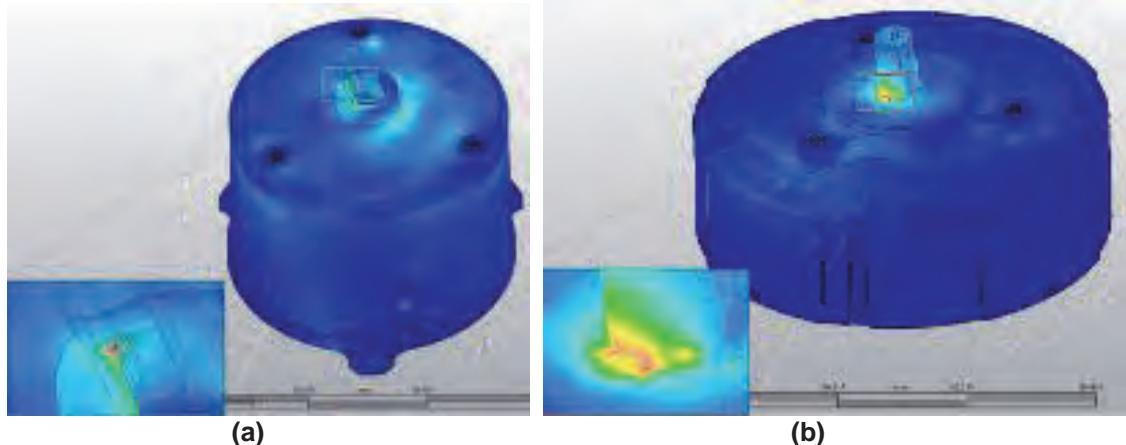


Figure 11. FEA results: (a) Pin Puller V.1 - shear load; (b) Pin Puller V.2 - shear load (right).

Finally, the response time has been computed, as part of the actuator analysis, for both Pin Puller versions. In order to fulfil the environment requirements (working temperature between -30°C and 125°C), wires with Austenite Start Temperature (A_s) of 150°C have been considered. Therefore, FEA have been developed in order to obtain the temperature profile along the wire axis during operation and the actuator response time. The actuator maximum response time at worst case environment (-30°C) has been estimated to be 4.3 s for version 1 and 2.8 s for version 2.



Figure 12. Built demonstrator of the both Arquimea Pin Puller versions: (a) devices of 500 N of stroke force; (b) devices of 100 N of stroke force.

Pin Puller as built Configuration

Demonstration models (DM) of both versions, Figure 12, were constructed in order to test the mechanical device concepts and to debug the design. The DMs have been constructed in Alumide material by rapid manufacturing process. Alumide is a composite of plastic and aluminum that provides a suitable resistance to prototypes for preliminary operation test. Moreover, this material does not conduct electricity that ensures the electrical insulation of the structure. Since the device reset is planned to be made manually by pulling the pin, a reset tool has been designed and built too. The reset tool can be recognized in Figure 12 next to the Pin Puller DM. Finally, the DMs contain commercial components, such as screws, cables, crimps and SMA actuators, for completing a successful demonstrator device of a Hold-Down and Release Mechanism. Figure 12(a) shows the demonstrator models of a Pin Puller with a stroke force of 500N. Good functional performances were obtained from both models. Promising performances

and some design concept improvements have been obtained for both versions of the device in this phase of the development. The designs presented in this work can be easily scalable to different sizes and requirements. Figure 12(b) shows the demonstrator model of a Pin Puller with 100 N of stroke force, in which an engineering model (EM) is currently under development.

Conclusions and Future Work

Arquimea has characterized the proposed SMA material (SMARQ), demonstrating the material capabilities to be used as a triggering actuator for space mechanisms. The material has shown a good behavior as Shape Memory Alloy. The project requirements in terms of operating temperatures, strain and force capabilities and lifetime have been satisfied.

A rotary actuator included in the QM of the DS for environmental conditions requirements of the MEIGA-MetNet Mission has been presented. DS will perform airborne dust opacity measurements on the Mars surface, as can be confirmed from the qualification campaign results obtained. The rotary actuator operational temperature range from -90°C to +25°C was an initial challenge that has been completely reached thanks to a correct thermal design and a proper control algorithm. The temperature range obtained exceeds the operational range presented for other SMA-based actuator for a Mars surface application as stated in [4].

Two complete Pin Puller mechanisms were conceptually designed and analyzed, with promising results. Demonstration models for both devices were constructed and tested, obtaining a successful proof of concept of the mechanisms. The results of the work presented show that SMARQ technology is ready to be used in the development of EM, QM and FM actuators for future space missions. Other potential applications are the design of actuators for multi-cycle operation, for working in hard environments, such as cryogenic applications, or for applications where an ultra-light weight is required. Finally, the technology developed during this project can be applied to other industrial applications outside the space market.

References

1. Duerig, T.W., Melton, K.N., Stockel D., and Wayman C.M. (Ed.). *Engineering Aspects of Shape Memory Alloys*. London: Butterworth-Heinemann, 1990.
2. Otsuka, K. and Wayman C.M. (Ed.). *Shape Memory Materials*. UK: Cambridge University Press, 1998.
3. Delaey, L. "Diffusionless Transformations". *Proceedings of Materials Science and Technology*, (1991), Vol. 5, pp 339-404.
4. Fernández, D., Cabás, R. and Moreno, L. "Dust Wiper Mechanism for Operation in Mars". *Proceedings of 12th European Space Mechanisms & Tribology Symposium (ESMATS)*, (2007).
5. Jenkins P.P., Landis A.G. and Oberle L.G. "Materials Adherence experiment: Technology IECEC-97339". *Proceedings of 32nd Intersociety Energy Conversion Engineering Conference*, (1997).
6. Collado, M., Martínez, D., Álvarez, F., Cabás, R., Moreno, L. and López, F. "Evolution of SMA Rotary Actuators for Space Applications in Mars Environment". *Proceedings of Actuator 10 – International Conference and Exhibition on New Actuators and Drive Systems*, (2010).

Design and Performance of the Telescopic Tubular Mast

Mehran Mobrem* and Chris Spier*

Abstract

The Telescopic Tubular Mast (TTM) has been under development at Astro Aerospace – Northrop Grumman Aerospace Systems for a number of years and has found several applications including deployment of the Large Sunshield on the James Webb Space Telescope. The TTM is composed of a number of large diameter tubes that are deployed and retracted using a Storable Tubular Extendable Mechanism (STEM). In order to study and evaluate the feasibility of utilizing the TTM concept for long boom applications a special design case (34.4-m long) was selected in 2005, which later was built and tested. This paper describes the design and analysis of this design case as well as testing performed. Special attention is given to the deployed stiffness and frequencies, which is a key requirement for space applications. Also, stabilization features required for the deployment are discussed and finally a feedback control system to drive the STEM deployer during the deployment is selected and the difficulties of controlling the system are discussed.

Introduction

The TTM is composed of a number of large-diameter thin-wall composite or metallic tubes as required to achieve a given deployed length, stowed envelope and structural characteristic. When deployed, the tube sections are latched together by multiple tapered pins to achieve a stable extended structure. These pins are withdrawn automatically to enable retraction. The Telescopic tubes are deployed and retracted by a version of Astro Aerospace's STEM deployer. The STEM deployer has a long history of being used in space from the earliest small satellites in the 1960s as antennas and gravity gradient booms to the current GPS series of spacecraft. For the TTM application, the STEM has been evolved into a higher force actuator capable of more than 445 N (100 lb) deployment force.

The TTM has to be deployed within a given time and it is desirable to have a constant velocity during the deployment or retraction. However, due to friction, latch up loads, and external tip loads, the velocity fluctuates. Also the friction and latch up forces fluctuate during the deployment/retraction depending on the individual segments. The STEM deployer inherently has a large dead band due to the winding/unwinding of its STEM element around the spool, therefore, each time the motor changes its direction it can not affect the deployment/retraction for a short period. Hence, the feedback control system should minimize the motor reversal during a given operation, e.g. deployment. Finally, it is desirable to limit the average velocity.

TTM Top Level Information and Background

The TTM test hardware is comprised of 17 telescoping tubes, excluding the fixed base tube. The tubes are optimized for stiffness, strength, and mass and are made of high modulus graphite composite with wall thicknesses ranging from 1.02 mm (0.040 in) to 0.38 mm (0.015 in). The tube closest to the fixed base is 31.8 cm (12.5 in) diameter, and tubes decrease in diameter by 1.3 cm (0.5 in) to the last tube at the tip which is 11.4 cm (4.5 in) diameter.

The tubes are nested inside the fixed base tube and the nested group of tubes is deployed using a STEM deployer that is attached to the fixed base tube. The STEM deployer pushes the group of nested tubes

* Astro Aerospace – Northrop Grumman Aerospace Systems, Carpinteria, CA

from inside the fixed base tube. Latching features built into each tube allow the tubes to latch together as the system is deploying and creating a stable structure once fully deployed. The latching features are explained below.

Stowed Design Features

The base tube is designed to support the tubes and STEM deployer for a typical spacecraft application. There are two sets of attachment points one at the base and one in the side close to the tip. Also there are graphite load rings at the tube tips to provide a stiff structure for supporting the payload. The stowed configuration of the TTM is shown in Figure 1.

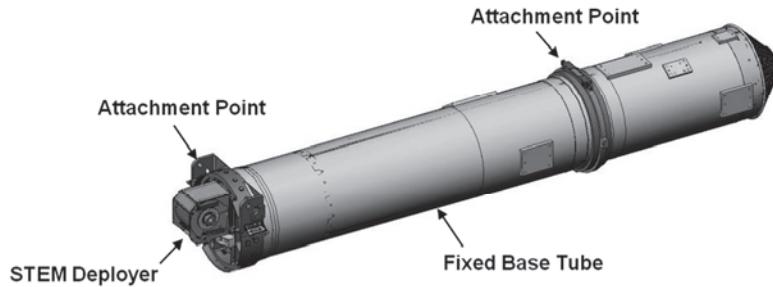


Figure 1. Stowed TTM

Deployment Design Features

There are three major components in the design to stabilize the TTM during its deployment. Each tube has three rails along the tube axis that are spaced 120 degrees apart to stabilize the rotation about the boom axis during the deployment. These rails also have secondary effects to increase the deployed stiffness. The second major component is a secondary stiffening ring at the base about one diameter apart from the latch ring to stabilize the rotations about the two lateral axes. Finally, there is one centralizer in each tube to support the STEM element and stabilize/improve its buckling capability. These main features of each tube that help stabilize the TTM during deployment are highlighted in Figure 2.

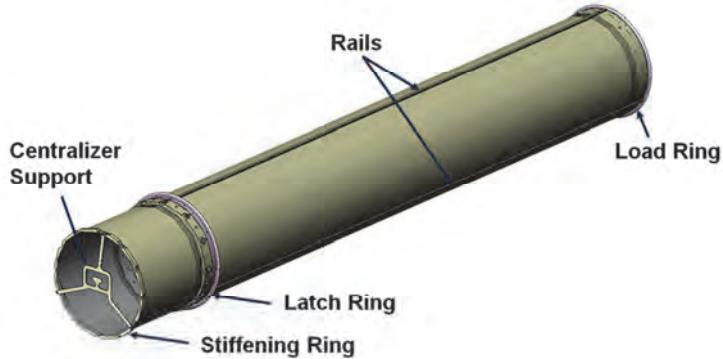


Figure 2. Tube Features

Deployed Design Features

The deployed TTM has nonlinear stiffness mainly due to local flexibility of the latching feature. The stiffness increases as the applied loads to the latch-pin increases. Several design features have been implemented to increase the deployed stiffness. A load ring has been added to each tube tip where the latch-pins are engaged to stabilize the local deformation of the thin walled tubes. As discussed earlier these load rings are part of launch restraint to support the payload during the launch. Also, the three

deployment rails along each tube add to the overall stiffness. Note that by pre-loading the latch-pins the stiffness would be increased and the non-linearity could be reduced. For many applications, there may be a type of tension load which could pre-load the TTM; however, if needed the STEM deployer could be utilized to do this function.

STEM Deployer

The drive system for the TTM is a STEM deployer powered by a brushless dc motor which pushes against the tip plate. The STEM consists of a "C" section of thin formed metal that is flattened so it can be rolled onto a spool for launch, as shown in Figure 3. Deployable booms in the STEM family are simple and extremely lightweight; they have been successfully deployed over 300 times in space without any known failures.

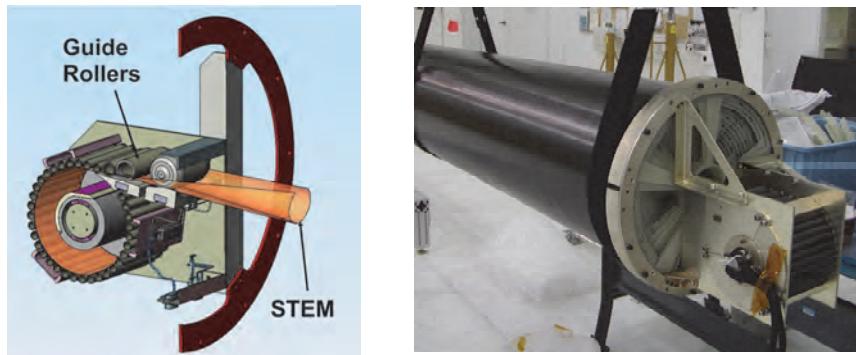


Figure 3. STEM device used for TTM deployment/retraction

The payload and package of stowed tube segments are pushed from the inside of the fixed external base tube by the STEM. When the package reaches the end of the fixed segment, the outer tube in the package latches to it. This tip deployment process repeats sequentially until all tubes are latched into place. The same sequence is reversed to retract. The innermost of the undeployed tubes is fixed to the tip of the STEM in order to stabilize the moving package of tubes.

To minimize the number of tubes, they are all the same length and are stowed coincident with each other. The latches fit in the annular gap between adjacent tubes in a stiffening ring at the lower end of each tube. The adjacent larger tube in turn necks down to a thin stiffening ring at the upper end. The stiffening ring helps to center and align the adjacent smaller tube and to lessen local deformations between the latched segments in bending.

Tube Latching

Small tapered pins are distributed circumferentially in the stiffening ring at the lower end of each tube. The pins are loaded radially outward by short springs to engage with tapered holes at the upper end of each larger adjacent tube, as shown in Figure 4. When stowed, the springs and pins are compressed by the interior surface of the adjacent larger tube. During

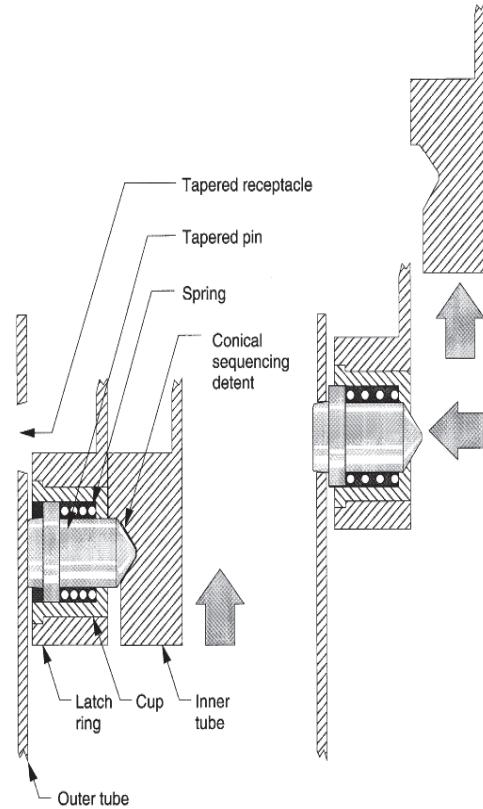


Figure 4. Tapered pins used for latching

deployment, the tips of the pins slide on the surface until they pop into the tapered seats to latch.

Sequencing

Since the tubes are stowed coincident to each other, each ring of compressed latch pins can engage the adjacent smaller ring with simple detents as shown in Figure 4. All the nested tubes are thus locked together so that they can be pushed as a package during deployment. When the latch ring in the outermost tube of the package locks it into deployed structure, the detents retaining that tube to the moving package of tubes are released. The now smaller package of moving tubes continues without interruption.

The male component of the detent on the interior end of the latch pin is conically shaped to make the latching function fail-safe. If one or more springs fail, the affected pin is forced out of the way by the female side of the detent, which acts as a ramp, as shown in Figure 4. Without the spring to preload the pin in the tapered receptacle, that pin cannot contribute to the deployed stiffness of the boom, however, deployment will not be impeded.

Retraction

To retract a given tube, its latch pins are pulled from engagement with the next larger tube by ramps in the next smaller tube. The ramps are hollowed out of the latch rings to engage conical rims at the male detent end of the latch pins, as shown in Figure 5.

Latch pins are alternated with retraction ramps and detents in increments around the circumference of each ring. Each successive tube in the assembly is indexed by one such increment relative to its neighbors so that everything meshes properly. The length of the trough is controlled so that the detents will engage before the deployed tube is unlatched, as shown in the second inset of Figure 5.

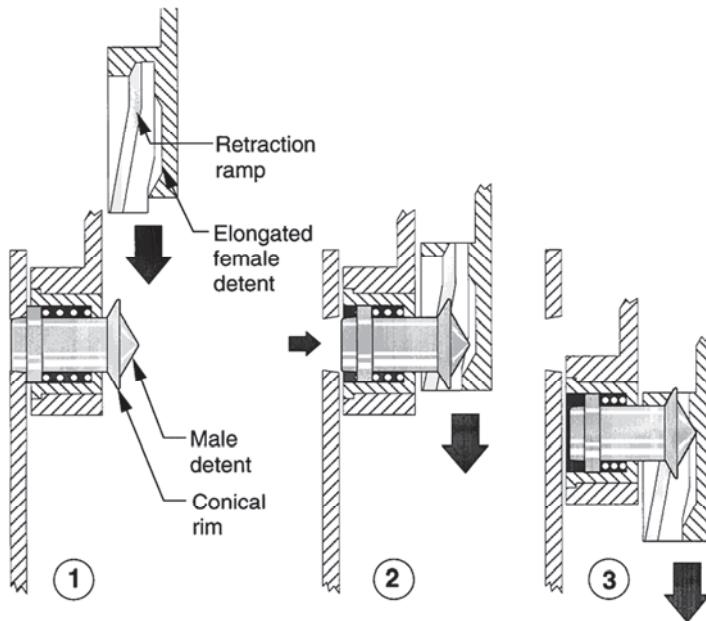


Figure 5. Boom retraction sequence

TTM Special Design Case

In order to study and evaluate the feasibility of utilizing the TTM concept for long boom applications, a special design case was selected in 2005 which was later built and tested. The key parameters and top level requirements for this design are:

- Deployed length of 34.3 m (1350 in) from bottom of base to tip
- Stowed length of 2.16 m (85 in)
- Mass is approximately 58 kg (128 lb)
- Deploy time within 14 minutes
- Stowed frequency should be greater than 35 Hz
- Deployed frequency should be greater than 0.1 Hz
- Mast should be able to retract by reversing motor
- Tip displacement during the deployment/retraction should stay within ± 17.8 cm (7 in)

Tube Properties

There are 17 telescoping tubes, excluding the fixed base tube. Table 1 lists properties for the minimum and maximum diameter telescopic tubes, along with Tube 9 which is the tube in the middle between the base and the tip. Tube 1 is the tube closest to the base tube and is 31.8 cm (12.5 in) diameter, while Tube 17 is the last tube at the tip and is 11.4 cm (4.5 in) diameter. Listed in the table are the different stiffness properties for each of the tubes. EI is the bending stiffness of the tube, GJ is the torsional stiffness of the tube, and EA is the axial stiffness of the tube.

Table 1. Tube Properties

Tube	Tube Diameter (cm)	Thickness (mm)	EI ($\times 10^3$ N·m 2)	GJ ($\times 10^3$ N·m 2)	EA ($\times 10^6$ N)	Mass/Length (kg/m)
1 (Max)	31.8	0.51	868.9	346.9	69.0	1.56
9	21.6	0.38	140.3	105.8	24.1	1.47
17 (Min)	11.4	1.02	81.1	41.9	49.6	1.93

Stowed Frequency Analysis

A stowed finite element model of the TTM was created to compute the natural frequencies. The fundamental computed natural frequency is 37.88 Hz which exceeds the 35 Hz requirement. The first ten stowed natural frequencies are listed in Table 2 and the first three mode shapes are shown in Figure 6. Note that these frequency results have not been validated by a test.

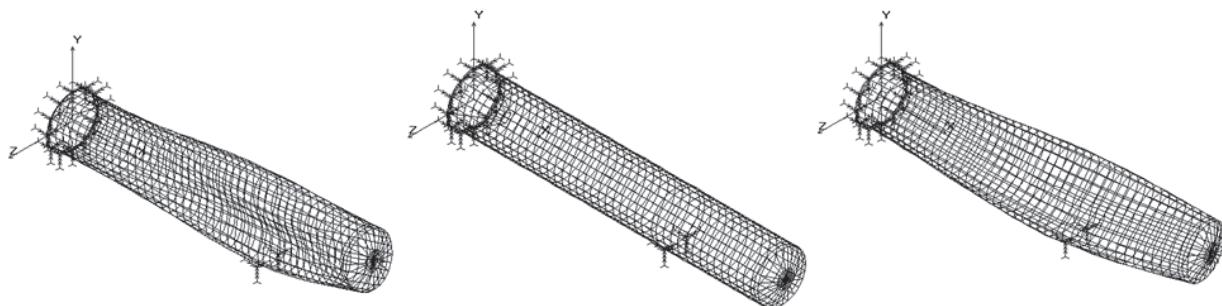


Figure 6. First three modes in the stowed configuration

Table 2. Stowed natural frequencies

Mode	Frequency (Hz)	Mode	Frequency (Hz)
1	37.88	6	62.92
2	48.69	7	69.23
3	51.83	8	76.58
4	52.68	9	82.42
5	57.46	10	85.28

Deployed Stiffness Analysis and Test

A deployed nonlinear FEM was created to determine the deployed stiffness, natural frequencies, and its load capability. The nonlinear FEM was used to determine the deployed stiffness under different load conditions and was validated by test. Measurements were performed on the deployed TTM to characterize its stiffness under different loading conditions. The test setup consisted of the deployed mast offloaded with a total of 17 helium balloons. Each balloon was attached to the tip end of their respective tubes as shown in Figure 7. The lift of the individual balloons was adjusted to the mass of the supported tube sections. The tip load was applied with a motorized slide mechanism that had a load cell and position transducer attached.



Figure 7. Deployed stiffness test configuration

Baseline Tip Load – No Preload

A baseline tip load test was performed with no preload. For this test, the mast was loaded in shear only at the tip to the levels shown in the plot in Figure 8. The blue curve in the figure shows the load-deflection characteristics of the mast with zero preload. The red line represents the predicted performance of the mast. The TTM measured stiffness correlates well with predictions, however it is lower at low amplitude and is higher at high amplitude compared to the predictions.

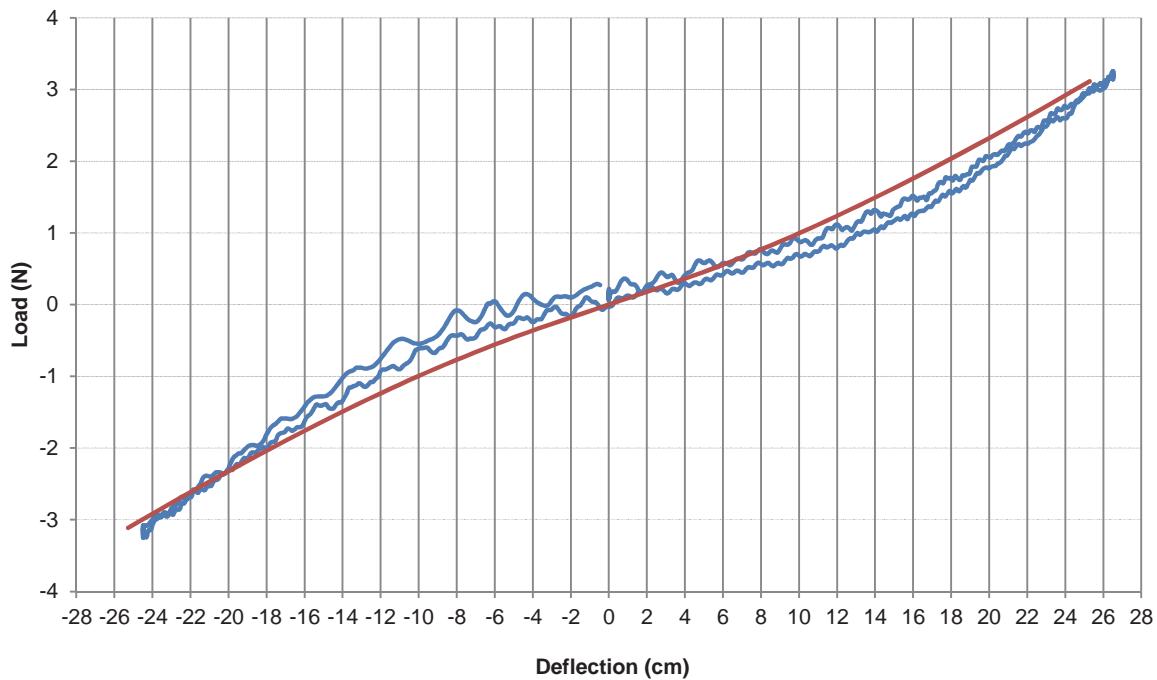


Figure 8. Plot of tip displacement versus load for the no preload load case

Deployed Preload Condition

The deflection of the fully deployed mast due to the application of a tip preload was also characterized. This type of loading generally relates to typical flexible solar panels or sun-shields under tension. The test configuration is shown in Figure 9. A typical 55.6-N (12.5-lb) load was applied in the direction shown at the tip and the resulting deflection was measured at the tip.

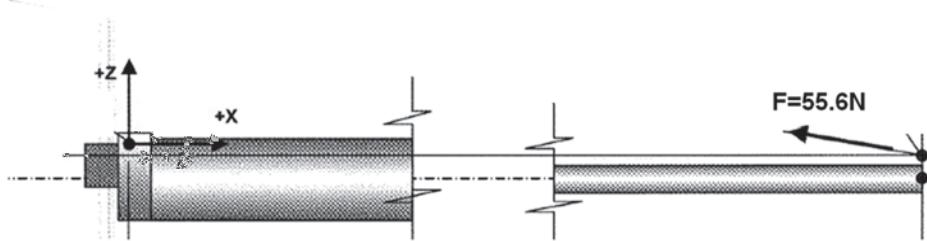


Figure 9. Deployed preload condition

The results of the preloaded test are shown in Figure 10. For this test, the mast was loaded with a 55.6-N (12.5-lb) tethered load, which creates an axial, shear, and moment load, and then an additional shear load was added at the tip to the levels shown in the plot. In this plot, zero deflection corresponds to the deflected shape under the tethered load, which was 13.8 cm (5.45 in).

The red line represents the predicted performance of the mast. This line shows the predicted tip deflection of 12.7 cm (5.0 in) under the tethered load versus the 13.8 cm (5.45 in) observed in the test. It was observed from this test that lower than predicted stiffness occurred at lower loads while higher than predicted stiffness occurred at higher loads.

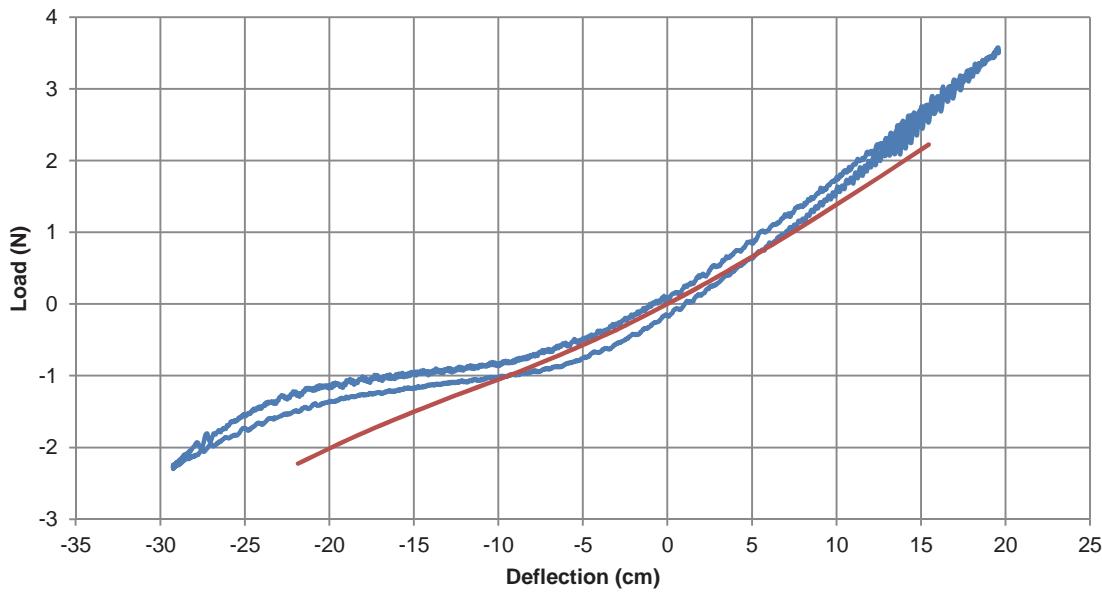


Figure 10. Plot of tip displacement versus load for the preload condition

Deployed Natural Frequency Analysis

A linear FEM was created from the nonlinear model with applied tethered loads to compute the natural frequencies. The fundamental computed natural frequency is 0.1 Hz which meets the 0.1 Hz requirement. Note the mode shape is orthogonal to the plane of load application where the boom stiffness is at minimum stiffness region. The first eight deployed natural frequencies are listed in Table 3 and the mode shapes are shown in Figure 11. Note that these frequency results have not been validated by a modal test. A detailed view of the deployed FEM is shown in Figure 12.

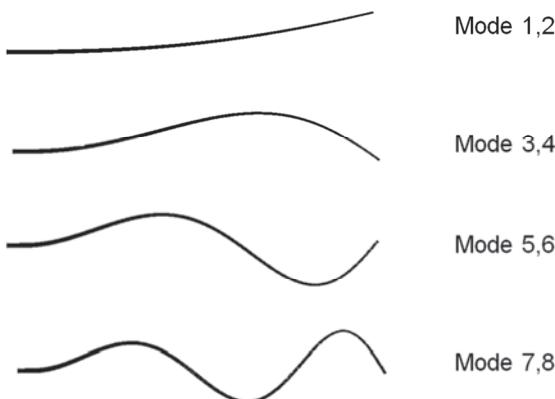


Figure 11. First eight deployed modes

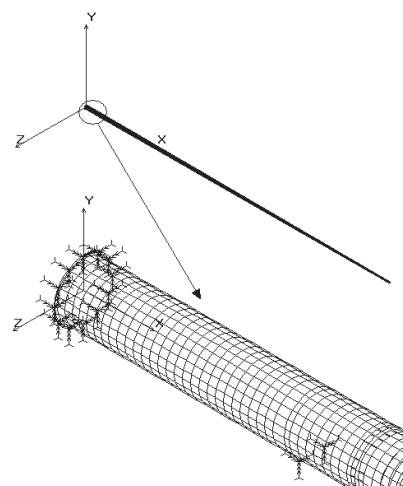


Figure 12. Deployed FEM

Table 3. Deployed natural frequencies

Mode	Frequency (Hz)	Mode	Frequency (Hz)
1	0.10	5	1.56
2	0.15	6	2.09
3	0.56	7	3.09
4	0.77	8	4.09

Deployment Characteristics and Control

The goal was that the TTM should be deployed within 15 minutes. It is desirable to have a constant velocity during the deployment or retraction; however, due to friction, external tip loads, and latch up loads the velocity fluctuates. Also, the friction and latch up forces fluctuate during the deployment/retraction depending on the individual segments. A typical resistive force during a segment latch up is show in Figure 13.

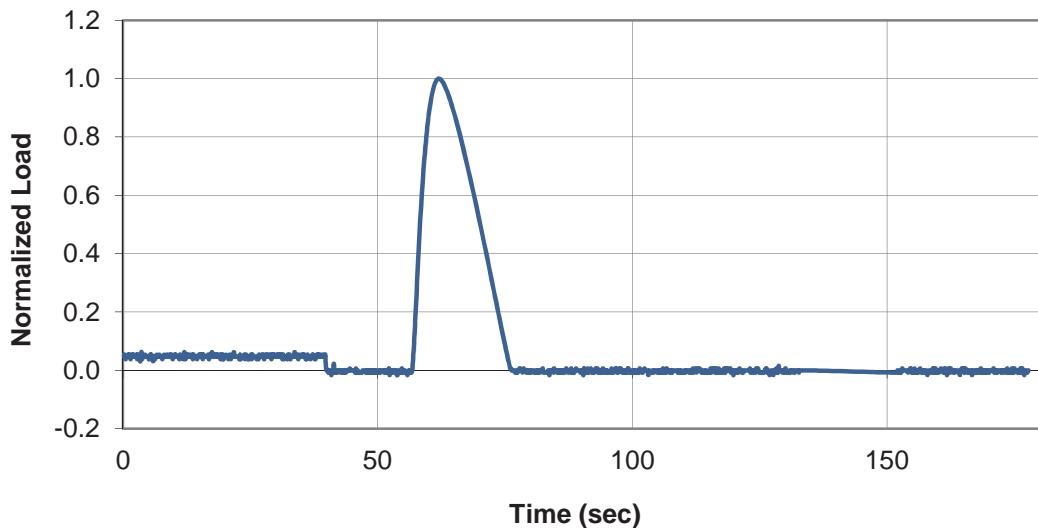


Figure 13. Typical latch loads during deployment

The drive system is a STEM deployer powered by either a brushless dc motor or a stepper motor which pushes against the tip plate. The STEM deployer inherently has large dead band due to the winding/unwinding of its STEM element around the spool, therefore each time the motor changes its direction it can not affect the deployment/retraction for while. Hence the feedback control system (required for brushless dc motor application) should minimize the motor reversal during the deployment operation. Finally, it is desirable to limit the average velocity.

Deployment Drive Feedback Control System

To achieve the deployment criteria, a feedback control system containing the following is considered (see Figure 14):

- Position loop
- Velocity loop inside the position loop
- Feed forward time dependent velocity profile - trapezoidal
- Time dependent reference position – integral of velocity profile
- Both velocity and position loops should be:
 - Stable for minimum inertia due to the backlash (motor inertia only) as well as maximum inertia
 - Open loop frequency bands should be less than 70% of the structural natural frequency
 - Nonlinear gains used in both position and velocity loops
 - Gain and phase margins should be greater than 10 dB and 40 degrees respectively
- Current limit is required to prevent high deployment force

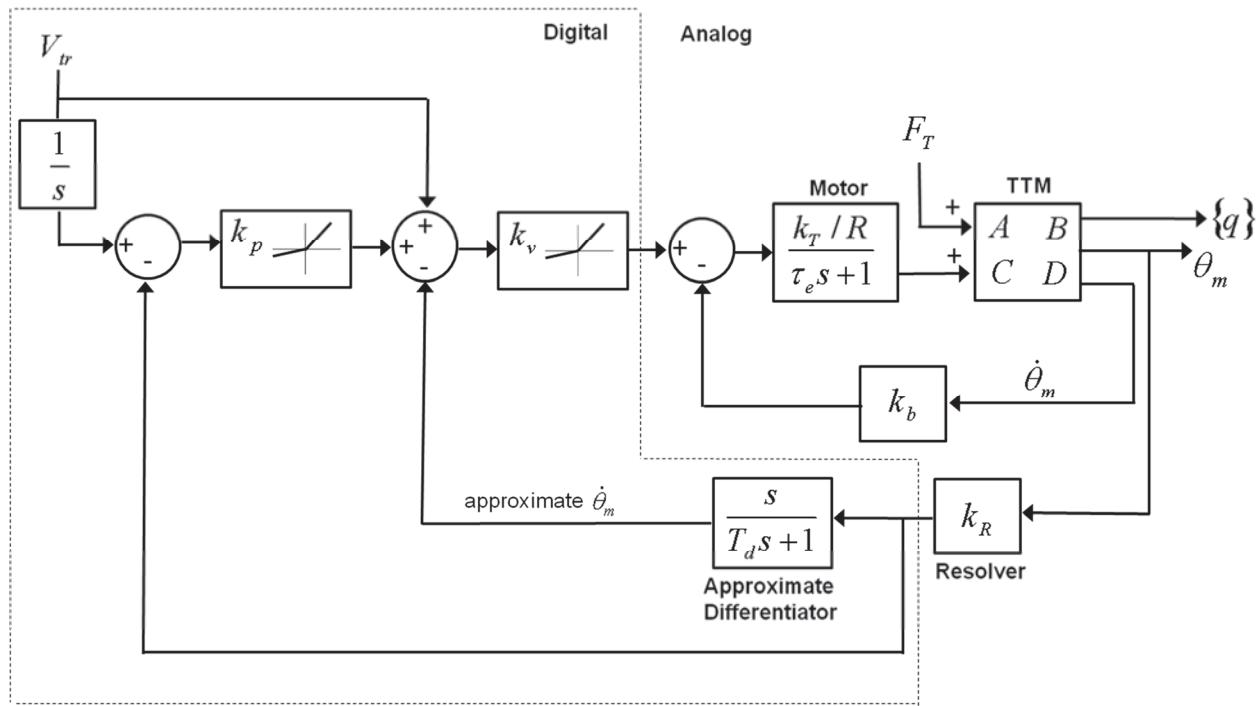


Figure 14. Control system block diagram

In Figure 14, V_{tr} is the translational drive reference velocity, T_d is the approximate differentiator time constant, L is the motor inductance, R is the motor resistance, τ_e is equal to L/R , k_T is the motor torque constant, and k_b is the back emf constant.

The gains for the control system are: k_p is the position loop gain, k_v is the velocity loop gain, and k_R is the resolver gain. It is desirable to have nonlinear gains in both the position and velocity loops in order to prevent the motor reversal caused by back winding in the STEM. A possible nonlinear control gain that can be implemented is a piece-wise linear gain that is high gain for lag and low gain for lead.

The TTM is a time variant system and, because of this, there are non-conservative forces during the deployment. These forces become significant as the deployment velocity and acceleration increases

[2,4]. A similar feedback control system was designed and tested for the Space Station Freedom Mobile Transporter [2,3]. For the Mobile Transporter, an avionics control breadboard simulator was designed to simulate and verify the operation of the Mobile Transporter control system.

The following dynamic models are used to derive the TTM system state space matrix [A,B,C,D]. Note that during deployment the length of the TTM is changing causing a change in natural frequencies.

Primary Dynamic Model

The primary dynamic model used for the design of the control system is shown in Figure 15. This model represents the deployment and axial vibration of the TTM. The moving mass M is the mass of the deploying tubes plus the mass of the payload and $f_{resistive}$ are loads due to friction, tube latching, and any external loads such as sun-shields tension and/ or space craft attitude control. For the STEM deployer, k_{STEM} is the axial stiffness of the partially deployed STEM and varies by length, θ_m and θ_s are the rotation of the motor and spooler, respectively, J_m and J_s are the inertias of the motor and spooler, respectively, and n is the gear ratio.

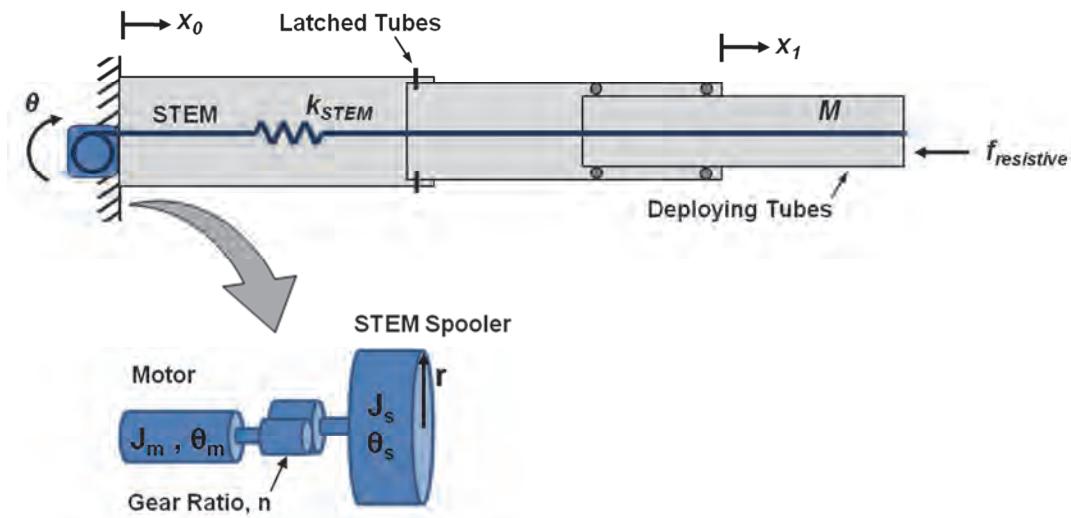


Figure 15. Dynamic model for control system

The equations of motion for the STEM deployer and the system of deploying tubes shown in Figure 15 are

$$M\ddot{x}_1 + k_{STEM}(x_1 - x_0) = -f_{resistive} \quad (1)$$

The axial natural frequency changes as the STEM deploys and the boom length changes. A plot showing the change in axial natural frequency as the system deploys and the length increases and moving mass of the tubes decreases is shown in Figure 16.

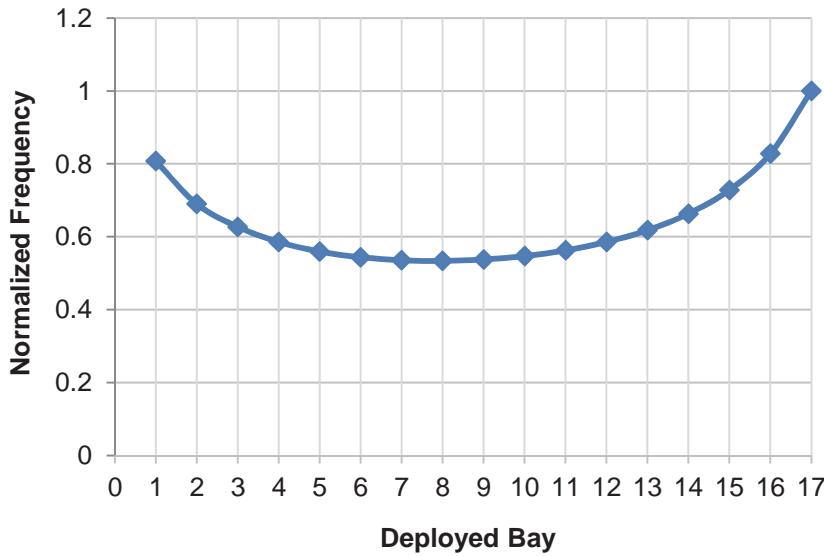


Figure 16. Plot of axial frequency versus deployed tube bays

Secondary Dynamic Model

The secondary dynamic model used for the design of the control system represents the lateral vibrations of the TTM during the deployment. This can be represented by an axially moving cantilever beam with a tip mass as shown in Figure 17.

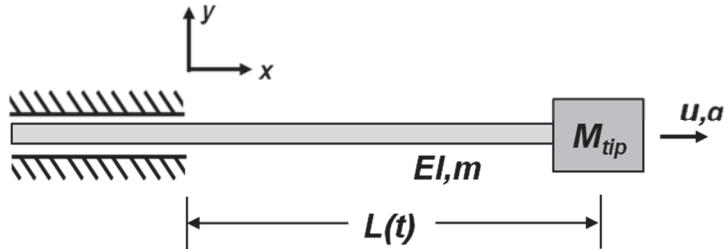


Figure 17. Cantilever beam with tip mass and time dependent length

The equation of motion for the system shown in Figure 17 for a cantilever beam whose length changes with time is given by [2]

$$\left[\frac{33}{35} m L(t) + 4 M_{tip} \right] \ddot{\eta} + \frac{33}{35} m u \dot{\eta} + \left[\frac{12EI}{L(t)^3} - \left(1.028m + 4.8 \frac{M_{tip}}{L(t)} \right) a - 0.6857 \frac{m}{L(t)} u^2 \right] \eta = 0 \quad (2)$$

where u is the velocity of the moving beam, a is the acceleration of the moving beam, EI is the bending stiffness of the beam, m is the mass of the beam, $L(t)$ is the instantaneous length of the beam, M_{tip} is the tip mass and η is the normal coordinate representing the lateral displacement y . Note that equation (2) has non-conservative forces which could become important depending on the deployment velocity and acceleration.

If the velocity and accelerations are small, equation (2) reduces to

$$\left[\frac{33}{35} mL(t) + 4M_{tip} \right] \ddot{\eta} + \frac{12EI}{L(t)^3} \eta = 0 \quad (3)$$

Control System Simulation

A simulation of the control system was performed using Simulink. A resistive force representative of the one shown in Figure 13 is used to simulate latching loads. Non-linear control gains are used for the position and velocity loop gains and a deadband of ± 7.6 cm (3 in) is used.

Simulation results for the TTM deployment are shown in Figures 18 and 19. Figure 18 is a plot of velocity versus time and includes deadband in the system. Figure 19 is also a plot of velocity versus time, but does not include deadband in the system. In both plots, time is in seconds and velocity is in meters per second.

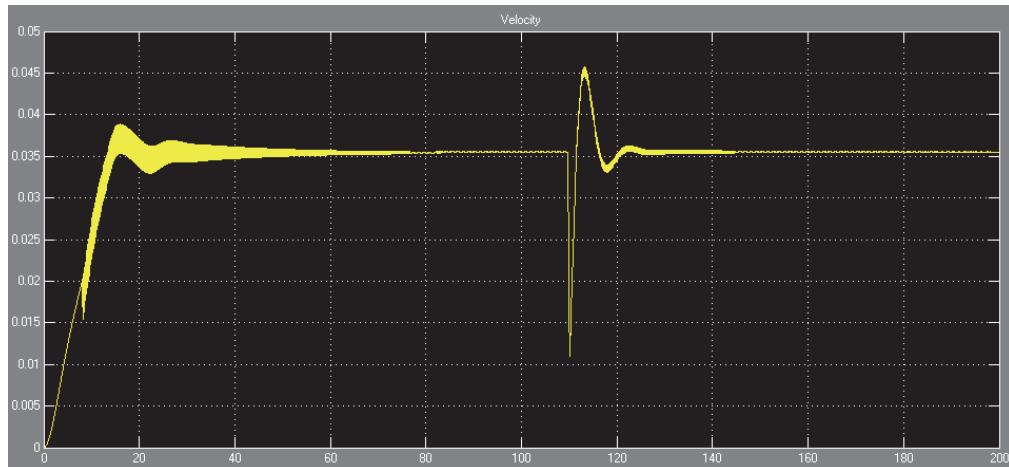


Figure 18. Velocity versus time plot with deadband



Figure 19. Velocity versus time plot with no deadband

Summary

A deployable and retractable telescoping boom that contains large-diameter, thin-walled composite tubes has been developed that is capable of high deployed stiffness. Tapered pins are used to control the deployment and retraction between the tubular sections and create a stable extended structure when deployed. The latch design and STEM work together to eliminate the need for segments to overlap when deployed giving a lightweight design.

The key parameters and requirements for the TTM study are given, and it is shown by analysis and test that the requirements are met. Frequency analysis on the deployed and stowed configurations was performed using FEA software to show that the frequency requirements are met. Testing was also performed on the deployed TTM to characterize the stiffness under different loading conditions. In all the load conditions, lower than predicted stiffness occurred at lower bending loads and higher than predicted stiffness occurred at higher loads.

Control of the deployment drive for the TTM presents several challenges due to the design of the STEM actuator and the latching loads during deployment. To analyze the system, a dynamic model was developed that includes the deploying tubes and the STEM motor and spooler. The equations of motion for the system were derived and a feedback control system was designed. The work done to date and the progress made on the TTM system are presented here.

References

1. Thomson, M.W. "Deployable and Retractable Telescoping Tubular Structure Development." *Proceedings of the 28th Aerospace Mechanisms Symposium* (May 1994).
2. Mobrem, Mehran and Mark Thomson. "Control Design of Space Station Mobile Transporter with Multiple Constraints." *First Joint U.S./Japan Conference on Adaptive Structures*, (November 1990), pp. 87-116.
3. Mobrem, M., Paden, B., Bayo, E., Devasia, S., "Optimal Output-Trajectory Tracking: Application to Mobile Transporter Avionic Breadboard." AIAA Guidance, Navigation, and Control Conference and Exhibit, (August 2000)
4. Taborrok, B., Leech, C.M., Kim Y.I., "On the Dynamics of an Axially Moving Beam," *Journal of the Franklin Institute*, Vol. 297, No. 3, (1974), pp. 201-220.

Development of Variable Reluctance Resolver for Position Feedback

Greg Leibovich^{*} and Sara Senanian^{*}

Abstract

The variable reluctance resolver (VRR) is commonly used in the automotive industry as a rotor position sensor. Its use in the Aerospace and Defense Industries has been limited due to inadequate accuracy performance. However, recent interest in the Aerospace Industry for VRRs as a viable alternative to conventional resolvers has driven the development of higher accuracy VRRs for use in angular position feedback applications. This paper presents the progression in the development of the VRR and provides information on the lessons learned during the completion of the first generation of single speed and multi-speed engineering units of VRRs. This first generation of engineering units was evaluated to identify potential design and manufacturing process improvements. Incorporating the lessons learned from the development of the first generation units resulted in an improvement in performance and manufacturability in the second generation of VRRs, making it a desirable option for future use in commutation of brushless DC motors.



Figure 1. Single-speed (left) and multi-speed (right) variable reluctance resolvers

Introduction

Resolvers are rotary motion feedback sensors used to provide angular position detection in a wide variety of environments; space, defense, automotive and oil exploration. For decades, conventional resolvers have been used for high precision mechanism position feedback and commutation in a range of adjustable speed drives; vector control induction motor, switched reluctance motor and brushless DC motor drives. Besides resolvers, optical incremental encoders and potentiometers offer an alternative solution for position sensing by producing precise incremental position information. However, optical encoders are susceptible to vibration, debris and high temperatures. Potentiometers are easy to use; however the potentiometer contains an electrically conductive wiper that slides across a fixed resistive element causing the possibility of considerable wear. Hence the life cycle of a potentiometer is limited and its sensitivity to vibration is of significance. Resolvers do not depend on moving electrical contacts for signal reliability and do not exhibit significant aging or changes to performance due to extreme temperatures or vibration.

^{*} Ducommun LaBarge Technologies, Carson CA

In addition, conventional resolvers transmit high accuracy angular data electrically in the thousands of a degree (arc-seconds) and consist of a stator, a rotor and a transformer assembly; each with its own winding as seen in Figure 2. Nonetheless, the conventional resolvers are intricate to manufacture and therefore labor intense and costly. Furthermore, in larger conventional resolvers, the transformers have been observed to delaminate and are difficult to rework or replace. The high cost and manufacturing complexity of conventional resolvers lead to the development of variable reluctance resolvers.

Unlike a conventional resolver, the VRR has no need for rotary transformer and it consists of a simpler design. All windings are located on its stator assembly whereas in conventional resolvers the stator core, rotor core, stator transformer and rotor transformer each contain windings as labeled in Figure 2.

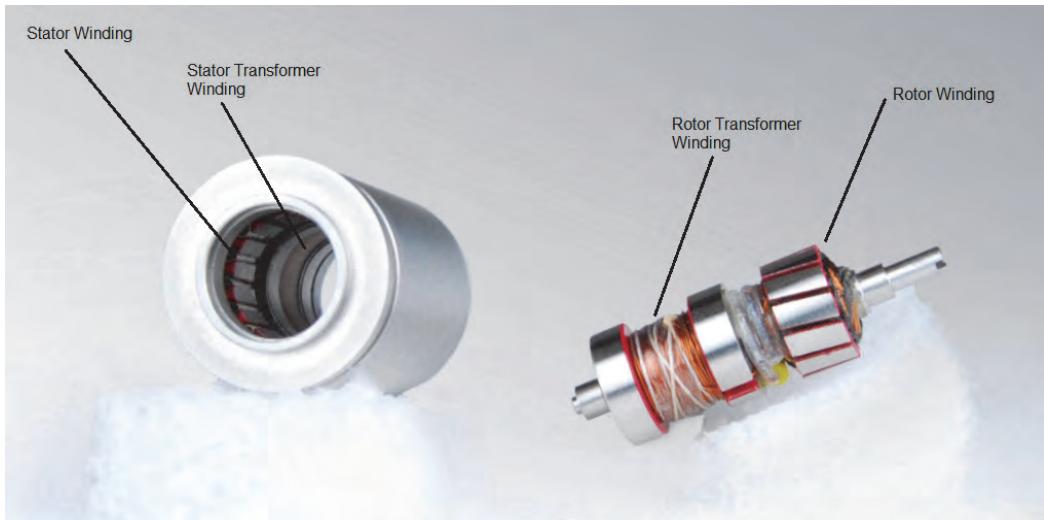


Figure 2. Conventional resolver with transformer

Furthermore, the study and experiments conducted by the Ducommun Team resulted in an improvement in the accuracy of the VRR making them competitive to convention resolvers particularly for the commutation of brushless DC motor drives in the Space and Defense Industries. This paper documents the development and qualification of the VRR for use in commutation of brushless DC motors that minimizes envelope size, mass and increases reliability.

The purpose of development of VRR

1. Provide resolver architecture for continuous operation without rotary transformer
2. Reduce amount of magnetic components and windings
3. Decrease the manufacturing complexity and fabrication cost
4. Reduced envelope size and mass

The VRR was developed to meet the following accuracy requirements:

1. Single speed accuracy to be less than 30 arc-minutes
2. Multi-speed accuracy less than 6 arc-minutes

Background

The VRR consists of stator core and a rotor core and is unique in that its rotor core is slot-less with no windings. Unlike conventional resolvers, the VRR is based on variable reluctance between the stator and rotor segments. The voltages of the output windings of the resolver vary as sine and cosine functions of the rotor angular position. The VRR is structured to vary the reluctance of the magnetic path between the stator and rotor core in accordance with equation (1) through the change in the length of the air gap (l) or the area of the air gap (A). From equations (2) and (3) it is easily determined that the variation in reluctance causes a change in the induced voltage in the sense windings. Therefore, varying the air gap

or coupling area will cause a variation in the reluctance and consequently cause a change in the voltage outputs.

$$\mathcal{R} = \frac{l}{\mu A} \quad (1)$$

$$\Phi = \frac{mmf}{magnetic\ reluctance} = \frac{Ni}{\mathcal{R}} \quad (2)$$

$$e = -N \frac{d\phi}{dt} \quad (3)$$

Where \mathcal{R} is the magnetic reluctance; l is the length of the air gap; A is the area of the air gap; Φ is the magnetic flux and e is the induced voltage.

For a multi-pole configuration, as seen in Figure 3, the structure is such that the variation in the length of the air gap between the stator and the rotor produces sinusoidal variations in the output voltages.

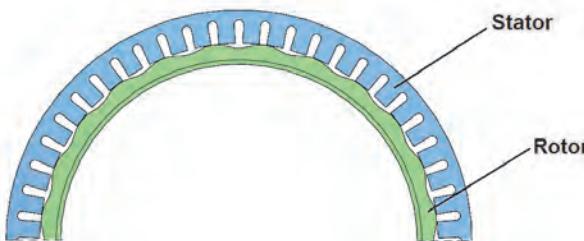


Figure 3. Structure of multi-speed variable reluctance resolver

For absolute position feedback a single speed variable reluctance resolver is used, which consists of a couple-pole configuration. The configuration of a couple-pole VRR varies the reluctance through the variation in the coupling area between the stator and rotor core segments. A unique circular rotor core is supported by two non-magnetic members, as seen in Figure 4. The rotor core provides a diametrical diagonal magnetic path from upper half of stator core to the lower half of stator core as illustrated below.

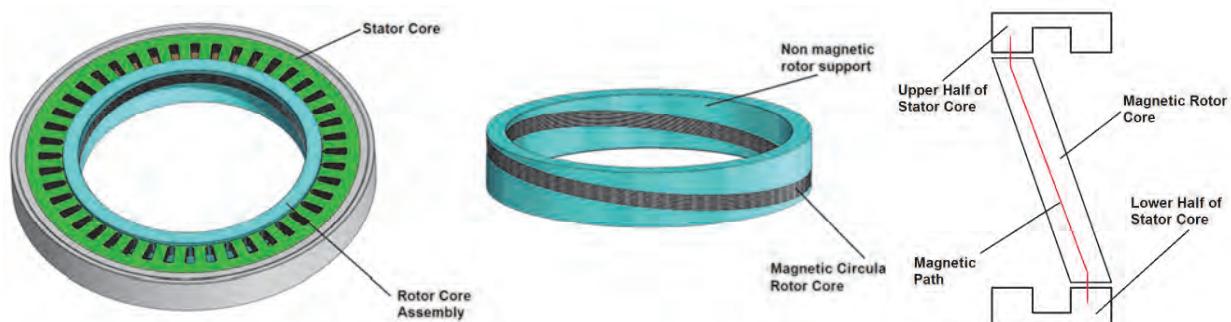


Figure 4. Structure of single-speed VRR

Development of Single Speed Variable Reluctance Resolver

Description of first generation single speed VRR

The architecture of the first generation single-speed VRR, as seen in Figure 5, consisted of two laminated stator cores and a single laminated rotor core. Each stator core, made of high permeability lamination, were stacked, bonded and insulated.



Figure 5. First generation single speed VRR

The two stator cores were then inserted into the back iron and aligned and then bonded to the back iron. The excitation winding was placed between the two laminated stator half cores diametrically, as shown in Figure 6, and the sense winding was inserted through both cores axially.

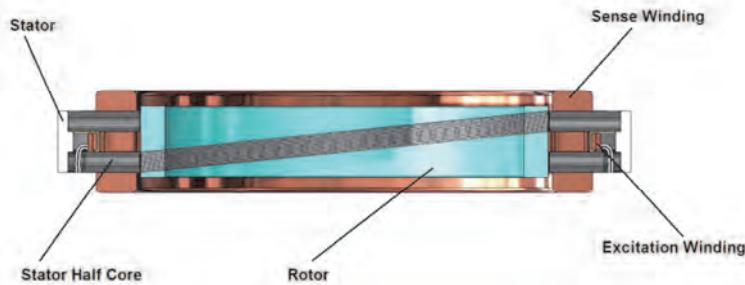


Figure 6. Architecture of the single speed VRR

The rotor core consisted of high permeability laminations, which were stacked and placed on a temporary hub against spacers on either side of the lamination stack and were bonded. The rotor core was designed as a laminated core in order to minimize rotor reluctance since a solid rotor has high reluctance due to eddy current losses. The laminated rotor core produced a high enough transformation ratio of the output voltage to the input voltage.

Shortcomings of first generation single speed VRR

During the manufacturing process and the functional testing, the following were issues which called for design improvements:

- The manufacturing process for the rotor core was extensive and consisted of several machining steps. After the rotor laminations were bonded lamination-to-lamination and lamination-to-spacers, the rotor assembly was machined on the outer diameter (O.D.), then removed from fixture and ground on the inner diameter (I.D.). Finally the rotor assembly was bonded to a hub and its O.D. ground to final dimension to improve concentricity. The several machining processes introduced various stresses to the assembly and jeopardized the bonding adhesive; which introduced de-laminations of the rotor core.
- The thickness of the insulation on the stator cores was inconsistent which contributed to the tolerance stack-up of the stator cores in the stator assembly. Furthermore, the insulation used which was Scotchcast Electrical Resin #260 (3M) was observed to chip off the stator teeth during testing and handling of the VRR.
- During accuracy testing, the accuracy of the single speed VRR was initially found to be approximately 85 arc-minutes as highlighted in Table I, which was much greater than the design

accuracy requirement of 30 arc-minutes. Following the initial accuracy test, various tests were conducted for different parameters to locate which were the greatest contributors to the accuracy of the resolver. The numerous tests included recordings of the signal outputs of the resolver from radial misalignment testing, axial misalignment testing, stator core alignment and repeatability testing. It was established that the stator core alignment had the greatest contribution to the accuracy. See Table I for accuracy readings obtained after the stator core alignment was improved with a significant increase in accuracy from 85 arc-minutes to approximately 48 arc-minutes. For rotor misalignment, the radial misalignment was found to be of higher contribution to the accuracy than axial misalignment with a deviation in the accuracy reading of approximately 9 arc-minutes at the off-set position of 25 µm (0.001 in) as seen in Figure 7.

Table I –Accuracy Test Results of Single Speed VRR

Angle (degree)	0	20	60	100	140	180	220	260	300	340	360
Initial Accuracy Test (arc-min)	0.0	-5.9	-17.8	17.5	44.2	84.4	-40.4	42.6	-48.0	-9.6	0.0
Accuracy after Stator Core Alignment (arc-min)	-0.3	-6.6	-13.1	-2.4	20.1	43.6	47.6	36.3	24.3	7.7	0.3
2nd Gen VRR Accuracy Test (arc-min)	0.0	-9.0	-14.9	-3.4	1.6	-5.3	-9.1	-7.7	6.3	5.6	0.0

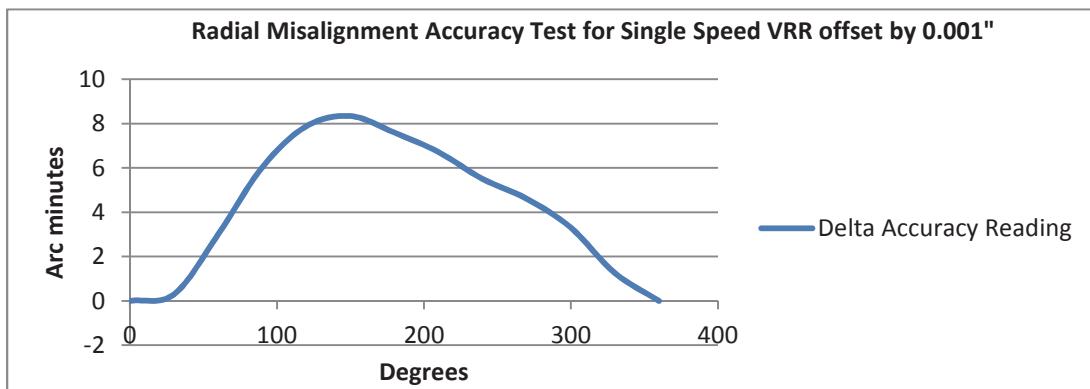


Figure 7. Radial misalignment test result

Lessons learned from the first generation Single Speed VRR

The observations made and the lessons learned from the manufacturing and initial testing of the single speed VRR were the following:

- Excessive machining of the rotor core assembly was causing de-lamination of the rotor core and needed to be dimensioned such as to minimize the machining required to achieve final dimensions.
- Based on the stator core alignment test, it became apparent that the variation in the insulation thickness affected the accuracy significantly; therefore it was found that masking the stator core surface at the outer edge prior to applying insulation was critical.
- Lastly, a final grinding of the O.D. of the rotor core assembly was observed to be necessary to increase concentricity since the accuracy was found to be greatly affected by radial misalignment.

Design improvements for the second generation single speed VRR

The lessons learned from the first generation were implemented in the next generation single speed VRR through the following design modifications:

- The stator and rotor cores were re-designed with the design objective of a solid rotor core in order to eliminate any possibility of de-lamination. This was obtained by increasing the slot area of the stator cores to increase the coil turns in order to compensate for the eddy current losses in the solid rotor and to achieve the required transformation ratio.
- The stator cores were masked at the edges and were electrostatic powder coated using the Scotchcast Electrical resin 5133 allowing for a thinner and more consistent insulation thickness with no chipping observed.
- All machining of the rotor core was minimized by machining the solid rotor core to final dimensions less the O.D. which once bonded to the hub would undergo a minimal O.D. grind to improve concentricity.

The second generation single speed VRR showed significant enhancement in performance once the design improvements had been implemented. Testing of the second generation VRR produced an accuracy reading of approximately 15 arc-minutes as listed in Table I. Comparing to the initial reading of 85 arc-minutes it was a great achievement.

Development of Multi Speed Variable Reluctance Resolver

Description of first generation multi speed VRR

The multi-speed VRR was designed and built with a single laminated stator core with specifically designed tooth profile for optimized sensitivity of variable air gap and a slot-less laminated rotor core. The resolver was developed with an axial length of 6.35 mm (0.250 in) offering a compact design, which resulted in a 30% reduction in mass compared to that of a conventional resolver of similar O.D. The excitation windings and the sense windings were placed on the stator core alone. Its air gap was varied such to produce a sinusoidal change in the magnitude of the output voltages of the two sense windings.

Observations and test results of the multi speed VRR

The performance of the multi-speed VRR was exceptional and produced accuracy test results much higher than required of the design. The short coming of the initial design was limited to the insulation material Scotchcast resin #260 which was chipping as it had in the single-speed VRR.

Accuracy testing was performed and the resolver accuracy was measured in every 1 degree increments from 0 – 360 degrees and its results are summarized in Table II. The highest reading was found at 350 degrees at a value of approximately 35 arc-seconds which is listed and highlighted in the Table. Comparing to the design requirement of 360 arc-seconds (6 arc-minutes) the multi-speed VRR performed much greater than anticipated.

Table II –Accuracy Test Results of Multi-speed VRR

Angle (degree)	0	20	60	100	140	180	220	260	300	340	350	360
Accuracy Test (arc-sec)	0.0	36.7	0.1	-21.5	27.9	6.5	-20.5	25.5	3.9	-24.9	35.2	0.0

Conclusion / Summary

The Ducommun team has developed Variable Reluctance Resolvers with sufficient accuracies to be in used in the Aerospace and Defense Industries in angular position feedback applications. The single-speed and multi-speed designs have been fully qualified and were shown to meet internal as well as external customer requirements. The latest development of the variable reluctance resolvers has made them competitive to conventional resolvers and offers an alternative solution in the application of brushless DC motor commutation.

FeF₃ Catalytic Influence on PFPE Lubricant's Lifetime under Loaded Conditions

Lionel Gaillard*, Antoine Mariot**, Catalin Fotea* and Roland Holzbauer[†]

Abstract

A Perfluoropolyalkylether (PFPE) oil was heated in an inert atmosphere under dynamic temperature control. The temperature profile allowed precise determination of the degradation onset temperature. The degradation temperature appears to be lower than literature values under the conditions used for this investigation. Other samples of PFPE oil were later tested with a Pin on Disk Tribometer under different temperature and loading conditions.

Introduction

While PFPE lubricants are widely used in mechanisms designed for aerospace industry because of their numerous advantages, it is known that they degrade quickly and heavily under boundary lubrication conditions, especially when in contact with 440C or 52100 stainless steels.

Numerous authors (1) (2) (3) (4) (5) (6) in the past decades suggested that degradation of PFPE oils under boundary lubrication conditions was catalyzed by the Lewis acid FeF₃ (Iron fluoride III). Some authors (3) even proposed the degradation mechanism was autocatalytic, which means it could continue for a while after the mechanical stress ceases.

In 1991, David J. Carré (2) proved indeed that PFPE does degrade in the presence of FeF₃ by reacting a branched PFPE and FeF₃ in a nickel-lined autoclave under inert atmosphere at high temperatures. The reaction is triggered in this instance at a temperature approximately 30°C below thermal degradation; however, high mechanical stress could have contributed to the high temperature excursions (7).

The recent experiment, on the other hand, has dealt specifically with the degradation temperatures and more importantly to precisely assess the triggering temperature for PFPE degradation. This is the first experiment that combined the precise temperature control for the heating ramp by using a state of the art Netzsch Simultaneous Thermal Analyser (STA) while monitoring the discrete changes that occur within the PFPE/FeF₃ mixture using Fourier Transform Infra-Red (FTIR) and a mass spectrometer. Furthermore, the experiment would provide further insight into the autocatalytic mechanisms as suggested by (3).

Experiment

The Netzsch STA consists of a dynamic temperature controlled furnace coupled with a Fourier Transform Infrared Spectroscopy and Mass Spectrometry (Figure 1 and Figure 2). The instrument is vacuum tight by design, the furnace is evacuated first at pressures of ca. 10⁻² mbar and is continuously purged with N₂ gas therefore the pressure inside the furnace is atmospheric during continuous operation.

* European Space Agency, Noordwijk, The Netherlands

** École Nationale Supérieure d'Arts et Métiers ParisTech, Lille, France

[†] Aerospace & Advanced Composites GmbH, Seibersdorf, Austria



Figure 1. Furnace (left) and mass spectrometer (right).



Figure 2. FTIR facility.

The fact that we were working at a more or less ambient pressure should not be an issue since even in high vacuum both FeF_3 and PFPE oil are expected to be present as a condensed form. In this case, the pressure dependence of the Arrhenius equation is low.

Approximately 5 mg of FeF_3 powder were mixed with ca. 100 mg of Fomblin Z25 PFPE lubricant in an aluminum crucible. Fomblin Z25 is a base oil used in various Maplub and Braycote greases. These quantities of FeF_3 were intentionally high to ensure that iron fluoride would be in excess. It was feared that the reaction rate with “realistic” amounts of FeF_3 (which is supposed to form as a near-monomolecular layer on real-life mechanisms (3)) would be too slow to be measured during a reasonable timespan. A “witness” cup containing only Z25 oil was also prepared.

The temperature profiles used for this exercise are shown in (Figure 3).

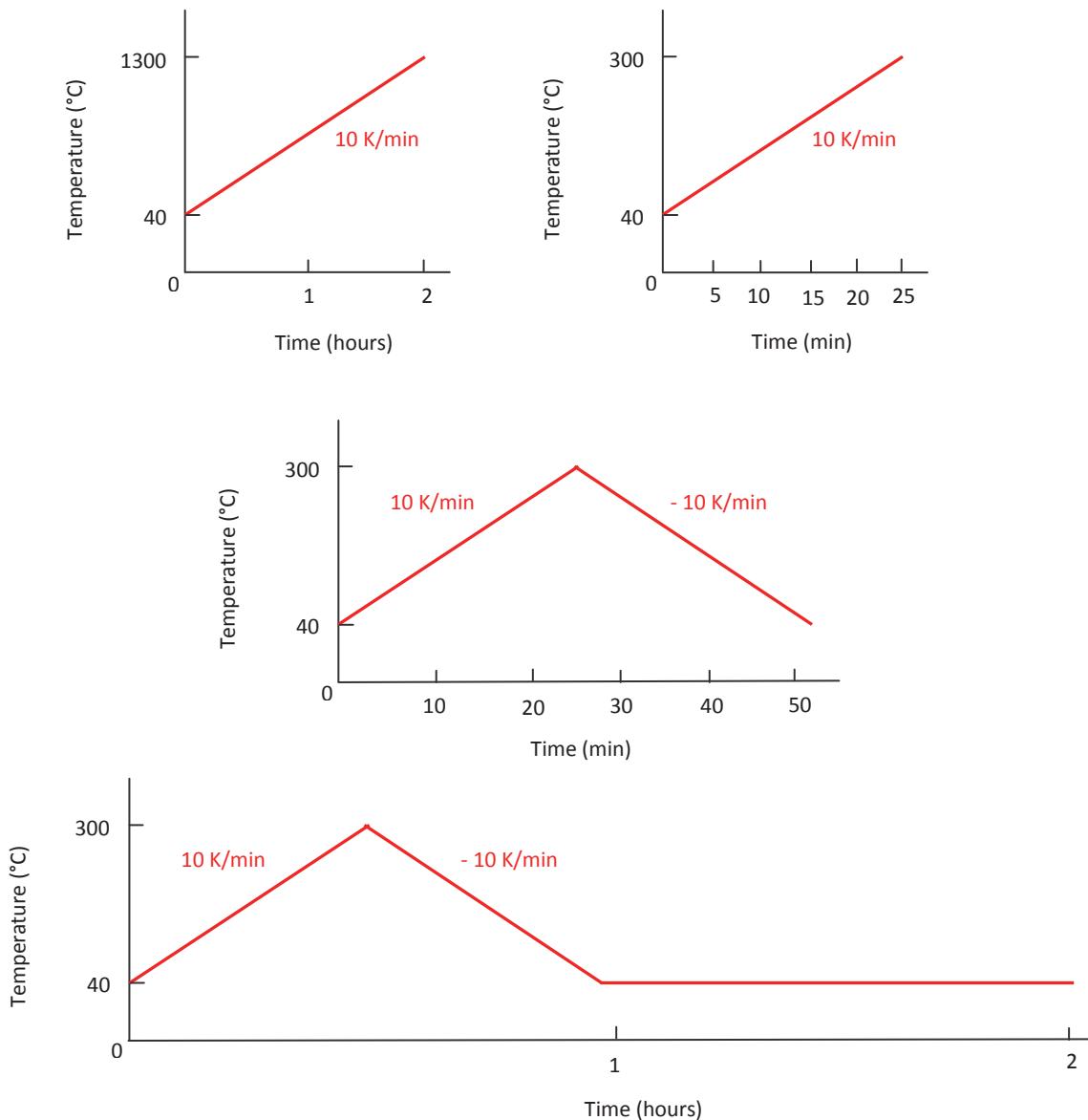


Figure 3. Temperature profiles.

At the time of writing this paper, the following tests were completed:

1. Neat Fomblin Z25 was heated to 1300°C using a 10 K/min ramp to assess the degradation temperature of the lubricant.
2. A mixture of Fomblin Z25 and FeF₃ was heated to 300° using a 10 K/min ramp.
3. A mixture of Fomblin Z25 and FeF₃ was heated to 300°C using a 10 K/min ramp and cooled down to 40°C using a -10 K/min ramp.
4. A mixture of Fomblin Z25 and FeF₃ was heated to 300°C using a 10 K/min ramp and cooled down to 40°C using a -10 K/min ramp, then maintained at 40°C for one hour.

The FeF₃ has never been clearly identified in an actual mechanism or test apparatus, even if its presence is very likely. Consequently, additional tests on a tribometer were run. The aim was to observe the gaseous compounds coming out of the degradation reaction. Although it would not be a definitive proof, finding the same degradation products and behavior as in the STA facility would greatly increase the

likeliness of the hypothesis. A Pin-on-Disc (PoD) tribometer was used in a high-vacuum chamber under temperature control, along with mass spectrometer analysis.

Results and discussion

The heating of neat lubricant to 1300°C determined the thermal degradation onset temperature of the Fomblin Z25 oil. Very precise onset points for the lubricant mass loss and the FTIR Gram-Schmidt reconstruction readings were observed. Figure 4 presents the temperature profile (red curve), the total mass loss of the oil (green curve), the differential scanning calorimetry (DSC) reading (blue curve), and the FTIR Gram-Schmidt reconstruction (black curve). The thermal degradation occurs at ca. 400°C.

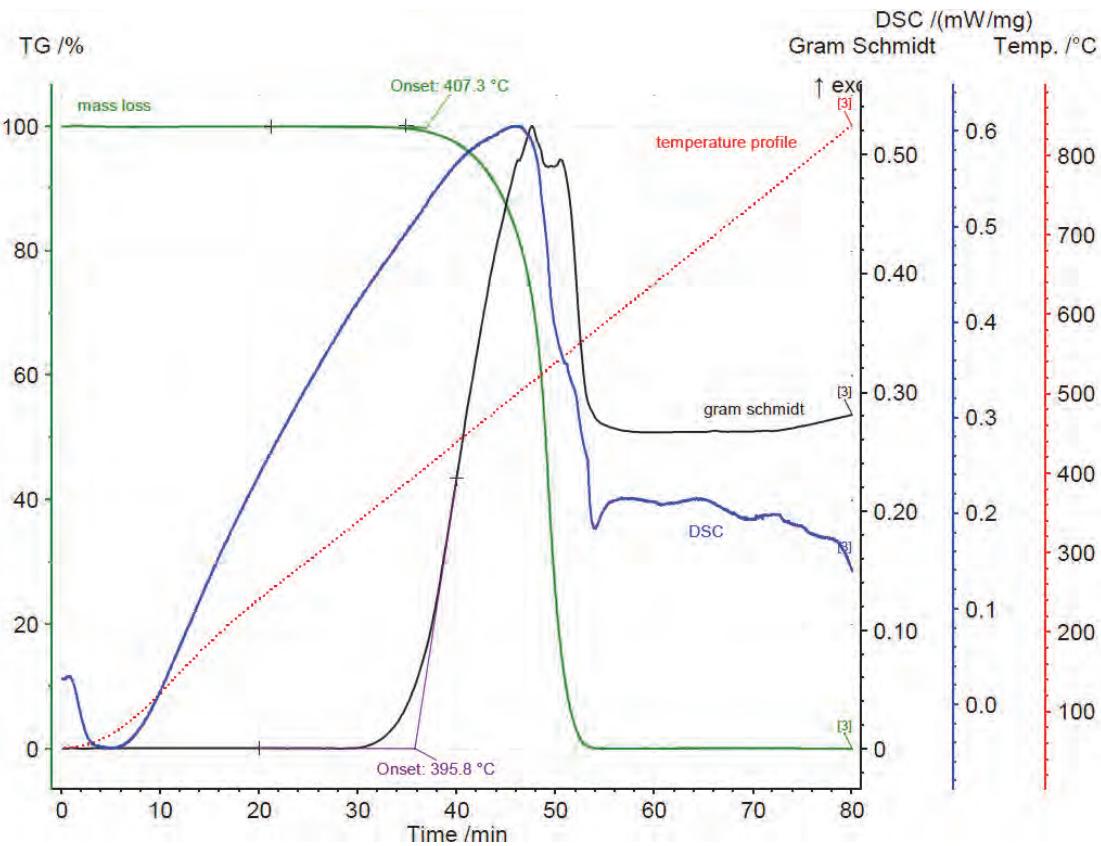


Figure 4. PFPE run to 1300°C.

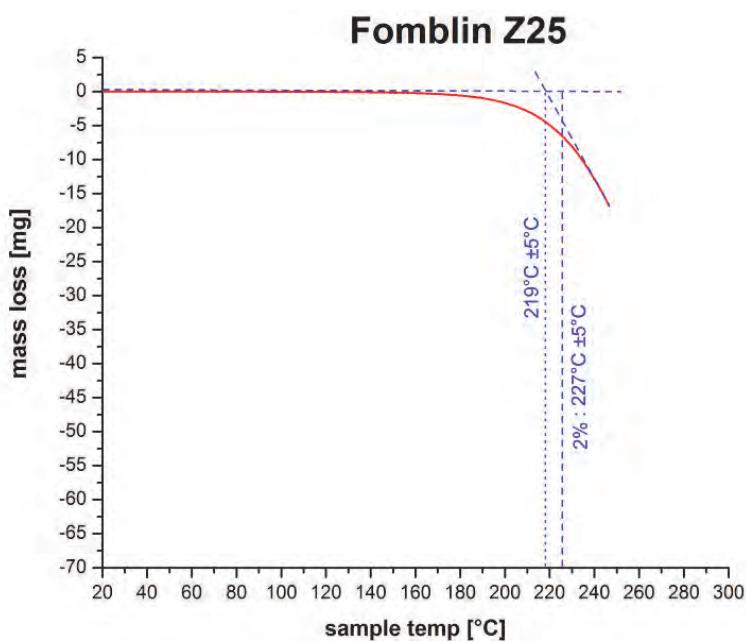
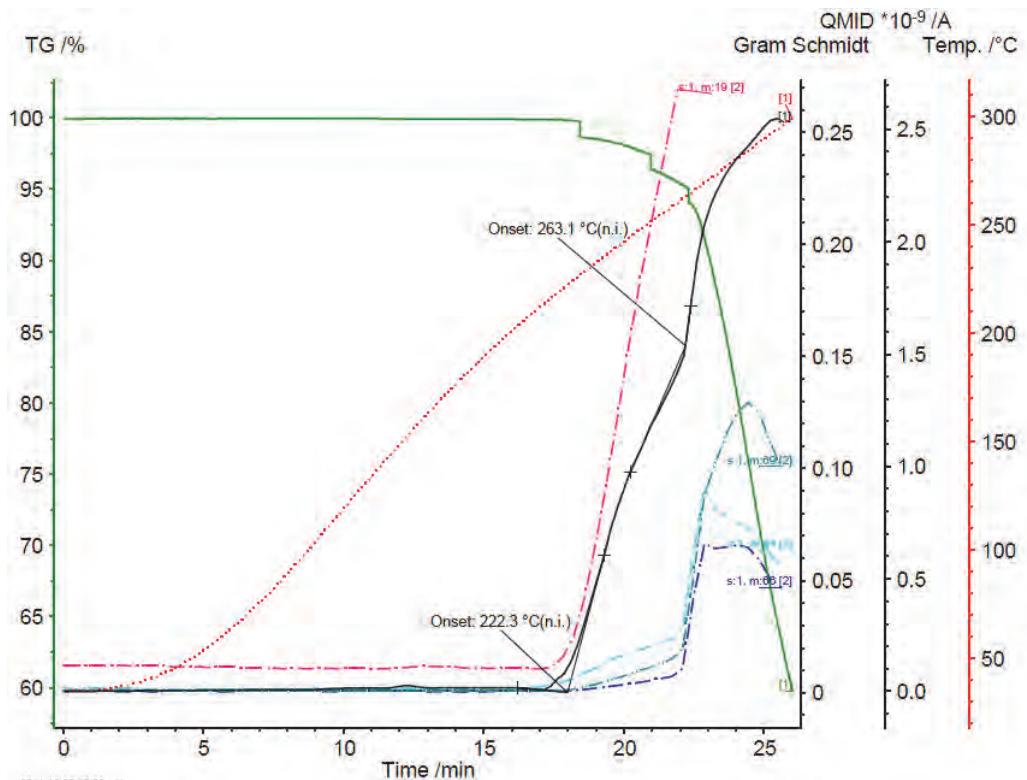


Figure 5. Z25 sublimation test under high vacuum.

Observation: the experiment was run at an ambient pressure, which means that under vacuum, sublimation will occur before the oil reaches 400°C. This was shown by a sublimation test run by AAC GmbH (Figure 5). Given those results, it was not necessary to go above the thermal degradation temperature, which led us to choose a 300°C maximum limit.

The second (PFPE and FeF₃ mixture heated to 300°C using a 10 K/min ramp) and third test (mixture of Fomblin Z25 and FeF₃ heated to 300°C using a 10 K/min ramp and cooled down to 40°C using a -10 K/min ramp) showed that some degradation was occurring at a much lower temperature. Figure 6 shows an onset point for the mass loss (green curve), FTIR Gram-Schmidt reconstruction (black curve) and mass spectrometer readings (dotted curves). Thus, the degradation appears to be triggered at ca. 220°C. Figure 6 presents the different gaseous products detected by the mass spectrometer as follows: the main peaks were observed at atomic mass units (amu) 19, 44, 47, 66 and 69. The 19 amu trace can be attributed either to electron-stimulated desorption (along with 1 and 16 peaks, not shown) (8) or to fluorine radicals coming out. The other traces are 44 amu: CO₂, 66 amu: COF₂ and its ionization product 47 amu: COF, all of them being predicted by the theory of FeF₃/PFPE reaction (3).



However, it has not been possible to compare the mass intensity of these traces between each experiment. Because of the presence of moisture inside the test chamber, the mass spectrum associated with water was exceeding the range of the mass spectrometer, thus rendering other readings inaccurate. Future tests should therefore carefully use amplification settings that do not make water traces exceed the range of the instrument.

Table 1. List of conducted PoD experiments.

Test 1 560 MPa, 20 °C	Test 2 560 MPa, 80 °C	Test 3 560 MPa, 120 °C
Test 4 850 MPa, 20 °C		Test 5 850 MPa, 120 °C
Test 6 1200 MPa, 20 °C		Test 7 1200 MPa, 120 °C
Test 8 1900 MPa, 20 °C		

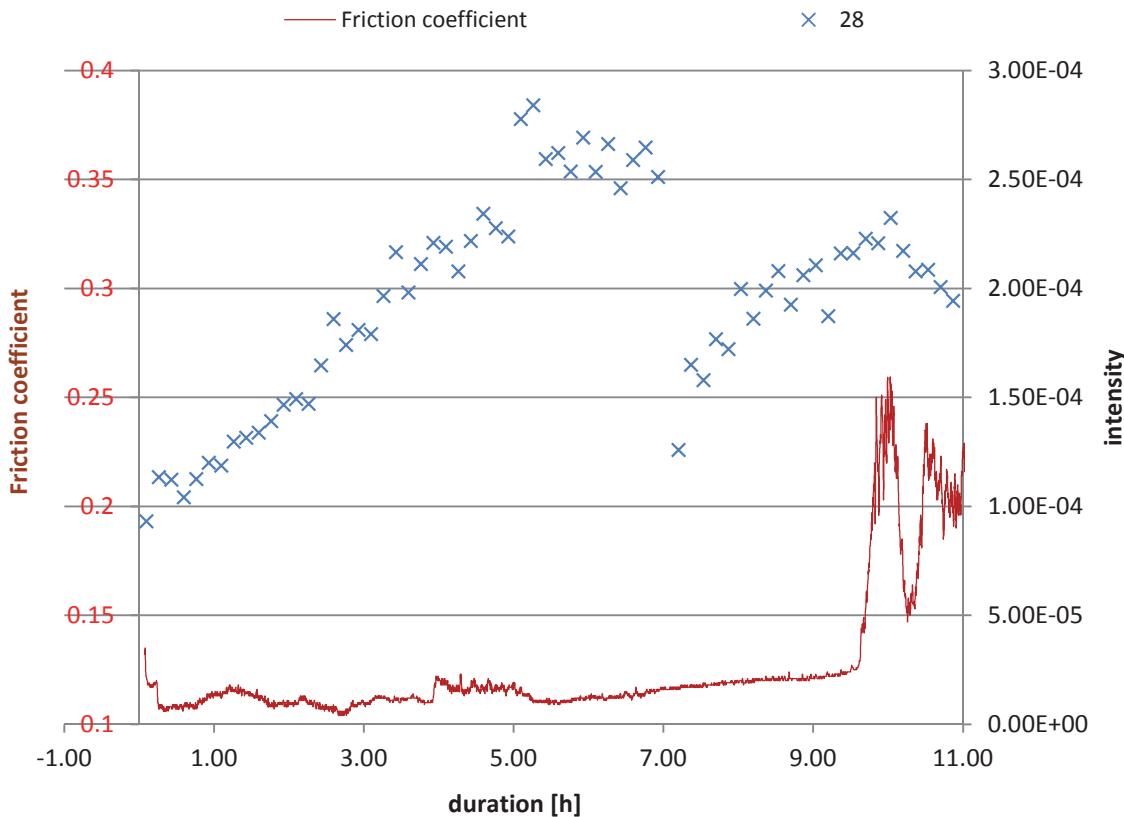


Figure 7. Example of MS readings from a Pin-on-Disc test (red curve: 28 amu, blue curve: 47 amu).

Conclusions

The current results have not allowed a precise reaction rate to be calculated at a given temperature, which would give a good estimation of this degradation mechanism's activation energy and therefore allowed us to propose a safe range for operating this grease in space mechanisms. This knowledge would also have allowed us to estimate whether the degradation reaction is truly negligible at ambient temperature or not. In this case, even stopped stages should be considered harmful for the lubricant. However, we did manage to show that the presence of FeF_3 in the mechanisms definitely and considerably lowers the lubricant's degradation temperature to a point that could be obtained through mechanical loading only (e.g., at ball/race micro contact level in a ball bearing).

Looking at the gaseous compound release during the Pin-on-Disk tests, it is also important to take into consideration that the outgassing rate of the grease under loaded conditions significantly differs from an unloaded grease. A prediction of grease outgassing for a long lifetime application shall take these effects into consideration and adapt the quantity of grease accordingly.

It has been noted that test facilities are easily contaminated by some chemical species. Care should be taken to follow proper "bakeout" procedures to ensure as much as possible that every trace of the previous test has been removed, especially in experiments where mass spectrometer data is important. Moreover, we would like to point out the importance of knowing in advance which spectra (and thus which peaks) are expected to be found in the mass spectrometer measurements, since expected species usually have complex spectra where various traces are overlapping.

Further tests within a pin-on-disc tribometer and/or the spiral orbit tribometer will now focus on observing a real-case degradation to assess if it can truly be correlated to the degradation reaction we studied here. In particular, the influence of mechanical loading and temperature will be monitored. During these tests, care shall be taken to carefully choose mass spectrometer settings that allow proper comparison of the readings coming from the different experiments. We expect that these tests will help us to better define safe ranges of operation for the Z25 grease, and conclude on the autocatalytic effect existence or not.

Bibliography

1. Carré, David J. *Perfluoropolyalkylether Oil Degradation: Influence of FeF_3 Formation on Steel Surfaces under Boundary Conditions*. El Segundo : The Aerospace Corporation, 1985.
2. —. *The Performance of Perfluoropolyalkylether Oils under Boundary Conditions*. El Segundo : The Aerospace Corporation, 1991.
3. Marchetti, Mario. *Aspects globaux et locaux de la mise en œuvre de la lubrification fluide en ambiance spatiale*. Lyon : INSA, 2000.
4. Morales, Wilfredo and Mori, Shiguyeki. *Reaction of Perfluoropolyalkylethers (PFPE) With 440C Stainless Steel in Vacuum Under Sliding Conditions at Room Temperature*. Cleveland : NASA Lewis Research Center, 1989.
5. Pepper, Steve V. *Effect of Test Environment on Lifetime of Two Vacuum Lubricants Determined by Spiral Orbit Tribometry*. Cleveland : NASA Glenn Research Center, 2011.
6. Zehe, M. J. and Faut, O. D. *Acidic Attack of Perfluorinated Alkyl Ether Lubricant Molecules by Metal Oxide Surfaces*. Cleveland : NASA Lewis Research Center, 1989.
7. Hsu, Stephen M. and Klaus, Erwin E. Estimation of the Molecular Junction Temperatures in Four-Ball Contacts by Chemical Reaction Rate Studies. *ASLE Transactions*. 1977, Vol. 21, 3.
8. Neave, J. H. and Joyce, B. A. The Origin of Spurious Peaks in Mass Spectra. *Journal of Physics. Applied Physics*, 1976, Vol. 9, 15.

Trade Studies for a High Torque Density Planetary Gearbox

Jeffrey Mobley*

Abstract

Sierra Nevada Corporation (SNC) has developed planetary gearbox design guidelines that significantly improve the torque capacity per unit volume for an optimized gearbox under a study funded through the NASA Phase II SBIR Lightweight Gearbox Technology Program. The design was based upon optimizing both the physical configuration and material selection of the gearbox design. As a part of this study, many different materials and material processes were evaluated for their suitability for use in lightweight planetary gearboxes for space applications. Calculation methods used to predict gearbox load ratings and expected life were also validated through test. This paper presents findings that have been extracted and edited from the final Phase II report published by SNC.

Introduction

Traditionally, planetary gearboxes used in aerospace mechanisms are based on conventional materials, processes, and designs. This usage has been primarily the result of rapidly paced schedules, and events taking place in a risk-adverse environment. Developing or honing new technology in the midst of a program is often impractical. This study provided the opportunity to research new combinations of materials and processes, as well as the opportunity to validate calculated gearbox ratings for capacity and life. The goal was to capitalize on this endeavor, in an effort to advance the technology used in the common gearboxes employed on planetary rovers and other similar space applications.

Alternate materials and material processes have the potential to improve the load capacity and/or life of planetary gearbox designs. But many of those materials and material processes have little to no heritage in space mechanisms. The key is to develop optimum material combinations that balance the performance limiting factors within a planetary gearbox. One of the limiting factors is the radial load capacity of the planet bearing or bushing. Though ball bearing analysis remains uncomplicated, a general concern with journal bearings is the limited availability of data. Such data includes information regarding pressure, velocity, and pressure-velocity ratings for specific material combinations, and space applications which differ from standard journal bearing testing.

Typical planetary gearbox designs used in space applications are not only based on the conservative guidelines set forth by the AGMA, but build additional margin throughout the system design. If confidence can be built in the calculated gear capacities for the applications and materials seen in space planetary gearbox designs, then it is possible to reduce the amount of margin in order to reduce the torque/mass ratio and still result in a highly reliable gearbox.

Prototypical Gearbox Design

A prototypical gearbox design was developed for use as both an analytical and test model. Every component in the prototypical gearbox design was carefully reviewed to optimize weight, facilitate the use of high capacity materials, and to ensure that manufacturability is maintained. The design was also easily reconfigurable with a variety of materials and finishes which facilitated its usage in further developing the proposed technologies. For the purposes of this study, the gearbox was designed to use a ring gear with five planetary gear stages with a ~1500:1 overall gear ratio, 48.3-mm (1.9-in) housing diameter (excluding flanges), and a 78.7 mm (3.1 in) overall length (excluding shaft extensions). Each stage uses optimized

* Sierra Nevada Corporation, Durham, NC

geometry, materials and construction techniques that are best suited for the individual stage. The design goal was to achieve the maximum torque capacity with an output speed of 3.33 rpm. The overall gearbox weight was 0.59 kg (1.31 lb). An overall view of the resulting prototypical gearbox is shown in Figure 1.

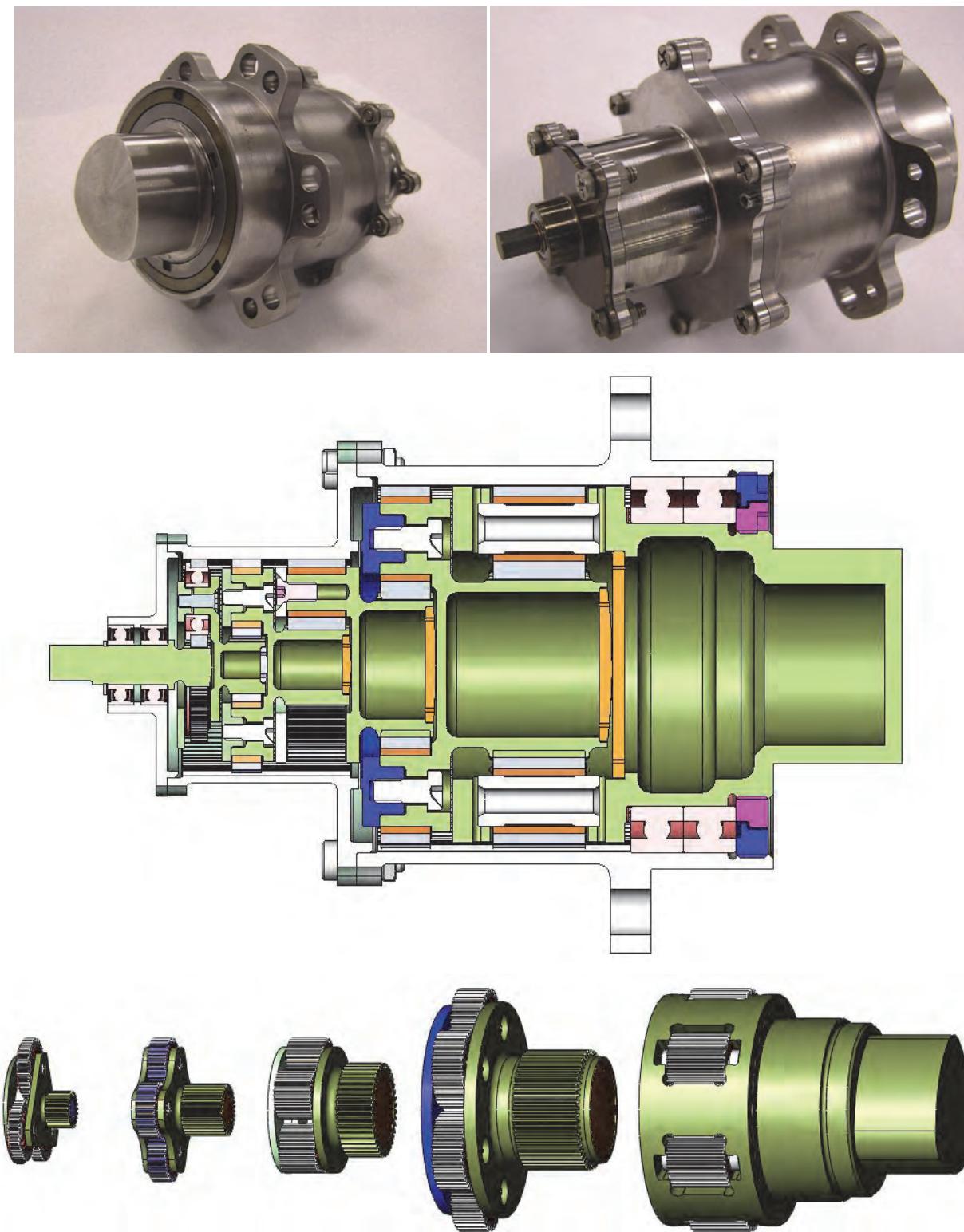


Figure 1 - Prototypical gearbox design

Prototypical Gearbox Rated Capacity

The prototypical gearbox design was analyzed per ANSI/AGMA 2001-C95. Allowable bending stress versus cycles and allowable contact stress versus cycles was extrapolated from the AGMA standard based on the material hardness used. Stress factors were selected to match typical space planetary gearbox applications as much as possible. Based upon the analysis, the following capacities were predicted (assuming a 1.5 Reliability Factor for 99.99% reliability):

- 38.6 N-m (342 in-lb) operating torque against the endurance limit (1E7 Cycles)
- 56.2 N-m (497 in-lb) operating torque at 3.33 RPM for 205.1 hr (Pitting Life = Bending Life)
- 89.5 N-m (792 in-lb) for short term operation of 4 hr or less
- 137.5 N-m (1217 in-lb) operating torque for momentary operation (bushing dynamic limit, ≤5 minutes rated gear operation at this load)
- 205 N-m (1812 in-lb) static torque limit for gears (2.0 Safety Factor)

Test Evaluation Parameters

Bushing Materials

For applications in which rolling element bearings are not suitable due to either capacity or packaging constraints, heritage planetary gearbox designs have traditionally utilized oil-impregnated SAE 841 bronze bushings. SAE 841 bushings have a Pressure-Velocity (PV) rating of 1.75 MPa-m/s (50 kpsi-ft/min) with a peak intermittent pressure of 28 MPa (4 kpsi). Often the bushing will be the limiting factor in the dynamic and/or static rating of the gear stage.

An alternate material under consideration is Toughmet 3AT by Materion Brush, a spinodal/copper/nickel/tin alloy. Toughmet 3AT has a published PV rating of 4.6 to 9.0 MPa-m/s (132,000 to 260,000 psi-ft/min) depending upon the surface finish of mating parts. Maximum low-speed pressure was not provided and the testing that generated the PV ratings for the Toughmet 3AT material was performed at speeds of 1.5-2.0 m/s (300-400 ft/min) with additional lubricant added during the test. Space planetary gearboxes do not allow any lubrication to be added during life and often operate at speeds at or below 0.5 m/s (100 ft/min).

It was decided to test both SAE 841 bronze and Toughmet 3AT bushings without providing additional lubrication and over a speed range closer to the typical space planetary applications. The purpose of the test was to determine if published PV ratings are valid and also to show a direct comparison between the two materials.

Gear and Journal Surface Treatments

The literature for Toughmet AT recommended Metalife Industries MLP as a surface treatment that could provide lower friction, higher PV ratings, and longer life in lubricant starved conditions. Metalife MLP is a thin dense chrome coating with a proprietary polymer compound added.

Oerlikon recommended adding their Balinit C coating to gear teeth and mating surfaces of bushings to extend life and capability. Balinit C is an amorphous carbon-tungsten carbide coating (WC/C) with a high surface hardness and a low coefficient of friction that claims higher bearing load capacity, lower sliding wear, improved scuffing resistance, and reduced pitting particularly in applications with boundary lubrication conditions such as slow moving gears in contact.

REM Chemicals recommended their Isotropic Superfinish (ISF) process which claims to eliminate break-in, reduce friction, and reduce contact fatigue. The ISF process involves a chemical conversion creating a micro thin soft layer that is removed by ceramic media. Multiple passes through the process resulted in removal of the peaks from the surface, while leaving the valleys as location for lubricant to remain during contact operation.

Shot peening of gear tooth faces was also considered as a method to increase the localized surface hardness of the tooth, thereby increasing gear pitting fatigue resistance. Another expected benefit of shot peening of gears is an increase in the bending fatigue resistance at the root of the tooth.

Many of these processes had not been previously performed on fine pitch gearing (64DP & 96DP) that is typical of lightweight gearboxes in space applications. These processes also had not been tested with space-grade lubricants which traditionally do not perform as well as their higher outgassing terrestrial counterparts. A development test was needed to determine which processes or combination of processes would add to the life and/or capacity of planetary gearboxes and may be suitable for future consideration.

Capacity Validation

AGMA analysis guidelines are typically conservative and do not always directly correlate to lightweight planetary gearboxes for space applications. Additionally, the parameters used in AGMA gear calculations were developed from testing larger gears, different environments, different materials, different lubricants, and different load conditions than typically experienced in Space applications. When testing is traditionally performed on a program, gearing is only tested to the loads and life specified for the application, and not tested up to or beyond the calculated rated loads and life of the design. Development testing was needed to validate the calculated allowable loads and life for the various base gear materials used and ensures that the calculations are not over stating the capability of the gearboxes.

Testing

Journal Bearing Test

In order to directly compare combinations of bushing material (SAE 841 sintered bronze vs. Toughmet 3AT), shaft/planet finishes (as-machined vs. Superfinished vs. Metalife MLP vs. Balinit C), and lubricant (Bray vs. Pennzane), a journal bearing test was formulated. Various combinations were tested to determine relative pressure and velocity limitations for both high speed/low torque and low speed/high torque scenarios. Testing was performed in ambient temperature and pressure due to numerous required test setup changes to accommodate each combination.

The oil impregnation from the SAE 841 bronze bushings coupled with relatively low hardness allowed the SAE 841 bushings to replenish the interface lubricant, absorb wear debris, and wear in any bushing surface damage to provide operation at levels higher than rated. The inherent hardness of Toughmet 3AT provided more uniform initial torque measurements, but in general these bushings failed at PV levels lower than the SAE 841 bushings and initial friction increases moved quickly to catastrophic increases in friction. REM Superfinishing displayed slightly reduced friction at the start of test, but overall results were mixed and there was not a conclusive improvement in life as a result of the process. Metalife MLP, when run against the Toughmet 3AT bushings, revealed a pressure limit of around 3.45 MPa (500 psi) at which point the coating began to break down regardless of speed. Balinit C shafts and gear blanks showed distinctly higher friction than other finishes and appeared to limit the SAE 841 material from recovering from initial onsets of increased friction. Pennzane formulated lubricants (Nye 2001 oil / 2000 grease) performed somewhat better than Bray formulated lubricants (815Z oil / 601 grease), but there was not a conclusive nor definitive trend.

The optimal configuration was determined to be SAE 841 bronze bushings running on hardened steel shafts and planet bores with no additional surface coating or treatment except for surface finishes held as tightly as feasible. One of the lessons learned was that any chamfers, fillets, or edge breaks on the contacting surfaces should be performed prior to performing the final machining operation on the journal surfaces to minimize the risk of concentrated areas of high contact pressure.

Heritage Phoenix SSI Gearhead Test

In order to obtain advanced test results on some of the materials and finishes while the Prototypical Gearbox parts were being fabricated, spare gear parts from heritage Phoenix SSI Actuators were modified, assembled, and tested. One gearhead was assembled with Balinit C coated parts and one was

fabricated with Metalife MLP coated parts. Both gearheads contained a mixture of shot peened and non shot peened parts. Both gearboxes were assembled with Toughmet 3AT bushings, Bray 815Z oil and Bracyote 601 grease. The gearheads were operated at constant speed with increasing torque until a significant friction increase was detected at the input. Units were then disassembled and inspected.

The Toughmet 3AT bushings displayed significant interface damage against both the planet posts and planet gears, in some cases seizing on the planet shaft. Due to the reduction in contact area and corresponding increase in contact pressure, shot peening increased the likelihood that both the Balinit C and Metalife MLP coatings would breakdown during operation. All of the Metalife MLP gear tooth wear surfaces showed some degree of coating breakdown, with the breakdown being more severe on the shot peened parts.

Metalife MLP was determined to not be as durable as Balinit C for gear teeth under the pressures seen. Test results supported the journal bearing test data which indicated that Toughmet 3AT bushing material is not appropriate for this application. Additionally, it was determined that shot peening is a detrimental process for fine pitch gearing, particularly if surface coatings are desired.

Prototypical Gearbox Test

Gearboxes representing each finish (No Finish, Superfinish, Balinit C) and lubricant (Bray, Pennzane) combination were assembled for test. One combination, Bray/Balinit C, was not tested due to damage sustained to a carrier pinion during assembly. The remaining gearboxes were run-in at 14.1 N-m (125 in-lb) for 4 hours and characterized for baseline efficiency at loads up to 56.5 N-m (500 in-lb). Two gearboxes with No Finish were loaded with a static output torque ranging up to 282.5 N-m (2500 in-lb) to verify static capacity. Both units held the applied load with no sign of damage, verifying the static torque rating.

One gearbox from each of the five configurations was tested through a 250 hr life test at 56.5 N-m (500 in-lb) external torque to verify rated life. This test was followed by 4 hours at 90.4 N-m (800 in-lb) to verify short term life. The Pennzane/No Finish, Bray/No Finish, and Pennzane/Superfinish gearboxes ran smoothly with no erratic torque spikes or significant changes in efficiency through the entire test. The Bray/Superfinish gearbox ran smoothly for the first 150 hours of the life test, and then started to show sporadic input torque spikes that would recover and recur, but never reached runaway levels. Efficiency testing on the Bray/Superfinish gearbox showed a reduction from 74% baseline to 56% post life. The Pennzane/Balinit C gearbox ran smoothly for the first 190 hours of the life test and then also started to show erratic torque spikes would recover and recur, but never reached runaway levels. Efficiency testing on the Pennzane/Balinit C gearbox showed a reduction from 73% baseline to 60% post life.

One Bray/No Finish gearbox and one Pennzane/No Finish gearbox were operated up to and beyond the rated maximum momentary operational torque limit or 137.5 N-m (1217 in-lb) with no signs of erratic input torque which would have indicated bushing failure. The test was halted at the capacity of the input drive motor. The Bray gearbox reached 175.4 N-m (1552 in-lb) while the Pennzane gearbox reached 145.5 N-m (1288 in-lb) maximum momentary torque.

Each of the life test gearboxes was disassembled and inspected. In general, Bray lubricant appeared darker and drier than Pennzane lubricant. The unfinished gearboxes revealed polishing at the gear meshes with no signs of significant surface degradation. The Superfinish/Pennzane gearbox appeared very similar to the No Finish/Pennzane gearbox. The Superfinish/Bray gearbox showed significant bushing wear in the 2nd stage. The Balinit C gearbox with Pennzane (only Balinit C gearbox tested) showed significant bushing wear in the 2nd and 3rd gear stages with several of the bushings cracked. Even with significant bushing degradation, these units continued to function with reduced efficiency, but no sign of imminent catastrophic failure. The external static torque on one of the No Finish gearboxes was increased up to 425.7 N-m (3768 in-lb) with no sign of internal damage, significantly exceeding the rated capacity of the gearhead. The load applied was halted due to the output shaft rotating within the mating interface of the external coupling.

Conclusion

SAE 841 Bronze proved to perform at rated levels even in a lubrication-starved environment with space grade lubricants. SAE 841 Bronze also provides extensive additional margin between initial friction increase and catastrophic failure due to the ability to replenish lubricant and absorb debris.

Toughmet 3AT did not perform to rated capacity most likely due to the inherent lubrication starved environment and the use of space grade lubricants instead of higher performing commercial alternatives. Unlike the SAE 841 bronze, initial onsets of friction quickly turned to catastrophic friction increases.

Metalife MLP provided lower initial friction than bare steel, but the coating broke down at relatively low operating levels, generating abrasive debris which resulted in a high wear rate. This coating may be suitable for bearing journals in high speed/low load applications but extreme caution would need to be taken. Metalife MLP did not appear suitable for use on gear teeth with any significant load.

Balinit C displayed higher friction in journal bearings than bare steel and was detrimental to the performance of the SAE 841 bronze material. It is therefore not recommended for use against bushings. While Balinit C was more durable on gears than Metalife MLP, once the coating was broken down the debris was very abrasive and resulted in extreme wear. Balinit C may help fatigue life on higher speed, lower torque gear stages, but should be avoided in higher torque stages of fine pitch gears to prevent coating breakthrough.

Shot peening resulted in significant surface roughness that could not be overcome by Superfinishing and resulted in swifter degradation of subsequent coatings of Metalife MLP or Balinit C. Shot peening is not recommended on 64DP or 96DP gears unless the process can be refined with extra fine media and reduced pressure, in which case additional testing should be performed.

REM Isotropic Superfinishing provided mixed results. Initial friction levels were improved and there was less debris observed in the lubricant after gearbox run-in. However, overall gearbox life was not conclusively improved by the process. Superfinishing should be considered for 64DP and coarser gearing that cannot be cleaned and re-lubed after run-in. There remained concern over the impact of Superfinishing on the gear profile for 96DP gears (and finer).

Gearbox rated capacities for short term, momentary torque, and static capacity were all validated through the testing of the standard No Finish gearboxes with additional margin shown. This data gives confidence moving forward that calculation techniques and assumed parameters are valid and gear designs can be pushed closer to their calculated limits to minimize mass and volume.

Flight Application

Sierra Nevada has incorporated design elements from this SBIR study into several programs that have been qualified, acceptance tested, and delivered. Significant programs included JPL Mars Science Laboratory Descent Braking Mechanism, JPL Mars Science Laboratory Low Torque Actuator Gearboxes (5 different gearbox designs), as well as other commercial Aerospace applications.

References

1. "D21507 Final Report: Lightweight Gearbox Technology Program Phase II SBIR." SNC
2. "ToughMet Plain Bearings – Performance with High PV." *Materion TechBrief*
3. "Enhancing Toughmet 3 Bearing Performance with Metalife Hard Coated Steel." *Materion TechBrief*
4. "Coated Components: Greater performance and reliability." Oerlikon Balzers, 2010.
5. Winkelmann, Lane et al "The Effect of Superfinishing on Gear Micropitting." *Gear Technology* March/April 2009.

Single Motion Actuated Shape Memory Alloy Coupling

A. O. Perez*, J. H. Newman** and M. Romano*

Abstract

The objective of the single-motion-actuated-shape-memory-alloy coupling (SMA^2C) is to produce a small, single motion actuator used to secure and then release the solar panels on a CubeSat, or other very small satellite, upon command. The SMA^2C consists of a nickel titanium (NiTi) cylindrical shape memory alloy (SMA) press-fit into a stainless steel bushing, surrounded by a Kapton foil heater, a spring, a holding bolt, and a polyetherimide isolation washer all in a structural housing. Heating the SMA above its activation temperature causes it to contract, permitting the spring to push the SMA, and therefore the holding bolt, out of the stainless steel bushing. This releases whatever the holding bolt is attached to from the CubeSat structure.

Introduction

In the past, CubeSats, very small satellites of about one to four kilograms, have used various ways to secure their solar panels while in their CubeSat launchers. Some have been simply held closed by the walls of the launcher itself. The CubeSat's solar panels would slide along the walls of the launcher and, when fully released, the solar panels would deploy. Sometimes the solar panel is secured by tying fishing wire around the solar panel and having a mechanism burn the wire for a controlled release. When this method is successful, it is quite simple and effective, but there have been premature releases occurring during vibration tests. In addition, there is a limit to the amount of force that the fishing wire can withstand, restricting its application to other types of deployments. SMA^2C is a release mechanism that addresses both control of deployment and capacity of holding force, which can be scaled for many applications.

SMA^2C Background

NiTi is a shape memory alloy with particular properties for our application. Shape memory alloys are a class of materials that exhibit a mechanical change in property with a non-mechanical input such as a temperature change. SMAs undergo three types of transformations; Austenite, Twinned Martensite, and Detwinned Martensite. In its natural state, SMA begins in its memory state also known as the Austenite phase. Once cooled it enters into the Twinned Martensite phase in which the crystal structures realign and produce a minimal change in overall expansion. If stress is not introduced during the Twinned Martensite phase and heated back up, the SMA's crystal structure returns back to its Austenite phase and a minimal amount of overall contraction occurs. On the other hand, when stress (σ) is added in the cooled Twinned Martensite phase, an increase in strain (ϵ) (expansion) of the Shape memory alloy brings it to the Detwinned Martensite phase wherein its crystal structure has been further modified. In order to go from the Detwinned Martensite phase back to Austenite phase, all that's needed is an increase in temperature. This will cause the crystal structure to return to its original memory state (contraction). The amount of overall expansion is closely related to the amount of stress added during the Twinned Martensite phase. Figure 1 is a visual representation of this process.

* Mechanical and Astronautical Engineering Department, Naval Postgraduate School, Monterey, CA

** Space Systems Academic Group, Naval Postgraduate School, Monterey, CA

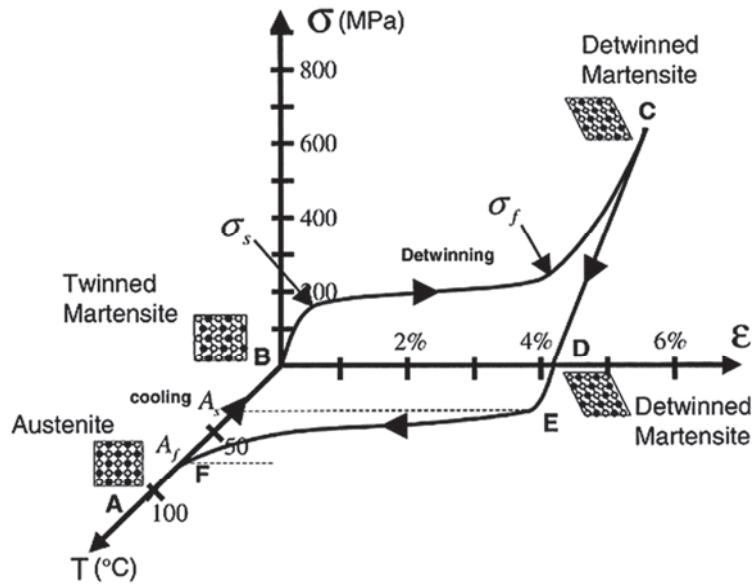


Figure 1. Shape Memory Alloy phases [1]

SMA²C press fitting

Assembly begins with a load cell in order to measure the amount of stress incurred on the NiTi during press fit. The outer bushing is placed inside the cradle and a little Isopropyl alcohol is dropped inside in order to clean and act as a lubricant during the press fit. The remaining cradle is then placed on top followed by the NiTi ring on the press pin. The press pin is then forced down causing the NiTi ring to be forced into the steel bushing as the load cell records the amount of force being asserted by the press pin. Figure 2 depicts the press fit assembly.

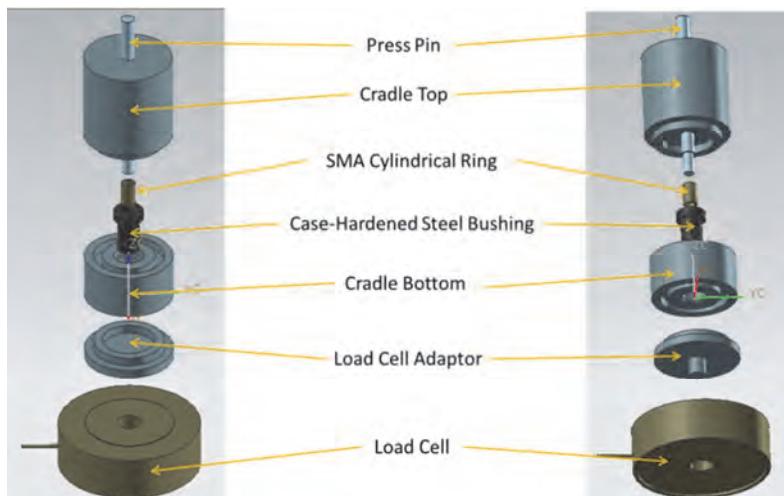


Figure 2. SMA²C Press fit [2]

SMA²C holding force

As mentioned above, the amount of stress induced between the Twinned and Detwinned Martensite phase is directly correlated to the the amount of strain (expansion) that the NiTi undergoes. This

expansion affects the amount of holding force when inside the bushing. In order to demonstrate this relationship, four different sample sets of NiTi rings were used with different outer diameters. They were each press fitted into a bushing of a certain diameter. The outcome was four sample sets, each with different interference measurements (difference between the outer radius of the NiTi ring and inner radius of the bushing). The sample with the greatest interference required greater force when press fitting the two pieces together, therefore increasing the stress induced. Because of this increased stress, the NiTi expands, leading to a greater force required to separate the two. Figure 3 plots the four different samples with varying interference and the amount of force needed to separate the NiTi ring from the bushing.

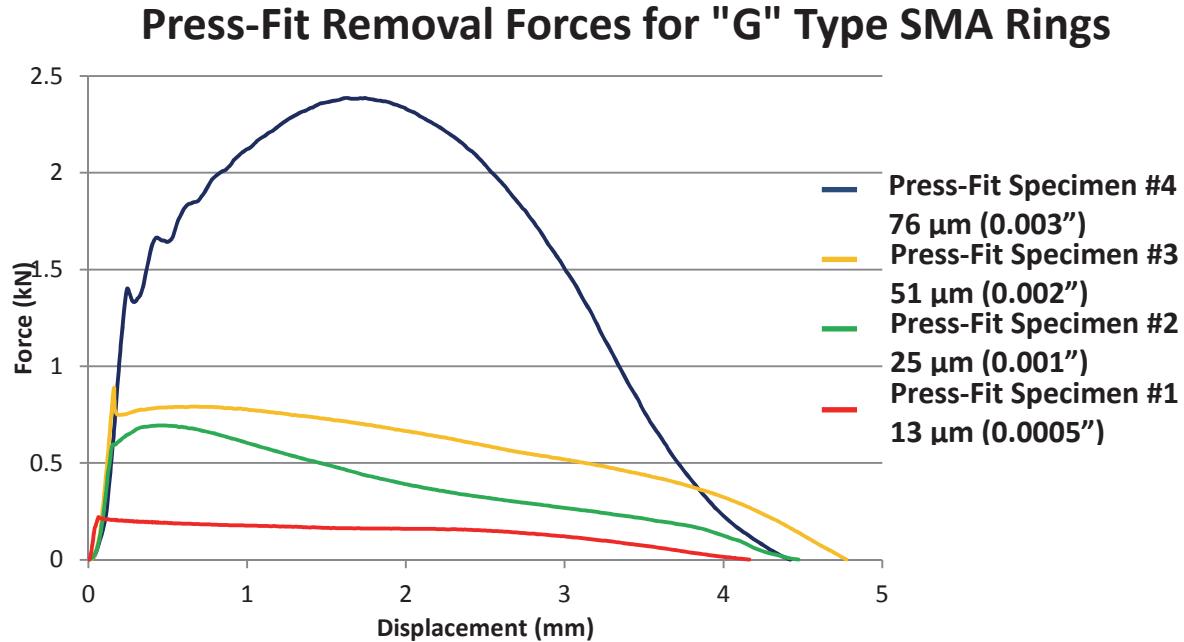


Figure 3. SMA^2C holding force [2]

SMA²C assembly

After the NiTi ring has been press fitted into the bushing, a polyetherimide isolation washer is placed through the bushing in order to thermally isolate it from the remaining assembly and the CubeSat. The bushing is wrapped with a Kapton foil heater and this assembly is then inserted into the outer housing. A push plate and spring are inserted on the other end. This push plate will provide the little push required to separate when the NiTi is heated in a zero gravity environment. Figures 4 and 5 depict the final assembly.

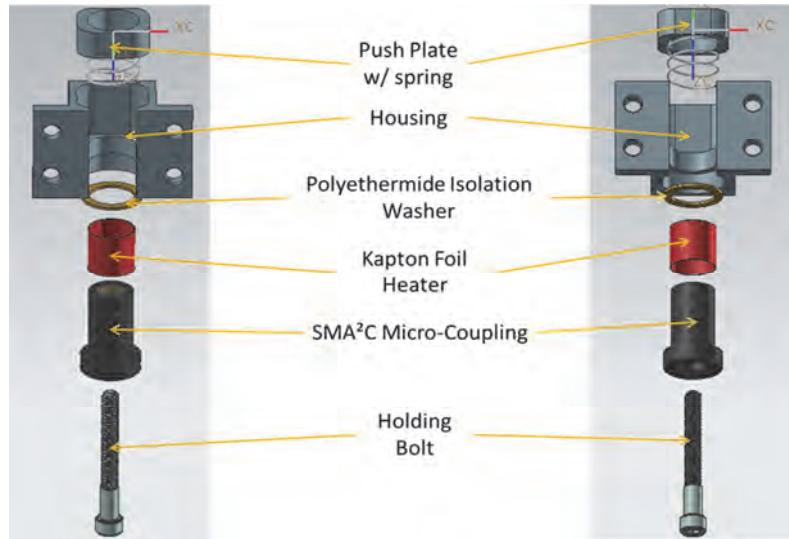


Figure 4. SMA²C final assembly [2]

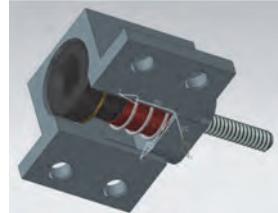


Figure 5. SMA2C assembled [2]

SMA²C release

The SMA²C housing would be secured to the bottom of the CubeSat. A retaining bolt would be inserted through the bushing and NiTi ring with the head of the bolt resting on the NiTi ring, and the other end secured to the solar panel. When commanded, current is sent to the Kapton foil heater, which then heats the SMA²C micro coupling. Once heated, the NiTi will shrink allowing it to be released from the steel bushing. The push plate and spring would help nudge the NiTi ring along with the bolt out of the bushing.

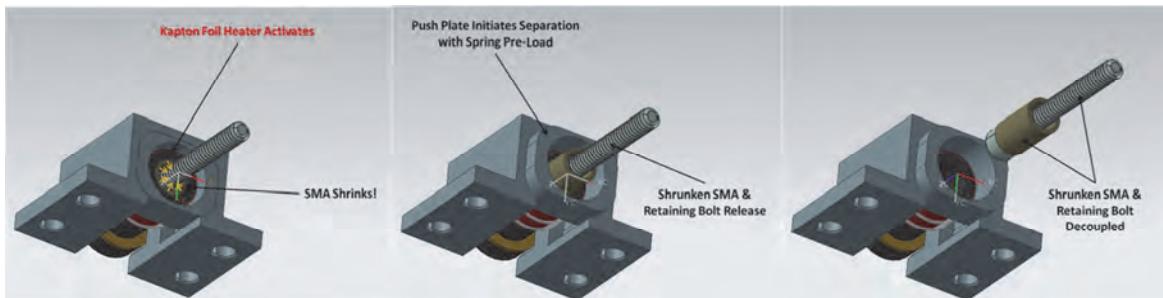


Figure 6. SMA²C release [2]

Conclusion

CubeSats, and other small satellites, require a mechanism to secure and to control the release of their solar panels and other deployables. One common practice is to use fishing wire to secure the deployable and cut it thermally at the desired time on-orbit to release it. Due to the limitation of the fishing wire's strength and reliability, especially during vibration testing, other release methods may be useful.

SMAs, when pressed fitted into another metal, provide a strong holding force which can be released with the addition of heat. The amount of holding force can be modified by simply adjusting the difference between the outer diameter of the SMA ring and the inner diameter of the bushing. Once heat is added to the bushing, the SMA contracts allowing the SMA and the bolt to release from the bushing.

References

- [1] D. C. Lagoudas – Editor, Department of Aerospace Engineering Texas A&M, *Shape Memory Alloys Modeling and Engineering Applications*; Published by Springer Science + Business Media, LLC © 2008.
- [2] Crane, William Mike. *Development of a Nano-Satellite Micro-Coupling Mechanism with Characterization of a Shape Memory Alloy Interference Joint*. MS thesis. Naval Postgraduate School, Monterey, 2010. Print

Development and Testing of a High Compact Stepper Motor Mechanism

Jörg Schmidt* and Greg Wright**

Abstract

The Laboratory for Atmospheric and Space Physics (LASP) has developed for the Mars Atmosphere and Volatile EvolutioN (MAVEN) mission an Imaging Ultraviolet Spectrometer (IUVS) instrument. A grating flip mechanism (GFM), inside the IUVS instrument, is based on a highly compact and innovative stepper motor solution to drive an optic in two precise, bi-stable positions. Rotation angle between positions was 90°. This paper discusses major design restrictions, unique design characteristics and lessons learned from the development up through environmental and performance testing.

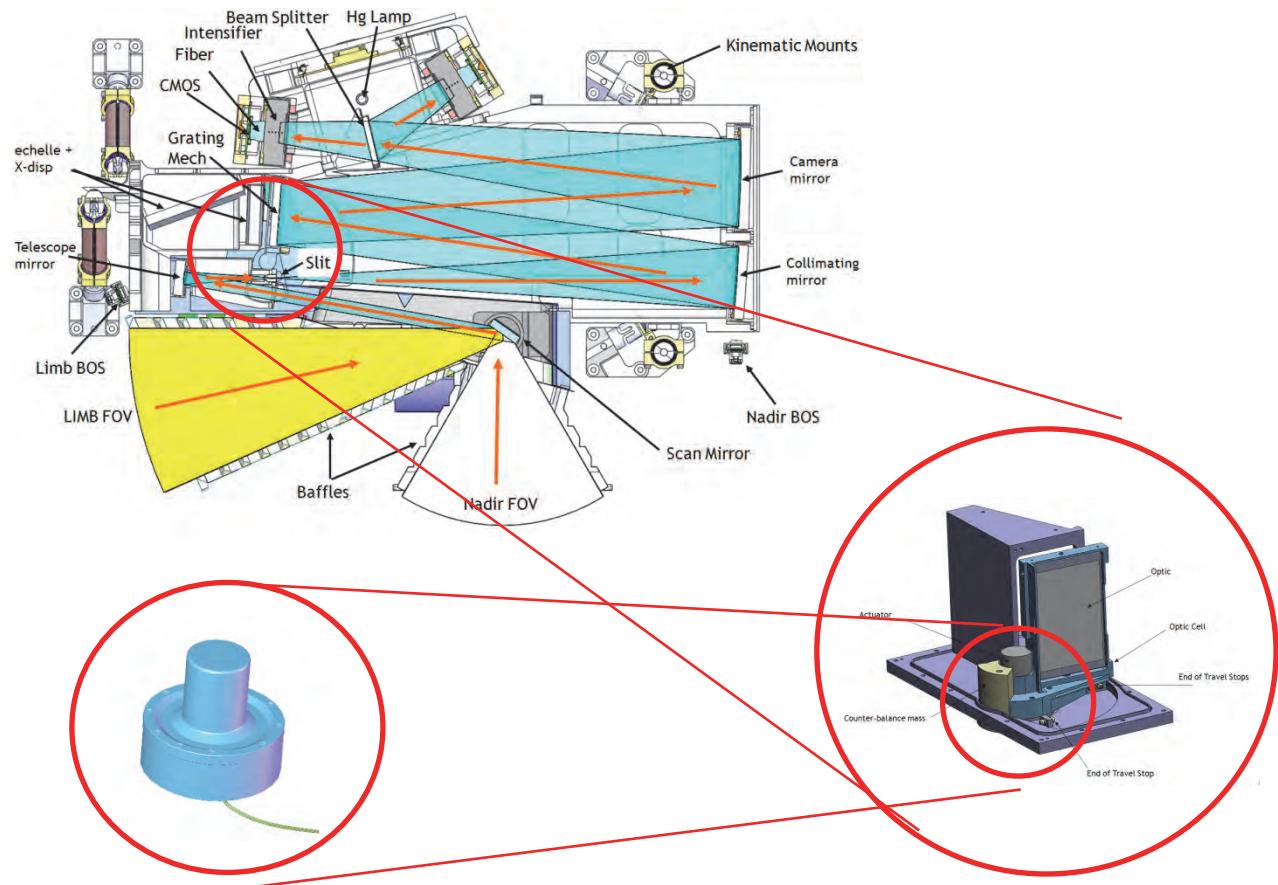


Figure 1. IUVS mechanism overview

* Phytron Elektronik GmbH, Grabenzell, Germany

** Laboratory for Atmospheric and Space Physics, University of Colorado, Boulder, CO

Introduction

Function of the GFM consists of turning a grating assembly inside two hard end stops. The position accuracy defines the systemic grating position. Very restrictive geometrical boundary conditions limited the degree of freedom for an actuator solution – especially with respect to axial length and diameter for the actuator. Standard components or “of the shelf” products were not applicable.

Low weight, high rigidity and functional safety were fundamental design criteria. The long-term cleanliness of the grating represents a systemically size for the spectroscope. To keep the probability and the various ways of grating surface contamination in a very low level, an effective design strategy had to meet all these criteria. This risk mitigation was the key point in the complete design concept. A much more compact construction had to be developed.

Mounted on the cover was the grating assembly with the counter balance mass. The rotation angle was 90°. Two hard end stops on both sides limit the rotation angle. Electrical limit switches detect both end positions. To facilitate the bi-stable positioning we added a flexible coupling between cover and planetary gear shaft. Our purpose was to turn the grating assembly very smoothly in to the end positions. A torque preload should hold the grating in the end position under unenergized conditions via detent torque. Motorization was done by a special modified hybrid stepper motor size VSS 25.200.0,1-X from Phytron.

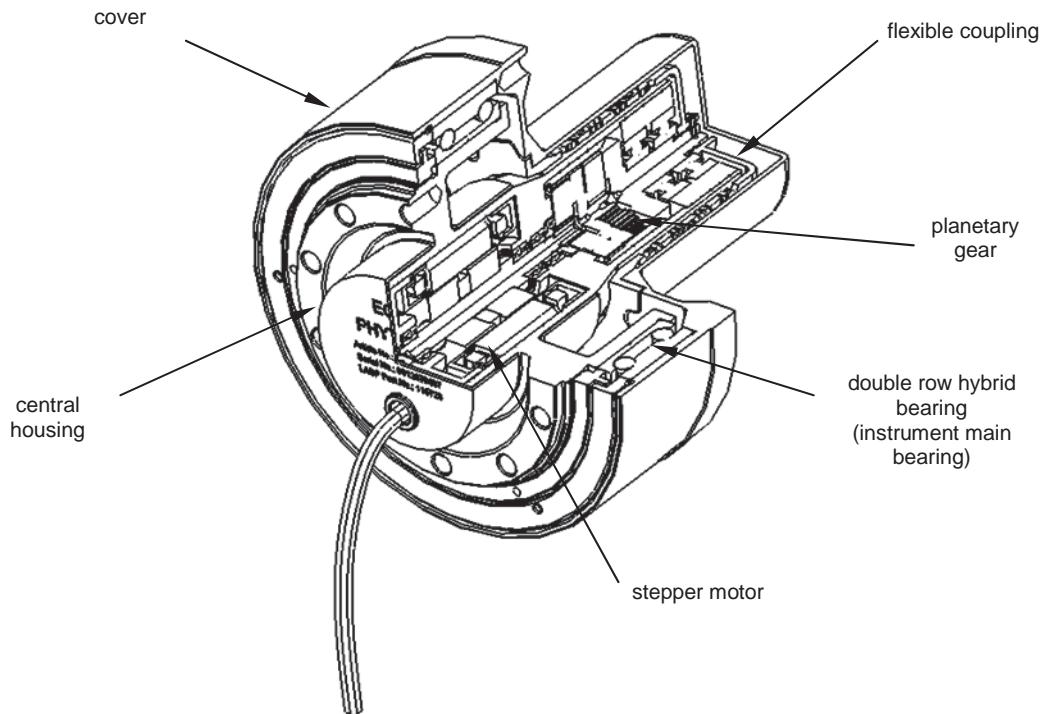


Figure 2. Integrated stepper motor mechanism

Main Functional Requirements

Thermal Constraints

The operating temperature range from -10°C (safety range -30°C) up to +40°C creates some different friction characteristics. Each lubricated bearing needs a little higher torque under cold conditions.

At begin of the project it was not possible to calculate the friction characteristic for the double row instrument bearing. Equivalent data were not available from the manufacturer. Due to the special construction, quality criteria, preload and specified materials, no similar bearing was usable for a representative friction test at that time.

36 balls in each bearing race, 72 balls in total. 144 wet lubricated single contact points creates a higher friction uncertainty. Torque loss with affects to the functional safety was a critical issue. Agglomeration effects during long time storage were an additional uncertainty. Other bearings in the mechanism and the lubrication inside the planetary gear increase the complex of friction problems. The thermal characteristic influences all parameters. These are well known effects.

On the other hand, the stepper motor, driven by a constant voltage driver, must create enough torque to overcome all static and dynamical friction parameters. The integrated 2-stage planetary gear with a ratio of 49:1 increases the available stepper motor torque.

Friction Torque Separation

To minimize the thermal induced torque reduction and uncertainty we try to split the consequences over the time. For a better understanding we must describe the process, to drive the grating assembly in to a hard end stop, in more detail. The stepper motor with 200 steps per revolution (=1.8°/full step) operates normally with a small magnetically load angle, depending on the torque load.

The planetary gear have a backlash of 35 arcmin and the very exact calculated and qualified flexible stiffness of the coupling allows us to drive with 4 motor full steps in the hard end stop. So, if we turn out of the end stop we can use the:

- stepper motor magnetic load angle
- planetary gear backlash
- flexible coupling stiffness

for a friction torque separation. If we turn the grating assembly out of the torque preloaded end position, the motor must not overcome all friction parameters at same time. In the first milliseconds, the complete motor torque is only necessary to overcome the motor internal friction torque (bearings, detent torque). Motor shaft began to turn.

The planetary gear is now positive preloaded due to the flexible coupling and began to turn with a much lower friction torque as normally required. The backlash reduces the coupling preload slowly and absorbed some vibrations (function like a damper). Some milliseconds later the planetary gear began to turn.

In a third step on the time line, motor and planetary gears were turning; the flexible coupling was used as a torque peak damper to overcome the friction torque of the instrument bearing. At -10°C, we need 34 mA and at -30°C only 37 mA starting current. So the engineering teams from LASP and Phytron played with the characteristic and performance of different design elements to create friction risk mitigation.

To drive in a hard end stop is from a friction and torque point of view not so critical due to the lower dynamical friction values. The worst case was to drive out of a hard end stop.

Final Concept Approach

Flexible Titanium Coupling

To get enough safety margins in the flexible coupling design, following the wisdom "expect the unexpected", we start with some different designs.

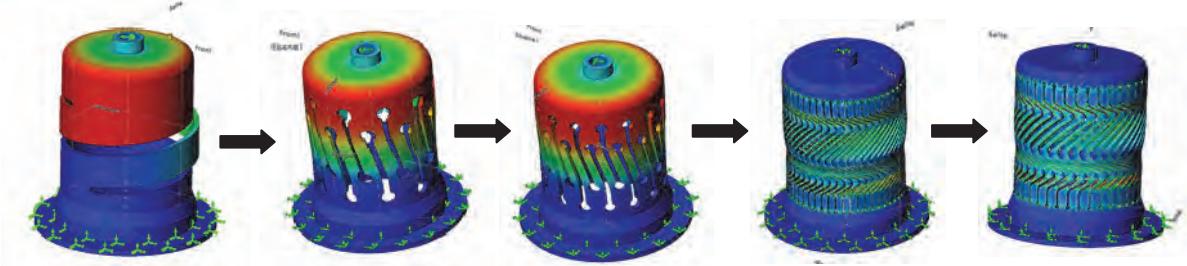


Figure 3. Evolution steps flexible coupling

Nearly 30 different models were calculated to find an optimal flexure structure. The stiffness was defined and the dimensions very hard restricted. Material stress reduction and the radial and axial dimensional changes were limited, too. We could reduce the internal stress from 724 MPa down to 54 MPa (= ~8%). Both parties recalculated the final FEM model. LASP with ANSYS, Phytron used COSMOS. The results correlated in the stress and dimensional changes very exact.

To reduce any risk in the later assembling and test phase, we decided to produce three different flexure structures in the couplings. So, three versions were manufactured and tested respective to the torsional stiffness. Calculated and final measured stiffness values were different. Similar results were found in [1].

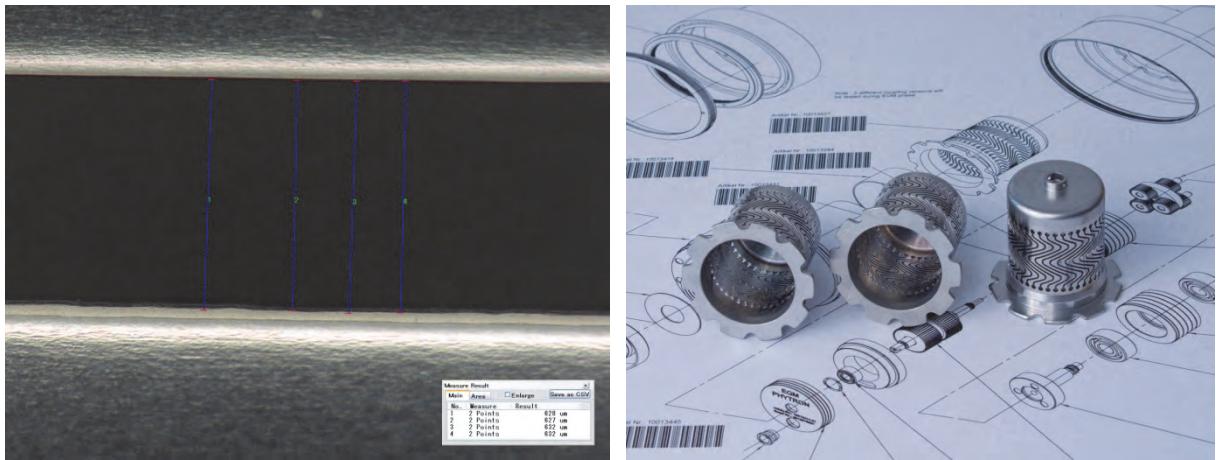


Figure 4. Structure of flexible couplings

Intensive studies of comparable flexible structures, which were used in other mechanisms e.g., titanium butterfly pivots [2] and their final tested characteristics, creates a higher confidence level for our design approach.

Central Housing Structure

The only constructive way to be able to press many requirements in a small space was to use a well coordinated conceptual design in hybrid joining technology. The central housing used all the advantages of the accuracy of CNC machines. At the same time, it represents the basic structure without soft joints.

To achieve excellent out gassing properties, the cover envelops the entire internal structure on 3 sides. Desorbing products will be dissipated controlled in one direction.

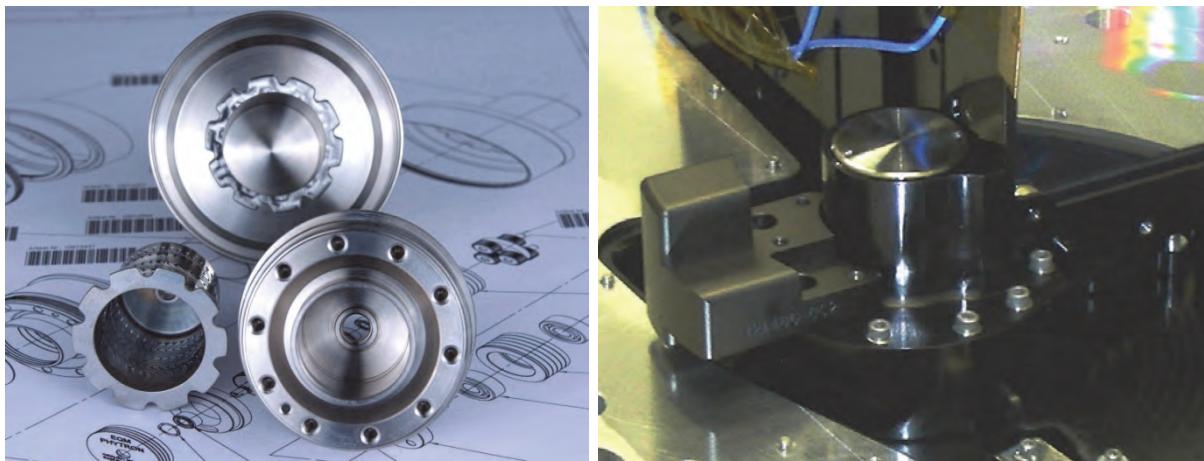


Figure 5. Main structural titanium parts and complete mechanism

Final Grating Flip Stepper Motor

To obtain detailed performance data from each assembly phase, several tiered test sequences have been defined. The performance data were therefore known at any time. The irreversibility of some assembly processes requires a precise line of action with parts which must absolutely comply with the requirements.

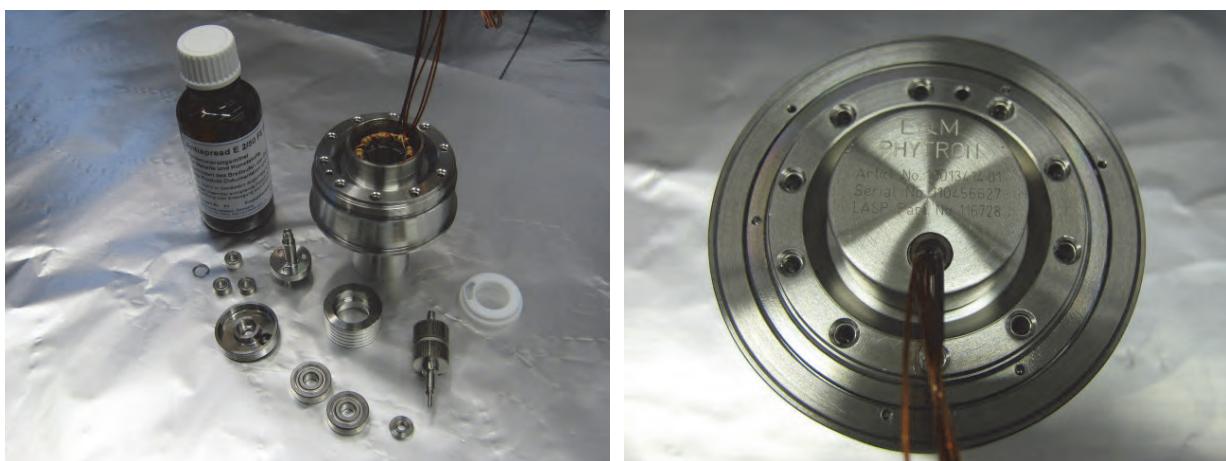


Figure 6. Final tested motor assembly

The complete unit can be connected with the IUVS instrument structure via 10 internal threads. Heli coil inserts prevent a fretting between the materials. The cover contains similar threads for the grating flip mechanism. Both mounting points are very close together. The stiffness of the large instrument hybrid ball bearing dominates the overall stiffness.

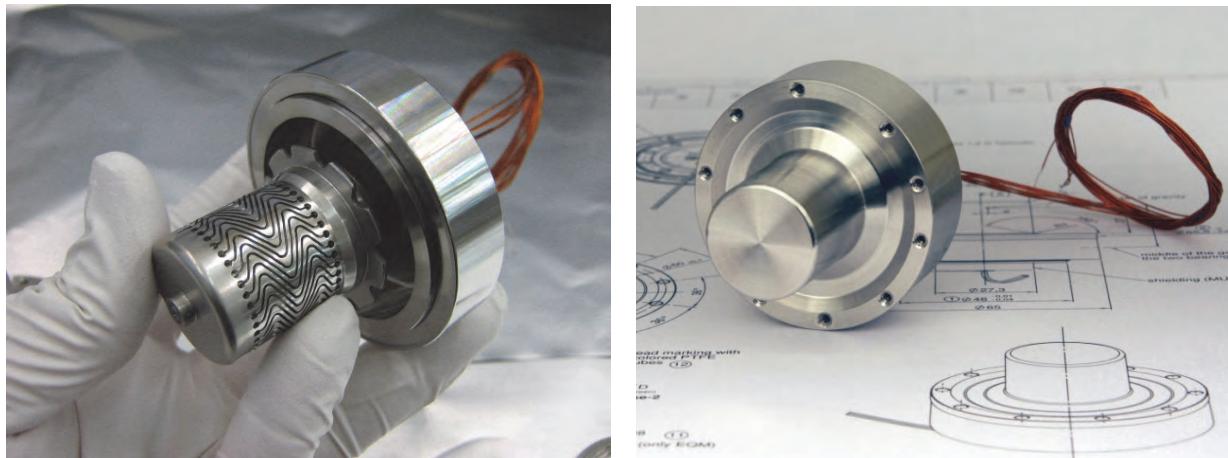


Figure 7. Final tested motor assembly

The flexible coupling separates two mechanical oscillating systems. One system is defined by the stepper motor, the planetary gear, and the upper part of the coupling. Vibration source is represented by the stepper motor. Second system is defined with inertias of the grating flip mechanism, the instrument ball bearing and the cover. Static and dynamic friction inside ball bearings and gears can have far-reaching repercussions on the damping properties.

Main Test Results

Outgassing Test Results

A residual gas analyzer (RGA) was used to measure the volatile impurities in the assembled actuator at +40°C. Results of the test indicate the actuator is suitable for the strict requirements of a FUV optical instrument – i.e. virtually indistinguishable from a clean vacuum chamber.

Vibration Testing

The EQU actuator was assembled into the GFM life test unit (LTU) and subjected to the corresponding qual-level vibration environment. Test levels included sine burst to 17 Gs and random vibe to over 10 Gs rms per axis. Following the testing the actuator performed smoothly and passed all post-test inspections.

Life Testing

Following the vibration testing the LTU was subjected to a thermally controlled vacuum life test which included over 6,000 cycles at a range of temperatures. The actuator met all operational criteria from -30° C to +40°C and passed the life test successfully.

Optical Repeatability Testing

The LTU was driven into the hard stop over 200 times, and the optical orientation of the grating was measured each time using an autocollimator. The position repeatability was measured at less than 10 arc-sec, which meets the mechanism requirements.

Conclusions and Recommendations

1. A sequence of several manufacturing processes reduces the coupling stiffness in a range of approx 40%. Result of different material properties and the unpredictable behavior in the rim zone. Our strategy, to create 3 different coupling versions, was very helpful at the end. Real tests were highly recommended in an early project phase.
2. Trust-based cooperation between the design teams at a very early stage of the project is the basis of innovative products.
3. The distribution of the entire starting friction in several temporally separated events represents an efficient way.
4. Adjusting rings made of titanium with fine threads creates difficult problems during assembling. Very precise inspection and deburring under the microscope is necessary.
5. The characteristic of both mechanical oscillating systems must match exactly together. Meant with "match" is naturally "out off-tune". At worst case, the system creates resonance or bouncing effects. In a complete representative "plug and play" system test, the performance characteristics should be verified in an early project phase. Alternative settings shall be provided in the degrees of freedom of control electronics or software intelligence.

Acknowledgement

The authors would like to thank Steve Steg and Heather Buck from LASP for some technical concepts, FEM calculations and technical discussions, Wahid Lahmadi from Phytron Inc. for all the project management support on this project.

References

1. Santos, I., et al., "HIGH ACCURACY FLEXURAL HINGE DEVELOPMENT", ESMATS 2005
2. Henein, Simons, et al., "FLEXURE PIVOT FOR AEROSPACE MECHANISMS", ESMATS 2003

Cryogenic Temperature Testing of NEA Fuse Wire Mechanism

Edwin Vega* and Geoff Kaczynski*

Abstract

NEA has over 10 years of continuous innovation in the field of space rated non-pyrotechnic release mechanisms. At the heart of our technology is the NEA patented Fuse Wire Assembly (FWA). NEA utilizes our patented FWA design across all our product lines to initiate the release operation of our restraint and release devices and our battery bypass switches. Most recently, as part of a deep space mission, cryogenic temperature testing was performed on our FWA down at 18° Kelvin (K). The testing discussed in this paper validates that the FWA, which is a critical component of the overall mechanism design, is robust enough to reliably operate in space at extremely low power levels and temperatures. In this paper, NEA will describe the cryogenic temperature tests along with test results. As the space community explores further into our solar system and beyond, this validation testing of our product enables new found confidence that existing technologies can be used for fielding deployable structure in deep space.

Introduction

All major space agencies and organizations are funding missions for spacecrafts to explore our solar system and beyond. As soon as a spacecraft leaves the earth orbiting environment, it experiences extreme cold temperatures with the background radiation of the universe. Today's missions require several staged deployments during multiple phases of their missions, such as entering orbit, decent, landing and deployment of instruments. For today's missions, the restraint and release device must be proven to operate in deep space cryogenic temperatures to ensure mission success.

The NEA release mechanism is used to provide restraint and release functions for critical deployment operations on spacecraft such as solar arrays, antennas, radiators and payloads after launch. The FWA in the release mechanism is a critical element. Each release mechanism's FWA is single or redundantly initiated. Actuation time variation between multiple mechanisms FWA is less than 10 milliseconds when a nominal firing pulse is applied to all units simultaneously.

Basic Design

The patented NEA FWA design is simplistic in operation and design. Upon receiving a specified electrical pulse of 1.2 amps or greater, the fuse wire breaks starting the release sequence of the preloaded release rod. The shock induced by release of the tensile load is typically less than 300 G's. Each FWA is fully refurbished after each ground-based test actuation. The principle of operation is as follows:

- A fuse wire is wrapped between two electric terminals.
- A process controlled load is placed on the fuse wire.
- When current is applied via the spacecraft firing system, the fuse wire heats lowering its yield strength.
- The fuse wire yields once the applied load exceeds the strength of the fuse wire.
- Breaking of the fuse wire allows the release system to activate and allow deployment.

* NEA Electronics Inc., Moorpark, CA

The electrical characteristics for the fuse wire assembly are time and current dependant as shown in Figure 1.

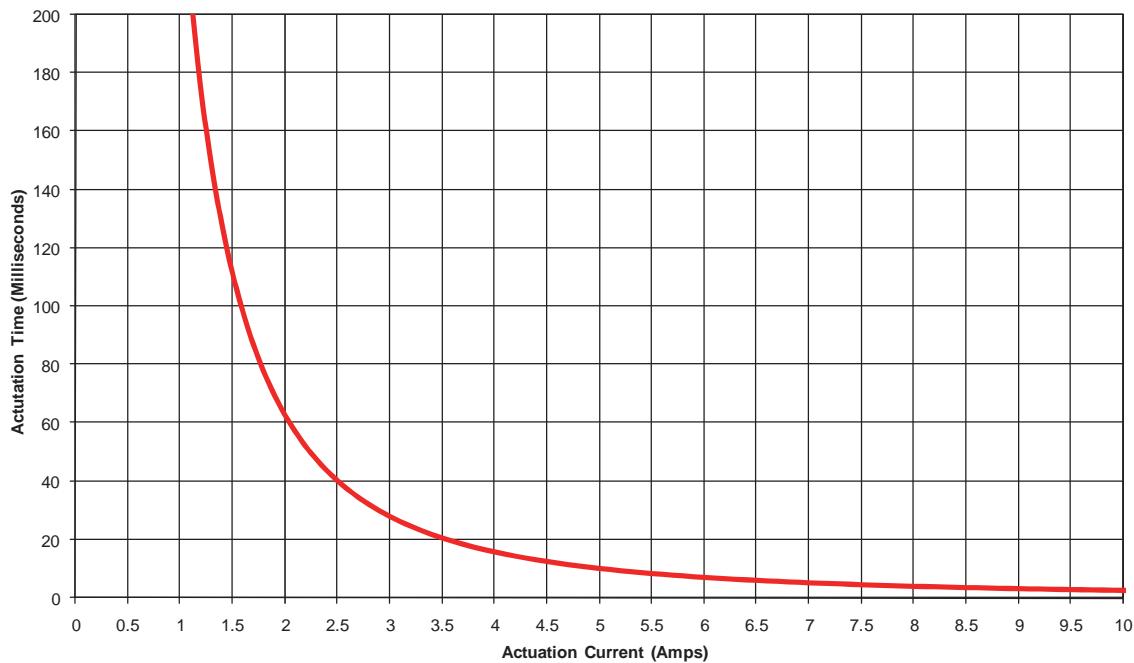


Figure 1: NEA Mechanism Actuation Curve

Extensive test data has shown that time for release is not significantly influenced by external operating temperature. See Figure 2 for data.

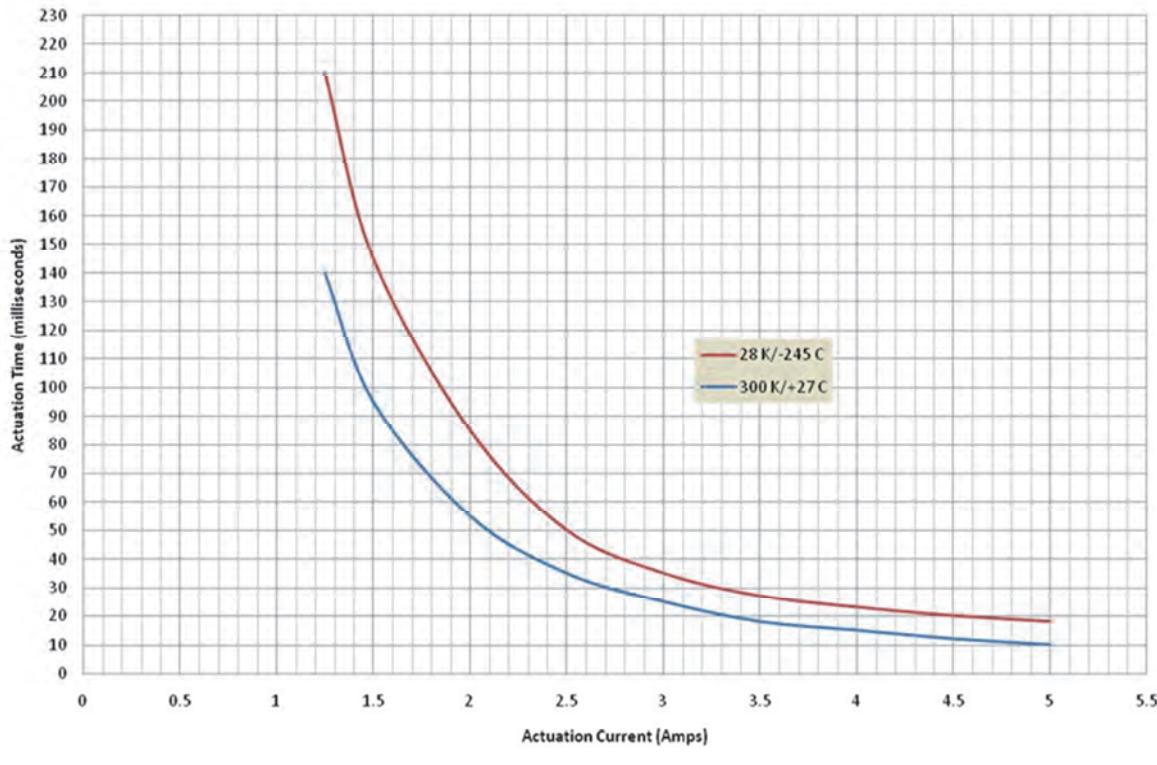


Figure 2: Fuse Wire Actuation Time vs. Temperature Curve

Cryogenic Temperature Testing

The intent of the Cryogenic Temperature testing was to verify if a typical NEA release mechanism could withstand cryogenic temperatures and successfully actuate to release the preload at these temperatures. Two units were used for the Cryogenic Temperature Test. These two units were flight worthy NEA 9103 release mechanisms. A preload of 11,120 N (2,500 pounds) was applied as shown in Figure 4.

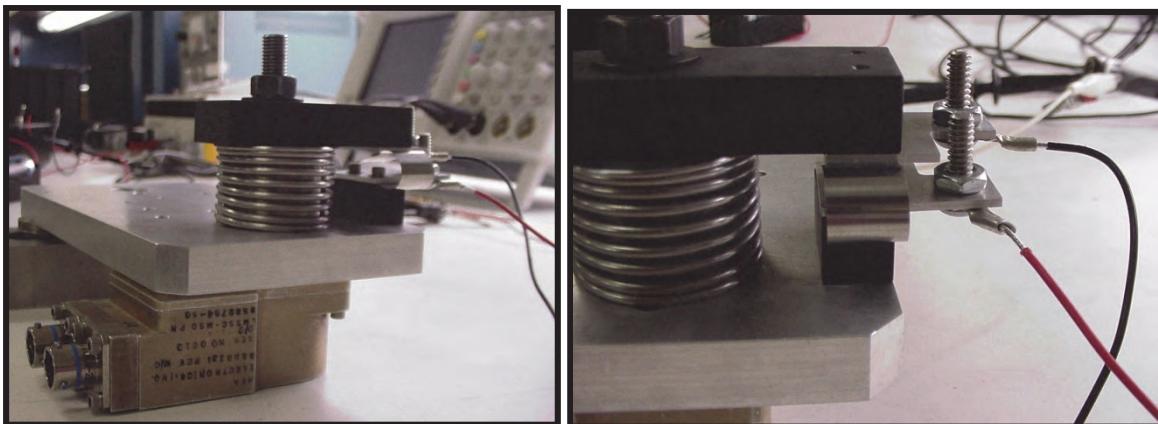


Figure 1: Cryogenic Temperature Benchtop Setup for the NEA Mechanisms

A voltage of 1.5 Vdc from a D-size battery was set across the switch plates. A 0.13-mm (0.005-in) thick stainless steel leaf spring was included as a temperature compensation element. When the mechanism was actuated, the ejection spring forced the insulator and corresponding switch plate away and caused

an open circuit. This verified successful release of the preload. The noise from the hardware hitting the bottom of the chamber also served as evidence of successful release of the preload.

The fuse wire resistances were taken at lab ambient temperature.

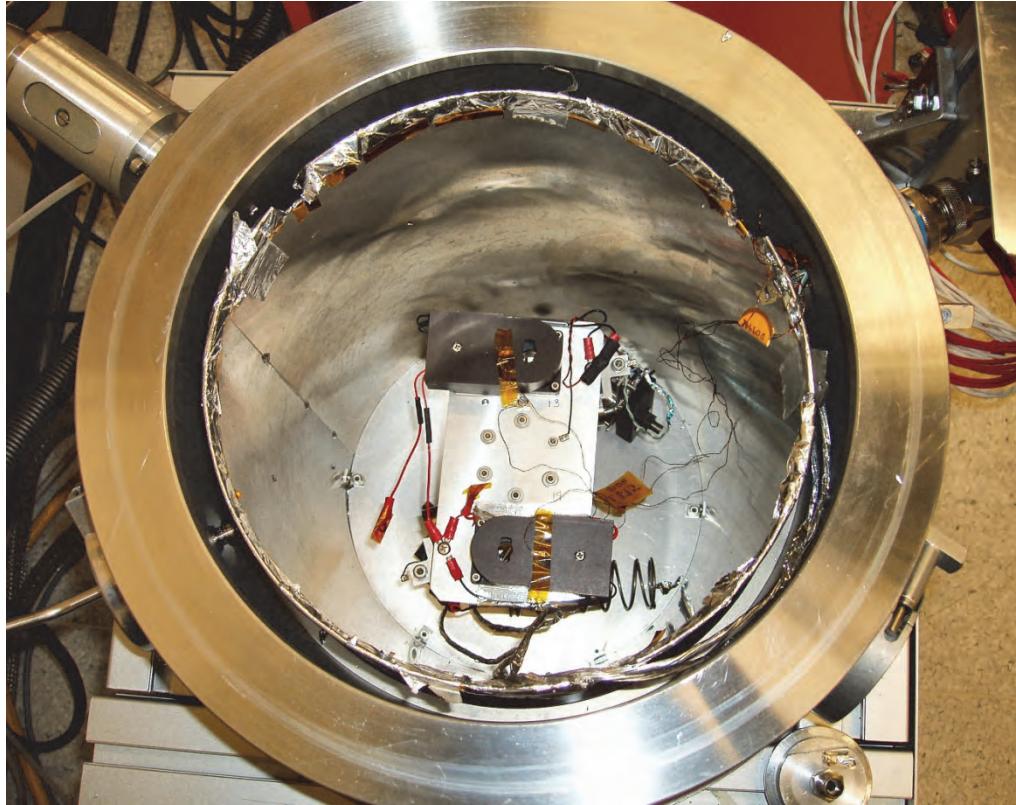


Figure 2: Cryogenic Temperature Test Setup for the NEA Mechanisms

Due to a limited number of chamber output leads, only the redundant circuit was actuated. The redundant circuits were wired so that each shared a common ground. The primary circuits were grounded to the plate so as to assist in reaching the temperature. Thermal diodes were taped to the cover of each unit. Once the test fixture was fastened to the mounting head of the cryogenic chamber, the resistances were measured again at lab ambient temperature.

The chamber as shown in Figure 5 was set to vacuum conditions and the temperature was decreased using liquid helium as the cooling media. The chamber achieved temperature stabilization at the targeted temperature of 10K after approximately 20 hours. After temperature stabilization was met, the unit temperature for both mechanisms was approximately 17K. The temperature of the mounting plate was 10.2K. Fuse wire circuit resistances were taken once again.

The continuity was checked for each of the switch plate circuits. The switch plate circuit for the first mechanism displayed continuity. The switch plate circuit for the second mechanism reads open. It was determined that the second unit would be actuated first, due to the fact that the switch plate circuit was open. Once the second unit was actuated, the switch plate circuit was re-connected. The switch plate pulse dropped from approximately 0.5 V to zero, indicating successful separation. The release rod and associated hardware could be heard hitting the bottom of the chamber. The unit successfully released the preload. The temperature of the unit dropped immediately after actuation.

The first unit was then actuated following the same procedure. Once the unit was actuated, the switch plate circuit voltage dropped from approximately 0.5 V to zero, once again indicating successful separation. The release rod and associated hardware could be heard hitting the bottom of the chamber. The unit successfully released. The pulse for the trigger circuit was shown re-connecting. This was an anomaly in the test setup. The captured scope plots of the actuation events are shown in Figure 6 and Figure 7.

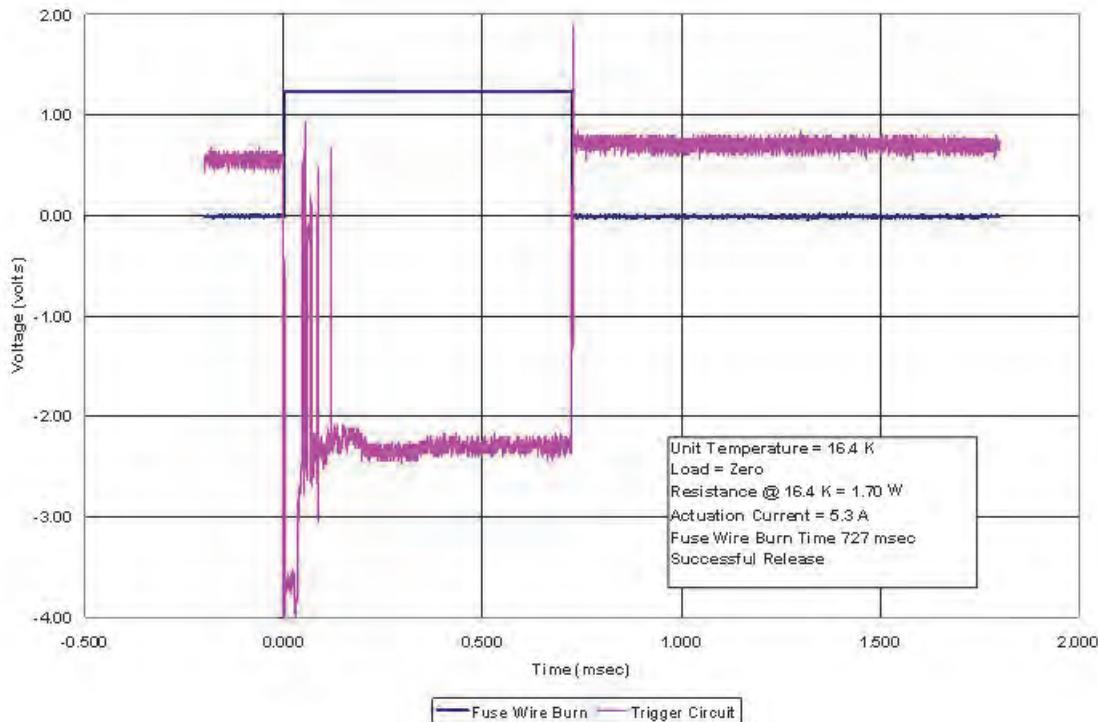


Figure 3: Actuation Plot for the First Release Mechanism

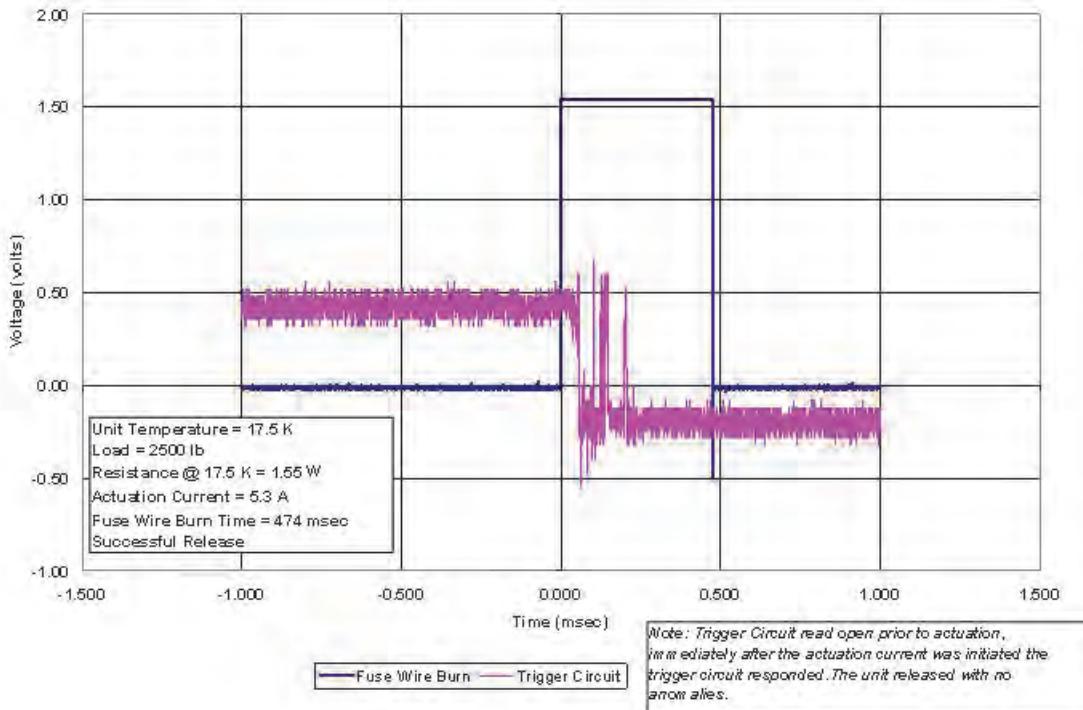


Figure 4: Actuation Plot for the Second Release Mechanism

Conclusions

Cryogenic testing has shown that the NEA FWA and mechanism reliably actuate at cryogenic temperatures. The fuse wire circuit resistance for each of the devices decreased by no greater than 0.3 ohms from lab ambient conditions compared to cryogenic vacuum conditions. The mechanisms successfully released at approximately 16K in both loaded (2,500 lb) and the unloaded conditions. Post test inspections revealed no physical degradation due to actuation. In particular, the restraining wire remained intact which would lead to a typical dissipation of strain energy and therefore a low shock output.

Developmental Testing of Electric Thrust Vector Control Systems for Manned Launch Vehicle Applications

Lisa B. Bates^{*} and David T. Young^{**}

Abstract

This paper describes recent developmental testing to verify the integration of a developmental electromechanical actuator (EMA) with high rate lithium ion batteries and a cross platform extensible controller. Testing was performed at the Thrust Vector Control Research, Development and Qualification Laboratory at the NASA George C. Marshall Space Flight Center. Electric Thrust Vector Control (ETVC) systems like the EMA may significantly reduce recurring launch costs and complexity compared to heritage systems. Electric actuator mechanisms and control requirements across dissimilar platforms are also discussed with a focus on the similarities leveraged and differences overcome by the cross platform extensible common controller architecture.

Introduction

The potential for ETVC systems to significantly reduce recurring launch costs, complexity, weight and volume, compared to electro-hydraulic systems of equivalent performance and reliability, soon may be realized on large launch vehicles for human space flight. ETVC systems have been used in the Apollo and Space Shuttle programs in the past. But conditions unique to the launch environment have up to now restricted their use for manned spaceflight to less powerful in-space applications. The lack of a suitable electrical power source and approved human rated power electronics that could be qualified to the launch environment, as well as the susceptibility of high voltage electrical power systems to corona discharge, have placed severe limitations on the power of these early manned systems.

Renewed interest in ETVC systems for high power launch vehicle applications is due to advances in key enabling technologies related to the source and control of electrical power. High rate lithium ion batteries, high-voltage, high-current insulated gate bipolar transistors (IGBT) and Field Programmable Gate Arrays (FPGA) are among the maturing technologies incorporated into the cross platform extensible controller architecture of the ETVC system tested and described in this report. The controller, battery modules and the integrated ETVC system based on a developmental EMA are the result of an internal research and development effort by Alliant Tech Systems, Aerospace Systems Group and Moog Inc., Space and Defense Group. Testing was performed in cooperation with NASA George C. Marshall Space Flight Center at its Thrust Vector Control Research, Development and Qualification Laboratory.

Among these maturing technologies, high power switching electronics such as the IGBT in particular has made it possible to further simplify actuator mechanisms and eliminate certain mechanical failure modes. IGBTs have been used extensively in the electric vehicle industry, not only to create the inverter circuits needed to power 3-phase Brushless Direct Current (BLDC) motors, but also as a key component in regenerative braking circuitry. How these technologies can reduce the mechanical complexity of an ETVC actuator will be seen in a comparison of the developmental EMA actuator mechanism with that of Apollo and Space Shuttle EMA.

The work presented in this report represents one phase in an ongoing development program aimed at demonstrating the maturity of high power ETVC systems and components for manned launch vehicle

^{*} NASA George C. Marshall Space Flight Center, Huntsville, AL

^{**} Raytheon – Jacobs ESTS Group, George C. Marshall Space Flight Center, Huntsville, AL

applications. The next phase of this effort will be to update a multi-channel electro-hydrostatic actuator (EHA) by adapting it to the common controller architecture while again utilizing advanced lithium ion batteries as its power source. In preparation, testing of the EHA in its present form was also carried out to baseline its performance.

Objectives of the Experiment

The primary goals of this experiment were to verify integration of the ETVC developmental hardware and to demonstrate functionality of the complete system. Flight specific performance requirements were not set. Moreover, this test was carried out with fewer battery modules than would be needed to achieve the full power capability of the actuator. As such, the system under test was considered to be underpowered and it was necessary to design control parameters accordingly so that peak power demands under the applied load would not exceed the capabilities of the available battery modules. Performance measurements are, therefore, meant more to indicate general functionality of a representative class of Thrust Vector Control (TVC) system, rather than in meeting a particular vehicle requirement.

Key test objectives:

- Functional integration of ETVC components
- Controller parameters tuned “in the field”
- Peak power draw and voltage droop controlled to acceptable levels
- Step and frequency response as expected for underpowered performance
- Battery cell temperatures stay near ambient
- Repeated operation on a single battery charge

For the functional demonstration, dynamic loads due to inertia and spring forces were supplied by two large Inertial Load Simulators located at the Marshall Thrust Vector Control Research and Development and Qualification Laboratory.



Figure 1. Electromechanical (left) and Electro-Hydrostatic (right) Actuators

In addition to the dual channel developmental EMA shown in Figure 1, tests were performed with the four-channel EHA also shown, to baseline its performance. This report presents data and the results of analysis for only the EMA.

Background

Control of a launch vehicle during ascent implies the ability to direct the vector of the thrust that it produces. Typically a pair of linear actuators, positioned so as to rotate an engine or nozzle about its bearing along orthogonal planes, act together to define a resultant thrust vector. High inertial load and the requirement to operate from sea level to near orbital altitude are characteristics of launch vehicle applications. This is in contrast to the low load, vacuum conditions of in-space applications. High powered TVC systems are needed to react against the inertia of an engine or nozzle, as well as against the stiffness of an engine gimbal or flex bearing, vehicle structure and propellant flex lines, at the slew rates necessary to maintain stable control of the vehicle throughout all phases of flight.

Heritage Electro-Hydraulic Actuation

Historically, high power demands could be met only by hydraulic systems. One means by which these systems could derive enormous amounts of hydraulic power was by accessing a pressurized propellant line in a liquid fueled rocket engine, such as in kerosene-based engines, at the cost of a slight performance loss to the engine. However, not all rocket propulsion systems are compatible with this approach. Therefore, auxiliary power generated by hydraulic turbo pumps and dedicated propellant systems have also been used in heritage hydraulic systems.

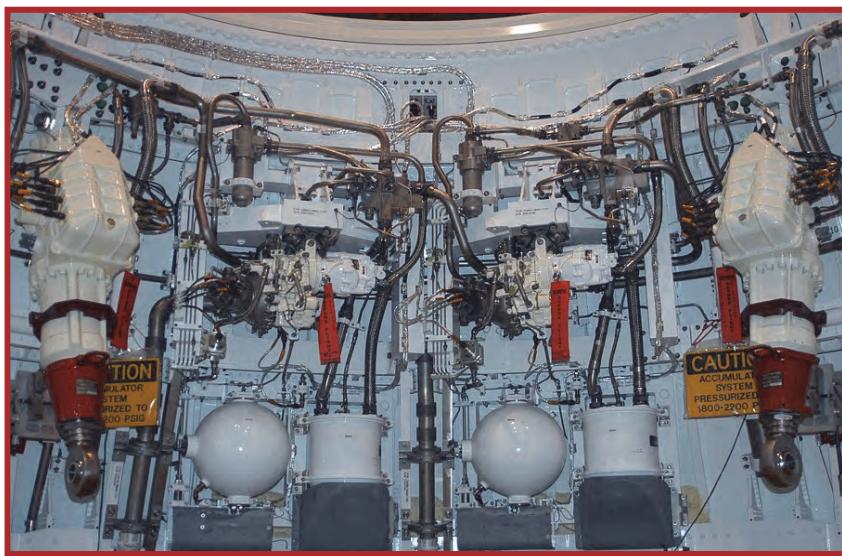


Figure 2. Heritage TVC System

The complex arrangement of discrete hydraulic components, seen in Figure 2 for the Space Shuttle Solid Rocket Booster, was typical of high power heritage TVC systems. It was common for such systems to have a long and elaborate process flow associated with their assembly. A major detractor that opponents of this particular approach often cite is that in order to drive the turbo pumps that generate the needed hydraulic power, these systems typically relied on the decomposition of toxic monopropellants such as hydrazine, a known carcinogen with costly storage, handling and safety concerns.

To deal with concerns about toxic monopropellants one could simply replace the heritage turbo pump with a fixed speed electric motor driven variable displacement pump, while leaving the rest of the heritage system unchanged. The trade in this case would likely be a slight increase in system mass and volume due to the lower energy and power densities of electrical power sources compared to that of monopropellant powered hydraulic turbo pumps. Another way to deal with these concerns would be to retain the turbo pump but substitute a less toxic monopropellant with equal performance, such as an ammonium dinitramide based liquid monopropellant. However, in either case, leaving the rest of the

heritage system unchanged means that the complex assembly of the discrete components of the overall system still remains a labor intensive process.

While there are certain benefits that may favor heritage electro-hydraulic systems in a trade of alternate TVC approaches, these are likely to be only in the short term. As available stores of heritage hardware dwindle and mature enabling technologies continue to further advance high power ETVC capabilities, these perceived benefits will inevitably diminish.

ETVC Systems

There are a variety of possible ETVC systems available based on the type of actuator and source of electrical power. But, in general, their inherent simplicity, compared to heritage systems, means that they can be expected to have lower operating costs because of simpler, less hazardous ground operations. The potential for less overall system weight and volume is also a possibility, in spite of the fact that electrical sources are not as power dense because of the many discrete heritage system components that can be eliminated. For example, a complete ETVC system like the EMA system tested and described in this report, or a similar one based on the mentioned EHA, would consist of only a pair of actuators along with a set of controller boxes and a bank of battery modules such as those shown in Figure 3.



Figure 3. Lithium Ion Battery Module (left) and Controller

The simplicity of the EMA and EHA systems and the streamlining of ground operations that they afford is a feature shared by another type of ETVC system, the Integrated Actuator Package (IAP). The best way to think of an IAP is as an entire electro-hydraulic system self contained within each actuator. The IAP takes advantage of the approach mentioned earlier of using a fixed speed electric motor and a variable displacement pump to generate hydraulic power. This strategy, partly because it does not have to deal with propellants or turbine exhaust, allows the IAP to more readily integrate each of the components of a conventional electro-hydraulic system into a self-contained package. Like the heritage electro-hydraulic system, servo valves are used to continuously interpret low power electric command current, measured in millamps, and, thus, regulate hydraulic power to either side of the actuator main piston. In this way, the IAP is very similar to the EHA.

Electro-Hydrostatic Actuation

The electro-hydrostatic actuator is another approach available for ETVC systems that possesses both electrical and hydraulic power system attributes. Unlike purely hydraulic TVC systems, EHA systems rely on an electric motor driven positive displacement pump, incorporated into the body of the actuator, to generate hydraulic power and meter fluid to and from a hydraulic cylinder. Like the IAP, all hydraulic components including the fluid reservoir, manifold, filters, etc. are incorporated into the body of the actuator, simplifying system integration and reducing the total volume of hydraulic fluid used in the overall system. The difference between these self contained systems is in the type of pump used and in the way position commands are interpreted, which for the IAP involves servo valves.

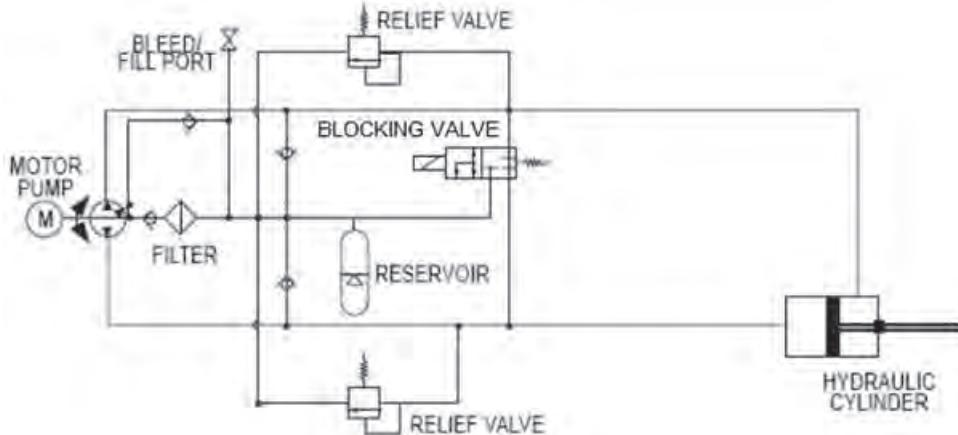


Figure 4. EHA System Elements

The schematic in Figure 4 shows the system elements of a typical EHA system and can be used to understand its operation. Position commands interpreted by a controller (not shown) are used to continuously update speed and direction of a reversible, variable speed, 3-phase BLDC motor. This motor drives a fixed displacement pump creating a hydrostatic pressure difference across the hydraulic cylinder. The fixed area of the cylinder piston translates this pressure difference into a force proportional to the speed of the motor which acts against the applied load. Finally, position and velocity feedback (not shown) is used by the controller to close the control loop on the commanded position. The EHA, which was also tested, is a four channel version of this same arrangement. Each of four identical channels responds independently to what are nominally the same commands. The hydrostatic pressure developed by all four channels combines at the hydraulic cylinder to create a net total pressure and sizing is sufficient to tolerate the failure of two channels without loss of the targeted performance. The blocking valve is used to remove an errant channel from the system by equalizing its pressure contribution and pressure relief valves are provided for safety. Sizing of the reservoir, depending on the application, is either determined by peak power demands or is based on the thermal capacity of the total hydraulic volume and the mission duration.

Electromechanical Actuation

The EMA, the simplest of all ETVC actuator types, is nothing more than a mechanism that converts electrical energy into the torque of a rotating variable speed motor and then into linear motion through a mechanical transmission. This ultimately puts energy into the motion of an engine or nozzle mass that the EMA must also be able to absorb as it brings this motion to a stop. In the case of the EMA tested, a 3 phase BLDC motor is used to both add and remove kinetic energy to the overall system. Many electric automobiles use BLDC motors and high power solid state switches to recover energy and improve mileage. But, whether recovered by the electrical power source, or simply dissipated through a resistive load, high power solid state switches such as the IGBT make it possible to handle high levels of excess kinetic energy electronically through motor torque. As a result, the mechanical brakes and clutches of older systems, with their potential for failure due to contamination and wear, are no longer necessary.

The architecture of the EMA system that was tested allows it to be single fault tolerant, with the redundancy of two active channels. Identical position commands, which on a vehicle would come from a flight computer, are sent to a motor controller on both of its command channels and telemetry feedback from sensors within the actuator is returned. Position feedback is measured directly by a dual channel linear variable differential transformer (LVDT). On the other hand, actuator velocity, the rate of change of the actuator rod end position, is not always a direct measurement. Often it is derived from electric motor velocity, which is much faster prior to gear reduction and, therefore, offers greater resolution. Motor velocity can be monitored using a generator or similar such device. Motor position can also be acquired

using a resolver or an encoder. In the case of the developmental EMA, resolvers are used for both motor position and motor velocity.

As illustrated in Figure 5, the outputs of two identical 3-phase BLDC motors are combined through spur gears to create a torque-summed moment upon a common ball screw mechanism. The ball screw is used in a rotating nut / translating screw configuration. It should be noted that because two channels are combined at a common ball screw, mechanical redundancy is lost at this point. There are several potential failure modes that can be identified for the common ball screw. Seizure of the ball screw mechanism preventing motion of the actuator at an inopportune time can be catastrophic. For the EHA and IAP, hydraulic power transmission through a main piston cylinder virtually eliminates potential jamming concerns assumed by electromechanical transmissions. The strategy for dealing with such failure modes in the EMA that was tested is to size each motor and drive train sufficiently so as to provide adequate torque to overcome some degree of potential mechanism seizure. It has been asserted by the manufacturer that deformation of the ball or race, by this means, or through wear, as well as any potential hazard of contamination, would likely result in only degraded actuator performance, but not failure. Based on manufacturer studies, it is expected that under such degraded conditions, the ball screw would simply behave like a nominal Acme screw mechanism.

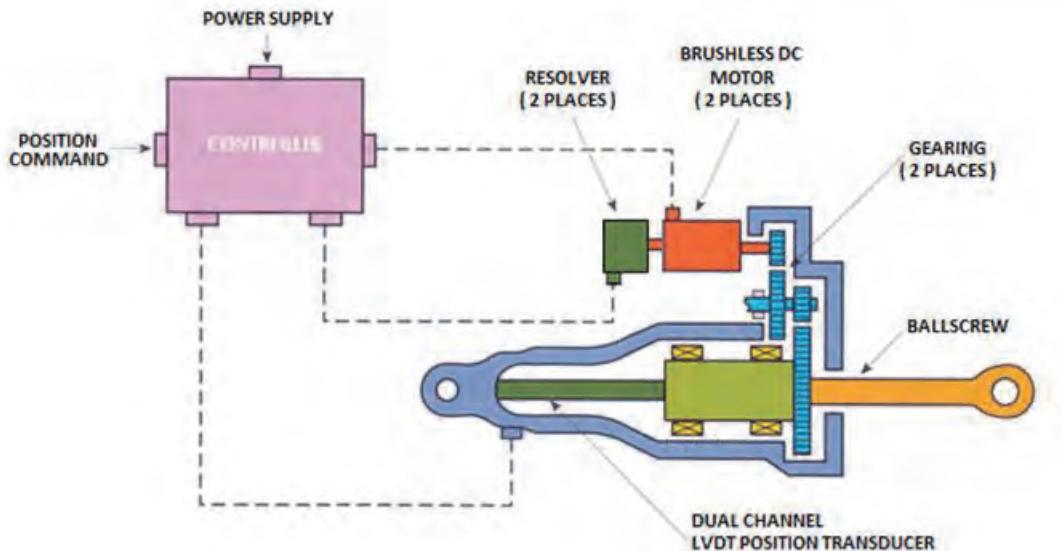


Figure 5. Dual Channel developmental EMA and Controller

Precedence for a multichannel EMA actuator with common drive train components can be found in the first ever ETVC system developed for manned space flight. The Apollo Service Propulsion System (SPS) which was relied upon to perform its mission critical trans-lunar injection maneuver, successfully employed a mechanically similar approach for its EMA. However, the Apollo EMA differed in its redundancy scheme in that it employed an active / standby system. The Apollo SPS was located within the Service Module of the Apollo spacecraft and utilized only after the Saturn launch vehicle had carried it into orbit. Therefore, the Apollo EMA is considered to be an in-space propulsion system, and this fact likely influenced the choice of an active / standby approach.

Another example where ETVC have been effectively used in manned space flight is found in the Space Shuttle Orbital Maneuvering System (OMS). The OMS, located near the aft end of the Space Shuttle Orbiter provided thrust to perform orbit insertion, orbit circularization, orbit transfer, rendezvous and de-orbit. These were maneuvers performed after Space Shuttle Main Engine cutoff, and, for this reason, the OMS is also considered to be an in-space propulsion system.

The Apollo and Space Shuttle EMA were both two channel actuators, which nominally operated one active channel, the primary channel, while the other secondary channel was reserved as a standby in the event of primary channel failure. This differs from the developmental EMA, which nominally operates two active channels, a scheme that is considered to be more reliable because of the probability associated with the standby channel not being available when called upon, a risk more often accepted for in-space propulsion than for launch because it is not always practical to require in-space systems to be active prior to launch.

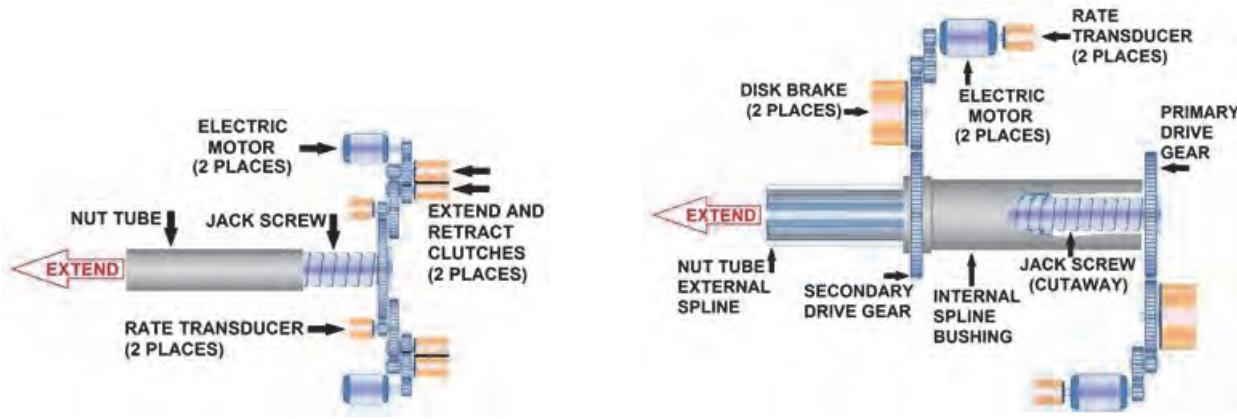


Figure 6. Active / Standby EMA Mechanisms

Careful consideration of the two mechanisms illustrated in Figure 6 will provide insight into some of the ways in which redundancy can be achieved by EMA systems and of their relative merits. The mechanism on the left utilizes two clutches with each motor to control the direction motor torque is applied to a common jack screw through a common drive gear. Braking is achieved by applying torque opposite the direction of travel. The nut tube and the jack screw on which it translates as the jack screw turns are single point of failure components. Likewise, the common drive gear and associated shaft and bearing are single point of failure components because these components are also shared by both channels.

The mechanism on the right of Figure 6 illustrates how redundancy can be achieved throughout the entire drive train including translational motion. As seen in this illustration, the nut tube will translate along its external spline due to the rotation of the jack screw or due to the rotation of the nut tube as driven by the rotation of the internal spline bushing. Disk brakes are used in this mechanism to prevent movement of the secondary standby channel while the primary channel is active, or vice versa. Significantly, these brakes are also used to arrest movement of the active channel and, thus, dissipate energy as motion of the engine nozzle is stopped.

Power and Control Considerations

Technology innovation efforts such as the More Electric Aircraft initiative by the Air Force and efforts by the commercial aircraft and automotive industries have led to many new advances in power electronics and direct current power sources. For aircraft applications, a bus voltage of 270 volts has emerged as more or less an industry standard. But, launch vehicle applications have unique considerations because of the altitudes traversed for which this voltage may be a concern. The dielectric constant of the air changes with altitude, making it easier at higher altitudes for high voltages to break down the dielectric barrier of the air in a process known as corona discharge. At still higher altitudes, susceptibility to corona discharge vanishes as the vehicle enters near vacuum conditions, which is why high voltages do not exhibit this particular concern on orbit. But, for launch vehicles this phenomenon can be potentially disruptive to sensitive electronics elsewhere on the vehicle, as well as to the TVC system itself. At sea level, thousands of volts are required to induce the onset of a corona discharge. For aircraft, a bus voltage of 270 volts is not a corona concern because it is well below the corona onset voltage at the altitudes where most aircraft fly. Many factors influence a corona discharge event. Atmospheric pressure and constituency, bus voltage and frequency, as well as conductor geometry, are all factors that play a

role. Use of a 270-volt bus for launch vehicle applications is based partly on the belief that design and construction standards, once developed and validated, can be applied to manage this issue.

The availability of approved high voltage, high current power electronics presents another challenge to high power ETVC systems for use in human rated launch vehicle applications. An effort by NASA to update requirements and its list of suitable parts for this application is underway. Addressing this concern and that of corona discharge susceptibility is a priority for proponents wishing to gain acceptance of powerful ETVC on large manned launch vehicles.

The use of FPGA by avionics has already gained wide acceptance for manned launch vehicle applications. Within the common controller architecture FPGA, allow control parameters to be tuned to specific applications and the needs of specific actuator classes. When the testing presented in this report was performed, the developmental EMA actuator was the highest powered example to which the common controller had yet been configured. Actuator classes already covered by the common controller in previous developmental tests include: an electromechanical rotary engine control valve actuator, an electromechanical launch abort system valve actuator, and a less powerful EMA. Control of an EHA is planned as future work.

The common controller leverages a modular architecture to increase its flexibility across dissimilar actuator platforms. As seen in the discussions of EMA and EHA mechanisms, actuator types differ not only in power requirements but also in instrumentation and control schemes. In a modular architecture, signal conditioning and instrumentation drive circuitry can be swapped out as required by a particular actuator type.

Laboratory Demonstration of Integrated EMA System

The integrated system test brought together all the elements of a single channel for one axis of a complete ETVC system. These system elements included the two-channel single fault tolerant developmental EMA, four high rate lithium ion battery modules and the cross platform extensible common controller. Testing was performed during August and September of 2011. It was during the first week of testing, when system integration and check out was performed, that it was necessary to modify control parameters for more optimal performance under test conditions. This modification satisfied the objective of demonstrating that control parameters were not merely factory preset constants but could be potentially changed in the field.

Developmental hardware was used for these tests rather than the more flight-like battery module and controller shown in Figure 3 because they were not available at the time these tests were performed. As can be seen in Figure 7, four developmental battery modules, each containing many individually matched cells, were combined to form a single bus.



Figure 7. Developmental Lithium Ion Battery Supply (left) and Common Controller

Test Setup and Procedure

The integration of the developmental EMA with the common controller and battery modules was done as illustrated by the interconnection diagram of Figure 8. In addition to the developmental hardware, this test setup also includes a Power Control and Regeneration circuit and the Universal Test Interface (UTI) needed to communicate with the common controller and translate telemetry into a form that could be recorded by laboratory data acquisition systems. Telemetry included commanded position, actuator position and force, motor current and motor velocity. The UTI and Regen circuit are Moog, Inc., Space and Defense Group proprietary hardware. The EMA, and Battery Modules used in this demonstration are NASA owned assets. The common controller is ATK and Moog jointly held proprietary hardware.

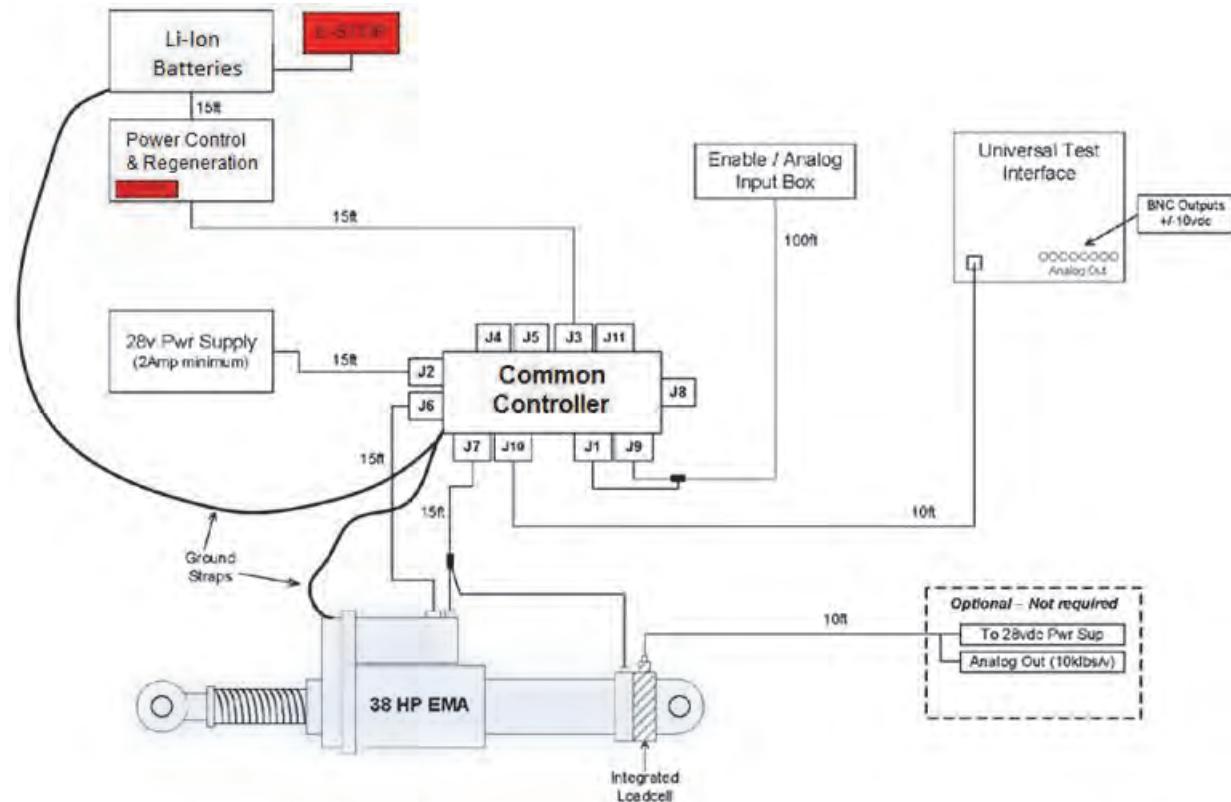


Figure 8. EMA System Test Interconnect Diagram

Battery cell temperatures at 38 separate locations were monitored by an Agilent model 34970A Data Acquisition / Switch Unit using Type-T thermocouples. Temperature logs were made during charging of the battery modules, as well as during testing of the integrated system. Logs would often cover several tests performed on a single day to track thermal data across consecutive runs. This also demonstrated the objective of repeated operation on a single battery charge. A voltage probe, visible in Figure 7, and a current probe applied to the Power Control and Regeneration circuit were used to verify that the integrated system was able to control peak power draw and voltage droop to acceptable levels.

One of two large single axis inertial load simulators was used to provide representative inertial and spring loads for EMA system testing. These test stands were designed by Marshall Space Flight Center (MSFC) engineering and are located at the Marshall Thrust Vector Control Research, Development and Qualification Laboratory in high bay 110 of building 4205 at the NASA Marshall Space Flight Center.

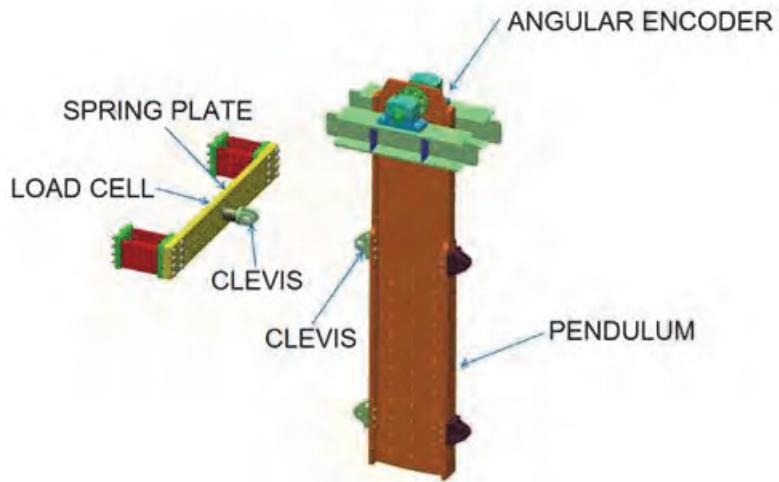


Figure 9. Schematic of large inertial load simulator

The developmental EMA was mounted between the two clevises indicated in Figure 9, as shown in the photograph of Figure 1. Each Inertial Load Simulator is instrumented to measure tension and compression forces applied by an actuator using a Honeywell model 3156-150K load cell that has a capacity of 667 kN (150,000 lbf). Pendulum position is measured to a system accuracy of 2 arc seconds using a Heidenhain RCN 729 absolute angular encoder.

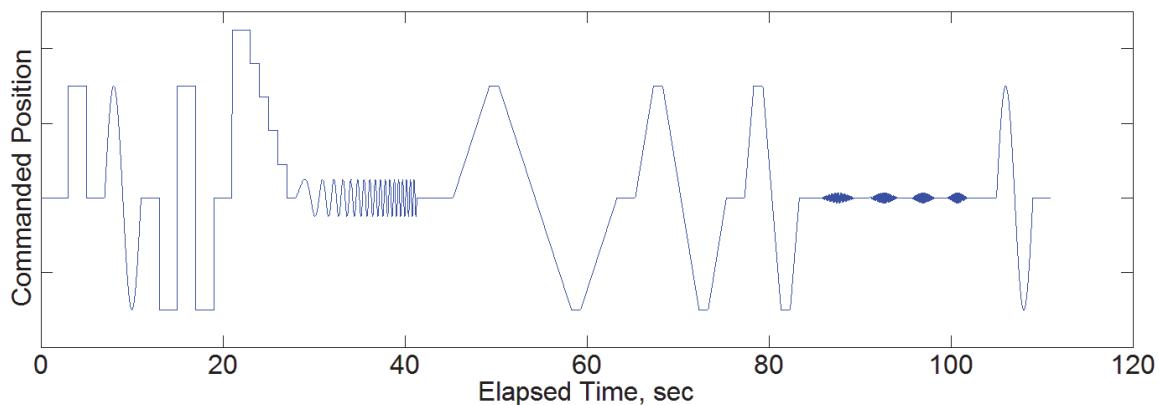


Figure 10. ETVC Demonstration Duty Cycle

Two programmed duty cycles were created to exercise the actuators through a series of steps, ramps, discrete frequency sine waves and frequency sweeps. The ETVC Demonstration Duty Cycle shown in Figure 10 is somewhat aggressive. Lasting 111 seconds, this duty cycle created a relatively high demand on the power source and controller during use, and as such far exceeded the demands typically placed on TVC systems in a realistic launch scenario. The ETVC Demonstration Duty Cycle consisted of the following sequence: Large amplitude steps in the extend and retract directions; A single period of a 1 Hz sine wave at the same large amplitude; A stepwise return to null done in 5 discrete steps; A continuous sine-sweep from 1 Hz to 16 Hz, inclusively; A set of large amplitude ramps; A set of four discrete sine waves, chosen to excite a structural resonance within the test stand; Another large amplitude single period sine wave at 1 Hz. This duty cycle was used for both EMA and EHA testing.

Lessons Learned

For EMA testing, it was necessary to first command the actuator away from null and then to displace the duty cycle accordingly. This was done because the type of LVDT used in this particular actuator created a control discontinuity as the actuator passed through null. The preferred solution would have been to change out the LVDT for one more optimally suited. However, schedule constraints did not allow for the exchange of this LVDT, so it was decided to simply avoid duty cycles that commanded the actuator through the null position.

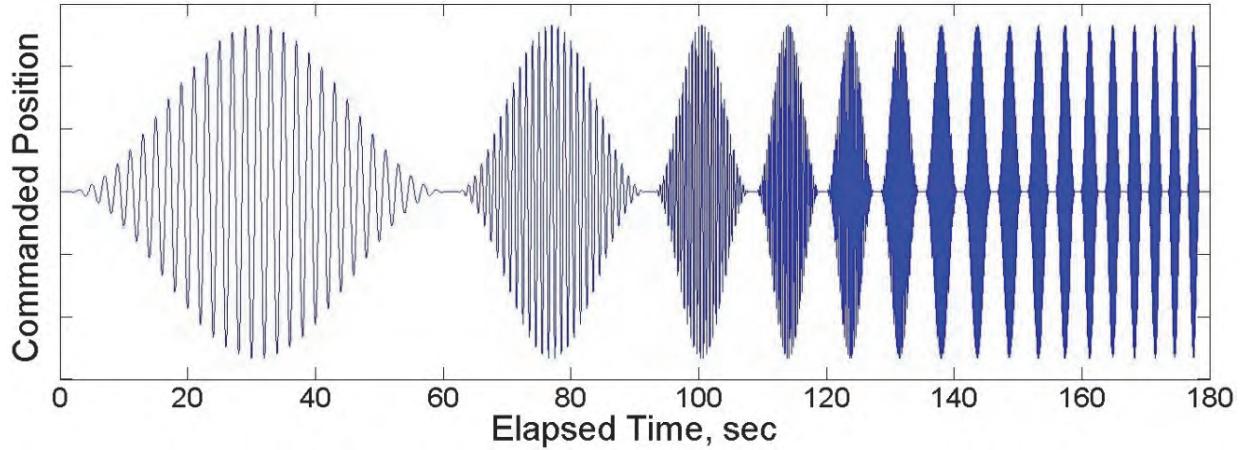


Figure 11. Discrete Frequency Duty Cycle

The discrete frequency response duty cycle shown in Figure 11 was the other programmed duty cycle used. It was generated to assess the frequency response of the integrated EMA TVC system. This duty cycle consisted of a set of 17 sinusoidal waveforms covering the frequencies 0.5 Hz, 1.0 Hz, 2.0 Hz, ..., 16 Hz. Unfortunately, a fixed number of 30 cycles was programmed for each frequency. The preferred method would have programmed a fixed duration for each frequency so that the number of data samples acquired would be equal. The duty cycle used resulted in a broadening of the individual spectral response curves with increasing frequency. Although this error was not identified at the time of testing, sufficient spectral data was present in the recorded command and response signals to perform the needed assessment.

To each of the 17 individual sinusoidal waveforms of the discrete frequency duty cycle a Hanning window was applied, creating a smooth, gradual rise in amplitude to a maximum followed by an equally gradual reduction of amplitude. A wait time of 1 second was introduced between each waveform. This technique was used as a result of lessons learned during a previous modal assessment in which it was observed that whenever abruptly starting and stopping sinusoidal waveforms an impulse component was introduced with its associated broadband excitation. This technique was verified by Fourier analysis to be a very effective means of applying monochromatic (single discrete frequency) excitation.

The recorded command signal and the actuator response, acquired via LVDT, were analyzed by applying a discrete Fourier transformation individually over time intervals corresponding to each successive frequency in the duty cycle. The highest four frequencies (13 Hz, 14 Hz, 15 Hz and 16 Hz) were discarded because the transform of the response did not meet the necessary criteria for inclusion. The coefficient of variation ($CV = \sigma/\mu$), representing the ratio of the standard deviation to the mean of a computed discrete Fourier transform, was used as this criterion. Only those responses for which the calculated CV was greater than 1 were selected.

Results and Conclusions

All test objectives were accomplished without any unexpected outcome. Functional integration of all developmental ETVC components was performed. Controller parameters were adjusted for smoother operation and to account for differences due to the larger inertial load at the MSFC laboratory facility compared to that at Moog facilities. This need provided an opportunity to demonstrate the ability to tune the controller "in the field". Peak power draw and voltage droop was demonstrated to be controlled to acceptable levels as was repeated operation on a single battery charge.

The dynamic behavior of the EMA system was determined for step and frequency response. Figure 12 shows the response of the EMA actuator to a large commanded step in the extend direction under the test stand inertial load. This step occurred at the start of the aggressive ETVC Demonstration Duty Cycle. Response as recorded by the LVDT and the optical angular encoder, which provided a much cleaner signal, are plotted along with the recorded command signal.

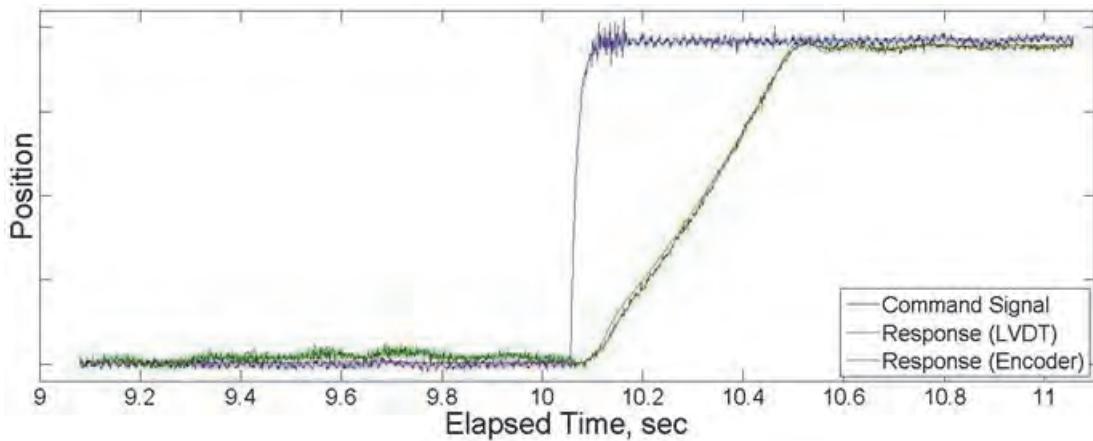


Figure 12. Step response of EMA actuator

Gain and phase response spectra of the underpowered EMA are shown in Figure 13. Poor performance above 4 Hz was expected under the inertial load and power limitations imposed by the test. Frequencies above 12 Hz were discarded because the response did not meet the acceptance criteria for inclusion. This is equivalent to the magnitude of the response being below the effective noise floor of the data acquisition system.

The highest battery cell temperature was recorded on 2 September 2011. The temperature log for that day, shown in Figure 14, captures a total of three EMA tests. A single thermocouple measured a single out of family temperature event at 2,010 seconds, elapsed from the start of the log, which corresponds to the end of the 2nd EMA test performed that day. At the same time, the temperature nearest that value, recorded by another thermocouple, was compared. The difference is not significantly greater than the standard deviation measured across all temperature data at this same time. This means that the amount by which this single value is out of family is insignificant. It should be noted that even for this worst case example, the rise in temperature was not appreciable, the temperature returned to an in family value post test and, in no case, did any cell temperature ever approach a level of concern.

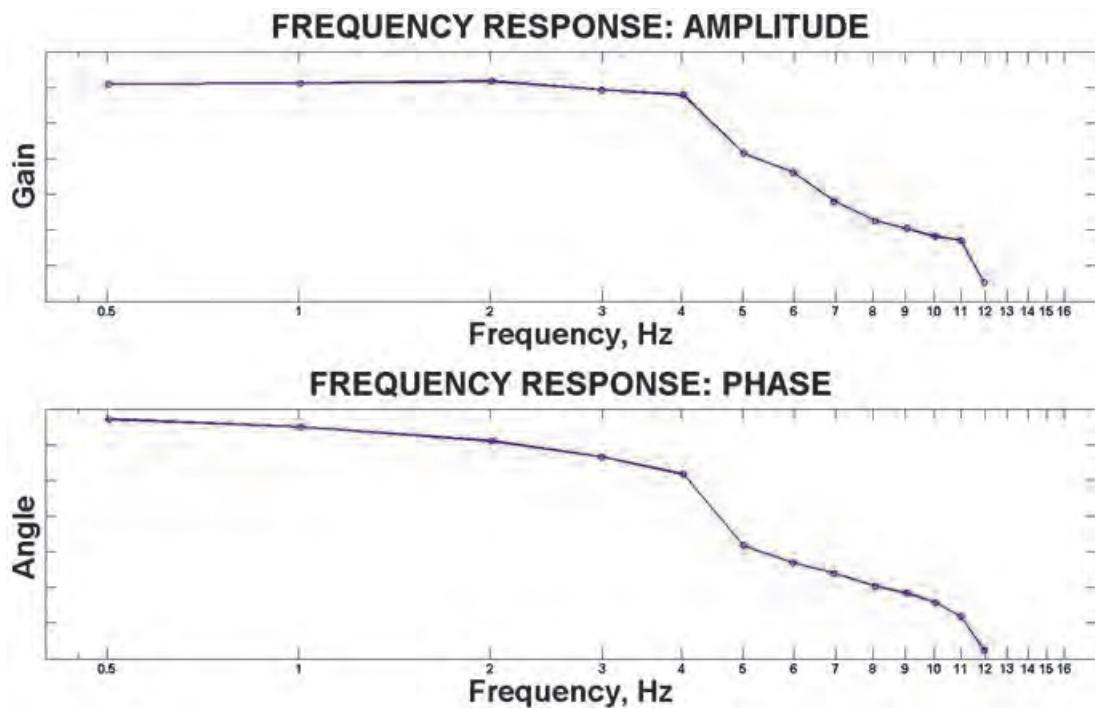


Figure 13. Gain and Phase Spectra of Underpowered EMA

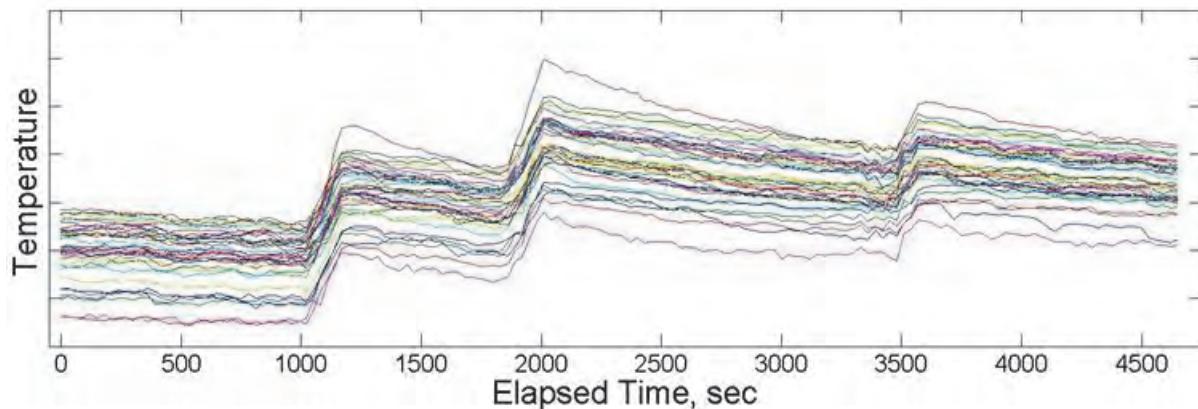


Figure 14. Lithium Ion Battery Temperature Log (worst case)

References

1. Garrison, Michael and Scott Steffan. "Two Fault Tolerant Electric Actuation Systems for Space Applications." Association Aeronautique et Astronautique de France (AAAF) Changes in Aeronautical and Space Systems, Challenges for On-Board Energy Conference, Avignone, France (26 - 28 June 2006).
2. Garrison, Michael and Scott Steffan. "Two Fault Tolerant Electric Actuation Systems for Space Applications." AIAA-2006-4939, 42nd AIAA/ASME/SAE/ASEE Joint Propulsion Conference, Sacramento, CA. (9 - 12 July 2006).
3. McMahon, William A. "Apollo Experience Report – Guidance And Control Systems: CSM Service Propulsion System Gimbal Actuators." NASA TN D-1969 (July 1975).
4. Wayne, Duke. "OMS/RCS Subsystem Presentation." NASA GNC Presentation at NASA Kennedy Space Center, (4 June 1996).

5. White, Robert A. "High Voltage Design Criteria." Marshall Standard MSFC-STD-531, George C. Marshall Space Flight Center (September 1978).
6. Dunbar, William G. "*Corona Onset Voltage of Insulated and Bare Electrodes in Rarefied Air and Other Gases.*" Air Force Aero-Propulsion Laboratory Technical Report AFAPL-TR-65-122, Air Force Systems Command, Wright-Patterson Air Force Base (June 1966).
7. United States Environmental Protection Agency. Hydrazine Hazard Summary-Created in April 1992; Revised in January 2000.

Development of High Temperature High Current Contact Technology in slipring Assemblies for the BepiColombo MPO & MTM Spacecrafts

Fabrice Rottmeier, Mikaël Krummen* and Mickaël Miler*

Abstract

RUAG Space Nyon has been selected to design, develop and test the slipring assemblies of the Mercury Planetary Orbiter (MPO) and the Mercury Transfer Module (MTM) spacecrafts for ESA's BepiColombo Scientific mission. The exposure of the spacecrafsts to the harsh thermal environment of this mission to Mercury has inhibited the use of standard high current contact technology in the design of MPO and MTM cylindrical slipring assemblies. In order to sustain the particularly high thermal requirements resulting from the combination of the thermal environment with the significant thermal dissipation of high current transfer at high temperature, new contact and electrical transfer technologies were developed and tested. Validation tests were performed on breadboard models (BBMs) with flight representative contact system at temperatures ranging from -33°C to +186°C.

This paper first presents the new developments integrated in the electric contact system design to meet the simulated thermal environment. It is then followed by a detailed presentation of the objectives and results of the validation tests. Lessons learned and the optimization of the design for the flight configuration are presented in the last sections of this article.

Introduction

Standard high current contact technologies used for space applications at RUAG consists of composite brushes soldered to a flexible copper beryllium blade. This flexible element provides a contact preload force that is designed to not only compensate the abrasive wear of the composite brush during its lifetime but also compensate for the preload loss due to the inherent creep of this material. The current is directly transferred from the composite brushes through the flexible blade. The composite brushes slide on hard gold-coated cylindrical tracks.

For the BepiColombo slipring assemblies, the high temperature environment inhibits the use of standard solder which has been replaced by a high temperature gluing compound. Consequently, current from the composite brush is not transferred through the blade, but through copper braids directly sintered into the composite brushes. This standard industrial process is for the first time used in a space application.

Additionally, composite brushes material has been adapted to the high-temperature environment while considering the need for reduced friction and low electrical resistance of the sliding contacts in vacuum conditions. Since this material differs from standard ones used by RUAG for space applications, validation tests have been performed to validate the new contact technology and the composite brush assembly for space applications.

Technology overview and main features

For the BepiColombo slipring assemblies, the high temperature environment inhibits the use of standard solder which has been replaced by a high temperature gluing compound. While providing a fixation system compliant with the local thermal environment, this new gluing system is relatively resistive, such that the electrical conduction through the flexible blade is not effective. In order to re-establish a low

* RUAG Switzerland Ltd, RUAG Space, Nyon, Switzerland

resistive electrical path between the composite brushes to the brush holder's electrical distribution system, ultra-flexible copper braids (two per composite brush) are directly sintered into the composite brushes. This standard industrial process is used for the first time in a space application. Sintering is directly performed by the composite brush manufacturer. This process implies very high temperatures, thus preventing the use of standard space cables with polymer insulation material. In order to minimize the parasitic stiffness of the cable assembly in the composite brush suspension system, ultra flexible copper braids are used. The reduced stiffness of these cables is obtained by using small diameter strands ($\varnothing 0.05$ mm) specially woven in 3 braids of 43 strands. As for all space applications, copper braids have to be silver plated. While standard space-grade cables commonly have a silver thickness of 2 μm , it was not possible to procure ultra-flexible braids in standard space grade with a silver coating thicker than 1 μm for this special type of braid.

At the other extremity of the flexible braids, standard soldered electrical connections could not be implemented due to the high local thermal environment. This connection has therefore been replaced by a terminal lug with the pair of flexible braids crimped to it.

In order to electrically insulate the flexible braids, PTFE heat-shrinkable insulating sleeves have been used. This material has been selected for two main purposes. While PTFE is fully compatible with the local thermal environment, it also has the advantage of shrinking at higher temperatures than the maximum predicted local temperature. This permits a control of the forming of the shrink sleeves in the production process while guaranteeing no further shrinkage during the operational life of this component. The control of the dimensions of the insulating sleeves has been considered important based on the observation of the ultra-flexible braid under the microscope. This particular braid construction has a very loose braid structure to minimize strand contacts during flexion. Therefore, a too tight sleeving will augment the stiffness of the insulated braids, affecting the stiffness of the flexible blade system. The diameter and thickness of the shrunk sleeves also plays a role in the stiffness of the system. The final definition of the PTFE sleeves for the ultra-flexible braids has been based on numerous stiffness tests in order to minimize the parasitic stiffness brought on by this electrical connection to the composite brush.

A 3D CAD view of the composite brush assembly is provided in the left side of Figure 1. A picture of a completed composite brush assembly for the production of the flight units is also shown on the right side of Figure 1.

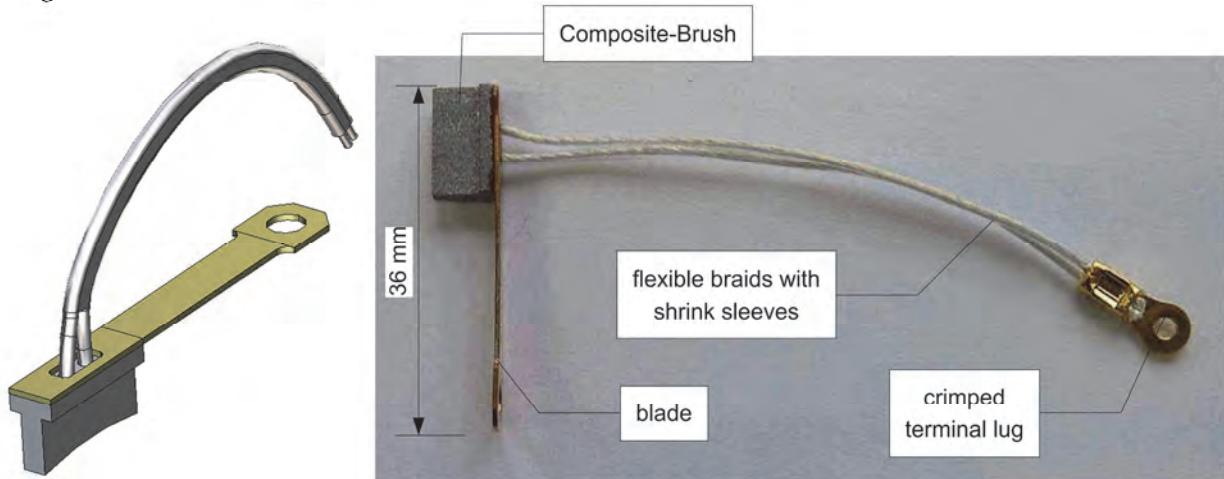


Figure 1. Composite brush assembly (CAD and final flight configuration)

Each composite brush assembly is designed to transfer 8.25 A in the worst case thermal configuration of the mission. The material of the composite brushes has been adapted to this high-temperature environment while considering the need for reduced friction of the sliding contacts in vacuum conditions.

The selected composite brush material basically consists of high silver content composite brushes with MoS₂ lubricant. Since this material differs from standard ones used by RUAG for space applications, validation tests have been performed to validate the new contact technology for space applications.

Validation Test Program

In order to validate the high temperature contact technology selected for the BepiColombo slipring Assemblies, the following validation test program has been established. The main objective of this validation test program was to verify that the selected composite brushes technology is adequate for the BepiColombo mission. Validation tests have been performed at component level as well as at system level on breadboard models fully representative of the newly developed contact system.

Component-level validation testing aimed specifically at the validation of the new gluing system, the validation of the sintered connection between the flexible braid and the composite brushes as well as the validation of the electrical performances of the new composite brush assembly.

Component-level validation tests specifically consisted of:

- Shear tests on the glued interface
- Microsections of the glued assembly
- Pull test of flexible braid sintered into composite brush
- Verification of electrical continuity between composite brush and blade
- Anthony-Brown test on silver coated flexible braids (red plague risk assessment)

In addition, the inability to procure ultra-flexible braids in full compliance with European Cooperation for Space Standardization (ECSS) requirements on silver coating thickness of copper wires (1 µm coating instead of 2 µm) has necessitated additional testing for the assessment on red plague contamination control.

Performance of the composite brushes in terms of electrical dynamic resistance, friction torque and wear has been characterized on breadboard models and compared to the initial design values. The validation tests have been conducted in parallel with the development of both MTM and MPO slipring assemblies for programmatic reasons. Both breadboard models have been used to validate the overall slipring assembly concepts with main focus on the new contact technology. These have been tested with respect to the various representative mission environments, which consisted of random vibrations, shocks, thermal vacuum cycling and accelerated life tests with intermediate electrical and mechanical functional tests.

Component-level validation tests

Mechanical validation tests of the new gluing system of the composite brushes mainly consisted of post thermal-cycling shear tests of composite brushes samples as well as analyzing microsections views of the composite brushes after performing the validation test campaigns. These two tests aimed specifically at the verification of the mechanical properties of the gluing system after aging. These tests are described hereafter, along with other components tests.

Shear test on glue interface

Shear tests were performed after 100 thermal cycles on numerous samples of the composite brush/flexible blade assembly by Aerospace & Advanced Composites GmbH - AAC. Table 1 summarizes the shear test results performed on two series of samples and reference samples (without thermal cycling). These results have demonstrated that the aging through thermal cycling has not impacted the structural integrity of the adhesive system that is fully compliant to the design requirements.

Moreover, the margin of safety with respect to shear force is significant, as in the real application, the composite brush experiences a shear force approximately 1000x smaller than the minimum ultimate shear force resistance when the slings's motion is initiated.

Table 1. Shear test results summary

Series 1	Shear Force	Std deviation
Thermocycled Samples (8 samples)	442 N	14 N
Reference Samples (2 samples)	448 N	4 N
Series 2		
Thermocycled Samples (8 samples)	427 N	20 N
Reference Samples (2 samples)	448 N	20 N

Figure 2 provides pictures of shear test samples after shear testing to illustrate the fracture mode of the composite brush glued assembly. The same fracture mode has been observed on all test samples.

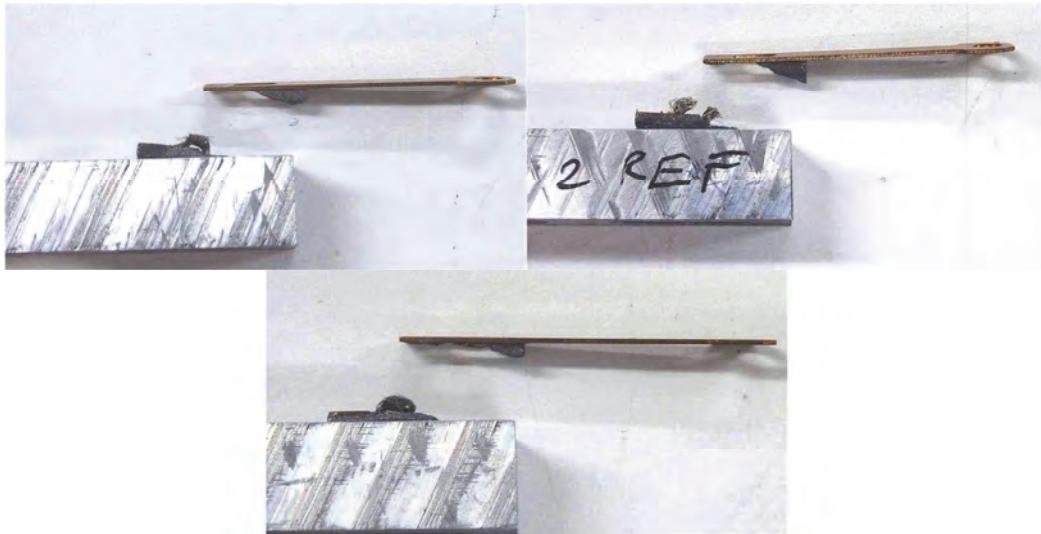


Figure 2. Shear test samples

Figure 3 illustrates the shear fracture propagation mode. A crack initiates on the side of the composite brush where it is held in the shear test fixture, and then propagates up to the glue interface, underneath the blade. The glue interface surface then breaks very quickly as the contact surface between the blade and composite brushes reduces rapidly. The initiation of the crack in the composite brush suggests that this component has a shear-stress limit lower than the glued interface.

Glue layer microsections

Examples of transverse micro-sections views of the composite-brush/flexible blade assembly made after life tests are presented in Figure 4. The Copper Beryllium blade section is shown on the top-half of the micro-section views (uniform color) and the composite brush sections on the lower half (marbled section). All micro-section views have shown that the integrity of the gluing system of the composite brushes is not compromised by both the thermal cycling and life tests performed on the breadboard models.

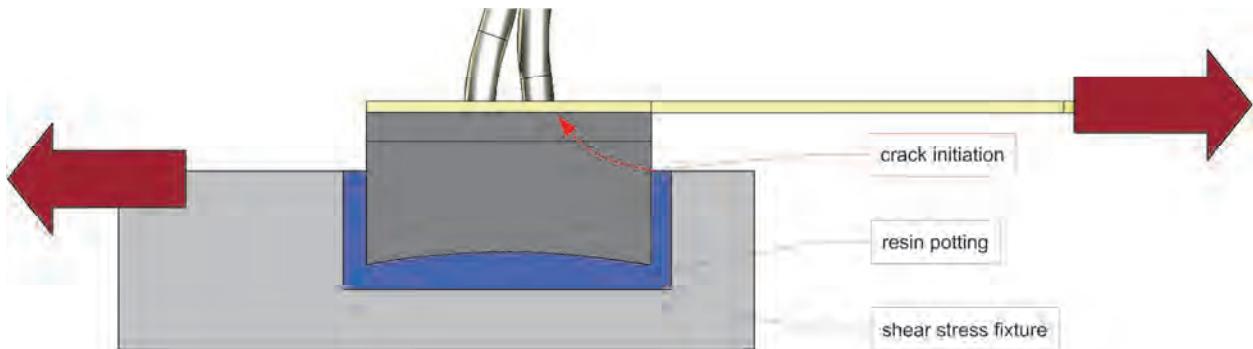


Figure 3. Shear test setup and fracture mode description

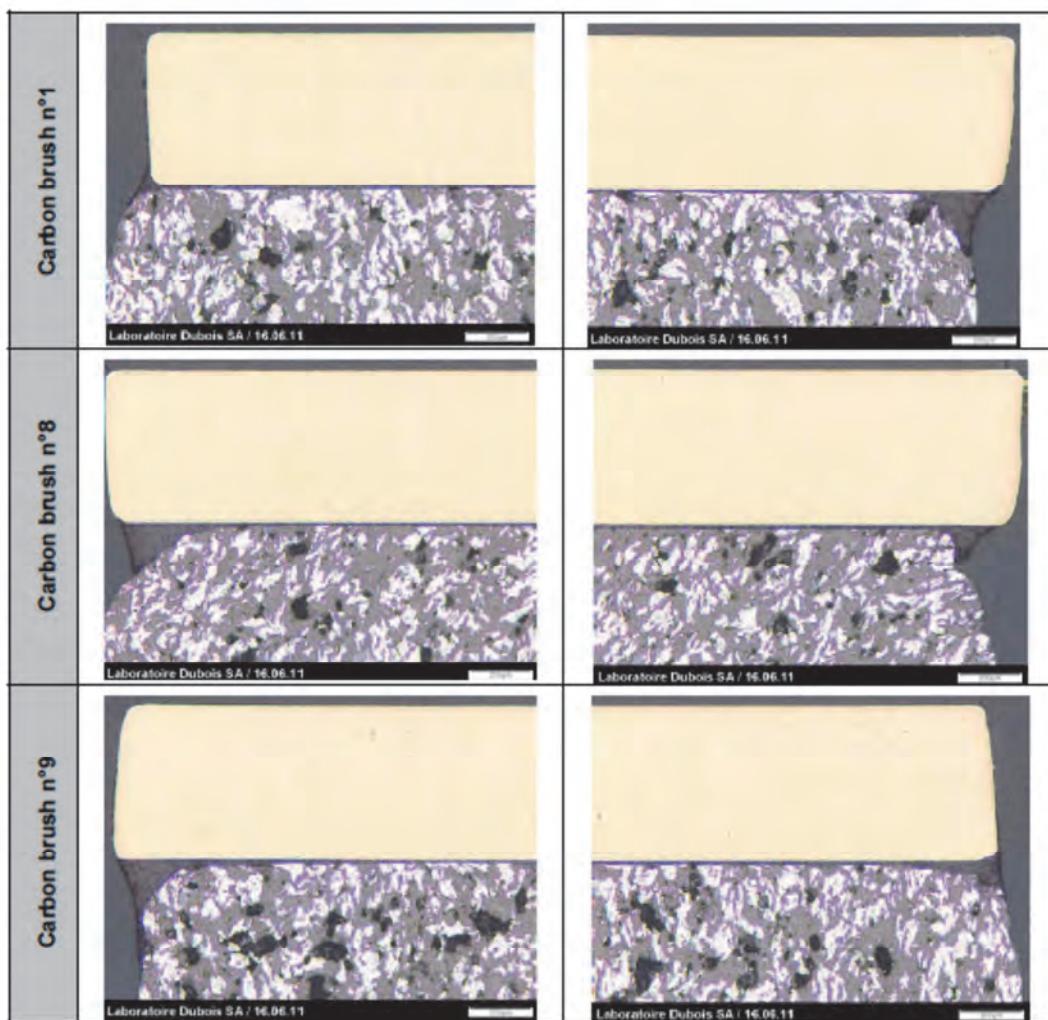


Figure 4. Example of composite brush micro-section views (© Laboratoire Dubois SA)

Pull test on composite brushes sintered cables

Flexible braids are directly sintered into the composite brush as part of the composite brush manufacturing process. In order to validate the proper mechanical fixation of the braids, pull tests have been performed by RUAG.

To assess the potential impact of thermal vacuum cycling on the mechanical fixation of the sintered braids, composite brushes from both breadboard models have been tested and the results compared with the ones obtained on the QM/FM composite brushes fabrication batch. The flexible braid pull test results are summarized in

Table 2.

Table 2. Pull test results summary

	Pull Force	Std deviation
composite brushes from BBMs (thermal vacuum cycled)	58.3 N	4.8 N
composite brushes from QM/FM production lot (not cycled)	52.5 N	2.8 N

No major impact of the thermal cycling on the resistance of the sintered connection can be observed from the pull test results. In fact, in most cases the rupture mainly occurred on the flexible braid rather than on the sintered joint. This is illustrated in Figure 5 on a composite brush assembly that encountered both fracture modes during the flexible braid pull tests.

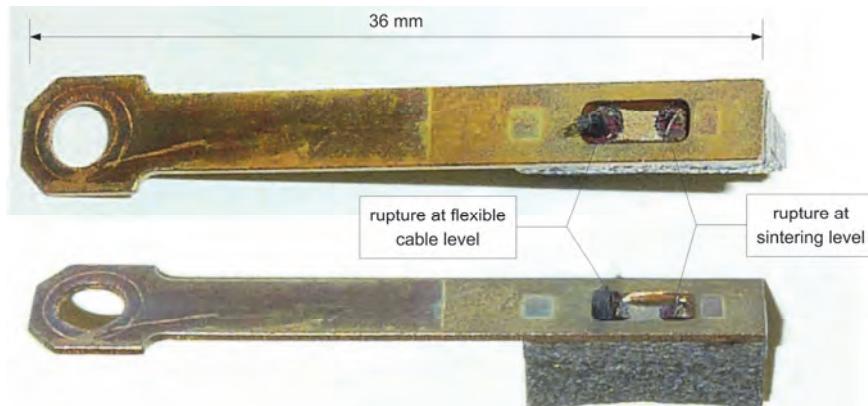


Figure 5. Pull test results on composite brushes sintered cables with both rupture modes

The maximum design loads on the flexible braids are generated by the vibration and shock environment and principally due to the inertial loads on the flexible braids. These loads are marginal with respect to the ultimate traction load.

These pull tests have proven the suitability of the sintered connection between the flexible braids and the composite brush for the BepiColombo slipring assembly design.

Electrical grounding between composite brush and blade

In this new composite brush Assembly the spring blades are not part of the electrical line anymore. Since the flexible blades are connected to the composite brush using electrically insulating glue at one end, and supported by a brush holder made of insulating material at the other end, the electrical grounding of the blades needed to be insured by tests or by the use of an additional grounding lug.

Continuity tests have been performed on the composite brushes assembly of both breadboard models after the validation tests. The tests were fully successful and proved that the electrical continuity was guaranteed between all blades and composite brushes, despite the use of electrically insulating glue.

Using a purely theoretical approach on the insulating properties of the thin layer of glue used, the spring blades should have been electrically insulated. However, the electrical grounding tests have enlightened

that the assumption of a uniform barrier of glue between the composite brush and the flexible blade is not realistic. In fact, a good electrical conduction between the blade and the composite brush is ensured by discrete electrical contact points arising from the high surface roughness of the composite brush in combination with the gluing process performed under preload. In order to guarantee the electrical grounding of the flexible blades during QM/FM production, an electrical continuity check is performed on every composite brush assembly.

Anthony-Brown tests on silver plated flexible braid

The applicable requirements from the ECSS call for a 2- μm silver plating thickness on copper conductors. While standard space grade cables commonly have a silver thickness of 2 μm , it was not possible to procure ultra-flexible braids in standard Space grade with a silver coating thicker than 1 μm for this special type of braid.

“Red Plague” is a well-known phenomenon that causes corrosion of copper on silver plated copper cables. The risk of occurrence is increased in the presence of humidity, particularly in condensed form. With the selected composite brush assembly, this is typically the case considering the thermally insulating sleeving of the flexible braids in humid atmosphere and submitted to temperature variations.

Samples of the flexible braid production batch have been equipped with the PTFE shrink-sleeves and provided to ESA’s Test Center (ESTEC). Anthony-Brown tests are currently being performed for the assessment on red plague contamination control.

Breadboard Model Validation Tests

The new composite brush sliding contact system has been validated at system level on two breadboard models (MTM and MPO slipring assemblies). Figure 6 provides a picture of one of these breadboard models for illustration purposes.

Both models shared the same composite brush contact system and were fully representative of the flight hardware in terms of materials, contact configuration and dimensions, with the exception of the number of tracks that was reduced in the breadboard models. The main implication is that the breadboard models have a reduced overall length with respect to the QM/FM design.

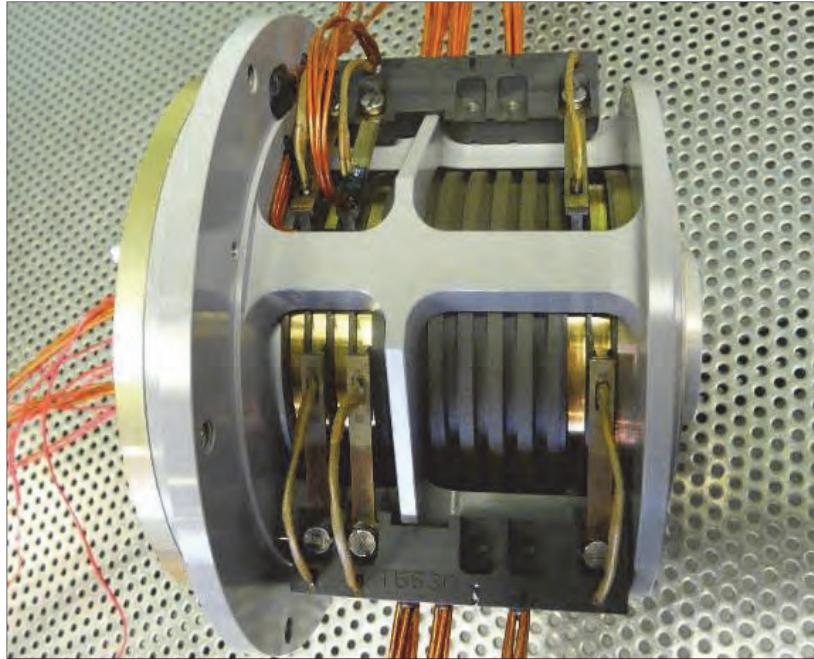


Figure 6. BepiColombo BBM 1 (configuration with contacts not fully populated)

The validation test sequence for both breadboard models is schematized in Figure 7. Breadboard model validation tests mainly consisted of mechanical vibration and shock tests, thermal cycling and life tests with numerous electrical functional tests to demonstrate the adequacy of the contact technology to this high temperature application.



Figure 7. Breadboard models validation sequence

In addition, the preload force drop due to the combination of the wear of the composite brushes and flexible blade material creep has been measured and assessed. These measurements were then used to compute the friction coefficient of the contact system from torque measurements performed both in air and in vacuum as well as with and without brush holders in order to remove the contribution of the bearings on the overall measured torque. The main results of these BBM validation tests program are described in the next subparagraphs.

Thermal vacuum cycling, mechanical and accelerated lifetime tests

BBMs have been tested under representative mechanical, thermal and accelerated lifetime (number of cycles including qualification margin) of the BepiColombo mission. During the lifetime testing, monitoring of the dynamic resistance and friction torque was performed, in order to measure the evolution of these critical parameters.

Figure 8 and Figure 9 present the static and dynamic RMS contact resistance evolution during lifetests (measured with a current of 1A). Both graphs show a slight increase with the number of revolutions, which reflects the impact of the generated wear particles on the sliding contact electrical characteristics. However, these resistance values remain very small and well within the specification.

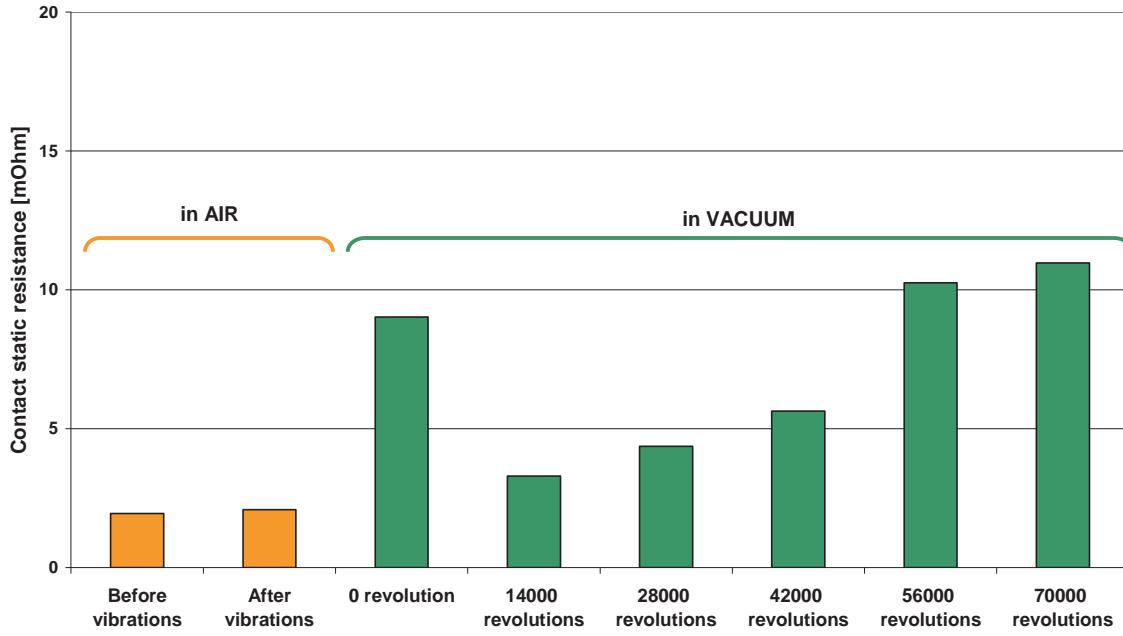


Figure 8. Static contact resistance evolution – RMS value

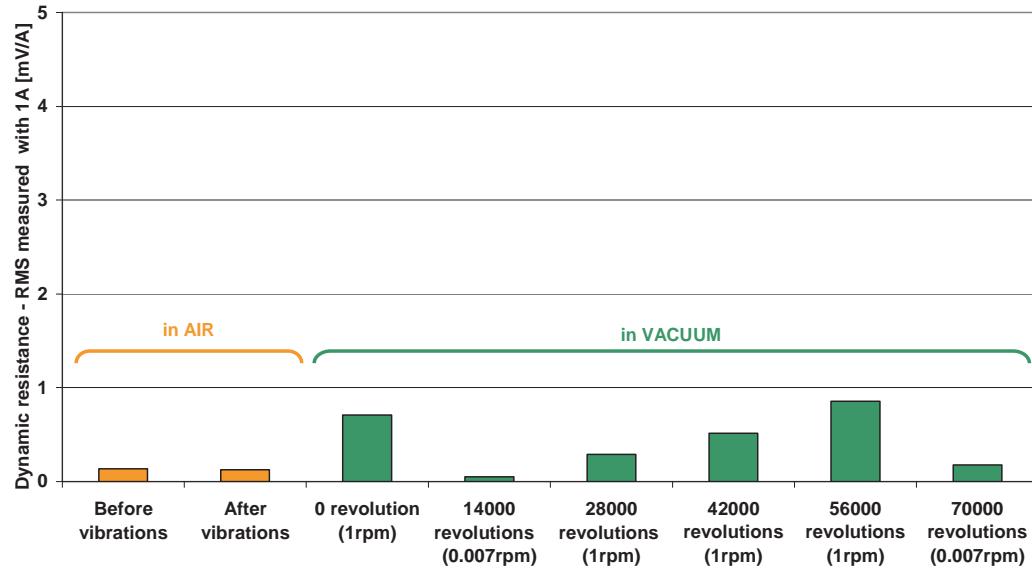


Figure 9. Dynamic resistance – RMS value

The design of the composite brush preloading system is inherently critical with respect to the mechanical environment, mainly due to the configuration of this system that has a concentrated mass at the end of a spring blade. The weight of the composite brush design has been minimized and the preloading system designed to avoid eigenfrequencies in the vibration frequency spectrum. Moreover, the mechanical dimensioning of the preloading system is such that lift-off of the composite brush is prevented as well. Vibration and shock tests have been performed on both breadboard models to validate the design of the composite brush suspension system and demonstrate that the composite brushes and tracks were not affected by these mechanical environments.

An illustration of the contact system after vibration and shock tests on a breadboard model is shown in Figure 10. Slight traces were visible on all tracks near the composite brushes. After close inspection, it

turns out that these marks were coming entirely from the local composite brush wear during vibration and shock tests. As a matter of fact, the rotation of the rotor was not rigidly blocked such that a reduced back and forth sliding movement was enabled. This local sliding created deposition of the composite brush wear particles on the tracks. These residues could easily be wiped off and a visual inspection of the gold-coated tracks under magnification did not reveal any damages or wear of the track surface. It should be noted that the dimensioning of the composite brush preloading system is such to avoid any lifting of the contacts under the applicable vibration and shock environment. The observed agglomerates of wear particles are typical of composite brush contact slipring designs and have already been previously observed by RUAG. These traces do not affect the performances of the contact system.

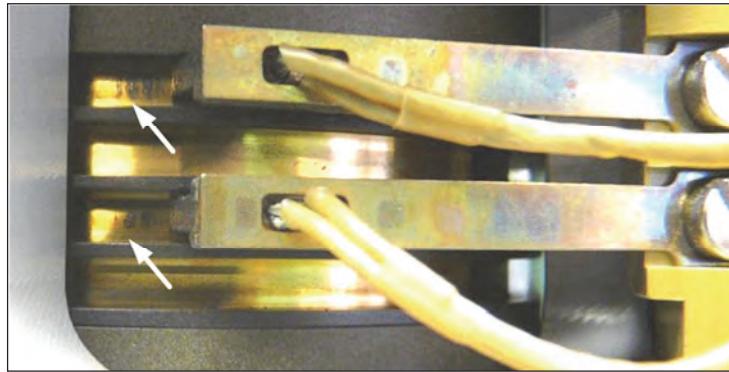


Figure 10. Wear traces due to composite brush sliding effect during vibration

In terms of accelerated lifetime testing, one of the breadboard models was subjected to more than 70'000 revolutions, which corresponds to more than seven times the specified number of revolutions for the BepiColombo mission. Thorough visual inspections of the tracks and composite brushes after life test and under magnification have shown that the overall conditions of the tracks and composite brushes were fully satisfactory. As a matter of fact, very limited amount of wear particles were found, and slight wear traces were visible on the tracks. The analysis of the total wear of the composite brushes demonstrated that the wear of the composite brushes was extremely limited, despite the number of revolutions experienced on top of the design life of the contact system. Moreover, the wear was observed to be uniform on all the composite brushes. It should be noted that the design life of composite brushes in industrial applications is at least more than one order of magnitude higher than the one tested in this application. Finally, the complete visual inspection of the breadboard model slipring assembly showed that it was still in a very good condition.

Friction coefficient

The friction coefficient of the electrical contact system plays an important role in the friction torque of a slipring assembly, mainly due the high number of contacts, and is, of course, an important parameter for the design of the drive assembly. In order to validate the friction coefficient used for the design of the BepiColombo slipring assemblies, torque measurements were performed in air and in vacuum as well as with and without brush holders in order to reject the torque contribution from the bearings. Measurements of the preload force of the composite brushes allowed the actual friction coefficient of the electrical contacts in air and vacuum to be calculated.

Figure 11 summarizes the friction coefficient measurement results. These data, besides enabling the validation of the total torque calculations for the slipring assemblies, have also shown that measuring the torque in air can be considered as worst case conditions for the definition of the qualification and acceptance test programs. These results furthermore confirm the adequacy of the selected composite brushes technology with respect to space applications.

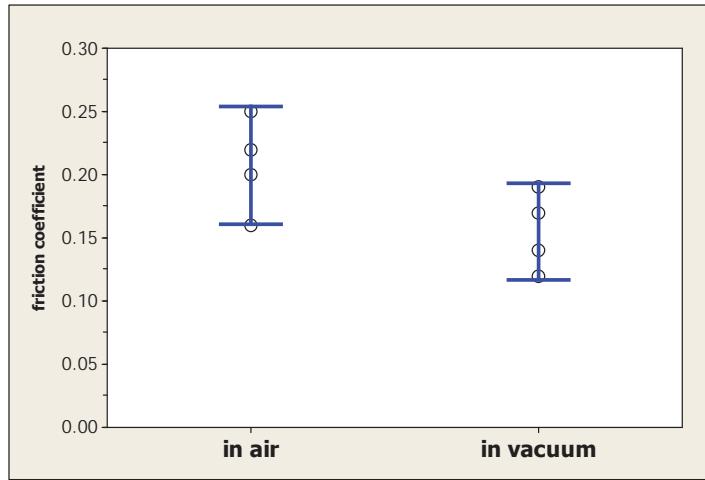


Figure 11. Friction coefficient measurement results

Dynamic contact resistance

Examples of the dynamic electrical contact resistances measured over a full revolution and after run-in of the composite brushes are presented in Figure 12. These measurements were performed at the nominal current of 12.5 A per track on four different tracks in air and vacuum. All results have shown a low electrical contact resistance in both vacuum and air conditions with great consistency between the different measured tracks. Moreover, the performances of the composite brushes are significantly better in vacuum environment, which, again, confirms the adequate selection of the composite brush material for space applications.

The RMS values of the dynamic electrical contact resistances are of particular interest, as contact resistance is a key driver for the thermal dissipation at the contact interfaces due to the electrical power transfer. This is particularly critical considering the thermal environment of the BepiColombo mission.

Figure 13 summarizes the RMS values of the dynamic contact resistance curves presented in Figure 12, with the addition of measurements performed before run-in of the composite brushes. These results show that with the selected composite brushes technology, RMS values of the contact resistance are very low, especially under vacuum. Composite brushes run-in also shows its benefits, with an overall reduction of the dynamic contact resistances. These results show that composite brush technology becomes optimal under vacuum and is furthermore improved by the effect of the run-in, which correspond to the flight configuration.

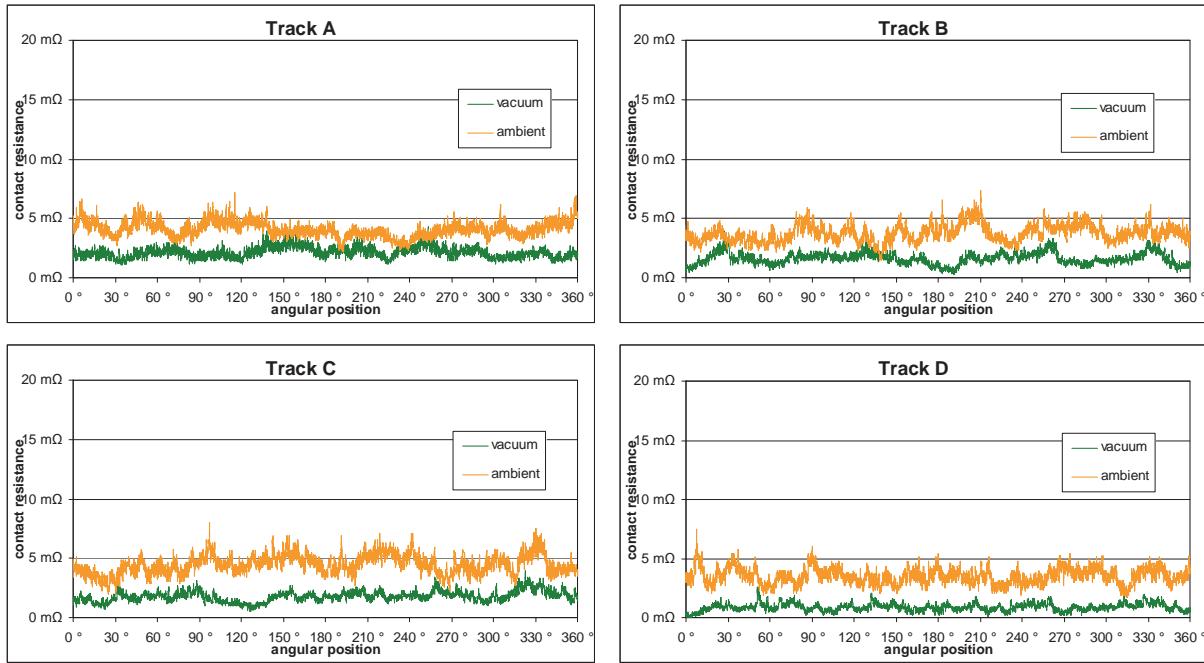


Figure 12. Dynamic contact resistance curves over 360° – VACUUM & AMBIENT (after run-in)

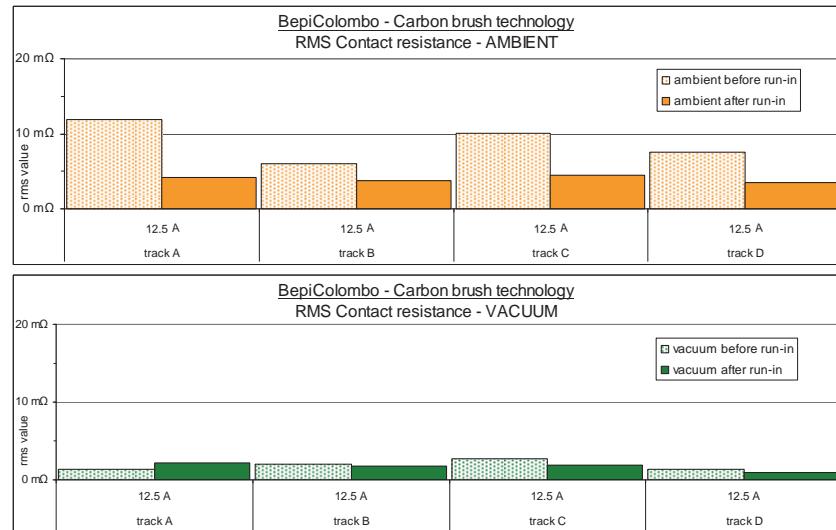


Figure 13. RMS dynamic contact resistance – VACUUM & AMBIENT (after run-in)
Lessons learned and improvements

Validation test programs performed at component and breadboard model levels have shown that the selected composite brushes contact technology is fully compliant with the BepiColombo requirements. In view of QM and FM slipping assembly production, some improvements are being carried out, namely:

- For the breadboard models, the composite brushes were manufactured as closely as possible to the cylindrical shape of the track, with the objective of performing a run-in directly on the assembled slipping assemblies. However, breadboard models tests have showed that wear is extremely low, and that a significant number of revolutions were required to obtain a perfect fit of the composite brushes to the tracks. Figure 14 illustrates the composite brushes contact surface before and after run-in tests performed on the breadboard models.

In order to accelerate the run-in process for the QM and FM production lines, the brush holder assemblies are run-in on a dedicated abrasive tooling representative of the final track dimension. In order to further accelerate the run-in process, wear particles are removed by a continuous flow of demineralized water during the run-in procedure.

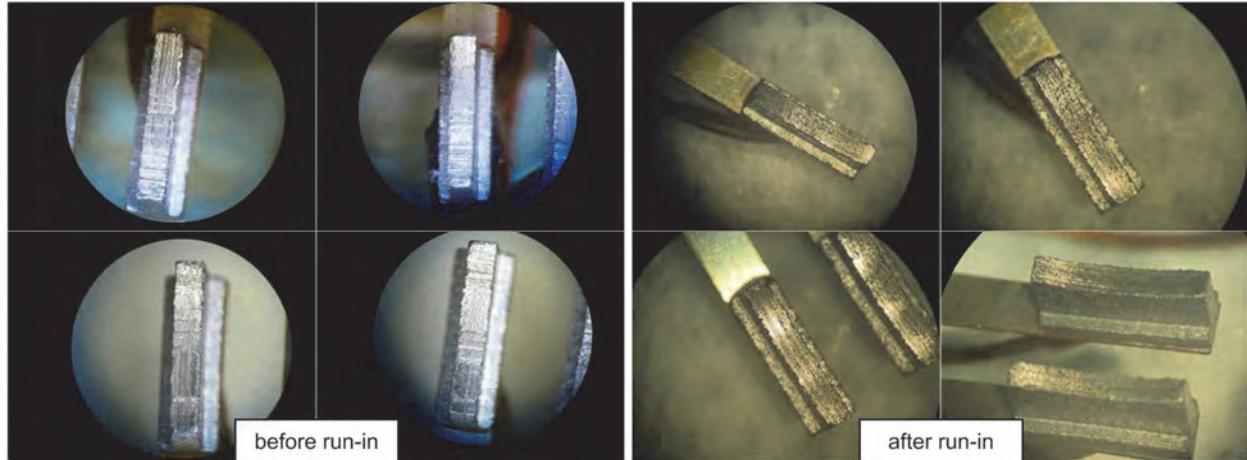


Figure 14 – Overview of composite brushes before and after run-in

- After thermal tests, a slight brownish coloration has been observed on the Kynar sleeves covering the ultra-flexible braids of the composite brushes. Initially translucent, with a pale yellowish coloration, they have slightly darkened most probably due to the harsh thermal environment of the experienced thermal test (see images on the left of Figure 15), which were close to the Kynar temperature limits. Additional tests performed on the Kynar sleeves of the breadboard models did not reveal any degradation of the mechanical and electrical insulation properties.

However, for the QM/FM design, it has been decided to switch to a PTFE-type heat shrink sleeve, which could sustain higher temperatures and avoid further shrinkage during the operational life of the slingshot assemblies. Additional thermal tests have shown that this shrink sleeve was not affected by the exposition to the thermal environment defined for the BepiColombo mission (see images on the right of Figure 15).

- In the initial design of the QM/FM slingshot assemblies, the flexible blades were grounded using an additional cable fixed to the opposite end of the composite brush using a terminal lug. However, continuity tests performed between the composite brushes and the flexible blades have all shown that the grounding of the flexible blades is ensured through the glued interface between the composite brushes and the suspension blades. The grounding cables have been removed in the QM/FM contact system design and replaced by a continuity test performed on each composite brush assembly during their production.

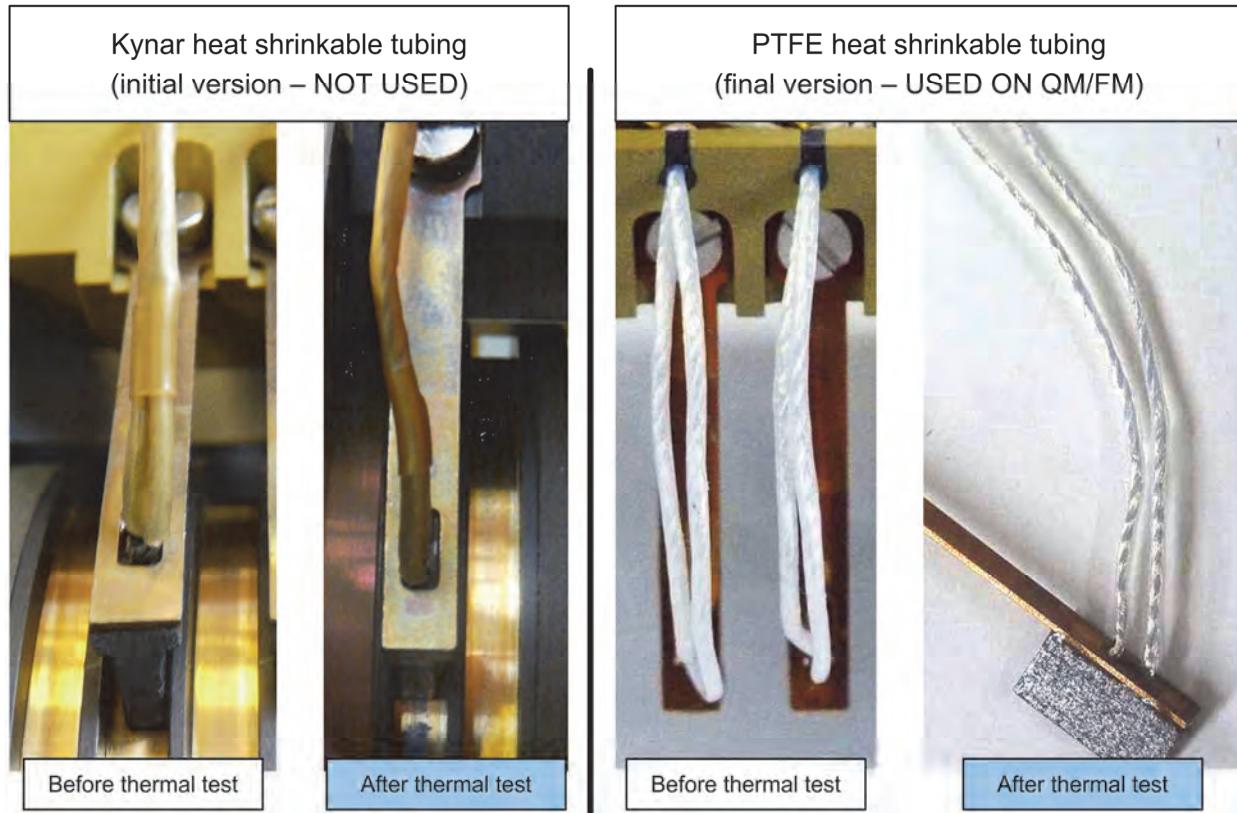


Figure 15. Change of heat shrink sleeve type (left: old, right: new)

- The gluing process carried out on the composite brushes flexible blade assembly during breadboard model production has shown that it requires careful attention. In order to enhance the QM/FM gluing process, the amount of glue and the location of its application have been defined and documented. Additionally, acceptance criteria have also been defined to guarantee a proper distribution of the glue, a precise alignment of the composite brush and in general a full repeatability of this process. Figure 16 illustrates the final configuration of the QM/FM composite brush as part of the acceptance criteria.

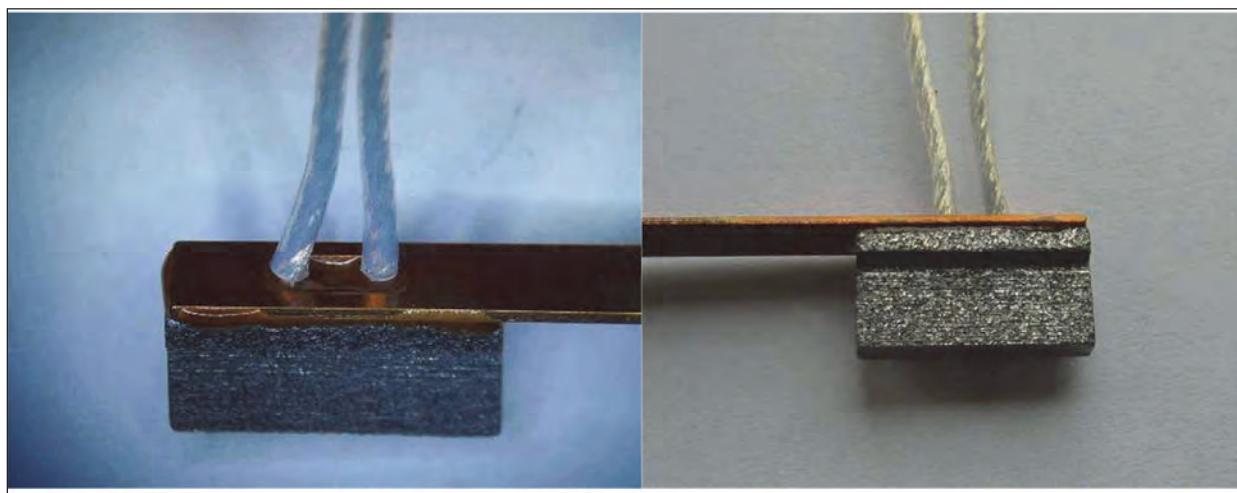


Figure 16. Close-up view of glued interfaces

Conclusions

Validation tests results have demonstrated the full adequacy of the high temperature high current contact technology implemented in the BepiColombo slipring assemblies. Moreover, the electrical dynamic resistance which has an important impact on the local thermal dissipation and consequently on the temperature distribution, appeared to be much lower than anticipated, validating the thermal simulation results with a comfortable margin.

Additionally, the demonstrated low friction and low wear properties of the composite brush technology are well above the required lifetime for the mission. Moreover, the selected material for the composite brush is well-adapted to space applications, as it behaves better in vacuum than in air.

Both validation campaigns (at component and at breadboard model levels), have helped in identifying important improvement points and lessons-learned. The production processes for the QM and FM manufacturing have been consequently enhanced. More specifically, the gluing and run-in processes, which are specific processes to the current application, have been updated and thoroughly detailed following these validation test campaigns.

Finally, it has been demonstrated that the selected composite brush assembly, including blade gluing, sintered flexible braids and heat shrink sleeves fulfills all mechanical, electrical and lifetime requirements of the BepiColombo mission.

References

1. Heinrich B, Zemann J, Rottmeier F. "Development of the BepiColombo MPO Solar Array Drive Assembly." Proceedings of the 14th European Space Mechanisms & Tribology Symposium, September 2011.

Lessons Learned to Avoid Coax Cable Failure in Moving Mechanical Mechanisms

Sheah Pirnack*

Abstract

Several programs have experienced anomalies due to cold welding of coaxial cables within Moving Mechanical Assemblies. Cold welding occurs when similar clean adjacent metal surfaces (like silver on silver or gold on gold) molecularly bond to one another given sufficient cleanliness, time, and contact pressure; as the name implies, it can and will occur in the absence of heat. This paper addresses the effects of cold welding in coaxial cables, outlines specific test results, suggests how to test for cold welding, and how to avoid the problem of cold welding in the design and material selection phase of a program.

Introduction

Within moving mechanical assemblies (MMAs), where any item is expected to move relative to another, cold welding can result in failure or severe performance degradation. Cold welds create a constraint where either the cold weld is strong enough such that the two surfaces are unable to move relative to each other or where movement / strain on the surfaces will cause early fatigue failure (such as local yielding, buckling or other low cycle fatigue damage) when the cold welded joint is flexed.

In a coaxial (or coax) cable, the condition of concern begins when cold welds develop a local constraint within the multiple layers of the cable; then through subsequent motion the induced strain initiates low cycle fatigue failure in the proximity of the cold welds including tensile overload and buckling. Additional motion has the potential to result in severe damage to the conductors intended to carry the signal/data. Not every test specimen showed cold welding between the silver-coated copper layers common to coax cable design and cold welding does not always lead to a damage level that affects Radio Frequency (RF) performance. Within this paper the construction of coax cable will be introduced, photos of where cold welding has been found will be shared, and contributing factors for cold welding will be discussed. Additional comments will be given on specific application susceptibility. Figure 1 has photos of two different cables whose failure was initiated by cold welding.

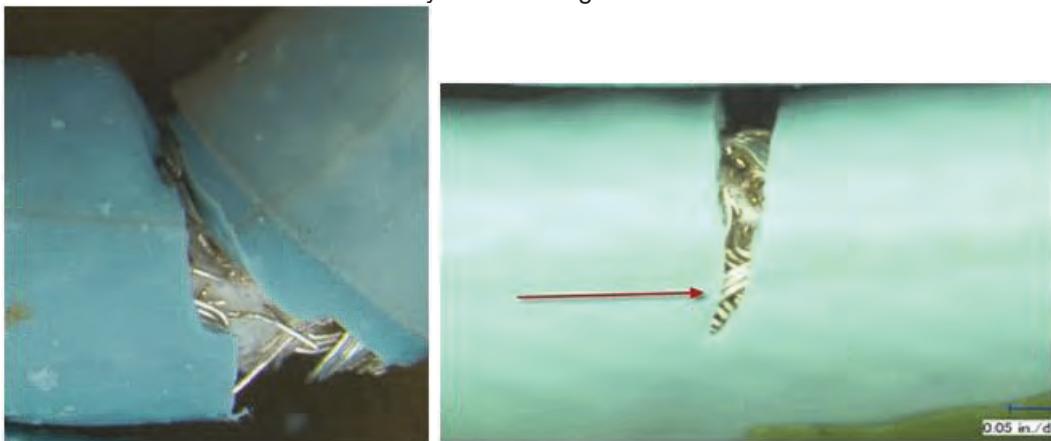


Figure 1. Failed Coax Cable: failure initiated by cold welding

* Lockheed Martin Space Systems, Denver, CO

Background

Within space flight Moving Mechanical Assemblies (MMA's) the cabling design, construction, and management should be an integral part of the design process: the cable should be chosen for its RF/data/power performance, space-compatible materials, flexing capability, and the cable management system should consider the cables' capability for bending through life without fatigue or instability compromising the functional integrity of the cable. When a coaxial cable is part of a MMA, specific features of the cable design as well as the mechanical features that manage the flexing and containment of the cable must be carefully considered. Insufficient attention to these mechanical design details can cause cold welding and/or subsequent fatigue failures in space hardware.

Coaxial cables are used as transmission lines for radio frequency signals; their applications include feed lines connecting transmitters and receivers with their antennas (data transmission / receipt). In coax cables the signal travels between the center conductor and the surface of the outer conductor separated by the dielectric. A typical flexible RF coax cable construction is shown and annotated in Figure 2.

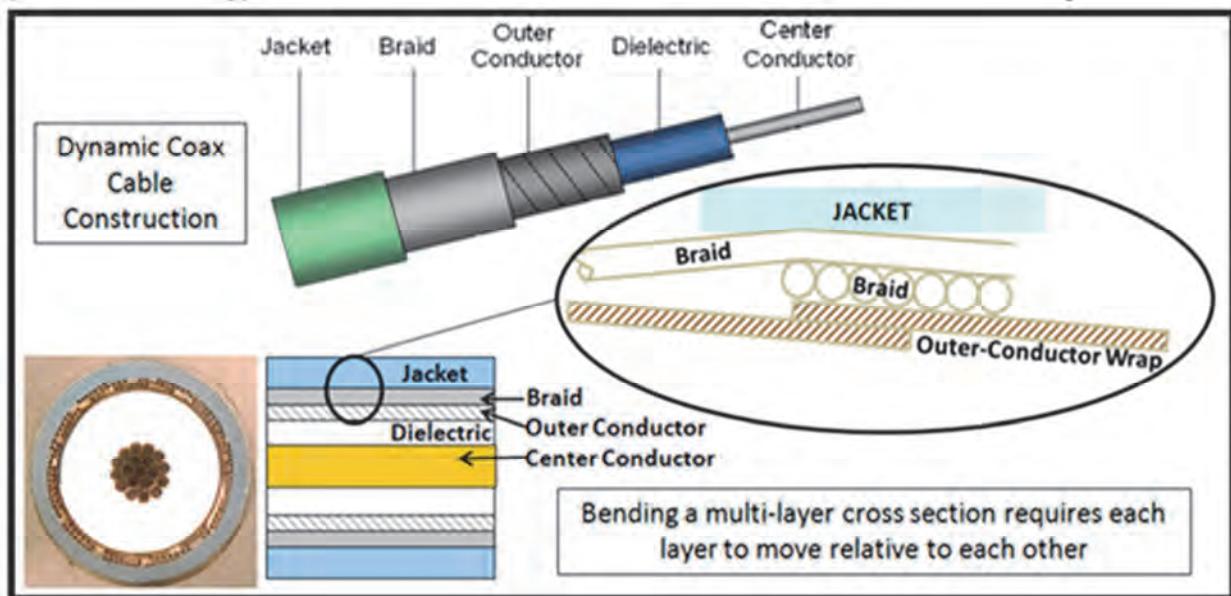


Figure 2. Construction of a typical Flexible Coax Cable (Design 1)

Within a MMA application a coax cable must maintain its insertion loss / frequency performance throughout flexing and life. The construction details are critical to a flexible coax cable's dynamic function. To maintain a high level of performance, the separation between the conductors has to be relatively constant through flexing/bending, the dynamic system (driving the motion) must be able to bend the cable, and the conductor's have to maintain electrical continuity when flexed (no gaps). For high performance flexible cable the jacket and dielectric are plastic (low modulus/bend easily) and the metal conductive layers are multi-layer components themselves: the woven braided shield, the spirally wrapped outer-conductor foil wrap, and the stranded center conductor. The assembly is held together with the protective jacket sleeve to both protect the cable and ensure no radial gaps are generated at the outer conductor (maintaining cable insertion loss stability).

The majority of aerospace coax cable designs' incorporates silver-coated copper center conductor strands, outer conductor foil, and braid (Ag coated Cu). Recall that cold welding occurs when similar clean adjacent metal surfaces (like silver on silver or gold on gold) molecularly bond to one another given sufficient cleanliness, time, and pressure. Within the typical construction for flexible coax cable there are multiple opportunities for the various layers to cold weld to themselves or each other because of their similar material construction.

Results of Testing

Cold Welds Observed in Cable

In a series of cyclic cable tests performed in vacuum, post-test destructive physical analysis (DPA) revealed evidence of cold welding in multiple specimens and multiple coax cable designs [Acknowledgments 1c]. Both silver to silver and copper to copper cold welds were observed. Cold welding was found between metal to metal surface layers within various coax cables - see Figure 3 and Figure 5 for evidence of cold welding within the cable constituents.

Cold welding in the center conductor can be identified by pulling individual strands apart; the evidence of cold welding is one or more strands are attached to the strand that is being separated from the group. As can be seen in the photo in the upper right hand side of Figure 3 what appears to be two strands bonded together is actually two center conductor strands cold welded along the whole length of the center conductor. Cold welding in a stranded center conductor reduces fatigue life properties of this critical component effectively acting as a deeper beam section that must conform to the same cable bending radius, producing a higher stress state than a single strand would [Acknowledgments 1b].

In multiple cable cyclic test specimens fretting, plowing, and material transfer due to the outer conductor foil layers cold welding and sliding relative to each other was observed [Acknowledgments 1c]. Not all cold welding affected the cable performance. When the foil was unwound from itself during DPA, intact cold welds were discovered in several specimens along the spirally wound length of the cable. The extent of the cold welding was dependent on the location along the cable, the type of cable, and the relative bending profile of that section of cable. An example of cold welding is pointed out in the lower right hand picture in Figure 3. Recall that an RF signals travel along the surface of the outer conductor. This type of wear and material transfer will not affect the cable's function if the outer conductor layer remains intact and continuous.

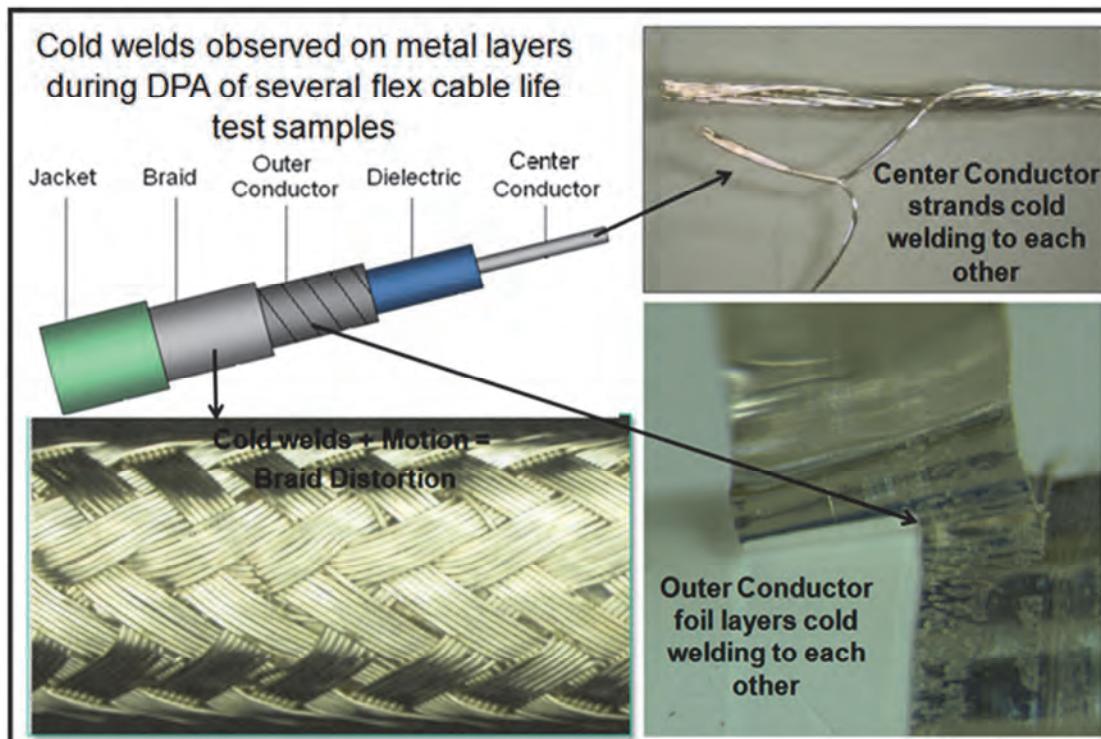


Figure 3. Cold Welds and effects of Cold Welds observed on all metal layers of coax cable

The photo in the lower left hand frame of Figure 3 reveals braid distortion along the length of the cable. The geometry and path of the seven (7) strand groups of woven braid are not uniform in their form; some strands are pulled away, or bent in an irregular shape, or, in an extreme case, an entire group of strands under local stress tensile yielded. The braid distortion is indicative of the braid strands sticking to each other or to the outer conductor foil layer underneath. With movement, the cold welding distorts or pulls the strands away from the woven group of strands that they originally followed. An X-ray of untested cable from the same lot cable is shown in Figure 4 (without distortion). An X-ray can be completed after test without DPA to look for evidence of cold welding in a cable by discerning if there is braid or conductor distortion.

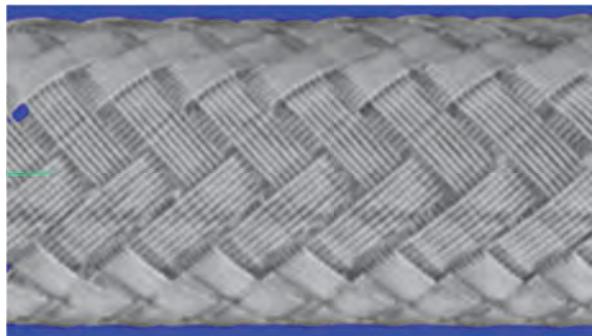


Figure 4. CT Scan / X-Ray Image of undistorted cable (braid visible)

Figure 5 is a photo of the same section of braid distorted cable within Figure 3 with sections of braid peeled away to reveal the cold welds and outer conductor damage/stretching and tearing. Evidence of braid to outer conductor foil cold welding is clear in Figure 5.

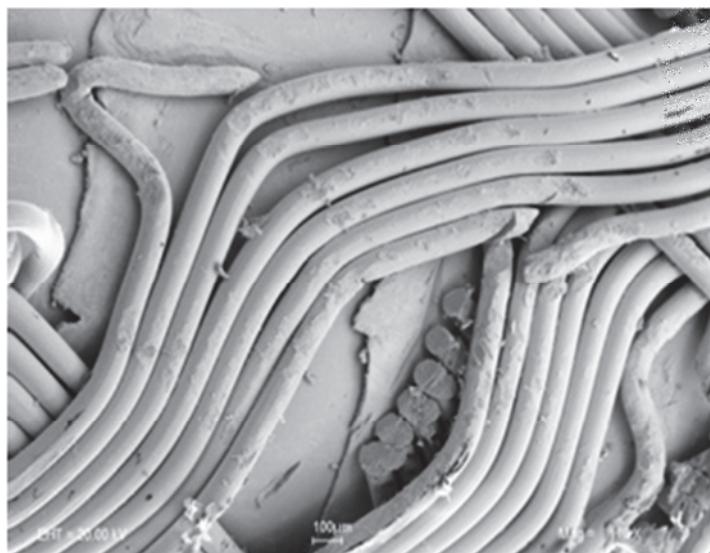


Figure 5. Image of Cold Welds observed between the braid and outer conductor (foil wrap) during DPA (some areas purposely cut away to make observation) [1c]

Recall that RF signals travel between the center conductor and the inner surface of the outer conductor layer with a precise separation set by the dielectric within coax cable. In the construction outlined above, the outer conductor foil is the main functional layer along with the center conductor. If either of these functional layers is damaged, a corresponding affect in insertion loss within the cable is realized: the

extent of insertion loss increase is dependent on the operational frequency range and the level of damage.

Susceptibility of Cold Welds in Cable: Choosing a flexible cable design

Not every cable test sample showed cold welding between the silver coated copper layers, and not all cold welding led to damage that affected the RF performance of the cable. So what is the potential for damage due to the layers cold welding? And what kind of cold welding is most damaging? How can it be adequately screened for? And if a cable management system was successfully qualified and life tested already, is that enough, regardless of seemingly small changes between cable production lots?

Multiple coaxial cables of different designs were tested in various conditions to determine the impact to the performance of the cable. Development testing, fatigue testing, life testing, X-ray inspection, material analysis and various other techniques were used to characterize the cable; RF performance parameters were used to monitor test units during testing. Different manufacturers and types of cables were tested with a construction outlined in Figure 2- will be referred to as Design 1. Some cables with an additional layer between the outer conductor spiral wrap and the braided shield were also tested and designs with this feature will be referred to as Design 2. A schematic representation of a Design 2 cross section is shown in Figure 6.

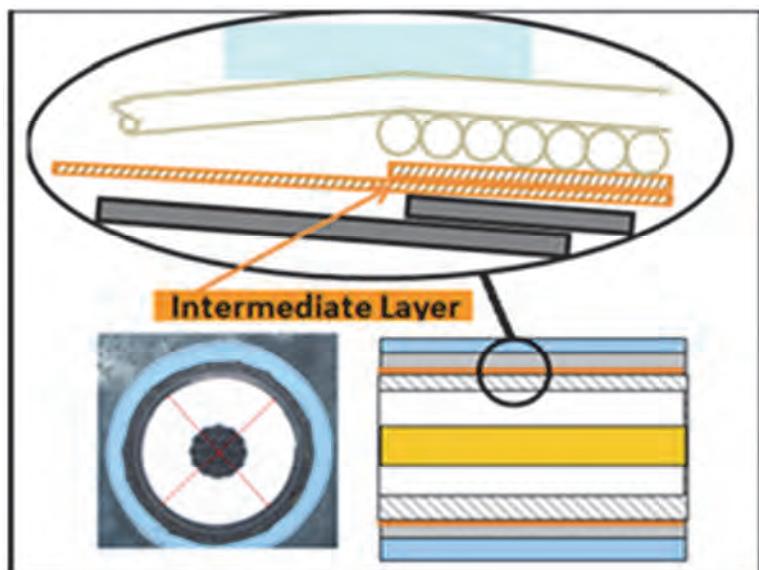


Figure 6. Design 2 of cable with addition of an intermediate layer

Three specific tests are summarized in Table 1: each test was conducted in an equivalent strain cycle and strain rate profile that encompasses appropriate life test margins in a vacuum chamber.

Design 1 of cable went through multiple tests but one lot failed life testing (Lot C) and one lot successfully completed life testing without degradation (Lot A). DPA of the cables revealed very subtle differences in material hardness, contamination levels, jacket pressure, and overall manufactured process / tightness but significant differences in cold welding and damage.

A key lesson learned from the results of the testing is a recommendation to complete vacuum life testing on every material lot of cable to ensure that manufactured lot differences won't have an impact on cable life performance. Subtle changes in contamination, material lot and manufacturing processes can impact the results of life testing even with the same design of cable.

Table 1

Design 1: Lot A	Design 1: Lot C	Design 2
Baseline Construction / design 1: Lot A initial build & lot of materials, no performance affecting damage observed	Construction / Design 1 same as Lot A, different build date and lot of materials; Cold Welding and damage observed in multiple layers along length of cable	Design 2 incorporated intermediate layer, multiple Design 2 cables tested, Sporadic Cold Welding between Outer Conductor layer observed with minimal damage.
Life Tests Successful (2 of 2 cables passed)	Life Tests Failed (2 of 2 cables failed)	Life Test Successful (6 of 6 cables passed)

Design 2 cables went through multiple tests, multiple permutations of profiles, and various other stress and fatigue tests in addition to the same level of testing of Design 1. Design 2 cable outperformed Design 1 cable. Two key features differentiate Design 2 Cable from the Design 1 cable: the intermediate non-silver coated copper layer between the outer conductor and the braided shield; and alloyed center conductor strands with a thicker outer silver coating. The failed Design 1 cable incorporated relatively pure copper strands coated with a thinner layer of silver within the center conductor strands.

In regard to cold welding, the intermediate layer prevents cold welding between the outer conductor and the braid by inserting a different material between the silver coated copper layers. This intermediate layer feature is believed to be the key difference preventing the most damaging occurrences of cold welds: cold welds that form between two separate layers in the outer portion of the cable. When the cable is put in bending, the outer layers are forced to move-slide relative to each other (more than the inner layers); if cold welds are present, instead of moving relative to each other by sliding, local yielding or pushing of surface materials occurs. Referring back to Figure 5, it is evident that braid to outer conductor cold welds initiated tearing and yielding in both layers through motion / bending of the cable.

The alloyed center conductor mitigates some level of the similar metal interaction required for cold welding, has better metal fatigue properties, and with a thicker layer of silver on each strand the silver is likely to transfer between strands acting as a lube or additional wear layer through plowing and compliance.

To mitigate the effects of cold welding in coaxial cables, the design and material of the cable for flexing applications should incorporate the two features mentioned:

- 1. Incorporate an intermediate layer between the outer conductor and braid of a different preferably non-metallic material. It will act as both a wear buffer and will prevent cold welding between the two outer most metallic layers of the cable. It also has the potential to mitigate insertion loss instability within cables (where the outer conductor loosens up over time developing a radial gap between adjacent wraps).**
- 2. Ensure the center conductor is a higher strength alloyed copper and that the silver coating on the strands has a well controlled thickness (thicker likely is better based on the test observations).**

Because of the many variables involved, a life test must be performed for each new design of cable even with the recommended features incorporated. In addition to design verification, an important lesson-learned was that coax cable construction and implementation can vary in subtle ways between production lots that can affect cold welding and fatigue capability, and therefore a life test should be performed for each production lot regardless of design similarity.

Monitoring RF Parameters for indicators to screen for a problem during Coax Cable Vacuum Testing

During vacuum testing of the Design 1 lot C cable RF data (TDR, IL, & VSWR monitored continuously) indicated that something was happening almost immediately after a test pause due to a chamber issue. Up until that point there was no indication of a cable performance change. Similar pauses occurred with the other cable lots/designs but the leading indicator (RF performance) was unaffected.

Soon after the restart of the test, the degradation of the Design 1 lot C cable was rapid. The initial indicator was a time-domain reflectometer (TDR) test where a discontinuity / spike identified damage in the bending portion of a cable. Through additional cycling an insertion loss “suck-out” or increase started to form in the highest monitored frequency range and moved towards the lower frequency ranges with additional cycles (RF performance monitored from 100 MHz – 20 GHz). The test was stopped to determine the cause of RF degradation. The RF performance was cable motion and position dependent indicating opening and closing of functional layers (impedance changes affecting loss). An in-situ x-ray inspection was completed with the test unit inside the vacuum chamber to determine the condition of the cable without incurring the risk of moving it. One of the x-rays images taken (courtesy of Aerospace Corporation) [Acknowledgments / Reference 2, 3] is shown in Figure 7. This x-ray happens to be same cable as shown in Figure 1 (left photo).

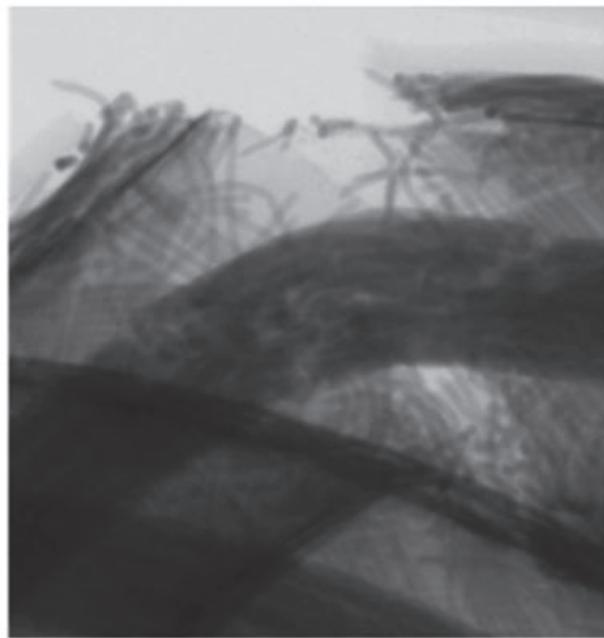


Figure 7. In-Situ X-Ray inspection photo taken of Test Unit in Chamber [2] reprinted with permission of The Aerospace Corporation

At the onset of the degradation the RF indicators implied a gap forming on the outer conductor functional layer (impedance change showing up as a TDR spike/ reflectance). Additional cycling caused the gap to propagate to a full circumferential crack around the cable and after a full breach was realized, additional cycling increased the separation along the length of the cable (gap grew larger). As the gap began to expand around the circumference of the cable, the insertion loss became evident in the higher frequency range and moved to the lower frequency ranges as the gap expanded and grew larger.

Based on bench-top testing completed at Lockheed Martin and repeated by Aerospace Corporation, (Acknowledgments 1a /References 2), the initiated crack would have had to have been at least 90 degrees circumferentially around the cable to show up in the highest frequency range (20 GHz). A crack development of 270 degrees about the circumference would impact the 10 GHz range. A full breach will

impact multiple frequency ranges with variable RF performance impacts dependent on the cable geometry, conductor condition, bending requirements, size of the gap, etc.. The bench-top testing completed at Lockheed Martin [Acknowledgments 1a] and Aerospace Corporation [2] mapped the rapid physical degradation to the RF indicators.

Prior to the significant RF degradation resulting from the damage as shown in Figure 7, there was no warning of an issue in the cable. Unfortunately this means if you can see a change in the RF, an issue is likely already present indicating some level of damage to the cable. There is no leading indicator of actual cold welding in the RF data until the damage is done. The effect of the cold welding condition occurs after a cable is moved and the damage is within the active cable layers. RF position dependent performance was due to the breach in the outer conductor foil layer opening (higher impedance) when bending the cable and closing (recovering) by reversing the bending / motion.

On a similar Design 1 Lot C cable, a partial breach of the outer conductor manifested itself in a similar manner, but was in a much lower strain area. Prior to DPA, a CT scan of the break area (this cable did not have a full circumferential break) was completed. The CT scan revealed that the center conductor had failed. The center conductor strands appear to have failed due to accelerated fatigue caused by increased bending from a partial breach. A likely contributor to the accelerated fatigue in the cable is an adjacent stiffness increase due to cold welded cable layers. The CT scan image of the break area is shown in Figure 8 as a section view so that the center conductor is visible; this image is of the same cable as shown in Figure 1 (right photo).

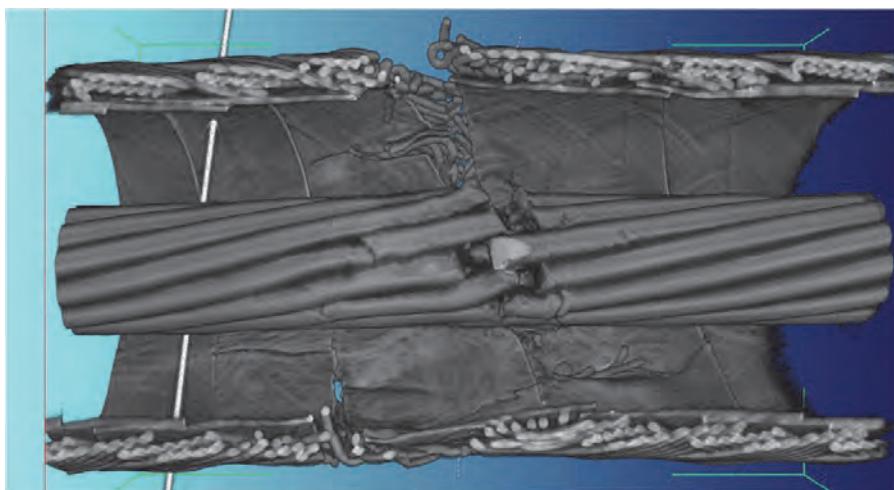


Figure 8. CT Scan inspection photo taken of a partially breached cable with center conductor condition shown (part of outer conductor / shield taken out of visible frame)

As can be inferred from the photos of damaged cables and the trailing RF indicator, it is imperative to test cables well to screen for this condition.

Experience has shown that cold welding has led to a progressive damage process and, while not proven experimentally, cumulative fatigue damage is expected to be a non-linear function of cyclic flexural amplitude times the number of cycles typical of metallic fatigue. Consequently, the design of the coax cable and the cable management system must be within proven fatigue capabilities for an expected mission angular movement profile [Acknowledgments 1b].

Possible contributors and/or additional areas of concern

References on cold welding indicate time is necessary for cold welds to form. Although it does not take very long for cold welds to form, continuously running a test without pausing has been shown in past tests to prevent cold welds from occurring. It is believed that in the test with the Design 1 Lot C cable that material conditions were right within the cable layers to cause cold welds, the time and opportunity was given in the test pause, and after restarting the test and inducing motion on the cold welded cable the damage progressed to a severe level. **Completing a cable test continuously without pauses impacts the cable layers ability to cold weld, potentially masking an issue in the cable.** Mechanism idle periods during a mission promotes the development of cold welds (to become more prominent or stronger), in effect accelerating the degradation in the cable when mechanism operation resumes. Complete cable testing as flight-like as possible to ensure that the operation and stopping or non-operation is adequately simulated. Conversely if the application requires the cable to continually move this may actually prevent severe cold welds from occurring.

Several vacuum life tests were run with Design 2 test cables. The most apparent advantage of the intermediate layer to cable performance is preventing the braid to outer conductor cold welding. It does not, however, prevent the various layers from cold welding to themselves (outer conductor wrap to adjacent outer conductor wrap or braid to itself). Some Design 2 cables were tested with a profile consistent with the other test units but with small angle dithers incorporated at each extreme (while similar cables did not undergo the small angle dithers). These dithers were not analytical contributors to fatigue so were not initially considered to affect the overall performance of the cable, but they did, however, have an effect on the condition of the cable noted in DPA. The cables that had small angle dithers incorporated into their test profile had cold welding between the outer conductors foil layers (lower right picture on Figure 3). The cold welds within the Design 2 test cable did not impact the RF performance of that specific cable but their significance in a design susceptible to multilayer cold welding may be severe. What was concluded from this result is that **small angle motion likely exacerbates cold welding as it contributes to cleaning the surface between the metals (but is not necessary for cold welding to occur if the surfaces are already clean).** Small angle dithers, although not a large contributor to fatigue can polish a surface, pushing barrier films away and cleaning the surfaces through movement. What is also theorized is that the cold welding did not impact the performance because it was only between the outer conductor and itself and not between the outer conductor and the braid. The motion that was being stifled at the sporadic cold welds between the outer conductors was made up for with adjacent wraps and layer motion.

Clearly the speed/motion profile used in the life test significantly affects the results of the life test. However a surprising result of the investigation indicated that the cables that were vacuum life tested at slower speeds, with pausing and dithers incorporated within the profile (versus a generic encompassing designed profile simulating accelerated cumulative fatigue) degraded more rapidly (with less motion and cycles). Understanding the subtle parameters of a critical contact surface is essential to make informed decisions on how to design a life test given typical time considerations. **Critical interfaces should be tested in as flight like manner as possible (Test like you fly).**

It has been asked whether a vacuum environment is necessary for cold welding to occur. In the testing completed during this investigation, cold welding in cables was observed for cables tested both vacuum and atmospheric conditions; however all of the critical testing for our investigation was completed inside a vacuum chamber. All DPA activities were performed under ambient laboratory conditions. It is believed by the author that the space vacuum environment exacerbates the condition of cold welding simply because it is a cleaner environment and without air to replenish a potential contamination source (ex. oxidation, nitrides, and water), cold welding is more likely to occur. One test result, although not statistically significant, between two similar cable specimens demonstrated that cold welding occurred more readily in the specimen tested in a vacuum environment (sooner within a similar cyclic test profile) versus the test specimen run in ambient laboratory conditions. Two previously published papers on cold welding within cables [4,5] also mention the affect of vacuum on cold welding.

Given sufficient time and pressure, two metals of similar composition in clean contact will form cold welds.

Applications of concern

Depending on the amount of motion required of the cable, cold welds may or may not be a problem. Depending on the geometry of the system, fatigue may or may not be an issue, but additional consideration to local low cycle fatigue of layers due to cold welding should be given. If cold welds form and the cables are not required to move during operation, then cold welding is not a concern. The following are application considerations regarding cold welding to keep in mind throughout the design, verification, or qualification life cycle of a program or MMA design:

Cables in or across single deployment mechanisms are generally NOT at risk:

- Cable primary failure mode is fatigue (yielding and buckling). Cold welds reduce the number of cycles / amount of motion required for local fatigue failure to occur. Single deployment mechanisms that have to operate once will not generally have excessive cumulative damage from fatigue (even low cycle local fatigue).
- Deployments generally occur at beginning of life (BOL). With relatively little time / motion relative to last "successful on-ground" test, damage from cold welds likely will not have the chance propagate to a failure within a single motion / deployment.

However:

- If the system has low force / torque margins there is some risk of higher force required to move / bend cable relative to what was tested initially if cold welds formed post launch / pre-deployment.
- If cold welds form prior to deployment and a very large motion/bending is required for the initial / first and only motion some damage might occur at deployment. The likelihood of cold welds forming and cumulative damage in one motion is low but should be considered in the context of the application.

Cables that are expected to operate and move over life (especially high cycle long life mechanisms) ARE at risk:

- Dithering motion and vibration can exacerbate cold welds by abrading the surfaces and creating atomically clean surfaces. A space vacuum environment also contributes to maintaining clean surfaces.
- Pausing, idle periods and non-operation between operation / motion cycles can exacerbate cold welds by allowing the two adjacent surfaces time to molecularly bond to one another and form stronger cold weld bonds.
- Bending the cable through any angular motion has the potential to cause damage to the layers within the cable particularly when the layers have cold welded or are sensitive to fatigue failure; but not all damage is life threatening - the cold welds' strength, the forced strain on the layers and the fatigue properties of the individual cold welded cable materials will determine the extent of the damage.
- Through multiple cycles of cold welded cables the extent of the damage becomes progressively greater and can lead to a full break / breach in a cable.

Aside from cables, the risks may be obvious, but it is worth mentioning that similar metal to metal contact interfaces requiring motion within mechanisms are at risk.

- If two surfaces are required to move relative to each other and there is no (non-metallic) barrier between them (lube, coating or otherwise) then cold welding can lead to failure (seizure / increased force to slide, move or separate; or low cycle fatigue) at that joint / interface.
- Any critical surface contact and motion between critical interfaces should be tested in as flight like manner as possible (Test Like You Fly). Recall cold welding is exacerbated by clean surfaces, time, and contact pressure, so ensure testing incorporates / encompasses these critical parameters.
- Dithering motion and vibration can exacerbate cold welds by abrading the surfaces and exposing the atomically clean metallic surfaces underneath. A space vacuum environment also contributes to maintaining clean surfaces (no oxidation, sulfides, water vapor, etc) – Test like you fly considerations should be validated.
- Pausing, idle periods and non-operation between operation / motion cycles can exacerbate cold welds by allowing the two adjacent surfaces time to molecularly bond to one another and form stronger cold welds. Sequence of initialization, deployments, and storage periods should be given consideration during a qualification of critical contact surfaces.
- A higher contact pressure and softer metallic interface contribute to a larger contact surface area and more energy at the interface to encourage the metals to share molecules, i.e., the higher the likelihood of cold welding. Reference 5 goes into further detail about the contribution of surface micro hardness of the constituents as it relates to cold welding.
- Material Lot Changes: Hardness, contamination/cleanliness, alloy/material difference, subtle construction differences/ machine and assembly setups all make a difference and should be considered when making a decision on whether cold welding is a concern in your system. Complete a life test on every lot of material for critical surfaces whether or not you have completed a life test in one version or design.

Conclusion

Moving cables are sensitive to changes in material lot and test parameters including vacuum, strain / motion, speed, and other test like you fly assumptions much like other components within moving mechanical assemblies. This was the conclusion after a multiple year investigation completed on coaxial cable for an aerospace Moving Mechanical Assembly. Fatigue has been widely discussed as the primary failure mode of flexing wire; however, other phenomena need to be considered when designing a cable to move over life. Cold welding, a condition in which welds occurs between similar metals in the absence of heat, can occur on cable layers if precautions are not put in place when choosing a cable design to use for a moving application. For coax cable it has been shown that cold welding between the outer braid and the outer conductor can lead to degradation in RF performance. Three key points were discussed during the course of this paper:

1. Life Test Programs are not usually driven by lot/date code changes, however, life testing for coax cable from each production lot is recommended
2. Coax Cable Designs to be used in life critical MMA's should incorporate a non-metallic intermediate layer to prevent multi-layer cold welding between any metal to metal layers. Additional attention should be paid to the lot construction of the individual metal constituents

including the center conductor. Ensure the center conductor is an alloyed copper (higher strength) and that the silver coating on the strands has a well controlled thickness (thicker likely is better based on the test observations).

3. Cold Welding happens with clean metal to metal contact. These lessons learned are applicable to other Moving Mechanical Assembly (MMA) components where sliding or rolling interfaces are metal to metal. Testing should simulate flight like conditions, sequences, and profiles to the maximum extent possible on any MMA especially considering the entire variable set that could potentially affect performance.

Acknowledgments

- (1) Lockheed Martin Space Systems (LMSSC) Data, Assessments from Team, and Findings:
 - a. Special credit goes to the RF Engineers for their extensive coax cable knowledge and testing
 - b. Analysis Group for their analysis expertise in macro and micro structures, metal stress/strain, fatigue and dynamic simulation work
 - c. Failure Analysis Lab for steady hands and patience dissecting tens and hundreds of cable specimens (DPA work) and documenting it beautifully.

Additional acknowledgements on the LM Team in Denver: Quality Lab for scanning and rendering all the CT scan cable images, and many more folks on the team that put in countless hours and thought ensuring our results were something we could rely on. Thanks to the whole Lockheed Martin, LM Customer, Aerospace Corporation, and Subcontractor Team for providing their time, resources, test samples, and units from which we gathered a lot of data and knowledge.
- (2) Also special mention of Bob/Robert Pan from Aerospace Corporation for being a facilitator of information transfer ensuring the contractor / customer and Aerospace team were in constant communication and providing additional data with Aerospace Corporation support through repeating tests for confirmation, refinement, and interpretation of results.

References

- (3) 2D In-situ X-Ray Image (Figure 7) courtesy of The Aerospace Corporation, Dr. Eric C. Johnson, Shant Kenderian, and Robert Pan, Space Material Laboratory.

Published Papers on Cold Welding:

- (4) Coaxial Cable Failure in a Spacecraft Mechanism, by Michael Chiu, Proceedings of the 34th Aerospace Mechanisms Symposium, Goddard Space Flight Center, May 10-12, 2000 where the solution for cold welding in cables was to replace design with a design that had a PTFE barrier between the wire braid and foil
- (5) Material Property Effects on Coaxial Cable Mechanical Failure, by R. B. Pan, J.B. Chang, C.C. Wan, Y. R. Takeuchi, R. McVey, and I. Chen Proceeding of the 36th Aerospace Mechanisms Symposium, Glenn Research Center, May 15-17, 2002 where it shows DPA results and postulates a failure mechanism that relates low yield strength associated with the low hardness values to the cold welding of similar material at the interface, rapid initiation of multiple crack sites and fast crack propagation.
- (6) Assessment of Cold Welding Between Separable Contact Surfaces Due to Impact and Fretting Under Vacuum; by A. Merstallinger, M. Sales, E. Semerad, Austrian Institute of Technology, and B.D. Dunn, ESA/ESTEC European Space Agency; STM-279, November 2009.

DLR's Dynamic Actuator Modules for Robotic Space Applications

A. Wedler, M. Chalon, K. Landzettel, M. Görner, E. Krämer, R. Gruber, A. Beyer, H-J. Sedlmayr,
B. Willberg, W. Bertleff, J. Reill, M. Grebenstein, M. Schedl, A. Albu-Schäffer, G. Hirzinger *

Abstract

Based on our long-term goal to develop “robonauts” for space and the experiences our research department accumulated in space robotics, this article describes recent design and development results at DLR’s Robotics and Mechatronics Center. Herein, we focus on lightweight robot arms, articulated hands and highly integrated actuation modules for space applications. We show how the development process started with fully sensorized, highly dynamic joint modules with state feedback control and led to seven degree of freedom (DOF) torque-controlled robot arms that enable innovative Cartesian impedance controllers. Further, we present two space robotics examples that are based on such modular actuation units. The first one is the ROKVISS experiment which has been launched towards the ISS in 2004 and returned to earth in 2011. The second is the Dextrous Robot Hand, DEXHAND, which we developed on contract with ESA. These two projects underline the strong interest to transfer our knowledge and experience from terrestrial robotic developments to innovative space technology.

Introduction

Currently, many operations in space, such as maintenance or new module assembly, have to be carried out by astronauts and expose them to a hazardous environment. These missions are associated with high risks and costs. While robotic systems are not yet ready to replace humans in space, they may provide an excellent support for astronauts. Supported by telemanipulation concepts, robots could be used for many of the Extra Vehicular Activities (EVA). Herein, robotic perception and partial autonomy could strongly simplify tasks for the astronauts. Further, methods like force feedback allow operators haptic interaction at distant locations. Besides near earth orbital activities, we believe that autonomous and semi-autonomous robotic systems will take an important role in planetary exploration scenarios.

In order to bring teleoperated systems to the International Space Station (ISS), the European Space Agency (ESA) is currently investigating different scenarios. We think that humanoid robots, like our terrestrial technology demonstrator “Justin”, (Figure 1) could fulfill ESA’s development goals within this context. Since the ISS is designed for humans, sending up robots with hands and arms is an obvious option that also NASA follows with its Robonaut [1]. In the case of a telerobotic scenario, humanoid robots simplify the mapping from the operator to the robotic system.

* Robotics and Mechatronics Center (RMC), German Aerospace Center (DLR), Wessling, Germany



Figure 1: Teleoperator using a head-mounted display to get 3D visualization and lightweight Robots (LWRs) as haptic input device with force feedback and "Justin" in telerobotic operation

This results in an intuitive operation that minimizes learning time as well as user fatigue and improves execution speed. Upon those arguments, ESA decided to develop an EVA capable hand/arm system. Based on the experiences of our lab with space robotics projects like ROTEX and ROKVISS, ESA assigned the development of the space-qualifiable hand to the DLR Robotics and Mechatronics Center (RMC).

Since space robotics applications require highly integrated, lightweight systems with low power consumption and high performance, DLR's robotic actuation technology and our longtime experience with a space robotic system may provide interesting solutions for future missions. Throughout this article we present our robotic drive train technology and its development process as well as two space related application examples. The next section) of this paper discusses the design of the DLR drive train unit including the in-house developed permanent magnet synchronous motors.

Furthermore, it describes how a terrestrial seven DOF arm is built based on these actuation units. A later section presents ROKVISS, our robotics component verification experiment that was operated at the outer surface of the ISS from 2004 to 2010. The interesting fact of this experiment is that we used a mixture of space qualified and off-the-shelf components and achieved very reliable long-term operation in space. Receiving the robot back allows us to collect valuable data about the effects of the space environment on the system. Furthermore, this paper describes the development of the EVA qualifiable Dexterous Robotic Hand, DEXHAND, for the ESA. All presented results are based on the Critical Design Review (CDR) status, giving an overview of the technical decisions with respect to the mechanical design.

DLR Drive Train

Developing actuators for dynamic and sensitive robotic systems is a challenging task. The broad range of applications and the intended interaction with the environment require characteristics that differ from common actuation scenarios in industry. The same robot, for example, has to deliver high torques at low speed in one application while it has to provide high dynamics in another. Since robotic actuators are usually attached to the moving structure, they also need to be small and lightweight. In order to reduce positioning errors and to avoid disturbances during reversing motions all gears should be free of backlash. Thus, the requirements for robotic drive trains are manifold. The most important ones are summarized in the following list:

- high torques at low speed or stand still
- low weight
- small sizes
- high dynamics
- high efficiency / low losses

- backlash free gearing
- sensor feedback (position and force-torque)

In the end of the 1990th no commercially available actuators could sufficiently fulfill those needs. Thus, at our institute, permanent magnet synchronous motors were developed that match the requirements. Being combined with very low backlash Harmonic Drive (HD) gears, they constitute high performance robotic actuation units. These units provide high dynamics and high link side torques due to low inertia parts and the high reduction ratios of the HD gears. Further, their low number of components reduces the probability of failure.

In the following, we present the development of our lightweight robotic arms with a focus on our modular actuation units. We begin at the motor stage and progress via the highly integrated actuation modules towards the complete robot.

The DLR brushless Motors

The key components of the DLR drive train concept are the permanent magnet synchronous motors developed at our institute. The so-called “Innen-Läufer-Motor” (ILM: German for “inside rotating motor”) is well suited for highly dynamic tasks involving frequently reversing motions. For maximum performance, all of our motors are sized to comply with available HD gear dimensions.

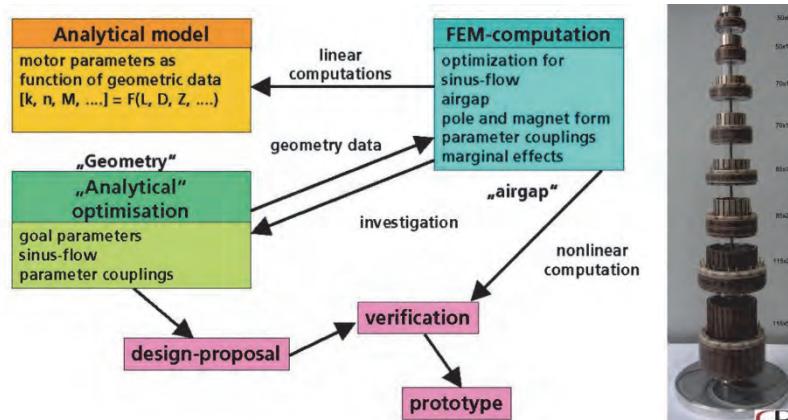


Figure 2: Concurrent engineering for the actuator design and the RoboDrive variations

During the two year development process we strictly followed a concurrent engineering and optimization process (see Figure 2) to achieve high dynamics combined with low losses and low weight. The complete design is based on extensive multi-physics simulations, considering electromagnetic, mechanical and thermal effects. In the final design short copper paths, very dense and optimized windings, strong neodymium rotor magnets and low inertia rotating parts are the main source of the high dynamics. Furthermore, the ILMs consist of a high number of pole pairs (ILM 25 and ILM 38 have 7 pole pairs all others have 10), which allow very accurate positioning and reduce motor ripples. Using wires with a large cross-sectional area allows the motor to handle large currents with low losses and thus, to produce very large torques at low angular velocities. To give a performance example, the torque/current constant of the ILM 25 (stator diameter of 25 mm) is $0.008 \text{ N}\cdot\text{m}/\text{A}$. The motor uses approximately 12.5 A (without saturation effect) to provide a torque of 100 mN-m.

The corresponding HD gears with 1:100 reduction ratio (HFUC8) for example has a nominal torque of 2.4 N-m, a repeatable torque of 4.8 N-m and a momentary peak torque of 9 N-m. The limiting factors for the motor torques are thermal constraints related to the passive cooling. In case of active cooling the torque output of our motors could be even increased. At the time of development the motors achieved a 50% reduction of weight and losses with respect to commercially available units with comparable torque

ratings. Currently, our motors are becoming the state of the art for high performance robotic drives and are commercialized by the company RoboDrive [2].

The DLR Actuator Units

As already mentioned, our motors are developed to comply with the ratings of Harmonic Drive gears. Together with those they form the core of our highly integrated actuation units. Aside those core parts, the units include power, data acquisition, motor control and communication electronics in a very dense package.

The amount of wires has been drastically reduced to two power (one for electronics and one for the motors) two communication lines (SERCOS is a ring) and one emergency stop. Due to the large hollow shaft of the motors these lines can be easily guided through a robot joint and thus remain inside the robot. Furthermore, the actuation units comprise a large set of sensors enabling sophisticated impedance and admittance controllers with underlying high performance torque or position control loops. These sensors are motor side position sensors for commutation and relative position measurement as well as link side absolute position and joint torque sensors (see Figure 3).

Aside the high performance, low weight and low losses, two properties of our actuation units are very interesting for space applications. First, the high torque capacity of the motors allows applying short and very strong “kicks” that could free the unit in case of cold welding within the bearings or the HD stage. Of course, in this case the power electronics has to be designed to supply large currents for a short time.

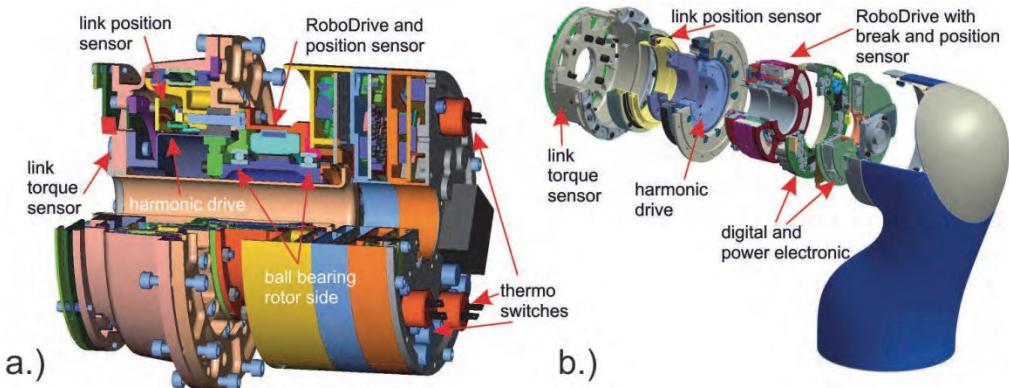


Figure 3: DLR drive train concept a.) ROKVISS unit - ILM70 - HFUC25, b.) Joint module of the LWR III

The second advantage is that the low number of mechanical components reduces the probability of failure (see Figure 4). In the following, the mechanical components of one joint unit are listed:

- stator
- rotor with magnets
- rotor bearing
- HD wave generator (WG)
- HD flex spline (FS)
- HD circular spline (CS)
- output bearing.

Within these components the rotor bearing and the WG bearing are the most crucial elements since the associated friction has to be overcome by the motor torque directly.

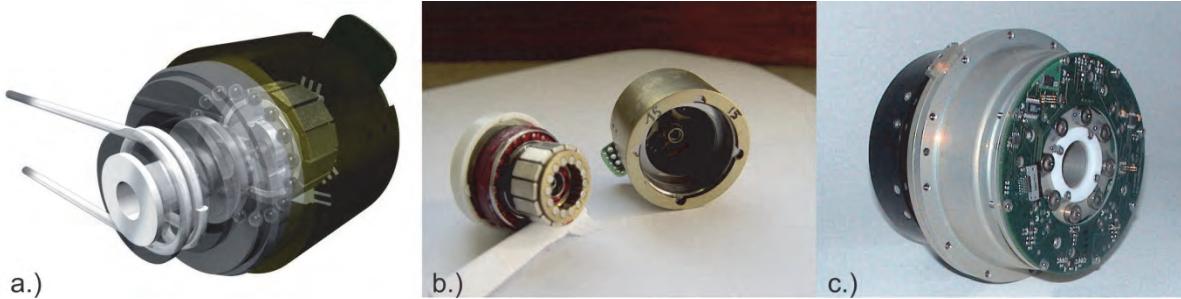


Figure 4: DLR drive train concept a.) DEXHAND unit CAD, b.) DEXHAND unit photo, c.) ROKVISS unit photo

In summary, the design of our actuation units allows highly dynamic and powerful operation as well as precise control in fine manipulation tasks. An example for the usage of this drive train concept within a space application is the joints of our ROKVISS experiment that is described in more detail later.

The DLR modular Arm

Developing, building and controlling lightweight robotic arms for a large variety of applications are a research focus at the DLR Robotics and Mechatronics Center (RMC). Starting with the Lightweight Robot I (LWR I) presented in 1994 via the LWR II of 1999 to the current model LWR III from 2003, we gained a lot of experience within this field. Due to the success within the research community and an initial market demand for such technology, in 2006 the KUKA GmbH started to commercialize the LWR III. A first small batch series was mainly provided to different research institutions.



Figure 5: a.) LWR III, b.) LWR as a KUKA product, c.) modular robot system “Justin” with 54 DOF

Currently, around hundred units are sold and the car manufacturer Daimler sees high potential for a factory-wide deployment of the LWRs. For them, especially attractive is the possibility of switching between torque-based and position-based control concepts. This is very promising for the solution of challenging assembly tasks.

Besides the innovative impedance and admittance control algorithms developed for our lightweight robots, its modular joint-link concept is one of the reasons for its success. Hereby, the underlying modular assembly system with only a few basic components concerning joint mechanics, electronics and links allows composing completely different configurations in a short time. Thus with three different single degree of freedom (DOF) robot joints and a two DOF wrist joint, different kinematic configurations can be easily assembled. For example, in addition to the symmetric version an asymmetric version (Figure 6) can be built. This is particularly interesting for space applications where the arm needs to be folded for stowing.

Again the design process for the joint and link modules followed a concurrent engineering process including kinematic and dynamic simulations as well as an FEM analysis. Supported by a link component library with variable parameters, virtual prototypes could be assembled, tested and optimized. One special result of this process is the ball-shaped two axis wrist joint (see Figure 7). This joint imitates the human wrist but achieves much higher mobility. Its short distance between the wrist pitch axis and the tool-center-point (TCP), helps to reduce the motion of the lower robot joints in case of changes of the TCP orientation. Furthermore, the wrist design enables two kinematic configurations, a common configuration with roll-pitch-roll axis and optional a roll-pitch-pitch configuration. To reconfigure the joint the short standard flange simply has to be replaced with an extended 90° bend flange. Another advantage of the wrist is that its cardan joint avoids singularities in an extended position and the reduced joint mass allows carrying larger payloads.

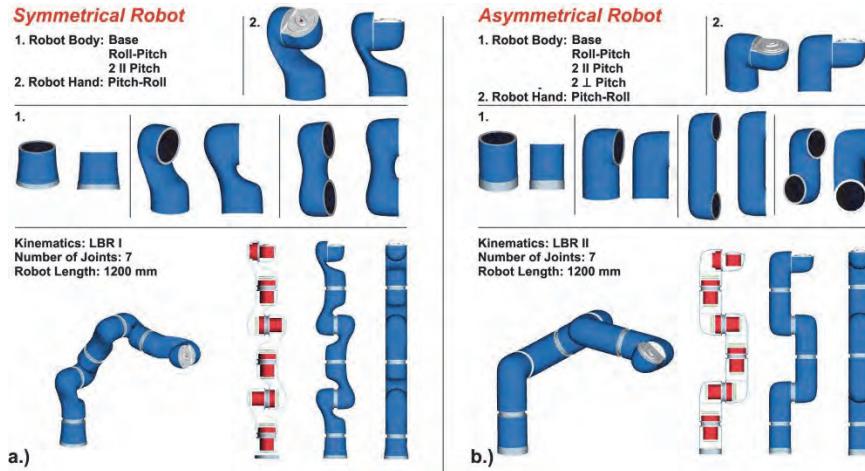


Figure 6: a.) symmetric LWR modules ,b.) unsymmetric LWR modules

The DLR lightweight robots are very well suited for a large variety of service robotics applications with their modular assembly, kinematic redundancy (7 DOF), the torque controlled joints, the low inertia and a load to weight ratio of nearly 1:1,. Some examples at our institute are the humanoid "Justin", the three arm co-worker scenario, several single arm manipulation tasks as well as the bi-manual input station for robotic experiments. The concept of highly integrated modular actuation units is further improved for the new DLR hand arm system as well as the DEXHAND. With their low power consumption and the above mentioned features our drive trains and complete robots provide interesting capabilities for future space missions [3].

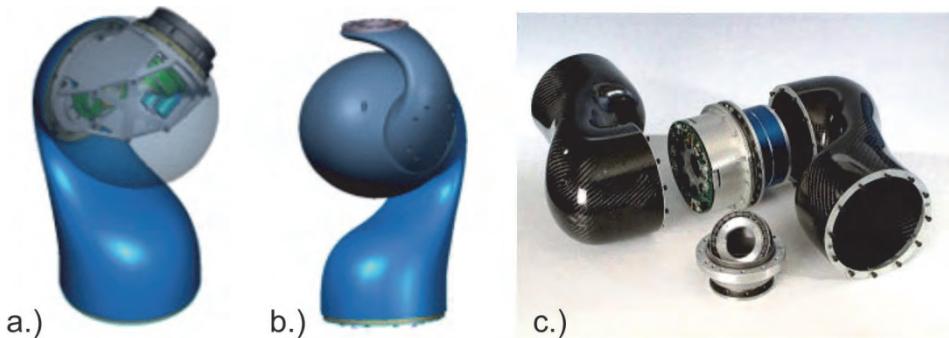


Figure 7: LWR cardanic hand module joint a.) roll-pitch-roll configuration, b.) roll-pitch-pitch configuration c.) LWR joint modules

ROKVISS

The German space robotic project ROKVISS (German:"Roboter Komponenten Verifikation auf der ISS") has just been finished. The system has been returned to earth early 2011 and the hardware is now subject to detailed analysis and advanced tests.

ROKVISS (see Figure 8) aims at the space qualification of DLR's LWR modules (modified for a space environment) with a reduced setup of a 2 DOF robot arm on the ISS. With this experiment DLR could prove the concept can use partly components-off-the-shelf (COTS) within a very tight and highly integrated mechatronic device based on the modular joint concept discussed previously.

After more than five years of successful operation and without any failure the innovative mechanical and electronic concept seems very promising for the use in space projects. Those projects are in the wide range of future robonaut applications as well as planetary robotic missions. Indeed what we are still missing in space are fast signal transmissions. One relay satellite could provide signal round trip delays of 0.5 seconds within a coverage times of around 40 minutes. This allows even haptic feedback, which is a major idea of our advanced telerobot control strategy using visual and haptic feedback [4].

ROKVISS was also a telerobotic demonstrator with real-time stereo-video transmission and tactile feedback. The telerobot success was the second major achievement of ROKVISS, besides the component verification. We believe that realistic telerobotics probably combined with partial or full autonomy will be needed in future space robotic applications [5-7].



Figure 8: ROKVISS photo of the experiment mounted on the ISS

The following subsection deals with the mechanical design and the detailed structure of the ROKVISS robot describes the friction analysis and shows preliminary results.

Mechanical System Design

In Figure 8a the overall ROKVISS is shown, while Figure 8b shows the joints as described in the previous section. Figure 8c shows ROKVISS in its position outside the ISS at the Zvezda service module.

The ROKVISS experiment consists of a small robot with two torque-controlled joints, mounted on a Universal Workplate (UWP). Each joint module consists of a power supply, a controller board, a power converter, the drive train and a torque sensor. Inside the robot there are 2 joint modules, a stereo camera, an illumination system, an earth observation camera and a power supply. A mechanical contour device is mounted on the UWP for verifying the robot's functions and performance (see Figures 8a and 8c).

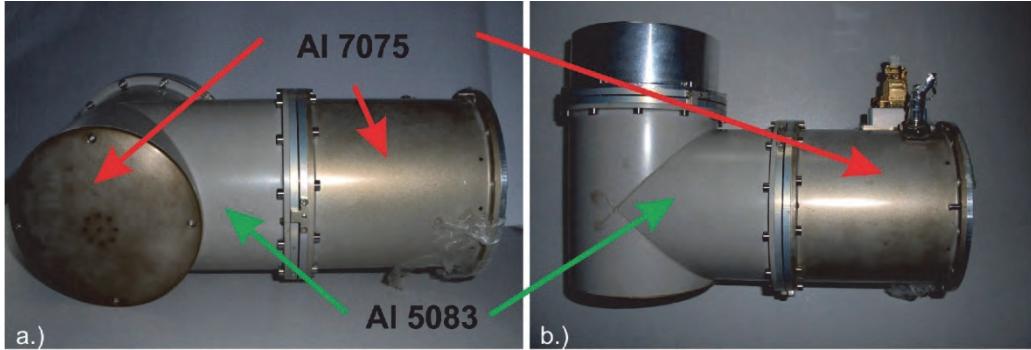


Figure 9: ROKVISS FM modules with color changes on the surface after return to earth

These two robot joints have been extensively tested and the joint parameters have been identified by repetitively performing predefined robot tasks in an automatic mode, or based on direct operator interaction. The automatic mode is necessary due to the fact that communication constraints limit the direct link experiment time to windows of only up to seven minutes when the ISS passes over the tracking station German Space Operations Center (GSOC). Figure 9 shows the returned two joint modules. After five years of operation on ISS differences on surface with its anodic treatment (LN9368 I 2101) of the two different aluminum alloys (AI 7075 | AI 5083) are obvious [8, 9].

Friction Analyses

The preliminary results of the on-orbit identification show that the total friction for joint 1 in space increased by about 50% compared to the friction on ground, taken at 20°C, under normal atmospheric pressure (Figure 10). However, only a small further degradation of the parameters has been observed so far during the mission. This friction change will be analyzed in the upcoming tests to determine if the lubricant (Braycote 601) and/or the guidance condition influenced this effect. The temperature dependency of the parameters is close to the range of identification uncertainty (Figure 10) [10].

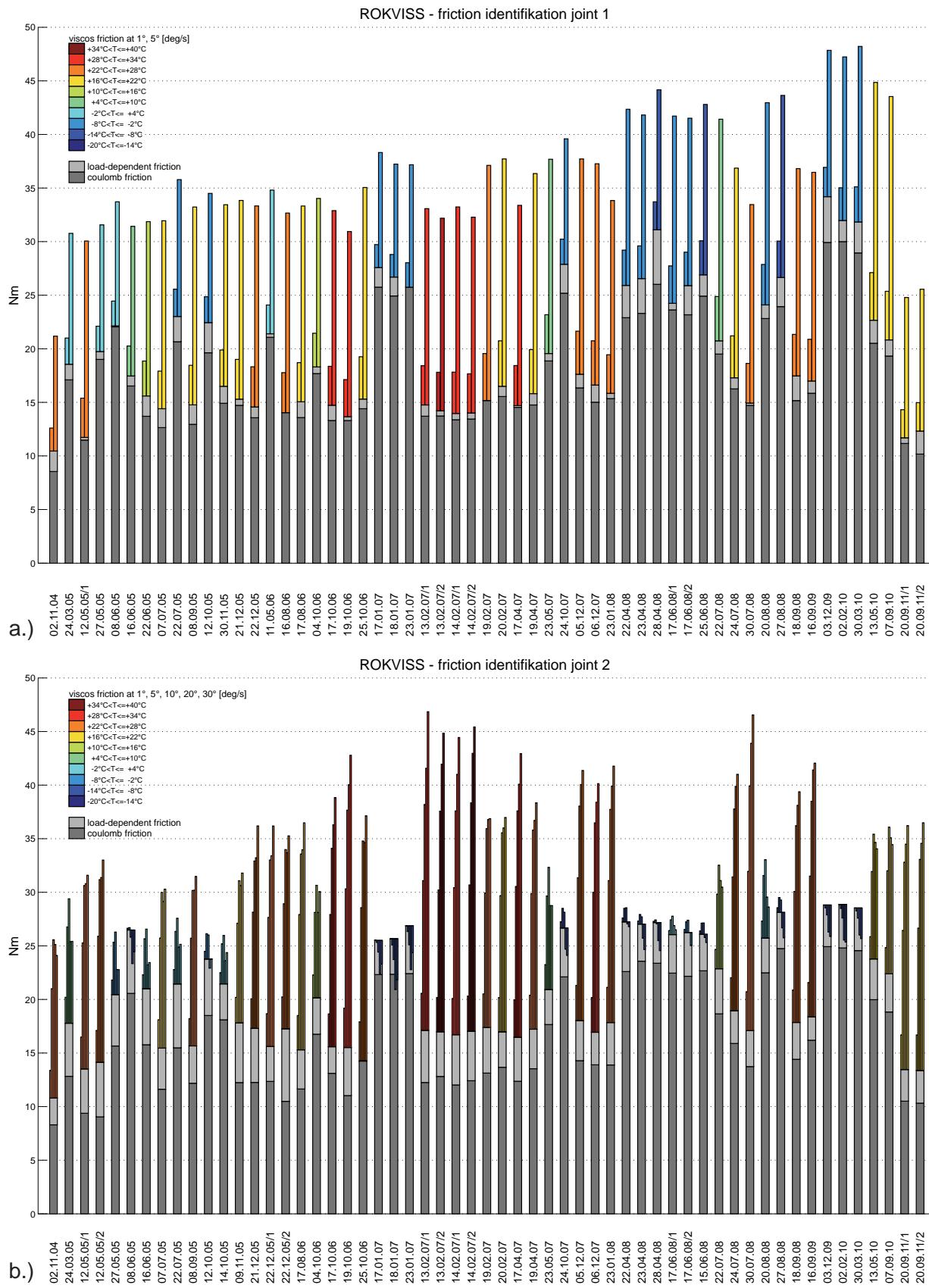
Conclusion for the Friction Identification

The friction in the two joints increased initially, already at the first experiment in space compared to the values measured on ground, but remained rather constant afterwards. All the controllers were robust with respect to these changes. The friction changes of joint 1 and joint 2 are different. Friction in joint 1 has the same structure as on ground, but values increased by 50%. The friction in joint 2 shows no more significant viscous friction and the total increase is lower than 20%. Since the same lubricant was used for both joints (Braycote 601), further experiments are planned in order to explain the different behavior.

To provide a better fit of measured and simulation data, a nonlinear (third order polynomial) function is required. However, due to the higher number of optimization parameters, their variance over different experiments is greater. A trajectory with a higher number of distinct velocities is needed in order to reduce the variance of the results.

Stiffness Identification

The main sources of elasticity in the joints are the flex splines of the HDs and the torque sensors. The elasticity is identified by contacting a rigid surface with the tip of the robot and by commanding a slowly changing force to the joints. Since the torque is measured after the gear-box, the stiffness can be easily identified with the available torque and position signal. The model torque is computed as a product of position increment and stiffness. The stiffness for joint 2 has a value around $4900 \text{ N}\cdot\text{m}/\text{rad}$ in space.



No significant differences between the stiffness values on the ground and in space are observed. Still, a change of about 15% can be observed. However, this deviation is within the range of the load dependent stiffness variation and the controllers are designed to be robust with respect to such uncertainties.

Conclusions

Though the ROKVISS mission was planned for one year, already after 8 months of operation the main goals of the mission were achieved. The hardware proved to work reliably under space conditions. The dynamical parameters of the joints, although somewhat different than on ground, show a small variation over time and with temperature. The controller structures proved to be robust with respect to these variations and to the used COTS elements. Within the cooperation with the Russian Institute for Robotics and Cybernetics in St. Petersburg (RTC) the mission of ROKVISS has been extended step by step up to end 2010. Then the collective decision has been taken to bring the main parts of ROKVISS down to earth. Currently we are in close cooperation with the RTC to accomplish tests and analysis of these modules. Initially, complete segment tests are planned to identify the behavior and especially understand the correlation between conditions on ISS, thermal vacuum chamber in the test facility and the conditions in the laboratory environment. With this experience we may gain the competence to build "Justin" for space application.

DEXHAND

The development of a torque controlled multi-fingered hand is also a domain in which the DLR has a long history [11–14]. The DEXHAND is designed to be able to perform a set of generic space oriented tasks. For example, the removal of a multi layered insulation (MLI) cover or the manipulation of a handle. This section presents how the design concept and the architecture of the hand are selected based on the hand capability requirements. As discussed in the previous sections, the DEXHAND is in line with the DLR overall goal to develop a complex two handed system for space application such as EVA assistance or substitution of astronauts [15, 16].

The first part that follows presents the main requirements for the system and explains how the general concepts have been selected and the overall architecture is described. The second part "reveals" the mechanical structure, the tendon actuation system and the torque sensor implementation. The fourth part gives an overview of the control system, controller architecture and the software distribution.

Requirements and Concept

The design of the DEXHAND is driven by its required capabilities. Some constraints are purely technical: operating temperature, maximum fingertip forces, joint velocity, but others are functional, such as grasping and operating a pistol grip tool (a space version of an electric driller). The desired capabilities must be translated into technical requirements that result in a trade-off between system complexity, capabilities, reliability, volume, weight and cost. Finally top level functional requirements have been defined, such as the DEXHAND shall be able to grasp the following EVA tools and to support their operations: Pliers, Scissors, Hammer, Tether, Scoop, Cutter, Allen Wrench et cetera.

Successful operation of the tools implies force closure of the grasp with respect to the preferably form closure which should be achieved. In the robotic community, hands are ranging from the simplest grippers to the most advanced biomimetic devices. The design space (i.e., the possible design solutions) of hands is extremely large, therefore, the first part of the project was to select a concept that would fit to the initial requirements. Examples of parameters that must be selected are:

- number of fingers
- number of degrees of freedom (DOF) per finger
- number of actuated DOFs
- placement of the fingers in the hand
- shape of the fingertips

- size of the fingers
- etc...

Certainly, each finger DOF brings more capabilities but increases the number of parts. The use of multiple small actuators instead of one large actuator, increases the capabilities to distribute power losses, might provide redundancy, and usually provides a better form factor. However, the raw power density is reduced. The control complexity and the number of sensors must also be increased in order to take advantage of the available degrees of freedom.

The principle parameters are selected based on the manipulation experience gathered with the DLR Hand II and DLR/HIT hand. A parameter refinement is done by simulating grasps with each object of the EVA tool list. For example, in order to perform trigger actuation of the pistol grip tool, while maintaining tool stability, it appears that at least three fingers are required. For fine manipulation, the shape of the fingertips is playing a key role. Several shapes are compared with respect to rolling, maximum load and the ability to pick up small objects. The DEXHAND is using a variable curvature with a flat end fingertip shape.

Finally, the DEXHAND development differs from the hand developments at DLR. This time the modularization borderline changes (see Section 1.2). For the LWR III the border of the modularization was at joint level. The Hand II (as well as DLR/HIT hand) modularization borderline is based on fingers. While the DEXHAND and as well the Hand Arm System (HaSy [14]) are based on motor modules as previously discussed.

Overall Architecture

The DEXHAND system is developed for use with a robotic arm (Dexarm) designed and realized by Selex Galileo. The hand has 12 actuated DOFs, distributed in 4 fingers with 3 degrees of freedom each. Figure 11 presents the latest state of the CAD model of one Finger and Figure 12 shows two photos of the DEXHAND prototype with housings and without. The actuation system is based on geared motors followed by a tendon transmission system (see first section). The motors are controlled using a combination of a DSP, FPGA and motor controllers. Joint torque measurements are available and realized with full bridge strain gauge sensors. Multiple temperature sensors are available to protect the system against overheating and freezing. The control system of the hand is able to run entirely inside the hand. The DEXHAND is required to communicate over a CAN bus with a common VxWorks communication controller. The communication to control the Dexarm is routed as well through a real-time VxWorks system. It will allow the hand and the arm controllers to be tightly synchronized in the future.

In the DEXHAND, modular fingers are used in order to increase the system reliability. It also improves the cost efficiency of the project. However, based on a kinematic analysis and the experience from the DLR Hand II, a special finger is used for the thumb. As shown in [17], the thumb deserves a special treatment in order to increase the hand dexterity. For example, in order to properly oppose to the other fingers the thumb should have at least twice the maximum fingertip force. The DEXHAND fingers are design to actively produce a fingertip force of 25 N (for the stretched finger) while withstanding 100 N passively.

Mechanical Design

The transmission system is using polymer Dyneema tendons and harmonic drives in order to bring the motor torque to the joints. The concept keeps the extremities (the fingers) with radiation uncritical electronics. The shielding strategy consists in housing the whole electronic system in an aluminum shell with at least 2 mm thickness.

This leads to a fully electro-magnetic interference (EMI) sealed hand body containing:- the drives, the power electronics and the communication electronics. The only exceptions are the torque sensors, based on strain gauges, and some temperature sensors, which have to be placed in the fingers. The design successfully encases all electronic systems in its protective housing.

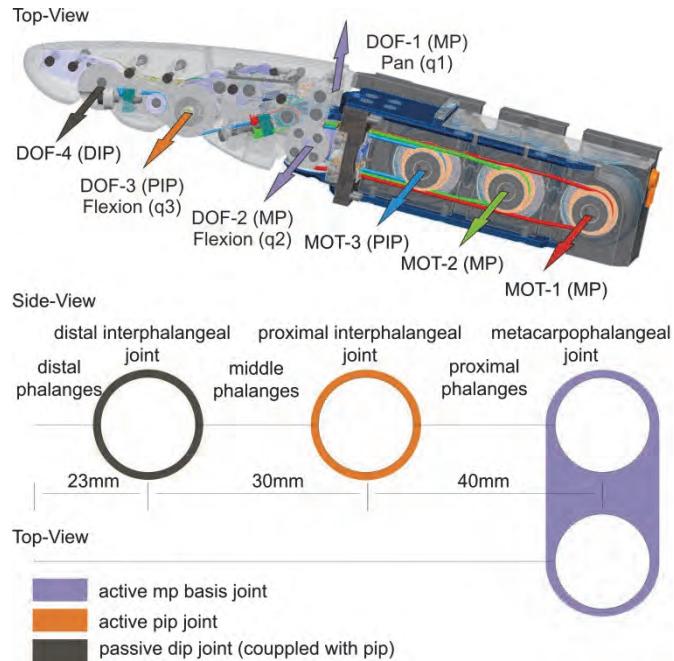


Figure 11: Actuation principle of the DEXHAND fingers

The cardanic metacarpophalangeal (MP) base joint is driven by two motors. Due to the coupling of the tendons in the MP joint the two motor torques can be used together for one DOF of the base joint. This aspect opens the possibility of using the same motors for the base joint and the proximal inter-phalangeal (PIP) joint. Indeed, due to the difference of lever length (pulley radius), the required torques are scaled dependent to each joint. The PIP joint has a fixed coupling with the distal inter-phalangeal joint (DIP) with a ratio of 1:1. In Figure 11 the section lengths, joint positions and definitions are shown.

The coupling matrix P , which relates motor velocity $\dot{\theta}$ with joint velocity \dot{q} is:

$$\dot{\theta} = P \dot{q} \quad (1)$$

$$P = \frac{1}{r_p} \begin{pmatrix} r_1 & r_2 & 0 \\ -r_1 & r_2 & 0 \\ r_{13} & r_{23} & r_3 \end{pmatrix} \quad (2)$$

Where r_p is the motor pulley radii, r_1 , r_2 and r_3 , are the joint pulley radii, and r_{13} and r_{23} are the pulley radius of the PIP tendons in the base. Given that the coupling matrix is not configuration dependent, the relationship can be integrated in:

$$\theta = P q \quad (3)$$

The motor unit for DEXHAND has been developed based on the DLR / RoboDrive (see section1) [2] ILM 25 motor including the gear of a harmonic drive HFUC8 with a transmission ratio of 100:1. The whole unit fits into a cylinder of 27-mm diameter and a length of 17.5 mm with a weight of 46 g (see section 1 Figure 4). The unit provides a continuous torque of 2.4 N-m with peaks up to 9 N-m which is the maximum peak torque of the gearing. In the DEXHAND, the motor has been electronically limited to 2 Nm for power reasons. Each actuated joint has a reference mark in the middle of its motion range. These reference marks are composed of a small magnet and a Hall-effect sensor located in the actuated joint. The joint torque measurement is implemented using a sensing body and full bridge strain gauges sensors (Figure 12). The torque sensors are all physically located in the proximal finger link. Therefore, the sensor for the PIP/DIP-joints measures the reaction torque of the coupling tendons.

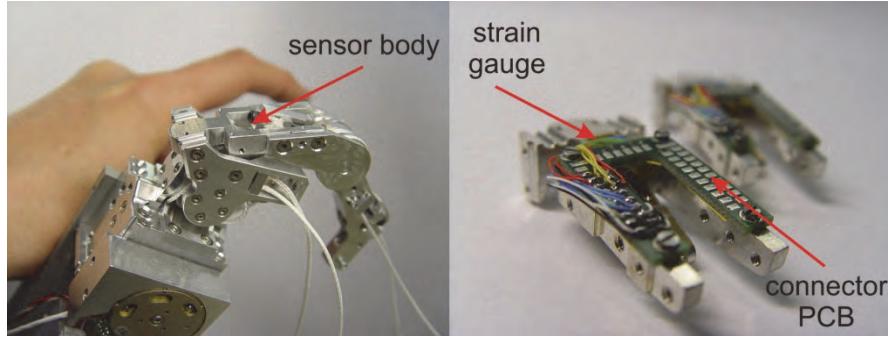


Figure 12: a.) Finger without housing, b.) Strain gauge sensor body

All sensors, except one of the reference sensors of the MP joint, are located and mounted in one mechanical part. This part also contains the pull relief of the wires, as well as the shield connection of the cable from the fingers to the electronics in the palm. This simplifies the assembly and the maintenance of the finger. Special care was taken in the design of the sensor body in order to prevent temperature drift. The force measurements obtained in a thermal chamber from -50° to $+70^{\circ}$ confirmed the measurement stability. The palm structure consists of 11 main segments. These segments are massive aluminum parts to improve heat transfer and increase the thermal inertia. The modules of the DEXHAND are four different ensembles representing the ring-, middle-, index- and thumb finger actuation units. A unit includes the tendon guidance from the motor pulleys to the MP and DIP joint. The palm surface mainly consists of the outer shell parts. Furthermore, all parts are designed without sharp edges. They are optimized for ideal thermal allocation and minimum resistivity (Figure 13 shows the hand without the palm grasp pads).

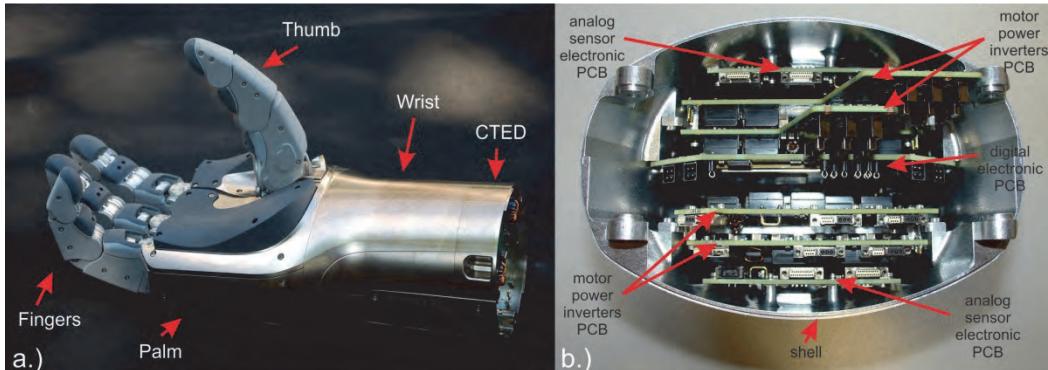


Figure 13: a.) Section view of DEXHAND with its components, b.) PCB placement in the wrist

The wrist houses all electronic parts. This includes the analog, the digital and the power circuit boards. The electronic boards are coupled to the palm assembly with connectors. The housing of the DEXHAND is composed of 2-mm aluminum shells. It is fully closed to provide good EM compatibility. During electro static discharge (ESD) tests with 4-kV impulse at the fingertip and palm structure no failure has been detected. The final DEXHAND design is presented in Figure 13a. Furthermore the compact and also fully integrated housing of the electronic inside the wrist is shown in Figure 13b.

Software and Control

As presented in the previous section, the hand comprises a DSP and a FPGA. The FPGA is used for low level, high speed functional blocks. In the DSP, functional blocks such as calibration tables, impedance control loop, communication, and safety systems are implemented. The controller itself is an impedance controller running at 1 kHz.

The communication to the system is done via a CAN bus, on which no hard real-time data is allowed. The commands to the system are always asynchronous. In order to establish telerobotic scenario, a VxWorks

real-time system is used to establish the data exchange between the data glove data source and the DEXHAND. Moreover, the system is used to monitor the communication bus and to provide a TCP/IP communication interface from any standard operating system.

Conclusion

After more than 20 years of torque-controlled lightweight robot development the third generation becomes a useful product now, where we have tried to use all present day available simulation and computational technologies to approach the technical limits. Taking into account its weight of 13-14 kg, its typical power consumption of little more than 100 watts, its load capability of around 8 kg, its motion speed based on maximal joint speeds of 180 deg /sec, it is probably one of the lightest robots that have been built so far. It is the basis for DLR's future space robot developments

The presented ROKVISS project has proven the capability of using the lightweight robot and motor unit concepts for space application. The experience acquired with the ROKVISS project influenced many decisions. We believe that upcoming tests and results from analyzing the returned hardware will even further improve the DLR space developments.

Furthermore this paper presented an overview of the DEXHAND project with its 12 motor units, its tendon driven actuation principal and its overall mass of 3 kg. The fingers proved to be capable of applying 25 N at the fingertip, and can withstand 100 N impact loads.

It should be noted that the biggest issue in terms of thermal control of DEXHAND are the digital electronic circuits, the power inverters and not the motors. Indeed, they have very little dissipation capabilities. The EM compatibility issue is mainly solved by using a thick enclosing aluminum shell, for the radiation issues only space qualified parts are used. The used commercial parts are qualified with TID tests. The control system runs entirely in the DEXHAND, complying with the very low communication bandwidth requirements.

Acknowledgment

We would like to thank the Bavarian Ministry that has made mechatronics a key topic of Bavaria's high tech offensive with lightweight robotics and articulated hands as central demonstrators. The authors would like to thank the DEXHAND and ROKVISS team at DLR, as well as, the ESA for the opportunity to develop an EVA capable hand. The DEXHAND Project has been founded with the ESA Contract No. 21929/08/NL/EM.

References

- [1] M. A. Diftler, R. O. Ambrose, S. M. Goza, K. Tyree, and E. Huber, "Robonaut Mobile Autonomy: Initial Experiments," in IEEE International Conference on Robotics and Automation, Barcelona, Spain, April 2005, pp. 1437 – 1442.
- [2] RoboDrive (2009) Website of the RoboDrive GmbH Company. [Online]. Available: <http://www.robodrive.de/>
- [3] G. Hirzinger, N. Sporer, A. Albu-Schäffer, M. Hahnle, R. Krenn, A. Pascucci, and M. Schedl, "DLR's torque-controlled light weight robot iii-are we reaching the technological limits now?" in Proc. IEEE Int. Conf. Robotics and Automation ICRA '02, vol. 2, 2002, pp. 1710–1716.
- [4] G. Niemeyer, C. Preusche, and G. Hirzinger, Handbook of Robotics. Springer Verlag, 2008, vol. ISBN 978-3-540-23957-4, ch. Telerobotics.

- [5] C. Preusche, D. Reintsema, K. Landzettel, M. Fischer, and G. Hirzinger, "DLR on the way towards telepresent on-orbit servicing," in Proc. Mechatronics & Robotics 2004, 2004.
- [6] C. Preusche, D. Reintsema, K. Landzettel, and G. Hirzinger, "ROKVISS - towards telepresence control in advanced space missions," in Proc. 3rd. International Conference on Humanoid Robots (Humanoids 2003), Munich and Karlsruhe, Oct. 2003.
- [7] B. Schäfer, K. Landzettel, A. Albu-Schäffer, and G. Hirzinger, "ROKVISS: Orbital testbed for telepresence experiments, novel robotic components and dynamics models verification," in Proc. 8th ESA Workshop on Advanced Space Technologies for Robotics and Automation (ASTRA), Noordwijk, The Netherlands, Nov. 2-4 2004.
- [8] K. Landzettel, B. Brunner, R. Lamariello, C. Preusche, D. Reintsema, and G. Hirzinger, "System prerequisites and operational modes for on orbit servicing," in Proc. ISTS International Symposium on Space Technology and Science, Miyazaki, Japan, May 30-June 6 2004.
- [9] G. Hirzinger, K. Landzettel, and et al., "ROKVISS robotics component verification on ISS," in Proc. of 'the 8th Int. Symposium on Artificial Intelligence, Robotics and Automation in Space - iSAIRAS, Munich, Germany, 2005.
- [10] A. Albu-Schäffer, W. Bertleff, B. Rebele, B. Schäfer, K. Landzettel, and G. Hirzinger, "Rokviss - robotics component verification on ISS current experimental results on parameter identification." in ICRA. IEEE, 2006, pp. 3879–3885.
- [11] J. Butterfaß, G. Hirzinger, S. Knoch, and H. Liu, "DLR's Multisensory Hand Part I: Hard- and software architecture," Proceedings of the IEEE Int. Conf. on Robotics and Automation, 1998.
- [12] C. Borst, M. Fischer, S. Haidacher, H. Liu, and G. Hirzinger, "DLR hand II: experiments and experiences with an anthropomorphic hand," in ICRA, 2003, pp. 702–707.
- [13] Z. Chen, N. Y.Lii, T. Wimboeck, S. Fan, M. Jin, C. H. Borst, and H. Liu, "Experimental study on impedance control for the five-fingered dexterous robot hand DLR-HIT II," Proceedings - IEEE IROS, 2010.
- [14] M. Grebenstein and P. van der Smagt, "Antagonism for a highly anthropomorphic hand arm system," Advanced Robotics, no. 22, pp. 39–55, 2008.
- [15] A. Wedler, M. Chalon, and et al., "DLR's space qualifiable multi-fingered dexhand," in Proc.:11th Symposium on Advanced Space Technologies in Robotics and Automation (ASTRA), vol. 11, ESA. ESA/ESTEC, Noordwijk, the Netherlands: ESA, 12 14 April 2011, p. Session 3a.
- [16] M. Chalon, A. Wedler, and et al., "Dexhand: A space qualified multi-fingered robotic hand," in Proc. IEEE Int Robotics and Automation (ICRA) Conf, 2011, pp. 2204–2210.
- [17] M. Chalon, T. Wimböck, M. Grebenstein, and G. Hirzinger, "The thumb: Guidelines for a robotic design," in IROS, 2010.

Mars Science Laboratory Rover Integrated Pump Assembly Bellows Jamming Failure

Michael R. Johnson^{1*}, Joel Johnson*, Gajana Birur*, Pradeep Bhandari* and Paul Karlmann*

Abstract

The Mars Science Laboratory rover and spacecraft utilize two mechanically pumped fluid loops for heat transfer to and from the internal electronics assemblies and the Radioisotope Thermo-Electric Generator (RTG). The heat transfer fluid is Freon R-11 (CFC-11) which has a large coefficient of thermal expansion. The Freon within the heat transfer system must have a volume for safe expansion of the fluid as the system temperature rises. The device used for this function is a gas-over-liquid accumulator. The accumulator uses a metal bellows to separate the fluid and gas sections. During expansion and contraction of the fluid in the system, the bellows extends and retracts to provide the needed volume change.

During final testing of a spare unit, the bellows would not extend the full distance required to provide the needed expansion volume. Increasing the fluid pressure did not loosen the jammed bellows either. No amount of stroking the bellows back and forth would get it to pass the jamming point. This type of failure, if it occurred during flight, would result in significant overpressure of the heat transfer system leading to a burst failure at some point in the system piping. A loss of the Freon fluid would soon result in a loss of the mission. The determination of the source of the jamming of the bellows was quite elusive, leading to an extensive series of tests and analyses. The testing and analyses did indicate the root cause of the failure, qualitatively. The results did not provide a set of dimensional limits for the existing hardware design that would guarantee proper operation of the accumulator. In the end, a new design was developed that relied on good engineering judgment combined with the test results to select a reliable enough solution that still met other physical constraints of the hardware, the schedule, and the rover system.

Introduction

The Mars Science Laboratory Mission - Overview

The mission consists of four discrete sections or phases:

1. Launch Phase
2. Cruise Phase
3. Entry, Descent, and Landing Phase
4. Surface Operations Phase

An exploded view of the assemblies that make up the spacecraft as it heads to Mars is shown in Figure 1. The Cruise Stage is jettisoned just prior to Entry, Descent, and Landing (EDL). The Backshell and Heat Shield are necessary components during the Entry portion of EDL. The Descent Stage contains fuel and rocket engines to provide a powered descent to the surface with a deployed Rover for a soft touchdown. After the Rover is on the surface, the Descent Stage is cut loose and flies away from the Rover's location.

* Jet Propulsion Laboratory, California Institute of Technology, Pasadena, California

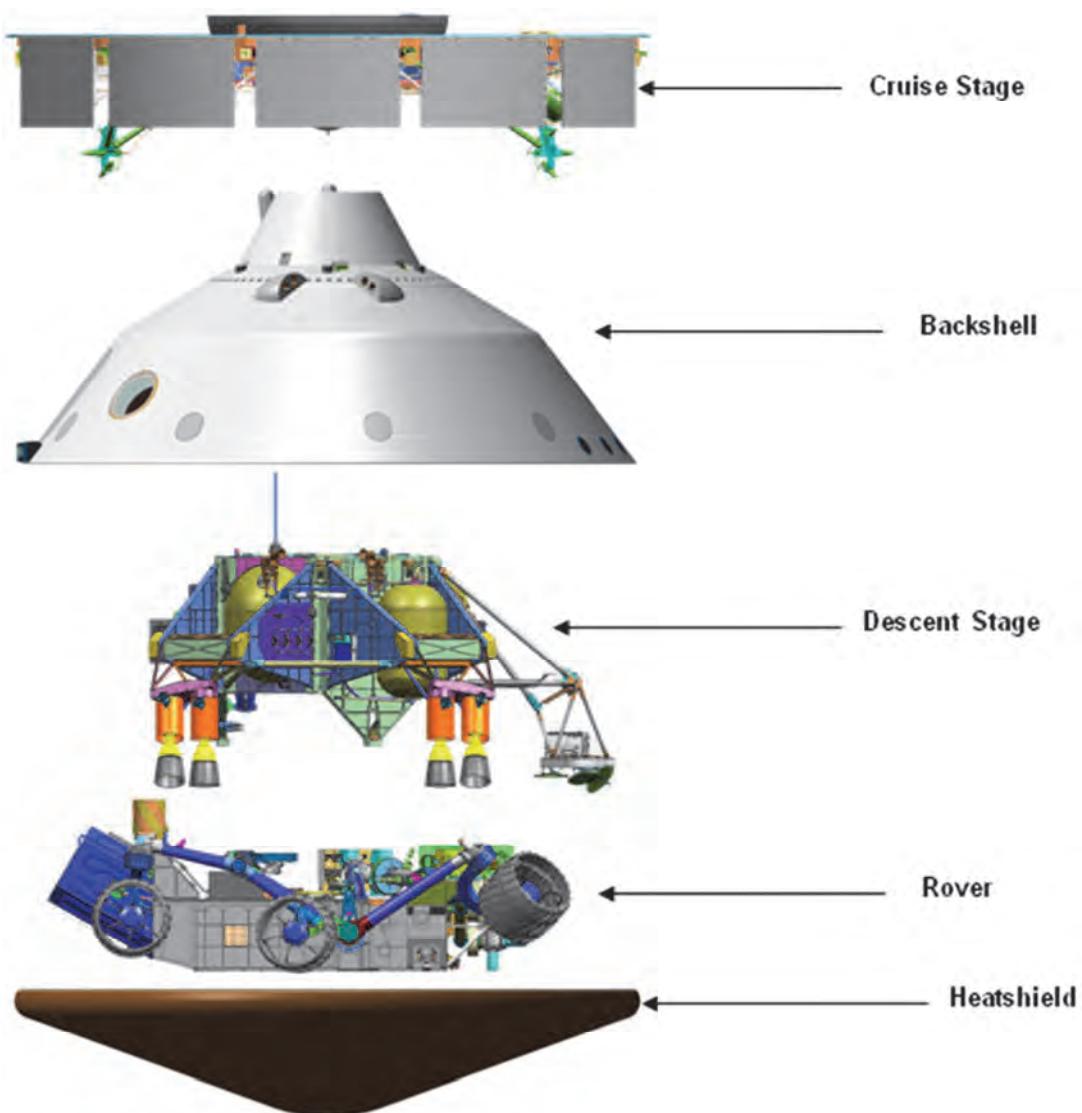


Figure 1. Mars Science Laboratory Spacecraft Major Assemblies

The Mars Science Laboratory Mission – Thermally

The cruise portion of the mission consists of the rover and cruise stage traveling from Earth to Mars over a period of 8½ months. During this time, power is provided to the cruise stage and the rover by solar panels located on the cruise stage and an RTG attached to the rover chassis. The RTG is located inside the spacecraft entry body. Heat generated by the RTG, as well as waste heat from the electronics, is transferred to radiators on the cruise stage using a system of pipes containing Freon R-11. This heat management system is called the Heat Rejection System (HRS). There are two separate fluid systems, one that is part of the cruise stage (CHRS), and one that is part of the rover assembly (RHRHS). More detail on these two systems is provided in references 1 and 2. The CHRS is no longer needed after the several month cruise period to Mars so it is vented and then jettisoned from the entry body with the Cruise Stage just prior to the Entry, Descent, and Landing phase. The separate fluid system within the rover must continue to operate throughout landing and the 690 Earth-day primary surface mission, as well as any extended mission time. The main function of the heat transfer system is to distribute heat around the rover assembly for the purpose of maintaining a smaller operating temperature range for the rover electronics than the environment would otherwise require. Heat is transferred from the RTG to the internal Rover Avionics Mounting Plate (RAMP) during cold periods. The fluid is directed to radiators when excess

heat must be exhausted. By utilizing the heat from the RTG and the fluid Heat Rejection System (HRS), the temperature range for the internal electronics assemblies is substantially reduced from -128°C to +55°C to a smaller range of -40°C to +55°C for the length of the mission.

Thermal Hardware Description

The thermal system for the rover and cruise stage are very similar. The hardware consists of an Integrated Pump Assembly (IPA), a gas-over-fluid accumulator, a significant length of fluid tubing, and heat transfer surfaces. The IPA consists of a motor, centrifugal pump, motor drive electronics, and directional valves for maintaining the coolant temperature. The valves direct more or less Freon to the radiators depending on the temperature of the coolant. A representation of the internal piping of the rover is shown in Figure 2 and the piping on the cruise stage is shown in Figure 3.

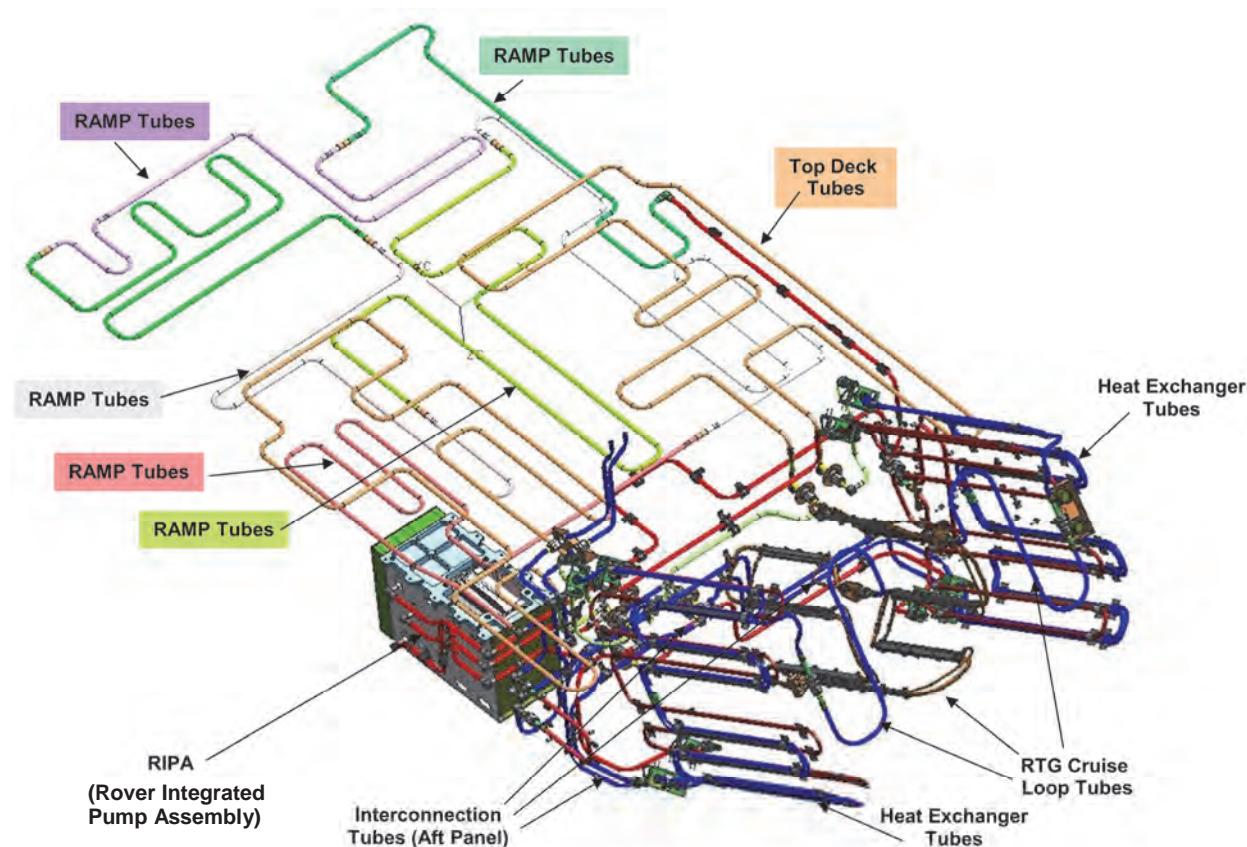


Figure 2. Heat Transfer System of Piping in the Rover and Around the RTG

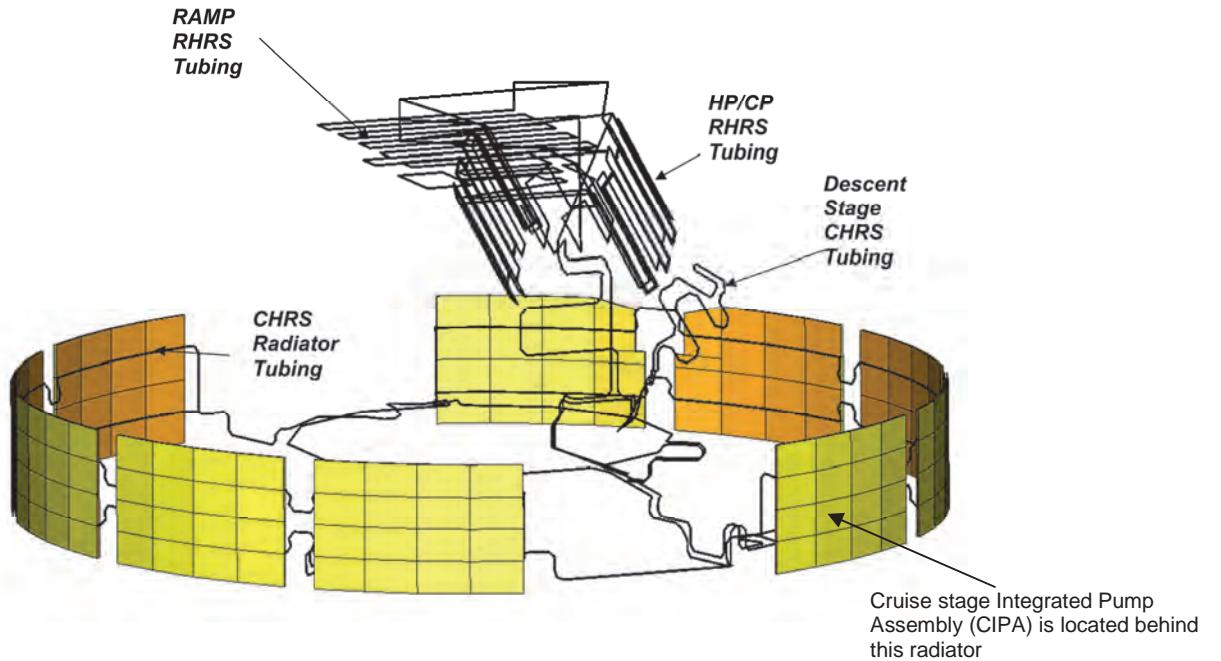


Figure 3. Heat Transfer System of Piping in the Cruise Stage and Relationship to the Rover System of Piping

Components of the Integrated Pump Assembly (IPA)

There are two separate IPA units, one on the Cruise Stage and the other on the Rover. The Cruise Stage IPA is called the CIPA and the Rover IPA is called the RIPA. A model of the RIPA is shown in Figure 4. The pumps provide the circulation power for the Freon R-11, the pressure transducers provide telemetry back to the system indicating the health of the fluid system, the directional valves divide the flow between the radiators and the RTG, and the accumulator provides expansion volume for the fluid in the closed system. The accumulator expansion volume is absolutely necessary because of the large thermal volumetric coefficient of expansion of the Freon of 20% per 100 degree Celsius change in temperature. Providing a volume for the Freon to expand into prevents the following failures:

- Mechanical failure of the system tubing due to over-pressurization
- Bubble generation from low pressure

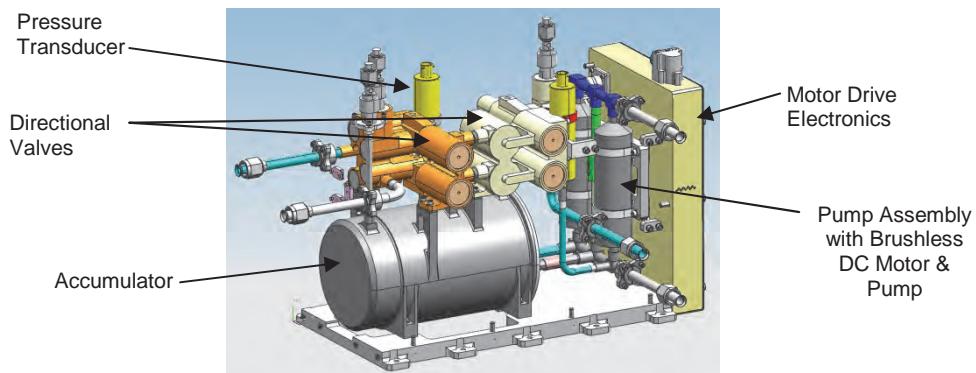
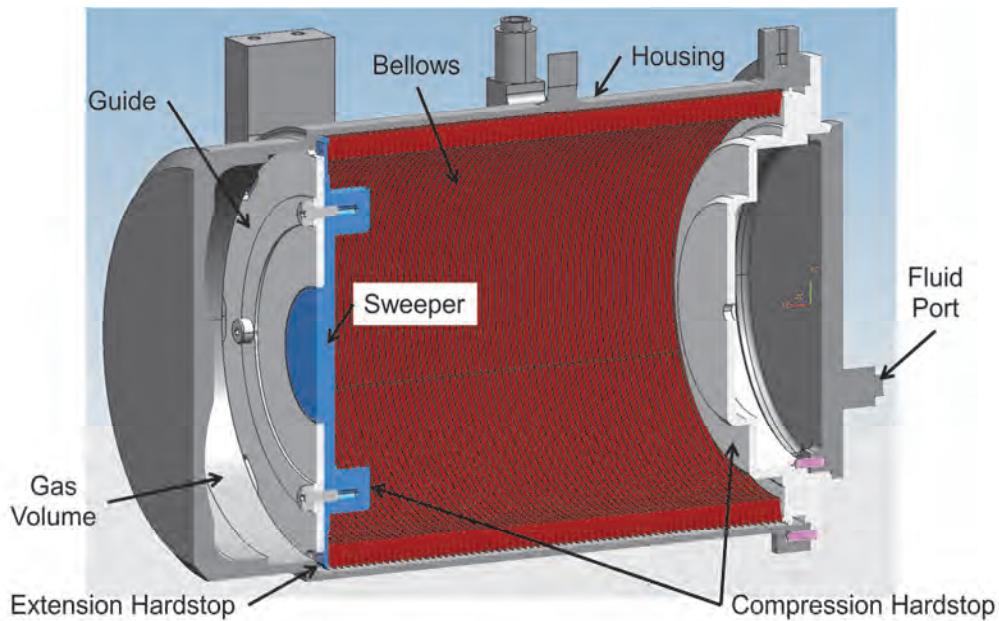


Figure 4. Rover Integrated Pump Assembly (RIPA)

The accumulator is a gas-over-fluid design that uses a metal bellows for the barrier between the fluid and gas. The gas is dry Nitrogen and the fluid is the system coolant of Freon R-11. A cross-section of the accumulator is shown in Figure 5.



**Figure 5. Accumulator Assembly showing bellows in fully extended position
(maximum fluid volume, maximum pressure of gas)**

The free end of the bellows assembly consists of a metallic sweeper to which a Teflon[®] guide disk with a larger outer diameter is mounted to provide low friction sliding on the bore of the outer accumulator housing. The bellows is prevented from stroking too far by a step in the housing bore that corresponds to the maximum design fluid volume increase along with the highest gas pressure. As fluid is removed from the accumulator, the gas pressure compresses the bellows until other features of the assembly act as a compression hardstop. This is the state of minimum fluid volume and minimum gas pressure within the accumulator assembly.

Failure Event

The initial functional testing of the accumulator assembly involved the following steps:

- Closing the accumulator assembly without welding (using a mechanical clamp) for a functional check
- Filling the bellows with fluid and removing any air bubbles (input tube upright)
- Pressurizing the gas side of the accumulator until the bellows is fully compressed
- Pumping fluid into the accumulator to extend the bellows, until the pressure difference across the bellows reaches a limiting value (this was the point where the bellows was calculated to be at full stroke with the guide seated against the step in the housing bore)
- Removing the pump connection
- Allowing the bellows to drain into a graduated cylinder to measure the amount of fluid the accumulator could contain
- Verifying that the fluid capacity of the accumulator is within specified tolerances
- If the assembly passes the test, weld the bellow end assembly onto the housing for a final flight seal
- Repeat the functional test above to verify no change occurred during welding

During final testing of one of the welded accumulator assemblies, the accumulator's fluid capacity appeared to be less than half the required value. Upon repeating the test several times, the capacity of the accumulator did not change. No test setup anomalies were observed and the accumulator assembly did not have any discrepancies that could account for the reduced capacity.

The accumulator assembly internals were then imaged using X-rays with the fluid in the accumulator at the limiting pressure difference. The picture in Figure 6 shows what was observed.

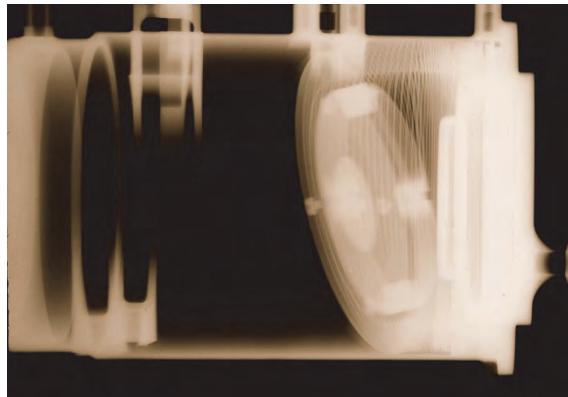


**Figure 6. X-ray of Accumulator Assembly showing bellows shape with the maximum allowable pressure difference across the bellows.
The accumulator fluid capacity is significantly reduced from the required value.**

The end of the bellows assembly with the sweeper and Teflon® guide had managed to tip to an angle where the piston would no longer move down the bore and had jammed in place. The force on the piston in the direction of extending the bellows with the maximum allowable pressure difference is 370 N, indicating the jamming force was quite high. When the fluid was removed, the bellows compressed flat against the compression hardstop (the right end in Figure 6) as designed. Repeating the test and measuring the fluid capacity indicated that the failure point was consistent and very stiff – meaning the location along the bore where the piston jammed did not move detectably when cycled between no fluid and the maximum possible fluid, limited by the allowable pressure difference across the bellows.

The X-ray was used to make measurements of the geometry of the failure location so it could be identified when the assembly was opened for inspection. Figure 7 shows some of the measurements made to determine the location and the possible source of the jamming.

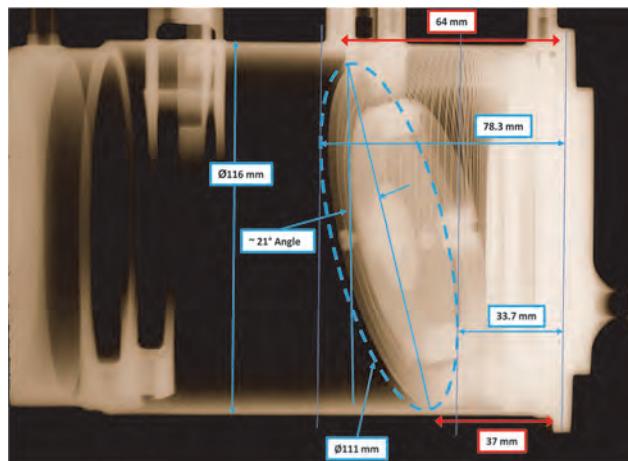


Figure 7. Measurements made using the X-ray of the Accumulator Assembly

It was clear there was some obstruction to the motion of the bellows guide that would hopefully be identified when the assembly was opened up and inspected. The next step was to carefully remove the bellows assembly from the housing to find the source of the jamming by cutting the weld off the end of the housing. Figure 8 shows what was found inside the housing assembly. The location of the residue seemed to indicate it was the source of the jamming, as indicated in Figure 9.



Figure 8. Tape adhesive residue on the housing wall, left behind from previous rework operation

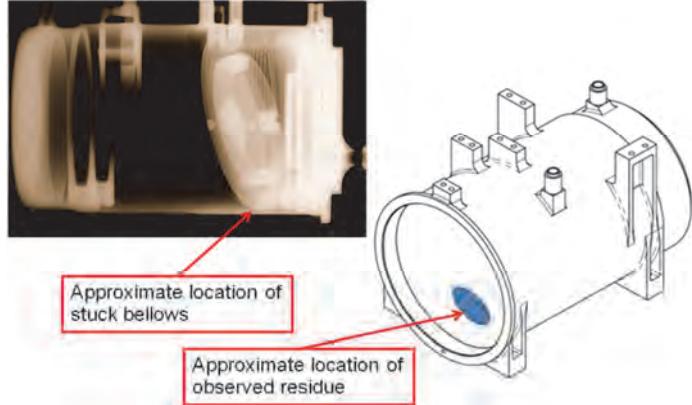


Figure 9. Location of tape adhesive residue correlates well to the tip-initiation point

The tape residue was cleaned from the housing bore and the accumulator reassembled. The test was repeated with the full expectation that the problem had been solved. The result of the test indicated no change in the behavior of the assembly, including the measured fluid volumes. The following analysis on the tipping phenomenon was performed (see Figure 10) to understand the sensitivity of the design to the variables involved. A description of the mechanical behavior model is presented.

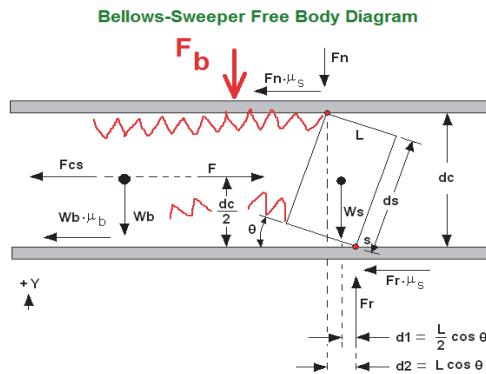


Figure 10. Free Body diagram of bellows assembly in housing

Mechanical Behavior Model Description

The free-body diagram variables include the weight of the sweeper (W_s), the weight of the fluid-filled bellows (W_b), the friction at the sweeper-to-housing interface (μ_s), and the normal force generated by a squirming bellows (F_b).

Prior to the tipping of the end of the bellows, F_b is zero. Once the end starts to tip, the bellows squirms upward and reacts against the housing wall. This additional normal force increases the frictional drag between the housing wall and the bellows surface, including the sweeper-to-housing interface.

An additional aspect of the tipping end of the bellows is how the contact between the Guide Disk and the housing behaves. The contact starts at a point and, as the tipping angle increases, this contact spot increases to an elliptical area. As the tipping angle is increased more, the contact patch splits into two small contact patches that travel around the housing surface. As the contact points get higher on the housing surface, the normal force necessary to balance the bellows squirm force, F_b , increases substantially. As the normal force increases, so does the friction force, increasing the tipping moment on the end of the bellows. This runaway behavior demonstrates that the tipping of the end of the bellows will eventually jam, and added force will not help to release it. See Figure 11 for a pictorial description of this phenomenon.

area. As the tipping angle is increased more, the contact patch splits into two small contact patches that travel around the housing surface. As the contact points get higher on the housing surface, the normal force necessary to balance the bellows squirm force, F_b , increases substantially. As the normal force increases, so does the friction force, increasing the tipping moment on the end of the bellows. This runaway behavior demonstrates that the tipping of the end of the bellows will eventually jam, and added force will not help to release it. See Figure 11 for a pictorial description of this phenomenon.

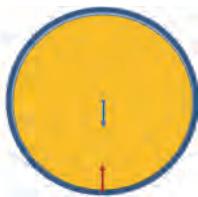


Figure 11a. Bellows straight, normal force on bottom is from weight only ($F_b = 0$)

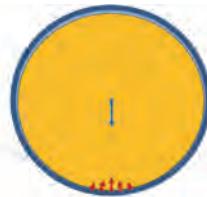
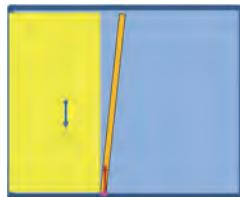


Figure 11b. Start of tipping, normal force on bottom is a small contact patch ($F_b = 0$)

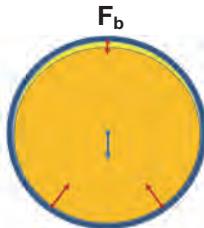
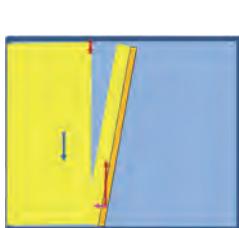


Figure 11c. Tipping angle has increased and contact patch has split into two discrete areas

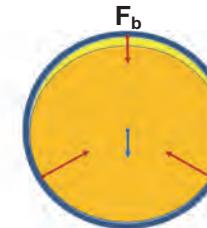
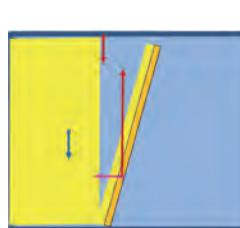


Figure 11d. As tip angle increases more, the contact areas move up the side of the housing. Radial force must increase to balance the bellows squirm force, F_b .

The most significant variable in this tipping and then jamming behavior is the friction force. The housing bores were cleaned very well to minimize the possibility for contamination. The Teflon® Guide Disk was relied upon for its low friction properties at the bellows-to-housing interface. No other Accumulator Assembly has exhibited this characteristic and it had not shown up in any of the environmental testing either.

Design History of the Accumulator Assembly

This accumulator design was not new. There was a Heat Rejection System on the Mars Pathfinder Lander in 1997, as well as one on each of the rovers, Spirit and Opportunity in the 2003 missions. The accumulator in the MSL mission was larger than any of the prior units because the volume of heat transfer fluid was much greater. The design was scaled up in size to accommodate the volumetric increase.

The mission life requirement for MSL is eight times longer than the Spirit and Opportunity rovers. The larger size of the accumulator and bellows assemblies coupled with the longer operational life required a cycle life test be performed. The cycle life test resulted in a fatigue failure of the bellows assembly. The bellows was redesigned to accommodate the higher life requirement by reducing the thickness of the convolutions a small amount. The bellows displacement then resulted in a lower stress level in the material. This had the additional effect of reducing the bellows stiffness, both axially and laterally.

The Next Version of the Failure Mechanism Hypothesis

When the elimination of the adhesive residue on the housing wall did not affect the failure results, the additional factor of the reduced stiffness of the bellows was considered. This would make the design even more sensitive to bellows tipping under smaller frictional forces, since the bellows stiffness helps keep the end from tipping by resisting the applied moment from friction with the housing bore. The reduced stiffness of the MSL bellows combined with a surface finish in the housing bore that was at the coarse end of the tolerance and some tape adhesive residue all seemed to have pushed this unit over the edge and initiated the tipping of the end of the bellows. Once it had started, the bellows continued to tip and jam at the same location, even though the adhesive had been removed from the bore. While a stress analysis indicated that the tipped distortion of the bellows should not have resulted in any yielding, and

there was no visual indication of damage or permanent deformation, it seemed that the bellows had taken a set that led to the repeatable failure. Additional stroke tests were performed with different orientations to gravity that indicated that the bellows was slightly biased to fail in the original location.

Design Change Options – Highly Limited

The opportunities for changing the design were explored at this time and included a new bellows assembly with a greater stiffness, reducing the stroke requirement, providing improved guidance of the end of the bellows, and increasing the length of the housing to accommodate more volume for some bellows guide options. The options that were possible in the schedule time available included reducing the stroke requirement and adding a guide to the end of the bellows. A new bellows could not be designed and fabricated in time and increasing the housing length was not possible since the rover had structure that would interfere with a longer housing. The option of reducing the stroke requirement did not actually solve the fundamental problem and would have required the temperature range to be less than the current system design provided, making this option unacceptable.

The remaining option of improving the design of the guide on the end of the bellows was pursued. The length of the outside of the accumulator housing could not be changed, but the inside of the housing had an option for moving the end-of-stroke hard stop 25 mm closer to the end of the housing. This did not affect the outer profile, making it acceptable in the tight volume the accumulator occupied within the rover chassis. While the housing could not be lengthened, the end-of-stroke hardstop inside of the housing could be moved closer to the end of the housing. This provided 25mm of additional interior length in which to implement the improved guide design.

What Guide Material and Length-to-Diameter Ratio is Acceptable?

The additional guide length that could be obtained without changing the outside length of the housing was 25 mm and the diameter of the bore of the accumulator was 111 mm. For a piston type guide, the standard wisdom is to have a length to diameter ratio of 0.5 to 2.0, with most ratios in typical applications near 1.0. The best that could be obtained within the constraints of the MSL application was 0.225. Additionally, the best material choice would be one with the following characteristics:

- Low friction with the stainless steel housing
- Minimal to no particle generation over the life
- A life cycle capability of 10,000 cycles
- A coefficient of thermal expansion (CTE) that is close to the bellows and housing values

The best choices for low friction involved polymers and the best CTE choices were metals. The choices from a particle generation and cycle life perspective crossed between polymers and metals. Lubrication of the metals was considered, but no lubricants had been qualified with the nitrogen gas fill valve. If the gas fill valve leaked at all, the system would fail due to loss of pressure on the Freon R-11. The leak rate of the fill valve had been verified with everything clean, and there was not enough time available to repeat the valve qualification with a lubricant, liquid or dry. This eliminated the use of an applied lubricant as a possible solution to the failure mechanism.

The analysis of the self-energizing jamming phenomenon showed that friction and initial tip angle are critical to a successful design. A larger radial clearance between the guide and the housing bore would allow the guide to rotate more before contacting the housing wall. The larger the initial contact angle is, the smaller the required friction to create a self-energizing jam. This demonstrates that smaller radial clearances are preferred. In addition, the CTE difference between the guide and the housing had to be considered. These properties determined the smallest radial clearance that could be selected for a particular guide material choice.

In order to answer the question of minimum acceptable guide length and material choice, manual testing was performed using the test assembly shown in Figure 12. The plates at the end of the assembly determined the radial clearance to the housing bore and the plates in the middle region controlled the effective length of the test guide.

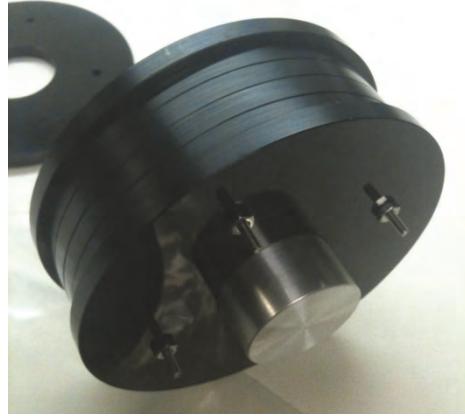


Figure 12. Test Guide Assembly - Used to qualitatively determine the best length and radial clearance combination using Delrin® disks

The test guide assembly was inserted into the test housing and the operator used the mandrel diameter to stroke the assembly within the bore. As the test guide was moving, the operator applied a moment to the assembly with the thumb and index finger. As moment was applied, some combinations of length and radial clearance would solidly jam, some would tip over freely, and others would get tight in the bore but not be self-energizing. The results of the testing are listed in Table 1.

Table 1. Results of Qualitative Manual Testing of Test Guide Assembly as a function of radial clearance and guide length using Delrin® disks

Length [mm]	Clearance, \emptyset [mm]					
	0.025	0.127	0.254	0.381	0.508	0.635
6.35	FAIL -	FLIP	FLIP	FLIP	FLIP	FLIP
12.7	FAIL	FAIL -	FAIL -	FAIL-	FAIL/FLIP	FLIP
19.1	FAIL	FAIL -	FAIL	FAIL	FAIL	FAIL-
25.4	FAIL	FAIL -	FAIL	FAIL+	FAIL+	FAIL
31.8	FAIL	FAIL	FAIL+	FAIL +	FAIL+	FAIL+
38.1	PASS -	PASS -	PASS	PASS	PASS	PASS -
44.5	-	-	-	-	-	PASS

FLIP = Piston could freely flip through 360 degrees, i.e. provided no tip restraint

FAIL - = Jammed badly, i.e. became stuck with little or no effort

FAIL = Would jam, but only when a moment was applied or was pushed at edge

FAIL + = Would jam, but took a lot of effort. Would not recover on its own

PASS - = Judged not to jam, but considered to be closer to jamming than others

PASS = Could not be made to jam

The manual testing indicated that a 38.1 mm minimum guide length was required; no length/clearance combination less than 38.1 mm was successful. However, the maximum possible length of the guide that could be implemented with the housing and structural constraints was 25 mm. The test results demonstrated that a Delrin® solution was not acceptable.

Since the longest possible guide length was 25 mm, a new set of tests were implemented with different guide materials and two different guide designs. The first test guide design was a solid cylindrical guide that was 25 mm long on a stainless steel mandrel. The second design was the same cylindrical guide with a mandrel and a slotted guide, with the slot in the circumference of the guide, similar to automobile engine piston ring designs. The slot allowed the CTE mismatch between the guide and housing to be accommodated in the expansion/contraction of the slot, rather than in the radial clearance between the guide and housing. This was crucial for high CTE materials, since a solid guide design would have required the guide to actually be smaller in diameter than the bellows themselves. The slotted guide was also placed on a stainless steel mandrel to provide support for the bore of the guide. Figure 13 shows the virgin Teflon® version of the guide.

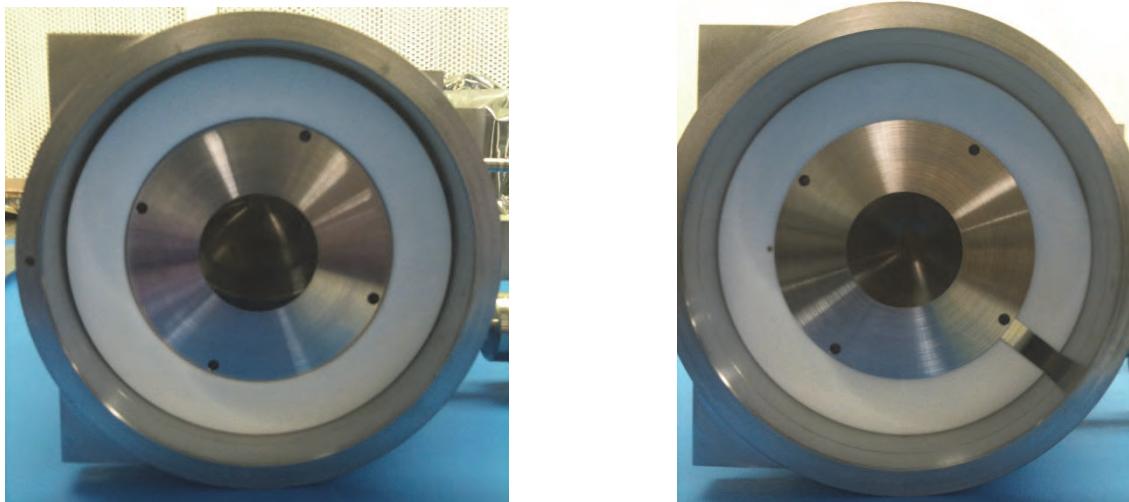


Figure 13. Solid and Slotted designs of the guide on Test Mandrel and inside the Test Housing with the largest possible radial clearance. Note that the slotted design springs outward, closing the radial clearance under all conditions.
(the terms Solid and Slotted refer to the circumference of the guide)

The different materials tested using circumferentially solid and slotted guides on a mandrel were

- Torlon® 5030
- Vespel® SP-3
- Delrin® 100 AF
- Teflon® 25% glass filled
- Virgin Teflon®

The testing was done manually with the same pass/fail criteria as was used in the previous Delrin® guide testing (see Table 1). The test guides were fabricated to diameters representing a nominal radial clearance at 25°C and the maximum radial clearance associated with the lowest temperature condition and the smallest manufactured outside diameter (Least Material Condition, or LMC). The results of this testing are listed in Table 2. Note that a solid Delrin® version was not tested. This was the version tested previously and represented in Table 1. For the Torlon® and Vespel®, the slotted versions were not tested

because the CTE of these materials did not require them to be slotted and the solid versions failed. Both Teflon® versions were successful, except that the solid version with virgin Teflon® had too high a CTE and lost all guiding function at cold temperature and least material condition.

Table 2. Results of Qualitative Manual Testing of Test Guides using circumferentially slotted and solid test items as a function of radial clearance [Nominal and Least Material Condition Cold (LMC Cold)], and material

Material	CTE [ppm/C]	Solid		Slotted	
		nominal	LMC Cold	nominal	LMC Cold
Torlon 5030	glass fill	16	FAIL		
Vespel SP-3	MoS2	52	FAIL		
Delrin 100AF	Teflon fill	100			FAIL
Teflon 25% GF	glass fill	100	PASS	PASS	PASS
Teflon, virgin		151	PASS	FLIP	PASS

The test results demonstrated that both glass filled and virgin Teflon® were acceptable candidates, though only a slotted design was acceptable with the virgin Teflon®. Additionally, the glass filled Teflon® showed signs of abrading the bore of the housing by capturing fine particles of housing material within and on the wear surfaces of the guide. This abrasion was deemed undesirable and the virgin Teflon® slotted design was chosen to proceed forward. The final design of the guide and hard stop for the flight assembly is shown in Figure 14 along with a representation of the original design, emphasizing the changes made to mitigate the demonstrated failure mode.

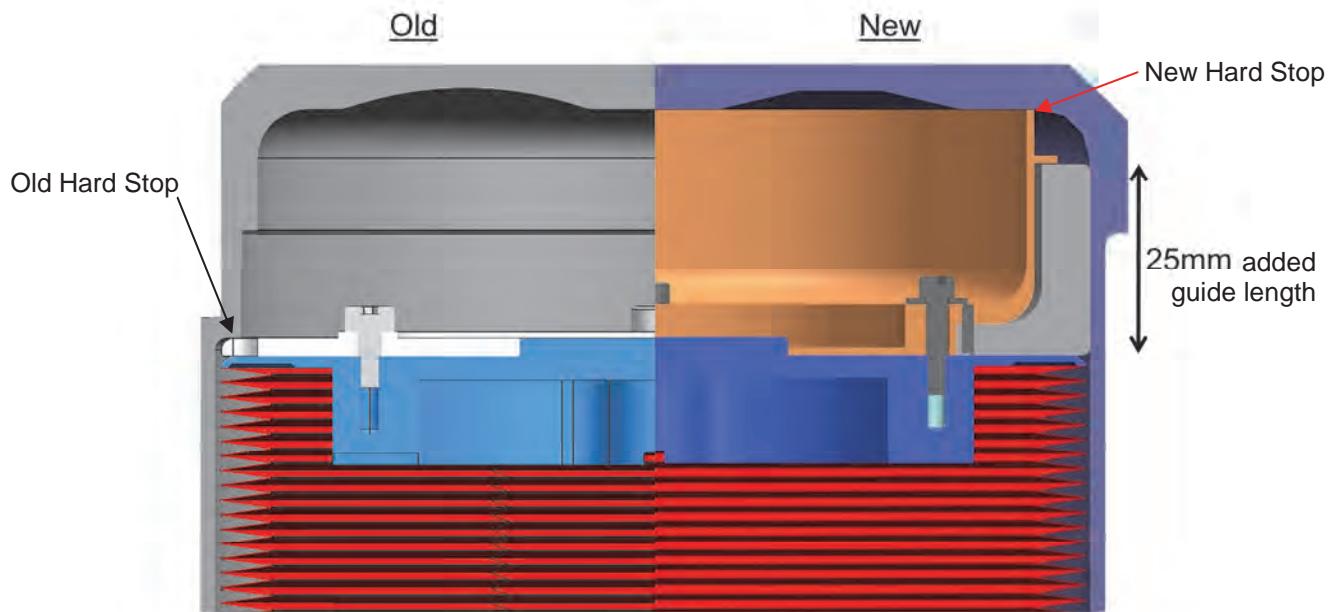


Figure 14. Original and Final designs of the end of the bellows assembly. The figure shows the bellows stroked to the maximum fluid condition and against the end-of-stroke hard stop for both design versions

Acceptable to Fly?

The final design of the bellows end guide was selected based on intuitive “feel” and engineering judgment. These are not exactly verifiable quantities that make an assembly ready to fly on a mission. The next challenge was to demonstrate, using quantifiable methods under worst case conditions, that the new design would not exhibit the previous functional limitation or any new failures. This was particularly difficult since the landing and launch environments present significant loading to the assembly, but they were not representative of the long life mission loads while the bellows is actually stroking within the bore. However, if the large loading of launch or landing were to initiate a self-energizing condition, then they were appropriate and representative to use for testing.

Upon studying the types of loading the unit would be subjected to during all of the phases of the mission, the worst case conditions consisted of combined radial and moment loading at the end of the bellows. The magnitude of the moment loading would be dependent on the stroke position of the bellows, which is a function of the temperature around the internals of the rover. In order to cover the conditions on the surface of Mars for the majority of the mission as well as the shorter term higher loading conditions, a combination of moment and radial loading conditions were formulated. It turned out that the maximum radial load could not be achieved along with the proper moment load due to the dimensional constraints of applying the loads to the bellows inside of the housing. Since the moment loading was determined to be the most detrimental to the operation of the accumulator, the moment loading was matched and the radial loading was allowed to be undersized.

The test loads were generated by attaching steel plates to the end of the bellows assembly and cantilevering them far enough to produce the required moment loading and best possible radial load. This was not possible to do with a closed and sealed accumulator, so it was performed with the nitrogen gas end cap removed from the end of the accumulator housing. Figure 15 shows the test setup.

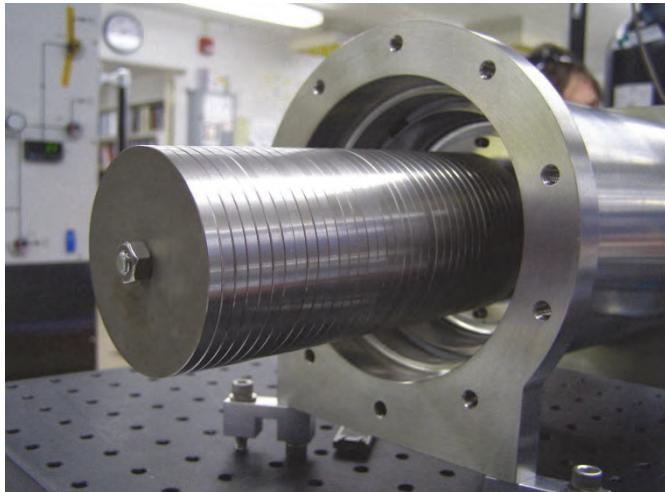


Figure 15. Stroke Testing of the final guide design under high loading conditions (load is equivalent to 3.2-g radial and 5.4 times the maximum flight moment)

The test loads were applied as shown above and the bellows stroked using internal pressure. The maximum allowable safe pressure difference across the bellows assembly was 38 kPa. The pressure difference across the convolutions that moved the guided end of the bellows in the housing was measured and recorded. There was no nitrogen gas pressure applied to bellows during the testing. This meant that the only force available to compress the bellows was its own internal spring force, which was very low. The results of this testing are shown in Table 3. Note that for the higher moment loads, the bellows did not retract on its own due to the friction force. This would not occur in a sealed and pressurized accumulator due to the presence of the nitrogen gas on the end of the bellows, forcing it to retract.

Conclusions and Lessons Learned

A bellows assembly without end guiding that must carry moment loads is a marginal design at best. A design without adequate end guiding relies on the internal moment stiffness of the bellows itself to prevent a significant rotation of the free end. If the radial clearance and friction conditions are beyond certain limits, then the rotation of the end of the bellows can quickly result in a self-energizing jamming condition that cannot be overcome.

With a piston guide of reasonable length, friction and the allowable radial clearance are extremely important design parameters because this mechanical configuration is very sensitive to these variables. The best option, where possible, is to use a lubricant to control the sliding friction. Otherwise, the lubrication function must be provided by careful material selections of the moving components. Polymers like Teflon® are great, but their CTE is large compared to metals and the applied contact pressure between the sliding surfaces must be limited. The slotted guide presented here worked exceptionally well to accommodate the large CTE difference.

**Table 3. Results from the load testing of the final guide design
(all bellows pressure values were well below the 38 kPa limit)**

Number of test plates	0	14	22	29	37
Added mass [kg]	0.000	1.540	2.368	3.093	3.921
Total mass [kg]	0.680	2.220	3.048	3.773	4.601
Total applied load [N]	6.671	21.778	29.901	37.013	45.136
Cantilever length [m]	N/A	0.069	0.065	0.072	0.096
Applied moment [Nm]	0.000	1.022	1.492	2.160	3.647
Equivalent Radial load [g's]	0.5	1.6	2.1	2.6	3.2
Equivalent Moment load (x Flight)	0.0	1.5	2.2	3.2	5.4
Bellows Pressure, kPa gage					
Guide started to slide, extending	0.34	2.4	5.2	9.3	7.9
Guide is halfway, extending	1.4	4.5	8.3	10.7	13.4
Guide is almost at hardstop, extending	3.1	7.2	10.3	13.4	16.9
Guide started to slide, contracting	2.4	0.34	†	†	†
Guide is halfway, contracting	1.4	†	†	†	†

† the drag was high enough to prevent the bellows from contracting on its own

References

1. Bhandari, P., Birur, G., Pauken, M., Paris, A., Novak, K., Prina, M., Ramirez, B., and Bame, D., "Mars Science Laboratory Thermal Control Architecture," SAE 2005-01-2828, 35th International Conference on Environmental Systems, Rome, Italy, July 2005.
2. Bhandari, P., Birur, G.C., et al, "Mechanically Pumped Fluid Loop Heat Rejection & Recovery Systems For Thermal Control on Martian Surface – Case Study of The Mars Science Laboratory," 36th International Conference on Environmental Systems, Norfolk, Virginia, July 2006.
3. Flexial Corporation provided experienced advice on the details of bellows analysis methods within the confined space of the accumulator housing. Flexial Corporation, 1483 Gould Drive, Cookeville, TN, 38502-3105, USA, www.flexial.com

Acknowledgements

This work was performed at the Jet Propulsion Laboratory, California Institute of Technology, under a contract with the National Aeronautics and Space Administration. Reference herein to any specific commercial product, process, or service by trade name, trademark, manufacturer, or otherwise does not constitute or imply its endorsement by the United States Government or the Jet Propulsion Laboratory, Pasadena, California. Copyright 2012 California Institute of Technology. Government sponsorship acknowledged. The authors wish to acknowledge the many individuals working on the MSL project, of which the thermal subsystem is a part of the greater whole. Dave Bame and AJ Mastropietro from the MSL Thermal team provided excellent support for the testing of the bellows at JPL.

Pacific Design Technology (PDT) in Goleta, CA is acknowledged for their excellent work in developing the pump assemblies and providing significant support for this investigation.

Development of the Descent Brake Mechanism for the Mars Science Laboratory

David Dowen*, Jeff Moser** and Jeff Mobley**

Abstract

This paper will describe the design and testing of an electromechanical damper assembly for the Mars Science Laboratory as well as provide the current program status. Unique test equipment was developed for verification of flight requirements and is presented. Included in this paper are the problems that arose during design and testing that are peculiar to a device intended to dissipate energy. Also discussed are the lessons learned relating to assembly and test anomalies and the resulting corrective actions.

Introduction

The primary mission of the Mars Surveyor Lander (MSL) program is to deliver the 900-kg Curiosity rover to the surface of Mars in the year 2012. Its "Skycrane" landing system uses a free-flying rocket-decelerated descent stage to set Curiosity down on the surface, which hangs on a 7.5-m-long bridle cord, without ever landing the descent stage or fully powering down the engines. This architecture enables safe delivery of Curiosity onto rugged terrain. A key component of the Skycrane landing system is the device which allows the rover to be lowered by a distance of 7.0 m to fully extend its bridle. The Descent Brake allows this deployment to happen quickly and with controlled speed that decreases toward the end of deployment for a soft stop at the full bridle length. The amount of energy dissipated by the Descent Brake during the event is approximately 24 kJ.

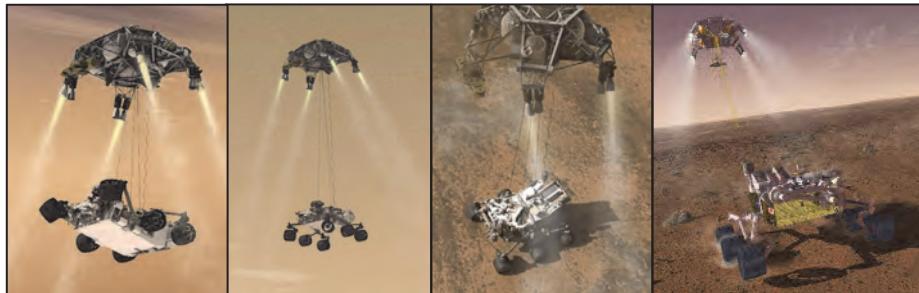


Figure 1 - Sky Crane Landing Sequence

Descent speed control is achieved passively by deploying the bridle cord from a tapered spool. The tapered spool allows an ending descent speed that is less than the average speed. The radius from which the cord deploys is decreased as the cord is deployed. Initially the vertical velocity of the rover is high relative to the angular rate at the input shaft. As the bridle deploys, the diameter of the spool decreases and the angular rate, at the shaft, increases relative to the rover's vertical rate. For this design, the torque is initially low at the Descent Brake, and then rapidly increases to slow the vertical rate of deployment, reference Figure 2. The design chosen to manage the drop converts the rover's potential energy into heat with an electrical generator, driven by the bridles wrapped on the spool and dissipating the rover's energy into a bank of resistors. This technique has the advantage of being completely passive, and unlike previous friction technologies, offers highly consistent performance over a wide temperature range.¹

* Sierra Nevada Corporation, Space Systems Group, Louisville, CO

** Sierra Nevada Corporation, Space Systems Group, Durham, NC

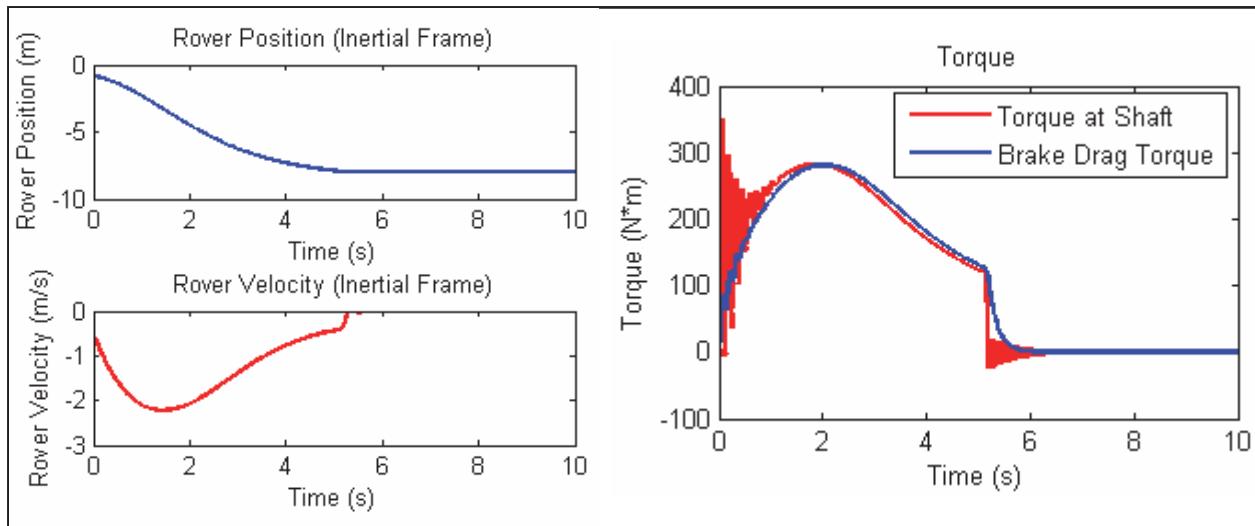


Figure 2 - Output from MSL Lowering Device Simulation¹

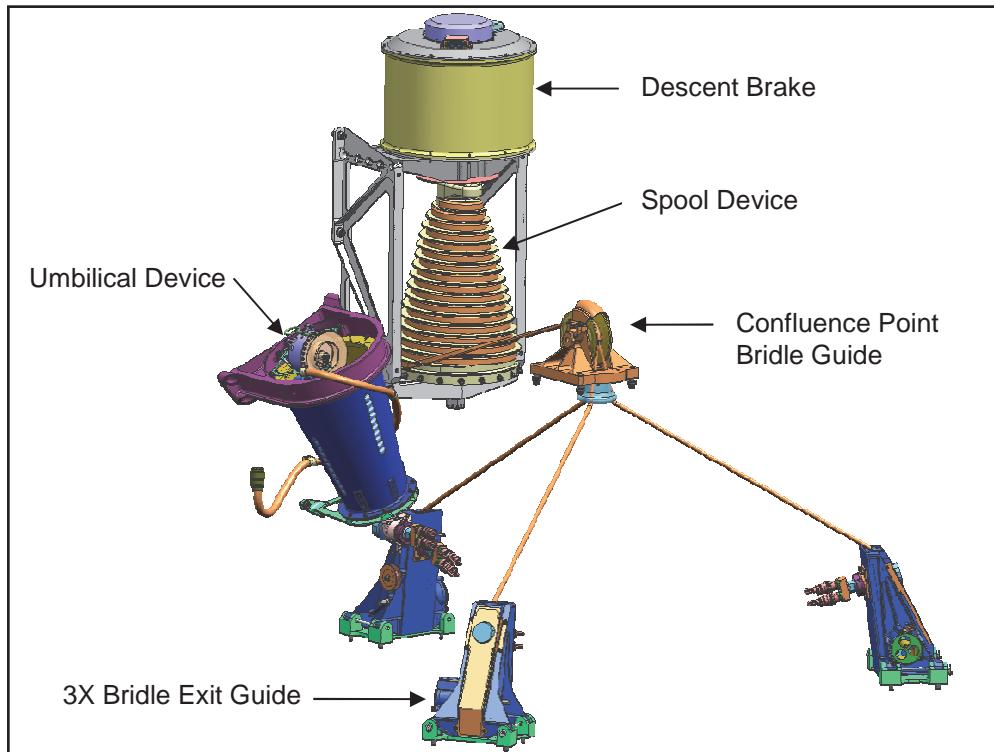


Figure 3 - MSL Deployment Mechanism

Descent Brake Requirements

Damping Performance

The initial nominal performance specification for the MSL Descent Brake required a nominal linear speed dependent drag of $10.6 \pm 2.3 \text{ N}\cdot\text{m}\cdot\text{s}/\text{rad}$ over a temperature range of -35°C to $+35^\circ\text{C}$.

Figure 4 shows the performance envelope allowed as it relates to shaft speed and torque. The performance of the Descent Brake design needed to remain in the performance envelope over all variations in manufacturing tolerances and environments.

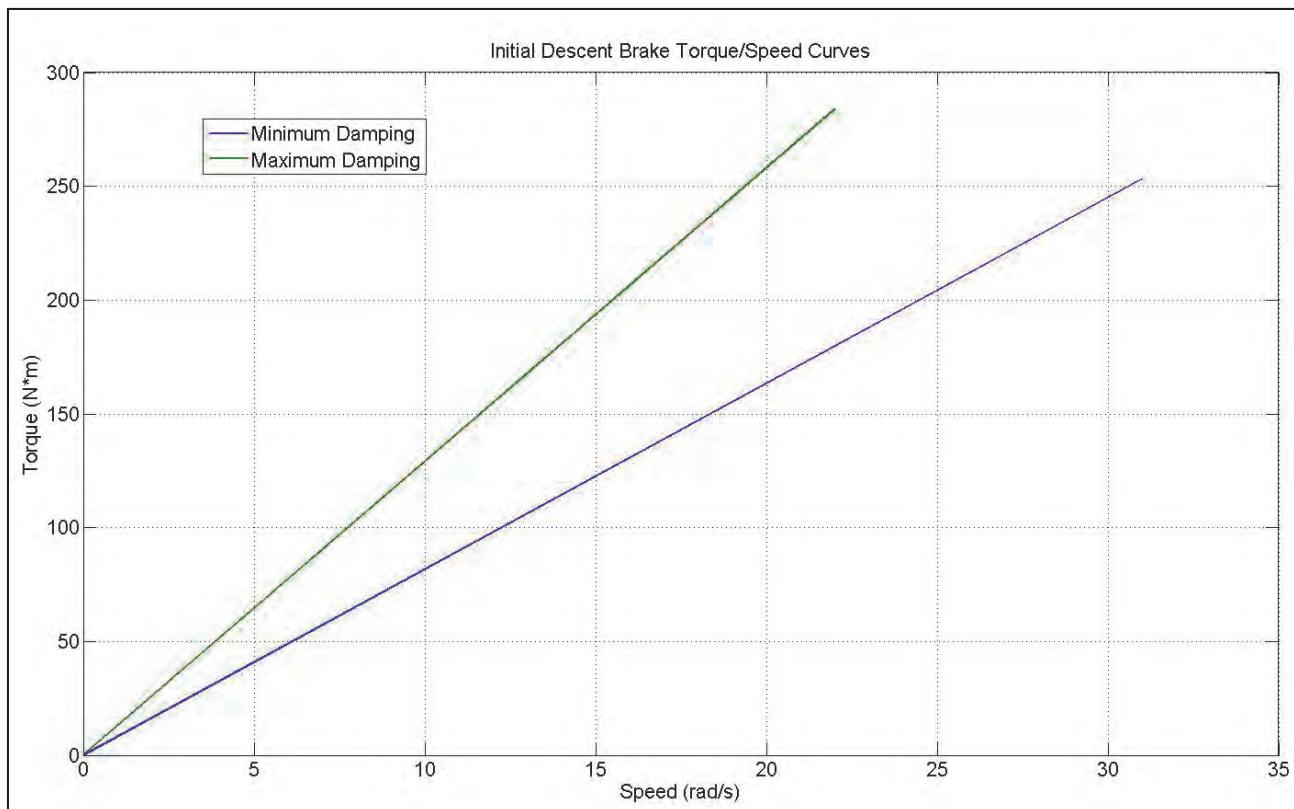


Figure 4 - Descent Brake Performance Requirement

Design Limits

Several other requirements key to the design were specified as design limits. These requirements from the initial specification were:

- Output shaft peak speed of 28 rad/s
- Instantaneous output shaft peak torque of 340 N·m
- Event duration of 7 seconds maximum
- Power dissipation capability of 9.5 kW
- Approximate envelope of Ø265 mm (Ø10.43 in) maximum outer diameter by 230 mm (9.05 in) maximum length (circular form factor)

Descent Brake Design

The initial step in the system design of the Descent Brake was to evaluate the driving requirements and establish design goals. The peak power requirement of 9.5 kW drove the design to require the majority of the power to be dissipated by a resistor bank. To ensure consistent performance with variation in temperature the resistor bank was designed around high reliability wire wound resistors with very low change in resistance over temperature ($\sim \pm 20 \text{ ppm}/^\circ\text{C}$). In order to minimize the generator winding copper losses (I^2R losses) it was desired that the generator winding current be minimized. To minimize the generator winding current, the generator voltage was designed to be as high as practical. In order to avoid corona issues, the maximum generator design voltage amplitude of 150 V peak was chosen.

To meet the desired performance requirement of nearly linear damping over the speed range, it was critical that the inductive reactance component of the generator winding impedance be minimized. The inductive reactance component of the generator impedance is a function of the generator winding

inductance, the number of generator poles selected and the shaft speed. The shaft speed was determined from the gear ratio selected. The gear ratio was selected to be as high as practical to balance the generator and gearbox sizes while still surviving the specified load conditions with margin.

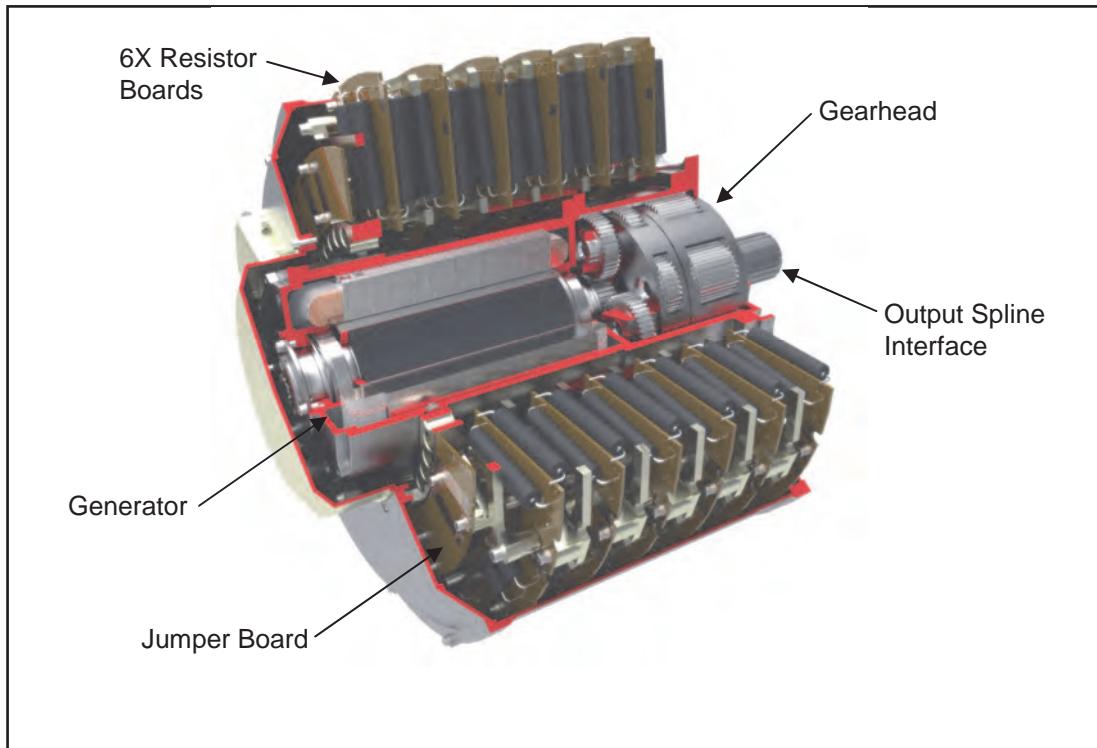


Figure 5 - MSL Descent Brake Assembly

Late in the design process several of the design limits changed as the Curiosity rover design matured. The damping ratio was modified to $9.45 \pm 0.15 \text{ N}\cdot\text{m}\cdot\text{s}/\text{rad}$. This change in damping ratio resulted in the peak momentary torque rising to $583 \text{ N}\cdot\text{m}$ and independently the peak speed to 36 rad/s . The Descent Brake design was evaluated for performance to these new requirements and fortunately was able to meet them by analysis except for the new maximum speed requirement. Operating at the new maximum speed requirement drove the rotor speed to over 1750 rad/s . This new rotor speed was 20% over the manufacturer's recommendations for the rotor bearings. A test rotor with bearings was used to show the bearings were capable of withstanding operation at the maximum speed requirements with no issues. The rotor bearing set was tested to speeds that equate to 40 rad/s at the gearhead input shaft. The bearings were inspected at SNC and by the bearing manufacturer after completion of the testing with no detrimental affects noted.

Descent Brake Components

Generator

From the established generator parameters, the generator design space was evaluated. Several generator designs of various geometry and number of poles were created. Each design was optimized to minimize inductive reactance while meeting all other parameter requirements. A Simulink model of the Descent Brake system was also created. The Descent Brake performance was evaluated for each generator design to determine the best generator configuration to meet the design requirements stated above using the system model. The generator configuration that ended up with the lowest inductive reactance was a 6 pole generator with a 1.1:1 length to diameter ratio. The chosen design showed very near linear operation of the generator damping over the required speed range.

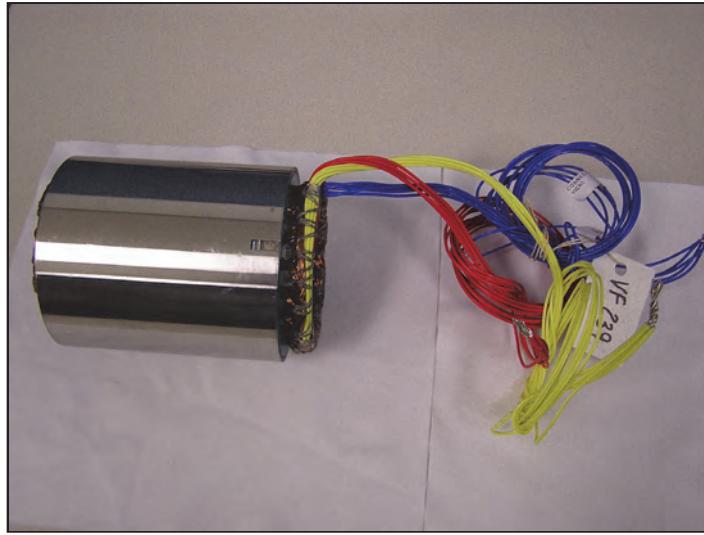


Figure 6 - 3 Phase Generator Stator Assembly

Gearbox

The gearbox is a high torque density, 3 stage planetary gearbox with an overall gear ratio of 48.8:1. The gearbox mass is 3.73 kg within an envelope of 98.55-mm diameter by 91.44-mm length (excluding flanges and shaft extension). Gearhead capacity was optimized using the gearbox design guidelines developed through the NASA Phase II SBIR Lightweight Gearbox Technology Program², including material selection, design features, and analysis techniques. The gearbox was designed for an operating high torque load case (322.5 N•m at 25 rad/sec), an operating high speed load case (298.8 N•m at 36 rad/sec), a momentary load case (583 N•m at 18 rad/sec) and a static peak torque case (700 N•m). The required life of the gearbox is only 8 cycles of 120 radians (960 radians total) for the operating load cases with the momentary load occurring no more than twice per cycle. With the relatively short life requirement, the gearbox was designed to provide positive margin for the specific loads and duration specified rather than being designed for endurance limit. Because of the high loads and speeds involved, significant attention was paid to imbalance of loads between the planets and the resultant net load applied to the supporting bearings. At the high speeds required, the centrifugal force on the planet bearings was factored into the analysis in addition to the resultant gear forces. Thermal impacts upon the lubricant during high speed operation were also considered.



Figure 7 - First, Second and Third Stage Carrier Assemblies

Resistor Bank/Structure

The design of the Resistor Bank for the Descent Brake was a challenge in packaging. The Resistor Bank consists of three 1.5-ohm phase resistances wired in a wye configuration. Each phase consisted of two Printed Wiring Boards or PWBs containing 25 resistors on each board. The resistors were set in series/parallel configuration to result in the required phase resistance. This number of resistors was also utilized to ensure the maximum power dissipated in any resistor never exceeded 10 watts. An additional PWB was used to make all the connections between the Resistor Bank and Generator Assemblies. The resistors were arranged in a radial pattern on the donut shaped PWBs due to the circular form factor of the required envelope. The PWBs were mounted onto aluminum chassis components that were optimized for weight under the required structural loads. Individual resistors of different values could be chosen to tune the damping of the assemblies as required to meet the desired requirement in the range of approximately 7.0 N•m•s/rad to 12.0 N•m•s/rad.

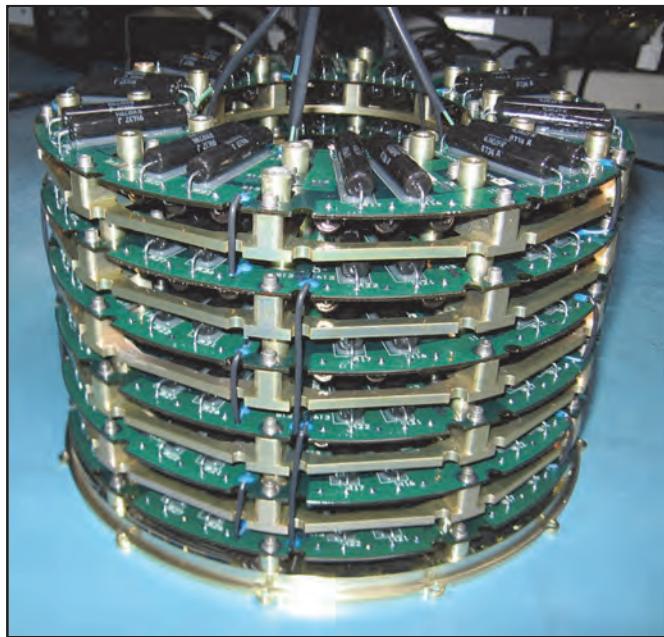


Figure 8 - Resistor Bank Assembly

Test Program/Equipment

Functional testing of the Descent Brake can be thought of as essentially dropping the equivalent of a Mini Cooper from the roof of a second story building on a spooled cable system. Although the requirements could be met with this type of test setup it was not ideal for many reasons. The functional testing needed to be performed in many different configurations including in a thermal vacuum chamber. The test method chosen was to use a brushless DC servo system to supply the required torque at the Descent Brake input shaft and a reaction torque cell to measure reacted torque at the mounting flange. The DC servo was sized to be able to meet all torque requirements without any gearing to keep sources of error at a minimum. This type of test setup allowed for a flexible test rig that could be adapted to many different scenarios. The DC servo system also allowed for flexibility in test profiles with only changes in programming. Figure 9 shows three of the test setups used for in-process, acceptance and qualification testing. The upper left photo shows the test configuration used for component level verification and resistor bank tuning. An additional torque cell is added between the generator rotor shaft and input to the gear head.

This allowed for easy measurement of gear head efficiency and generator performance in the system. The upper right photo shows the ambient test configuration for a fully assembled Descent Brake. This

setup was extremely robust and allowed for consistent test results from the Descent Brake. The bottom picture shows the test configuration for thermal vacuum testing. This setup is essentially the same as for ambient except the addition of a fluid coupling to pass torque through the thermal vacuum chamber wall. Although the fluid coupling does have some drag associated with it, the magnitude is small compared with the torque input so had little affect on the overall test results.

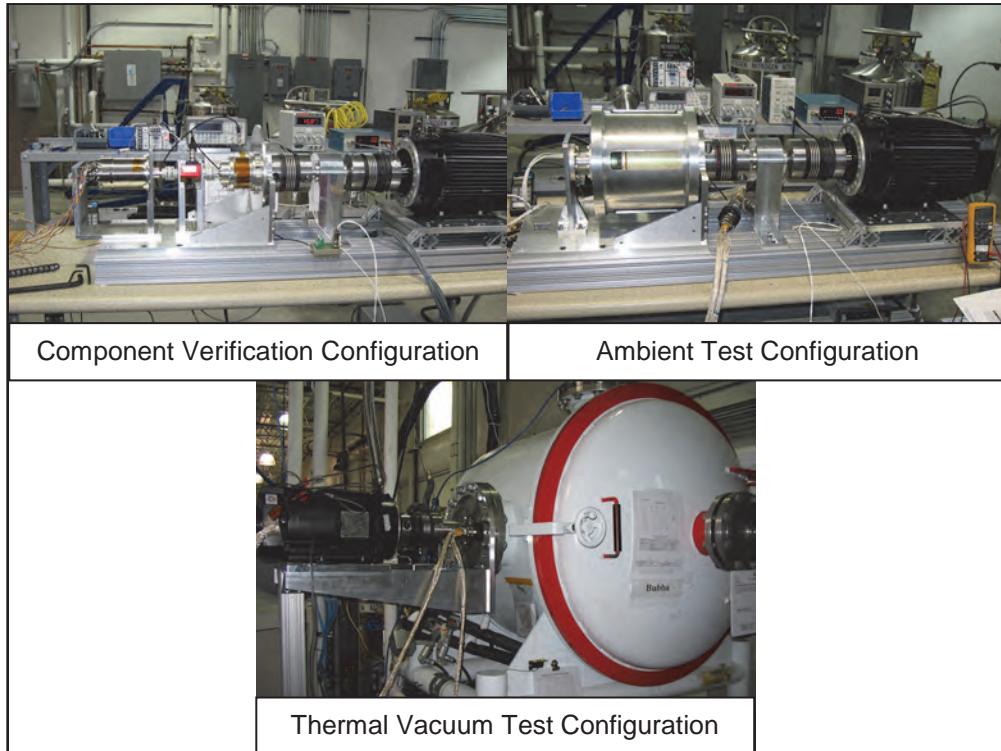


Figure 9 - Performance test setups

The tests performed on the flight Descent Brake included the following:

- Structural/Stiffness test
- Initial ambient functional test
- Vibration test
- Ambient functional test
- Thermal cycling
- Functional testing at thermal extremes
- Final functional test

The flight unit completed all acceptance testing without issue. The measured damping rates for the functional tests performed were 9.51 N•m•s/rad during initial ambient, 9.42 N•m•s/rad during thermal vacuum hot extreme, 9.51 N•m•s/rad during thermal vacuum cold extreme and 9.36 N•m•s/rad during final ambient functional testing. The torque vs. speed curves for these tests are shown in Figure 10 and shows the consistency of operation under varying environmental conditions.

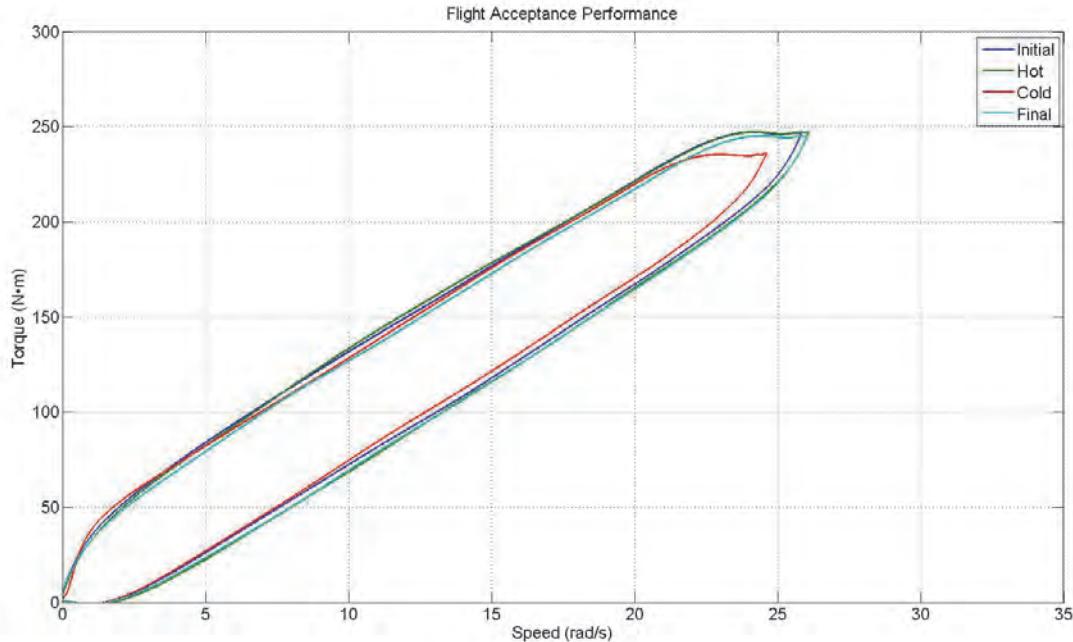


Figure 10 - Flight Acceptance Performance Curves

The Qualification Unit completed the same tests as the Flight Unit with the addition of shock, more extreme temperature limits during thermal vacuum and life testing. All tests were completed with no issues. After completion of the life test the qualification unit was disassembled and all parts inspected. No issues were found during the inspection.

Lessons Learned

Collaboration and Robust Design Margins

One of the biggest challenges on the program was reacting to changes in requirements throughout the program and in particular after completion of the design phase of the program. At the point the last requirement changes occurred there was a lot of schedule pressure to complete the program to support launch date at that time. Fortunately, the gearbox and resistor bank were designed to take advantage of the required envelope and had adequate design margins. We were able to perform analysis to the new requirements and show that the gearhead and resistor were still compliant. The generator rotor bearings were the only components we could not show compliant to the higher limits via analysis. This verification was handled through empirical testing and turned out to be a nonissue. The highly collaborative environment cultivated between JPL and SNC throughout the program was instrumental in working through the requirement changes effectively. This type of relationship is a necessity in order to effectively work through a program with dynamic requirements.

Robust Test Set

Besides the design of the deliverable hardware, the test set was also a challenge. The size of the Curiosity rover drove torque and speed test requirements outside our normal range. Using the large direct drive DC servo system worked extremely well. The combination of size and flexibility allowed us to perform many different tests in essentially the same test setup.

Development Test Anomaly

The generator rotor is composed of three main parts, a stainless steel rotor hub, permanent magnets and a thin metal rotor band. The permanent magnets are bonded to the stainless steel rotor hub and the rotor band is thermal fitted over the outside diameter of the permanent magnets. The function of the rotor band is to provide secondary mechanical retention and to protect the magnets within the air gap between the rotor and stator. Under nominal conditions there should normally be 0.25 mm (0.010 in) clearance, typical for this type of device, between the rotor band outside diameter and the stator inside diameter. During

initial testing of the development generator, abnormalities in the generator torque were noticed during in-process run-in. The generator was disassembled and it was found that the rotor band had been rubbing the generator stator inner diameter, reference Figure 11.

In order to determine the cause of the rubbing, all the dimensions were verified and a rotor deflection analysis was performed. The result of the analysis was that everything appeared correct. The only abnormality noticed in the test data was that the no load generator torque measurements indicated higher than expected torque. No load generator torque measurements are an indication of the losses in the generator magnetic core and bearings. From the higher than expected generator torque, it was determined that approximately 50 W of power was being generated in the rotor band at the higher speeds due to varying magnetic field. In a normal generator design, the magnetic field in the rotor band does not vary to the extent that any significant losses are generated in the rotor band. However, the optimization done to the generator stator design, in order to minimize inductive reactance, created larger than normal magnetic field variation in the rotor band. The rotor band is a thin metal band which is primarily in direct contact with the rotor magnets. The rotor magnets are Samarium Cobalt, which has relatively low thermal conductivity. Due to the relatively low thermal conductivity of the magnets, the 50 W of power generated in the rotor band caused the rotor band temperature to increase. Due to this, the band expanded significantly which caused it to rub the generator stator inside diameter. Normal operation duration for the Descent Brake is seven seconds, which does not generate enough heat to cause the interference. This issue did not show up until the run-in was performed for 1 hour in each direction at 6 rad/s.



Figure 11 - Rotor Development Issue

Since the rotor band is not exposed to significant varying magnetic field in a normal generator design, it is typically made from a material that has appropriate mechanical properties for the application. In this case, the material initially chosen was beryllium copper. Power losses due to magnetic fields are a function of the electrical conductivity of a material. Beryllium copper has an electrical conductivity of approximately 20% that of pure copper. To solve the band power dissipation issue, the beryllium copper rotor band was replaced with a one made from Inconel. Inconel has an electrical conductivity of approximately 2% that of pure copper. The Inconel band resolved the power dissipation issue.

Although the operation time of the Descent Brake is relatively short, understanding all the environments the device is going to be used in is critical to achieving a robust design.

Commercial Components

Another issue encountered in the manufacturing process was the use of commercial needle roller bearings. Roller bearings were implemented in the design to support the planet gears on the second and third stage carrier assemblies due to the high radial load and speed requirements at these locations. These bearings were procured from a commercial vendor using their standard materials. The 440C Stainless Steel rollers were fine, but the carbon steel cages had corrosion issues even though they were coated with a proprietary silver plating. Strict corrosion prevention process had to be implemented to ensure parts with corrosion did not end up in the assembly.

Conclusions

Ultimately, the program achieved successful completion of validation testing of the Descent Brake design for the qualification unit. High level collaboration between JPL and SNC led to the successful assembly and test of the flight unit. The flight unit has been integrated into the rover and completed system level testing. This included a system level drop test in January, 2011. The total drop time during this test was within 0.1 second of the predicted time. The Curiosity rover is currently in transit to Mars, it was launched November 26, 2011, and is scheduled to land on Mars on August 6, 2012.

Acknowledgments

This work was funded by JPL under Subcontract 1293381. The authors wish to express appreciation to Ted Iskenderian, JPL Mechanisms Engineering Manager, for his work on the Descent Brake and their assistance in the production of this paper. BUD and Curiosity images courtesy of JPL.

References

1. Gradzial, M.J. and Holgerson, K.J. "Mechanisms for Lowering Tethered Payloads: Lessons Learned from the Mars Exploration Program" IEEE Aerospace Conference Paper No. 1030, Big Sky, MT, March 2008
2. Mobley, J. "D21507 Final Report: Lightweight Gearbox Technology Program Phase II SBIR" SNC

Mars Science Laboratory Differential Restraint: The Devil is in the Details

Elizabeth Jordan*

Abstract

The Differential Restraint, a mechanism used on the Mars Science Laboratory (MSL) rover to maintain symmetry of the mobility system during the launch, cruise, and entry descent and landing phases of the MSL mission, completed nearly three full design cycles before a finalized successful design was achieved. This paper address the lessons learned through these design cycles, including three major design elements that can easily be overlooked during the design process, including, tolerance stack contribution to load path, the possibility of Martian dirt as a failure mode, and the effects of material properties at temperature extremes.

Introduction

The Differential Mechanism, a series of linked, passive pivots, is a component of the Mars Science Laboratory's rocker-bogie mobility design. The differential acts as a motion reverser for the suspension system. The Differential Restraint was designed to prevent the rotation of the Center Differential Pivot (see Figure 1) of the Mars Science Laboratory mobility system during the launch, cruise, and Entry Descent and Landing (EDL) phases of the MSL mission.

The Mars Science Laboratory is JPL's next generation Mars Rover, known to the public as "Curiosity". The mission launched on November 26, 2011 on an ATLAS V rocket and is scheduled to land on Mars on August 5th, 2012. The rover mobility system incorporates the heritage rocker-bogie suspension design which was invented at JPL for the first Mars rover missions. The large size of the rover, approximately nine feet in length, requires the mobility system to be folded during the cruise stage of the mission. During the Skycrane phase, in which the rover is lowered to the ground via bristles and a descent stage (see Figure 2) the rocker arms of the mobility system are released from their stowed positions and allowed to rotate about passive pivot joints until the four rockers latch in their ready-for-touchdown positions. The Differential Restraint is the last of the mobility restraints to be released, via a pyro, approximately 2 seconds before rover touchdown.

* Jet Propulsion Laboratory, California Institute of Technology , Pasadena CA

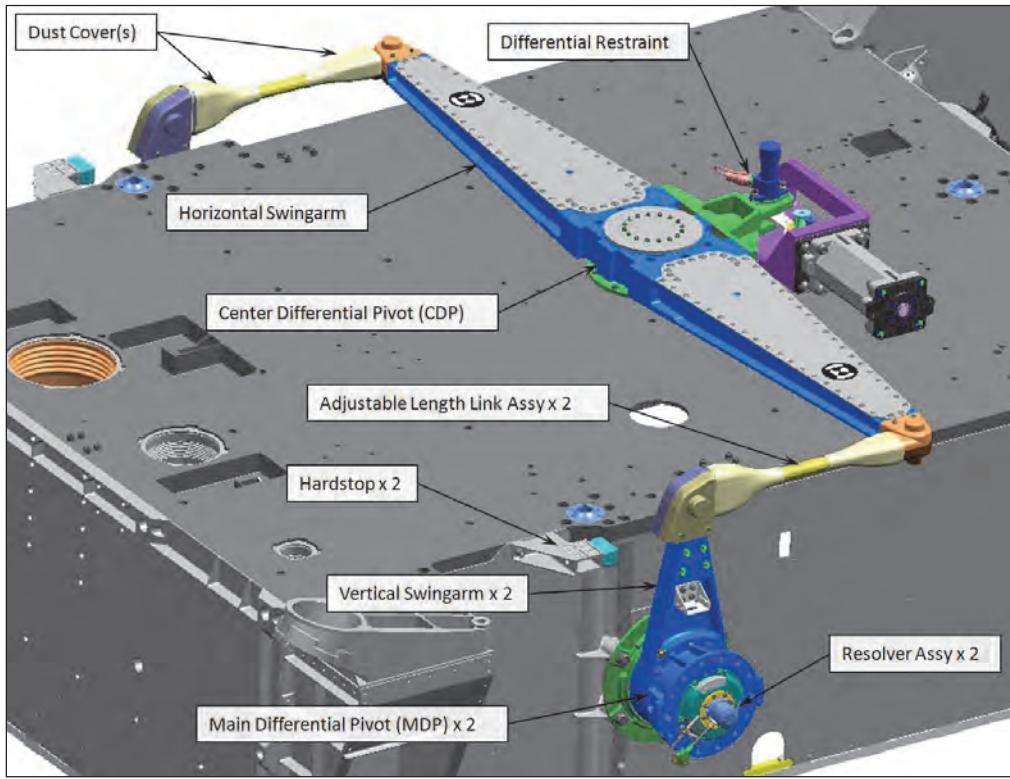


Figure 1: Key Components of the MSL Mobility Differential Suspension System

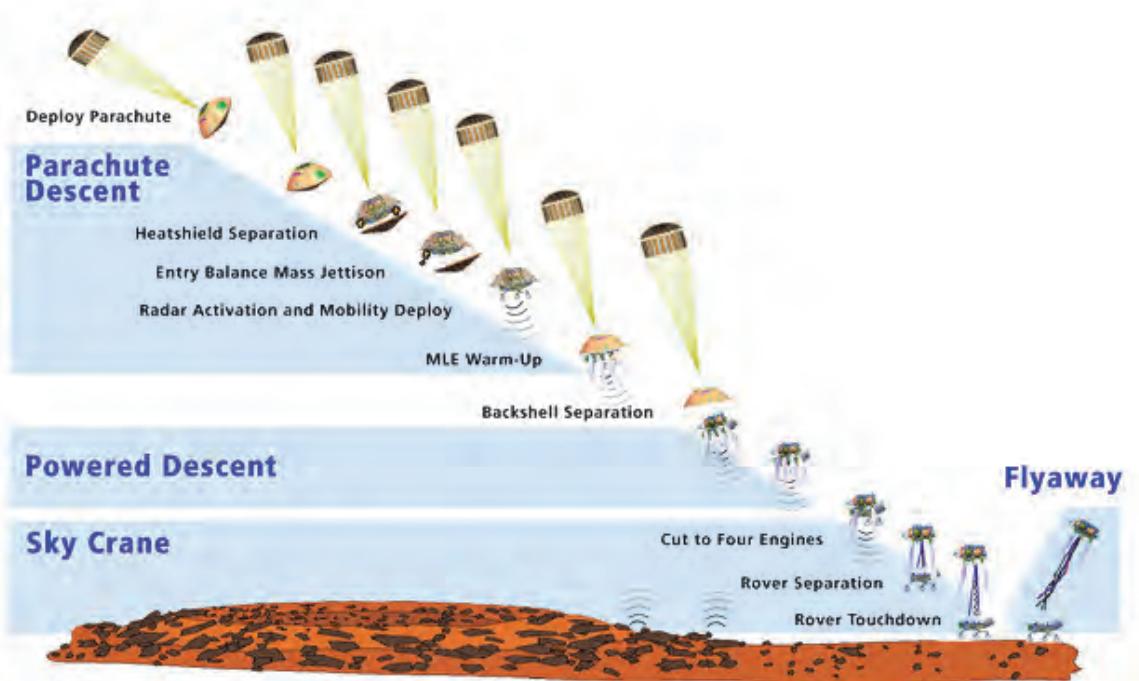


Figure 2: MSL Entry Descent and Landing Overview Diagram

Differential Restraint Design Development and Description

The Differential Restraint is a passive mechanism which relies on the compression of a series of Belleville Springs to limit the degree of rotational motion allowed at the Rover Mobility Center Differential Pivot during the Cruise and EDL phases, as well as to absorb and dampen the energy associated with the violent mobility deploy and latch events. Since the rover mobility system is also the vehicle's landing gear it is critical that the 6 wheels are in, what is termed, their "ready-for-touchdown" state, or as close to 6-wheels flat as possible when the vehicle impacts the Martian surface. The Differential Restraint enables this goal by limiting the rotation of the passive center pivot joint, known as the Center Differential Pivot (CDP), to a small angle, keeping the two sides of mobility, port and starboard, nearly balanced. Once the chassis dynamics, namely, chassis pitch and roll from the effects of the mobility deploy and latch events, have settled out the Differential Restraint is released, via a pin-puller pyro just prior to rover touchdown.

Design History

The driving load case for the Differential Restraint is derived from the near-simultaneous deployment (and end of travel latch events) of the mobility rockers during the Skycrane phase of EDL. In the event of actual simultaneous latch events of the port and starboard sides, large shear loads are expected at the CDP. Alternatively, if the deployment and latch events are staggered from port to starboard large moments are created about the CDP, which the Differential Restraint must absorb. The original Differential Restraint design was a rigidly pinned interface between the externally mounted mobility Differential and the top deck of the rover chassis which prevented nearly all motion, except for the small amount of slop between the pin puller pin and interfacing monoball (see Figure 3).

Approximately one year after the mobility Critical Design Review the increasing maturity of the ADAMS dynamic model produced a drastic increase in the predicted moment and shear loads at the CDP. This had the effect of creating significant negative margins in the original piece parts of the Differential Restraint; including the AerMet pin of the 3/8" Pyro, the shear pins and bolted joint which interfaced to the Rover top deck, as well as the Rover top deck itself. In late 2008 it was concluded that a completely new restraint design was required. The new design was to be analyzed, built, tested and integrated before the (then) planned 2009 launch. In addition to the tight timeline constraints, the re-design effort was further complicated by the fact that the hardware interfaces were already fixed, the available space was incredibly limited, and the 3/8" pin puller was the only feasible option for pyro devices.

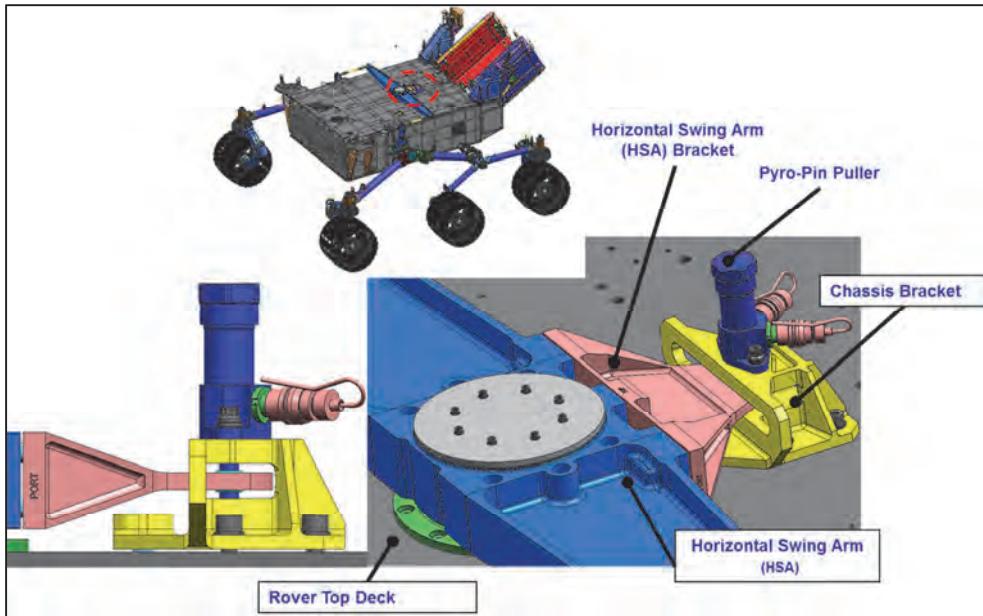


Figure 3: Original, Rigidly Pinned, Differential Restraint Design Concept

Since the rover top deck interfaces were already built, and the pyro device was already qualified and delivered the new design had to find a means by which the loads that the Center Differential Pivot would impart on these critical interfaces could be significantly decreased. The new design relied on the principle of applying a (theoretical) torsion spring at the center of the Differential Pivot which would absorb the large impact energy. After running idealized dynamics simulations, a spring rate of approximately $200,000 \text{ N}\cdot\text{m}/\text{rad}$ was selected as the stiffness that would reduce the impact loads enough to prevent negative margins in mobility and chassis hardware but still restrain the mobility system from excessive motion during launch, cruise and the initial stages of EDL enough to be able to ensure that the mobility system was in its “ready-for-touchdown” state in time for landing. The new restraint was designed to accommodate the worst case combined loading event as predicted by a 2000-run Monte Carlo ADAMS dynamic model of the MSL EDL system.

Implementing a torsion spring at the Center Differential Pivot (CDP) was impossible due to packaging and size issues so it was decided that the Differential Restraint would use a 3-bar crank-slider approach to turn rotation into linear actuation (see Figure 4). Combinations of large Belleville washers in series and parallel were implemented to achieve the extremely high spring rate that was required in the limited space available. A rod, known as the Spring Plunger, was used to actuate the two stacks of Bellevilles. One stack is compressed from positive moments while the opposite stack is compressed by negative moment loads at the CDP (see Figure 5). The Spring Plunger, made from Titanium, was threaded at one end to allow it to be joined to a Clevis, which in-turn was connected to a Linkage with a Monoball in each end (see Figure 6 and Figure 7).

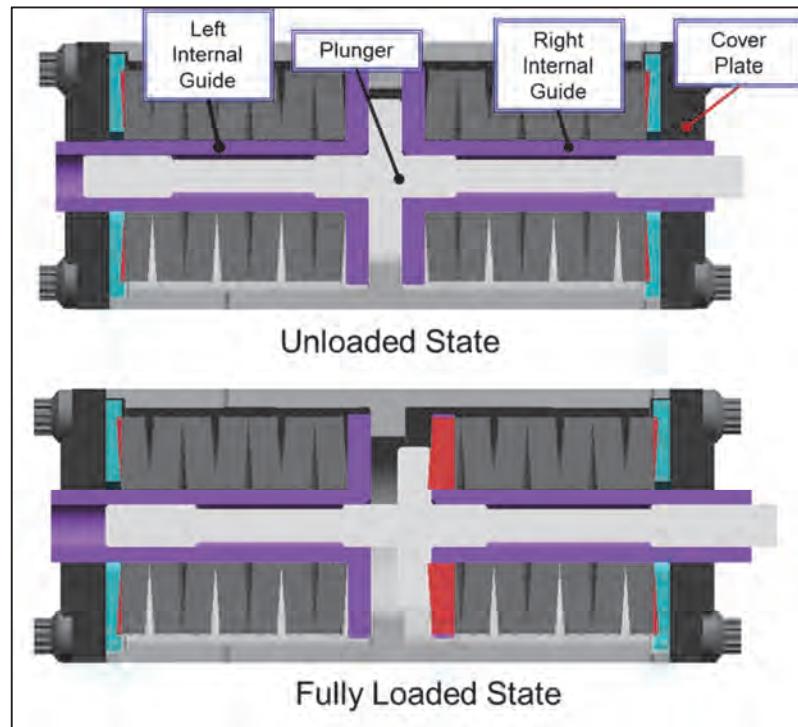


Figure 4: Crank-Slider Diagram of Differential Restraint

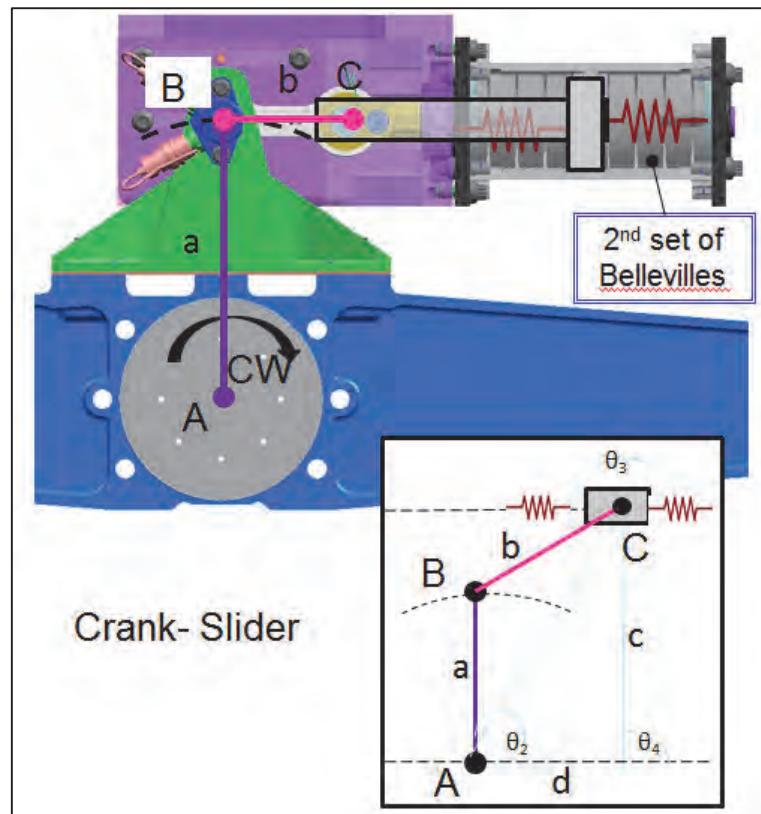


Figure 5: Belleville Spring Cross-Section Loaded and Unloaded States

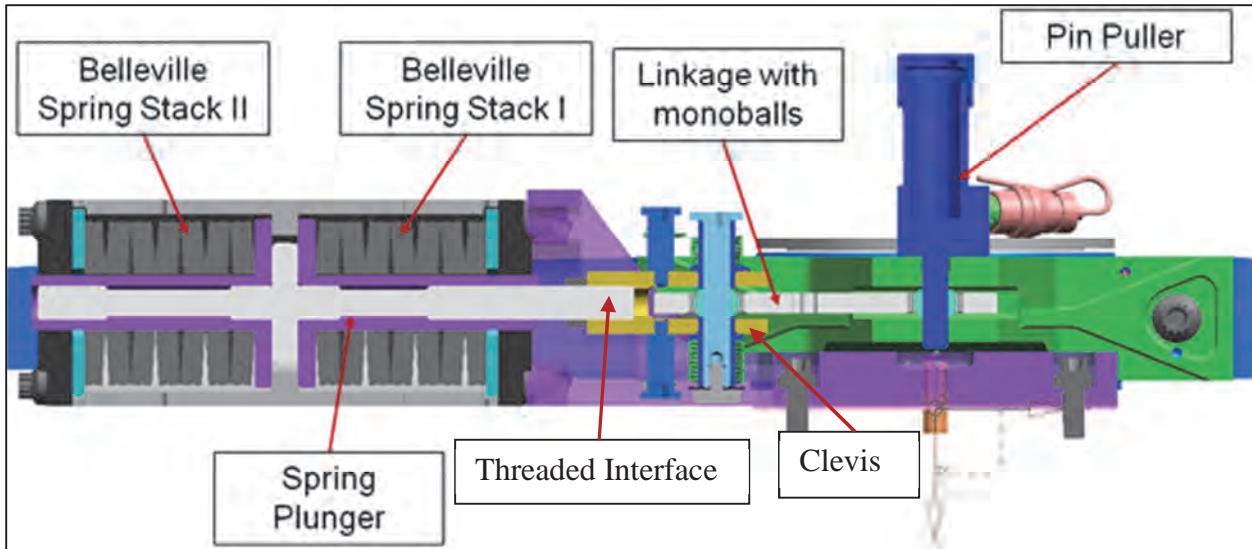


Figure 6: Cross Section of Differential Restraint Mechanism

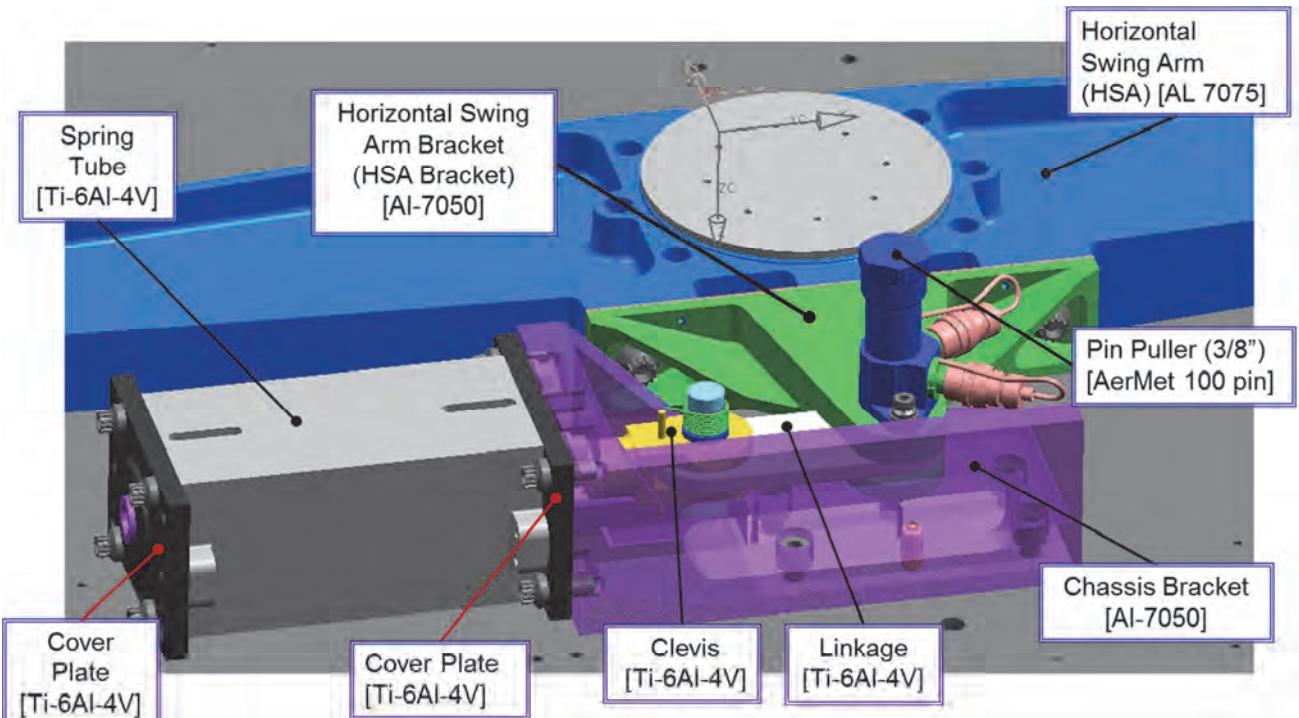


Figure 7: Differential Restraint Mechanism Nomenclature Overview

Tolerance Stacks and Stress Analysis

Test Failure

With the delay of the MSL launch the new Differential Restraint hardware was built but the planned component level testing of the hardware was delayed in an effort to conserve funds. In July of 2009, the Differential Restraint was integrated to the mobility differential system (see Figure 1) on the Dynamic Test Model of the MSL rover, in preparation for the differential system static test. With the restraint in place, the test was designed to load the entire differential system and generate a large moment load about the

Center Differential Pivot by pushing on an additional lever arm connected at the Main Differential Pivot Interface. At 90% of the full test load the measured load began to drop rapidly and an audible snap was heard. Upon investigation it became apparent that the Spring Plunger had catastrophically failed at the point of thread termination at the interface between the Spring Plunger and the Clevis (see Figure 8).

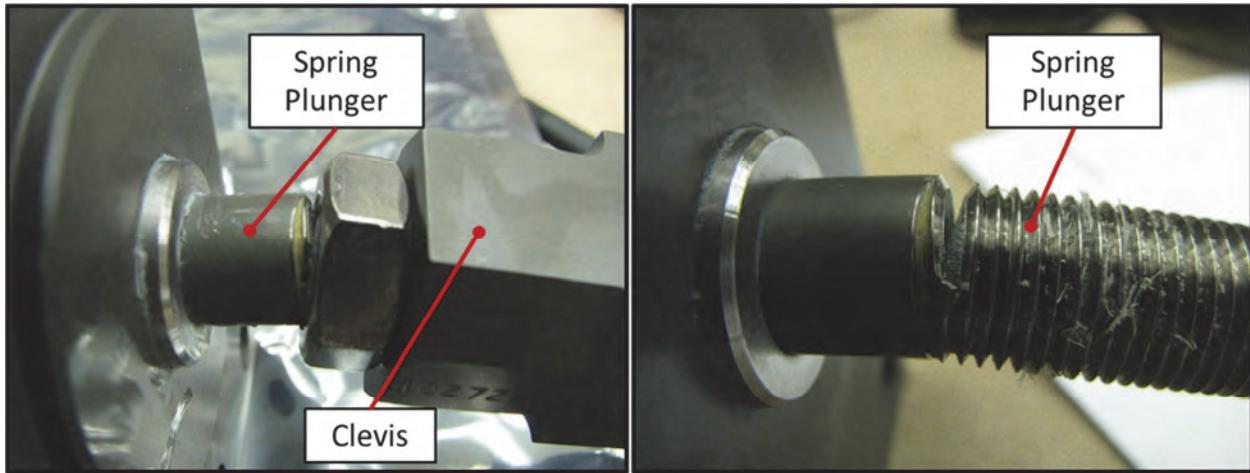


Figure 8: Failed Differential Restraint (Left) Disassembled from Clevis (Right)

Determining the Cause of Failure

Since the component level tests of the Differential Restraint had been skipped a wide array of failure causes existed that needed to be examined. Linear sliding mechanisms are often avoided at JPL on principle. This fact made the theory that one of the sliding surfaces between the Spring Plunger, Internal Guides, and Bellevilles had jammed, thereby preventing actuation of the mechanism, a prime suspect. Another theory was that the Spring Plunger, which was made from Titanium, had been made by a fraudulent vendor, and that imperfections in the material caused the crack initiation. The lack of a thread relief callout on the Spring Plunger drawing was also considered as a possible cause of failure, as was the large bending load on the Spring Plunger.

Failure Theories:

- Jammed sliding surfaces
- Fraudulent Titanium
- Improper thread termination on Spring Plunger
- Excessive bending load on Spring Plunger

The leading failure theory, that the sliding surfaces had jammed and prevent motion, was disproven in two ways. First, a line of Braycote, the lubricant used inside the Belleville Spring Assembly, was left on the Spring Plunger from where it had entered the Belleville Spring Assembly. By measuring the distance between the grease marks left on the Spring Plunger, it was possible to approximate the distance traveled between the start of test and the time of failure to be 5.46 mm (0.215 inch). At the load applied at the time of failure the total compression of the Belleville Spring stack was predicted to be 5.59 mm (0.220 inch). The close proximity of these values was strong evidence that the Spring Plunger did in fact slide along the Internal Guides and compress the spring stack as intended. Furthermore, the shape of the load deflection curve measured during the test exactly matched the prediction (see Figure 9), including the inflection point where the stiffness of the Belleville Stacks drops by one-half due to only one stack being compressed after the initial motion during which both stacks are in the load path. If the mechanism had jammed the applied load versus displacement would have spiked significantly rather than following the predicted linear line before dropping off when the Spring Plunger yielded and eventually snapped.

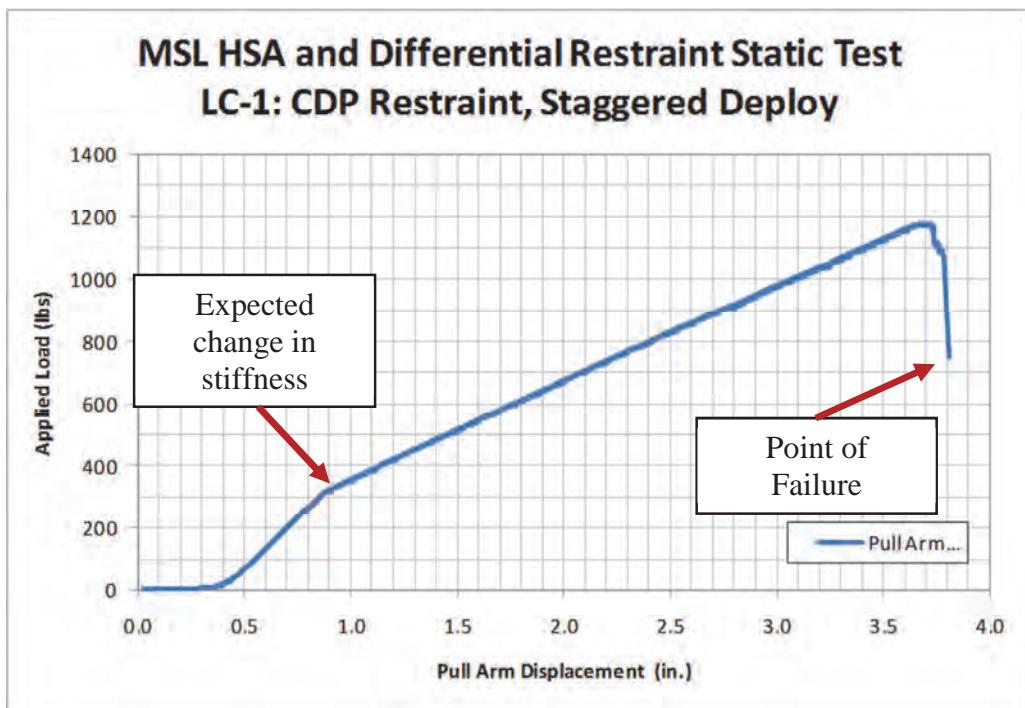


Figure 9: Applied Load vs. Pull-arm Displacement measured during failed Static Test

Upon inspection of the material certs for the Spring Plunger it was confirmed that the material was from Western Titanium. However, upon SEM inspection of the failed threads (see Figure 10) it was determined that the failure was ductile and there was no evidence that a material imperfection initiated the crack.

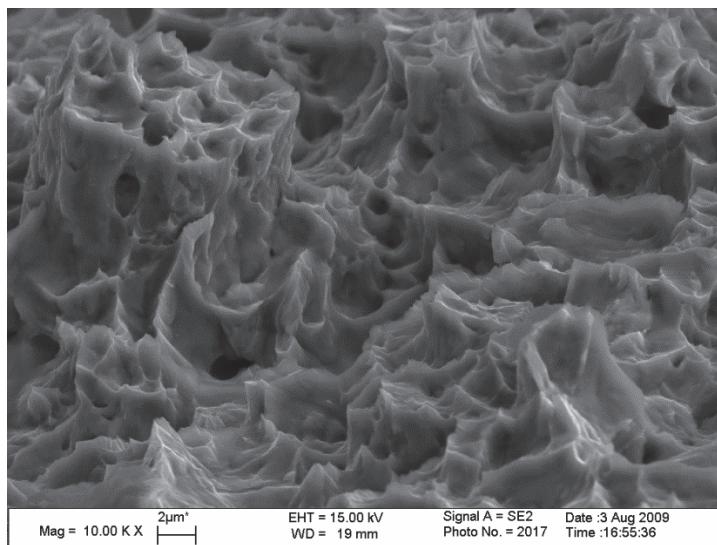


Figure 10: 10kX magnification of Spring Plunger Fractured Surface

Bending Loads

The Spring Plunger was originally analyzed for a bending load which would be applied as the Center Differential Pivot rotated. Since the Differential Restraint mechanism was designed to limit the rotation of the Center Differential Pivot to $\pm 2^\circ$, the total misalignment between the line of action of the Linkage and the Spring Plunger was calculated by assuming a worst case rotation of the CDP to be 5° . If the CDP were allowed to rotate 5 degrees the misalignment between the line of action of the Linkage and the

Spring Plunger axis caused by this rotation would be 0.5° . With these assumptions the Spring Plunger was shown to have very small, but positive, margins of safety at the root of the threads. What was thought to be a very conservative analysis, (doubling the expected rotation of the CDP) was in fact not nearly conservative enough.

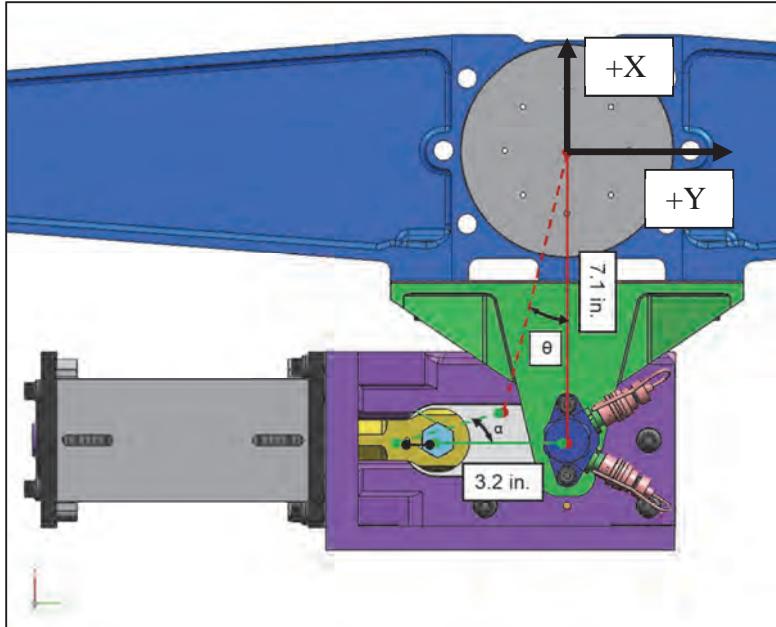


Figure 11: Line of action misalignment due to rotation of Center Diff. Pivot

In the post failure analysis the total angular misalignment between the Linkage force vector and the Spring Plunger was further scrutinized. It quickly became apparent that the misalignment caused by the rotation of the CDP was actually one of the smallest contributors to the overall misalignment. More significant misalignments were due to piece part misalignments due to imperfect shimming of the mechanism, the vertical slop of the Linkage in the mouth of the Clevis and Horizontal Swingarm Bracket, the slop of the Center Differential Pivot in its own bushings, and the elastic deformations of the Chassis Bracket and the Rover Chassis top deck. The maximum possible misalignment was calculated to be 2.2 degrees (see Figure 12), which was over four times what was initially accounted for in the Spring Plunger stress analysis.

Angular Misalignment

(Include RSS where applicable)

Misalignment Source	ΔX	ΔZ	ΔRX	ΔRZ
	[in.]	[in]	[°]	[°]
1.0	1.1 Sprng Stack Deflection (.215")	0.00458		
	1.2 HAS Shim	0.02		
	1.3 Chassis Bracket Shim		0.02	
	1.4 Monoball to HSA		0.0233	
	1.5 Monoball to Clevis		0.0094	
	RSS	0.020518	0.03211	
1.0 RSS_X_Z		0.03811		
2.0	2.1 CDP Translation	0.022	0.013	
	2.1 RSS_X_Z	0.02555		
	2.2 CDP Rotation about X/Y		0.0448	
	3.1 Chasis Bracket Elastic Deformation (8443 lbf)	0.0031	0.0053	0.629
	3.1 Sum_X_Z	0.0084		
3.0	3.2 Top Deck Elastic Deformation (8443 lbf)	0.0045	0.0290	
	3.2 Sum_X_Z	0.0335		
	3.3 Clevis Elastic Deformation		0.0188	
	3.4 Spring Plunger Elastic Deformation		0.0442	

RSS (1.0,2.1,3.0)	0.0749	0.6290	0.0822
Angular Misalignment (1.0,2.1,3.0)	2.0614	0.7112	

RSS (1.0,2.2,3.0)	0.0834	0.6290	0.0822
Angular Misalignment (1.0,2.2,3.0)	2.2154	0.7112	

Figure 12: Differential Restraint Angular Misalignment Calculations

Recovery From Failure

Immediately following the failure of the Differential Restraint many senior engineers began taking a closer look at the restraint design. They highlighted the fact that the restraint poorly implemented the concept of a crank-slider because the point at which the crank grabbed the slider was not at the center of the slider but rather it was offset- the link between the Clevis and the Spring Plunger was at the end of the Spring Plunger rather than the middle of the Spring Plunger (see Figure 13). Many engineers advocated redesigning the restraint to properly implement the theory of the crank slider; however limited schedule and funds made a complete redesign impractical. Instead, the design concept and most of the original hardware was kept intact, but key components were changed from Ti-6Al-4V material to significantly higher strength steel. By remaking two components and modifying two additional ones it was possible to quickly and relatively cheaply make the restraint design work.

Using the interaction formula:

$$R_c + \sqrt[3]{R_s^3 + R_b^3} = 1$$

R_c = ratio of compressive stress to yield /ultimate stress

R_s = ratio of shear stress to yield/ultime stress

R_b = ratio of bending stress to yield /ultimate stress

it was possible to predict the allowable side load, and hence the misalignment angle between the Spring Plunger and Clevis that a steel Spring Plunger could withstand, if the Flight Limit Load was applied axially. After calculating the misalignment angles that would produce yield and failure for a Spring Plunger made from steel it was decided that the values calculated were too close to the worst case possibilities predicted by the tolerance analysis to make simply changing the material a comfortable approach. Therefore, in addition to changing the material, the Spring Plunger diameter and thread diameter was increased. With the larger Spring Plunger diameter, and the material swap from Ti-6al-4v to steel, the new Spring Plunger would be able to withstand 4.24° and 4.29° misalignments before yielding and ultimately failing respectively. Additionally, a thread relief was added to the Spring Plunger thread termination (see Figure 14) to prevent excessive stress concentrations.

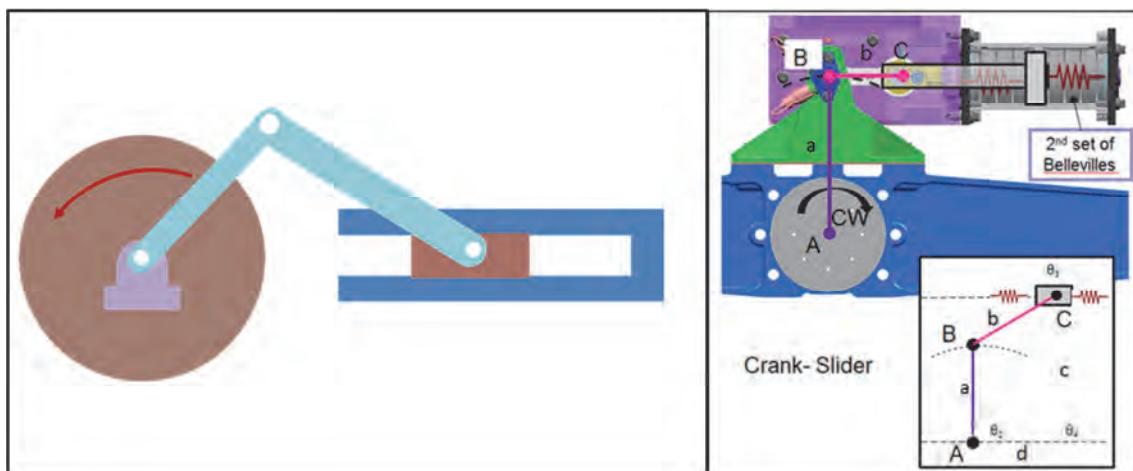


Figure 13: Comparison of “proper” crank-slider design methodology vs. Differential Restraint Design

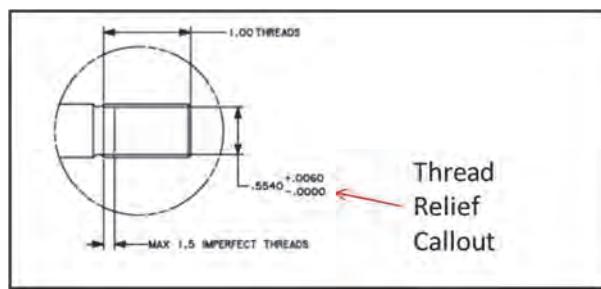


Figure 14: Spring Plunger Thread Termination Callout

Key Findings:

- Tolerance stacks and shimming procedures affect load paths- Make sure to account for this in stress analysis
- The location of pivot joints in kinematic mechanisms is extremely important- Failing to follow best practices early-on can cause unexpected difficulties down the road
- Proper thread relief callouts on drawings is essential for limiting the effect of stress concentrations

- Although not always the most elegant design approach- making a design “good enough” rather than ideal can be a more effective approach for saving time and money

Lubrication and Vacuum Bake

Since it was a concern that the properties of the lubricant used in the Differential Restraint, Braycote 601EF, could be altered by vacuum bake, the vacuum bake out, required for all MSL hardware to meet contamination and planetary protection requirements was performed prior to performing life and component level testing on the Belleville Spring stacks. Upon removing the Differential Restraint components from a 50 hour, 110°C vacuum bakeout an oily substance was noticed on the bottom surface of the mechanism. Upon chemical analysis of the substance it was determined that it was the lubricant Braycote 601EF. According to the Braycote 601EF product data sheet, the temperature range for Braycote 601EF is -80°C to 204°C, however the viscosity at these temperatures had been overlooked. At a temperature of 99°C Braycote 601EF has a viscosity of 45 cST, which is approximately midway between the room temperature viscosities of Honey (73.6 cST) and Olive Oil (24.1 cST). When viewed in this context it is not surprising that the Braycote flowed and leaked out of the assembly when baked at 110°C.

The Differential Restraint, Belleville Spring Assemblies were weighed before and after entering vacuum bake. With the knowledge of the decrease in weight due to vacuum bake and the knowledge of the mass of Braycote originally in the assembly it was determined that the Engineering Model and Flight units lost between 10 and 12% of their original Braycote lubricant due to the leak. Despite the loss of lubricant the stiffnesses of the Belleville Spring stacks measured during thermal characterization testing were well within the range of predicted and acceptable values and it was deemed unnecessary to add replacement lubricant to the assemblies.

By exposing the potential for Braycote to leak from the assembly the unfortunate leak that occurred during vacuum bake turned out to be a blessing in disguise, in that it focused attention on a failure mode that would have otherwise been missed. Due to the hardware's proximity to critical lenses for imagers on the Rover, focus was shifted away from the concern over the Belleville spring rate which was vetted through testing, to how to prevent the Braycote from leaking during flight and possibly contaminating other sensitive hardware. The actuation of the Spring Plunger through the Belleville Spring Assembly and its ability to squeeze Braycote out of the Belleville Spring Assembly like toothpaste became a concern. This problem was solved by adding a cover over the end of the Belleville Spring Assembly to catch any Braycote squeeze out (see Figure 15). Kapton shields were epoxied over the witness holes in the Belleville Spring Assembly (see Figure 15) to close out those leak paths as well. With these new covers in place the venting ratios of the Belleville Spring assembly came under scrutiny. A balance was struck between closing vent paths and preventing the Kapton tape from being blown off during depressurization by poking pin holes in the Kapton covers.

Key Findings:

- Just because a material is advertised to work over a specified temperature range doesn't mean it will work the same over the specified temperature range-make sure to understand all key material parameters over the expected temperature range to avoid surprises
- Consider “Band-Aid” solutions carefully while fixing one problem to avoid creating another

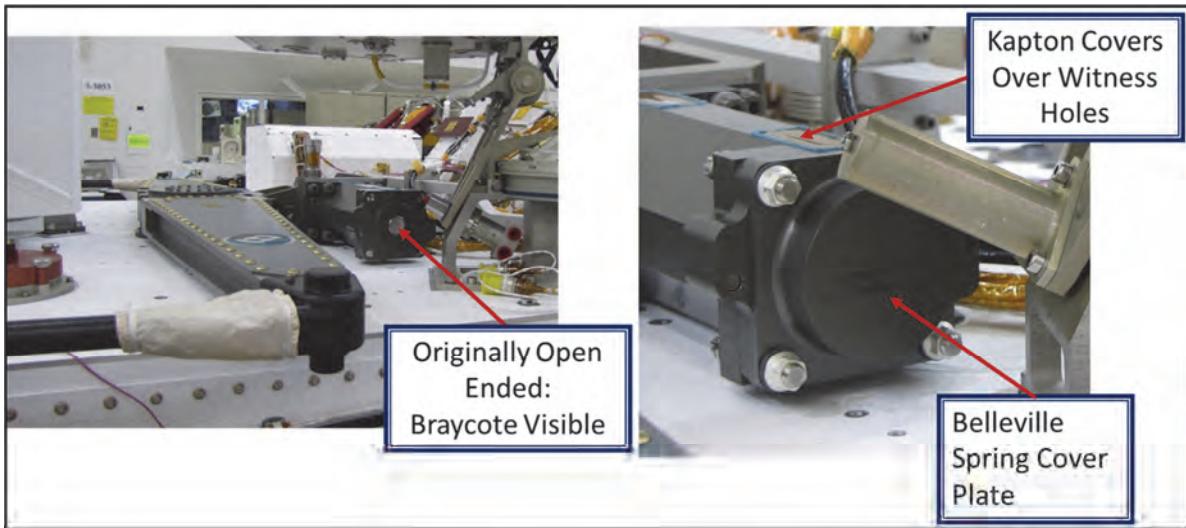


Figure 15: Before (Left) and after addition of Braycote leak path closures (Right)

Working in a Dirty World

As part of the final preparations for launch and closeout of the Verification and Validation matrices, the testing performed on all of the Rover pyros was summarized in order to ensure the Rover had been properly and completely tested. Although the pin puller used in the Differential Restraint had been qualified and testing had been completed at the sub-system and system level tests over temperature one concern was raised that the pin puller had never been fired in a dirty environment. None of the rover release pyros had been tested in dirt because they are fired shortly after the rover enters the Mars atmosphere while the rover is still connected to the Descent Stage and approximately one-hundred feet above the surface. The Differential Restraint pin puller, however, is fired much later in the deploy sequence, when the rover is approximately 2 seconds from final touchdown. Not only is there dust expected in the atmosphere at the level of the firing of the Differential Restraint pin puller, but the Descent Stage rocket engines are also expected to kick up significant quantities of Mars dirt into the atmosphere. The tight clearances between the Horizontal Swingarm Bracket bore and the pin puller pin (nominal 0.0015" diametral clearance) created a concern that small particulates of sand/dust could get stuck between the two surfaces and jam the joint, thereby preventing retraction of the pin. Additionally, there was a concern that if debris were to enter the pin puller device itself the retraction of the pin could fail.

Two tests were conducted to demonstrate the ability of the Differential Restraint Pin Puller to successfully retract in the presence of large quantities of dirt. Hardware which mimicked the Flight hardware clearances and tolerances was used to perform the test. This hardware had previously been used to qualify the pin puller for release while subjected to large lateral loads over temperature and varying percentages of NASA Standard Initiator charge. An acrylic chamber was built to sit around the Differential Restraint mock hardware and a GN2 line was setup with two inlets to the container to create a simulated dust storm. In total, 700 ml of dust simulant was added to the chamber, including 600 ml of cohesionless fine grain sand, which was used in traverse testing characterization for the MSL rover, 50 ml of JSC-1 lunar soil simulant and 50 ml of BP-1 dust (see Figure 16). GN2 was pumped into the chamber at 345 kPa (50 psi) for 30 seconds prior to firing the pin puller to create the simulated dust storm.

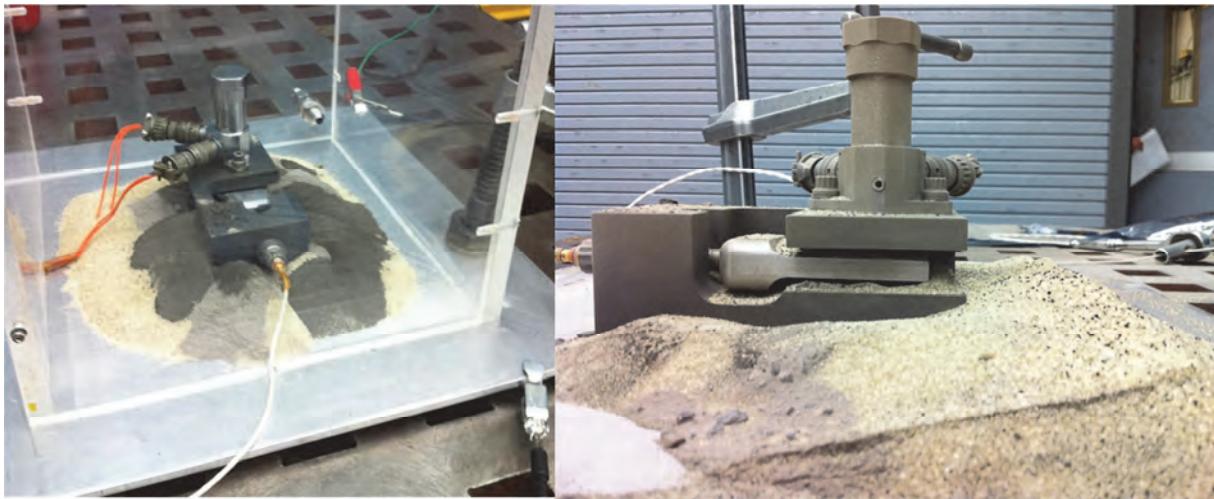


Figure 16: Dirty Pin Puller Test Setup: Pretest (Left), Posttest (Right)

The first test involved a dual firing of 100% charged NSI while the second test involved only a single NSI charged to 100%. Both tests included the application of the flight limit lateral load applied to the pin puller pin through the use of a strain gaged bolt connected to the Linkage hardware simulator. Both tests resulted in successful retraction of the pin puller. Upon inspection of the pin puller pin, Linkage monoball, and Horizontal Swingarm Bracket bore after the test no unusual wear marks or scoring were found, indicating that the fine grains of dust and sand had not jammed or impeded the retraction of the pin. The monoball in the Linkage, did however, have a significant increase in drag due to the presence of dirt in the lubricant on the monoball increasing the rolling friction between the ball and race. The increased drag in the monoball is not significant, however, since it did not provide enough resistance to jam the pin and prevent it from retracting.

Key Findings:

- Consider operational environments during the design of hardware (ex. how particulate contaminants affect hardware clearances and failure modes)
- Pin Pullers can successfully operate in the presence of fine grain particulates

Summary

The design of the Differential Restraint for the MSL mobility system involved striking a difficult balance between strict load and deflection requirements with the tight design space available. In total, three major design iterations were required to get the Differential Restraint from concept to the launch pad, and along the way some interesting lessons were learned. The first redesign effort was required when the loads model drastically increased the predicted maximum loads. The failure to consider the shimming procedure and misalignments allowed for by piece part clearances and tolerances was a costly mistake which led to the failure of the design in a major system level test causing the entire design to be subjected to major scrutiny and redesigned for a second time. The tolerances and clearances, when considered, allowed for over four times the assumed misalignment between the axis of the Spring Plunger and the Linkage which proportionally increased the bending stress in the Spring Plunger. The absence of a proper thread relief callout on the Spring Plunger drawing provided an easy target for scrutiny of the design, but was also easily corrected in the redesign efforts. The leaking of Braycote during vacuum bake should not have been a surprise, but the failure to assess the meaning of the viscosity of the lubricant at high temperatures led to the requirement of yet another design Band-Aid, the implementation of which would have neglected the effects of depressurization and rules of thumb for venting ratios except for a last minute catch of the newly created issue. The development of the Differential Restraint was not a linear or

elegant process, but important lessons about tolerance stacks, lubricant leak paths, and even the use of pyrotechnic devices in dirty environments were learned; the knowledge of which will hopefully inform the design of future mechanisms for space applications.

Acknowledgements

This research was carried out at the Jet Propulsion Laboratory, California Institute of Technology, under a contract with the National Aeronautics and Space Administration.

Mars Science Laboratory's Dust Removal Tool

Kiel Davis*, Jason Herman*, Mike Maksymuk*, Jack Wilson*, Philip Chu*¹,
Kevin Burke**, Louise Jandura** and Kyle Brown**

Abstract

The Dust Removal Tool (DRT) is designed to expose the natural surfaces of Martian rocks obscured by layers of dust deposited by aeolian processes. The DRT, contained within a cylinder 154-mm long and 102-mm in diameter, has a mass of 925 grams. Using a single brushless DC motor, the DRT removes dust from an area 45 mm in diameter. During the dust removal process, a set of brushes articulate to maintain surface contact as they rotate at high speed. The DRT belongs to a special class of aerospace mechanisms designed to interact with unstructured extraterrestrial surface objects and environments. The wide range of rock surface characteristics along with severe resource constraints makes the DRT solution non-trivial. The mechanism features a high reduction single-stage planetary gear box and pivoting brushes that both offered lessons learned. The flight unit DRT was integrated with the MSL rover in early 2011 and is currently on track to begin surface operations at Mars' Gale Crater in August 2012.

Introduction

The Dust Removal Tool (DRT) is a critical component of Mars Science Laboratory's (MSL) Sample Acquisition, Sample Processing and Handling (SA/SPaH) subsystem. The aeolian-deposited reddish iron oxide dust that covers everything on the surface of Mars masks many characteristics of rocks and makes it difficult for scientists to identify optimal rock targets for further interrogation and possible sample acquisition. For instance, as shown in Figure 1, dust layers only microns deep can obscure many visual clues to a rock's origin (e.g., color or emissivity, cracks and inclusions) from instruments like the MSL's MastCam and Mars Hand Lens Imager [1]. MSL's Alpha-particle X-ray spectrometer (APXS), a key source of information about a rock's elemental composition, is effectively blinded by layers of dust as little as 5 microns deep [2]. It is therefore critically important to remove dust from the surface of rocks.

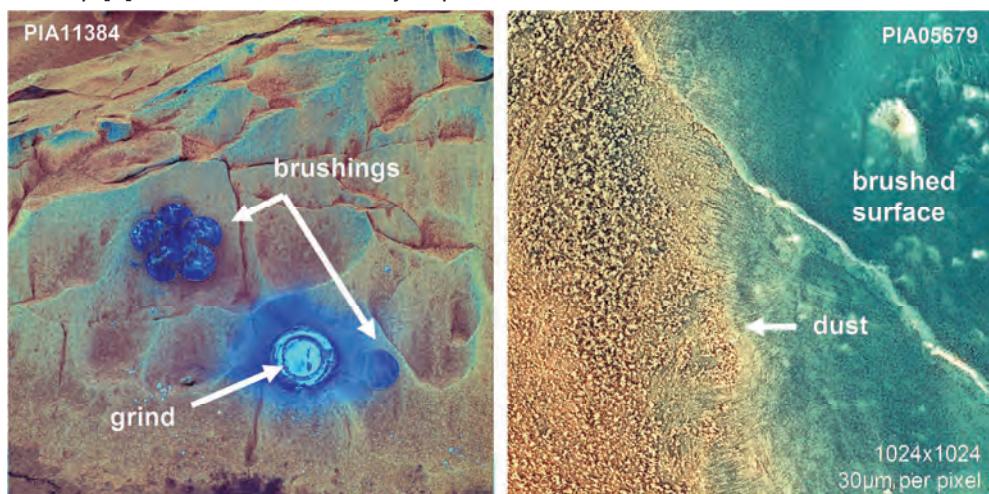


Figure 1. Left: MER Spirit Pancam false-color image of Mazatzal on Sol 86 after numerous Rock Abrasion Tool brushing and grinding operations; Right: MER Spirit Microscopic Imager false-color image of Mazatzal on Sol 79 after a RAT brushing operation. Image credit: NASA/JPL-Caltech/Cornell

* Honeybee Robotics Spacecraft Mechanisms Corp., New York, NY

** Jet Propulsion Laboratory, California Institute of Technology, Pasadena, CA

Planetary scientists may have first appreciated the dust's complicating effect during the Mars Pathfinder mission where APXS data were contaminated by dust and meaningful inferences could only be drawn through a process that assumed an amount of dust that had to be subtracted from the spectra [1]. Unlike Mars Pathfinder, the Mars Exploration Mission rovers Spirit and Opportunity both carried a tool for doing away with the dust a rock's surface. This tool, developed by Honeybee Robotics, is called the Rock Abrasion Tool (RAT) [4]. The RAT's primary purpose is to remove the rock's weathered rind by grinding an area 45 mm in diameter to a depth of 5 mm. By accomplishing its primary objective it naturally has to also remove surface dust. The RAT is equipped with brushes for sweeping away cuttings produced during the grinding process – see Figure 2. During the initial stages of RAT development, it was never envisioned or required that the RAT's brushes be used to strictly brush away surface dust layers. But through experimentation before and during the MER mission, it was eventually found that the RAT's high-speed brush, which protruded several millimeters beyond the grinding wheel's reach, is particularly effective at removing even fine layers of dust from all manner of rocks including those with pitted, vesicular surface textures.

The RAT can also accommodate a large degree of surface topography variation and robotic arm (IDD) positioning error due to its design architecture and 3 degrees of freedom. Prior to brushing or grinding, the IDD preloads the RAT against the surface of the rock via the RAT's butterfly mechanism (see Figure 2). The RAT has three actuators including a Z-axis actuator which moves the grinding wheel and brushes linearly toward and away from the rock surface. Once preloaded, a RAT software algorithm employing all three actuators, detects the rock's local surface position in the Z-axis reference frame. The RAT grind brush is then positioned with respect to the surface such that its bristles are engaged and the grinding wheel is not engaged. In this way, the arm positioning error is rendered more or less moot and successful brushing is achieved on a wide range of uneven surfaces.

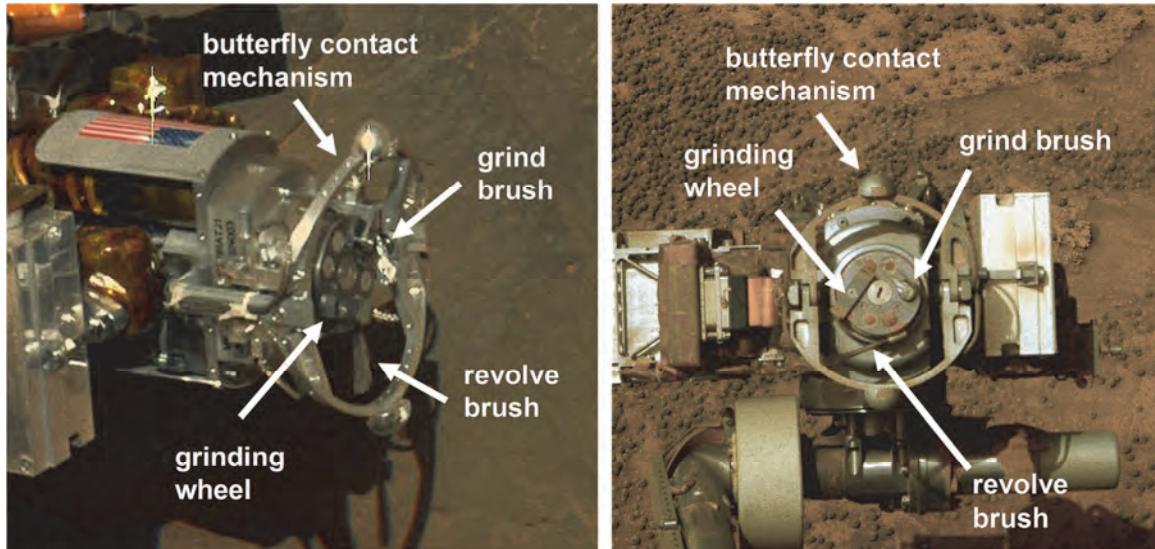


Figure 2. Left: MER Spirit RAT on Mars prior to its first operation on Adirondack rock; **Right:** MER Opportunity RAT on Mars after many operations. Image credit: NASA/JPL-Caltech/Cornell

The original plan for MSL was to include a next generation RAT with all the same functionality as the MER RAT but designed to last longer and penetrate stronger rocks [5]. However, that tool was eventually descoped by the JPL flight project office in 2007 to meet project budget constraints. This left the MSL science team without a method for clearing the blinding dust from rock surfaces. So later in 2007 a new effort was initiated to develop a tool, the DRT, designed solely for the purposes of removing dust.

Like other MSL mechanisms [6], the DRT is designed for very long life in very harsh conditions. But the DRT is unique and interesting for at least two reasons. First, as a device that directly, physically engages

an extraterrestrial object (rock) so as to manipulate this object's characteristics in some way, the DRT belongs to a special class of aerospace mechanisms. In this context, it is interesting and informative to future missions to understand how the DRT design solves the difficult problem of adequately removing micron-scale particles from a rock's uneven and often pitted surface. Second, from a pure mechanisms perspective, the DRT offers a valuable data point for planetary gear box designers along with other lessons. Due to extreme volume constraints, there was just enough room for a single stage planetary gear reduction necessary for meeting torque margin requirements. Practical limits of planetary stage reductions are considered 3:1 (lowest, planets become very small) to 10:1 (highest, sun becomes very small). A ratio closer to 5:1 is the most balanced with the highest performance rating and is therefore more common in space mechanisms designs. The DRT design incorporated a 10.4:1 single stage planetary gear reduction which pushes the limits of what is conventionally considered practical.

This paper will provide an overview of the DRT including requirements, design, manufacturing and qualification testing. It will present some of the key trades made during the development process including brush articulation kinematics and bristle geometry to maximize the reachable workspace. A significant part of the paper will deal specifically with brush pivot torque margin problems, the planetary gear design and related test results.

DRT Overview

The DRT is mounted on the MSL robotic arm (RA) turret as shown in Figure 3. Once placed on a rock by the RA, the DRT's primary functional requirement is to clear dust layers up to 2 mm deep from an area on the rock's surface no less than 45 mm in diameter – this diameter is driven by the APXS field of view and RA positioning accuracy. Like the MER RAT, the DRT is expected to face all kinds of rocks with diverse surface textures and topographies. Unlike the MER RAT however, the DRT only has a single actuator and is not preloaded against the surface. The design must therefore accommodate robotic arm positioning error in addition to varying local rock surface topography. These new design and operational constraints were challenging and required a substantial departure from the heritage RAT brush design.

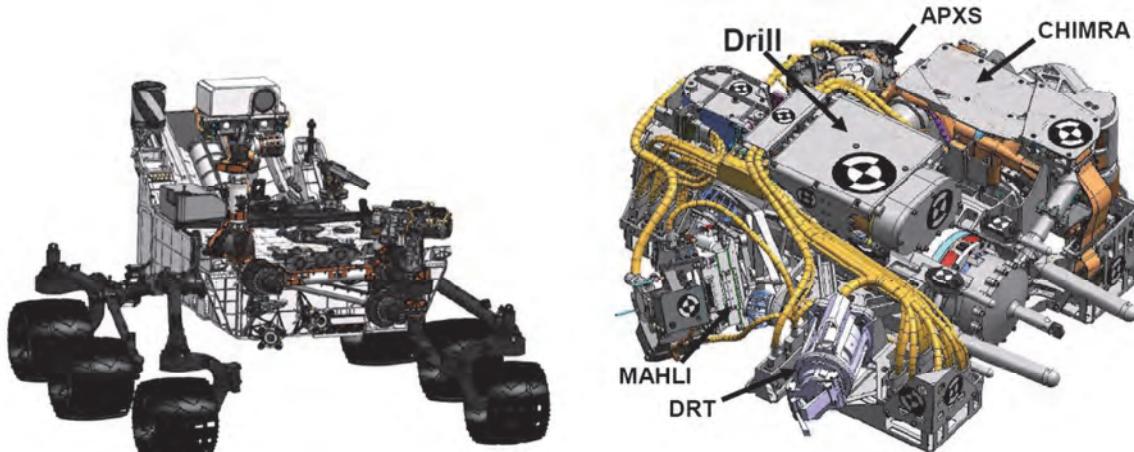


Figure 3. Left: MSL rover; Right: SA/SPaH turret with DRT. Image credit NASA\ JPL-Caltech [6]

To deploy the DRT, the RA first confirms the rock surface location using various contact sensors on the turret and then positions the DRT at a safe stand-off distance (not in contact with the rock). The DRT motor is then energized such that the bristles spin at relatively high speed and the RA then moves the DRT toward the rock surface to a position where the bristles are theoretically engaged. The DRT engagement position and angle may be off by as much as 10 mm and 15°, respectively, in any direction due to RA positioning error. The DRT motor current and encoder are monitored for a stall condition, but otherwise it is an open loop operation where the DRT motor is left energized for a period of time

(~60 seconds) to sweep the rock. The RA then pulls the DRT back away from the rock while the bristles are spinning at low speed so as not to inadvertently foul the cleared area with a sudden stop and dragging of the bristles (an undesirable effect observed during testing). The DRT motor is then de-energized while in free-space.

In addition to the single actuator and RA operational constraints, the other major constraints included the allowable volume and mass for the DRT and the fact that the DRT had to employ a particular JPL-supplied motor model. The DRT was to fit in a cylindrical envelope approximately 134-mm long and 141 mm in diameter. The allowable mass was 950 grams which included the mass of the motor (350 grams). The DRT design was to assume that the motor could provide 28 mN-m of torque at 10,000 rpm.

The DRT engineering challenge could then be boiled down to designing a set of brushes with the reach and compliance to meet the primary functional requirement (i.e., sweep a 45-mm diameter) across the range of surface topography and texture scenarios while not exceeding the tool volume, mass and motor limits. The resulting DRT fit within a cylindrical envelope 154-mm long and 102 mm in diameter and weighed 925 grams. The mechanism is comprised of a JPL-supplied motor integrated with a Honeybee custom-designed planetary gearbox which drove a sub-assembly called the brush block. The brush block consists of an asymmetric set of brushes each on spring loaded pivot (hinge) in order to accommodate the wide variation in surface geometry. A resistive strip heater is bonded to the outside of the planetary gearbox. A rotating post at the center of the brush block guards against overloading the tool's brushes against the rock.

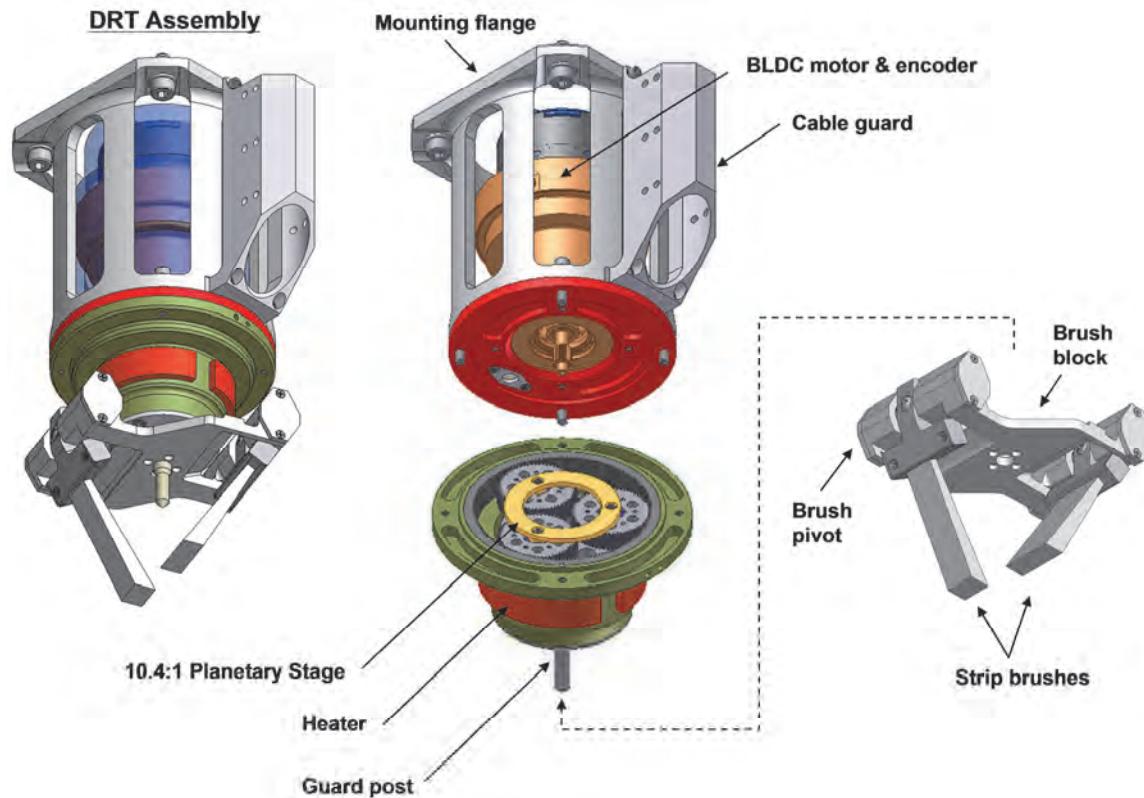


Figure 4. Dust Removal Tool

Brush Block Subassembly

The brush design process was heavily informed by a prototype testing program that lasted beyond the Critical Design Review. Rocks and dust analogs were supplied to Honeybee by JPL. A test and measurement methodology was established which quantitatively assessed brush performance. Per its equipment specification, the DRT dust removal capability was to be demonstrated by clearing 70% of dust particles less than 500 microns by surface area from a natural surface. It was especially important to clear the center of the 45-mm diameter area. Images of the surface were captured via digital camera and analyzed in software to determine the size of the area cleared by the tool. Additionally, the DRT would be required to perform dust removal operations up to 150 times on Mars and therefore a 2x demonstration (300 operations) would need to be performed with the final brush life test model. So quantitative measurements of bristle wear and brush shape degradation were also made to project life.

Initially the team considered several variants of the very simple “brush-on-a-stick” concept (left most image in Figure 5) but soon realized that bristle compliance alone was not enough to compensate for large surface height variations without massive increases in parasitic drag on the motor. Furthermore, relying on bristle compliance also worked the bristles much harder causing wear and flexing that shortened bristle life. So the notion of allowing the brush bristles to pivot about a spring loaded hinge was quickly adopted. The brushes can pivot up to 30° so that large surface height variations (10-20 mm) can be accommodated. By using a soft spring with a flat spring rate to keep the bristles loaded against the rock surface, the bristle contact force and resulting motor torque changes very little.

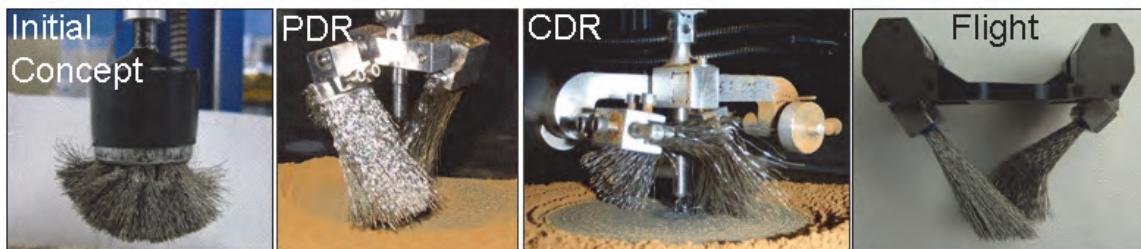


Figure 5. Brush design evolution

		Requirements and Restrictions						
		45 mm Diameter Circle	> 70% Clean	Center Clearing	Avoid Bristle Entanglement	Volume Envelope Restrictions	< 50 N Reaction Load into Turret	< 5 Micron Dust
Brush Geometry	Brush Width							
	Brush Length							
	Wire Bend							
Brush Holder Geometry	Brush Offset Distance from Center							
	Brush Separation Distance							
	Brush Symmetry							
	Brush Pivot Axis Distance from Center							
	Brush Angle							
	Spring Preload							
Software and Placement	Brush Speed							
	Approach Algorithm							
	Retract Algorithm							
	Engagement Distance							
	Brush Duration							

Figure 6. Matrix showing the major brush related design/ performance drivers

Many parameters were discovered to have an effect on the performance of this dual pivoting brush design. These parameters and their relationship to design/performance requirements are illustrated in Figure 6. Following is a summary of findings associated with key brush parameters:

- **Brush offset distance from center** – A large offset distance made it difficult or impossible to clear the center of the 45-mm diameter area; a small offset increased the chances of bristle entanglement around the center post or with bristles from the other brush.
- **Brush separation distance** – Naturally if the brushes were too close they became entangled; a minimum separation distance (~8 mm) was established which yielded best performance (minimal entanglement).
- **Brush symmetry** – It was found that with a symmetric brush design, it was impossible to clear the center of the 45-mm diameter area without severe bristle entanglement; an asymmetric brush design was adopted where one brush (Inner Brush) overlaps and clears the center and most of the area while the other (Outer Brush) assists with clearing the outer part of the area.
- **Engagement distance (brush angle)** – The engagement distance is the distance between the DRT and the rock surface as measured from the tip of the center post to the rock surface; being too close (<10 mm, shallow brush angle) resulted in a poorly cleaned surface while being further away (>10 mm, steep brush angle) resulted in better clearing and better ability of the bristles to pluck dust out of vesicular pits and crevices.
- **Brush width** – There seemed to be a critical brush width (~15 mm or $\frac{1}{3}$ the required cleared area diameter) where thinner brushes produced very clear surfaces of smaller diameter and wider brushes produced less clear surface of larger diameter.
- **Wire bend** – Straight bristles had a very difficult time removing fine particles from voids and crevices unless the engagement distance was large enough; forming a bend in the bristles enhanced their ability to “scrub” the surface even at shallow brush angles (close engagement).
- **Brush speed** – Speeds less than 300 rpm did not impart enough energy to effectively remove particles, instead the brushes just pushed the particles around in a circle; at speeds greater than 300 rpm, the brushes are much more effective at clearing the particles – a big difference between 300 rpm and 500 rpm was observed while a negligible difference between 500 rpm and 1000 rpm was observed.
- **Approach algorithm** – Not spinning the brush block while approaching the rock occasionally produced large reaction forces and at times no “center clearing”; spinning while approaching rock reduced axial force on DRT, resulted in symmetric pivoting of brushes and helped to clear the center of the 45-mm diameter area.
- **Retract algorithm** – Spinning at high speeds (or not spinning at all) while retracting tends to pull dust and debris back into cleared area; spinning at lower speeds (100 rpm or less) tends not to drag or eject material into clean areas.

Ultimately, all of the prototype testing resulted in the final flight brush design shown in the far right-hand image in Figure 5. The DRT flight brush bristles were made of a material similar to RAT brush bristles [4]. A brush manufacturer delivered straight brushes of a specified width and Honeybee formed the final brush geometry by bending the bristles around mandrels per a template and potting with a suitable flight-grade adhesive. The bristles were then trimmed to length. At two points in the process the bristle wire and brush assemblies underwent ultrasonic cleaning for contamination control (CC) and planetary protection (PP) reasons. Samples were sent to JPL for CC/PP analysis and approved for flight.

The spring-loaded brush pivots (hinges), Figure 7, were designed to keep the brushes lightly loaded against the rock surface across large variations in surface height relative to the DRT. The pivots allow the brushes to rotate 30° from hard-stop to hard-stop. The whole brush block assembly is designed to withstand inadvertent loading by the RA up to 200 N. This is one reason the pivot shaft is supported by bushings as opposed to small ball bearings. Spring-energized Bal Seals protect the bushings against dust ingress. The Bal Seals were match fit with the shaft to reduce the parasitic drag to near zero at standard temperature and pressure – a similar procedure was used with success for the RAT grinding wheel shaft

and Phoenix Icy Soil Acquisition Device cutting bit shaft [4][7]. The shaft is spring-loaded against a hard-stop by dual torsion springs. End cover-plates with integral spring arbors enclose the spring-bushing area. The pivot shaft-bushing-spring system is dry lubricated.

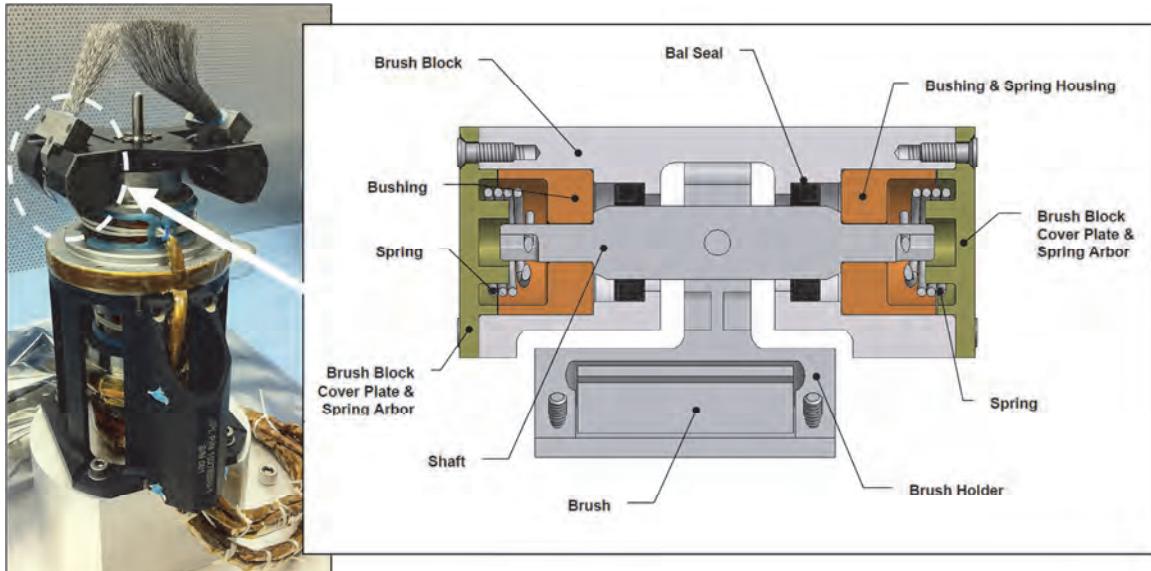


Figure 7. DRT Brush pivot

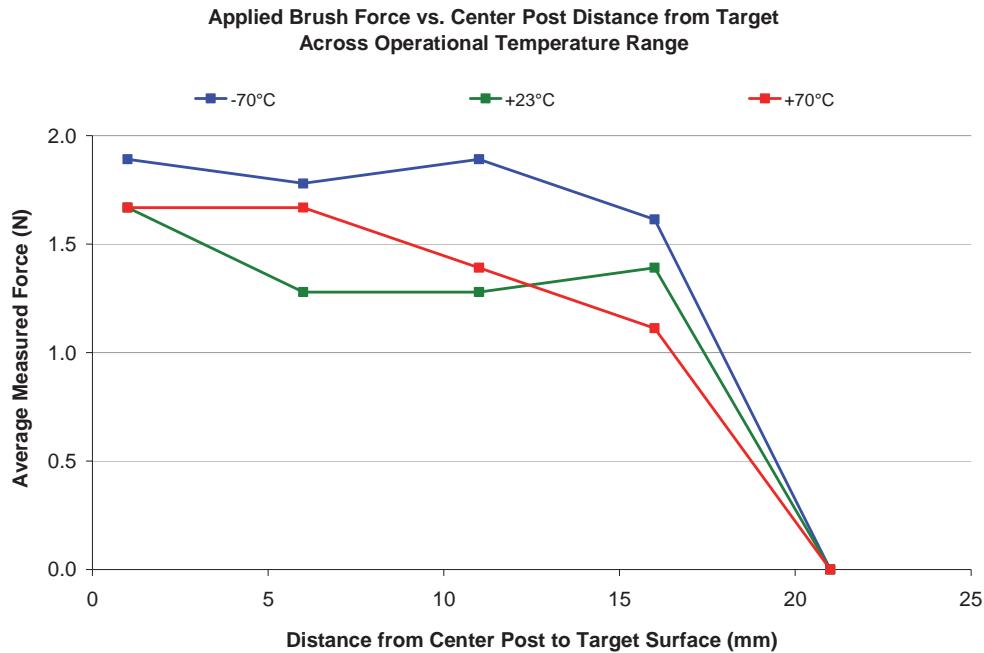


Figure 8. DRT Flight Model brush contact force vs. surface height

Sizing the pivot's springs was an exercise in threading the needle. On the one hand, the springs needed to be strong enough to keep the brushes in contact with the rock over the complete range of pivot motion (including at its relaxed hard stop). And on the other hand they needed to be soft enough such that the brush contact force at the fully compressed pivot position caused very little drag on the motor and the motor torque margin requirement would be met. It only took on the order of 3 N of bristle contact force to achieve the allowable motor current limit. So the springs were designed to deliver about 1.4 N of contact

force at the fully compressed pivot position and the spring rate was selected to be as flat as possible such that the contact force was about 0.4 N at the lower hard-stop.

The brush block subassembly was dynamometer tested across the operational temperature range (-70°C to +70°C). Instead of using a torque wrench to directly measure the torque supplied by each pivot axis over the range of motion, a test was designed to measure the net contact force delivered by both brushes against a contact plate instrumented with a load cell. At each temperature set point, the instrumented contact plate was translated toward the DRT brush block as the brush block was spinning at low RPM – this mimicked the flight operational concept. The DRT and contact plate translation stage were configured horizontally such that gravity should not have been a factor. Force measurements were taken at 21 mm (1 mm beyond the brushes reach), 16 mm, 11 mm, 6 mm and 1 mm between the center post tip and the contact plate. Measurements were not taken in the reverse order to quantify friction drag on the pivot axis. The results of this test, shown in Figure 8, were nominal (i.e., the springs produced forces that were within the expected range).

Brush Pivot Problem/Failure Report

Following the dynamometer testing of the DRT Flight Model (FM) and Engineering Model (EM) units and the subsequent delivery of the FM, the DRT EM was performance and life tested across the operational temperature range. During these tests, the EM motor was energized to spin up the brush block while it was positioned above a rock surface in the thermal vacuum chamber. Once at speed, a linear translation stage (ground support equipment playing the part of the RA) moved the DRT to a position of engagement with the rock. After a period on the rock, the motor speed was decreased to a lower setting and the DRT was retracted off the rock. This test procedure was consistent with the manner in which the tool would be used during the mission.

During the -70°C tests, it was observed the EM Inner Brush did not return all the way to its hard-stop following the low speed retraction from the rock. Instead it stopped a few degrees away from the hard-stop. However, the Inner Brush did return to its hard-stop position following the nominal 10-second 900 rpm run. The EM performance and life testing continued until the EM had successfully met its dust removal performance requirements after 2x life (greater than 300 brushing operations).

The Problem Failure Report process was initiated to capture the anomalous Inner Brush behavior and subsequent root cause investigation. The concern was that the pivot (unassisted by centripetal force) was not meeting its torque margin requirement. Per the DRT equipment specification, all actuators were required to demonstrate a minimum margin of 100% on torque required for operation under worst-case conditions where Margin = $(\text{Actual}/\text{Required} - 1) * 100\%$. In this case, the EM Inner Brush pivot spring (the actuator) had apparently failed to supply enough torque to overcome friction and return the brush to its hard-stop. The requirement in this case is that the spring be able to supply twice the torque required to overcome the friction opposing a return to hard stop – this would be considered a margin of 100% or factor of safety (FOS) of 2.

The first thing the team did was to revisit the pivot analytical model used during the design process as well as the as-built in-process test data and dynamometer test data. According to the manufacturing documentation the measured seal drag on the EM's Inner Brush pivot was 50% higher than that of the EM's Outer Brush and both the FM Inner and Outer Brush. This appeared to be the smoking gun. Unfortunately however, the team realized that the dynamometer test approach inadequately demonstrated the torque (or force) margin and it was impossible to draw any further conclusions about the pivot spring's torque margin. Pursuing the seal drag theory, it was hypothesized that seal contraction at cold temperatures had caused the drag torque to spike on the EM Inner Brush seal-shaft combination because it was perhaps past the "knee in the curve" known to exist in these types of configurations. So measurements of seal drag versus diametral interference were made at room temperature using gage pins to create a model (see Figure 9) and the maximum theoretical seal contraction was calculated. According to the model, the EM Inner Brush would have a margin less than 100% (FOS < 2) but the

margin should still be comfortably positive ($FOS > 1$). It was clear that something was missing from the model.

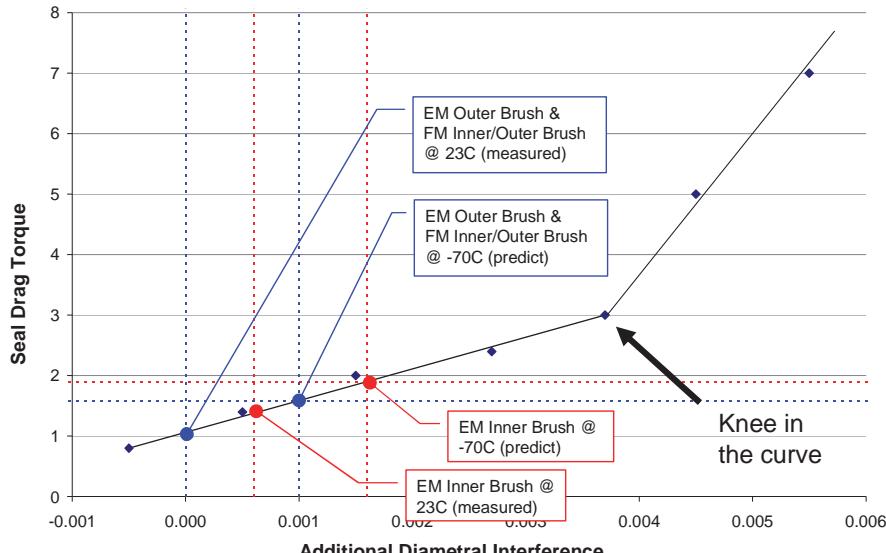


Figure 9. Seal Drag Model

Next a complete disassembly of the EM Inner Brush pivot was performed and documented. Unfortunately, other than very minor evidence of components rubbing (dark marks), there was no clear culprit explaining the problem with the EM Inner Brush pivot. The EM brush block was reassembled and the unit was sent to JPL for further testing.

At JPL, tests were performed at temperature on both the EM and FM to more directly measure the pivot's drag and spring torque and thereby achieve a clear demonstration of torque margin. A general model of the pivot behavior is shown in Figure 10 and assumes drag torque is equal in both directions and of course opposes the direction of motion. So in one direction, the measured torque is the sum of the spring and drag torque. While in the other direction, the measured torque is the difference between the spring and drag torque.

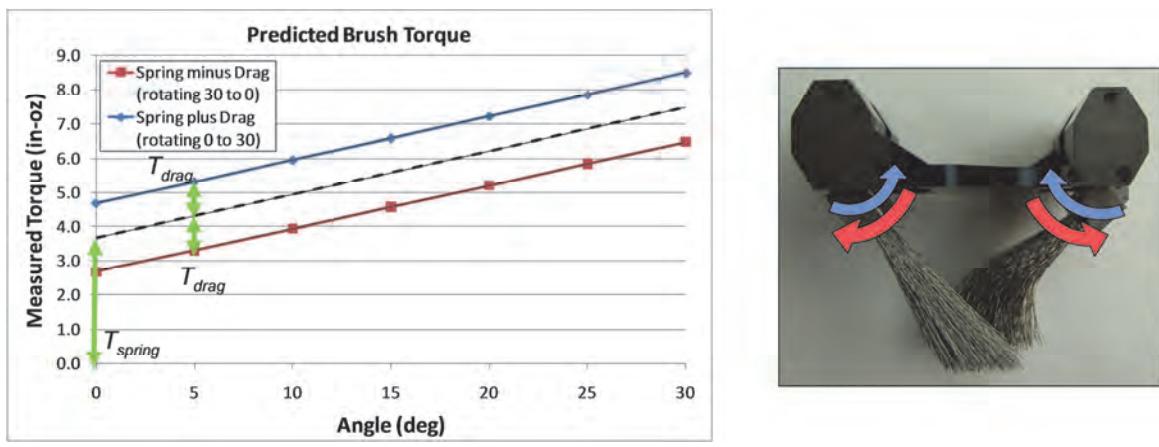


Figure 10. Pivot spring drag torque model

The JPL test results are shown in the columns labeled “0 rpm” in Table 1. At 0 RPM, the brush block pivots demonstrated a margin of 100% or more ($FOS \geq 2$) in only one instance for the EM and only one

instance for the FM. In many cases, negative torque margin was calculated. The JPL tests confirmed that the DRT pivot design did not meet the torque margin requirement.

Table 1. DRT Pivot Torque Factor of Safety (FOS) Test Results (min. required FOS: 2.0)

Temp (°C)	Test #	EM DRT				FM DRT			
		Inner Brush		Outer Brush		Inner Brush		Outer Brush	
		0 rpm	900 rpm						
+70	Test #1	2.00	6.96	1.24	4.64	1.51	5.59	1.33	4.69
	Test #2	1.78	6.54	1.23	4.60	1.83	6.44	1.56	5.54
+20	Test #1	1.30	5.03	1.58	4.85	1.27	4.79	1.87	4.85
	Test #2	1.23	5.28	1.42	4.63	1.17	4.60	2.20	6.20
-30	Test #1	0.67	3.34	0.61	2.27	0.96	3.61	1.05	3.28
	Test #2	1.06	3.58	0.54	2.29	0.74	3.13	0.52	2.13
-70	Test #1	0.76	2.22	0.47	1.50	0.43	1.87	0.51	1.64
	Test #2	0.57	2.04	0.35	1.33	0.38	1.78	0.64	1.77

Next calculations were repeated to determine the torque margin when taking into account the centripetal forces acting on the brushes when the motor is spinning the brush block at 900 rpm – this was the speed used at the end of each performance test brushing operation after the DRT had been retracted away from the rock. These calculations are shown in the columns labeled “900 rpm” in Table 1. It was determined that operating the DRT at 900 rpm produces a calculated centripetal force that will reliably return the brush pivots to their hard stops. The minimum FOS for the FM in this case is 1.64 (Outer Brush Test #1 at -70°C).

No further work was done to determine root cause and no hardware changes were called for as a flight operations rule that spins the DRT brush block at 900 rpm before each use was deemed an adequate solution by the review board.

Motor & Gearhead Subassembly

A challenge in the DRT design was to overcome the torque margin constraints due to the required use of a predefined motor. Based on the motor performance specifications, torque amplification was necessary and a custom single-stage planetary gearbox was designed (ref. Figure 11). The pinion of the motor was predefined as a long-addendum spur gear. This was likely done to avoid undercutting and increase the load capacity and life of the small pinion, necessitating the use of modified profile planet and ring gears.

Actuator margin analysis (ref. Figure 12) was performed based on those performance parameters as well as thermal limitations provided by JPL based on heat-up analyses. Various parameters were also estimated including seal and bearing losses as well as operational torque. The latter was estimated based on data from brush development tests.

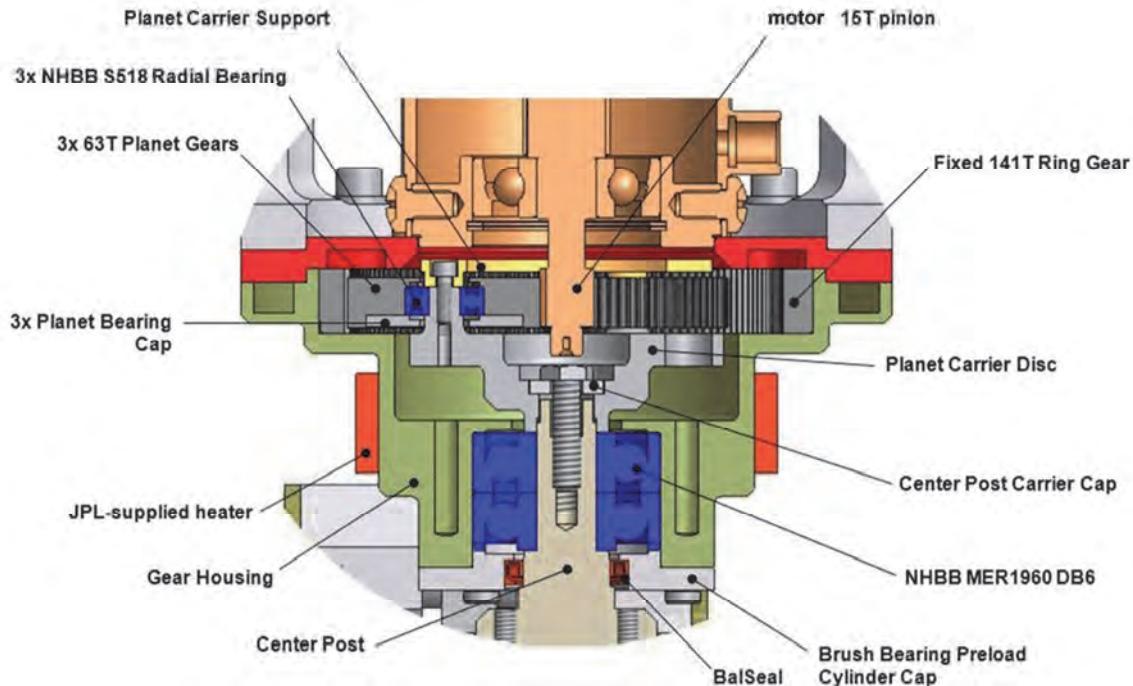


Figure 11. Cross Section of Gearbox Assembly

Analysis predicted that a 10.4:1 reduction ratio gave a torque margin of 140% and a thermal dissipation margin of 475% which exceeded the 125% requirement for a CDR-level design. Reducing the ratio to 6:1 decreases those margins to 41% and 99%, respectively. The gearbox single-stage ratio selection of 10.4:1 is somewhat unconventional when considering planetary gearbox rules of thumb which limit the highest practical reduction ratio to 10:1 due to decreased pinion size and increased sliding within the gear mesh (i.e. decreased efficiency and life).

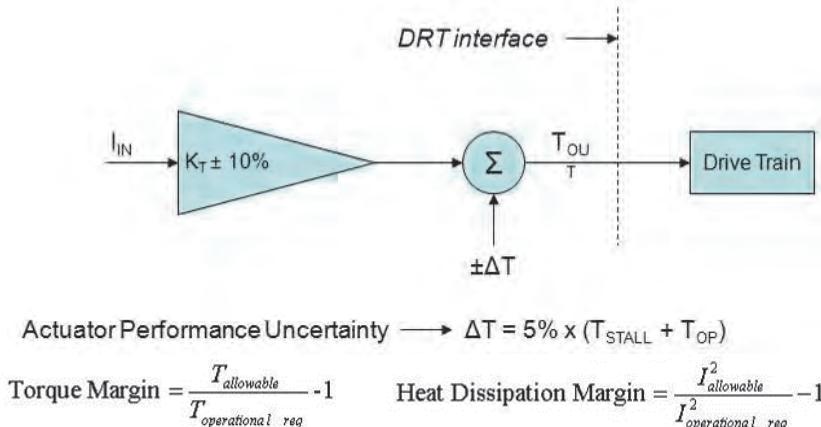


Figure 12. Actuator margin analysis methodology

The specific sliding ratio (SSR) is defined as the sliding velocity divided by the rolling velocity at the gear mesh. The SSR varies along each gear mesh. A higher SSR means that a gear mesh design has relatively more sliding action compared to a lower SSR and would therefore have increased friction and decreased efficiency and life. Therefore it is desirable to design a reduction stage to minimize the SSR within the constraints of other driving requirements. The rate of change of the SSR along the line of action should also be minimized for similar reasons.

The DRT required a high single-stage ratio in order to maintain torque margin on the motor as previously discussed. This in combination with a pre-defined 15T pinion fixed the gear proportions. Figure 13 shows how the SSR at the sun-planet gear mesh for the 10.4:1 design changes during a single mesh cycle. Looking at the lowest and highest points of single tooth contact (LPSTC and HPSTC respectively), i.e., the critical stress jump points, the SSR does not exceed a magnitude of 1.0. The worst-case SSR value occurs on the dedendum of the planet during recess action with a magnitude greater than 3.0. Because the SSR is less than 1.0 at both the LPSTC and HPSTC, the DRT gear design was deemed acceptable.

Other analyses included gear life analysis based on the American Gear Manufacturers Association (AGMA) standards 2001-D04 and 908-B89, backlash analysis, and momentary overload analysis. Backlash analysis included contributions from manufacturing tolerances as well as the operational thermal range to ensure that backlash existed under worst-case stack-up conditions. This was validated via accurate involute profile simulations. Momentary overload calculations included a combination of AGMA 2001-D04 and finite-element analysis (FEA) depending on the gear material selected.

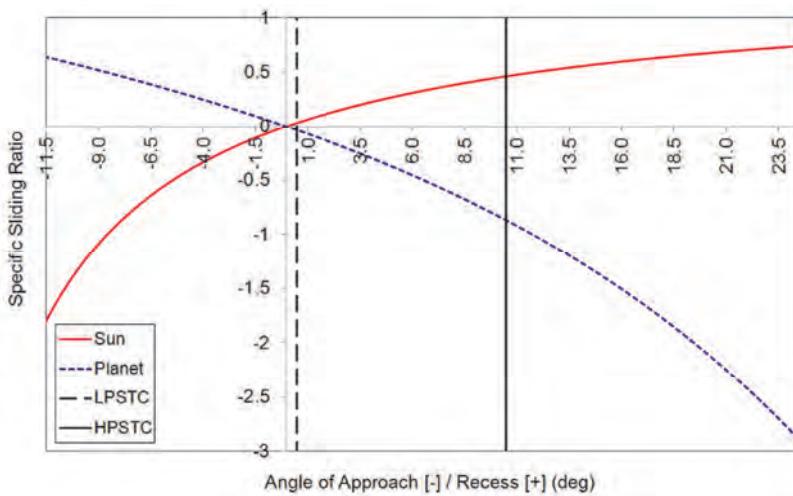


Figure 13. Sun-planet gear mesh specific sliding ratio

To validate the above analyses and verify that the DRT gearbox efficiency was acceptable, the DRT was subjected to output axis dynamometer testing across the operational temperature range. Dynamometer data was acquired at temperature set points (+70°C, +23°C, -55°C, & -70°C) at multiple motor voltages (6, 10, 16 and 22 volts). Speed-torque and current-torque profiles were created. The motor torque constant (K_t) values calculated from the dynamometer data, as shown in Figure 14, match up well with the K_t values measured for the A300 motor prior to integration with the DRT gearbox. This data shows the capability to design efficient planetary gearboxes with relatively high reduction ratios given careful gear tooth profile selection and analysis.

DRT-integrated A300 K_t values				A300 K_t values		
Temperature	6 Volts	10 Volts	16 Volts	22 Volts	16 Volts	21 Volts
+70°C	CCW	CCW	CCW	CCW	CCW	CCW
+23°C	18.0	19.4	20.0	19.2	20.0	20.7
-55°C	18.8	20.4	19.8	20.1	21.1	21.0
-70°C	19.9	20.2	20.5	20.3	N/A	N/A
	21.4	22.0	20.3	20.7	23.1	23.1

Figure 14. DRT-integrated A300 K_t values across the protoflight thermal range are shown on the left. A300 K_t values (not integrated with DRT) are shown on the right.

Lessons Learned

Parasitic Torque Model Shortcomings – The brush pivot drag torque model clearly came up short based on the test results and observations presented above. The lesson learned is to do a more thorough job validating models earlier in the development process (i.e., prior to CDR). The model used in the design process incorporated test data for seal drag from a past program – this data may or may not be valid as it was seal drag for higher operating speeds as opposed to the near static situation measured during the torque margin tests discussed above. One source of drag that may have been overlooked is the friction between the spring and arbor. It is difficult to predict how torsion springs end constraints will behave. Often torsions springs (especially those with few turns and short legs) will cant or cock to one side causing part of the spring to rub against its housing or arbor in an unanticipated manner. This can introduce drag and strange behavior that is difficult to model.

Test Program Inadequacy – In designing a test program that saved time by directly measuring brush contact force over the pivot range of motion, the team overlooked the fact that the test method was not going to collect all the data needed to verify the pivot spring torque margin requirement. Force measurements were taken in only one direction as opposed to both directions which is required to quantify losses due to internal drag. Additionally, while there are benefits to testing in a manner consistent with how the tool would ultimately be used, it was an error to omit a test that isolated the pivot spring and drag torque at temperature. Instead the bristle compliance was included as an unobservable variable in the same test. The lesson learned is to test pivot or hinge torque margin at the pivot/hinge level and to be sure to make a torque measurement in both directions so as to isolate the drag torque from the spring torque.

High-Reduction (10.4:1) Planetary Stage – While not ideal, it was demonstrated that given careful tooth profile selection and analysis, a relatively high-reduction (10.4:1) planetary stage can be an efficient torque amplifier.

Image Processing Provided Easy, Objective Measurement Method – Surface cleanliness can be a very subjective quality that is hard to define. Using image processing algorithms to measure cleanliness and brush performance turned out to be very easy. Its objectivity and ease allowed personnel to focus on collecting more data rather than fiddle with complicated alternative measurement techniques. This method could be used for other more general purposes like quantifying the amount of wear particulate generated in a mechanism over time.

Conclusion

MSL is scheduled to land at Gale Crater on Mars in August 2012. Using the rover's Dust Removal Tool, Earth-bound scientists will sweep away the blinding dust that eventually coats every object on the Martian surface. Spectrometers and cameras will take aim at these freshly exposed surfaces and will gather information that will allow scientists to decide whether those rocks may harbor evidence of organic materials or not. The DRT promises to be as instrumental to MSL's success as the RAT was and is still to the success for MER.

The DRT development process had many challenges. From engineering a brush design that utilizes a single actuator and can deal with 20-mm surface height variations to determining proper methods for testing such a novel device, there were many things learned over the course of the project.

There was a significant discrepancy between a key mechanism analytical model and the tested performance of that mechanism. The root cause of this large discrepancy has not been identified yet. But important lessons were drawn from the experience. In the future, greater consideration will be given to validating such analytical models earlier in the development process and performing component level verification tests on the flight hardware to isolate key parameters.

Acknowledgements

The DRT team at Honeybee Robotics would like to acknowledge and thank the team of scientists, engineers and managers at NASA JPL that offered their input during the DRT development process. The DRT marks the third time that Honeybee has developed a flight qualified robotic end-effector for a landed Mars mission through close collaboration and teamwork with JPL.

References

1. Bishop, J., et al., 2002, A model for formation of dust, soil, and rock coatings on Mars: Physical and chemical processes on the Martian surface, JOURNAL OF GEOPHYSICAL RESEARCH, VOL. 107, NO. E11, 5097, doi:10.1029/2001JE001581.
2. MSL Science Corner: Alpha Particle X-ray Spectrometer, <http://msl-scicorner.jpl.nasa.gov/Instruments/APXS/>
3. Rieder, R., et al., 1997, The chemical composition of the Martian soil and rocks returned by the mobile Alpha Proton X-ray Spectrometer: Preliminary results from the X-ray mode, Science, 278: 1771-1774.
4. Myrick, T., et al., 2004, Rock Abrasion Tool, Proceedings of the 37th Aerospace Mechanisms Symposium, NASA Johnson Space Center, May 19-21, 2004
5. Herman, J., Davis, K., 2008, Evaluation of Perflouropolyether Lubricant Lifetime in the High Stress and High Stress-Cycle Regime for Mars Applications, Proceedings of the 39th Aerospace Mechanisms Symposium, NASA Marshall Spaceflight Center, May 7-9, 2008
6. Okon, A., 2010, Mars Science Laboratory Drill, Proceedings of the 40th Aerospace Mechanisms Symposium, NASA Kennedy Space Center, May 12-14, 2010
7. Chu, P., et al., 2008, Icy Soil Acquisition Device for the 2007 Phoenix Mars Lander, Proceedings of the 39th Aerospace Mechanisms Symposium, NASA Marshall Spaceflight Center, May 7-9, 2008

A Zoom Lens for the MSL Mast Cameras: Mechanical Design and Development

Daniel DiBiase*, Dr. Jason Bardis* and Rius Billing*

Abstract

The Mars Science Laboratory (MSL), scheduled to land on Mars in August of 2012, brings with it the most advanced set of instruments yet to land on another planet. One of MSL's primary science instruments, Mastcam, was originally scoped to be the first zoom lens camera to operate on Mars. After descope and an 11th-hour reinstatement, zoom lens assemblies were built and mechanically qualified for the MSL mission in less than 12 months. Although they passed mechanical functional and life testing, the zoom lenses did not demonstrate superior optical performance (in the limited time available for optimization) compared to fixed focal length (FFL) lenses built following the earlier zoom descope. As a result, the Mastcam instrument does not have zoom capability as initially planned; it is equipped instead with 34mm and 100mm FFL lenses. Nevertheless, the design, development and qualification of the zoom lens mechanisms resulted in several valuable lessons learned. The Mastcam zoom lens, designed to operate in the severe environment of the MSL mission for one Martian year (approximately 2 Earth years) with 2x margin on life, is described along with the issues that were encountered in fabrication, assembly and testing in an accelerated schedule.

Introduction

Mastcam Instrument Description and Background

On November 26, 2011 NASA launched the Mars Science Laboratory (MSL) on its way to Gale Crater on Mars to learn more about the Red Planet's climate and geological history. On or around August 6, 2012 the MSL rover, built by the Jet Propulsion Laboratory (JPL) and named "Curiosity," will land and begin its 687-day mission to explore and gather scientific data to assess whether Mars ever had, or still has now, an environment able to support life¹. To carry out this mission, the Curiosity rover is outfitted with the most sophisticated array of scientific instruments ever sent to land on another planet. A Mast Camera system, or Mastcam for short, is one of the primary scientific instruments on the rover.

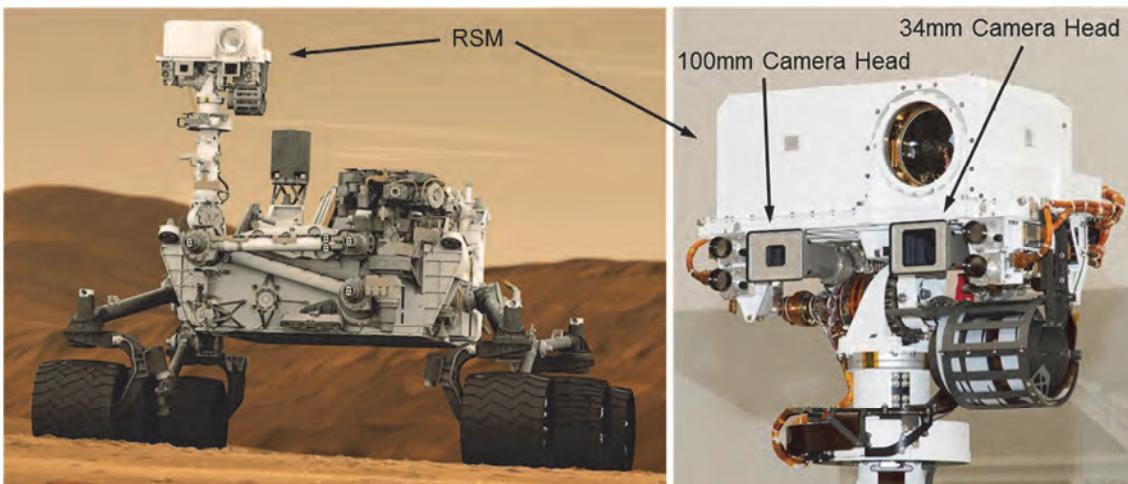


Figure 1: Mastcam on Curiosity, the Mars Science Laboratory Rover
Image Credit: NASA/JPL-Caltech

* MDA Information Systems, Inc. - Space Division, Pasadena, CA

Mastcam, shown in situ in Figure 1, consists of two camera heads mounted on the rover's Remote Sensing Mast (RSM), along with paired digital electronics assemblies located inside of the rover. The Mastcam camera pair, providing a humanlike perspective 2 meters above ground level, will serve as the "eyes" of Curiosity, in a similar fashion to that of the Panoramic Cameras (Pancam) on the Mars Exploration Rovers (MER), Spirit and Opportunity. These cameras will provide color images and high-definition video of the rover's surroundings, gather information about nearby terrain, and assist driving, navigation and sampling operations. Images can be combined for panoramic views and 3-D effects. Each Mastcam camera head is equipped with 8 different optical filters, changed via a filter wheel mechanism, providing a total of 13 unique filter options. The Principal Investigator of this instrument is Dr. Michael C. Malin of Malin Space Science Systems (MSSS).

Some of the new features that the Mastcam system will bring to Mars^{2,3,4} are:

- Active focus capability: A lens group is mechanically actuated for focus between 2 m and infinity.
- Differing Effective Focal Length (EFL) lenses: One camera head features a 34 mm focal length, f/8 lens while the other features a 100 mm focal length, f/10 lens. The 34 mm EFL lens provides a wide field of view: a 15° square field of view obtains 450 µm per pixel images at 2 m distance and 22 cm per pixel at 1 km distance. The 100 mm EFL lens enables detailed images of distant objects: the 5.1° square field of view takes images with a scale of ~150 µm per pixel at 2 m distance and 7.4 cm per pixel at 1 km distance.
- A Bayer pattern filtered CCD detector, providing natural color (i.e., what the human eye would see) pictures and video of Mars.
- Ability to take 720p high-definition video (1280 by 720 pixels) at approximately 7 frames/second.
- Electronics within each camera head can process data independently of the rover's central processing unit and can store thousands of images or several hours of high-definition video with 8 GB of internal memory. Thumbnails can be sent to Earth for the science team to review before full resolution images are transmitted (or discarded). The camera head electronics can analyze images for best focus and also combine in-focus portions of multiple exposures for greater depth of field images in a process called focus stacking or z-stacking. The electronics can be updated with new software when desired.

Variable focal length, though originally planned⁵, will not be part of Mastcam's capabilities. Variable focal length, "16x zoom" lenses (the subject of this paper) were designed, and later built, for Mastcam to provide a wide range of imaging and video capabilities. The 16:1 zoom lenses allow for wide field of view images at 6.2 mm EFL (f/6.2), telephoto close-ups at 100.4 mm EFL (f/10.5), and any EFL between these extents, all with the same lens. Zoom lenses would have also enabled stereo (3-D) video recording and quicker acquisition of stereo images.

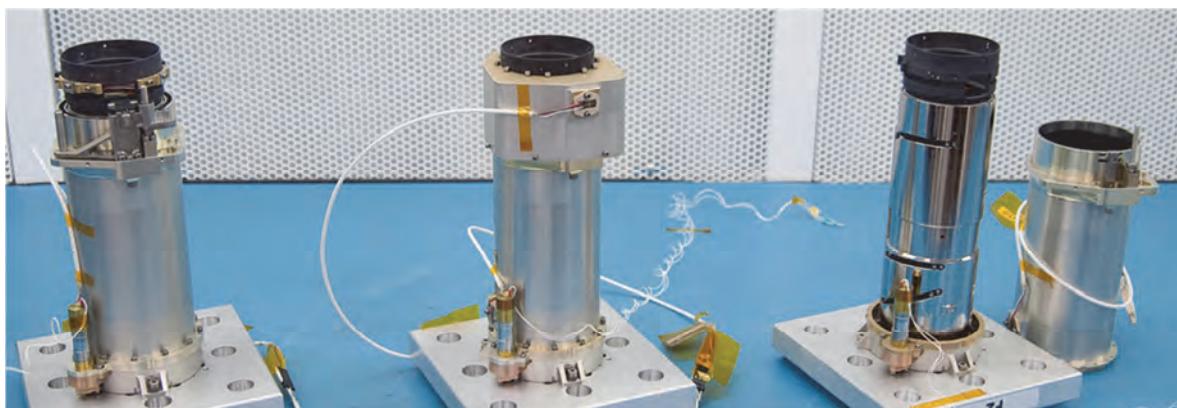


Figure 2: Mastcam Zoom Lens Assemblies

In 2007, late in the design phase, the zoom capability was removed from the Mastcam lens by MSL project management for risk and cost reduction purposes. The project redirected the team to design and

build the fixed focal length (FFL) lenses (34 mm and 100 mm), which were completed after a tight 18-month development and are currently in transit to Mars. The zoom lens design, meanwhile, was put on hold until January 2010 when James Cameron, a co-investigator for Mastcam, made a personal visit to NASA Administrator Charles Bolden to request the reinstatement of the Mastcam zoom lenses. Ultimately this request was granted and in late February, with funding in place, the zoom lens development effort was resumed. This effort resulted in three fully integrated zoom lens assemblies (2 flight units and 1 life-test unit, shown in Figure 2 at various stages of integration) being completed in December, 2010, and tested into March of 2011. Although these assemblies passed mechanical functional and life testing, the initial optical performance of the zoom lenses, while adequate over most of their focal range, was not as good as that of the FFL lenses. With little time for optical adjustments and further testing before the November 2011 launch date, the 34 and 100 mm lens assemblies, which did fulfill all science objectives for the Mastcam instrument, were chosen over the zoom lenses for the MSL mission.

The development of both the zoom and FFL lens assemblies for Mastcam was a collaboration between MSSS, the prime contractor for JPL and responsible for the optics and electronics design and assembly, and MDA Information Systems, Space Division, contracted by MSSS to design and build the lens mechanical assemblies. In this partnership, MSSS and MDA also developed the Mars Hand Lens Imager (MAHLI), another MSL science camera, which is mounted on the end of Curiosity's robotic arm and shares many features and mechanisms in common with the Mastcam mechanical lens designs⁶.

Paper Scope

This paper presents the mechanical design of the Mastcam zoom lens, along with issues encountered during assembly, integration and testing. Although not part of the MSL mission, the Mastcam zoom lens is one of a few instruments with actuated optics designed to operate on the Martian surface and the only Mars instrument thus far to offer optical zoom capability with a design proven through life testing. Not covered in this paper is the Mastcam FFL lens assembly design, which contains a focus mechanism almost identical to the MAHLI focus mechanism described in reference 6.

Zoom Lens Design

Design Overview

The Mastcam zoom lens, shown in Figure 3, packs both a zoom mechanism and focus mechanism within a volume approximately the size of a 473 ml (16 oz) can of soda (a cylindrical volume roughly 6.5 cm in diameter by 18 cm long.) The zoom mechanism adjusts EFL by moving 3 lens groups, each through unique motion profiles, with one actuator. The focus mechanism independently positions a fourth lens group driven by a second actuator for active focus. A filter wheel mechanism, driven by a third actuator, and located aft of the zoom mechanism and in front of the CCD detector, selects 1 of 8 optical filters.

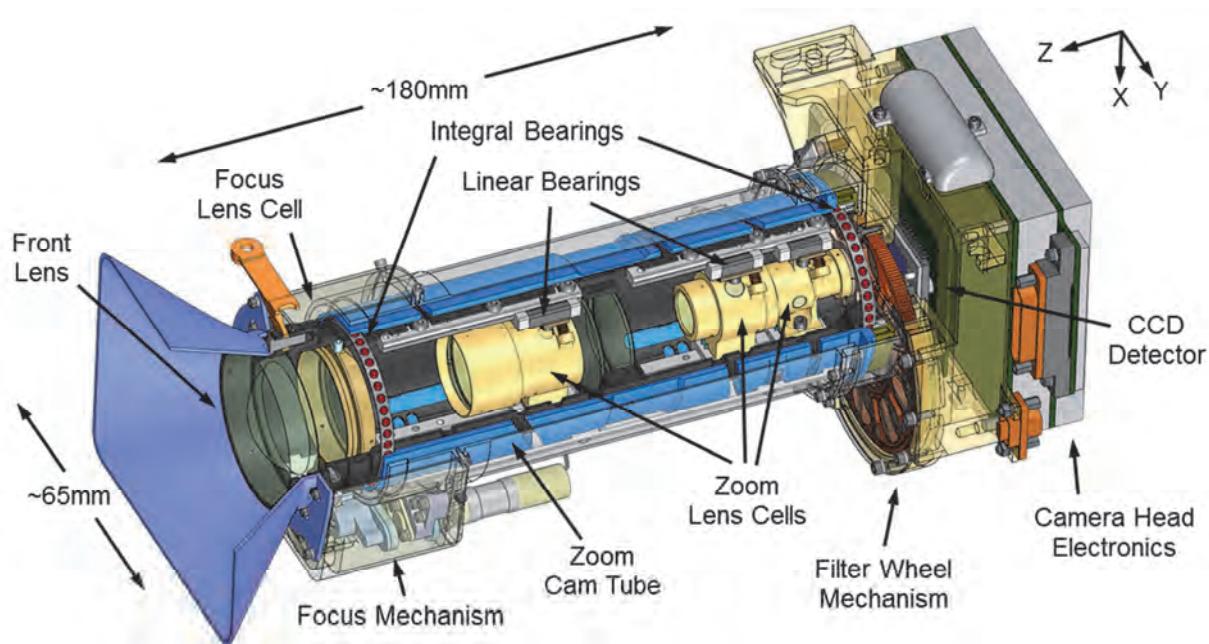


Figure 3: Zoom Lens Design Overview

The design maintains strict alignment requirements for the moving lens groups, mounted on linear bearings, over their range of travel and throughout operational environments without detriment from backlash or thermal distortions. The lens structure is aluminum, which has good specific strength and stiffness and good thermal conductivity to reduce distortion-inducing thermal gradients. Wherever possible, lens assembly parts are fabricated from this material. Flexural features are used where parts of differing coefficient of thermal expansion (CTE), such as the linear bearings, are fastened to the lens structure.

The following design constraints drive the Mastcam zoom lens mechanical assembly design:

- 687 days (1 Martian year) minimum lifetime with a 2x test demonstration factor
 - 300,000 focus cycles
 - 1,300 zoom cycles
- -55°C to +40°C operational temperature range
- -135°C to +60°C survival temperature range
- 160G quasi-static launch load
- 900 gram maximum mass (including optical elements, not including electronics)
- > 0.4 optical MTF at 68 lp/mm
- Distortion > -10% at 6.2 mm EFL, < +3% at 100.4 mm EFL
- Control positions of 21 optical elements (as tight as 0.005 mm decenter and total indicated runout alignment of moving lens groups)
 - 3 moving zoom lens groups with unique but coordinated motion profiles
 - 1 focus lens group with independent motion control
 - 2 stationary lens groups

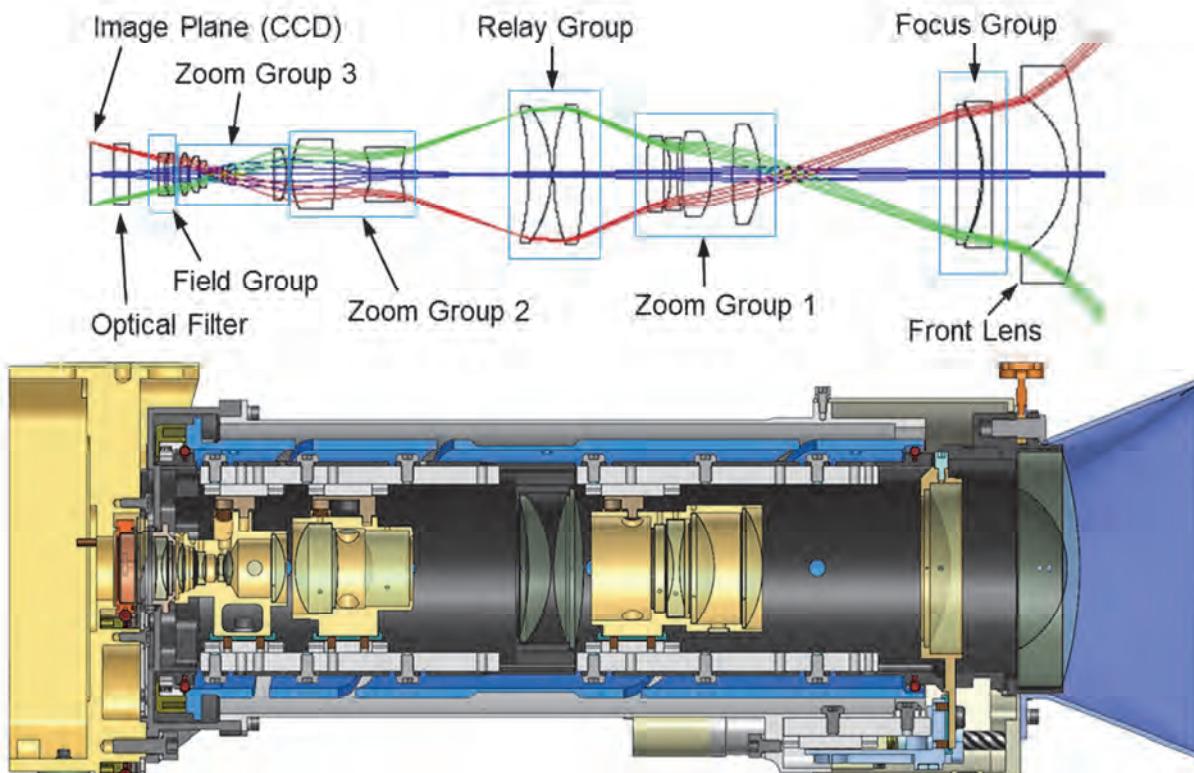


Figure 4: Zoom Lens Optical Design

Optics

The optical system for the Mastcam zoom lens, shown in Figure 4, consists of 20 powered optical elements, ranging in approximate diameter from 5 mm to 5 cm and made from a variety of Schott® glasses, as well as an optical filter changeable via the filter wheel mechanism. Total glass mass is approximately 80 grams. The powered elements are arranged in 6 lens groups (4 moving and 2 stationary groups) plus a single fixed element at the front of the lens assembly:

- The fixed front element serves a double duty of closing out the zoom lens assembly, thereby sealing the lens mechanisms from the dusty Martian environment.
- Directly behind the front lens element lies the moving lens doublet of the Focus Group. The focus mechanism actuates the Focus Group axially over a ~9 mm range of travel to provide focus at distances from 2 meters to infinity.
- The lens quartet of Zoom Group 1 resides behind the Focus Group. It moves over ~38 mm of travel and is one of three lens groups actuated on a unique profile by the zoom mechanism.
- Next in the optical path, the stationary relay lens doublet, or Relay Group, is held by the inner housing of the lens assembly.
- The Zoom Group 2 lens doublet is located behind the Relay Group. Zoom Group 2 is actuated axially by the zoom mechanism through a ~22 mm range of travel on its unique motion profile.
- Behind Zoom Group 2, a lens sextet in Zoom Group 3 is also actuated by the zoom mechanism along a third unique profile through ~22 mm of axial travel.
- The Field Lens Group is a stationary doublet that resides in the aft end of the lens assembly, in front of the filter wheel assembly.
- Last in the optical path, before the Bayer pattern filtered CCD detector, is one of 8 optical filters that can be changed by the filter wheel mechanism.

Each optical element and lens group is required to be positioned within prescribed tolerances. The tightest and loosest tolerance required of the moving groups is provided in Table 1 for the listed degrees of freedom (DOF). These tolerances were drivers for the mechanism design.

Table 1: Alignment Tolerance Ranges for Moving Lens Groups

DOF Name	Tolerance Value	Description
Decenter	0.005-0.030 mm	The radial distance (in orthogonal directions, X and Y) between the nominal optical axis and the center of the element or group
Tilt	0.0002-0.0012 radian	The angular tilt of the element or group about X and Y axes
Despace	0.03-0.10 mm	The axial distance (in Z direction) between an element or group and its nominal axial position

Drive System

The three zoom Mastcam mechanisms are powered by stepper motors with planetary gearhead speed reductions (256:1 for the zoom and focus mechanisms and 16:1 for the filter wheel mechanism). Like the MAHLI focus mechanism, the driving pinion in the zoom and focus mechanisms is supported on a duplex pair of angular contact ball bearings. These bearings are significantly larger than those within the motor gearhead and therefore can endure higher driving loads. Shown in Figure 5, a custom Oldham coupler connects the output shaft of the motor gearhead to the pinion gear. The pinion in the filter wheel mechanism, discussed later, is attached directly to the output shaft of the 16:1 gearhead because driving loads are low.

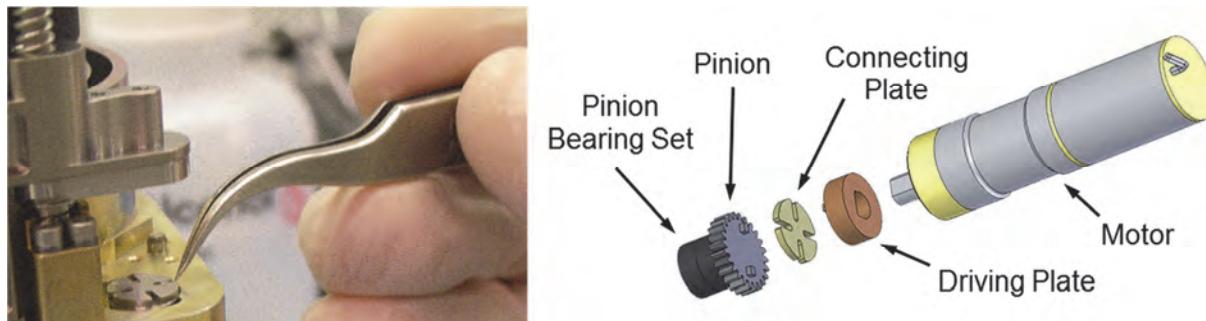


Figure 5: Oldham Motor Coupler

Zoom Drive System

The zoom mechanism, shown in Figure 6, moves the three lens groups simultaneously with a drive system resembling the MAHLI focus mechanism⁶: 1) The stepper motor rotates a pinion gear through the Oldham coupler; 2) the pinion meshes with a gear cut directly into the cam tube; and 3) cam tube rotation moves each zoom group axially along linear bearings following motion profiles prescribed by cam slots cut 295 degrees around the circumference of the cam tube. Each end of the cam slots serves as a hardstop for the zoom groups. Electroless nickel (eNi) coats the cam surface as well as the integral gear on the cam tube for wear resistance. Plating thickness encompasses the full depth of Hertzian contact-stress fields. The edges of the cam surface are rounded with fillets that both aid coating processes and reduce stress concentrations. Further detail and rationale for the cam design is discussed in the Lessons Learned section. A radial bearing serves as a cam follower with a twin bearing used for preload, as described later, in the cam slot.

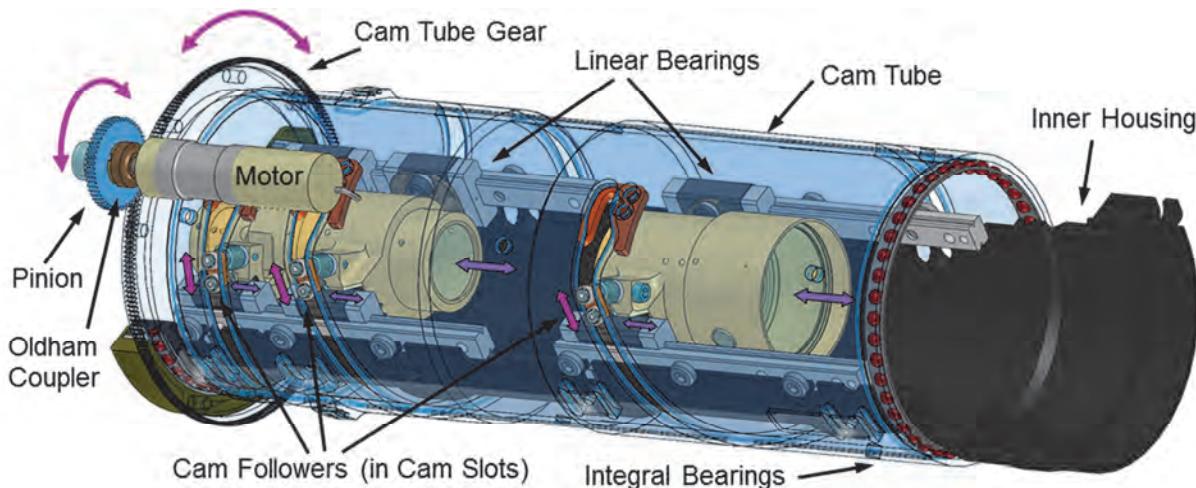


Figure 6: Zoom Mechanism Drive System

When the zoom mechanism is not used, the cam-follower bearings can be driven into launch restraints at the aft end of the cam slots. Figure 7 shows how the launch restraint, attached to the inside wall of the cam tube, raises the follower bearing off the cam surface, holding the follower bearing pivot on a ramp in such a way that the bearing is free from contact and therefore unloaded. Material for both the pivot and the restraint ramp was selected to minimize galling in this sliding interface. The launch restraint primarily protects against launch loads but can be used at other times, such as during rover driving operations.



Figure 7: Launch Restraint for Cam Follower

The cam tube rotates on a pair of bearings with raceways integral to the cam tube and the inner housing on which it rides. The rational for and development process of these integral bearings are described in the Lessons Learned section. Although this type of design poses higher wear-life risks compared to a standard bearing set, machining raceways directly into the aluminum parts obviates steel parts and eliminates distortions due to CTE mismatch. With the exception of the cam tube, all integral raceways are treated with a hard anodic coating (Type III per MIL-A-8625) left unsealed for maximum wear resistance and polished for smooth finish. The raceways on the cam tube are coated with eNi along with the rest of this part. The anodic coating was not suitable for the cam or gear teeth, as explained in the Lessons Learned section, and applying both anodize and eNi (the coating needed for the cam and gear surfaces) on the cam tube part proved prohibitively difficult.

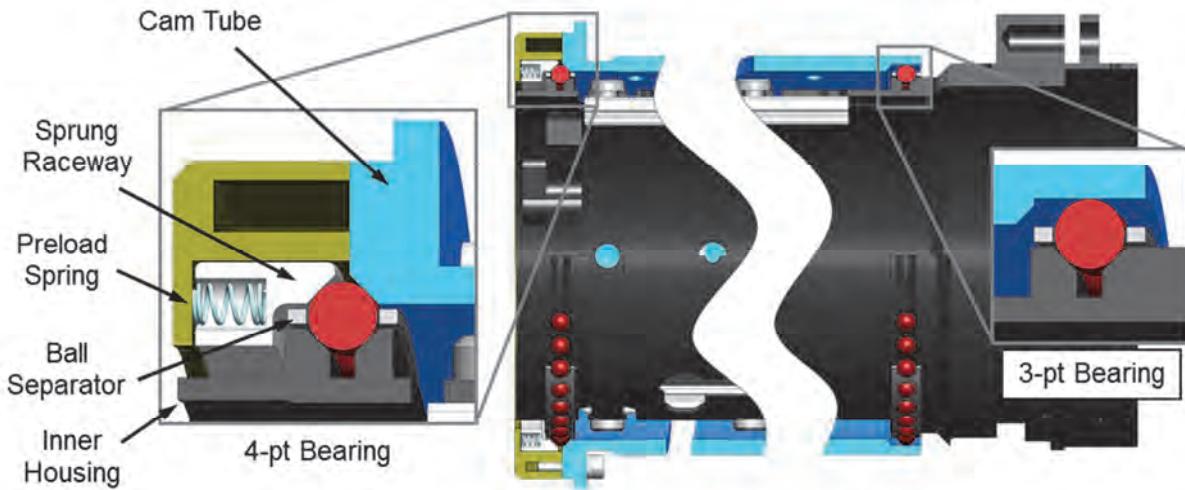


Figure 8: Integral Bearings

The integral bearings, shown in Figure 8, consist of a 4-point bearing at the aft end of the cam tube and a 3-point bearing at the forward end. The 4-point bearing establishes axial position of the cam tube. A set of small, axially-acting springs preloads one raceway. The springs are housed on the backside of this raceway in a radial pattern of blind holes with a precise depth to protect the springs from over-compression. This scheme allows for adjustment of the total spring force by varying the number of springs installed. The 3-point bearing provides moment stability for the cam tube while allowing for axial compliance. Custom ball separators, made from aluminum and coated with eNi, ensure smooth operation by preventing contact and scrubbing between neighboring stainless steel balls.

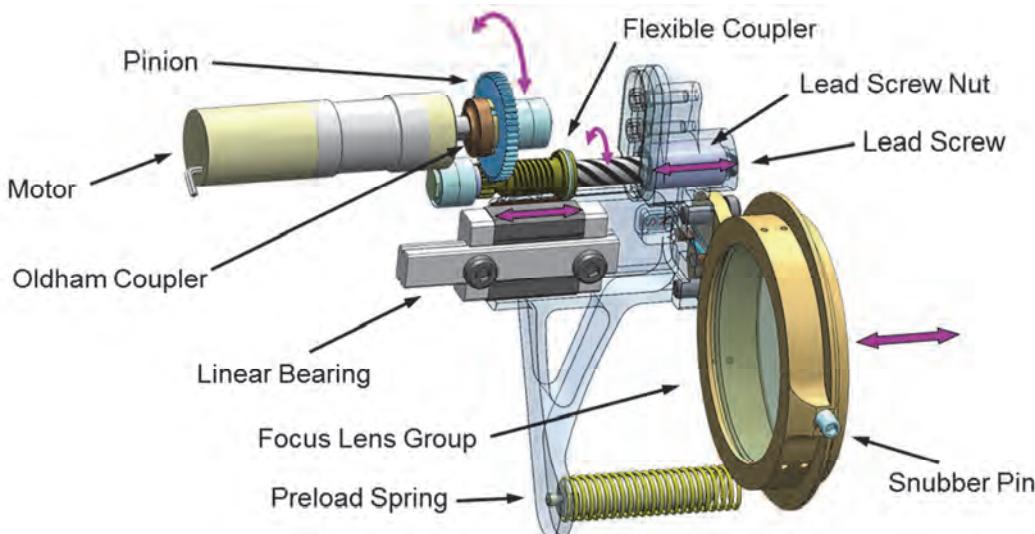


Figure 9: Focus Mechanism Drive System

Focus Drive System

The focus mechanism, shown in Figure 9, moves the focus lens group with the following drive system: 1) the stepper motor rotates a pinion gear through the Oldham coupler; 2) the pinion gear drives a smaller spur gear, increasing speed to meet focus speed requirements, supported by a duplex pair of angular contact ball bearings; 3) the spur gear rotates a 2-start lead screw through a custom 2-start helical flexible coupling; and 4) the lead screw drives the focus group axially along a linear bearing via a lead screw nut captured within the focus lens cell subassembly. The lead screw is made from stainless steel; the lead screw nut is brass, which prevents lead screw wear. Wear debris from the brass nut, potentially

detrimental to optical performance, was shown in tests to be adequately contained within the lubricant grease mixture. The focus group motion is limited by hardstops that contact the linear bearing slide at both ends of the travel range.

A snubber restraint pin limits launch and rover driving loads on the single linear bearing that supports the focus group. The pin, located on the focus lens cell opposite from the linear bearing, travels along an axial slot in the lens structure. The pin makes contact with the slot during high lateral loads, limiting the strain in the linear bearing. The helical coupler is protected from overstraining by stops that limit the axial displacement of the lead screw which would otherwise tend to over-extend or over-compress the coupler.

Filter Wheel Drive System

The drive system of the filter wheel mechanism consists of a spur gear set as shown in Figure 10. The pinion, mounted directly to the motor gearbox, drives an eNi-coated bull gear machined directly into the wheel holding the filter elements. This wheel rotates continuously to position any one of the 8 optical filters in the light path; the mechanism is balanced and does not have hardstops or launch restraints. The wheel is supported on a 4-point integral bearing similar to that used for the cam tube in the zoom mechanism.

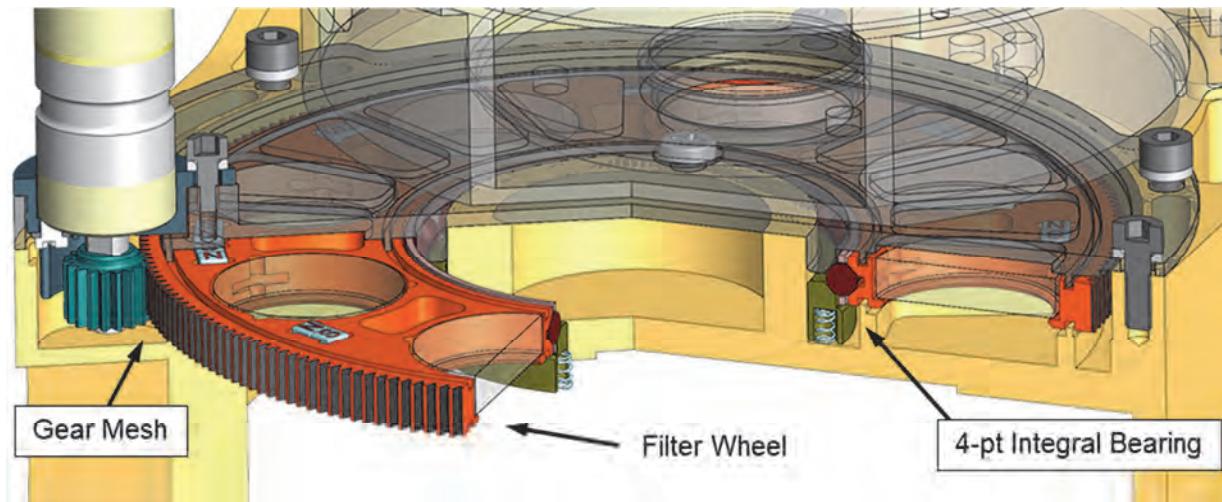


Figure 10: Filter Wheel Mechanism Drive System

Lubrication

Although initially designed to operate with dry lubricant, the Mastcam mechanisms are lubricated with Castrol Braycote® Micronic 601EF grease due to a programmatic decision to reduce wear-life risk at the expense of additional power required for heaters. A perfluorinated polyether (PFPE) based lubricant, Braycote® exhibits low outgassing properties, important for minimizing optics contamination, and excellent cold temperature performance, enabling the mechanism to meet requirements at temperatures as low as -55°C and to provide limited operation down to -70°C. Braycote® 601 additionally contains a corrosion inhibitor useful for protecting the ferrous surfaces in the mechanisms during pre-launch operations. To reduce friction further, tribological surfaces are polished with lay direction aligned with wear and/or friction direction.

A Nyebar® fluorocarbon barrier coating (type Q), with a low surface-tension, non-wettable surface, stops lubrication migration by preventing capillary action of the Brayco® 815Z base oil on part surfaces. By holding the lubricant in place, the barrier coating serves a dual purpose of reducing contamination risk to the optics and extending lubricant wear life. Fears of an incompatibility between the fluorocarbon Nyebar® barrier coating and the PFPE based Braycote® lubricant^{7,8,9} were allayed with a simple test that showed over 4 years of active repulsion of the lubricant by the barrier coating when applied with a specific process.

Sputter-deposited Molybdenum Disulfide (MoS_2) is used on the zoom mechanism launch restraints, in a belts-and-suspenders approach complementing the Braycote® grease, because the active surfaces in this interface undergo sliding wear (versus more benign rolling wear) and are subject to impact loads during launch. The MoS_2 coating, fully compatible with Braycote®, is applied to both sides of this interface: the restraint ramp and the follower bearing pivot body.

Motor Control

The stepper motors are driven by MSSS-developed electronics at 2.2 volts and a 5 KHz PWM frequency at approximately 100 pulses per second. The motors are commanded to run a prescribed number of open-loop steps depending on the operational scenario. Position feedback is not required for operation. However, each mechanism provides position confirmation at one or more points along the range of travel via a latching Hall sensor and activating magnet pair(s). The magnet pairs, comprised of two magnets facing the Hall sensor with opposite poles, create a highly contrasting magnetic field and resulting sharp trigger threshold. In the zoom mechanism two trigger points signal when the cam followers are located in the launch restraints and again when halfway through the cam tube rotation. The focus mechanism has one trigger point along its range of travel. The filter wheel employs nine trigger points, one for each filter position and a ninth to index wheel rotation. If necessary, optical performance of the camera provides another means of feedback using analysis of image quality to determine positions of the focus, zoom, and filter wheel mechanisms. This simple open-loop control system has benefits but also revealed weaknesses discussed in the Lessons Learned section.

Optics Mounting and Preloading

Despace or axial position of each moving lens group is controlled by the actuating mechanism. The decenter and tilt alignment of moving groups are constrained by linear bearings. Preload devices counteract both axial backlash in the mechanisms and play in the linear bearings to minimize the effect that loads and gravity direction have on optical performance. Preload level is a compromise between accommodation of operational scenarios and tribological stress in wear surfaces. For example, wear-life duration is unacceptably short if the lens groups are preloaded to counteract all loads witnessed during rover driving scenarios.

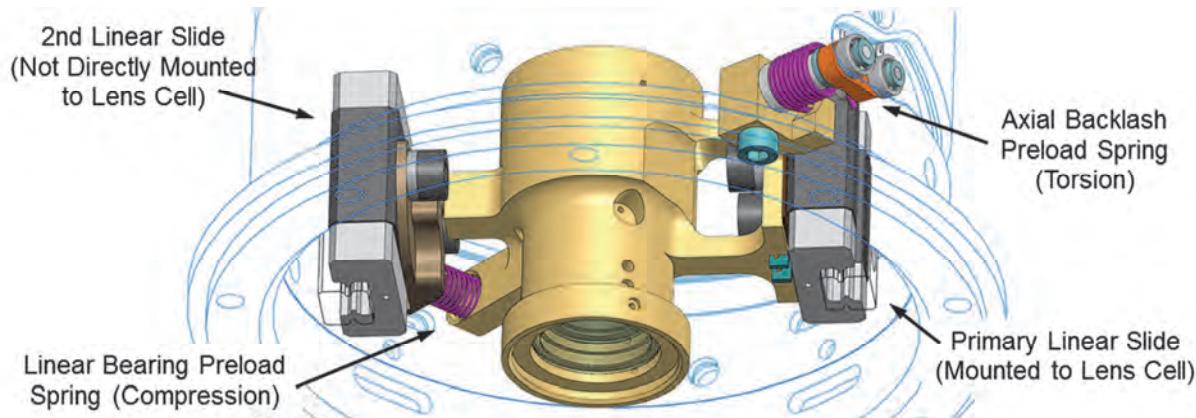


Figure 11: Zoom Group Preload Mechanism (Zoom Group 3 Shown)

Two independent schemes, shown in Figure 11, are employed to preload each of the three tightly packaged, simultaneously moving zoom lens groups. First, in order to remove play in the linear bearing on which the zoom lens cells are mounted (i.e., the primary linear bearing), a compression spring pushes against a second linear slide, opposite from the primary linear slide. This secondary slide is not attached to the lens cell, but pulled along by a pin loosely fit into a hole on the lens cell. The force on the lens cell from the compression spring counteracts movement in tilt and decenter directions from play in the primary linear bearing. Secondly, two follower bearings, preloaded via a torsion spring against either side of the driving cam slot of the zoom mechanism, remove axial backlash affecting despace position.

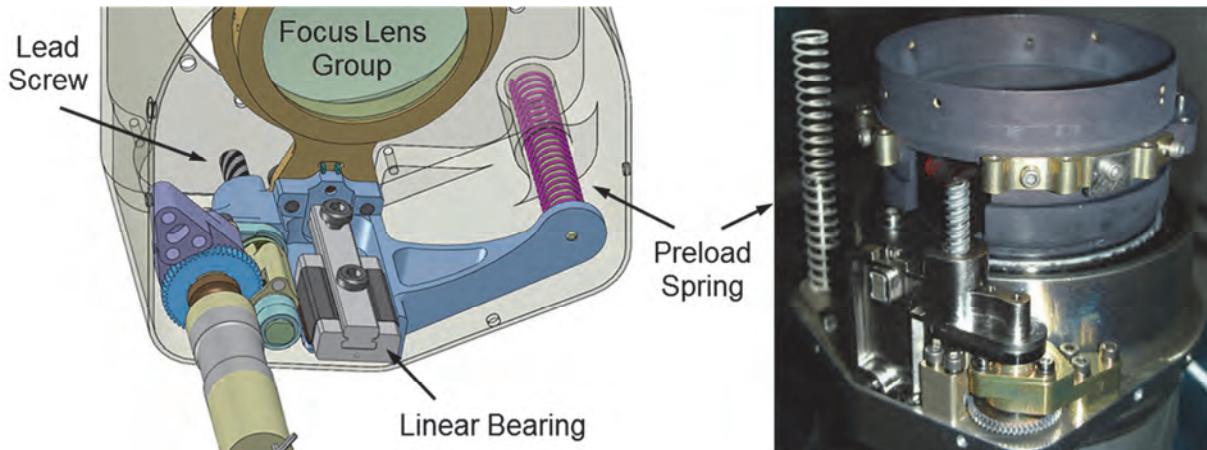


Figure 12: Focus Group Preload Mechanism

The Focus Group, like the MAHLI focus lens group⁶, utilizes a single compression spring, shown in Figure 12, for preload in all directions. The spring, mounted to the fixed structure of the lens assembly, applies a force to the Focus Group that counteracts backlash in the lead screw. This spring force also creates a moment and removes the play in the linear bearing. The long arm feature on the focus group places the spring at the location necessary to create this moment while keeping the spring force relatively low.

Lessons Learned

The nature of the zoom lens mechanisms designs posed high risks for meeting life cycle requirements of 1 Martian year operation plus margin. A large number of unique frictional interfaces created numerous failure points. The ability of each interface to withstand design loads was not completely understood, especially in the case of the coated aluminum surfaces. For these reasons a regimen of component life tests was planned and executed to 3x life requirements in order to prove the design. When appropriate, the tests were performed at temperature extremes as well. These tests revealed several issues with the baseline design. Two lessons learned from component tests are discussed below.

Integral Bearing Design for Smooth Operation

The unorthodox design of the integral bearings poses a risk to meeting lifetime wear requirements for the zoom mechanism. However, employing a traditional steel bearing set is prohibited by the unacceptable strain that would result over the temperature range. Relatively large diameter bearings are needed to accommodate the light path, the optical elements, and the moving lens carriers housed within. Typical steel bearings would undergo CTE-driven contraction differentials with the aluminum lens structure. The diametral mismatch would, with tightly fit parts, deflect and stress the delicate cam tube as well as the lens structure on which the cam tube mounts. This strain would move optic elements out of alignment, degrading camera performance. The integral bearing architecture poses no such CTE issues. In addition, the integral approach has a smaller form factor and less mass compared to a standard bearing set.

The integral bearing scheme is less precise than a traditional bearing, but precision is not critical in this application. These bearings do not influence zoom lens cell decenter or tilt alignment which are maintained by their linear bearings as described previously. Although the integral bearings do determine axial position through the cam slots in the cam tube, axial (despace) position requirements are less restrictive than other alignment parameters.

A relatively benign loading profile is also conducive to the integral raceway methodology for this bearing set. The linear bearings support most of the mass in the mechanism by restraining the lens cells and optic elements in all but one degree of freedom. Except in the axial direction, the integral bearings support only

the cam tube. When the integral bearings are loaded from acceleration in the axial direction, the complete set of balls supports the load, moderating contact stress.

The aluminum raceways require a hard coating to protect the surface from breakdown and wear despite low loads. Aluminum is relatively soft and will not withstand even light friction or Hertzian contact stress. Making matters worse, direct contact between aluminum and Braycote® oil leads to a detrimental chemical reaction. Aluminum forms Lewis acids that catalytically decompose the PFPE oil¹⁰, a process known as the "brown sugar" effect, which causes premature failure of the lubricant. The Type III or "hard" anodic coating on the bearing raceways blocks this reaction and protects the aluminum surfaces. This coating is very hard, resists abrasion and can bear contact stress well. The coating is applied to a thickness that encompasses the depth of the contact-stress boundary.

In the first round of component testing, problems arose for the integral bearings because of a polytetrafluoroethylene (PTFE, aka Teflon®) additive that was used as a lubricant in conjunction with the anodize coating (before wet lubricant was incorporated to the design). The additive was specified to be applied per AMS-2482 Type 1 (MIL-A-63576 Type I), a process believed to impregnate PTFE into the pores of the anodic coating. Initial component tests revealed that the PTFE material, evidently deposited in a layer on top of the anodize surface, would peel off in small flakes with the appearance of white dust or powder. This PTFE debris stuck together in clumps that jammed in the integral bearings and impeded rotation. Additionally, the debris posed an unacceptable contamination risk to the optics. Further investigation revealed that impregnating an anodic coating with PTFE is not physically possible because the long chain polymer molecules of PTFE are larger than the pores in an unsealed anodic coating¹¹. Claims of PTFE impregnation of anodize with the various emulsion processes available at this time have not been substantiated to the authors' knowledge; a surface coating is the more likely result of any such process. Fortunately the adverse effects of the PTFE coating in this application were discovered using test hardware. The PTFE coating was eliminated early before the design had been finalized.

Further testing, without the PTFE coating, revealed other complications with the integral bearings, however. Bearing rotation was uneven and unpredictable due to large variation in required driving torque (i.e., torque ripple). Investigation revealed that smooth operation was impeded by adjacent balls running into and scrubbing against each other in the full complement configuration baselined for these bearings. Several methods of relieving ball scrubbing were tested, including using ball separators, reduced ball quantities, balls of alternating sizes, and balls of differing materials. Ball separators clearly provided the smoothest operation of any design.

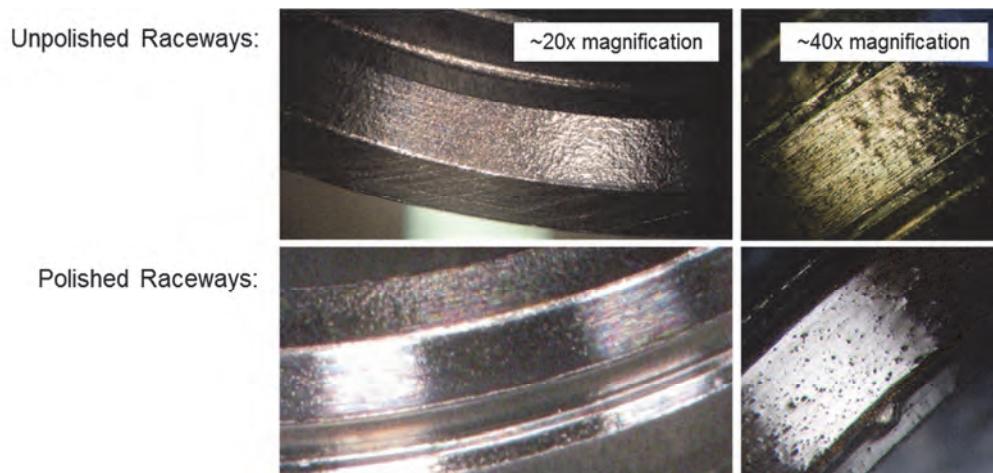


Figure 13: Unpolished and Polished Anodized Raceways

Further reduction of torque ripple was achieved by polishing the anodic coating. As applied, the anodic coating has an undulating, albeit smooth, "orange peel" surface finish as shown in Figure 13. After

removing a small percentage of the coating thickness through the polishing process, most of the unevenness was eliminated, leaving a relatively flat, hard surface. Together with the ball separators, the polished raceways resulted in consistent smooth operation for the integral bearings. Polishing also improved wear margins by reducing friction and lowering stress from uneven rolling. The final configuration of the integral bearings survived approximately 71,000 rotations during their individual component life test. Drive torques for the integral bearings at the end of this test were equal to or less than baseline torque measurements taken at the start of testing.

Hard Coatings for Aluminum Alloys

As demonstrated by the integral bearing testing, the Type III anodic coating is an excellent way to protect a relatively soft base material, such as aluminum. The anodic coating is extremely hard and strong, but it is brittle, a weakness that was made obvious in early tests of the cam/follower-bearing interface. Within the first 10% of the initial cam interface component life test duration, the cam surface exhibited complete failure. The anodic coating broke and chipped away, disintegrating under the load of the follower bearing until only bare aluminum remained on the cam surface; resulting debris finally seized the cam-follower bearing.

At the time of initial component life testing, the baseline cam surface width was optimized for minimal mass of the cam tube part. The tube wall thickness and resulting cam surface width was relatively thin, enabling the follower bearing to contact the entire width of the cam, including the cam's edges as shown in Figure 14, as it rolled along the cam surface. Anodic coatings on aluminum, especially the MIL-A-8625, Type III anodic coatings, contain periodic flaws and cause embrittlement of the base metal, an effect which is aggravated near sharp corners or small radii. For example, anodic coatings 0.025 mm thick will regularly exhibit such problems on radii less than 0.76 mm; as the anodize thickness increases, this effect is exacerbated¹². The cam surface, having relatively sharp corners in the early design and coated with a relatively thick anodize, abounded with embrittled material and corner flaws at its edges. Under pressure from the follower bearing, the coating chipped out and initiated failure of the cam surface during the component testing. It was surmised that similar problems would also exist in the small teeth of the gear integral to the cam tube, not yet tested, if finished with an anodic coating.

Unlike the integral bearing tribulations, relatively little schedule remained for making design changes when the cam interface test failed. Here modifications had to fix the problem successfully with as few iterations as possible. Several tribology experts were consulted with this constraint in mind. With their advice, a three-pronged approach was adopted to mitigate program risk quickly. A multi-faceted line of attack was aimed at eradicating the problem even if one or more of the changes did not produce results.

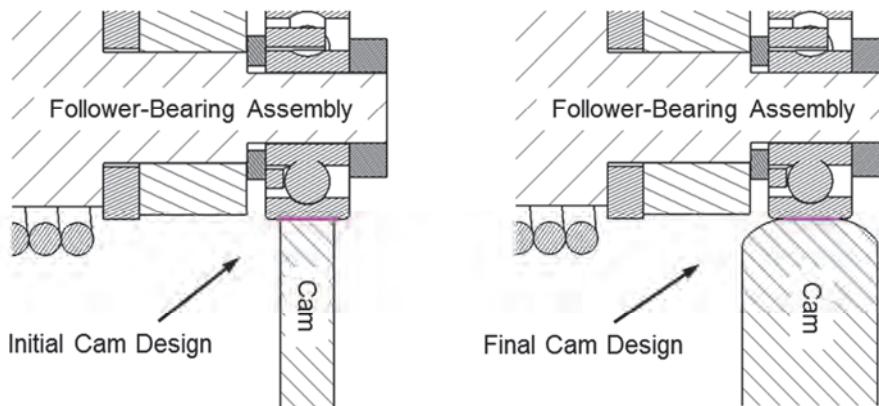


Figure 14: Cam Geometry Changes (Cross-Sectional View)

The first part of the approach modified the geometry of the cam surface to improve coating coverage and reduce edge stress concentrations. The cam tube wall thickness was increased, as much as space in the converging design allowed, to more than double the original thickness. While the actual flat of the cam

surface remained about the same size, the edge radii, made tangent to the cam surface and blended with the tube OD and ID, increased significantly. Figure 14 shows how the thicker cam tube wall provided a gradual transition to the cam flat compared with the initial design, a change anticipated to be more conducive to good coating results. The cam flat is toleranced to lie within the width of the follower bearing, preventing contact with the edge of the bearing and resultant line contact-stress concentrations¹³. The mass increase from the thicker-walled cam tube was compensated by adding more springs to the integral bearing sprung raceway, slightly increasing the preload spring force on the bearing.

The second part of the approach reduced the torsion spring preload force in the cam-follower assembly. As a result, contact stresses in the cam surface were reduced considerably. A consequence of this change was loss of preload during most rover driving operations, due to the springs being overpowered by opposing mass accelerated during bumpy rides. But this capability was not considered critical; the change had no impact to the science objectives of the mission.

The final piece in the recovery strategy replaced the anodic coating with electroless nickel (eNi). Electroless nickel was chosen from among many hard coating choices for its beneficial hardness and strength properties, because it could be applied uniformly over complex geometry in thicknesses that would encompass the depth of the Hertzian contact-stress fields, and also because it was perceived to be a fairly common and available coating. The eNi coating was specified per SAE AMS2404E (MIL-C-26074E) with a bakeout temperature that would not change the temper of the aluminum base material. Phosphorus content in the eNi was selected and specified for adequate strength properties considering contact-stress levels in the tribological interfaces.

Mock-up parts were fabricated for the cam component life test per the new design approach. The testing produced successful results. Over 80,000 passes of the follower bearing over the cam were achieved with little wear, while drive torque remained unchanged from baseline measurements. By the time this component life test was conducted the programmatic switch to wet lubricant had also been made, which undoubtedly helped to a considerable degree. However, successful completion of the life tests proved to be only half the battle for the cam interface.

Following the successful test results described, the design changes were made to the flight parts. Problems were encountered, however, in cam tube pathfinder parts during the eNi coating process. Applying a high-quality eNi coating to the cam tube proved extremely challenging. It was discovered that most coating vendors are set up to make aesthetic eNi coatings and are not prepared to finish complex geometry with a flaw-free, "tribological-grade" coating that minimizes the effects of friction. Even flaws not noticeable without magnification, such as those shown in Figure 15, can initiate deterioration or cause uneven operation and possible jamming of the small camera mechanisms if located on features like the cam or gear teeth, where surface finish is critical. Consequently, all parts were examined under at least 25x magnification for quality control before acceptance.



Figure 15: Successfully eNi-Coated Cam Tube and Common eNi Coating Flaws

Producing a flaw-free, high-quality eNi coating on a part with only one critical surface proved challenging, and often required several coating runs for success. Applying an acceptable coating on a cam tube possessing gear teeth, integral bearing raceways, and the three cam slots (all of which needed a high quality finish) as shown in Figure 15 was much more difficult. Over a half-dozen vendors failed to provide an eNi coating of the necessary quality. Coating thickness, coating chemistry, part orientation, part surface contamination, coating bath contamination, bath agitation, and bath temperature required precise control; all were determining parameters for an acceptable coating. The attention to detail necessary to fine-tune these conditions demanded a continual focus from capable and patient engineers; it was not a task that could be handed to someone accustomed to the typical process used for a plumbing fixture, for example. These challenges were surmounted with a dedicated vendor. The parts used in the zoom lens assemblies were successfully coated with eNi and proven in over 1,300 zoom cycles executed during the lens assembly life test.

Control Scheme Repercussions for Testing Stepper Motors

An additional lesson learned about testing stepper motors used with position feedback systems such as Mastcam's emerged during mechanical lens assembly functional testing. The Mastcam motor control and feedback system employs a minimal approach: position knowledge is controlled by tracking step count commands sent by the electronics in the camera head. This simple control system has inherent benefits of low cost, low complexity and reduced vulnerability to failure, but it depends on reliable stepping of the motor when commanded. If position knowledge is lost due to stepping malfunction, camera operation becomes inefficient because time is consumed to reestablish mechanism position. Camera operation was sensitive to skipping more than 1% of commanded steps, a level of skipping typically not exceeded in a robust design. After integration, however, several Mastcam stepper motors exhibited a propensity to skip steps more often than this, even under nominal mechanism loading.

An investigation was undertaken to isolate the root cause of the motor skipping. The motor, gearbox, and mechanism were all suspect, with emphasis placed on the mechanism because the motors had previously passed performance functional testing. This endeavor revealed an unplanned benefit of the Oldham coupling in the zoom and focus mechanism. The separable nature of this design lent itself to easy torque characterization of the fully assembled mechanisms without the motor in place. With a shaft inserted into the drive hole of the Oldham coupler, in place of the motor output shaft, a torque wrench measured the mechanism actuation torque through the entire range of travel. The filter wheel mechanism, without this feature, was a simpler mechanism and could be evaluated easily by hand. Such characterization showed that the mechanisms were working nominally, requiring torques well within the motor limits. (Testing did show skipping sensitivity related to the pinion/gear mesh of the filter wheel mechanism, but this behavior was shown to not be the root cause of the motor skipping phenomenon.)

Further testing of the motor revealed that the cause of the skipping behavior resided within the stepper motor or motor gearbox. Skipping incidence increased with higher torque loads but was clearly evident with no load as well. The behavior also did not appear to be a resonance issue dependant of inertial loading from the mechanism. Certain motors were proven to skip consistently up to 6% of steps while the unloaded output shaft was rotated. It was not clear if the issue originated in the motor itself or in the motor gearbox, but anecdotal evidence pointed towards the gearbox. The gears in the small diameter gearboxes were apparently very difficult to fabricate, causing delays in delivery. Worth noting is that duplicate spares of these motors leftover from the MER mission, obtained for performance comparison testing, did not exhibit the skipping behavior. The gears in these older motors were reportedly produced by a different vendor who was no longer available for the MSL effort.

This behavior was not discovered until late in development because motor testing (both at the vendor pre-shipment and after receipt, pre-integration) did not measure or quantify missed steps. Torque capabilities were assessed without regard for the percentage of skipped steps, which are not easily noticed at levels of occurrence under 10%, when outside the context of the mechanisms. As a result, motors not suitable for the planned driving scheme were accepted and integrated with the camera mechanisms.

The skipping issue was never completely characterized or solved due to schedule and budget constraints. Had the optical performance of zoom lens assemblies been better, the highest functioning motors may have been chosen for flight, as the skipping problems did not appear to compromise acceptable mission performance. Even when skipping to the degree described was observed, measured torque margins were robust. Furthermore, several motors had passed full MSL flight qualification testing, including 2x life testing, by the time that the skipping issue arose. The motors ultimately used for the mission in the fixed focal length Mastcam and MAHLI cameras had not exhibited skipping behavior problems.

Conclusion

The mechanical design for the Mastcam zoom lens presented a significant challenge of meeting stringent optical requirements in the severe Martian environment. This challenge led to non-standard solutions and unique designs for the mechanisms in the zoom lens. While the initial design failed in several areas, subsequent changes fixed these problems, enabling successful life testing of the fully integrated mechanism assembly.

Reassessing baseline assumptions, when necessary, was a large part of this success. Examples include reducing preload spring forces, and resulting alignment expectations, and using wet lubricant with increased heater power. Fundamentals were important as well: careful bookkeeping of details in each frictional interface, consultation with tribology experts, and many hours spent in trial and error. Early component tests mitigated the impact of failures by uncovering numerous flaws when changes to the design were still possible. Additionally, these tests brought to light defects on a more discrete basis where they could be worked out individually rather than in the context of a complex system. Expedited testing, however, posed its own hazards, as demonstrated by the stepper motor skipping phenomenon, a case where not all parameters were accounted for or understood.

Although the zoom lens, left with little to no time for alignment adjustments, became a victim of the optical performance achievements of the fixed focal length lenses, its mechanisms were shown to be robust in the context of the MSL mission. Curiosity will not have the benefit of Zoom Lens Mastcam instruments while it explores Gale Crater and beyond during its quest on Mars. However, given time to optimize optical performance, the zoom lens and its mechanisms are poised to explore distant worlds on a future mission.

Acknowledgements

The Mastcam mechanical lens assemblies were designed at MDA Information Systems, Inc., Space Division, in Pasadena (MDA) (www.MDAInformationSystems.com) under contract to Malin Space Science Systems (MSSS) (www.msss.com). Michael C. Malin (MSSS) is the Mastcam Principal Investigator, and the engineering work for the cameras was overseen by Mastcam Instrument Manager, Michael A. Ravine (MSSS). The authors give special thanks to Robert Bell and Rick Gelbard at Panavision for initial direction and support in the design effort; Jeffrey Lince of Aerospace Corp. for his expertise with MoS₂ lubricants and assistance with tribological testing; Larry Lipp for his tribological knowledge and support; Yuichi Ikeuchi of IKO Nippon Thompson Co., LTD. for his knowledge of linear bearings; Keith Campbell at Castrol Industrial for his expertise on the Braycote® lubricants; Greg Levanas for help trouble-shooting motors; and Mark Balzer of JPL for his willingness to share mechanism knowledge and advice. Also, the authors thank the Mastcam review board members, and all other reviewers, for their time and help guiding the project. Finally, the authors thank Helen Aslanian, Jennifer Baker, Todd Cameron, Cole Corbin, Sean Dougherty, Rene Espinosa, Richard Fleischner, Richie Gov, Jay Harland, Ross Hironaka, Jacques Laramee, Brett Lindenfeld, Anthony Matthews, Todd McIntosh, Richard McKenzie, Jim Ostroff, William Reed, Chris Thayer, Dorian Valenzuela, and Tom Vanderslice of MDA for their tremendous sacrifice and work developing the Mastcam lens assemblies. The Mastcam project could not have been completed without the dedication and energy placed forth by them as well as many others at MDA and MSSS.

References

1. NASA/JPL "Mars Science Laboratory." Website, cited 2 January 2012 <<http://mars.jpl.nasa.gov/msl>>.
2. Malin Space Science Systems "Mars Science Laboratory (MSL) Mast Camera (Mastcam)." Website, cited 2 January 2012 <http://www.msss.com/all_projects/msl-mastcam.php>.
3. NASA/JPL "MSL Science Corner: Mast Camera (Mastcam)." Website, cited 2 January 2012 <<http://msl-scicorner.jpl.nasa.gov/Instruments/Mastcam/>>.
4. Malin, M. C., M. A. Caplinger, K. S. Edgett, F. T. Ghaemi, M. A. Ravine, J. A. Schaffner, J. M. Baker, J. D. Bardis, D. R. DiBiase, J. N. Maki, R. G. Willson, J. F. Bell III, W. E. Dietrich, L. J. Edwards, B. Hallet, K. E. Herkenhoff, E. Heydari, L. C. Kah, M. T. Lemmon, M. E. Minitti, T. S. Olson, T. J. Parker, S. K. Rowland, J. Schieber, R. J. Sullivan, D. Y. Sumner, P. C. Thomas, and R. A. Yingst. "The Mars Science Laboratory (MSL) Mast-Mounted Cameras (Mastcams) Flight Instruments." *41st Lunar and Planetary Science Conference*, Abstract 1123 (2010).
5. Malin, M. C., J. F. Bell, J. Cameron, W. E. Dietrich, B. Hallet, K.E.Herkenhoff, M. T. Lemmon, T. J. Parker, R. J. Sullivan, D. Y. Sumner, P. C. Thomas, E. E. Wohl, M.A.Ravine, M. A. Caplinger, and J. N. Maki. "The Mast Cameras and Mars Descent Imager (MARDI) for the 2009 Mars Science Laboratory." *36th Annual Lunar and Planetary Science Conference*, Abstract 1214 (2005).
6. DiBiase, D. R. and J. Laramee. "Mars Hand Lens Imager: Lens Mechanical Design." *Proceedings of the 2009 IEEE Aerospace Conference* 7–14 March 2009, Big Sky, Montana (2009).
7. Jones, W. J. Jr. and M. J. Jansen. "Lubrication for Space Applications." NASA CR-2005-213424, p. 6.
8. Hilton, M. R. and P. D. Fleischauer. "Lubricants for High-Vacuum Applications." Aerospace Report TR-0091(6945-03)-6 (SMC-TR-93-14) (15 March 1993), p. 37.
9. Stone, D. and P. Bessette. "Chapter 8: Liquid Lubricants." In *Space Vehicle Mechanisms: Elements of Successful Design*, edited by P. L. Conley, 185-213. New York: John Wiley & Sons, Inc., ©1998, p. 208.
10. Conley, P. L. and J. J. Bohner. "Experience with Synthetic Fluorinated Fluid Lubricants." *Proceedings of the 24th Aerospace Mechanisms Symposium* (1990), NASA CP-3062, pp. 213-230.
11. Stevenson, Milt Jr. Vice President and Chief Technology Officer, Anoplate Corporation, Syracuse, NY. Telephone interview, 7 February 2012.
12. MIL-A-8625F "Anodic Coatings for Aluminum and Aluminum Alloys." US Military Specification (10 September 1993), pp. 16-17.
13. Norton, Robert L. *Machine Design: An Integrated Approach*. New Jersey: Prentice-Hall Inc., ©1996, pp. 518-519, Chap. 7.

Wet Chemistry Automated Sample Processing System (WASP)

Juancarlos Soto*, James Lasnik*, Shane Roark* and Luther Beegle**

ABSTRACT

Ball Aerospace & Technologies Corporation (Ball Aerospace) was commissioned by the Jet Propulsion Laboratory (JPL) to produce a wet chemistry automated soil sample processing mechanism that can be used for planetary wet chemistry sample preparation. Over a three-year period, Ball Aerospace designed, fabricated and performed end-to-end tests to meet JPL's performance parameters. The final product of this effort is called the Wet-chemistry Sample Processing System (WASP). WASP is an integrated system capable of autonomously accepting 100 mg+ of solid fines within a sample cell, combining the fines with 2 mL+ of solvent, heating and containing the mixture at 200°C for 1 hour+, and finally filtering/aspirating the liquid analyte from the processed cell. The WASP carousel with 30 sample cell assemblies currently exhibits a total mass less than 15kg making it field portable in a variety of situations and contexts.

1.0 INTRODUCTION

One of the main goals of NASA in the exploration of the Solar System is to determine if life exists or has existed anywhere beyond planet Earth. In most analytical investigations, there is a need to process complex field samples for the unique detection of analytes, particularly low concentrations of organic molecules that may identify extraterrestrial life. To analyze samples, they can either be carried back to Earth or processed in situ. By automating the processing of samples in situ and using a single integrated system, size, weight, development costs and time all can be minimized. When compared with the time and expense of bringing samples back to Earth from other celestial objects for processing and analysis, in-situ processing of samples should prove a significant cost savings measure.

This paper describes a Wet-chemistry Automated Sample Processing (WASP) system to be used in situ [1-3]. WASP is a simple and robust device that can process up to 30 separate soil samples and send the extracted material to instruments in a fluid form. WASP is capable of capturing and sealing a soil sample, mixing it with up to three different solvents, heating and pressurizing the analyte mixture in the test cell for extended periods, then aspirating/filtering the post-processed liquid analyte for subsequent chemical analysis.

WASP consists of a LabVIEW-enabled laptop computer, support electronics, and four primary mechanical subsystems: 1) sample cell subsystem, 2) carousel/cell-positioning subsystem, 3) capping subsystem, and 4) fluid handling subsystem. All aspects of WASP are programmable and controllable through a LabVIEW software interface. Rigorous subsystem-level testing and comprehensive end-to-end functional testing was performed to optimize performance and enhance reliability. Each of these subsystems is described further in Section 3.0.

* Ball Aerospace & Technologies Corp., Boulder, CO

** Jet Propulsion Laboratory, California Institute of Technology, Pasadena, CA

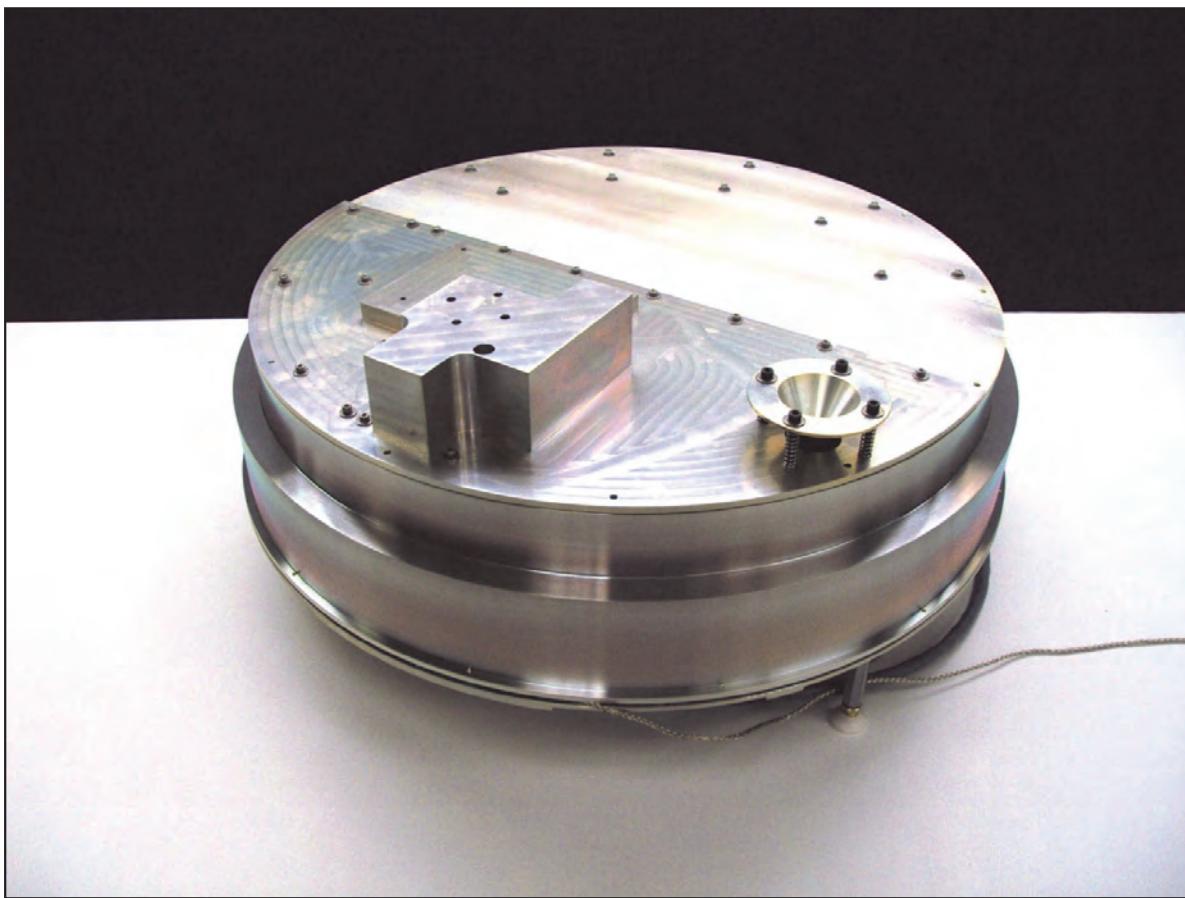


Figure 1. Wet-chemistry Sample Processing System

This project was funded by NASA's Mars Instrument Development Program (MIDP), and directed by Dr. Luther Beegle as the principal investigator (PI) from JPL. Ball Aerospace performed the design, construction, and demonstration under subcontract to JPL.

2.0 REQUIREMENTS AND OVERVIEW OF FUNCTIONALITY

2.1 Requirements

To develop a sample processing platform that could be used on multiple missions, the PI set a baseline list of requirements for planetary science investigations. The device could include more capability as long as these requirements were met and the project stayed within budget. An underlying design goal during development was to craft the mechanism such that it is as close to a flight-like system as possible, while operating within cost and schedule. Requirements included: (a) mechanism capable of processing 20 samples, each capable of holding a 100 mL of solid material and be mixed/processed with a reagent solvent; (b) the ability to process methanol at high temperatures and pressures in the range of 150°C and 10.3MPa (1500 psi) for a period of 1 to 2 hours; (c) as little risk of sample cross contamination as well as instrument delivery cross contamination as possible; and (d) the delivery of the soil sample into the sample cell. As the mechanism developed, initial requirements were met and exceeded by maintaining a flexible and modular design, and productive and regular communication with the PI.

The design consisted of a screw on cap which provided the practicality of reuse. The reusable sample cell drove the WASP design to increase in complexity, but it provided greater serviceability for field use and lowered the refurbishing costs of the assembly. The minimum number of sample cells was increased by 50% and the processing temperature and pressure requirements were 200°C and 13.8 MPa (2000 psi).

By increasing the minimum test cell quantities to 30 test cells, the mechanism scalability was demonstrated while maintaining the mass goal of less than 15 kg.

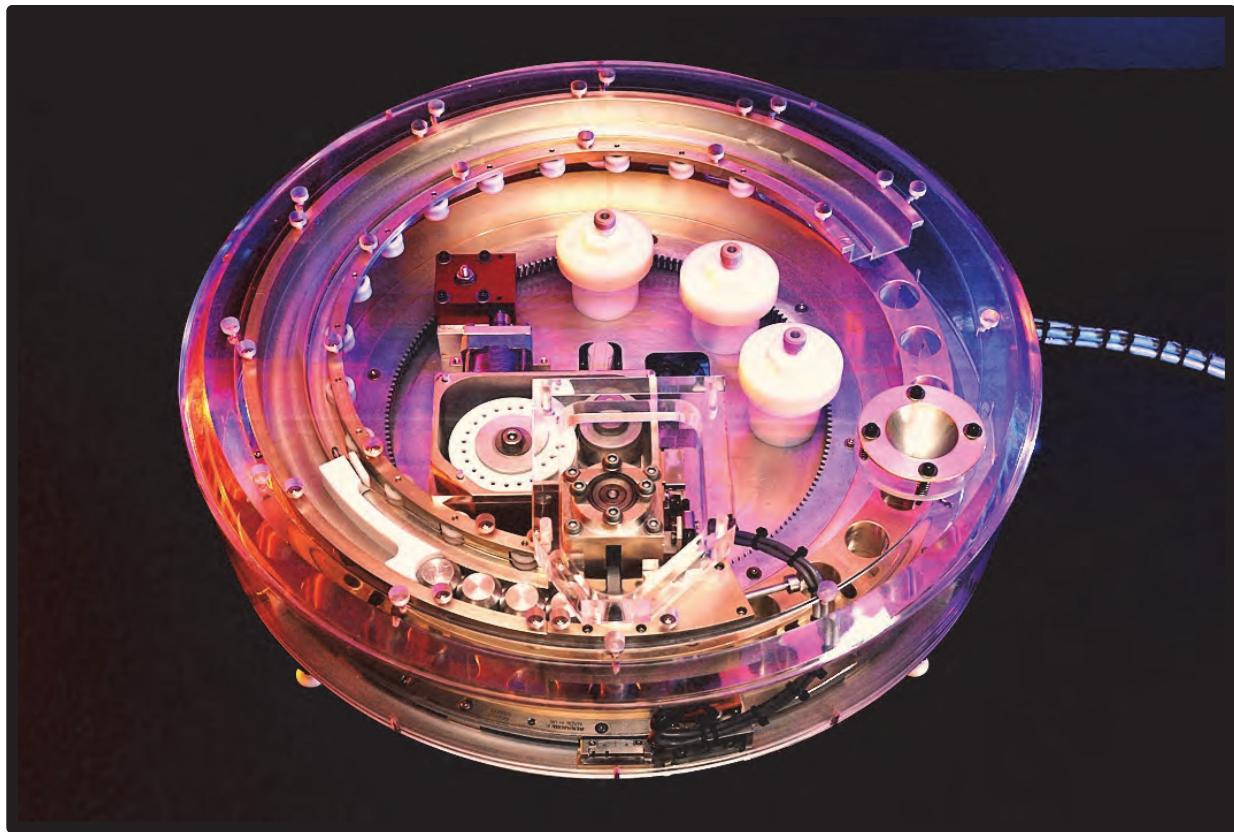


Figure 2. WASP Internal Components – shown in see thru housing

Because of budget limitations, the fluid handling pump and valve components that have been selected do not have direct links to space-rated components. However, their method of operation does mimic that of the space-qualified, solenoid-driven fluid control devices that are manufactured by Valcor Engineering Corporation. By focusing funds and capacity on the challenging aspects of the sample cell design instead of developing existing technologies such as space qualified valves and pumps and using commercial-off-the-shelf (COTS) components when appropriate, the design goals were achieved and enhanced. WASP evolved to include 30 reusable sample cells and three fluid reservoirs.

2.2 Operation and Functionality

This section explains the components of the WASP mechanism and how the components interact with each other. Figures 3 and 4 provide a visual reference for what these components are and where they are located on the mechanism (reference Figures 3 and 4 to associate the descriptions below):

- a) The mechanism is initialized and a sample cell is positioned underneath the inlet funnel
- b) The funnel is lowered into the cell
- c) A solid sample is delivered into the funnel, flowing into the sample cell
- d) The sample cell is driven to the capping station
- e) The capping arm is raised, allowing a cap to slide under the arm and load the capping station
- f) The capping arm drives the cap down into the sample cell, blocks other caps from feeding into the capping station, and pushes the cell into a bore hole feature containing an injector needle
- g) The test cell bottoms out at a hard stop and the capping arm pushes the cap until it snaps into place and seals the sample cell

- h) As the test cell bottoms out into the injector needle, the needle pushes the bottom plunger valve open
- i) While the test cell is bottomed out in the injector station, a solvent is selected on the multiport valve and then pumped into the sample cell
- j) The capping arm is retracted and a spring housed under the sample cell pushes it back to its neutral position; an O-ring keeps a seal with the needle, preventing any leaks as the plunger valve closes
- k) The sample cell is now driven to the heater station where it makes contact with electrical terminals to provide power to the cell's heater; temperature is monitored by an infrared thermistor
- l) Once temperature and dwell time is achieved, the sample is positioned back under the capping station and allowed to partially cool down
- m) After cooling the sample (to lower internal pressures), the capping arm is actuated and the sample cell driven into the needle of the injector assembly
- n) A delivery port is selected and a fluid pump actuated to extract the solute form the sample cell
- o) After the solute is delivered, another port is selected to rinse the tubing and inject the cleaning residue into the emptied cell.
- p) After cleaning the solvent plumbing, the capping arm retracts and the sample cell goes back to its neutral position and the mechanism is ready to process another sample

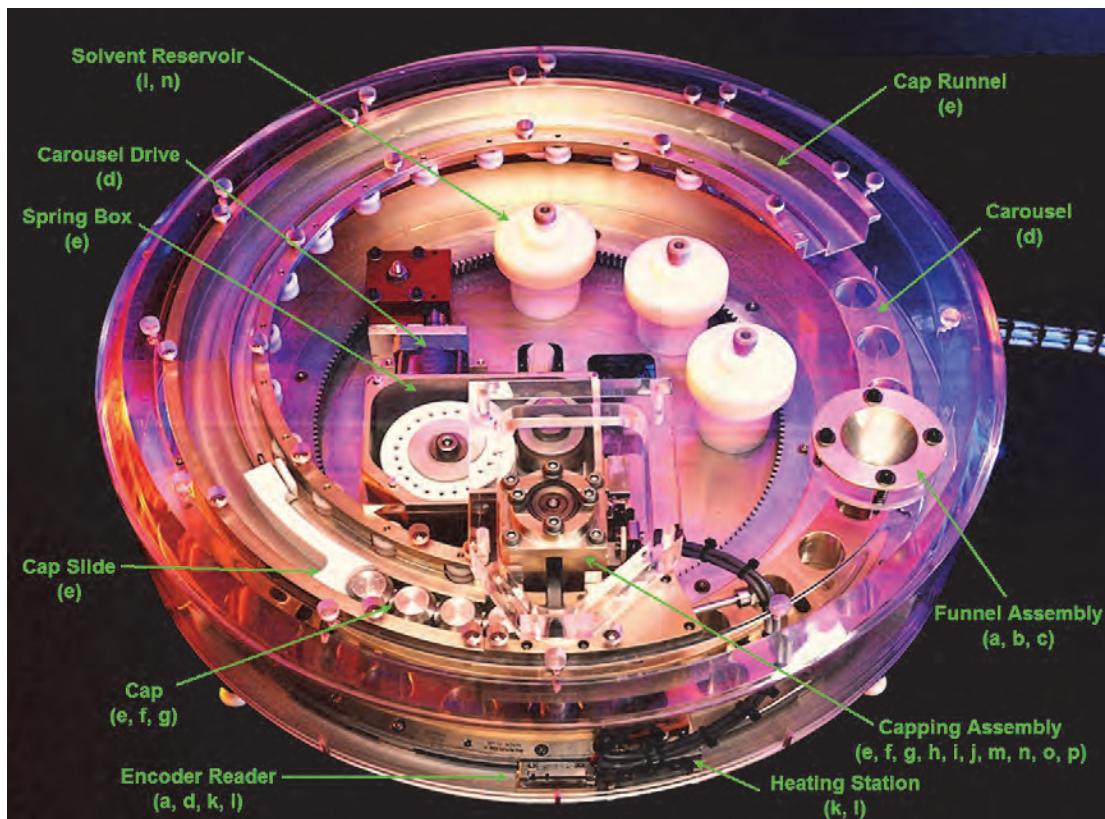


Figure 3. WASP Components – Mechanical Components

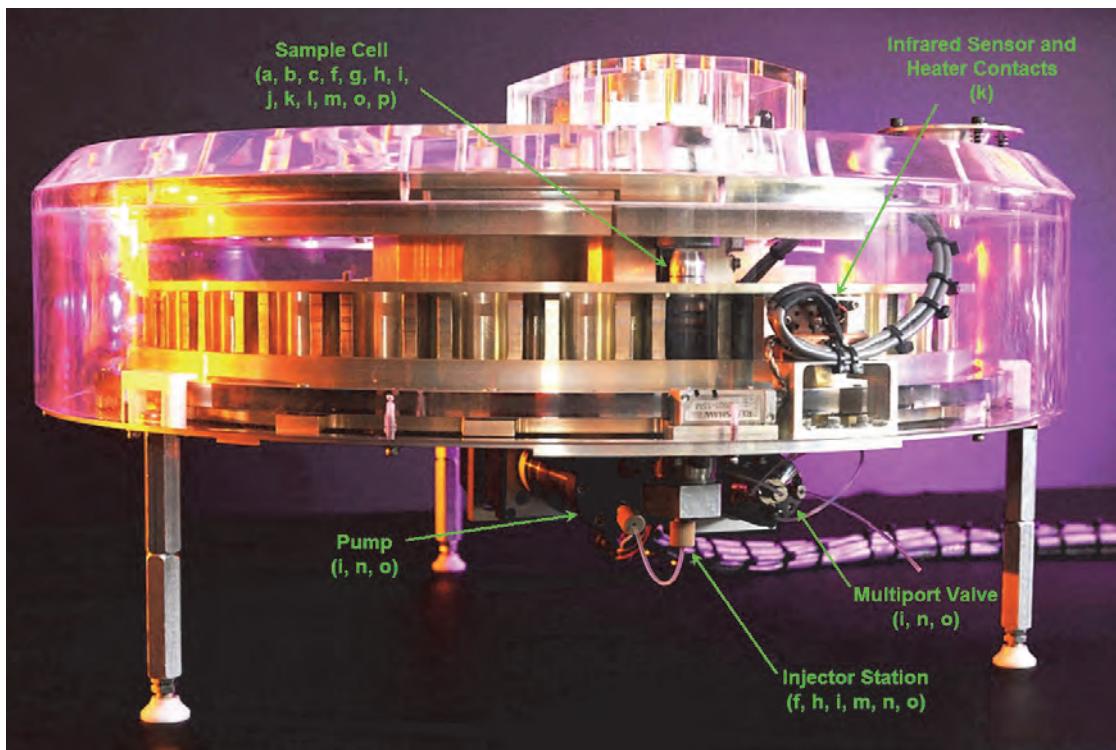


Figure 4. WASP Components - Fluid System

3.0 MECHANICAL SUBSYSTEMS

WASP's integrated system consists of control software and electronics, and four multifunction mechanical systems as listed above and further described below (sample cell subsystem – including the inlet funnel, carousel/cell-positioning subsystem, capping subsystem, and fluidics management subsystem).

To minimize the number of mechanisms required to perform all the required operations for a field wet chemistry processing system, many of the mechanical drivers/motors perform several functions. Additionally, the design included improvements to the sample inlet and interface with the sample cells to reduce the risk of sample cross contamination and increase the general cleanliness of the mechanism. This capability was not part of the original scope for this project but was imperative to address. See Section 4.0 for more information.

3.1 The Sample Cell Subsystem

The sample cells are the key component of the WASP mechanical design. The sample cells determined the approach we needed to take in designing the sample delivery, capping mechanism, fluid injection, sample extraction, and overall sizing of the mechanism. The sample cell was the first component we developed, and the one that took the most research and development.

The sample cell subsystem consists of a cylinder with two open ends. One end is fitted with a valve port and the opposite end is the sample inlet, which is capped after the sample is delivered, creating a sealed vessel. An external heater is bonded to the cylinder and external rings attached, acting as electrical heater contacts. An optical reflector is slipped onto the sample cell and used to accurately read the cell temperature with an optical infrared thermometer. Part of the cell's internal components includes a filter to prevent the sample from clogging the valve port.

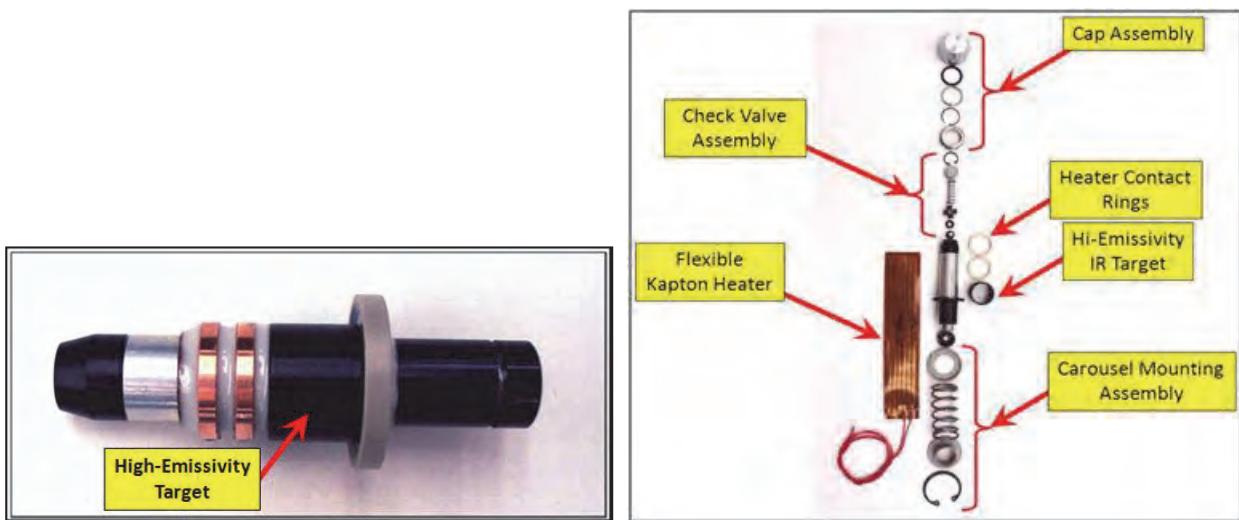


Figure 5. Sample Cell - Components

The ability to heat the sample with methanol at high pressure (200°C and 13.8 MPa) for a minimum of 1 hr is a critical requirement for WASP. A high pressure vessel is required that can be capped, sealed, heated, and accessed to extract the processed solute. Methanol is a very challenging solvent to seal, given that it is a small molecule with high vapor pressure, and it is also highly corrosive to rubber and most synthetic polymers. To seal the pressure vessel the most promising chemical and temperature resistant materials were determined to be Teflon.

An engineering development unit (EDU) of the capping module was developed to perform a proof of concept. This EDU assembly was of essence, ensuring the development of a successful approach showing the means to seal the sample cell and the cap feeding mechanism. If the sample cell capping was not properly developed, no further progress could be attained expanding the other subsystems for WASP. The use of a prototype capping device that reliably demonstrated the capping process and helped understand its nuances was an invaluable investment in resources providing the highest returns. This assembly helped develop the required features on the caps and the mating components, ensuring a smooth process when capping the cells. The EDU capping module consisted of a COTS linear motor that plunged the caps into the sample cell, and a cap feeding assembly that was synchronized with the capping actuator to control the cap flow. Because motors add significant cost, an approach was determined to control the cap feed rate and cap the cells with a single actuator.

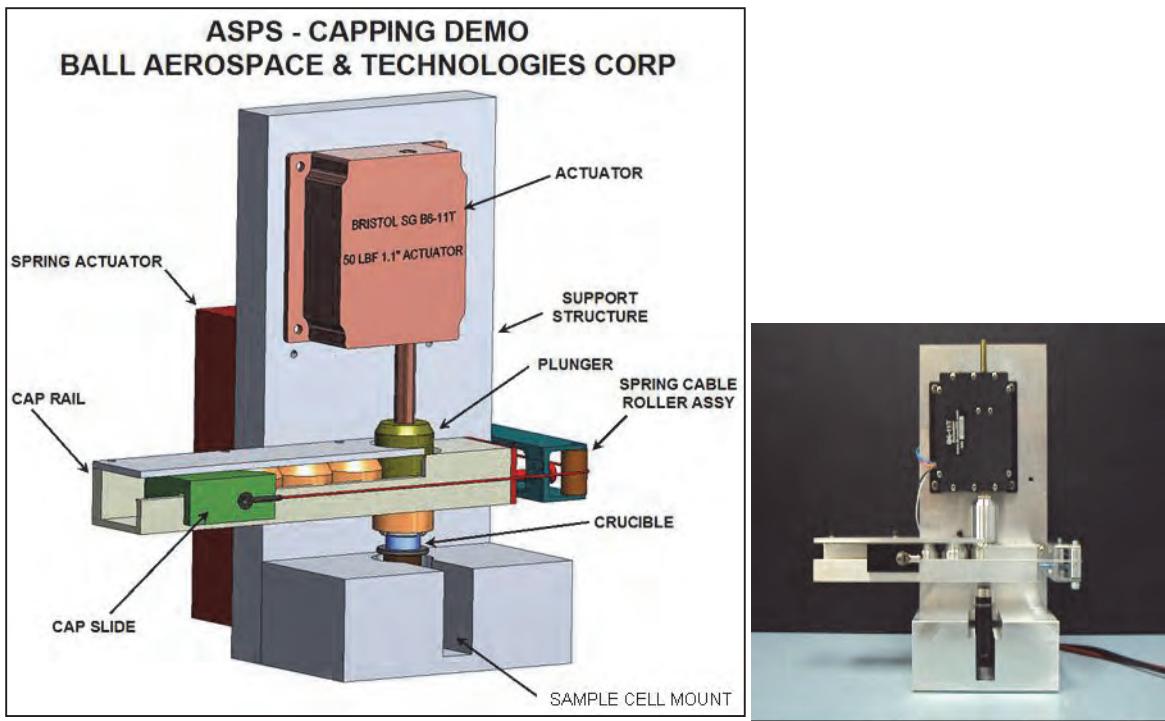


Figure 6. EDU - Capping Station

A cap rail guide or runnel with a Teflon slide to house and store the caps was designed to feed the caps into position. The Teflon slide was passively actuated with a constant force spring box that pulled the cap slide and forced the caps into the capping station underneath the plunger. To prevent the caps from jamming, the plunger, or capping head, attached to the motor shaft was elongated to block and control the dispensation rate. To ensure the caps were properly captured when positioning them in the capping station, a spring loaded cap guide was developed that slid to receive the next cap before the plunger was fully retracted to allow the cap to slide into position for the next actuation.

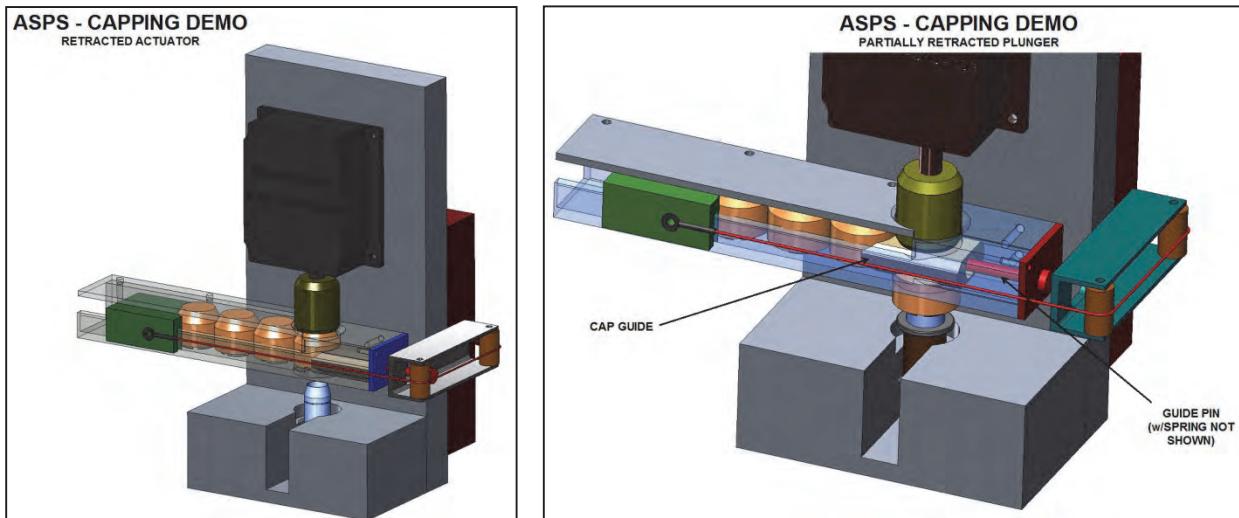


Figure 7. EDU Capping Station - Capping Sequence

The caps are self-aligning to allow for misalignments and position themselves when applied under load. Fillets and chamfers are used on the interfaces wherever required to assist the cap flow and help the transition into the sample cell. Chamfers on the sample cell cylinder avoided damaging the seals during the capping process and helped the cap position itself as it was pressed on. This chamfer angle took some debugging. Testing showed that the hard Teflon seals resulted in high peak loads to get the O-ring over the sample cell; therefore, it was necessary to reduce the abruptness of the angle on the chamfer to reduce peak loads. Later cell designs incorporated a longer chamfer which reduced the capping loads to a more linear response and also served as a self-aligning feature for the caps.

After developing the capping approach the next step was solvent injection and sample extraction. A Zirk fitting type of valve was the initial baseline, but the operational temperatures and pressures directed the search for other options as these components could not meet our requirements. A valve based on O-ring technology was developed for its low cost, relatively mature technology solution, and parts availability. Because O-ring based valves are susceptible to particulate contamination, a means to keep the solvent and sample from contaminating the valve was required. Filtering of the liquid sample after solvent extraction was accomplished by a two stage approach: a paper filter to capture the coarse particulates, and a COTS metal sintered cylinder to act as the refining filter that also works as a spring retention interface to keep the valve closed.

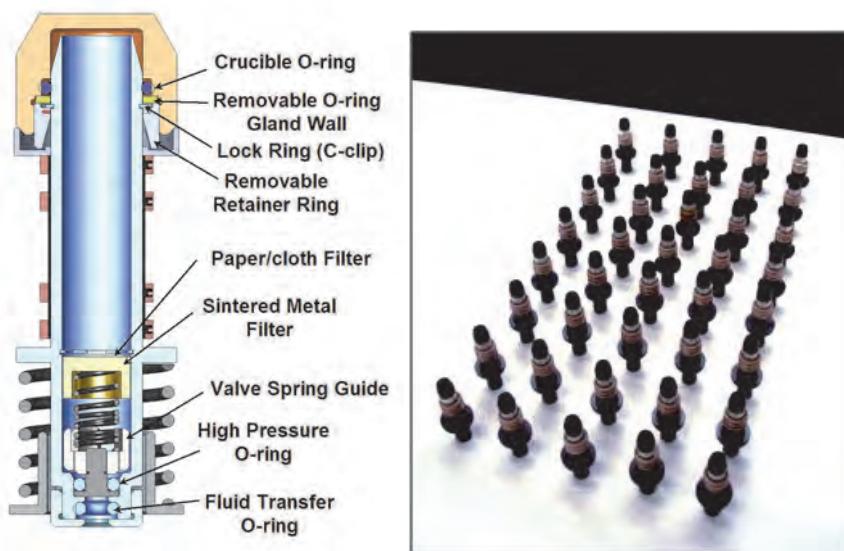


Figure 8. Sample Cell Cross Section

After developing the sample cell sealing and valving, the heating approach was addressed. To increase heating efficiency, reduce complexity, and provide redundancy, each sample cell has its own heater assembly. Kapton heaters were selected for their affordability and reliability. To reduce weight, cost, and wiring complexity, the heater leads to the sample cells were eliminated by incorporating heater contact rings instead of flying leads. To monitor the cell's temperature, a remote infrared sensor captures the cell's temperature; this option removed the requirement of having localized thermocouples installed on each sample cell. To power the heater, the sample cell is positioned by the carousel to a heating station with matching connectors that slide and contact the contact-rings. Once contact is achieved, power can be applied to the heater; simultaneously, the infrared sensor monitors temperature. This heating station can be easily duplicated to provide redundancy.

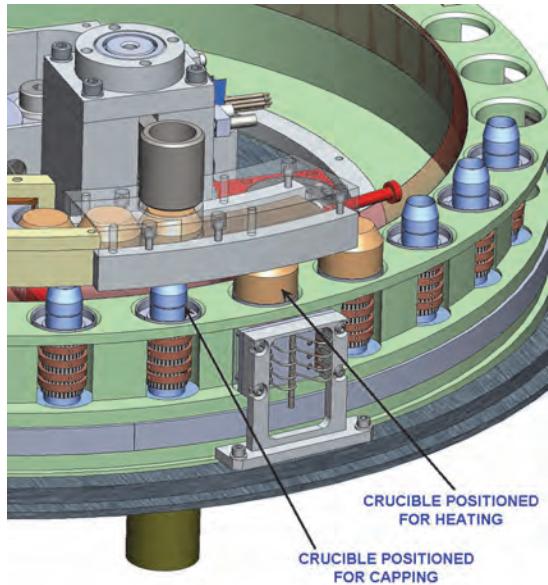


Figure 9. Heater Station

The capping of the test cell proved to be a challenge and the design-kernel for the overall mechanism development. Initially, the sample cell was developed with a single-use flight mission in mind. This approach led us to develop a simple test cell that proved successful after some development. However, we quickly realized of the cost-impact this approach would have for ground testing and further development. For this reason, a re-usable cap and sample cell was developed. Although the new reusable cap added more complexity and initial cost, it served the end user in the long run, reducing overall development costs. We also choose the harder and more difficult Teflon seals to ensure we had a viable design.

A final feature to the sample cell was the addition of a dust tray that is sealed when the cell is capped. The dust tray serves as an alignment and vibration damping feature and dust contamination mitigation device.

3.2 The Carousel System

The carousel system serves as the housing and positioning mechanism for the sample cells. It houses 30 test cells and drives them by means of a stepper motor and a worm drive reduction gearing. The worm drive gearing is used to get a mechanical advantage and to lock out the carousel when stopped. Position control is managed by an optical encoder and reduction gearing, resulting in position accuracy of 0.3 millidegrees. Because the carousel houses the test cells, it acts as a structural support platform through which most loads to the sample cells react. To manage these loads, the carousel is mounted on a large bearing, double sealed, and housed in a labyrinth seal to minimize bearing contamination.

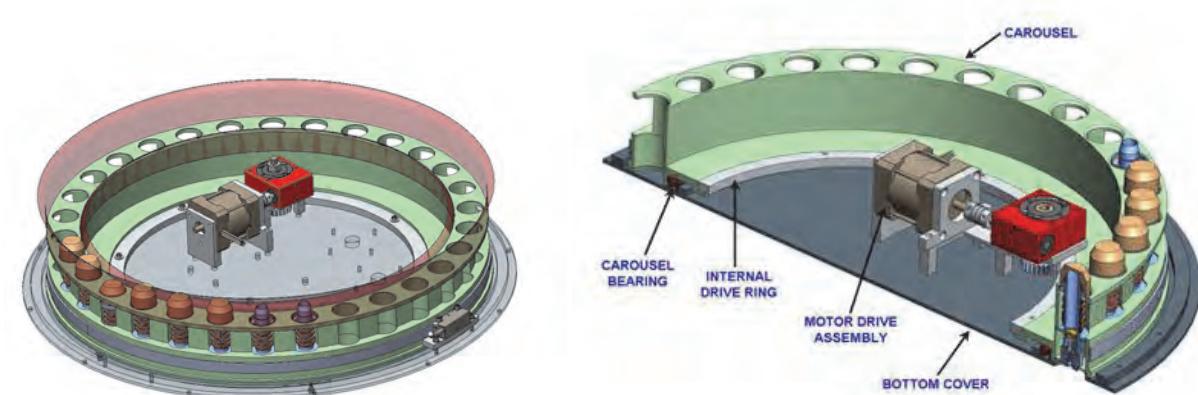


Figure 10. Carousel Assembly

The carousel positioning and repeatability is crucial to prevent damage during any operation, such as sample delivery, capping, heating, and solvent delivery. To obtain these goals, several approaches were considered: motor step counting, mechanical telemetry, and even a bar code approach. We chose an optical encoder because of its accuracy, turnkey solution, relatively low cost, and ability to mount the encoder ring on the outside of the carousel, which allowed the use of the inside area of the carousel for installing other components. The encoder output was integrated with readily available software drivers and subroutines that integrated with the WASP control software based on LabVIEW.

To move the carousel, a ring gear is bolted to the inside wall, close to the bearing to minimize tooth gear loads. A pinion gear attached to a worm drive gear box is used to drive the ring gear with enough gearing reduction to achieve position accuracy, torque margin, and a means to lock the carousel. The worm gear assembly is driven by a COTS stepper motor with flight history and vacuum compatible.

To facilitate assembly and refurbishing of the sample cells, a quick access port was designed into the bottom of the WASP cover through which each cell is accessible and easily removed by taking out a circlip that holds the cell in the carousel. For flight, an internal and external skirt can be added to further mitigate particulate contamination.

3.3 The Capping Subsystem

The primary function of the capping subsystem is to seal the sample cells and to drive the cells into the injector station of the fluidics subsystem. To accomplish this process, the capping subsystem requires a cap feeding assembly, and a capping arm to drive the caps into the sample cell and push the sealed cell into the injector station. The capping arm is driven by a similar setup as the carousel drive: a geared worm drive with an attached stepper motor, and a linear encoder to determine the arm position. As a backup system, mechanical switches are used to determine failed modes and reset the mechanism.

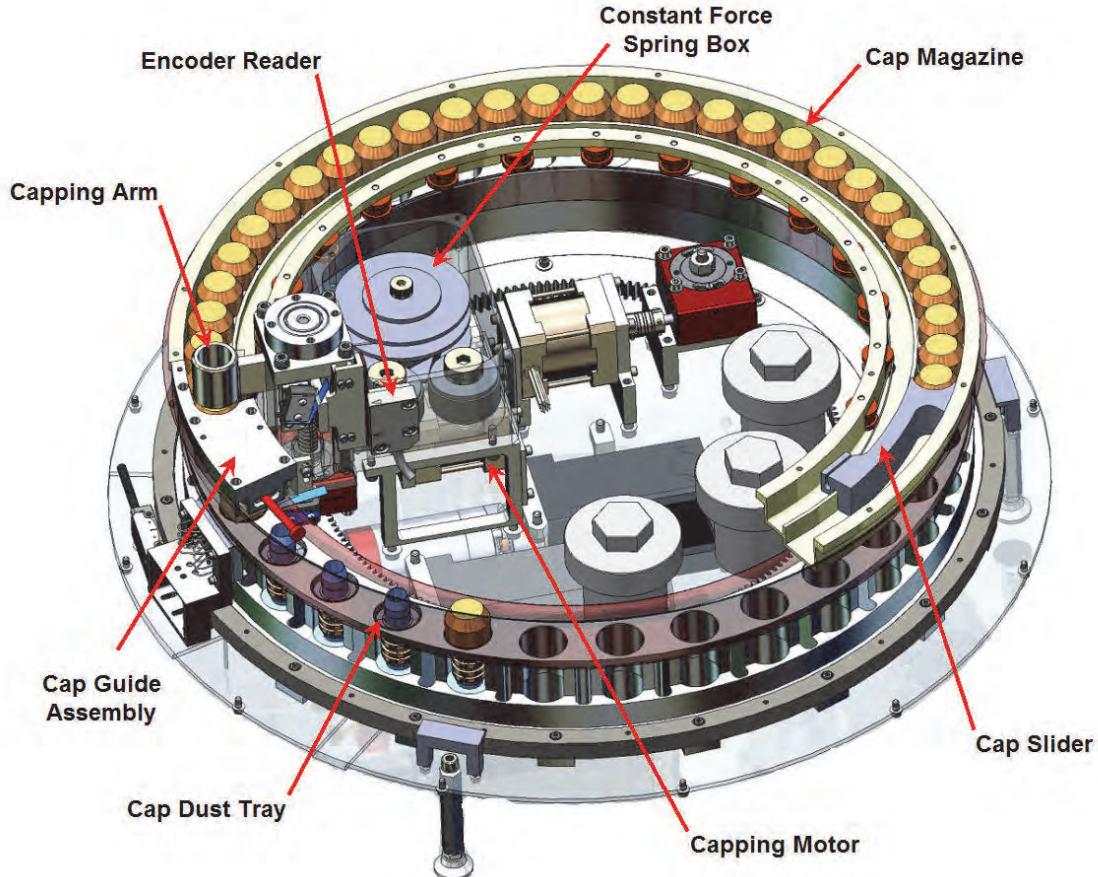


Figure 11. Capping System

The cap feeding assembly is a passive mechanism driven by constant force springs. All the sample cell caps are placed in the runnel and driven into the capping station by a cap guide made of Teflon. A cable is attached to the cap guide and routed along the runnel with rollers, and feeds into a redundant constant force spring box. The feeding of the caps into the capping station is managed by the capping arm. The cap feeding assembly was designed to only provide caps into the capping station when a new sample cell requires it. The arm was designed to block the caps from feeding into the capping station when the capping arm is driving a cap downward to seal a sample cell. When a new cap is required, the capping arm is driven upward to allow a cap to slide underneath. To insure that the cap does not get jammed, a cap capturing slide pops from the opposite side to capture the new cap. As the new cap is pushed into position, the capturing slide is pushed back to its stowed position. At this point the cap is still supported by the caps on one side and the capturing slide on the other. When the command is given, the capping arm begins to push the cap downward and blocks other caps from feeding into the capping station. The cap and capping arm engage through matching chamfers to center the cap onto the sample cell. As discussed in the sample cell section, the chamfer on the cell ensures the cap has enough run for the cap to self-align and seal in place.

The capping arm is driven by an ACME screw supported with bearings and Belleville washers to prevent jamming when bottoming out the assembly. The ACME screw is driven by a worm drive gearbox that is connected to the same type of stepper motor as for the carousel. Similar to the carousel, the worm drive is used to stop and lock motion. The worm drive gearing is designed to lock out the capping arm at any position. Because of the high mechanical gearing, special attention was given to the bracket design to ensure the mechanism would not self-destruct if the capping arm was driven past its operational limits.

The components were designed so that the capping arm can hard stop at either end without breaking anything. During normal operation, position is managed by the linear encoder; however, in case of losing control of the capping arm, mechanical switches are positioned at either end of travel.

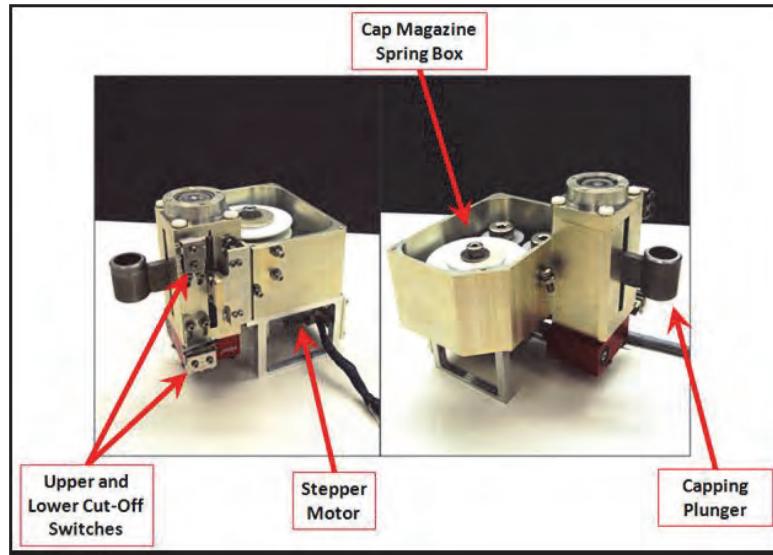


Figure 12. Capping Mechanism

The secondary function of the capping assembly is to engage the sample cell to the fluid transfer station. This subassembly consists of the injector housing, injector needle, and a spring loaded injector guide.

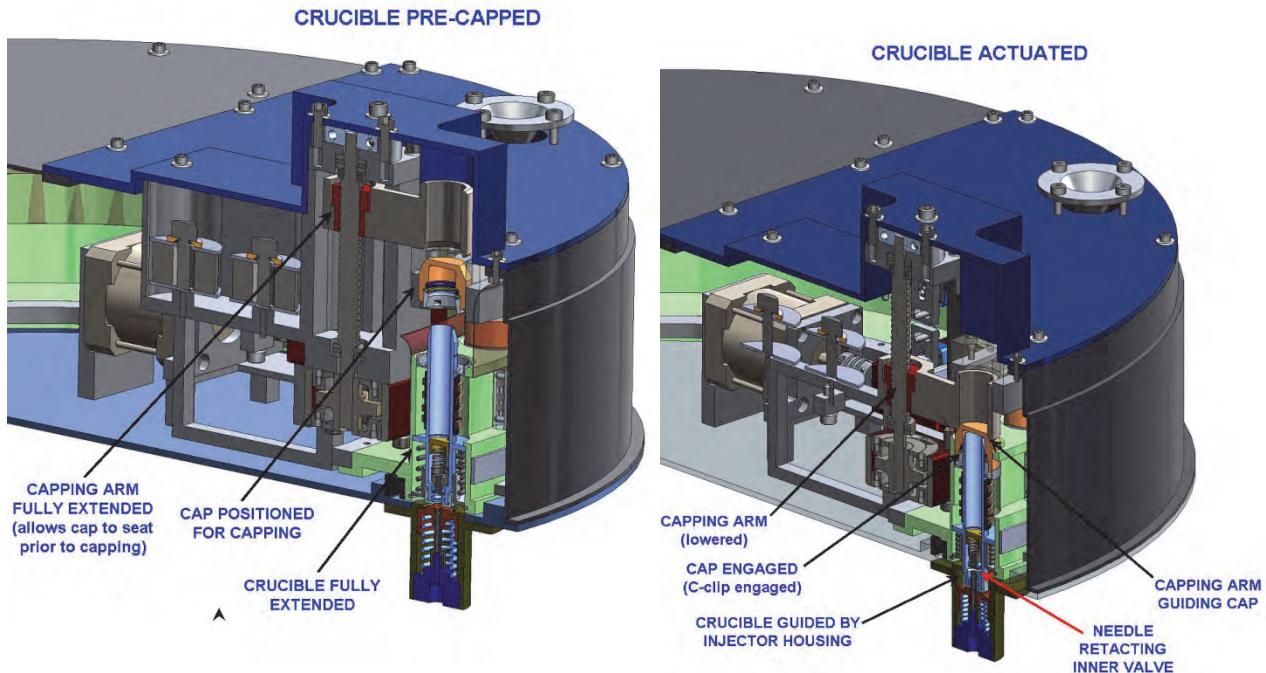


Figure 13. Capping Mechanism - Actuation – Section View

As the sample cell is driven into the fluid transfer station bore, the injector guide reacts against the bottom of the sample cell and aligns the injector with the bottom cell valve, while supporting the injector from

getting bent; the capping arm continues driving the sample cell until the valve is fully open and the injector fully sealed in the sample cell.

3.4 The Fluidic Management Subsystem

The fluidic subsystem consists of three fluid reservoirs, a multi-port valve, a pump, and a fluid transfer station.

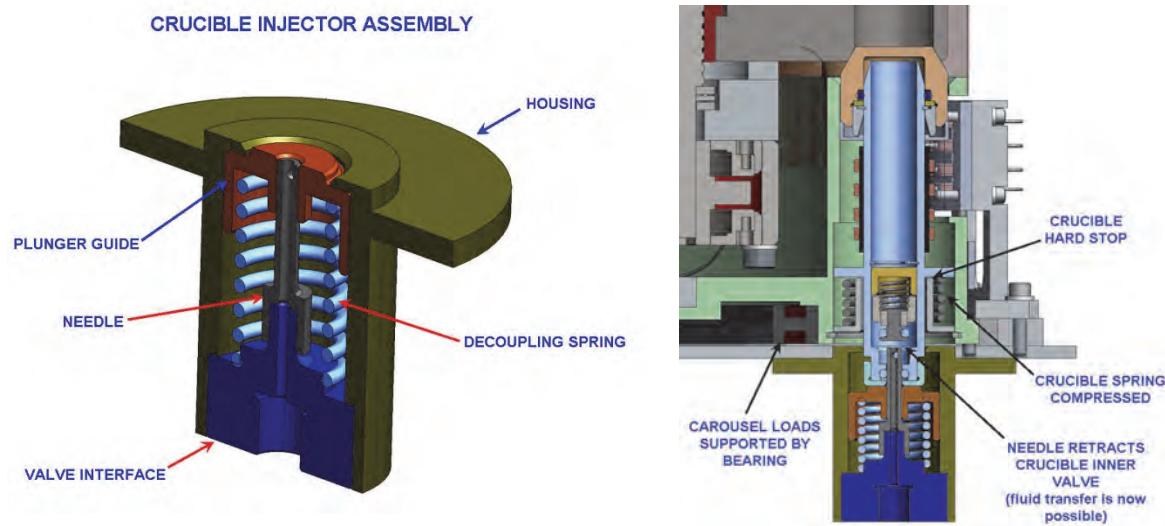


Figure 14. Fluid Transfer Station

The fluid transfer station consists of an injector needle with a spring loaded guide to support the needle when engaging the sample cell. The spring guide acts as a backup system in case the sample cell spring in the carousel fails, in which case, as the capping arm backs out, the spring guide will push out the sample cell from the fluid transfer station and allow the mechanism to continue functioning. If this failure would occur, the failed sample cell would simply drag along the bottom of the WASP housing.

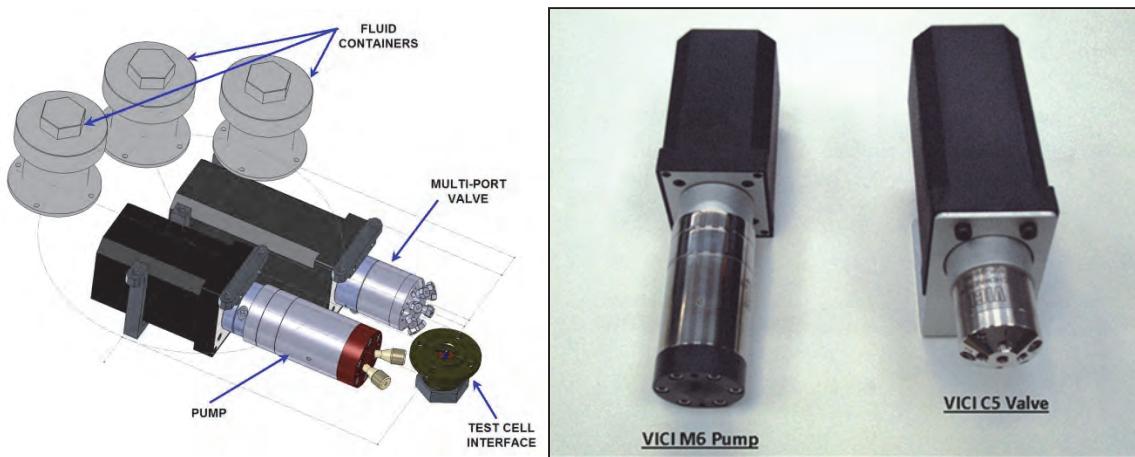


Figure 15. Fluid Management System

The finalized WASP fluidics subsystem incorporates a COTS VICI 4-position valve and a COTS VICI Cheminert M6 pump to select and deliver fluids from three custom Teflon reservoirs. The custom fluid reservoirs reside internal to the carousel and the design assumes water, methanol and oxalic acid as the three fluids of choice. The M6 bi-directional pump is capable of delivering fluids with an accuracy and

precision of $\pm 0.5\%$ and -0.1% , respectively, at flow rates of 10 mL/min when exposed to a maximum backpressure of 100 psi (0.69 MPa). Plumbing consists of COTS 1/16" (1.6-mm) OD, 300-nm ID PEEK tubing and COTS zero-dead-volume PEEK compression-style fittings. A relative layout of the solvent delivery subsystem is shown in Figure 16, depicting the pump, valve, and sample cell injection interface. A block diagram depicting basic fluid delivery pathways is illustrated in Figure 19. After each extraction cycle, fluid lines are flushed with a desired clean solvent back into a used sample cell in order to mitigate sample cross contamination.

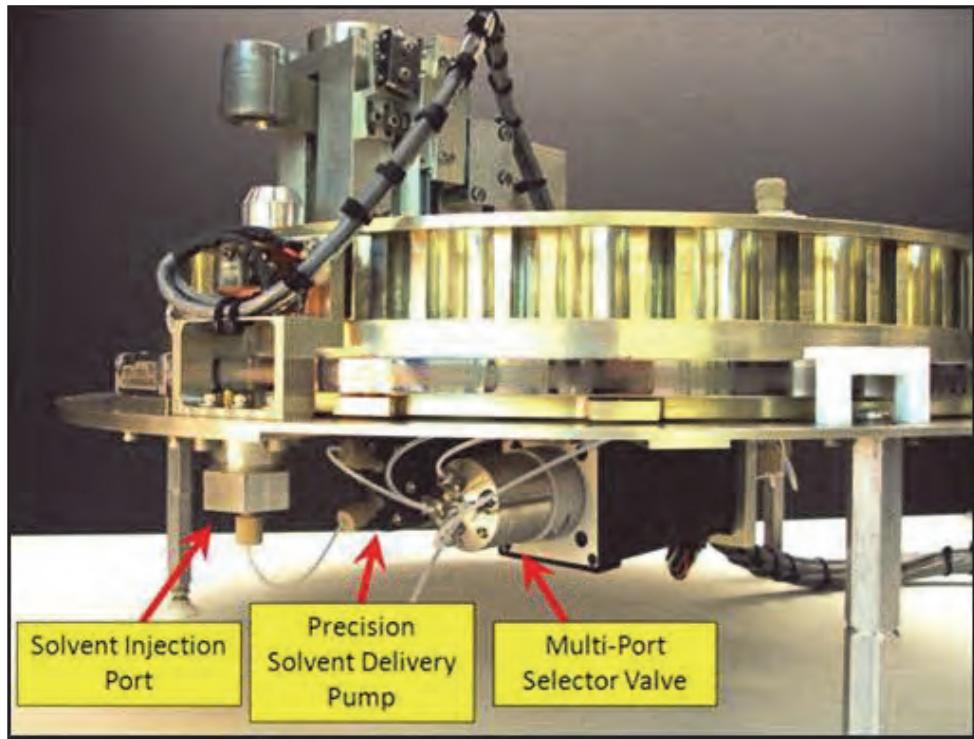


Figure 16. Fluid Management System

3.5 Additional Considerations: Inlet Funnel

The sample introduction was not part of the scope for this project. However, because an inlet is required, some development was done to address the means by which the sample is introduced into the test cells. How the sample is introduced to the test cells is critical in minimizing cross contamination of samples. Because the sample will be manually introduced, we used a funnel to guide the sample into the test cell. The funnel can be lowered into the sample cell, so that the neck of the funnel recesses inside the cell when delivering the soil sample. The funnel assembly is supported and guided by pins with springs under it to prevent the funnel from falling in and jamming the mechanism, and passively return it to its stowed position after use. An ultrasonic motor was attached to the funnel to excite the sample particles downward.

For flight, antistatic adhesion coatings will be applied to the funnel to minimize dust clinging onto the funnel surface due to electrostatic effects; Ball Aerospace has developed a coating that minimizes these effects in dry and dusty environments. The funnel's plunging step into the sample cell and the funnel's ultra-sonic motor actuation would be automated to ensure proper sample delivery.

4.0 CONTROL SOFTWARE AND ELECTRONICS

A great deal of consideration was placed upon developing a software command and telemetry interface that is highly intuitive and user-friendly, while also maintaining an elevated degree of versatility and customization. Given that the system is nominally intended to operate with an opaque aluminum cover—with all core mechanisms being visually inaccessible—Figure 17 illustrates that there is a wide array of LED indicators made available via the software interface, which provides an easily-decipherable display of general system status and positioning. This interface approach ensures that the user will never lose track of any system parameter during normal operation.

In addition to an assortment of intuitive LED indicators, the system is largely controlled via an interactive message center that provides the user with instructions, buttons, numeric inputs, indicators and/or plots that appear, disappear and automatically update depending upon user-initiated commands. For the advanced user, a quick-setup option is available that will allow the user to input predetermined sample processing parameters if desired.

A collection of versatile subroutines have been developed to perform the following tasks:

- Initialize the WASP carousel to its home encoder index.
- Initialize the WASP carousel to sample cell index #1. This move is relative to the home encoder index.
- Move the carousel to a user-specified cell index. This move requires the carousel to be initialized to cell index #1.
- Initialize the capping mechanism to its home encoder index.
- Move the capping mechanism to apply a cap and/or engage with the solvent delivery needle. This move is relative to the home encoder index.
- Move the capping mechanism to an intermediate position to allow the carousel to spin, but not allow another cap to feed. This move is relative to the home position.
- Turn the WASP heater on or off.
- Acquire an analog temperature measurement from the infrared thermocouple.
- Drive the VICI pump to dispense or aspirate a user specified volume of solvent at the user specified flow rate.
- Position the VICI valve at a user specified position.

These subroutines are used in multiplicity throughout the main WASP LabVIEW user interface state machine. The front panel of the main WASP user interface is depicted in Figure 18.



Figure 17. Screenshot of the WASP LabVIEW user interface

The input parameters tab of the software interface is pictured in Figure 19, and the existing software algorithm block flow diagram is shown in Figure 20.

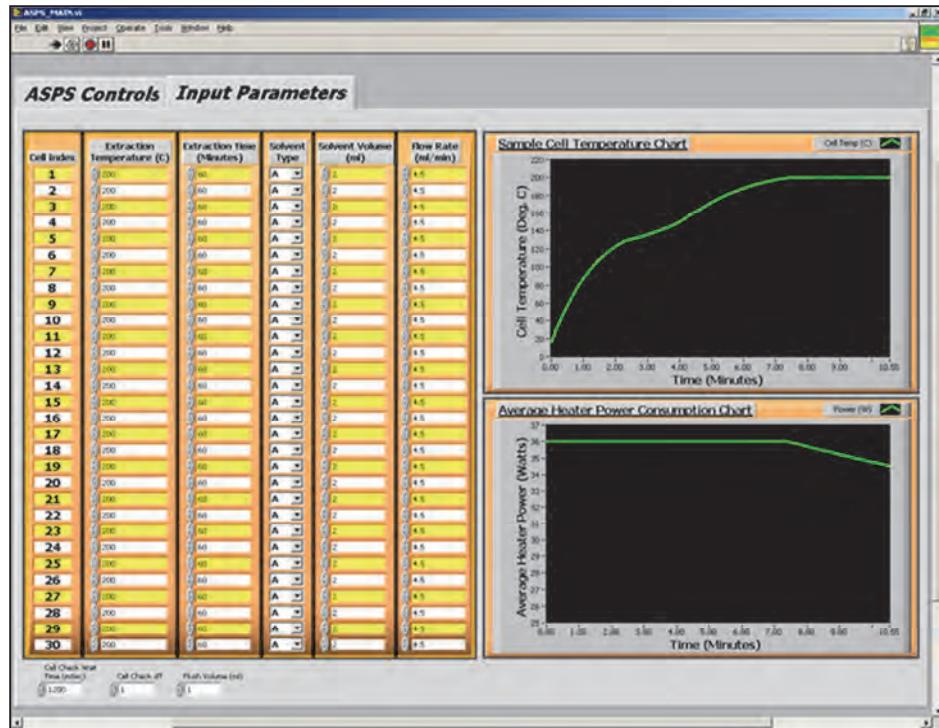


Figure 18. WASP Software User Interface, Input Parameters and Plotting Panel

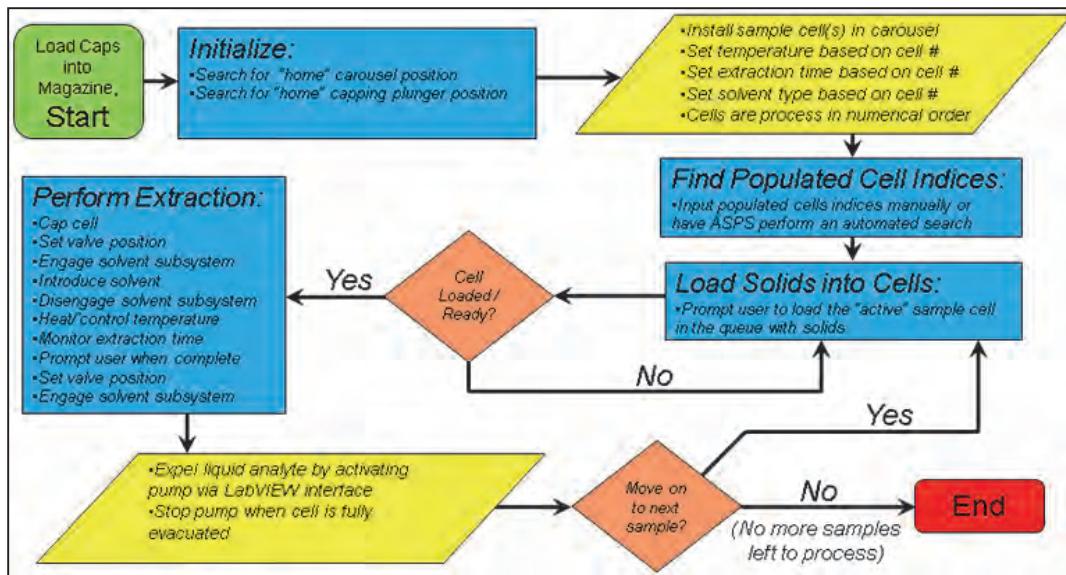


Figure 19. Updated WASP Software Algorithm Flow Diagram

4.1 ASPS Electronics Overview

COTS National Instruments (NI) hardware controls all aspects of the WASP system and was integrated in conjunction with the software interface as outlined in above. An NI 2-axis stepper motor controller controls the motors responsible for positioning the carousel and capping plunger; and a PCI-7332 board with four DIO ports that are used for heater modulation, as well as four analog inputs that capture the infrared temperature sensor telemetry. A NI Universal Motion Interface Connector Block serves as the central hub, to which all motion devices, heaters and thermocouples/thermistors are connected. The pump, valve, motor, and infrared temperature sensor also utilize COTS driver and amplifier modules in order to operate.

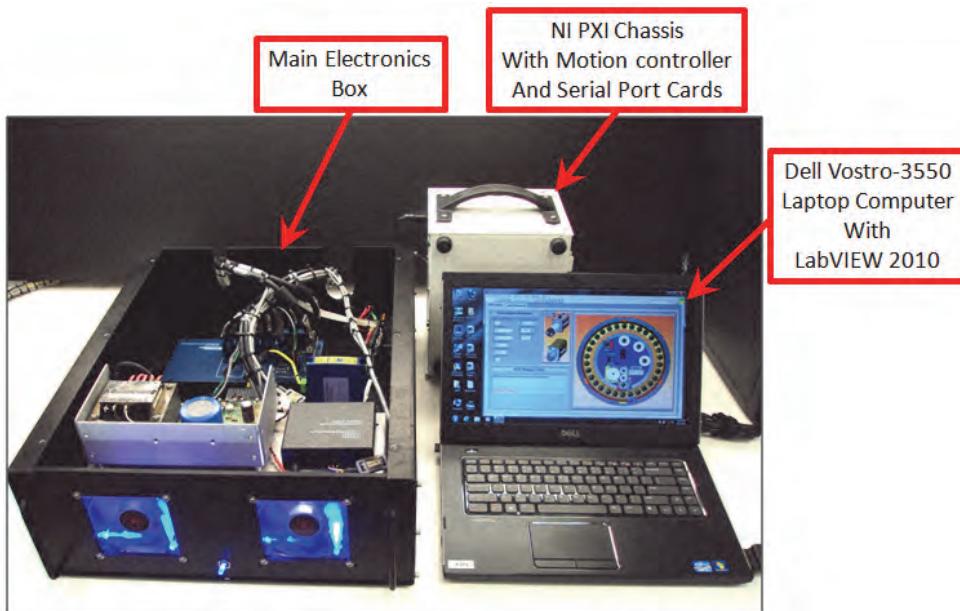


Figure 20. WASP electronics box CAD model

The existing system is compatible with either a single 110 VAC grid outlet or a 28 VDC supply (e.g., batteries, bench-top DC supply). This approach allows for a convenient power option in a laboratory setting, but would also make powering the ASPS system in the field with two standard car batteries—connected in series—a viable option as well. The WASP primary bus voltage will be +28 VDC, which was selected because it is a spacecraft bus voltage that is commonly available. As such, if 110 VAC option is used, the AC voltage will first be converted to +28 VDC. The end result is a single electronics box with a single three-foot cable bundle leading from the computer, and a single six-foot cable bundle leading to the carousel as shown in the picture in Figure 20.

4.2 Integrated System Calibration

The integration and calibration of the WASP took significant effort throughout the program. By treating each subsystem as an independent component, it made it easier to later integrate each subsystem into the WASP chassis. However, all the components had to work in conjunction, and timing and sequencing was of essence. A transparent cover was designed through this process to observe and help develop the timing and sequencing of events. This tool became indispensable developing the mechanism.

Calibration of the VICI pump and valve simply amounted to programming vendor-furnished calibration constants into the COTS controller/driver boxes' EEPROM via an RS-232 interface. Due to the nature of these devices, they should never require recalibration. The initial capping and carousel motion control setup calibration, however, was much more complex and required extensive trial and error in order to optimize the performance of each mechanism. Given that the WASP structure and mechanisms have intentionally been designed to be extremely stiff and rugged, it is anticipated that the system will be able to perform hundreds of cycles without requiring recalibration.

5.0 CONCLUSION

Over a three-year period of performance, Ball Aerospace successfully completed the design, fabrication and end-to-end testing of a field-portable Wet-chemistry Automated Sample Processing (WASP) system. Ball has demonstrated that the integrated system is capable of autonomously accepting 100 mg+ of solid fines within a sample cell, combining the fines with 2 mL+ of solvent, heating and containing the mixture at 200°C for 1 hour+, and finally filtering/aspirating the liquid analyte from the processed cell. The integrated WASP carousel with 30 sample cell assemblies currently exhibits a total mass less than 15kg and either meets or exceeds all of the performance goals. The WASP field-portable platform was delivered to JPL the week of October 17th, 2011.

6.0 REFERENCES

1. J. Lasnik, J. Soto, S. Roark, L. Beegle (2011) "Automated Sample Processing for Future Mars Astrobiology Missions" 42nd Lunar and Planetary Science Conference, abstract 1589.pdf (2011)
2. L. Beegle, J.P. Kirby, A. Fisher, R. Hodyss, A. Saltzman, J. Soto, J. Lasnik, S. Roark, "Sample Handling and Processing on Mars for Future Astrobiology Missions," IEEEAC Paper # 1602 (2011)
3. K.P. Kirby, S. Halabian, I. Kanik, L. Beegle, S. Roark, J. Lasnik, J. Soto, "Automated Sample Handling and Processing on Mars for Future Astrobiology Missions," Astrobiology Science Conference, Abstract 5392.pdf (2010)

Refinement of a Low-Shock Separation System

Chuck Lazansky*

Abstract

This paper discusses the design of Marman Clamp-band Separation Systems, and several lessons learned by SNC over 12 years and multiple programs. Historically, there have been enough failures associated with Marman band designs that practical design guidance is publicly available. Utilizing a shock-dissipating release device has allowed us to sidestep many of the typical challenges associated with Marman systems and helped create a highly robust design baseline that differs significantly from the traditional system.

An overview of the purpose, components, and function of a clamp-band system will be presented. Common failure modes of this type of system will be discussed, and how these can be addressed. Early examples of successful SNC systems will be reviewed (NANOSAT, Orbital Express). Much of our early work on Clamp band systems and release devices was performed collaboratively with SAAB-Ericsson (now RUAG). The heritage design was refined recently to meet a challenging set of requirements for the EELV Secondary Payload Adaptor (ESPA Grande). By retaining the proven features of the design, we built an optimized sub-24 inch (61 cm) separation system with high stiffness, low-release shock, and a compact envelope.

Overview of Marman Clamp Separation Systems

A “Marman clamp” or “Marman ring” is a generic ring clamp used to join two cylinders butted together at the ends. “Marman Products” was the name of the company which first produced this type of clamp in the 1930s¹. The Marman clamp was a sensible choice for spacecraft separation in the 1960s, as spacecraft stages are usually comprised of butted cylindrical structures of truss/beam construction covered with a skin. Separation of these structures normally entails severing the bolted connections. The advantage of the Marman clamp was to reduce the number of bolts to be severed for release, improving reliability.

The first Marman clamps were a flexible strap or band held around a series of circumferential V-wedges over the angled flanges of mated cylinders². Load was retained by tensioning the strap such that the wedges could hold the ring flanges together with no gapping under the worst load case. A redundant release could be achieved by severing 1 or 2 (or more) bolts that hold the flexible band/strap in tension. This allows the V-wedges to move radially outward, freeing the mated flanges. Bolt cutters, pyrotechnic or frangible bolts are historically common choices for the release element. Release of these systems results in significant shock as the band strain energy (and pyrotechnic shock) is dissipated. Typically there are features to retract and “park” the band after release to prevent the band from interfering with release of the deployed payload. Marman Clamp separation systems (also known as “V-bands”) have been used successfully on many missions. A generic system is shown in Figure 1.

Other features typical of these systems include indication of positive spacecraft separation with switches or continuity loops in electrical connectors, and kickoff springs sized and balanced to provide proper separation velocity and attitude.

* Sierra Nevada Corporation Space Systems Group, Louisville CO

Design of a Separation System

Marman Clamp systems usually share the design objectives below. All three design objectives should be kept in mind and balanced against each other (along with weight and cost):

1. Create a stiff connection to the payload under worst case load conditions; retain until deployment
2. Release the payload upon command, with proper separation dynamics, minimal imparted shock, and no “re-contact” between separated payload and band or any other part of sep system (including debris from pyrotechnic release)
3. Create robust processes for installation, preloading, and testing of flight system, compatible with proper safety measures

Figure 2 shows the components of a typical system. The band is tensioned to the required preload, compressing the shoes (V-wedges) radially, generating axial preload, clamping the rings together. The clamped rings behave like a preloaded fastener head, creating predictable joint stiffness as long as gapping between the rings does not occur. Most systems have no trouble being stiff in axial compression, as the joint acts as a solid cylinder. Stiffness under axial tension is more difficult to achieve as the load path goes from flanges to the clamped toes of the joint to the mating flange.

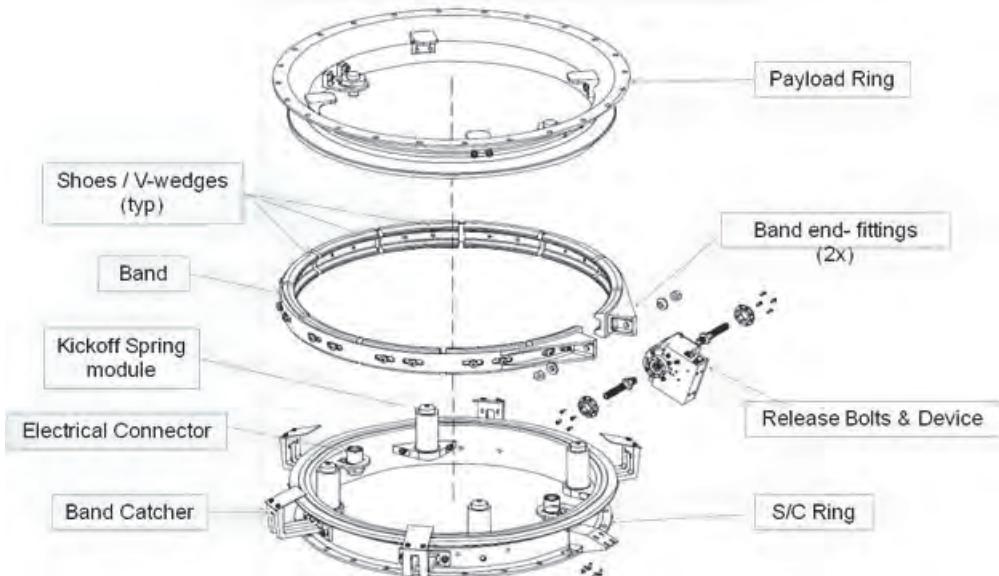


Figure 1: Generic Marman Clamp System

Table 1 shows a comparison of the traditional Marman system design approach to the alternative approach taken in our systems. These differences will be discussed in more detail to illustrate why our approach is an improvement.

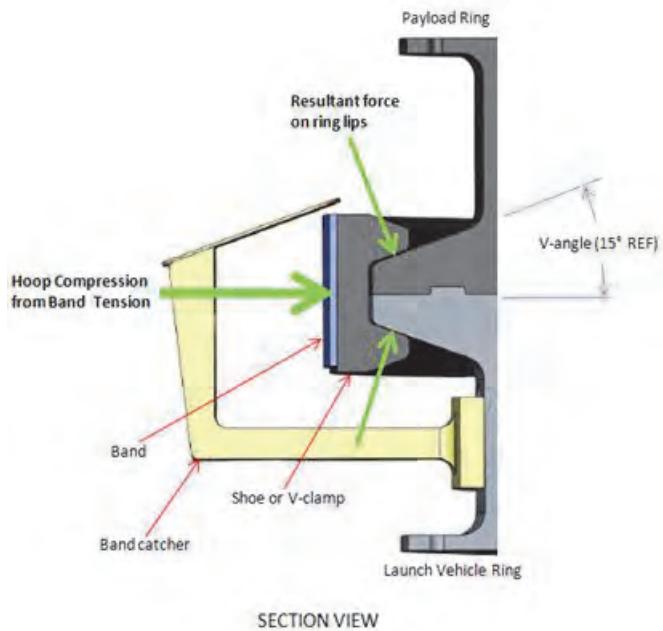


Figure 2: Generic Marman Clamp System Section

Table 1: Design Comparison: Traditional versus Improved Separation Systems

Feature	Traditional Marman Systems	Improved Separation System
Release Element	Pyrotechnic or frangible bolt separation	High-reliability, shock dissipating release device
Number of release points	2 release points minimum, 3 or more for larger rings	Single point release, redundant initiators
Band	Thin, flexible "strap" of steel (un-controlled shape)	Thicker, less flexible machined Alum band of controlled shape with free-state larger than installed state for release energy
Band Dynamics	Less predictable release dynamics; Dependent on band strain energy for release, Springs and/or tethers (extractors) to assist release and move band away from rings into catchers; Straps to contain ends of band after release	Predictable release dynamics due to controlled shape; Band "spring" energy sufficient for release, catchers "park" band away from rings after release; tethers and straps not necessary
Band End fittings	Trunnions w/ spherical ends connected to strap, or riveted "bathtub" fittings	"one-piece" band with integral machined ends (bathtub fittings); release bolts at each end have spherical washers
Band preload	Lower preload, lighter system	Higher preload, stiffer/stronger system
Interface Rings	Lighter weight on "flyaway" ring, shear lip, controlled gap, longer lips, angle >20 deg to reduce tension requirement	Matched stiffness, short lips for direct load path, minor inner "gapping" acceptable, smaller angle (15 deg)
Clamps/Shoes/V-Wedges/Retainers	Aluminum, Titanium, or steel	Aluminum w/ Titanium for highly loaded end shoes
Install and preload process	Set preload w/ bolt torque or strain gauges, tap band to equalize; pyrotechnic safety practices	Instrumented bolt indicates load, no tapping - single segment band w/ proper lubrication; reduced safety requirements
Preload Indication	Bolt torque, strain gauge on band or bolt(s)	Calibrated, Instrumented bolt

General Design considerations

Good design practices for any highly loaded system also apply to Clamp band systems:

Stress-Corrosion Cracking: These systems will be preloaded to the flight load, and remain loaded, possibly for months, until launch and deployment. Stress corrosion cracking has caused sudden failure in clamp band systems, so using materials with an A-rating for Stress-corrosion cracking is essential. Minimizing potential stress concentrations with controlled fillet radii, controlled thread roots, and rolled threads on loaded bolts is normal practice.

Minimizing Thermal Effects: Thermal strains can cause changes in band preload. Load drift should be avoided by using materials with similar coefficients of thermal expansion for rings and band, and shoes (to a lesser extent). Aluminum is a typical choice for rings. Shoes are typically titanium or CRES steel, and band is normally CRES steel. An all-aluminum design (with the exception of titanium in the more highly loaded shoes at the band ends) is preferred by SNC as will be discussed further.

Control of friction: This is critical at moving interfaces, especially between shoes and band, and shoes and rings in order to prevent lockup, equalize loading in band and prevent cold welding between rings and shoes. Surface finish (roughness) and solid-film / dry-film lubricants (DFL) MoS₂ ($\mu \sim 0.1\text{-}0.15$) and Dicronite® DL-5 ($\mu \sim 0.05$) are commonly seen in clamp band systems. With aluminum rings, chromate conversion coating followed by DFL provides $\mu \sim 0.1$. One tradeoff is that reduced friction between the rings, and between shoes and ring lips increases the required band load, but improves release performance and reliability.

Release Device

Traditional Marman clamp systems have used explosive bolt technology to load and release the band. The obvious disadvantages of these for this application are high release shock and inability to test the flight unit. While these devices have been used with success in clamp band systems, they present a number of other design issues to be solved which can complicate the design.

Multiple release points on the band have been recommended with pyro-bolt technology: 2 release points for systems up to 18 in (46 cm) and 3-4 for 60 in (152 cm) or greater³. This is primarily to add redundancy for release in the event of a pyro failure. Multiple release points also are recommended to allow more symmetric expansion of the band, to help it clear the rings. However, this approach increases chance for non-uniform loading of band/rings, and complicates release dynamics as multiple devices must operate simultaneously. More release points also increases the need for extraction features or added hardware to actively pull the band away from the rings such as springs and tethers. This adds parts and complication to the design, and increases system weight (more bolts, trunnions, tethers, springs). That weight may be better used to improve margins elsewhere in the system to improve stiffness (rings, band, etc.).

Inadvertent bending loads are common in Marman clamp systems and have been responsible for flight failures (overload, stress corrosion, or concentration in roots or creep of explosive bolts). Some technical literature suggests that despite good trunnion design, the failure mode may be inherent in the perpendicularity tolerancing of bolt head and nut threads and seats. Previous failures in these areas have been addressed with the addition of spherical seats or other misalignment features, and use of greases at the bolt attachments.⁴

Explosive bolts have other well-known drawbacks. Flight units cannot be tested. Margins are determined statistically, through lot testing. There are also safety concerns of unintended release. NASA design guidelines state that all debris from pyro-technic release should be contained – as in the case of exploding bolts, bolt cutters, etc.

During our early work with these systems, we developed a release device specifically for clamp band separation. The Clamp Band Opening Device (CBOD) uses patented FASSN (Fast-Acting Shockless Separation Nut) technology to dissipate stored strain energy resulting in extremely low shock to

Spacecraft and payloads. Use of a high-reliability release device allows for one release point. This not only addresses the above shortcomings of pyros, but drives the design of the entire system in a very favorable direction.

The CBOD (see Figure 3) consists of two bolts with opposite hand, high lead threads which engage the same central flywheel nut. The flywheel is fixed, and released, with a retractable pin. When the CBOD is stowed, it functions as a single long bolt, which engages the ends of the clamp band with a simple nut at each end. The band preload creates tension in the CBOD bolts, which exert a back-drive torque on the flywheel. Upon release of the pin, the flywheel is free to spin, releasing both bolts (and the band ends). CBOD slows the release event, dissipating band strain energy into rotational kinetic energy of the CBOD flywheel. This allows for higher band preloads without excessive release shock. Excess release shock can create unpredictable band behavior, potential rebound of the band, and possible damage to the vehicle or spacecraft.

Redundancy in CBOD is achieved with the use of a pin pulling device with dual NASA standard initiators (NSIs). This is the smallest and lightest part of the release device, and a very efficient means of meeting redundancy requirements. The CBOD is fully-resettable for multiple uses, with replacement of the NSIs only. The CBOD has controlled thread-form, rolled threads, and each is proof-tested. Margins on CBOD are verified by proof-load testing, and release performance of every flight unit is tested at component level and after integration. A Small CBOD version has $\frac{5}{16}$ -in (8-mm) bolts and 3500-lb (15.6-kN) rating; the larger version has $\frac{1}{2}$ -inch (13-mm) bolts and a 13,500-lbf (60-kN) rating. The CBOD has been used successfully in over 450 Flight band releases.

Several pyrotechnic system failures have been associated with failure of the explosive bolt⁵. Higher design margins are possible with the CBOD compared to explosive bolts since the latter must balance margins of retention and release against each other. Mounting configuration of the CBOD includes spherical seats for the end of the bolts and ensures CBOD is loaded purely in tension. High design margins, and an 18,500-lb (82.3-kN) component proof load test (~1.4x nominal load) on the CBOD cover potential overload encountered during or after preloading.

A single release point band equipped with the CBOD allows for a new design approach in which the band release is not dependent on stored strain energy in the band, or on external springs & tethers. Instead, the band is fabricated to a free-state which is larger in diameter than the rings. This creates stored elastic energy in the stowed condition and positive motion of the band away from the rings upon release. This will be discussed in more detail, to illustrate how the device has driven the improved design.

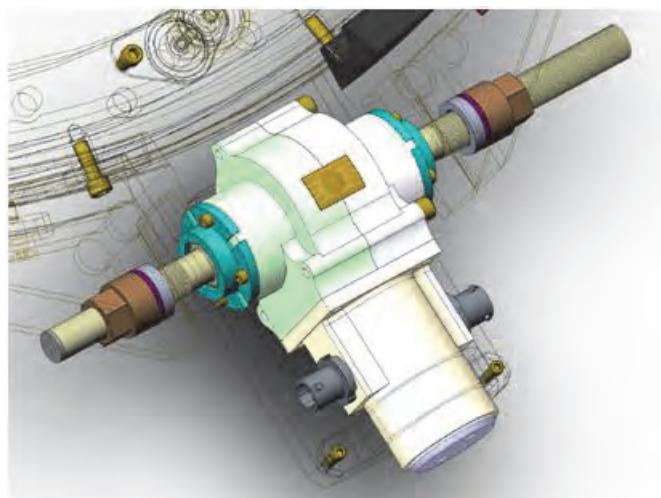


Figure 3: 13,500-lb (60-kN) Clamp-Band Opening Device (CBOD)

Band

The band (or “strap”) is the most highly-loaded element and is the primary carrier of all loads in a well-designed system. All forces acting to separate the clamped joint including shear, bending moments and axial loads should be reacted by tension in the band -- for reliable performance of both release device and clamp band. This also ensures that loads are more easily quantified, preventing the possibility of overload. The band also contains most of the strain energy, which requires a ductile material with high elongation. Resistance to stress corrosion cracking is also a key requirement as this has been cited as a cause in previous clamp system failures⁶.

The band must have fittings at the ends to engage the release device. These fittings are typically either trunnions or deeply gusseted “bathtub fittings”. Because of the large strains in the system as load is applied, there is potential for misalignments, which can impart unintended loads into the tensioning bolts or release device. The end-fittings should be equipped with spherical seats to ensure the bolt sees only tension. It is also important to keep the tangential line of action of the bolts as close as possible to the band to minimize bending moments and radial load on rings caused by these moments. Attachment points need to have extra margin due to the potential to overstress these during installation as load is applied and increased.

Most traditional systems have used a thin steel band (thus the term “strap”) to carry the tensile load (most systems are in the range of 3,000 to 10,000 lb (13 kN to 44 kN) depending on size)⁷. This seems like a good choice for the load retention design objective. It is easy to fabricate from band or sheet stock and secure end-fittings with rivets or screws. The disadvantage is the dynamic behavior of a thin-steel band (sized to carry the static loads) during release. Insufficient strain-energy in the band is a known failure mode. In one case, a design combined the shoes and band into one piece (in aluminum) and during a test, the band hung up on the rings and did not come free. The system was revised with separated shoes and steel band increasing strain energy, correcting the problem⁸. At the same time, excessive strain-energy in an overly flexible band (such as a thin steel “strap”) can lead to a chaotic release dynamic and re-contact between the band and ring.

We have found that a one-piece Aluminum band, from 7075-T7351 (stress corrosion cracking resistant), with integral “bathtub fittings” is an ideal approach. First, it is a similar material to rings and shoes in our design, eliminating CTE effects and load drift. Second, it removes the reliance on high band strain energy for the proper release dynamic. We design for a known installation deflection (i.e., known force) by machining a one-piece aluminum band to a free-state dimension such that the installed diameter provides a known strain energy (see Figure 4). This type of band springs outward, free of the rings on its own, creating a robust release dynamic. After release, the band remains rigid enough to prevent re-contact with the rings. One drawback of this is that the deflection of installation adds to the total stress state in the band, but thickness of the band can usually be adjusted to achieve proper margins.

Manufacturing cost for the band is higher with a one-piece aluminum band, which is machined from plate-stock, compared to a steel strap. But this cost is recouped by fewer parts in the assembly, by eliminating separate end-fittings and the attachment method (screws or rivets). Springs or tethers to extract the band are also unnecessary with this approach, resulting in a simpler, more robust system with less analysis, less assembly effort, and less testing.



Figure 4: One-Piece Aluminum Band Machining

Rings

Since a stiff connection is a primary design objective, it makes sense that the stiffness of the rings (both spacecraft and launch vehicle sides) should be as high as possible, limited by weight and/or envelope. Deformation of one or both rings has been identified as a failure mode in clamp band systems⁹. The term “ring rolling” was coined for severe ring deformation under band and applied loads. Ring rolling is a collapse of the ring under hoop compression due to increased radial loads or unintended local loads. This can cause loss of band tension, bending loads at the release device or separation bolts, or in severe cases, the band coming free of the ring lips. Rings should also be of uniform stiffness along circumference, with no structures or attachments that alter stiffness (thus deflections) around circumference. This applies to both radial and torsional stiffness. Local force concentrations can result in deflections and create instability of the band.

For the same reason, rings on each side should be as close as possible to *each other* in stiffness. An accepted guideline for these systems is that the spacecraft ring must be at least 70% of the stiffness of the adapter ring¹⁰. This ensures rings share load and do not deform excessively. To maintain the stiffness of the entire system the load path between the bolt circles on each ring and the clamped lips on each ring should be as short and as direct a load path as possible. A proven approach to achieving this has been to maintain a small gap between the ring lips so the ring-to-ring contact point is closer to the bolt-circles, rather than having the load path extend out to the clamped lips. We have achieved good stiffness results by simply keeping the toe of the ring short, and not intentionally gapping anywhere. Keeping the toe short also reduces stress in the v-wedges.

In clamp band systems, gapping between the rings is considered unacceptable and a sign that the load limit has been exceeded. During early development work, we found that a small gap could be formed on the ID of the rings (0.005 - 0.010 in / 0.13 - 0.25 mm) due to deflection of the rings under band load and applied axial load. These gaps did not impact the stiffness of the joint or the performance of the system (did not cause non-linear load vs. deflection. Also, it did not cause shock or dynamic responses typical of gapped systems). We concluded that small local gaps at the ring interface (not complete gapping) are due to elastic deformations of rings and clamp and should not be considered a failure criterion. The reason to prevent gapping is to maintain stiffness of the joint, and if stiffness measurements show proper performance with local gapping present then this is an acceptable condition. There is support for this position in a previous technical paper on the subject¹¹.

Historically, most systems have used a half-angle on the flanges in the 15° – 30° range¹² (see Figure 2). Larger angles increase the band load required to prevent gapping, but smaller increase risk of lockup between ring lips and v-wedges for reliable release. The ring lips (and mating surface on the v-wedges) are a critical release interface and require a dry-film lubricant. This provides a friction coefficient of about 0.1, and prevents lockup between wedge and lips. It also prevents cold-welding or galling with the v-wedges, and ensures proper sliding to allow even loading of the band as tension is applied. We also

recommend use of the same lubricant at ring interface mating surfaces (unless electrical grounding requirements through this interface preclude it).

The rings of most systems contain an angled step or lip on the mating surface of the rings normally referred to as a "shear lip". It can appear that this step is intended to react payload shear loads. In our view, good systems do not react shear loads with a lip on the rings since this can lead to large local axial loads in the ring, causing deflection and possible ring rolling. Despite the name implying shear load capability of this feature, the shear lip is only a locating feature to help mate the rings during integration, which is helpful with heavy payloads. We call this feature a "centering ramp", since our approach is to react shear loads with band tension.

Other approaches for reacting transverse loads between the rings have been used successfully. Cup/cones at the ring surfaces have been used successfully, but increase the risk of unintended tip-off. Another successful design for reacting shear loads is shear pins inserted axially through each v-wedge, mating with axial slots in the ring lips all around the outer diameter. But shear pins must precisely fit mating rings and shoes, and can make for expensive, fussy fits. Generally cones, pins, or splines to take shear loads may save ring weight but add tolerancing and machining difficulty, and can interfere with clean spacecraft separation. They may also make integration and mating of rings much more difficult, especially with large spacecraft. There is support for increasing band preload to take shear, rather than having separate shear features¹³. It may be that shear features are added in order to keep band tension low to show higher margins or reliability, and to save overall weight.

Shoes / Clamps

The shoes (also called "clamps", "v-wedges" or "retaining wedges") transmit hoop compression from the band into axial compression between the rings. They must also resist the full axial tension acting to separate the payload from the spacecraft. Ideally the shoes would cover the entire circumference of the rings, but the release device is normally in-line with the band and requires a small area with no shoe. The shoes at each end of the band carry higher radial load due to the moment arm created by the offset between the release device and the band lines of force. This offset should be minimized but is difficult to eliminate. Excessive offset, and poor support of the ends of the band can lead to band end deflections and bending moments dumped into the release device. This could lead to premature release, or failure to properly release the band. Since the end-shoes carry higher loads, they should be made of a higher strength material such as titanium, compared to the remaining shoes which we make from aluminum 7075 (for similar thermal expansion with rings and band). Relatively short, angled faces minimize engagement of the shoes on the ring lips. This reduces stresses in the shoes, and improves release performance.

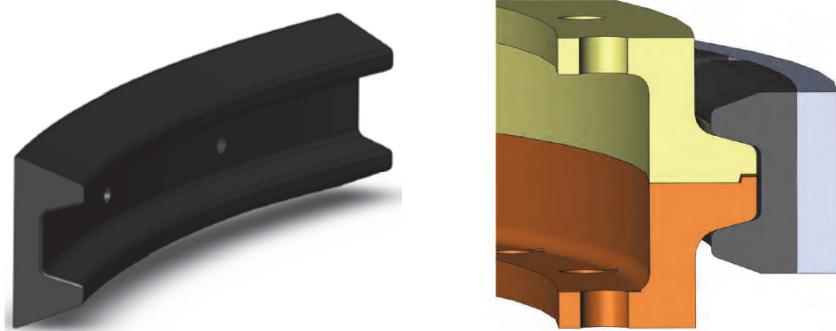


Figure 5: Shoe example (left) and Shoe fit on mated rings (right)

Proper mating between the shoe and the angled ramp of the rings is critical. The half-angle on the shoes matches that on the rings: (15 degrees typical & recommended). The shoes must have freedom to self-align at this interface, so all of the shoes' mounting points have degrees of freedom. Shoulder bolts in that back of each shoe, riding in slots in the band, allow the shoes to move along band during tensioning,

helping the band to load evenly as tension is applied. It also helps prevent potential bending overload of the shoulder bolts. Since the shoes move relative to the band and ring during loading it is important that the shoe position is monitored or actively controlled (with spacers, for example) as band load is incrementally increased.

We use a dry-film lubricant (DFL) on all shoe surfaces. This mitigates any potential for cold-welding and ensures a low and relatively controlled friction value between the shoe, ring lips, and band. In addition, a thin layer (0.003 in / 8 µm) of Teflon tape may be used on the back of each shoe to further reduce static friction with the band. Some technical literature warns against the use of Teflon between shoes and band, for the possibility of decay of preload due to cold-flow of the Teflon¹⁴. We have not experienced preload loss using this thin Teflon layer, and any small change in film thickness would have a negligible impact on band tension. The Teflon tape does require inspection after each load and release cycle, and can easily be refurbished when necessary.

The number of shoes is not critical as long as there are enough to keep the shoe length down. The longer each shoe, the greater the radial distance the shoe must move to clear the ring lips. Shorter shoes also reduce potential binding between the shoes and ring lips from small rolling deflections in the rings under load. Early in our clamp-band work we selected 12 shoes based on other similar systems, and have used this number successfully in our 17-inch (43-cm) and 24 (61-cm) systems.

Band Release and Band-catching Features

Clamp band systems normally have features which receive the band after release and “park” it where it cannot interfere with the separating rings. “Recontact” or “rebound” of the band into the rings can interfere with successful separation. Some systems actively retract the band with tethers and/or springs to move the band into catchers. Catchers normally consist of a radial stop for the band at some safe diameter away from the ring lips. Some systems have used energy absorbing features in the catchers such as a crushable element to reduce system shock.

The release behavior of a highly loaded, flexible, thin strap of steel could be hard to predict or control. Since the strain energy in our systems is mostly dissipated by the CBOD, shock absorption is not required at the back of our catchers to prevent rebound, simplifying their design. The stored elastic energy of the deflected band causes the band to spring free from the ring lips, so no tethers or retraction systems are required. An angled piece of Elgiloy spring at the top of the catcher deflects the band away from the deployed ring and into a rest position within the catcher (see Figure 2).

We use high-speed video extensively to study the band release dynamic in a new design. By observing band behavior with high-speed video, we can make changes or adjustments to ensure the band expands symmetrically from the rings, and cleanly separates. Catcher locations can be tuned to ensure the band is received in the correct places to limit band motion and potential rebound. During a flight build, virtually every band release from confidence testing through acceptance is filmed and reviewed for proper release dynamic and any anomalies which might otherwise go unseen.

Separation Dynamics

Kickoff springs between rings are used in clampband systems to provide the proper separation velocity for the payload. Normal separation velocities are in the 30.5 cm/sec (1 ft/sec) range and there is typically some maximum allowable tipoff rate specified. Electrical Connectors that cross the separation plane, and separation switches, require energy to separate and can impart forces to the rings during deployment. To minimize tipoff, the net forces driving ring separation must be balanced around the circumference. Placing matched pairs of switches and connectors 180° is normal practice in clampband design. Kickoff spring forces are balanced by including features for tuning spring force within the kickoff module. This could be accomplished by testing and matching opposed sets of springs, but adjustability can be included with little added effort, expense, and weight.

High-speed video is used to observe the separation dynamic and measure velocity and tipoff rate. High-speed video during development is key to understanding and tuning release dynamics of system. This

includes the design and location of catchers and springs, and removing features which interfere with band motion away from rings and into catchers. The challenge in the setup is creating a mass simulator and off-loader that is representative of the flight release condition. The Nanosat clampband system was successfully tested in a zero-g flight to verify proper separation dynamics (which is not as expensive as one would think).

Installation and Preloading

The ground installation procedure is critical to set the band properly for flight. Specific tooling and processes for installation and preloading are an important part of the design effort and should be considered earlier rather than later as this can drive aspects of the design. A controlled, safe, and repeatable process is necessary and must be used in qualification and acceptance testing, as well as during integration. Development of ground support tooling and reset and preload procedures are critical to mission success. If possible, it helps to understand how the payload is to be integrated. How will kickoff springs be compressed and rings mated? How is the access to fasteners, and to the release device? Is there sufficient room to use any support tooling for the tensioning process?

Safety concerns must also be addressed. Traditional safety measures were taken to avoid an unintended pyrotechnic release. Regardless of the type of release element used, redundancy is required during loading of the band. In most systems we have seen, the tensioning tool serves as a backup to prevent catastrophic release due to a failure during load application. Shearing shoe fasteners during preloading is a potential failure mode. Shoes must be properly spaced before loading, and monitored as band load is increased, to accommodate band stretch. A shoe spacing tool can be used to ensure shoes and fasteners are positioned for maximum travel and even loading of the rings. Position of the release device is similarly adjusted and controlled as load is increased.

Ensuring the band loads evenly is critical for safety. Tapping around the band with a small mallet is the traditional recommended method, but is definitely not desirable as a practice. During development testing a reliable process for ensuring uniform band stress during loading must be developed by instrumenting the band with strain gauges in several locations (~5). We've found in our systems that with controlled friction between the band and the shoes, tapping is not required for uniform band loading.

Accurate application of band preload is difficult in systems which do not include direct, calibrated load sensing devices. In many cases this has led to over-design of Marman band systems to cover variations in preload application of up to $\pm 25\%$. The CBOD uses an instrumented bolt to accurately set a known preload to the tensioning band, which can be verified prior to launch. The instrumented bolt eliminates inaccuracy of torque measurements or sensitivity to friction at fastener interfaces to indicate proper preload. It also eliminates need for strain gauges on band, and affords better accuracy via factory calibration (strain gauging band during development testing is still required to ensure band loads evenly). In the case of the sub-24-inch (61-cm) system, specific hydraulic tooling was developed for ground support. Features were incorporated into the band ends to mate with the hydraulic loading tool (see Figure 6).

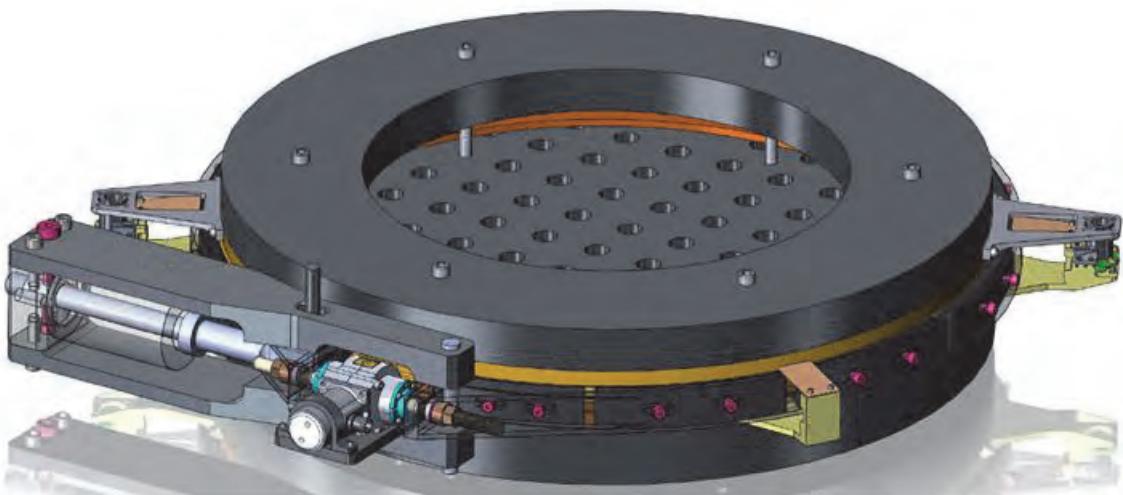


Figure 6: Hydraulic Loading Tool in-place, rings mated to fixture plates

Preliminary Sizing, Analysis, and Test

Marman systems are prone to stack-up of design margins resulting in over-designed (and overweight) systems. Analysis uncertainty, probabilistic load cases, margin-on-margin can drive design loads excessively high. Choose realistic load cases with reasonable margins to size band, shoes and rings as these have a big impact on system weight. A reasonable choice is to design and test to 1.25x worst case load predictions. Maintaining high margins on the release element (>2.00) has been recommended, and allows for any increase in loads, with a relatively low impact on system weight¹⁵.

With design loads defined, a band tension can be determined such that complete axial gapping of the clamped joint will not occur at the maximum load case (an exception is small localized gapping due to elastic deformations). Initial band load is determined using a standard set of equations used for Marman systems, derived from a force balance about the clamped section¹⁶:

$$\text{Axial Line Load: } W_{\text{axial}} = F_{\text{axial}} / \pi D$$

$$\text{Moment Line Load: } W_{\text{moment}} = 4M / \pi D^2$$

$$\text{Total Line load: } W_{\text{total}} = W_{\text{axial}} + W_{\text{moment}}$$

$D = \text{ring diameter}$ $\beta = \text{ring ramp half-angle}$ $\mu = \text{coefficient of friction}$

$$\text{Band Preload estimate: } P_{\text{band}} = W_{\text{total}} D (\tan\beta - \mu) / (1 + \mu \tan\beta) \sim W_{\text{total}} D \tan\beta \text{ (neglecting friction)}$$

A margin on gapping of 1.25 is normally applied to this result. The above loads allow for initial sizing and modeling of band, shoes rings, and other components. Finite Element Modeling is then used to analyze for stiffness and model system gapping behavior under load.

Not surprisingly, all agree on the need for extensive development testing to validate any separation system design. Testing is performed to confirm analysis results for system stiffness and gapping loads, and to validate or refine the flight band tension callout. Tests verify uniform loading of the band and proper stowing using the stow and load procedure steps. High-speed video is used to verify proper release performance of the band and system. These development tests are all performed prior to a comprehensive qualification test program.

Examples of Early Low-Shock Separation System Designs

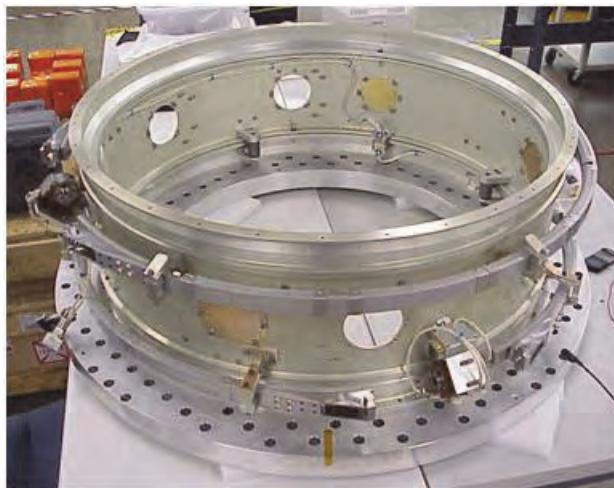


Figure 8: Orbital Express Separation System using 2 RUAG Bands and SNC mini-CBOD

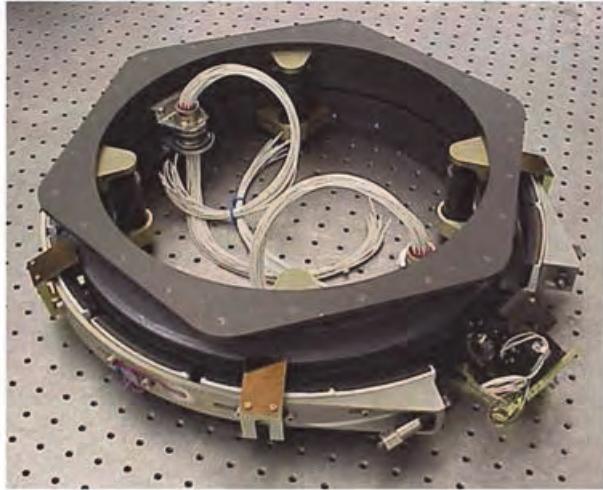


Figure 7: SNC NANOSAT 43-cm (17-inch) Separation System with Mini-CBOD

Orbital Express Separation System

- Utilized a 37" (94-cm) Soft Separation System High Performance Clamp Band by RUAG with Clamp Band Opening Device (CBOD) by SNC
- Primary structure between NEXTSat and ASTRO during launch and initial on orbit activities
- Separated NEXTSat and ASTRO on flight and release intermediate structure so that subsequent mates and demates using the OE docking system can occur
- One Flight unit delivered
- Line Load: 32 kN/m (184 lbf/in)
- Band Preload: 14.7 kN (3300 lbf)
- Band Yield Stress Margin*: 1.54
- Launched in 2007

* with SFy = 1.1, SFu = 1.4

Nanosat Separation System

- Developed for AFRL, collaborative effort with RUAG
- Four flight units delivered
- 17" (43-cm) interface diameter
- Clamp Band Opening Device (14-kN / 3250-lbf preload Mini-CBOD) imparts extremely low shock to Spacecraft and payloads
- Protolight test program included Band Proof load test, Thermal cycling, Random Vibration, Static structural testing, and Kick-off/Tip-off verification. Shock response characterized.
- Line Load: 42 kN/m (240 lbf/in)
- Band Preload: 14.7 kN (3300 lbf)
- Band Yield Stress Margin*: 0.42
- Launched in 2004, Delta IV Heavy Lift

Development of Sub-24" (61 cm) Separation System

For ESPA and ESPA-Grande applications, the secondary payload is cantilevered relative to the launch axis and space is at a premium along this line (see Figure 9). The required stack height (payload interface to ESPA ring interface) was 2.0" (5 cm), or roughly half that of the NANOSAT system. Stiffness and load requirements were increased compared to our heritage systems. Load requirements for ESPA are based on a 660-pound (300-kg) payload, with c.g. located 20 inches (51 cm) axially from the interface with the Separation System with inertial loads of 8.5G applied in two directions simultaneously¹⁷. This presented a challenging set of requirements for the sub-24" system (interface bolt circle diameter is just under 24.00" (60.96 cm)). With a desire to retain as many aspects of successful previous designs as possible, the design was revised to meet or exceed the specified requirements for ESPA Grande. The first step to a qualified design was to complete the design and analysis predictions, and fabricate an engineering model for testing.

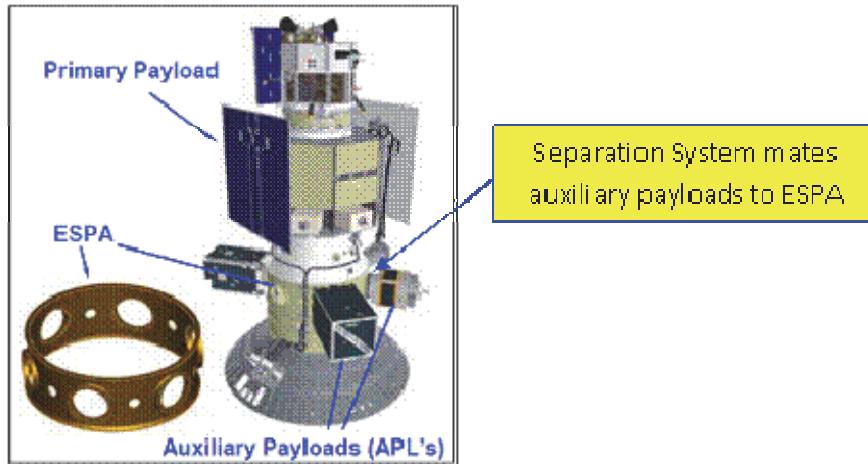


Figure 9: ESPA Separation System

To fit the required envelope, and to maximize stiffness, a major revision was made to the heritage ring profile (see Figure 10). The stack height of the system was reduced to within the required 2.0" (5 cm). Mounting flange of both rings were moved inboard of the tensioning band to improve load path and increase stiffness. This makes mounting fasteners less accessible, but is easily addressed by either accessing fasteners through holes in the ESPA ring, or installing rings prior to mating the payload to the adaptor ring. Preliminary stiffness analysis showed that the scaled, reduced height ring profile did not meet our stiffness goals, so the section was again revised. We thickened sections and shortened toes on each ring to improve stiffness and load path. These revisions resulted in roughly 3-fold improvement in stiffness, as seen in Figure 11.

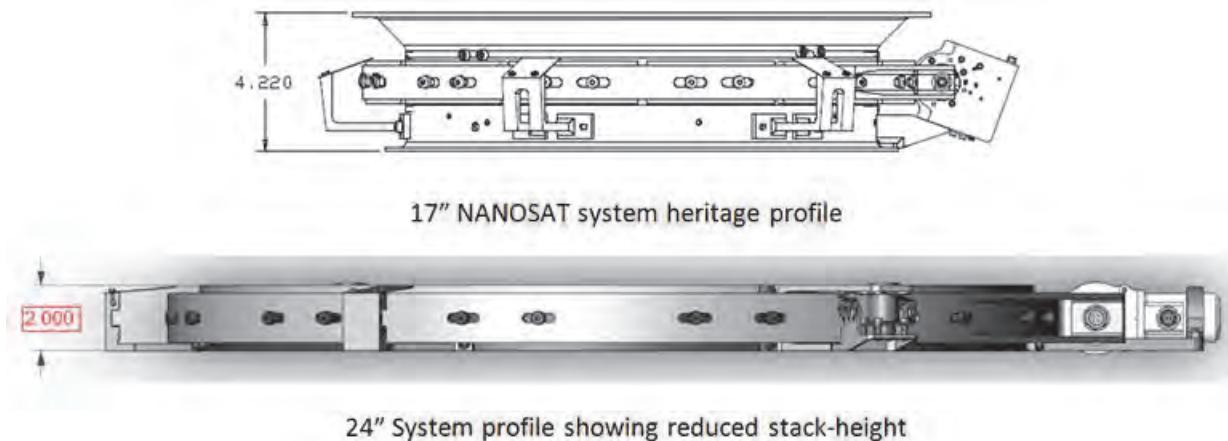


Figure 10: Profile Revision: Heritage design to sub-24" system

Catchers, switch mounts, and kickoff spring modules were also reduced in height. Fitting of kickoff spring modules into the smaller envelope was a challenge. The 660-lb (300-kg) payload mass requirement and 1 ft/sec (30 cm/sec) separation velocity (V_{sep}) goal required a larger amount of spring energy in a smaller volume than our prior designs. Our goal was to keep the kickoff spring module confined to the radial space between the rings, as a baseline. For our engineering system, we designed around a commercially available spring, and added 2 kickoff modules (total of 6) versus the heritage 4. Payloads up to $\frac{2}{3}$ the maximum load will achieve the V_{sep} target. Additional kickoff energy for future programs would be added by increasing the number of modules, utilizing volume inside the ESPA ring, or both.

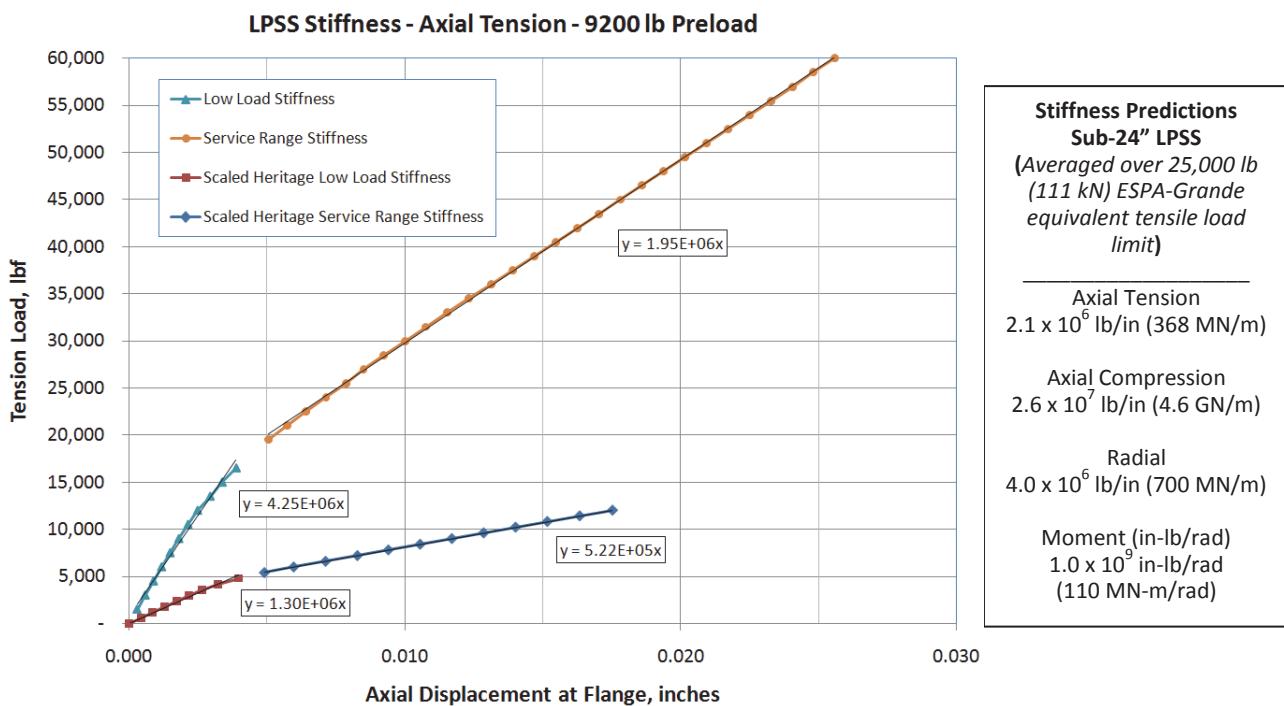


Figure 11: Results of ring profile revision on sub-24" predicted system stiffness

To maximize the load capability of the system (beyond the ESPA Grande requirements), the high-load CBOD (13,500 lb / 60 kN) was incorporated. Band thickness was increased to handle the larger CBOD loads, and it was found that the band stress associated with deforming the band from its free-state to the installed diameter was higher than expected, severely limiting the gains of a thicker band. The thickness of the aluminum was adjusted to maintain similar installed force with previous designs. To improve margin on gapping load, the ring half-angle was reduced to 15° from the 20° baseline.

The final band design (Aluminum 7075-T7351) uses a nominal 9200-lb (41-kN) band preload (10,000-lb (44-kN) proof load), with a yield stress margin of 0.05 and an ultimate stress margin of 0.22 (with SFy = 1.1 and SFu = 1.4, and a preload uncertainty factor of 1.1). The predicted stiffness and load capability for this size system is excellent even though only 75% of the CBOD load capability is used. The 9200-lb (41-kN) nominal band load in the sub-24 LPSS allows the CBOD to show >100% margin.

Analysis predicted local gapping of .0015" - .0035" (38 µm – 89 µm) at joint heel at the nominal 9,200-lb (41-kN) band tension, depending on the stiffness (or constraint) of the interfacing structure on each ring. Our FEM showed that this gap was an artifact of the hoop compression stresses of higher band tension on our ring geometry, with negligible effect on system stiffness. The load and location at which "true" gapping occurs were also predicted by FEM (see Figure 12). At an axial load of 67,500 lbf (300 kN) (about 2.7 times ESPA Grande equivalent axial loads, not shown on chart), a gap forms at the heel, such that only a small contact point at the toe remains, changing the system stiffness to ~ 1.27E+06 lbf/in (222 MN/m).

Summary / Conclusion

Using an understanding of the design features of a robust clampband system, we were able to scale a heritage design, reduce profile, and increase stiffness and load capability. Design and analysis of the sub-24 Low-Profile Separation System are complete, and engineering hardware has been assembled (see Figure 12). At the time of this writing, the sub-24" system is poised for development testing in early 2012 to confirm the analysis results and determine the true load capability.

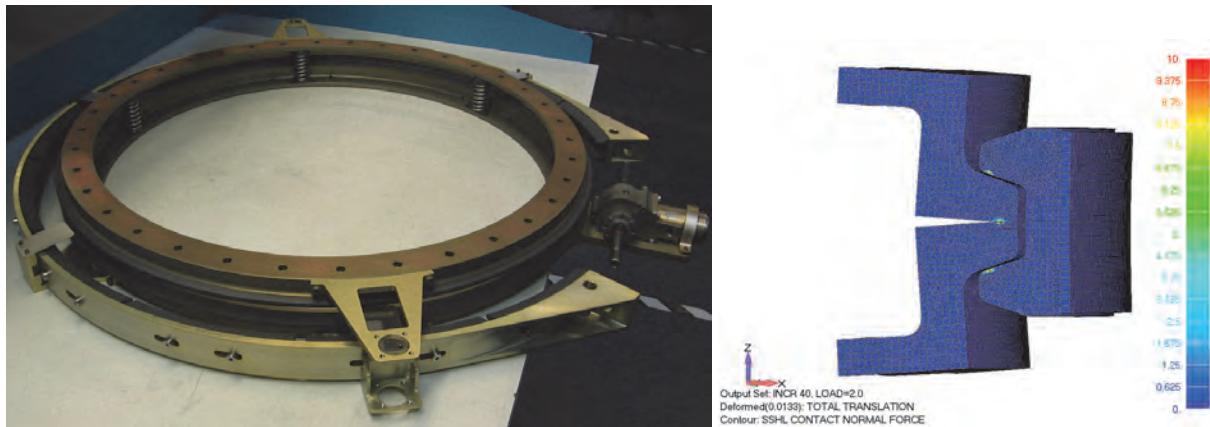


Figure 12: Engineering Development Unit of sub-24" (LPSS) and FEM

References

1. Wikipedia.org, "Marman Clamp" search word.
2. Morse, B & Wittmann, A "Shear Load Carrying V-Clamp for Spacecraft Application", 1992.
3. NASA, GD-ED-2214, "Marman Clamp System Design Guidelines", pp 4.
4. GOES-IJK Separation System Study, Astrotech Space Operations Inc, February 1987.
5. GOES-IJK Separation System Study, Astrotech Space Operations Inc, February 1987.
6. Marman Clamp Design, J.O. Mayor, SAI, April 1991.
7. GOES-IJK Separation System Study, Astrotech Space Operations Inc, February 1987.
8. GOES-IJK Separation System Study, Astrotech Space Operations Inc, February 1987.
9. Marman Clamp Design, J.O. Mayor, SAI, April 1991.
10. NASA, GD-ED-2214, "Marman Clamp System Design Guidelines", pp 5.
11. GOES-IJK Separation System Study, Astrotech Space Operations Inc, February 1987.
12. GOES-IJK Separation System Study, Astrotech Space Operations Inc, February 1987, pp D-2.
13. Pegasus-SELVS, Clamp Band Design Philosophy, Brian Morse, OSC, December 1992.
14. GOES-IJK Separation System Study, Astrotech Space Operations Inc, February 1987.
15. Purdy, W & Hurley, M "The Clementine Mechanisms" Presented at the 29th Aerospace Mechanisms Symposium, May 1995.
16. Stadnick, S. "Analysis Techniques for V-Band Coupling Designs", Hughes Aircraft Company, April 1975.
17. Lessick, D & Marrujo, T "ESPA Rideshare Users Guide", Department of Defense Space Test Program, May 2010.

Ares I Linear Mate Umbilical Plate and Collet

William C. Manley*, Gabor J. Tamasy* and Patrick Maloney*

Abstract

This paper will present umbilical carrier plate design and testing performed at KSC for the ARES 1 Upper Stage. The focus will be on the innovative linear mate ground carrier plate and electric solenoid actuated collet mechanisms. The linear mate ground umbilical plate is a unique, two-piece, design where an outer plate is first aligned and locked to the vehicle, and then an inner plate translates to engage the commodity connectors. The collet uses a spring-loaded over-center mechanism and redundant electric solenoids to release a traditional collet locking device. A high level discussion of the umbilical arm will also be presented as a corollary to the umbilical plate designs.

Introduction

Umbilicals discussed in this paper were designed to support the Constellation Program Ares I launch vehicle shown in Figure 1. The Constellation program was initiated in 2006 to build a human rated launch vehicle to replace the aging Space Shuttles. The Kennedy Space Center (KSC) Launch Pad was redesigned for the Ares I rocket to use the clean pad concept. The launch tower is now located on the Mobile Launcher (ML) platform, as shown in Figure 1. The launch tower was designed to house the T-0 umbilical arms, T-0 sway damper and stabilizer, and the crew access arm, along with all the ancillary support equipment.

* NASA Kennedy Space Center, FL



Figure 1. Ares I Vehicle on Mobile Launcher

The umbilical arms utilize a tilt up counterweighted configuration and rotate up as the vehicle rises from the ML. The tilt-up umbilical arm (TUUA) design is shown in Figure 2. This is relevant because the motion of the arm for connecting and disconnecting from the vehicle is a major driver in the design of the ground umbilical carrier GUCP (umbilical plate) and the linear mate mechanism. The GUCPs are located at the end of the TUUA umbilical arms. A typical GUCP (Ares I Instrument Unit) is shown in Figure 3. The GUCP houses the QDs for transferring fluids, ECS (environmental control system), and electrical power/data between the ground and the vehicle. In this innovative design, the two primary functions of the GUCP are separated. The first function of attaching to the vehicle is done by the Outer Plate (OP) and the second function of transferring commodities between the ground and vehicle is done by the linear mate Inner Plate (IP). The other innovative mechanism introduced in this design is the fail safe T-0 solenoid actuated collet which structurally connects the GUCP to the vehicle during ground operations. These umbilicals have the potential to improve the performance and reduce the cost of the next NASA rocket to launch from Cape Canaveral.

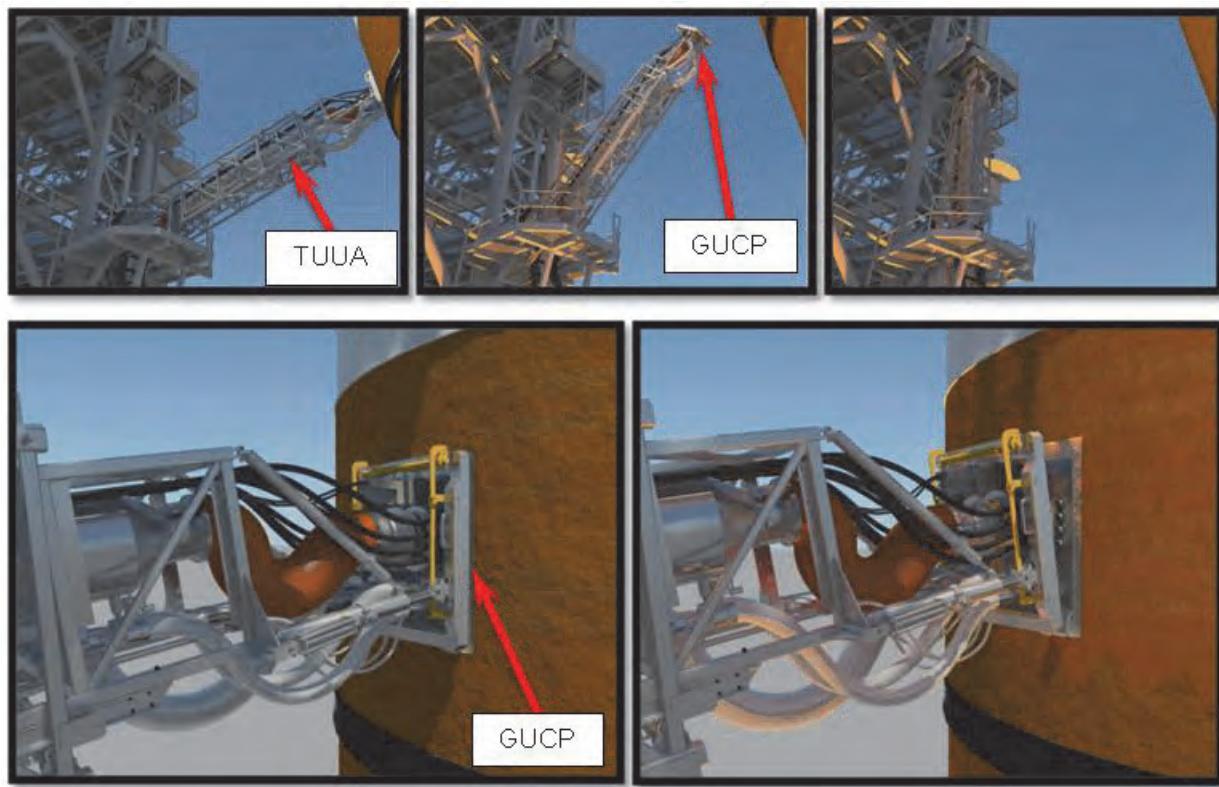


Figure 2. TUUA Model Disconnecting and Tilting Up

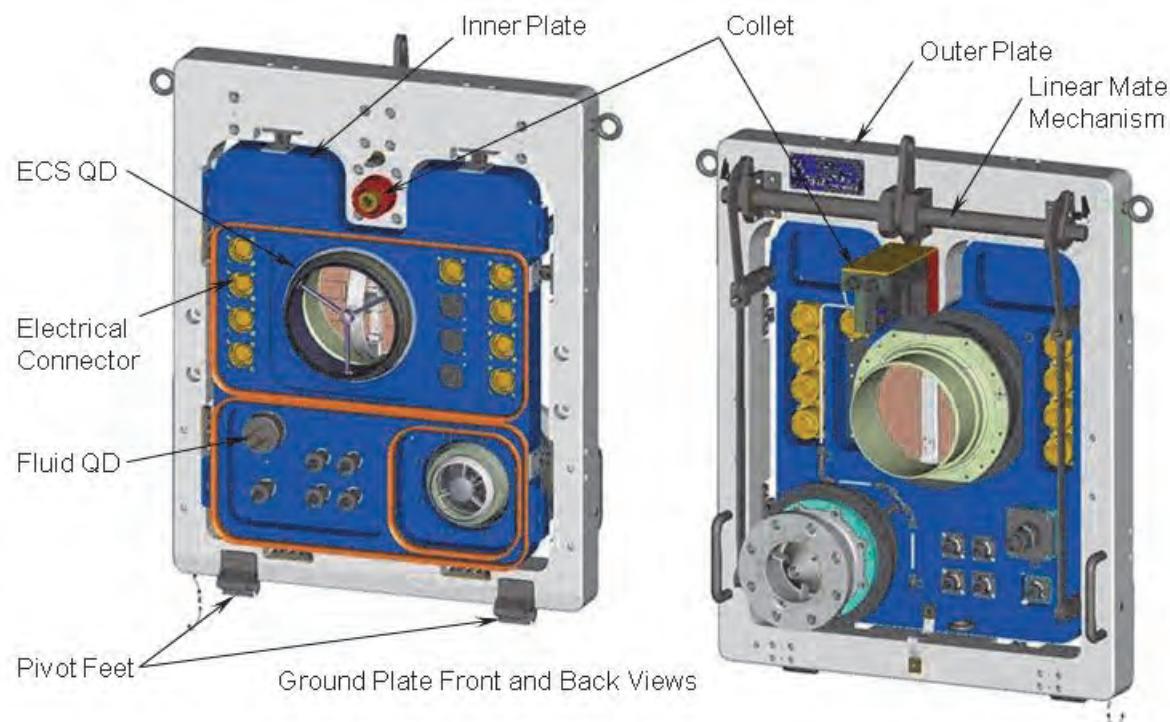


Figure 3. Ares I GUCP (Instrument Unit)

GUCP Function and Mechanisms

The umbilical has two primary functions. One is to transfer fluid commodities and electrical power/data between the rocket and ground. The second is to provide a safe T-0 disconnect to remove the commodities connections at the time of launch.

Connecting the Umbilical

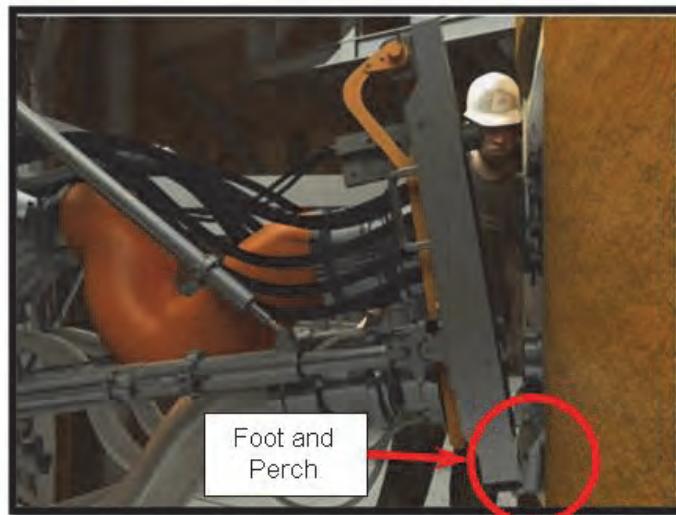
In this design the outer plate (OP) provides the connect/disconnect function from the vehicle and the structural interface designed for ease of connection and safe disconnection at T-0.

Connection of the GUCP to the vehicle is done in the VAB (vehicle assembly building). To make the connection operation ergonomically friendly, it is preferred to have the GUCP in a tilted back (foot-forward) orientation shown in Figure 4. The GUCP starts in a 10° tilt back position and is extended by actuators on the TUUA toward the vehicle with the pivot feet at the bottom being the leading portion. In this process the technician guides the GUCP forward and visually verifies that the pivot feet are aligned to the vehicle perch (foot bracket). After the pivot feet are engaged, they form a hinge, which allows the GUCP to pivot up to the vertical (0°) position as it is being pushed forward. At this point the collet located at the top of the OP is engaged to lock the GUCP to the vehicle's flight umbilical plate. The linear mate mechanism makes this process much easier by allowing the QDs to be retracted and not in contact with the vehicle while the GUCP is being connected. After the outer plate is connected to the vehicle, the linear mate mechanism is used to extend the inner plate (IP) and plug-in all of the ground connections in one motion. The components of the linear mate mechanism are shown in Figure 5.

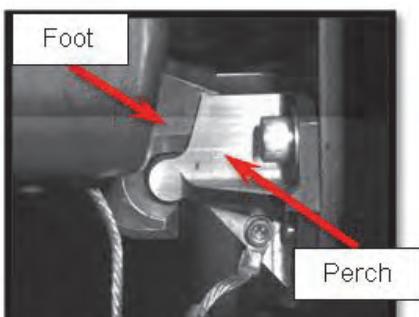
Step 1 – Extend GUCP to Engage Pivot Feet



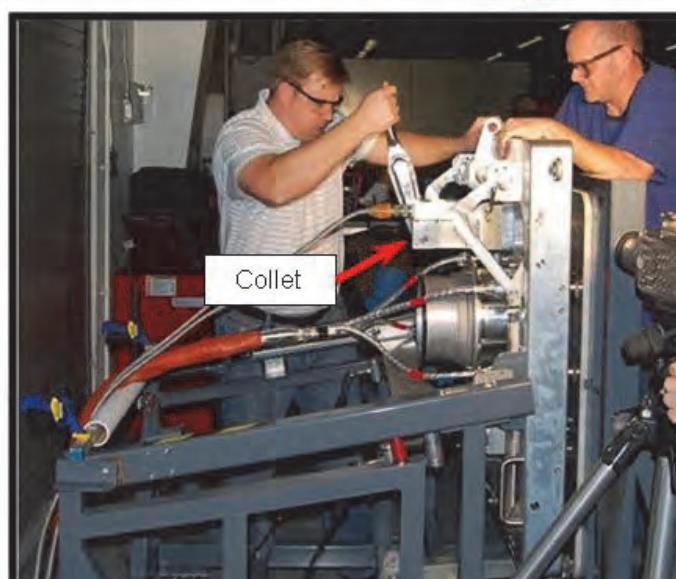
Pivot Feet Prior to Connection



Step 2 – Rotate Plate to Vertical and Engage Collet
Outer Plate is now aligned and locked to vehicle (Picture from testing)



Pivot Feet Connected
(Picture from high speed testing video)



Step 3 – Linear Mate Mechanism
Translates Inner Plate to Engage Commodity Connectors

Inner plate translates to engage commodity connectors as actuation nut is manually rotated. Mechanism is locked with two ball lock pins and remains locked through launch.

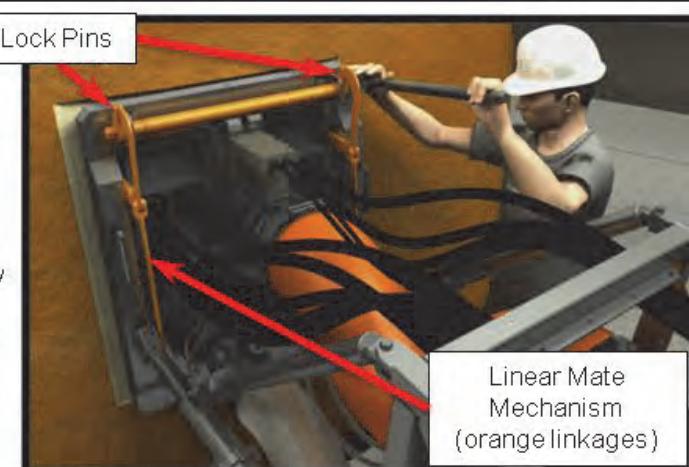


Figure 4. Umbilical Connection Sequence

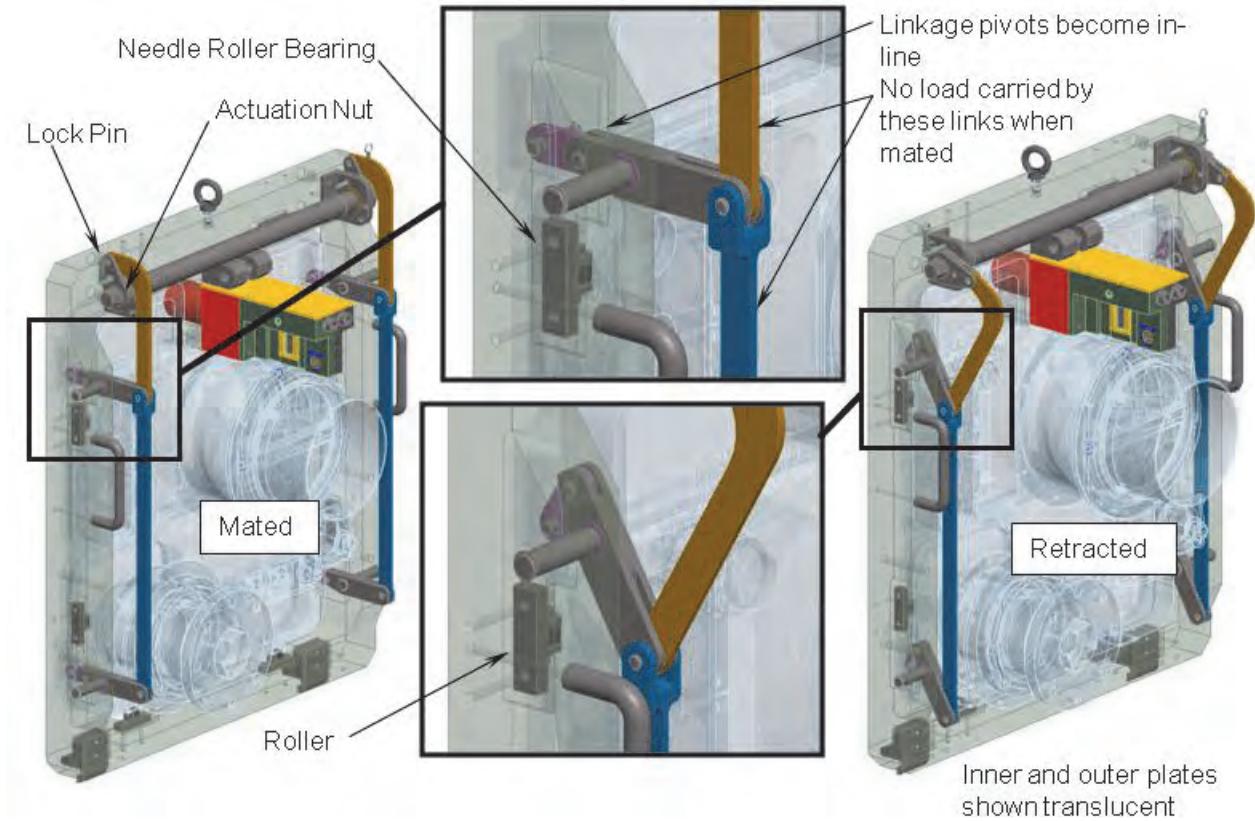


Figure 5. Linear Mate Mechanism Details

The linear mate mechanism consists of a series of parallel linkages that move the inner plate approximately 38 mm (1.5 inches). The inner plate is supported on eight needle roller bearings shimmed for a precise alignment and smooth in/out translation. The linkages are moved by turning the actuation nut with a standard 1-1/8 inch wrench as shown in Figure 6. In the mated position the load bearing linkages are in a straight (singularity) position which transfers all of the reaction loads into shear on the pins and has zero forces in the latching (gold) and horizontal (blue) linkages in Figure 5.

The 6061-T6 Aluminum 6061 plate carries up to 44,500 N (10,000 pounds) of separation load when all lines are pressurized. The deflection and stresses in the plate and mechanism were analyzed with FEA (finite element analysis) to ensure they were within acceptable safety margins. Deflections of the inner plate were limited to 1/8 inch and all the components have a minimum stress safety factor of 2:1 for yield.

Complexity added by the linear mate mechanism is more than overcome by the problems that it solves. The two-step mate operation provides high confidence for technicians by aligning the umbilical prior to mating the critical connections. Linear engagement allows mating of fluid and electrical connectors in the same operation. Previous angular mate umbilicals made electrical connections in a separate operation after the initial mate.

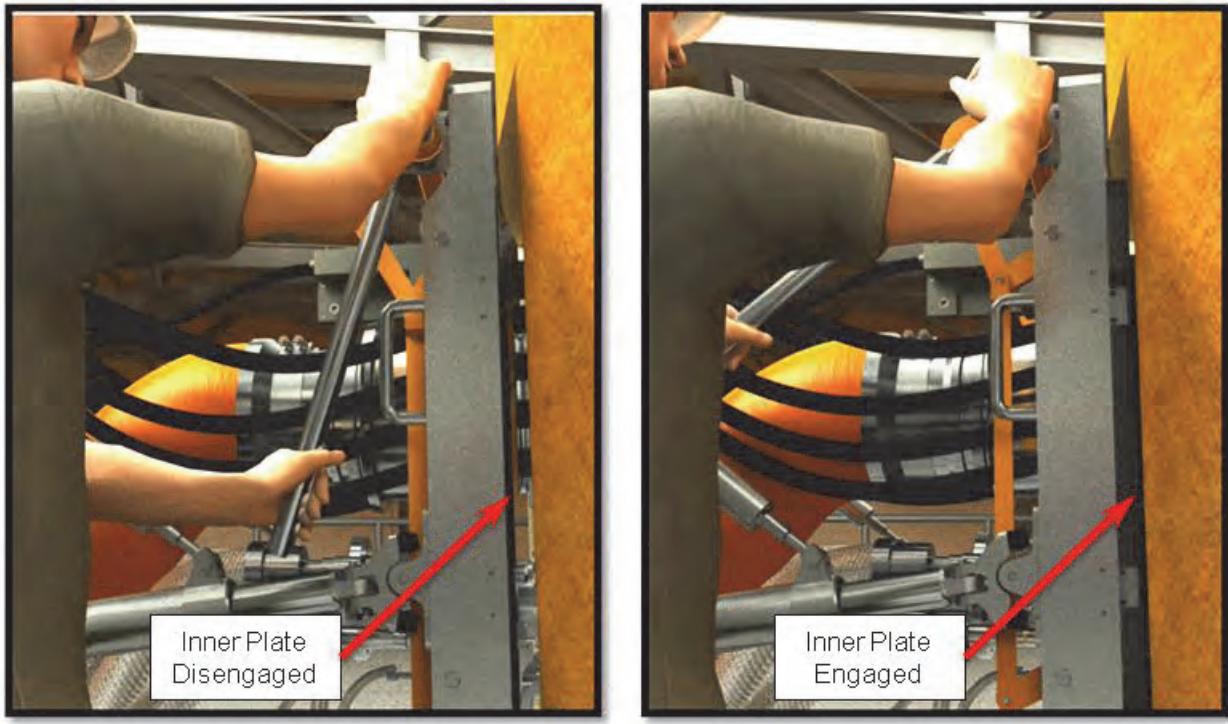


Figure 6. Linear Mate Mechanism Engagement – Inner plate translates to engage commodity connectors as actuation nut is manually rotated. Mechanism is locked with two ball lock pins and remains locked through launch.

Disconnecting the umbilical

The TUUA arm is passively (counter weight) biased to tilt up and pull away as the GUCP releases. At T-0 the command is given to release the collet. First the GUCP pivots away from the rocket approximately 10° about the hinge line of the pivot feet. Once the GUCP has pivoted, the toe of the pivot foot is no longer engaged with the vehicle receptacle. At this point the TUUA pulls the GUCP away from the vehicle and begins to tilt-up to the retracted position. The rise of the TUUA/GUCP is tuned to match the speed of the vehicle. It takes approximately 4 seconds to disconnect and stow the GUCP.

Ideally there is no net force applied to the vehicle during disconnect (some small forces may be present due to vehicle drift and other misalignments). The linear mate mechanism is in the forward (plugged-in) locked position during disconnect, resulting in an angular separation of the QDs. Compliance in the QDs allows for an angular disconnect. This was verified through extensive testing with the prototype GUCP to make sure no QD damage occurred during angular disconnect.

Fail safes are built into the design. In case of a collet release failure, a frangible pin is sheared by the vehicle motion which releases the GUCP. Force for the secondary release is transferred to the GUCP from the TUUA by a wire rope. A high momentary load is transferred to the vehicle during the secondary release.

After release, the GUCP is retracted into a safe house where it is protected from the rocket exhaust blast forces and contamination. Figure 2 shows the retract sequence. A cover plate is extended over the QDs, which are facing up after retraction, to environmentally seal and protect them from the rocket exhaust. After launch the ML is returned to the VAB where the GUCP is inspected and refurbished for the next launch.

Solenoid Actuated Collet

A locking device with a highly reliable release method was required for the GUCP. Designs such as collets, ball lock devices, pneumatic actuation, and non-explosive actuators (NEA) were evaluated. Ball locks, used on many heritage designs, are load limited when compared to collets. Pneumatic actuation is simple, but requires an expensive redundant pneumatic control system. NEA, also called a burn wire device, uses an electrical signal to melt a wire that retains the locking device. Replacement operation time and unit cost were very high for the NEA. The collet locking device was chosen due to success on Space Shuttle and X-33 designs. A solenoid actuated collet release mechanism was developed for the Constellation program for use in T-0 separation of the flight and ground umbilical plates, as well as T-0 release of drop weights in the Vehicle Stabilization and Damping System. It uses a simple, yet effective method for locking and releasing the collet, thus making it very easy to use and extremely reliable. Early testing of the mechanism has proven both of these to be true.

The collet is loosely based on a heritage Space Shuttle and X-33 program designs. Similar to collets used as tool holders in machining equipment, this collet consists of a round bar with a tapered surface that is split into multiple ‘fingers’ to allow radial displacement. These particular collets are made from a beryllium-copper alloy to take advantage of its non-sparking property when struck, thus preventing the ignition of residual hydrogen at the umbilical interface. The inner diameter of the collet is smaller than the outside diameter of a coaxial pin. When the pin is driven forward, through the small diameter of the collet, it expands the collet fingers, as shown in Figure 7. When the collet is inserted into a matching receptacle, and the pin is driven into the fingers, it locks the two pieces together.

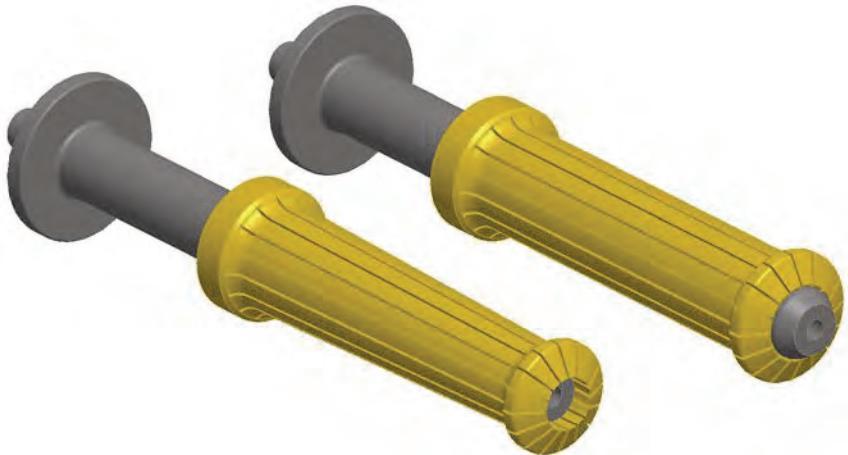


Figure 7. Collet Expanded and Collapsed (nominal) – Machined part with flexible fingers expands to engage flight receptacle when pin is inserted.

The innovation for this particular collet, shown in Figure 8, is the use of an over-center mechanism to drive the pin forward, lock it into place, and then release the pin. A cam is rotated to drive the over-center linkage from an unlocked to a locked position, storing energy in a spring connected to the coaxial pin during the motion. The spring rate was chosen based on data collected from the X-33 program collet testing, which showed the pin needs approximately 1112 N (250 pounds-force) to pull the pin. A 175 N/mm (1000 lbf/in) spring was chosen to provide 3336 N (750 lbf) to pull the pin, which is three times the expected load. Once the linkage is pushed past center, the energy in the spring attempts to force the linkage to continue in the same direction, but the motion is restrained by a fixed hard stop. Figure 9 show the linkage in the locked and unlocked positions. Since the spring is still exerting force on the linkage, it effectively locks it into place. This locks the coaxial pin inside the collet and prevents the collet fingers from collapsing. In this particular mechanism, the over center mechanism is only past center by about 1.27 mm (.050 inch) and needs about 100 pounds-force to push the linkage past center.

An electric solenoid is perfect for this application since they can exert a lot of force but only over a small distance. In this case, a pair of commercial-off-the-shelf (COTS) solenoids were wired into independent circuits for redundancy. Each solenoid sits adjacent to one of the linkages in the mechanism. When 60 VDC is applied to the solenoids, each one applies over twice the expected force to drive the linkage past center. The stored energy in the spring then pulls the coaxial pin out of the collet fingers. An elastomer bumper is installed to absorb some of the impact from the pin.

A prototype of this collet mechanism was fabricated by the in-house machine shop at KSC and has undergone some preliminary testing. When both solenoids are energized simultaneously, the collet mechanism is released from the receptacle in about 8 ms. If only one solenoid is energized, to simulate a failure of a solenoid, the collet releases in about 12 ms. During the Ground Umbilical Carrier Plate testing mentioned later in this document, the collet underwent over 150 mate/de-mate cycles without any degradation in performance. With only a few launches per year for the Constellation program, this simulated over 20 years of use. Only some minor wear due to abrasion was noted at the pin and collet interface.

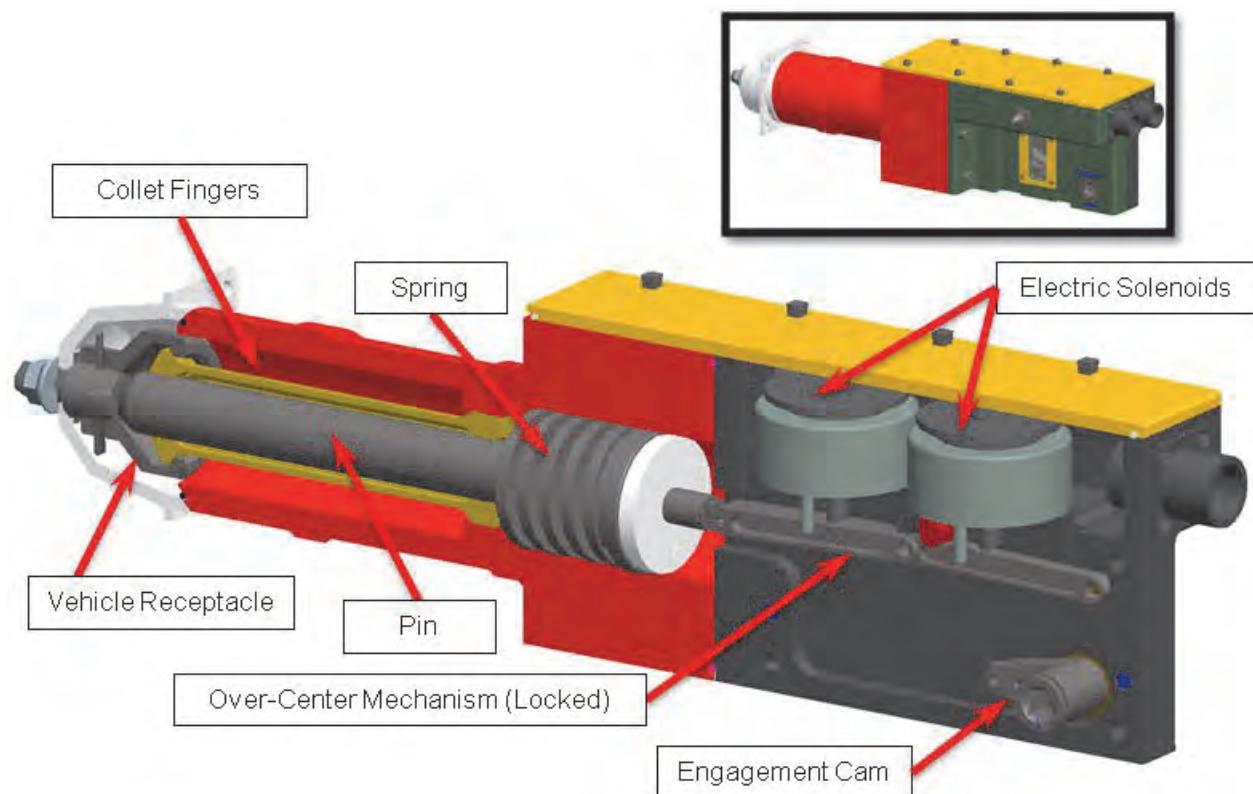


Figure 8. Solenoid Actuated Collet – Locked to vehicle receptacle

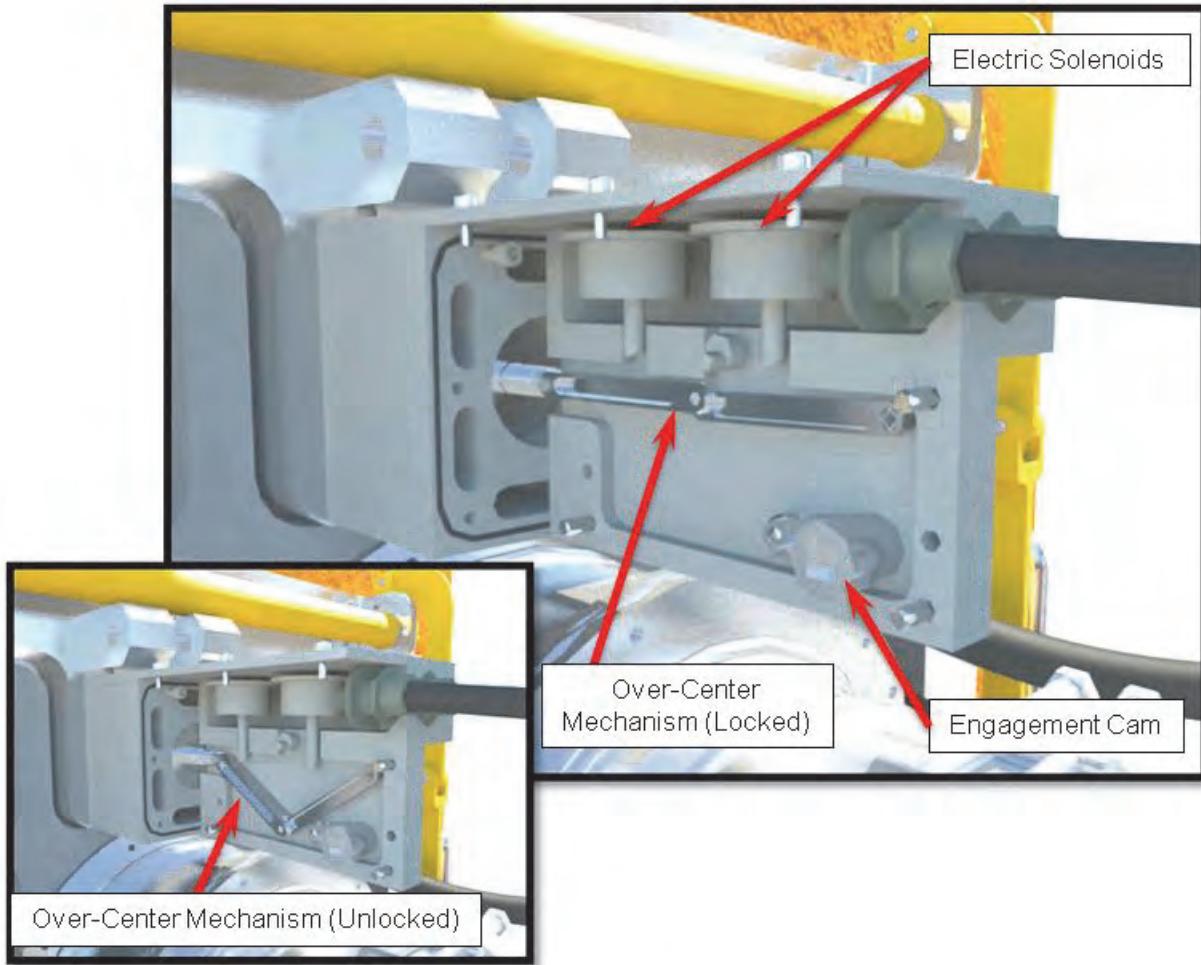


Figure 9. Solenoid Actuated Collet - Locked and Unlocked Positions

Even though it is Ground Support Equipment (GSE), the collet uses NASA-STD-5017, "NASA Technical Standard: Design and Development Requirements for Mechanisms" for design of flight mechanisms as guidance. All rotating joints feature redundant rotating surfaces and sliding joints are coated in friction-reducing material. The stored energy in the spring is more than twice what is expected to release the pin and each solenoid exerts twice the expected force on the over-center mechanism. These design details result in an extremely reliable mechanism for releasing loads of up to 44,500 N (10,000 lb). The solenoid actuated collet has other applications, such as a replacement for high cost pyrotechnic release devices.

Testing and Lessons Learned

Development of the linear mate GUCP was conducted through a series of design and test prototypes which incrementally demonstrated the efficacy of this design. Lessons learned from previous programs were used throughout the design to improve the operation and safety of the umbilicals.

One of the first items tested was the counterweighted tilt up arm design. A full scale prototype TUUA was built and tested with our Launch Simulator as shown in Figure 10. This testing proved the original design concept, helped validate the dynamic models, and pointed out some needed design improvements such as shock absorber sizing, and GUCP attachment strut design improvements.

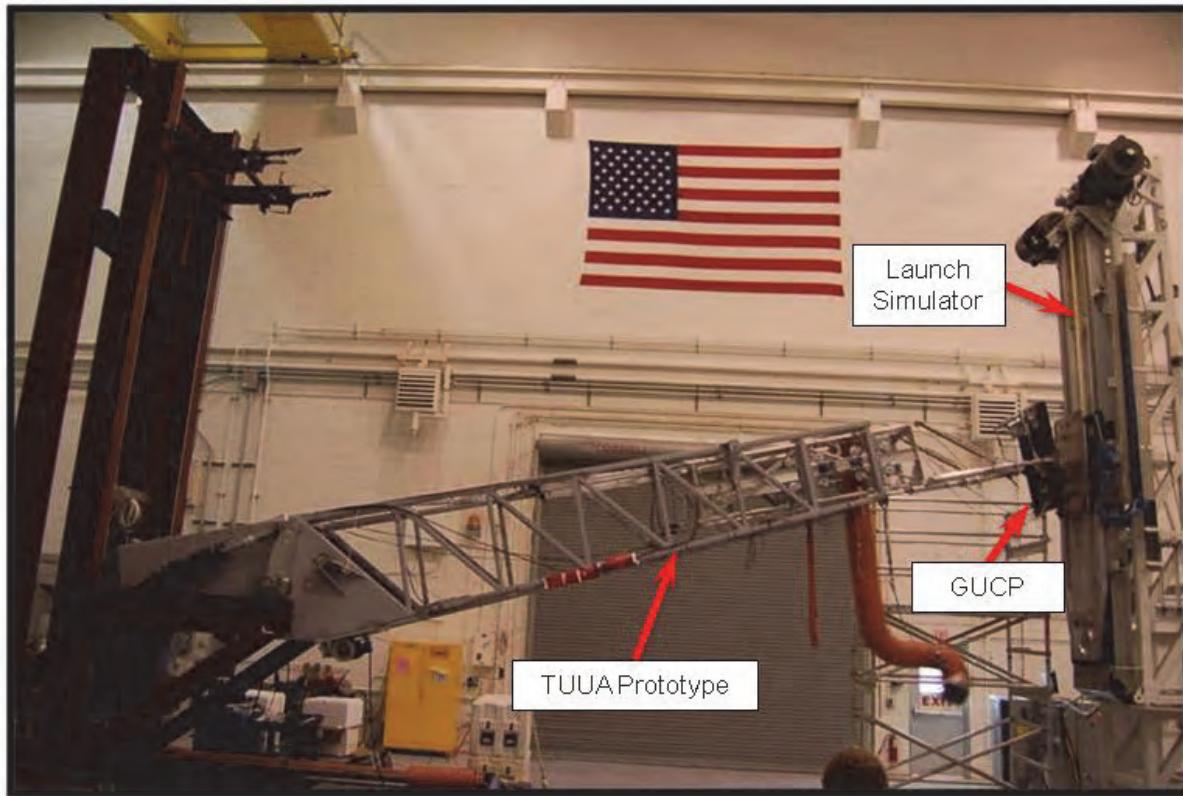


Figure 10. Prototype TUUA Testing

This sequence of connecting and disconnecting the umbilical incorporated many of the lessons learned from previous programs. Experience from the Shuttle program Tail Service Masts (TSM) umbilical drove the pivot foot design and alignment method, allowing the new design to eliminate the laborious adjustment of the GUCP pivot foot. Umbilical mating actuators were also built into the TUUA to make positioning of the heavy (nearly 400 lb) GUCP much easier.

Other critical components were tested, such as the electrical and fluid QD angular mate and demate functions. Some of this testing is shown in Figure 11. It was discovered that angular mating, which was the traditional method in previous umbilicals, was going to be a problem. Previous systems required fluid connectors to mate through a low angle as the plates were joined. Physical restrictions required a much higher mate angle for the ARES I umbilicals. Electrical connectors were damaged and the critical cryogenic fill QD did not align properly.

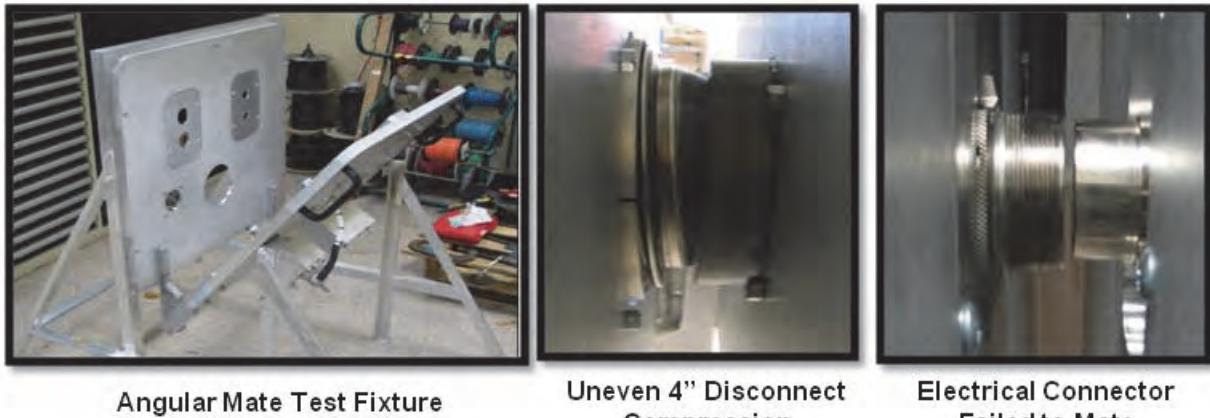


Figure 11. QD Mate/Demate Testing

The linear mate mechanism was the solution to the problems discovered during angular mate testing. Angular demate was still possible because of the extraction motion from the receptacles did not require a precise alignment. Angular compliance in the QD design allowed for the 3°-5° rotation during disconnects.

Once the design of the linear mate GUCP was completed, a fully functional prototype was built and put through extensive functional testing. A special test fixture was built, shown in Figure 12, to simulate mating and demating dynamics, measure loads, and verify all the functions of the GUCP.

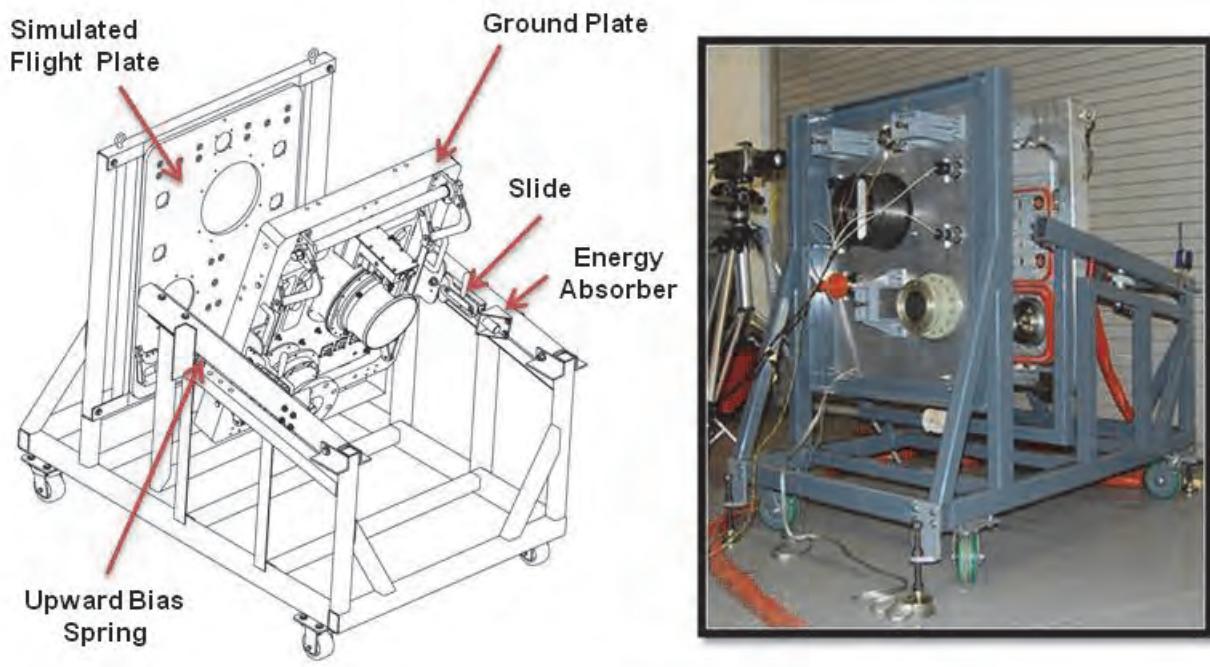


Figure 12. Umbilical Plate Test Fixture

Experience with the Saturn and Shuttle swing arms, and the Shuttle ET (external tank) vent drop down umbilical was incorporated during the design of the TUUA. The design of the TUUA and linear mate GUPC eliminated many of the drawbacks of these previous systems, such as the complexity of the drop

down design, and the much more fail safe tilt up motion of the arm vs. APOLO swing arms which could endanger the vehicle during a retraction failure. Another lesson learned and corrected in this design was the operation where the Space shuttle umbilicals plates were connected first, then the electrical connectors were installed. The separate operation avoided the angular mate problems, but created extra work, delays and higher cost.

Conclusion

Over the 4 year period since the start of the Constellation program KSC has developed a new generation of improved state of the art umbilicals. These new umbilicals draw on 40 years of experience and incorporate many improvements such as the TUUA, linear mate GUCP, and solenoid actuated collets. These umbilicals have the potential to improve the performance and reduce the cost of the next NASA rocket to launch from Cape Canaveral.

Complexity added by the linear mate mechanism is more than overcome by the problems that it solves. The low risk two-step mate operation provides high confidence for technicians. This umbilical combines the precision alignment of a linear umbilical with the simple demate function of a traditional angular umbilical. Linear engagement allows mating of fluid and electrical connectors in the same operation.

The solenoid actuated collet is a new method to reliable release a high load. The use of redundant solenoids is an all new method for T-0 umbilical systems. The combination of the release and engagement function into a single over-center mechanism is the key to the simple operation. The solenoid actuated collet has the potential to replace many high cost pyrotechnic release devices.

The development effort is not over. In the next phase a fully flight certified version of the umbilical is being built and scheduled to be completed in early 2012. This umbilical will be fully functionally tested at KSC using a vehicle motion simulator with cryogenic fluid transfer, and will be put through a full range of launch, abort, and simulated environmental conditions. The collet will also be used during this test providing more valuable data and life cycle testing. The goal is to use it for the future SLS (Space Launch System) rocket to be launched from KSC.

GMI Spin Mechanism Assembly Design, Development, and Test Results

Scott Woolaway*, Michael Kubitschek*, Barry Berdanier*, David Newell*, Chris Dayton*
and Joseph Pellicciotti**

Abstract

The GMI Spin Mechanism Assembly (SMA) is a precision bearing and power transfer drive assembly mechanism that supports and spins the Global Microwave Imager (GMI) instrument at a constant rate of 32 rpm continuously for the 3 year plus mission life. The GMI instrument will fly on the core Global Precipitation Measurement (GPM) spacecraft and will be used to make calibrated radiometric measurements at multiple microwave frequencies and polarizations. The GPM mission is an international effort managed by the National Aeronautics and Space Administration (NASA) to improve climate, weather, and hydro-meteorological predictions through more accurate and frequent precipitation measurements [1]. Ball Aerospace and Technologies Corporation (BATC) was selected by NASA Goddard Space Flight Center (GSFC) to design, build, and test the GMI instrument. The SMA design has to meet a challenging set of requirements and is based on BATC space mechanisms heritage and lessons learned design changes made to the WindSat BAPTA mechanism that is currently operating on-orbit and has recently surpassed 8 years of Flight operation.

Introduction

The Global Microwave Imager (GMI) instrument is one of the payload instruments on the Global Precipitation Measurement (GPM) core spacecraft and must be spun continuously at 32 revolutions per minute (rpm) $\pm 0.3\%$ on-orbit for the 3 year operational life of the instrument to provide the desired geolocation for the science data. The GMI Spin Mechanism Assembly (SMA) is the electro-mechanical bearing and power transfer assembly mechanism that spins the GMI instrument payload, see Fig. 1. The SMA design has to meet a challenging set of requirements and is based on Ball Aerospace and Technologies Corporation (BATC) space mechanisms heritage and lessons learned changes made to the WindSat BAPTA mechanism that is currently operating on-orbit and has recently surpassed 8 years of successful Flight operation. Early WindSat mission anomalies were described and published in a NASA 38th Aerospace Mechanisms Symposium (AMS) paper [2].

This paper will focus on the GMI instrument system requirements, the SMA design to meet those requirements, the integration and testing of the assembly, and lessons learned throughout the GMI SMA program. The design and development of the SMA will be described with a design overview, component development with suppliers, piece-part fabrication, and the drive component level test summary. The verification and validation testing of the SMA assembly to demonstrate compliance to performance and environmental requirements has been completed and will be discussed in greater detail later.

The GMI SMA drive consists of a pair of angular contact bearings separated axially on an AlBeMet™ (Aluminum Beryllium Metal Matrix) shaft and housing, driven by a 3-phase DC torque motor, with a 2-speed (1x/64x) resolver used for commutation and position feedback, a despun tube, a Slip Ring Assembly (SRA), and a rotary transformer. The rotary transformer is used to provide the electrical input to the resolver, which avoids running the low-level resolver excitation input signals across the sliring interface. The incorporation of the rotary transformer into the SMA was one of the WindSat BAPTA ‘lessons learned’ design improvements, after it was suspected that passing the low-level excitation

* Ball Aerospace & Technologies Corp., Boulder, CO

** NASA NESCC Goddard Space Flight Center, Greenbelt, MD

signals for the resolver across the slipring interface was a potential source of, or contributor to, the WindSat on-orbit spin anomalies [2].

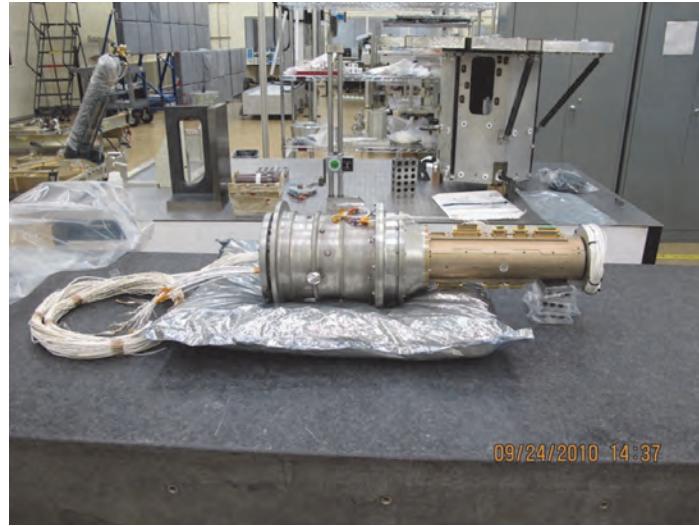


Figure 1. The completed Flight 1 SMA Assembly

The SRA is mounted on the top of the SMA drive and provides an electro-mechanical interface to pass all of the GMI instrument electrical signals and power from the spun-side payload (RF receiver signals, power, telemetry, etc.) across the spinning interface to the stationary-side of the GMI instrument to the GPM spacecraft. The SRA consists of a preloaded angular contact bearing pair, gold-on-gold, double v-groove type brush to ring design, with a total of 124 electrical circuits (rings), and it is wet lubricated. A despin shaft with bellows coupling is used to provide the mechanical despin interface to the stationary upper instrument calibration assembly structure and provide a slight misalignment capability between the bearing pair in the SMA drive and the bearing pair in the SRA. Bearings, lubrication, and material choices will be discussed later in this paper along with the selection and sub-assembly level testing of the drive components. The completed SMA drive is approximately 8.6 inches (22 cm) in diameter by 24.15 inches (61.34 cm) long from the instrument interface base to the top of the SRA, See Fig. 2. A brief overview of the control system architecture and SMA drive electronics will also be described briefly later on in this paper.

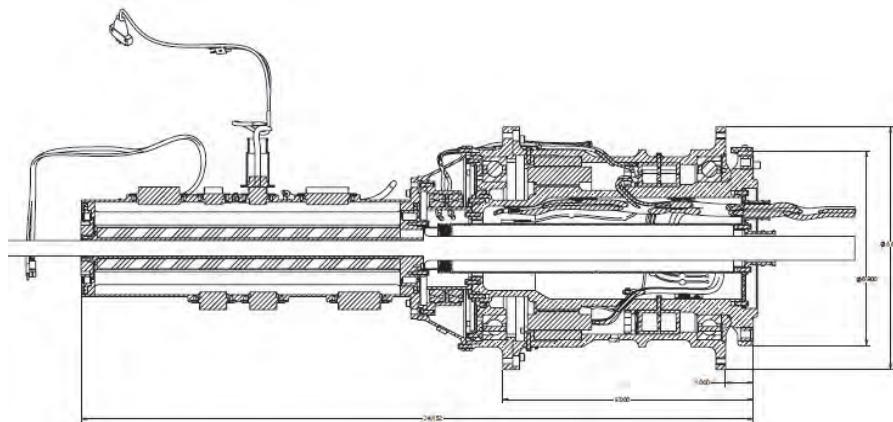


Figure 2. Cross-section view of the SMA

The SMA Assembly has to meet all of the challenging and design-driving requirements, such as: instrument deployed stiffness and pointing accuracy, minimize weight, and carry launch loads, long life reliability for continuous operation on-orbit and ground operations, integration and test demands. Table 1 shows the list of the main requirements that drive the design of the SMA.

Early in the design and development of the GMI instrument it was recognized that there were several risks associated with the successful completion of the SMA. The highest risk identified was the intermittent on-orbit uncontrolled spin anomalies associated with the WindSat instrument [2]. All the recommendations from the WindSat anomaly investigation lessons learned and BAPTA build were incorporated into the design of the SMA. The list includes: specific electronic design changes, procurement of the SRA, and addition of a rotary transformer to avoid passing the resolver signals across the SRA. These along with other potential SMA risks were closely tracked through the duration of the SMA design, procurement, integration, and test program.

Several risk mitigation actions were undertaken to reduce the chance of unanticipated anomalies becoming significant schedule or flight issues, including: the early procurement and testing of Engineering Model Units (EMUs) for the SRA, rotary transformer and resolver drive set components, and motor control electronics. In addition, early assembly and extensive testing of the completed SMA before it was integrated into the GMI instrument proved to be a wise strategy and well worth the investment. It provided the needed flexibility and time to identify and resolve issues before they could significantly impact the flight units, or worse, drive GMI instrument cost and schedule.

It should also be noted here that the anomalies experienced by WindSat occurred relatively early in the on-orbit history of the satellite, an instrument and drive operational work-around was developed quickly for the instrument and drive so no significant observational time was lost. Very infrequent spin-downs (approximately 1-2x per year) have continued to occur, but the operational work-arounds developed were immediately employed and been successful. WindSat BAPTA has now recently surpassed 8 years of continuous on-orbit operation, without any additional anomalies in the past 18 months [2].

Design Description and Details

The SMA is a bearing and power transfer assembly originally based on past BATC space mechanisms design heritage and experience going back to the 1960s-70s with several spinning or spin-stabilized small satellites (i.e., The Orbiting Solar Observatory (OSO) 1-7 satellite series, 1961-71). They were designed, built, and tested by the then Ball Brothers Research Corp. (BBRC), which is now BATC, and that have all had very successful on-orbit records. The DSCS II drive in the 1980s was the fundamental architecture for the WindSat BAPTA design and one of the DSCS II drives operated successfully on orbit at 30 rpm for over 23 years. The GMI SMA is based on the WindSat BAPTA design that BATC designed, built, tested, and delivered to U. S. Naval Research Laboratories (NRL) in 2001, for the WindSat instrument that is flying on the Coriolis mission.

Since the SMA design is based on so much past, and recent, successful BATC flight heritage, there was a very real priority given, and effort made, to keep the design of the GMI SMA as close as practical to the design of the WindSat BAPTA mechanism. The only changes made were to address the issues associated with, and the lessons learned incorporated from the WindSat BAPTA, or in a few exceptional instances, because the system level requirements for GMI were different and necessitated it. But every effort was made to design the other new elements of the GMI instrument around the design of the SMA, wherever sensible, to avoid impacting the flight heritage integrity of the SMA design.

The most significant change to the SMA design was the addition of a rotary transformer, the result of an effort to avoid passing the low level excitation and return signals of the resolver across the SRA interface. If the resolver signals drop for a long enough period of time, the motor commutation can be severely affected, resulting in the loss of operational rate or position control resulting in a controlled spin-down. For this reason, the decision was made early on to alter the basic SMA configuration by adding a rotary

transformer to the design. The addition of the rotary transformer added a significant amount of weight, approximately 2.0 kg, power, and some minor complexity to the control system electronics design but the trade decision was made that the added mass, power, and complexity was worth the risk mitigation that was gained by making this aspect of the design more robust.

Table 1. SMA Design Driving Requirements

Requirement	Predicted Performance
Rotation Rate /Control Rate shall be $32 +/- 0.3\%$ RPM Range shall be 0 – 33 RPM	$32 \pm 0.3\%$ RPM 0 – 33 RPM
Spin axis Align to base shall be < 75 arcsec Wobble shall be < 30 arcsec 3 sigma	49.6 arcsec (RSS) 11.5 arcsec (RSS)
Position Uncertainty Tach pulses/rate control position accuracy ≤ 60 arcsec	44 arcsec (32 tach pulses / rev)
Stiffness First mode > 50 Hz (in GMI assy) Deployed First Mode > 6 Hz De-spin torsion > 7.6 Hz	60.8 Hz > 7.6 Hz > 7.8 Hz
Mass 20.4 kg maximum	20.29 kg
Torque Margin 1.5x on known's, 2x on variables	0.222 MS
Operating and Non Operating Temperatures On-orbit Op: 0 to +50C Survival: -35 to +55C	10 to 15C Op
Design Life 38 months on-orbit op + 12 months I&T + 2.4 months op storage (2 yr @ 10%); total life reqmt 52.4 months	99.721% reliability 0.13 MS SMA lube 0.38 MS SRA lube

All the other changes to the SMA design were primarily within the SRA. For instance, the SRA for BAPTA had 137 rings, whereas, for GMI the SRA needed to have 124 rings for all the GMI signals. The BAPTA SRA manufacturer acquired and combined with another supplier. Extensive time and effort was spent to recover the BAPTA SRA heritage design. That proved to be a much tougher task, as it turned out, than anyone anticipated. The basic design and production knowledge was essentially still there, but a few of the critical process details of exactly how to produce the product as desired, why it was important, and what the impacts were was lost, and had to be re-created, to meet the specification requirements of the design.

The most obvious challenge in the early SMA development was trading either adapting the drive to meet the GMI instrument interfaces and requirements, or alternatively, adapting the GMI interface (or derived requirements) so that the SMA design configuration would, or could be made to meet them without adversely affecting the functional and performance heritage of the drive or principle critical elements. One of the biggest of these challenges was converging on an instrument interface and load path for the GMI instrument that would be consistent with the load capacity and stiffness of the SMA bearings and drive configuration.

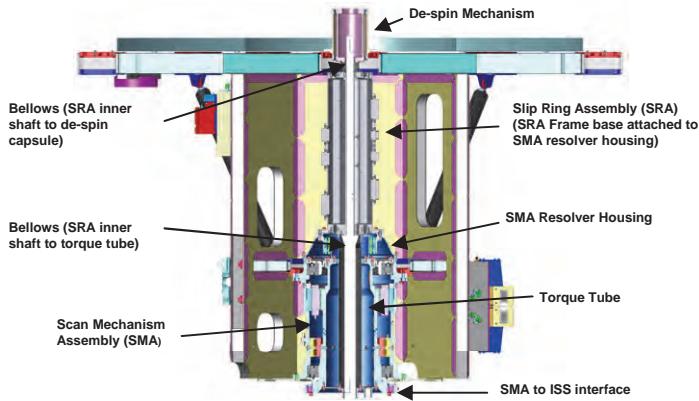


Figure 3. Cross-section of the GMI Instrument Bay Structure (IBS) with the SMA installed

Figure 3 shows a cross-section of the primary structural elements of the SMA within the GMI instrument. A critical factor in the final configuration of the instrument architecture was the analytical determination that the GMI Instrument Bay Structure (IBS) would have to be restrained for launch in order for the SMA bearings and design to remain the same as the heritage drive. Substantial effort and care was taken in the IBS design and structural analysis to ensure that the load path from the IBS launch restraints, to the IBS structure, and transferred thru the SMA structure during launch were maintained to acceptable levels to meet adequate margins of safety with modeling and testing uncertainties.

The SMA drive design was also analyzed for adequate stiffness to meet the deployed frequency first mode requirement after the launch restraints and main reflector have deployed on orbit. Figure 4 shows the stowed and deployed structural analysis Finite Element Models (FEM) used for the stowed and deployed stiffness determination and the first modes, respectively.

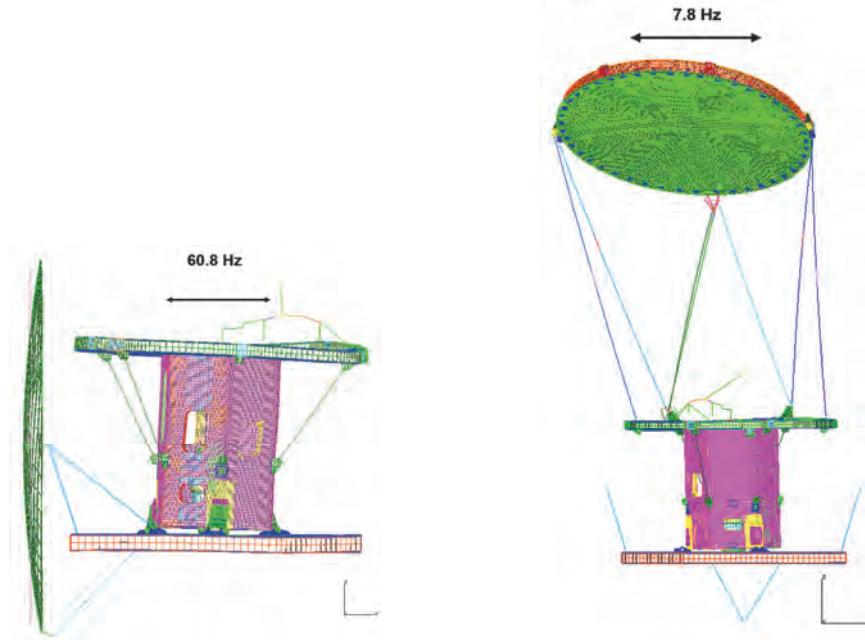


Figure 4. Finite Element (FEM) model of GMI instrument with SMA and launch restraints meets the first mode stowed frequency requirement (>50 Hz), meets the first mode minimum deployed frequency requirement (>6 Hz) predicted on-orbit

The electronic control system architecture was adopted and leveraged from the WindSat BAPTA electronics and software to perform the speed and position control tasks for GMI. The model includes an analog controller used to control SMA rate, a control plant that includes models of the motor (transfer function with current feedback loop) and disturbance torques, and feedback sensor that models position sensor with noise and velocity calculation via position differentiation. Further detail of the control system modeling and verification testing are beyond the scope of this paper.

Component, Material, and Lubrication Selections

The design-driving components for the SMA were, not surprisingly, the challenging procurements of the SRA, the resolver, rotary transformer, and the motor. However, since this design application requires such a long life (75million revolutions) and reliable performance over the entire life, the bearings, bellows, and lubrication are just as critical to the ultimate success of the drive. Figure 5 shows a cross-section of the SMA.

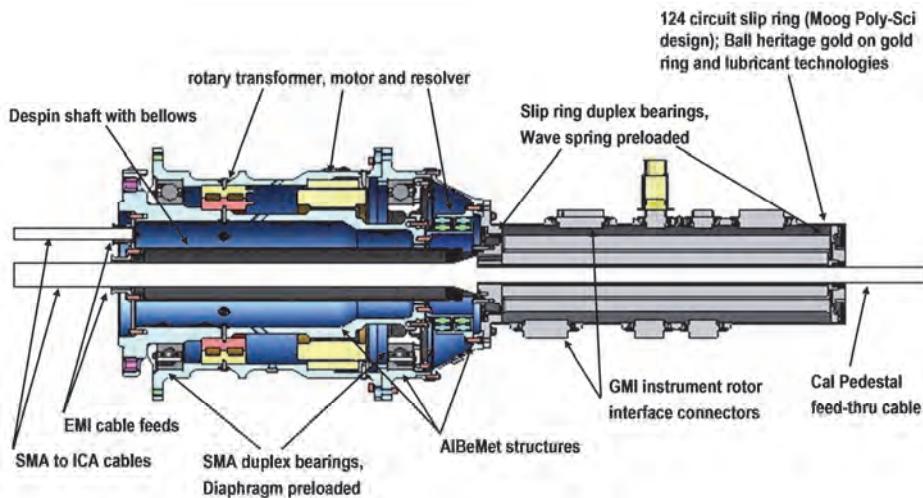


Figure 5. Cross-section of the SMA design with drive component labels

As previously mentioned, the SRA is a heritage design procured from Moog Components Group (formerly Poly-Scientific and Electro-Tech Corp.). The SRA configuration consists of an angular contact bearing pair, a gold-on-gold, double v-groove type brush to ring design with a total of 124 electrical circuits (rings) that are wet lubricated. The SRA brushes are a solid gold alloy and each brush pair rides in the hard gold over soft gold double v-groove rings. See Figure 6. This is a heritage design which dates back to DSCS II drive in 1980, and was similar to the WindSat BAPTA design with minor modifications. The PAO wet lubrication system is a BATC proprietary formulation and process [3] first demonstrated on the WindSat BAPTA SRA and will be life-tested in the GMI Life Test Unit (LTU) SRA discussed in section 5 of this paper.

The primary drive and control components; motor, resolver, and rotary transformer were all procured from Axsys Technologies, now owned by General Dynamics AIS. The motor is an external rotor 3-phase brushless DC torque motor with a skewed and redundant winding design. The motor design parameters; $K_t = 320 \text{ oz-in/amp}$ (2.26 N-m/amp), cogging torque = 13 in-oz (9.2 N-cm), peak torque = 639 oz-in (4.51 N-m) (at 1.71 amps max. current), air gap = 0.023 in (0.58 mm), and weight = 7.02 lb (3.18 kg) near identical to the heritage motor used on WindSat BAPTA. See Figure 7.

The resolver and rotary transformer were procured as matched sets with redundant units mounted on common hub and sleeve designs. The resolver design is the BAPTA heritage 2-speed (1x/64x) resolver used for commutation and position feedback. The combined resolver/rotary transformer set was specified

to have a reduced 30 arcsec minimum accuracy (at room temperature) and a 6 arcsec maximum electrical zero shift over temperature ($\pm 20^{\circ}\text{C}$), and a rotary transformer weight = 3.9 lb (1.8 kg). The resolver mounting alignment requirement = 0.0005 in (0.01 mm), air gap = 0.016 in (0.41 mm), and resolver weight = 1.52 lb (689 g) were all heritage designs too. See Figure 8.

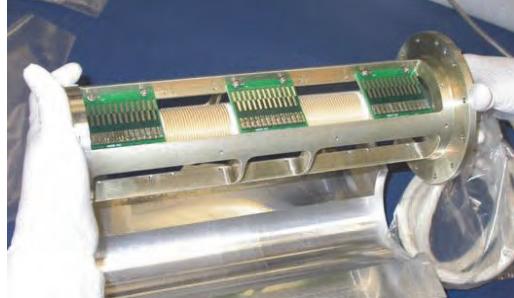


Figure 6. Slip Ring Assembly (SRA) showing double gold brush pairs, double v-groove gold rings



Figure 7. BAPTA 3-Phase DC torque motor



Figure 8. BAPTA 2-speed Resolver (1x/64x)

It is probably becoming clear that ‘Flight Heritage Design’ does not always mean it is truly ‘flight’ heritage. There is no such thing as 100% heritage based design; materials are altered, processes change, suppliers change, and requirements, or specific applications change loads, environments, or other critical conditions that may affect the design performance in sometimes dramatic ways.

The main SMA drive consists of a pair of preloaded angular contact bearings separated axially on an AlBeMet™ (Aluminum Beryllium Alloy Material) shaft and housing. The bearings are ABEC 7 (ABEC 5 balls), 52100 steel bearings procured from NSK Corp. (formerly manufactured by RHP, England) and is a heritage component except for a manufacturing change by the new vendor to improve the inner raceway curvature and dam height. These changes were modeled in the structural analysis and taken into account in the lubrication analysis that still shows a slightly positive margin of safety (MS = 0.02) at End of Life (EOL) for the number of stress crossings and with the mean Hertzian contact stress of the 110 lb (489 N) preloaded bearings, which is acceptable. The bearings are precisely preloaded and ‘snubbed’ by means of a titanium diaphragm and snubber. Several axial deflection vs. force measurements were taken during assembly to confirm the correct preload and snubber gap were achieved in the assembly. The lubrication for the SMA main drive bearings is a Nye Synthetic Oil with Rheolube grease and is heritage BATC tribology elements [4].

The SMA primary structural housings and inner shaft elements were fabricated out of AlBeMet™ which contains 62% Beryllium and 38% Aluminum and was chosen because of the material properties; mainly for high specific stiffness and heat conduction, compared to other more common aerospace structural materials. However, because of the Beryllium content in this alloy, it does require special handling to prevent human exposure to any particles that could be generated from the parts.

Finally, it should be mentioned here that a despin shaft with bellows coupling is used to provide the mechanical ‘despin’ interface to the stationary upper instrument structure, calibration assembly, and to account for any minor misalignments between the bearing pair in the SMA main drive and the bearing pair in the SRA. There is also another preloaded angular contact pair that supports the Calibration Pedestal and the upper IBS structure, this bearing configuration is referred to as the Despin Mechanism in the GMI instrument. Those bearings are being life-tested as well but the design of that mechanism is not included or mentioned further in the discussions in this paper but similar issues and constraints apply. The bellows life test was a significant effort at Tara BelFab.

Integration Experience, Test Setups, and Test Planning

The SMA drive successfully completed performance and environmental (thermal vacuum and EMI) acceptance testing in Nov. 2010, and met all of the sub-system requirements that were to be verified via test. The objective of this testing was risk reduction for verifying the critical functional and performance requirements early in the integration and test program, so that any issues found in the SMA integration with the electronics, performance or environmental testing could be addressed at the sub-system level, months before the SMA is integrated into the GMI instrument.

The test setups for performing the acceptance testing are briefly described here. The electronics integration, commutation offsets, initial spin testing, and baseline performance tests were all run in the clean room with the SMA mounted within the Inertial Test Fixture (ITF), See Figure 9. The completed SMA is seen within the test fixture along with the circular instrument mass and inertia simulator plate mounted on the SMA. The square shaped torque tube plates around the SRA above the SMA are seen and are used to interface with the optical encoder, torque transducer, and brake during the torque margin and rate testing.



Figure 9. SMA mounted in test fixture to prepare for acceptance test in the clean room.

Once the ambient testing was successfully completed, the test setup was loaded into the Thermal Vacuum (TVAC) chamber and the article under test was taken thru one complete survival thermal cycle with 4 hour minimum dwells at each temperature extreme. Then all the acceptance tests were repeated in the TVAC at the operating temperature extremes, see Figure 10.

Performance Test Results

The results of the acceptance testing of the SMA, including measured rate control, position accuracy, pointing alignment, wobble, and power dissipation over operating temperature ranges in vacuum, are summarized in Table 2.

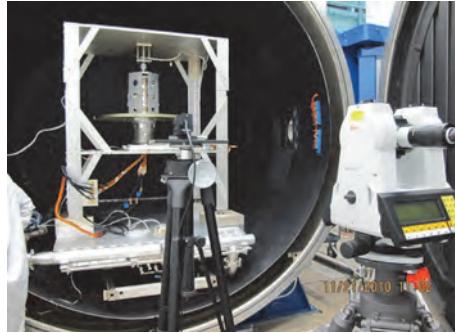


Figure 10. SMA mounted in inertial test fixture and loaded into chamber for TVAC Testing

The SMA torque margin was only tested in the cleanroom at ambient temperature but the drive current was monitored over temperature during operation. The torque margin can be calculated by knowing the motor constant K_t (which is essentially constant over temperature) and measuring the current at the operating temperature extremes. Then the change in current is due entirely to the change in bearing and SRA drag torque or the drive, within the measurement uncertainty of the torque transducer.

Table 2. SMA Tested Performance vs. Requirements

Requirement	Measured / Tested Performance
Rotation Rate /Control Rate shall be $32 + / - 0.3\%$ RPM Range shall be 0 – 33 RPM	$32 \pm 0.1\%$ RPM 0 – 33 RPM
Spin axis Align to base shall be < 75 arcsec Wobble shall be < 30 arcsec 3 sigma	< 15 arcsec (RSS) < 5 arcsec (RSS)
Position Uncertainty Tach pulses/rate control position accuracy ≤ 60 arcsec	50 arcsec (32 tach pulses / rev)
Stiffness First mode > 50 Hz (in GMI assy) Deployed First Mode > 6 Hz De-spin torsion > 7.6 Hz	60.8 Hz (GMI level test) > 7.6 Hz (GMI deploy test) > 7.8 Hz (GMI deploy test)
Mass 20.4 kg maximum	20.3 kg
Torque Margin 1.5x on known's, 2x on variables	0.87 MS
Operating and Non Operating Temperatures On-orbit Op: 0 to $+50^\circ\text{C}$ Survival: -35 to $+55^\circ\text{C}$	10 to 15°C Op
Design Life 38 months on-orbit op + 12 months I&T + 2.4 months op storage (2 yr @ 10%); total life reqmt 52.4 months	BAPTA 8 yrs. on-orbit to date, SRA and SMA Bearing Life Tests Begun

The rate control was measured independently with an optical encoder and compared to the tachometer/resolver feedback data. In this way, we measured and compared the rate control of the drive as commanded and the resultant rate, by performing an interpolation between any 2 points in the sample data set, and calculating the error between the encoder and the resolver information for rate and position.

The rate control and position knowledge of the drive was very good and well within the specified required accuracy. See Table 2 for SMA test results.

The current was monitored during GMI instrument level before and after environmental tests including vibration, acoustics, EMC/EMI, and TVAC testing. Figure 11 below shows a summary of the SMA motor current monitoring and trending during GMI instrument level testing. Characteristics to note are that the motor current is higher during ambient environment testing due to the air drag on the main reflector and reflector deployment assembly in the cleanroom. The motor current measurements also show that the bearing drag torque in vacuum is higher at cold temperature as expected and predicted. The variation in motor current at cold is due to cycling of the SMA operation heaters at or near cold operating temperature.

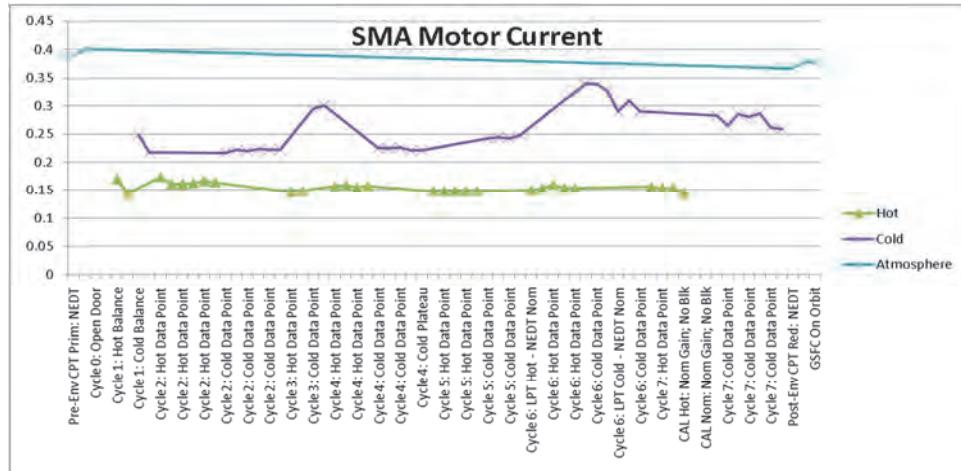


Figure 11. Summary of SMA motor current monitoring and trending thru GMI environmental test

Additionally, the SMA bearings and Slipring Assembly (SRA) have each begun a life-test program. The SMA bearings (3 preloaded bearing pairs) began testing Dec. 2010, see Figure 12. To date, the bearings have completed a survival temperature cycle, followed by 30 days of ambient operation, then 8 operational temperature cycles (1 day each at operating temperature extremes each cycle), 60 days back at ambient, and 30 days at each temperature extreme, all under vacuum and rotating at 32 rpm. That is just over 3.5 million revolutions or 3.4% of the total 104 million cycles (1.25x Flight Model total life) test objective. The test articles and test setups were all performing nominally for all the specified test conditions as initially planned.



Figure 12. SMA main bearings Life Test setup and preloaded bearing capsules (3 pairs)

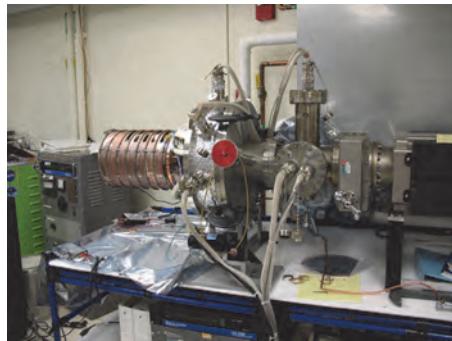


Figure 13. SRA life test Setup with the SRA Life-Test Unit (LTU) inside a small chamber ready for TVAC test

The SRA was configured in a vacuum and temperature controlled (TVAC) setup (Figure 13) and began a life test in May 2011. This SRA assembly will also see one month of ambient operation, then one survival temperature cycle with 8 hour minimum dwells at the temperature extremes, followed by 8 thermal cycles to the operating temperature extremes (1 day dwell duration at each extreme) while rotating, and then 1 month at each temperature extreme before returning to 60 days running at ambient temperature before repeating.

However, during the first cycle cold it was discovered that the dewar/chamber being used to chill the SRA assembly was not functioning properly and could not achieve the cold survival temperature, or remain stable enough to meet requirements at the cold operating temperature for the duration of the test. So the decision was made to purchase another chiller for the chamber with more cooling capacity to meet the requirements with adequate margin for desired stability at both cold survival and operating temperatures. The new chiller has been installed and the SRA assembly has been taken cold and successfully completed the first cold survival cycle and 7 cold operating cycles to date.

The temperature profile and durations were designed to give roughly 80% of the revolutions at the on-orbit predicted temperature (essentially room temperature, in this case), 10% of the cycles at hot operating, and 10% of the cycles at cold operating by the EOL of the Life Test. It was also found to be very important to monitor and control the temperature gradient across the bearings and rotating to spinning elements in both the bearings and SRA life test units under test. The Life Tests are expected to run continuously for the next 5 years and accumulate approximately 104 million cycles or revolutions on each test article. It is possible that the Life Test may be extended beyond the projected life if the life test is successfully completed, in order to gain qualified Life Test data for similar longer life missions.

In October, 2011 the SMA bearing life test was briefly stopped for a few weeks due to an apparent increase in bearing torque of one of the bearing pairs. After further investigation, it was found that the strain gage used to measure the bearing pair torque external to the housing was found to have become misaligned and broken, giving a falsely high torque reading (Figure 14). The decision was made to break vacuum, rework GSE setup, replace the strain gage, and restart the test. The Life-Test was restarted in late November 2011 and has been running without incident since then.

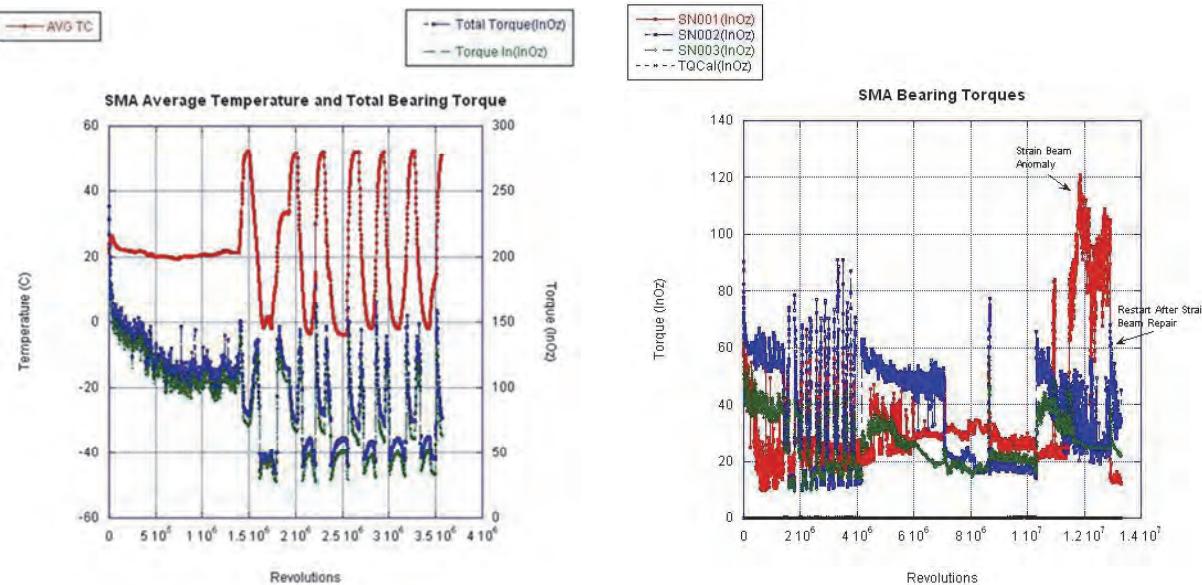


Figure 14. SMA main bearings life test temperature, bearing torque baseline over temperature, and total number of revolutions just prior to torque rise latter attributed to GSE strain gage

Figure 14 shows the average bearing temperature, total bearing torque, and torque measured going into the life test assembly over the revolutions completed to date [5], as well, as the faulty torque readings later concluded to have originated from a misaligned bracket and broken GSE strain gage in the SMA bearing life test setup.

Table 3. GMI Instrument and SMA vibration test and design analysis for launch environments

Random Vibration

Frequency (Hz)	ASD Level (g^2/Hz)	
	Qualification	Acceptance
20	0.010	0.010
20-50	+2.83 dB/Oct	+0.56 dB/Oct
50-800	0.024	0.012
800-2000	-2.83 dB/Oct	-0.56 dB/Oct
2000	0.010	0.010
Overall	6.0 G_{rms}	4.7 G_{rms}

Sine Vibration

Frequency	Limit Level	Protoflight/ Qualification Testing	Acceptance Testing
5-50 Hz	4.8g	6g	4.8g

Design Limit Loads

GMI Axis	Launch Vehicle Direction	Design Limit Loads (g)
X	Axial	10.0
Y	Lateral	8.0
Z	Lateral	8.0

Conclusions and Future Work

The SMA was integrated into the GMI instrument assembly, continued through the rest of the instrument final integration, and successfully completed all instrument-level performance and environmental testing including vibration testing, see Figure 15, to levels outlined in Table 3 above, at the end of January 2012.

The GMI instrument level vibration testing verified the stowed 1st mode frequency requirement. The SMA deployed stiffness was also measured and verified during the GMI Instrument level test program in the final flight configuration with the main reflector and Reflector Deployment Assembly installed and deployed on the IBS, see Figure 16.

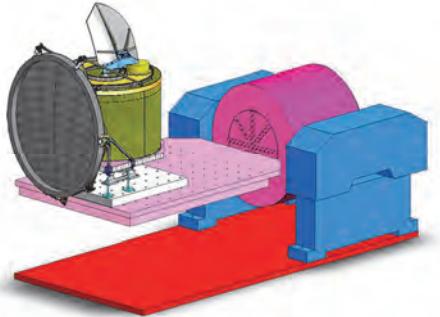


Figure 15. GMI Instrument during vibration testing on vibration test table in stowed configuration

The GMI instrument will also successfully completed a static and dynamic spin balance measurement and balancing program both in the cleanroom and in vacuum, to separate and eliminate the effects of air drag on the spin balance results. There has been extensive work done in this area and this subject alone is worthy of another paper in itself [6]. The GMI instrument was successfully completed, delivered to Goddard Space Flight Center, and integrated onto the GPM spacecraft in early March 2012.

Finally, the SMA Bearing and SRA Life Tests will continue for the next 4-5 years and updated status reports will be completed at least once a year until the completion of the tests, assuming the test data remains nominal until the tests are complete.



Figure 16. GMI Instrument during initial SMA Spin testing in Cleanroom with the reflector deployed

A special thanks to Sergey Krimchansky of GSFC for his input over-seeing the technical work on GMI and for his support in writing these technical papers.

References

1. Newell, D., Rait, G., Ta, T., Berdanier, B., Draper, D., Kubitschek, M., Krimchansky, S. "GPM Microwave Imager Design, Predicted Performance and Status", *Proceedings of the 2010 IEEE International Geoscience and Remote Sensing Symposium (IGARSS)* Publication Date: July 25, 2010
2. Koss, S., Woolaway, S. "Lessons Learned From the WindSat BAPTA Design and On-Orbit Anomalies", *Proceedings of 38th NASA Aerospace Mechanisms Symposium*, Langley Research Center, May 2006.
3. Pierre, W. "GMI Spin Mechanism Structural Analysis", *BATC Internal SER Report No. 2307821B*, Ball Aerospace and Technologies Corp., Nov. 2008.
4. Dayton, C. "Slipring and SMA Bearing Lubrication Analysis", *BATC Internal SER Report No. 2242913D & 2241045D*, Ball Aerospace and Technologies Corp., Oct. 2008.
5. Hoffman, C. "Status of the GPM/GMI Bearing Life Test", *541/Materials Engineering Branch Memorandum No. MEB-2011-025*, Ball Aerospace and Technologies Corp., Apr. 2011.
6. Ayari, L. "GMI Rotating Mass Balance Uncertainty", *BATC Internal SER Report No. 2324813A*, Ball Aerospace and Technologies Corp., Jun. 2009.

Lessons Learned from the TIRS Instrument Mechanisms Development

Jason Budinoff*, Richard Barclay*, James Basl**, Konrad Bergandy**, Thomas Capon*, Bart Drake**, Michael Hersh*, Chris Hormann**, Edwin Lee**, Adam Matuszeski*, Armani Nerses*, Kenneth Pellak**, Kermit Pope**, Joseph Schepis* and Ted Sholar**

Abstract

This paper describes the many lessons learned during the design and development of several mechanisms for the Landsat Data Continuity Mission (LDCM) Thermal Infrared Sensor (TIRS) instrument, built by an engineering team at NASA Goddard Space Flight Center (GSFC). Several mechanisms were developed for TIRS including an arc-second precise mirror positioning system, a launch lock for a 90-lbm (41-kg) cryo-cooler assembly, and a large deployable earth shield. These mechanisms were developed over a 2 year period, and several obstacles were encountered and subsequently solved prior to delivery.

Introduction

The LDCM satellite will launch into a low polar orbit in late 2012. LDCM will provide earth resources data continuity between the currently operational Landsat 5 and Landsat 7 missions and the Joint Polar Satellite System (JPSS) Missions. It will provide a high spatial resolution complement to the lower spatial resolution, higher temporal sampling JPSS data set. LDCM will be carrying TIRS, an actively cooled, nadir-looking, mid-infrared imager. TIRS on LDCM is a 100-meter spatial resolution push-broom imager whose two spectral channels, centered near 10.8 and 12 microns, split the spectral range of the Thematic Mapper (TM) and Enhanced Thematic Mapper (ETM+) instruments¹.

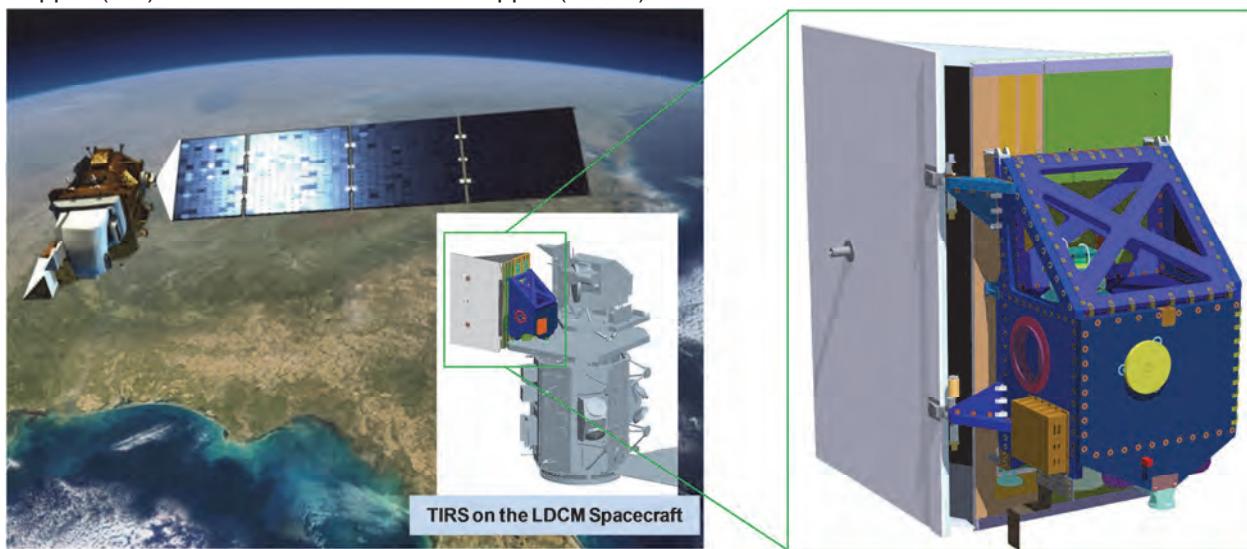


Figure 1. LDCM will launch in late 2012 carrying the TIRS Instrument. The LDCM spacecraft is shown in orbit in the left figure. The TIRS instrument is shown on the right with the large white earth shield panel deployed.

* NASA Goddard Space Flight Center, Greenbelt MD

** Stinger Ghaffarian Technologies Incorporated, Greenbelt MD

[†] Orbital Sciences Corporation, Dulles VA

[‡] Vantage Systems Incorporated, Lanham MD

The TIRS instrument has 3 mechanisms and a set of mechanism control electronics, all built at GSFC. All of the mechanisms were developed on very compressed schedules, resulting in increased development risks. Each mechanism had unique development problems which were successfully overcome.

Scene Select Mechanism (SSM)

TIRS requires multi-scene calibration every orbit, so a flat scene mirror is used to switch the instrument field of view between nadir, cold space, and a warm black body calibration target. The Scene Select Mechanism will rotate and hold the scene mirror in position within ± 9.7 radians using closed-loop digital control. The location of the SSM within the TIRS instrument is shown in Figure 2.

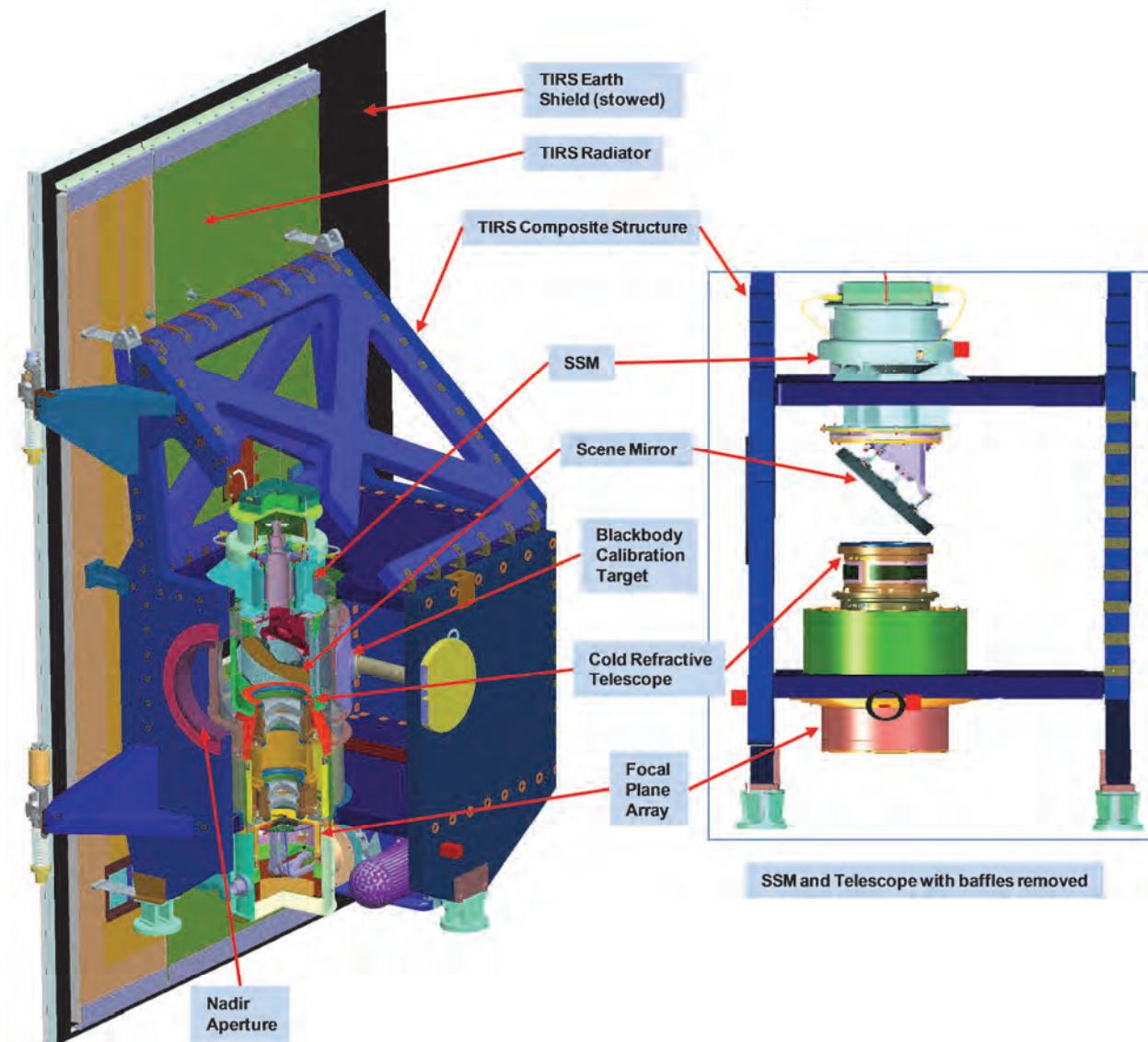


Figure 2. The SSM is located in the heart of the TIRS instrument, just above the cryogenic telescope. The quarter section view on the left shows the location of the SSM within the TIRS instrument structure. The figure on the right shows the SSM above the telescope. Baffles and secondary structures have been removed for clarity. Note the close proximity of the edge of Scene Mirror to the cold telescope, which radiatively drives the mirror temperature down.

Earth Shield Deployment Mechanism (ESDM)

As TIRS is a cryogenic instrument, it must reject a large amount of heat to keep the focal plane array at the operational temperature of 43K. In order to keep the radiator to a reasonable size, a 2.5-m² deployable earth shield panel is used to block albedo. This earth shield is stowed at launch, and is rotated & locked into position by the ESDM. The ESDM is shown in Figure 3.

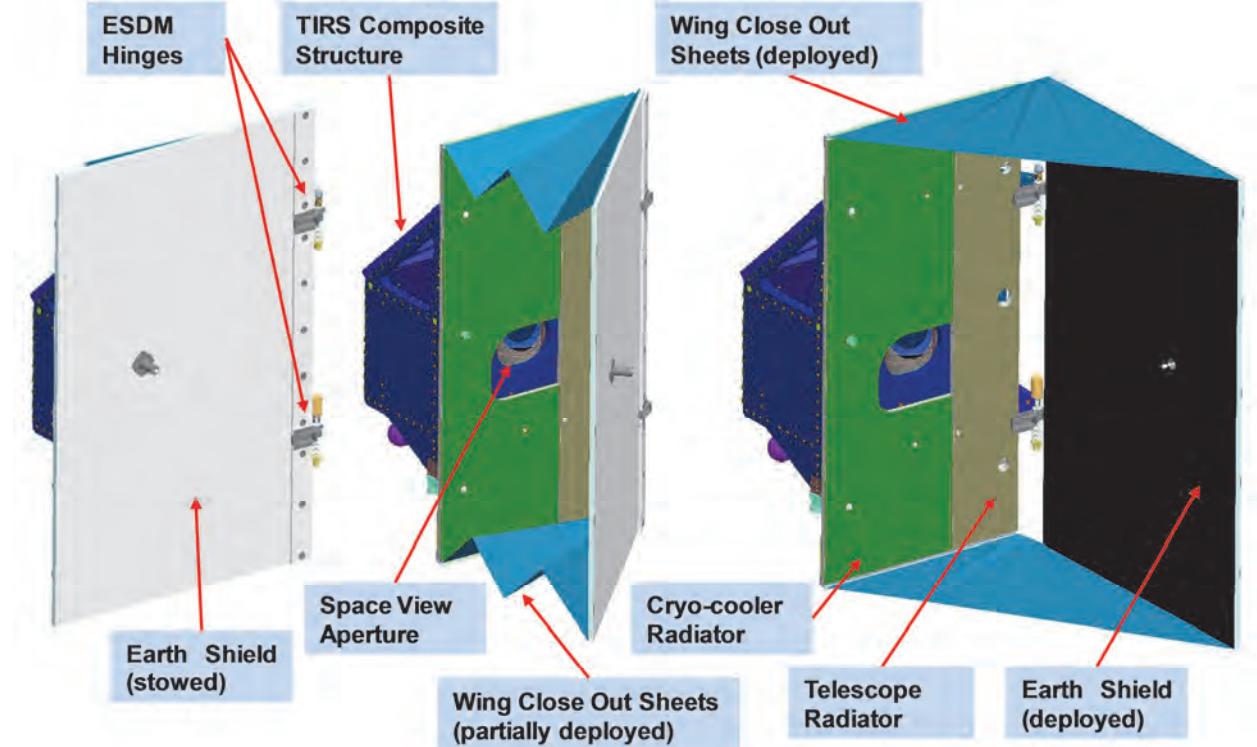


Figure 3. The ESDM deploys the large Earth Shield panel from the stowed position flush with the radiators 90 degrees to the deployed position. The left figure shows the panel stowed. The right figure shows the panel fully deployed.

Cryo-Cooler Launch Lock (CCLL)

TIRS is actively cooled by a Stirling cycle cryo-cooler mounted beneath the instrument. This cooler is a source of jitter and is separated from the instrument by a passive vibration isolation system consisting of damping flexures. The flexures are too soft to survive the launch environment without a launch lock. The CCLL mechanism constrains the cryo-cooler supporting structure during launch and is released on orbit prior to instrument operations.

Scene Select Mechanism

The SSM is a single axis, precision mirror positioning mechanism, capable of 3 μradian stability. It can be driven in either direction for unlimited rotations. The rotating mirror is dynamically balanced over the spin axis, and does not require launch locking. Several configurations were traded before the SSM flight architecture was finalized². The mechanism is shown in Figure 5. The SSM met or exceeded the driving requirements defined in Table 1.

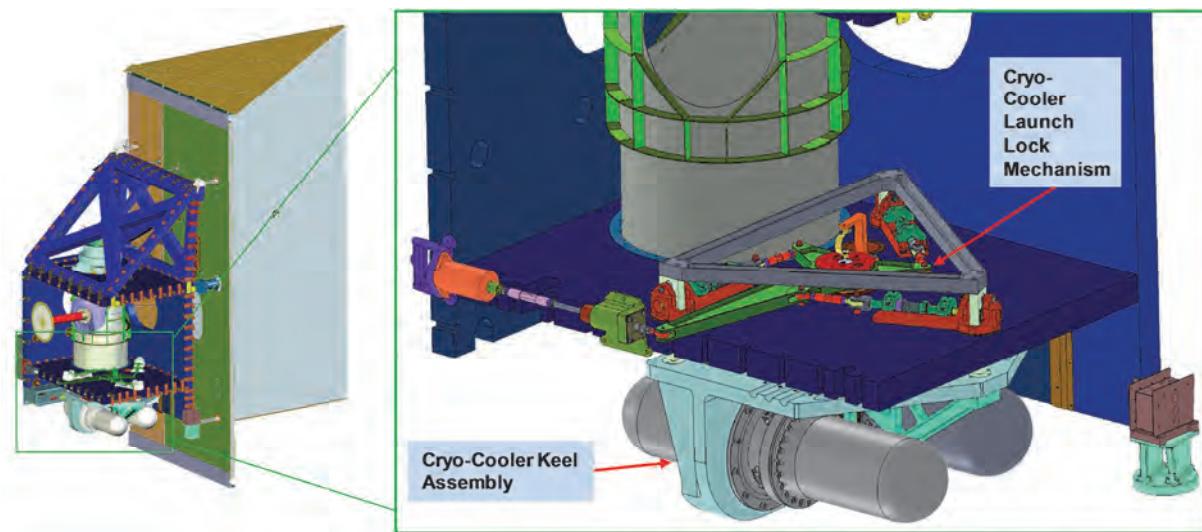


Figure 4. The CCLL is located within the TIRS instrument. The instrument side panels are removed to show the launch lock and the cryo-cooler keel structure that it restrains.

Table 1. SSM Driving Requirements

Requirement	Value
Mass	33 lbm (15 kg)
Power	6 W average
Mirror Size	8.15 x 5.87 in (207 x 149 mm) elliptical
Knowledge	$\pm 9.7 \text{ } \mu\text{radians}$ over 34 minutes
Stability	$\pm 9.7 \text{ } \mu\text{radians}$ over 2.5 seconds
Duty Cycle	100%
Thermal Operational	0 / +20°C stable to $\pm 1^\circ\text{C}$
Thermal Survival	-50° / +40°C
Lifetime	3.25 years on orbit
Redundancy	A/B side block redundancy
Operational Cadence	Stare nadir for 30-40 minutes Rotate 120° in <2 minutes to space view Stare for ~30 seconds, Rotate 120° in <2 minutes to blackbody view Stare for ~30 seconds Rotate to 120° in <2 minutes to nadir view

Structure

The SSM will operate at a nominal 7-10°C; the scene mirror it rotates will be near 0°C. To minimize heater power, low thermal conductivity titanium 6Al4V was chosen for the primary structural material. The 8.15 x 5.87 in (207 x 149 mm) scene mirror is made of an aluminum 6061-T6511 extrusion with a gold optical surface coating; the back is bare. The mirror is secured to a titanium mount with three aluminum 7075-T6 flexures to minimize thermal deflection of the mirror surface. The flexures are pinned to the mount then float bonded in place with Stycast 2850 epoxy to the mirror to reduce assembly-induced moment loading of the mirror. The mirror mount is bolted and liquid pinned to the SSM rotor shaft. The shaft is suspended in the bearing housing with a pair of angular contact ball bearings. The bearing pair is mounted within the bearing housing, which serves as the main housing of the SSM. Three radial legs extend from the housing and provide the mounting interfaces to the instrument. The encoder code disk

and motor rotor are bolted and liquid pinned to the shaft. The motor stator mount houses the stator, and attaches to the non-mirror end of the SSM. The motor stator mount is a separate part from the bearing housing so that it can be shipped to the motor vendor for stator build up independent of the rest of the SSM. Similarly, the mirror mount is a separate part from the shaft to allow concurrent, independent assembly. The motor mount, mirror mount, and rotor shaft are finished in Tiodize type II for corrosion protection. The bearing housing was not Tiodized; it was left bare since it is almost entirely covered with strip heaters and other thermal control components which require non-anodized surfaces to minimize the generation of thermal hot spots.

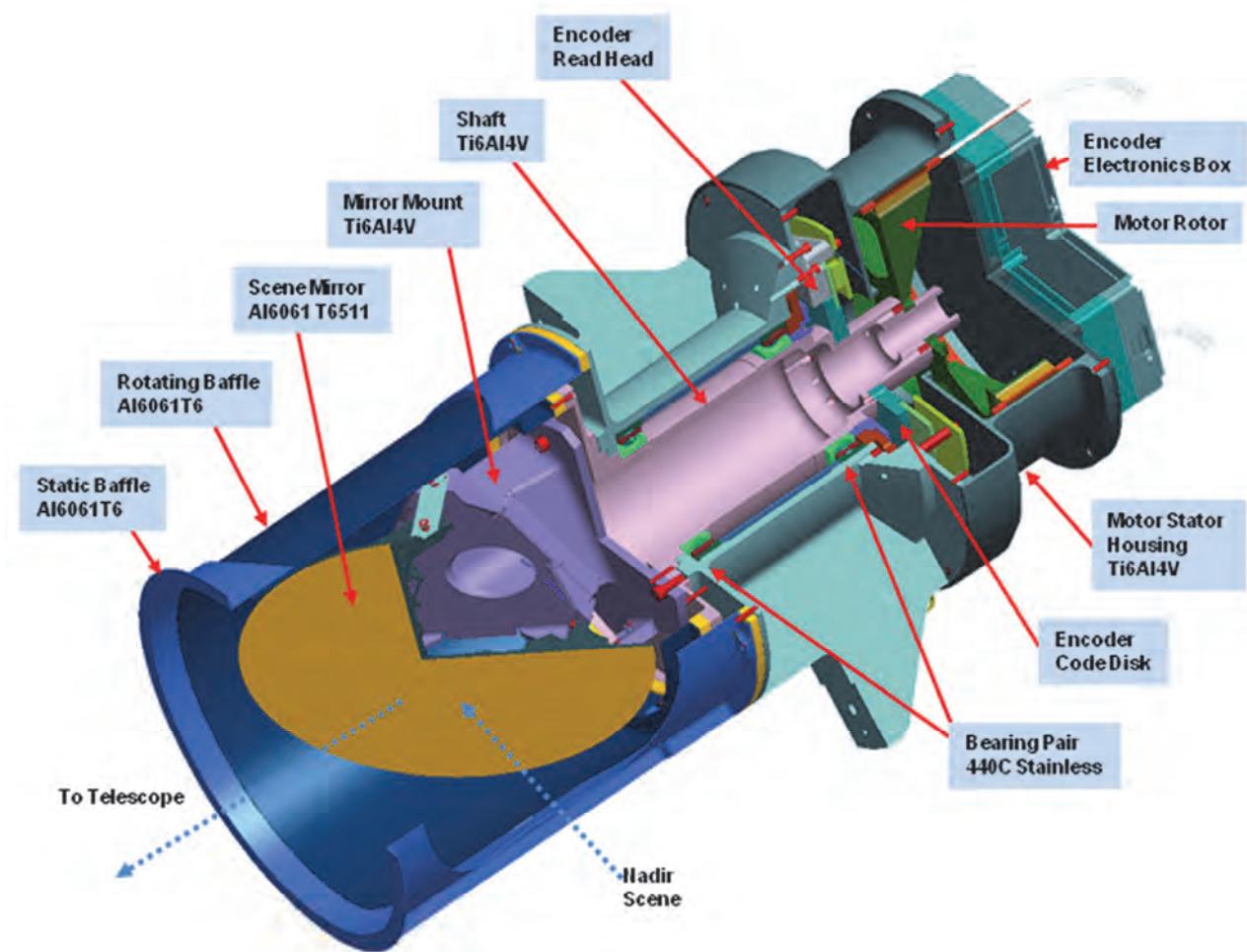


Figure 5. Internal detail of the SSM is shown in this quarter section view.

Several features were introduced to facilitate handling, reduce risk, and ease testing. Lift points and shipping interface points were independent of the flight interface points. This protected the precision flight interface from possible damage and wear from the numerous shipping and handling operations prior to installation in the instrument. A quartz optical cube was bonded to the motor housing to provide a boresight reference, facilitating SSM alignment and shimming into the TIRS instrument. Mirror pointing and stability measurements were referenced to this fiducial.

Baffles

A fixed aluminum baffle is fitted over the mirror end of the SSM, attached to the bearing housing. An aluminum rotating baffle, attached to the shaft, protects the back of the scene mirror and the mirror mount from the cold space view and hot blackbody view thermal loads, and reduces stray light introduced into the telescope.

Actuator

The SSM is driven by a frameless, brushless, direct-current “zero cog” motor with redundant windings and damping coils. The 2-phase, 48-pole, moving magnet motor has an air gap of 0.4 mm, and a motor constant of 1.79 N-m/amp (253 in-oz/amp).

Bearings

The SSM uses a duplex pair of back-to-back mounted, 70-mm bore angular contact ball bearings with a 25-degree contact angle. The bearings are bonded in place to ensure stability at the pradian level. They are hard preloaded to 50 lbf (222 N), with the preload calculated to drop to 25 lbf (111 N) at the operational cold temperature. The bearings use tri-cresyl phosphate coated 440C balls in a phenolic cage, with 440C races. Pennzane lubricant is utilized; specifically an oil + grease slurry (50% each by weight) of Nye 2001 ultra-filtered synthetic oil and Nye Rheolube 2000 grease. The oil is also vacuum-impregnated into the retainer. Lubricant retention is provided by labyrinth seals sized for < 5% mass loss over the mechanism lifetime. Lubricant surface migration is prevented by the application of Nye-bar surface barrier coatings within the labyrinth seals. Since twice the estimated bearing lifetime (including margin) was only 100,000 cycles, a full flight fidelity life test was not performed. Instead, a life test using only a pair of bearing cartridges, with identical preload and thermal conditions, was executed successfully.

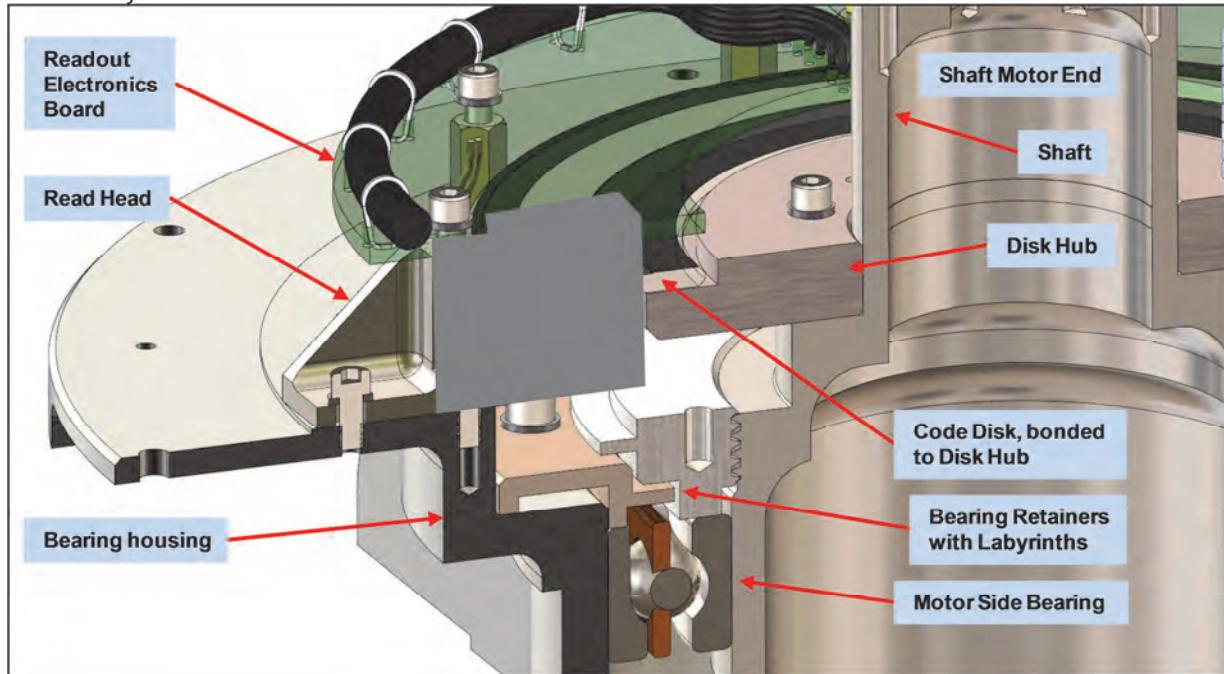


Figure 6. Optical encoder is shown in this section view mounted on the SSM with the motor removed.

Encoder

The SSM uses a 22-bit, pseudo-absolute optical encoder, which is an incremental unit that emulates an absolute encoder with a software counter and index pulses. The encoder has redundant read heads and drive electronics cards shown in Figure 7. The 125-mm code disk is fixed with liquid pinning to the rotating shaft. The read heads are fixed to the bearing housing. The encoder is shown in Figure 6. The

motor stator housing fits over the top of the read heads, encapsulating them; an integral contamination shield protects the encoder from any potential particulates coming from the motor area. The encoder drive electronics are housed in a dedicated enclosure, which is mounted to the cover of the motor stator housing. The encoder design has some flight heritage as it is based on the pseudo-absolute architecture from the National Polar-orbiting Operational Environmental Satellite System (NPOESS) Preparatory Project (NPP) satellite Cross-track Infrared Sounder (CrIS) instrument.

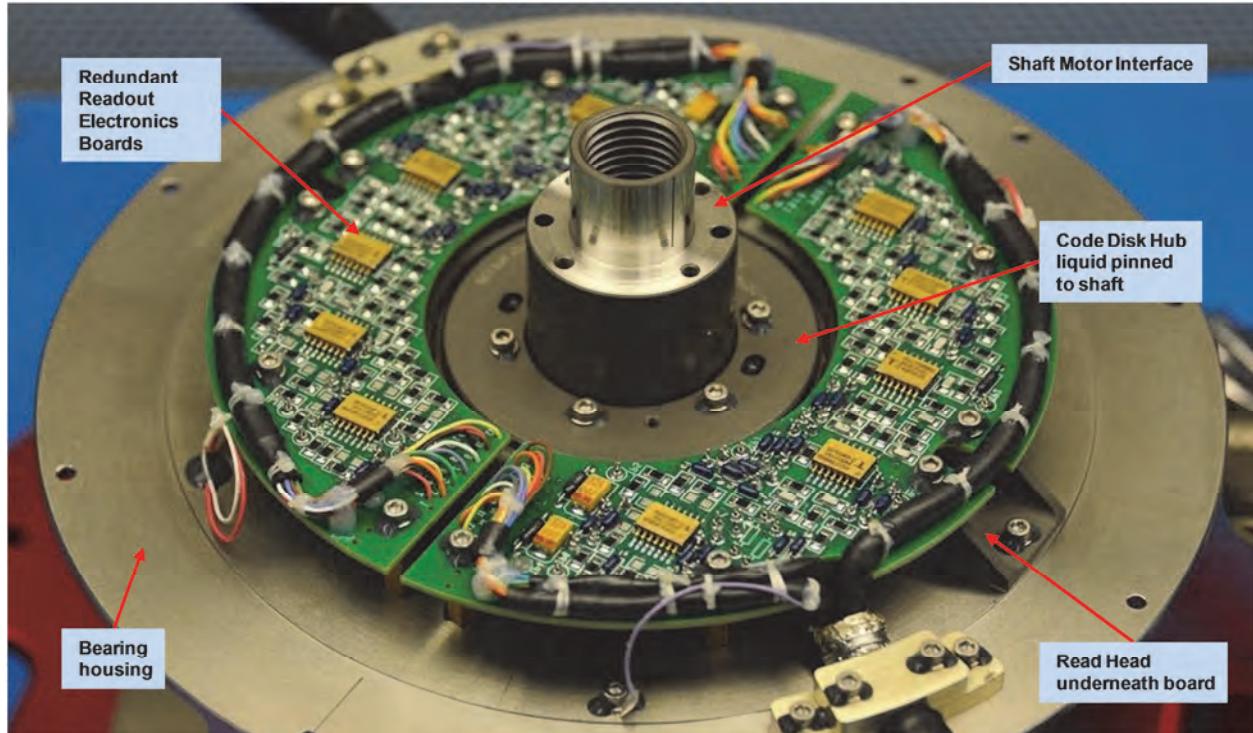


Figure 7. The optical encoder is shown mounted on the SSM with the motor removed.

Scene Select Mechanism Development Issues

Conceptually, the SSM is a very straightforward mechanism: it is single-axis, direct-drive, without a launch lock. However, a challenging stability requirement, a complex thermal gradient, a custom digital servo-controller, and most of all a compressed schedule complicated the development. Many obstacles were encountered and overcome; the most significant technical issues are described below. Schedule and management issues also occurred but have been described previously¹.

The importance of functional breadboards

At the beginning of the development effort, the control engineers required hardware that could be used to develop the arc-second-level servo controller be available much earlier than we could expect to receive the actual motors and encoders. The hardware would need to have at least a 22-bit encoder and a similar motor to be useful to the development.

A commercial 24-bit absolute encoder was procured from the same vendor that was to deliver the flight unit. These units were available on a short delivery. The digital output from this unit was identical to that which would be delivered for flight; i.e., from a telemetry standpoint, it was electrically identical. A spare 2-phase, frameless brushless DC motor that was similar in performance to the flight motor was fortuitously available. A commercially available back-to-back duplex (DB) bearing pair equivalent to the flight design was quickly procured.

A simple aluminum bearing housing and spindle were fabricated, and the bearings installed with a spring preload. The frameless motor was installed at one end of the shaft, and the encoder code disk and read head installed and aligned at the other end. While this configuration did not exactly mimic the SSM (which has the motor and encoder on the same end of the shaft), this was adequate for initial controls development.

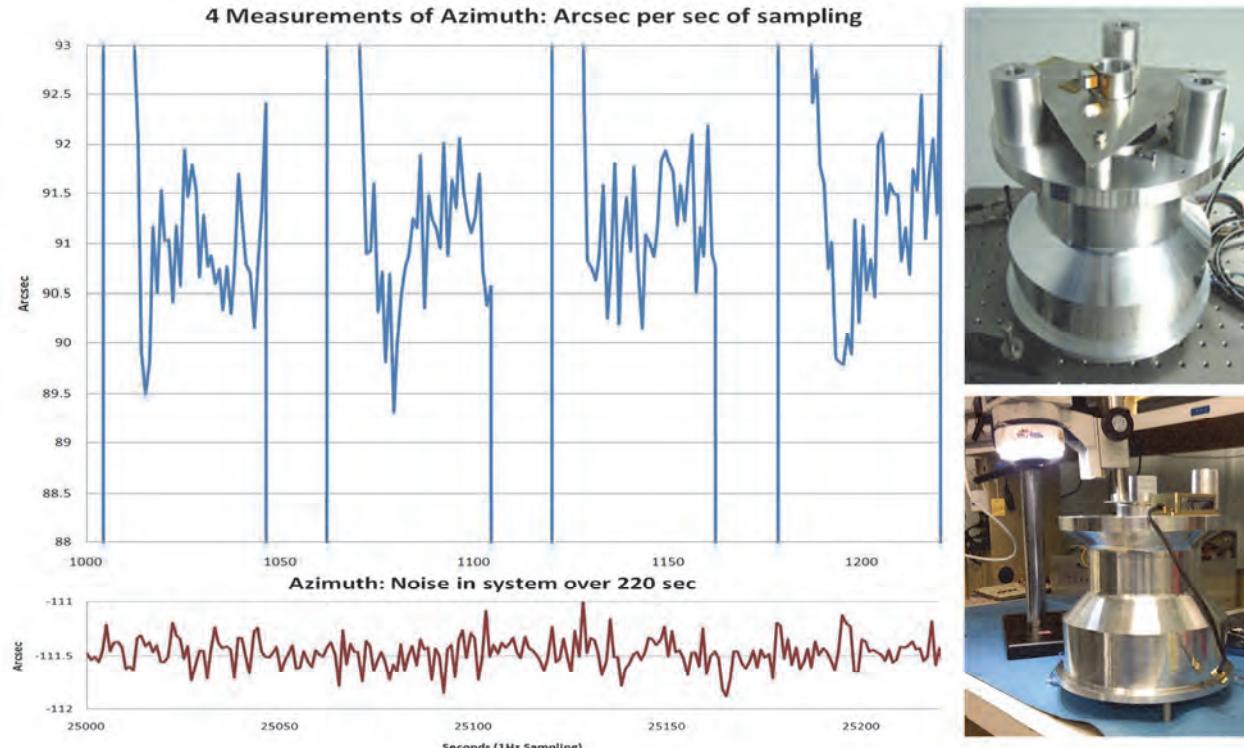


Figure 8. The SSM functional breadboard used a leftover frameless motor from another program mounted with commercial bearings and an industrial 24-bit encoder to demonstrate positional stability that exceeded the SSM requirements in a laboratory environment. Stability measurements were within 2.5 arcseconds with less than an arcsecond of noise.

This breadboard unit was available for use over 6 months before the encoders were delivered. This allowed the control electronics team to build a set of functional breadboard electronics much faster than if they would have waited for the flight hardware. An optical cube was bonded to the shaft, and an autocollimator was used to measure the stability and repeatability of the shaft position. This allowed 24-bit positioning stability and knowledge to be demonstrated in the laboratory. This was an important technical milestone which gave program management confidence that the SSM controller could be delivered on schedule. The unit, and some sample performance data is shown in Figure 8.

Lesson Learned: Create a functional breadboard using components that can be procured quickly as early in the program as possible. These components do not need to be expensive. It will facilitate breadboard-level controls development, demonstrate performance in a laboratory setting, and potentially identify technical issues early.

Critical assembly procedures should be practiced to reduce risk

In order to meet the arc-second-level stability requirement, critical bearing shaft and bearing housing surfaces had to be ground to tight tolerances and the bearings epoxied in place. Then the critical encoder code disk mounting surface on the shaft and the read head mounting surfaces on the bearing housing are ground true to the as-assembled spindle axis. These operations occurred at the encoder vendor which

allowed the encoder to be “built up” directly onto the flight hardware. This would save many weeks of development time; the vendor did not have to build a GSE spindle, and calibration testing could occur on the flight spindle. It also saved the time of de-integrating the encoder system from the GSE spindle and re-integrating (and re-calibrating) onto the flight spindle.

This process meant that the bearings would be epoxied in place at the encoder vendor. Since this would clearly be a risky process (epoxy could get into the bearings), a practice bearing shaft and mechanism housing were fabricated from aluminum. These breadboard parts, with a flight equivalent, commercial grade DB bearing pair, were used to validate the bonding procedure. A dry build, where the bearings are installed without epoxy, was done to fit check all of the components prior to the wet (with epoxy) build. NASA engineers were on site to supervise the dry and wet build operation, ensure that no epoxy had migrated onto the bearing faces, and verify that proper preload was applied. The process was successful, and prevented a major mishap during the flight procedure.

Many months later, during the flight bearing installation procedure, it was noticed by vendor technicians that the flight bearings did not look correct during the build; the wrong face of the bearing was visible. Further inspection revealed that the back-to-back preload marking on the outer race of the bearings had been erroneously reversed by the bearing manufacturer. If the bearings were installed according to the preload markings, as specified by the procedure, the bearings would have been installed face to face, as opposed to back to back. This error was identified because the procedure was practiced (with non-flight, correctly marked bearings), and the assembly technician and supervising engineer knew which side of the bearings should be visible in a correct installation. If this had not been noticed, it is possible that the error would have been allowed to occur on the flight and flight spare unit as all of the flight bearings were incorrectly marked, not just one pair. The error would not have been discovered until very late in the program during environmental testing, when the SSM flight and flight spare would not meet stability requirements.

The only corrective action would have been to disassemble the SSM and to assemble a new bearing housing. This would have taken several months and would have been devastating to the program. Another option would have been to fly the unit with degraded performance, resulting in lower data quality. This was avoided thanks to a sharp-eyed engineer noticing that the dry build installation did not appear correct, even though, according to the markings on the bearings (and per the installation procedure), they were installed correctly. A review of the documentation provided to the bearing vendor showed that the bearings were incorrectly marked by the vendor. The markings were not inspected upon delivery as they were not removed from their sealed bags until installation to minimize potential contamination.

Lesson Learned: Practice critical procedures with expendable hardware. The same personnel that practice must be the same that assemble the flight hardware. Supervisory engineers must be expert in all aspects of the operation so subtle errors, which may be overlooked even by experienced technicians and quality assurance inspectors, can be avoided.

The importance of preload analysis

The SSM has the scene mirror at one end of the rotating shaft and the motor and encoder at the other. The scene mirror shares a view of the warm Earth and a cryogenic telescope. The mirror edge is within 0.5 in (12.5 mm) of a 150K infrared transmission lens and cold shroud. This drives the mirror to be cold, about 0°C, and the optic mount at 2°C. At the other end of the mechanism, the SSM motor is dissipating power and tends to be warmer, up to 21°C. In addition, the bearing housing has heaters which cause a hot region between the bearings. The overall result is a combined standing set of axial (between the bearings) and radial (across the races) gradients. However, the axial and radial gradients were different for the motor end and mirror end bearings.

A calculation of what preload was to be applied at room temperature, such that the system would cool down to the operational preload of 25 lbf (111 N), was undertaken. An initial, simplified calculation estimated that the operational thermal conditions would cause little change in the preload applied at

ambient conditions; the axial and radial gradients would cancel each other out. However, this analysis did not consider the differing conditions between each bearing, and indeed it was unknown how to create this complex gradient case in current bearing analysis codes such as COBRA and Bearings10C.

A bearing specialist was consulted and a bearing analysis code was modified to consider the dual gradient case. The results of the new analysis showed that the preload would decrease with temperature, and the ambient assembly preload should be 50 lbf (222 N). This result was counter intuitive; in a hard mounted, DB configured bearing pair, preload usually increases as the shaft cools relative to the housing. This analysis showed just the opposite was occurring. The gradients combined to decrease the preload as the temperatures of the mechanism decreased.

Due to the new analysis results, the ambient assembly preload was doubled to 50 lbf (222 N) at assembly. While preload was not directly measured after assembly, performance of the life test bearing cartridges and environmental test performance of the flight SSM indicate that the operational preloads were adequate.

Without the combined gradient analysis, we would have preloaded the bearings to 25 lbf (111 N) at ambient; which would have yielded a low operational preload (close to zero!) likely resulting in our not meeting the stability requirement and potential ball sliding leading to lubricant degradation.

Lesson Learned: Do not underestimate preload analysis for precision positioning applications if your bearings are subject to complex thermal conditions. Many resources exist within the space mechanisms community that can support complex preload analysis, and they should be utilized.

Lesson Learned: For precision pointing mechanisms in harsh, poorly defined or complex thermal environments, consider a compliant bearing support technique, such as a preloaded, diaphragm-mounted outrigger bearing to maximize flexibility to the unknown thermal conditions without sacrificing precision. Diaphragms are usually larger in diameter than a typical hard mounted or compression spring preloaded configuration and it is better to allocate the additional volume required during the conceptual design phase than attempting to acquire it later in the program.

Heritage does not mean perfect

The architecture of the 22-bit encoder used by the SSM was chosen based on heritage from a previous mission, with some modifications as many heritage board-level, radiation-hardened electrical components were no longer manufactured. Upon delivery of the encoder unit, already built into the spindle assembly at the vendor, encoder function was verified, the motor was installed and the rest of the mechanism built up. The encoder position signal was used for closed loop position control, and motor commutation.

Initially the SSM function was demonstrated successfully in laboratory conditions. Four months before delivery, just before environmental testing of the SSM was to begin, the position error detector in the Mechanism Control Electronics (MCE) began to trigger. The error detector is a watchdog that triggers the motor to power off and resets the controller whenever the difference between the 24-bit commanded position and the 24-bit encoder position exceeds a user-defined threshold for more than 4 consecutive 200-millisecond samples³. The threshold value is set to ~2 milliradians; this is eight times larger than typical startup transients. Note that the MCE is based on a 24-bit absolute position sensor, but the encoder that was flown was 22-bit. This is because the initial MCE development was done using a commercial 24-bit absolute encoder. The flight 22-bit encoder position output was right padded (addition of 2 extra bits of zero value) to 24-bit to minimize changes between the breadboard and flight MCE.

The error detector was triggering because the most significant bits of the encoder position output would reset to zero values, but not when the encoder was actually resetting. This was the error. The reset occurred randomly, on timescales from hours to days, on both the A side and the redundant B side of the encoder system. At first, electromagnetic interference (EMI) due to inadequate grounding or non-flight harness was thought to be the culprit, due to the sporadic nature of the occurrence. Grounding schemes

and harness fidelity were improved, and the error event frequency decreased, but still occurred. The encoder vendor attempted to replicate the error at their facility with spare units that were not yet delivered, but could not. This indicated that the cause was due to some condition with the flight configuration, and was related to electrical noise.

A detailed noise review of the MCE and proprietary vendor encoder electronics was undertaken, and the problem was traced to a specific point in the encoder readout circuit. Of the 22 binary bits of position information returned by readout circuit, the most-significant bits were generated by a counter circuit. The least significant bits were generated by an interpolation circuit. The reset was traced to the counter circuit. The design of this circuit had heritage. However, analysis showed that it was potentially susceptible to noise. The noise generated by the MCE, even though of low level, was adequate to occasionally reset the counter bits to zero, corrupting the encoder readout. Unfortunately, being four months before delivery, there was no time to rework the MCE or the counter circuit. Random resets of the SSM would have been unacceptable to instrument operations and would greatly reduce science efficiency. A work-around had to be developed.

The error would occur as the upper most significant bits (MSB) of the counter were reset; the lower interpolated bits were unaffected. A solution was developed which assumed that the mechanism most significant bits were not changing; i.e., the mechanism was stable to 1.3 arc-minutes so the upper bits of the error signal would be zero. The corrupted bits could be ignored, and precision position maintained using only the least significant interpolated bits³. The reset could occur randomly in this mode and not affect the positioning of the fine positioning mirror. However, there is no way to determine if a reset event actually occurs while in this mode. This mode was referred to as the fine pointing mode.

The only drawback to the fine pointing mode is the possibility of violating the underlying assumption that the actual error will not exceed the range of the lower bits. If the real error grows too large, this assumption is violated, and it is possible that the controller could drive to the wrong position. To ensure the limit would not be exceeded, an operational measure was put into place. The mirror should never be commanded to move from position to position while in fine pointing mode.

The fine-pointing mode effectively mitigated the noise-induced, MSB random reset error and allowed operations of the instrument to be unaffected. It should also be noted that the reset error never occurred again once the SSM and MCE (with flight harness) were integrated into the instrument, suggesting noise in the test setup as the culprit.

Lesson Learned: Heritage in a system should not be used as an excuse to reduce analysis. A signal integrity analysis, which would have identified the counter circuit noise vulnerability during the design phase, was not done in order to save time, and justified because of the heritage of the system.

Never skip the bake out

At the conclusion of thermal vacuum testing of the TIRS instrument, a small smudge was discovered on the scene mirror, at the cold end of the SSM. Further examination showed not only the smudge, but a fine layer of contamination, looking much like a light fogging of the entire mirror surface, was discovered. The smudge and contamination are shown in Figure 9. Further analysis showed that this was a film of Pennzane, which had outgassed from the bearings and onto the cold optical surface of the scene mirror, and the cryogenic lens surface adjacent to it.

The bakeout step was omitted from development at the vendor in order to save schedule. The unit would have had to leave the vendor facility for a vacuum bake out, and this would take at least 2 weeks assuming immediate availability at the external bake out facility, or a NASA facility. A thermal exposure test was done (not in vacuum) at the encoder vendor of 50°C and the risk was assumed by the project.

There appeared to be no lubricant outgassing issues during SSM component thermal vacuum testing. However, the contamination could have been building up during component level testing, and continued

to build up to a visibly detectable level during the instrument test. It should be noted that the film did not degrade the science performance of the instrument or the performance of the SSM during the thermal vacuum testing. The film collected on the scene mirror and the first surface of the cold telescope lens; the two coldest surfaces closest to, and below the bearings. There was no detectable Pennzane contamination above the bearings near the warmer encoder code disk and encoder read head optics. The contamination was left in place as it did not affect the instrument and was not worth the cleaning risk.

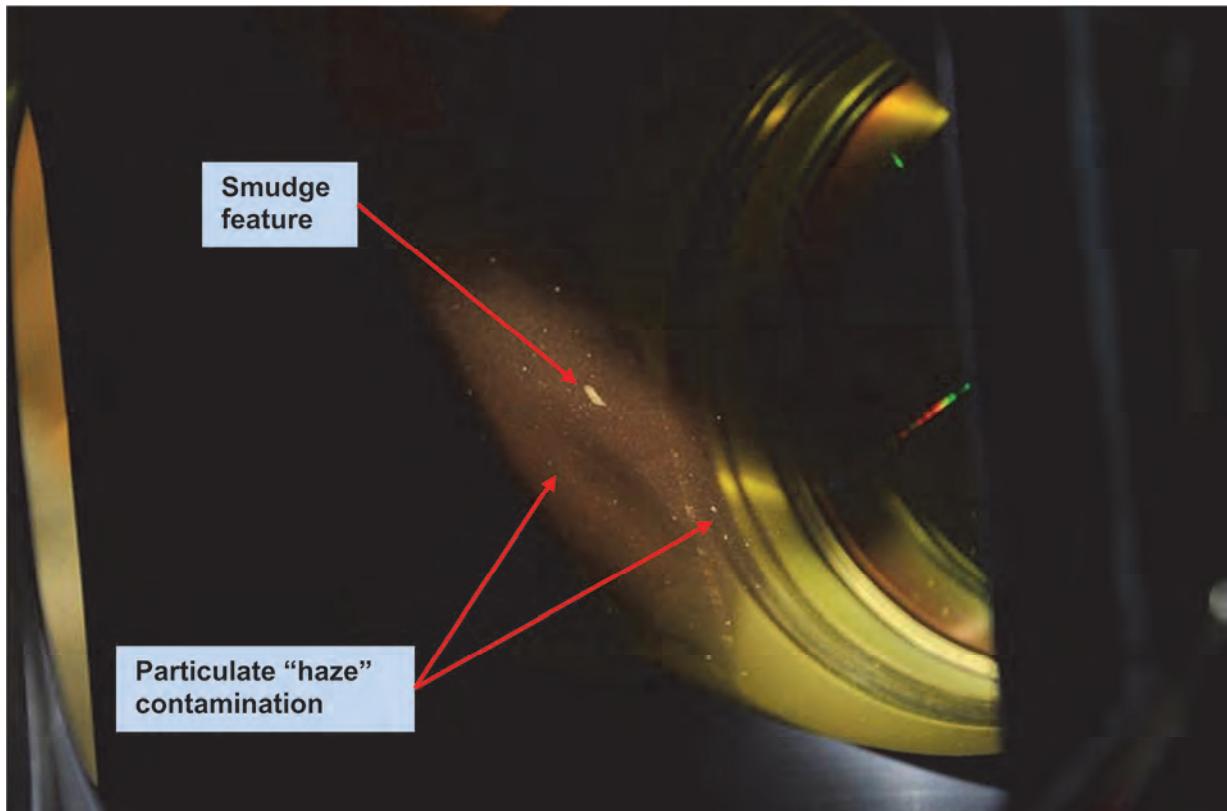


Figure 9. After instrument level thermal vacuum, a smudge was detected on the scene mirror and a haze of pennzane was discovered on the mirror surface. The figure shows the surface of the scene mirror as viewed from the exterior of the instrument.

Lesson Learned: While the contamination did not affect the instrument or mechanisms performance, a bake out would have prevented it. If the instrument operated in different wavelengths or a different lubricant was used, science performance could have been adversely affected. The bake out should have been done after spindle assembly but before installation of the optical encoder and scene mirror to prevent contamination of the main optical surface, code disk or read head optics. It was again confirmed that contamination builds up on the coldest surfaces close to the outgassing points, and even the best labyrinth seal, properly coated with a barrier film, will not prevent the escape of outgassed lubricant. Note that even with a bake out, lubricant outgassing will never be completely eliminated, only significantly reduced.

Lesson Learned: Visible and high-resolution photographic inspection of critical mechanisms optical surfaces must occur before, during (if possible) and after critical development events if possible. Proper photographic documentation did occur at the instrument level but at the mechanisms component level was of inadequate resolution to be useful for surface contamination detection.

Earth Shield Deployment Mechanism

The ESDM consists of a pair of spring-driven hinges and a release/restraint mechanism which allow a large earth shield panel to rotate 90 degrees from the stowed to deployed position. The large, 2.5-m² earth shield is a composite panel with carbon fiber facesheets and aluminum honeycomb core; it is shown in Figure 10. The overall architecture has all active elements housed on the instrument side of the hinge line; no harness is passed through the hinges. Triangular mylar "wing" sheets, used to close out the ends of the earth shield panel, were folded between the earth shield panel and the radiator panel. These wings were pulled along and unfolded as the earth shield rotated to its full deployed position. The major requirement was the instrument/spacecraft uncompensated momentum requirement; no more than 158 N·m of uncompensated torque and 25 Nms of momentum could be generated by this deployment. The driving requirements for the ESDM are summarized in Table 2.

Table 2. ESDM Driving Requirements

Requirement	Value
Earth Shield Dimensions	78 x 50 x 0.625 inch (1.98m x 1.27m x 15.8 mm)
Earth Shield Mass	24.9 lbm (11.3 kg)
Deployment Angle	90 degrees
Deployment Time	≤ 60 seconds
Uncompensated Momentum	≤ 25 Nms
Uncompensated Torque	≤ 158 Nm



Figure 10. The Earth Shield shown in the stowed configuration during TIRS instrument integration.

Damped Actuator

The two ESDM latching hinges were based upon the deployable solar array panel hinges used on the Lunar Reconnaissance Orbiter (LRO) spacecraft. They were powered by stowed energy, using torsion springs. The torsion springs (one in each hinge on the hinge line) were sized to provide positive deployment torque margin even if one of them failed. Each spring hinge contained a locking pawl which engaged when the deployment angle reached 90 degrees. This prevented any type of backdriving, and positively locked the panel in the deployed position. In order to accommodate thermal expansion and contraction of the panel, one of the hinges had axially floating bearings that were compliant to small linear deflections along the hinge line axis.

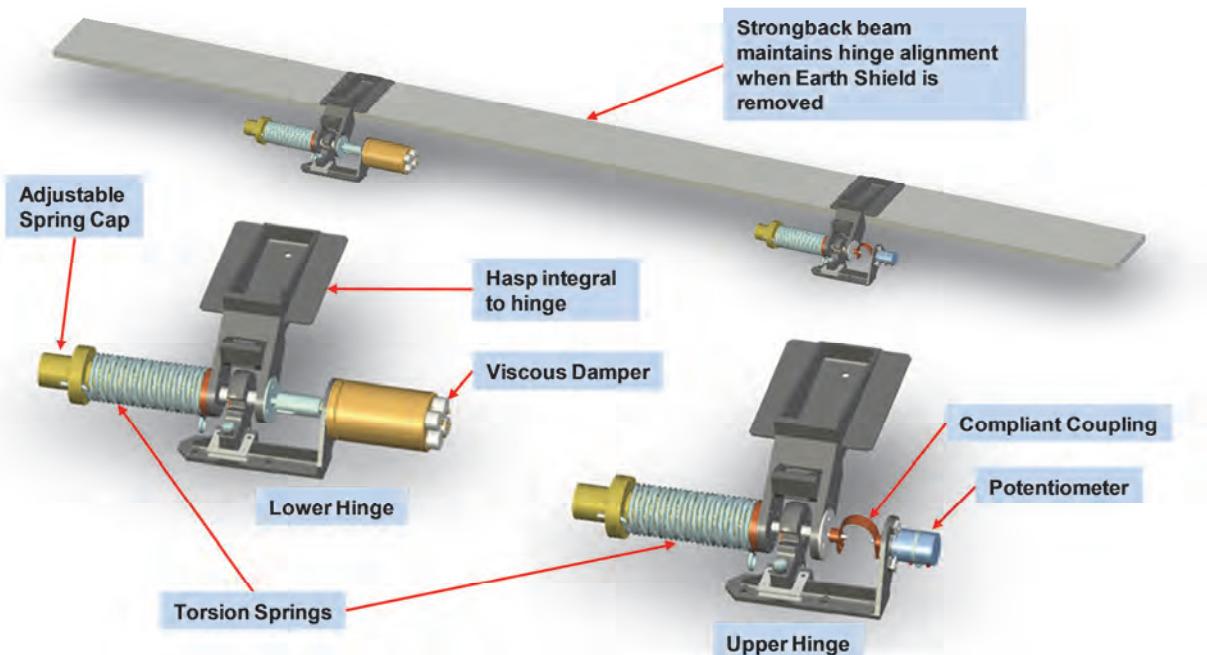


Figure 11. The Earth Shield hinge system. Two spring-powered hinges drive the deployment. One hinge mounts a rotary damper to significantly reduce the angular velocity while maintaining high torque margin. The other hinge mounts a potentiometer to provide position feedback. The strongback beam allows the hinges to maintain relative alignment when the Earth Shield is removed.

The torque generated by the drive springs had to meet the torque margin requirement specified in the GSFC Gold Rules; it also had to meet the one failed spring success criteria. This resulted in the springs being strong enough to deploy the earth shield with enough velocity to exceed the uncompensated momentum requirement. In order to not exceed this requirement, a viscous fluid damper was used to reduce the deployment velocity, without significant reduction of the deployment torque margin. The heritage LRO viscous damper was utilized.

Due to the large size of the earth shield panel, it is removed from the instrument before shipment to the off-site spacecraft integration facility. The panel would be re-attached after the instrument was integrated to the spacecraft. To ease detach/re-attachment hinge alignment issues, and to facilitate testing, an intermediate stiff beam structure, or “strongback”, was introduced between the hinges and the earth shield panel. The hinges attached the strongback to the instrument, and the earth shield rode on the strongback. The earth shield could be easily removed from and reattached to the strongback without disturbing the hinge alignment. This configuration allowed the ESDM to be tested without disturbing the hinge alignment, and without the flight earth shield (using an equivalent inertia simulator).

Sensor

A potentiometer provided coarse position. The same model of potentiometer that was successfully flown on the LRO solar arrays was used.

Release/Restraint Device

A single-point, command-releasable restraint device was used to prevent the spring-powered hinges from deploying the earth shield. Two compliant snubbers were used to share launch loads with the hinges and the release restraint device.

The device used was an Ejector Release Mechanism (ERM). The model flown is rated for 1000 lbf (4.4 kN) of holding force. It utilizes a shape-memory alloy which, when heated, releases a threaded cap which is held in place with a ball lockup type of lock. It releases with very low shock. It is manually resettable, and no hardware change out is required between testing and flight; the same hardware that is tested is flown. The ERM-1000 is shown in Figure 12.

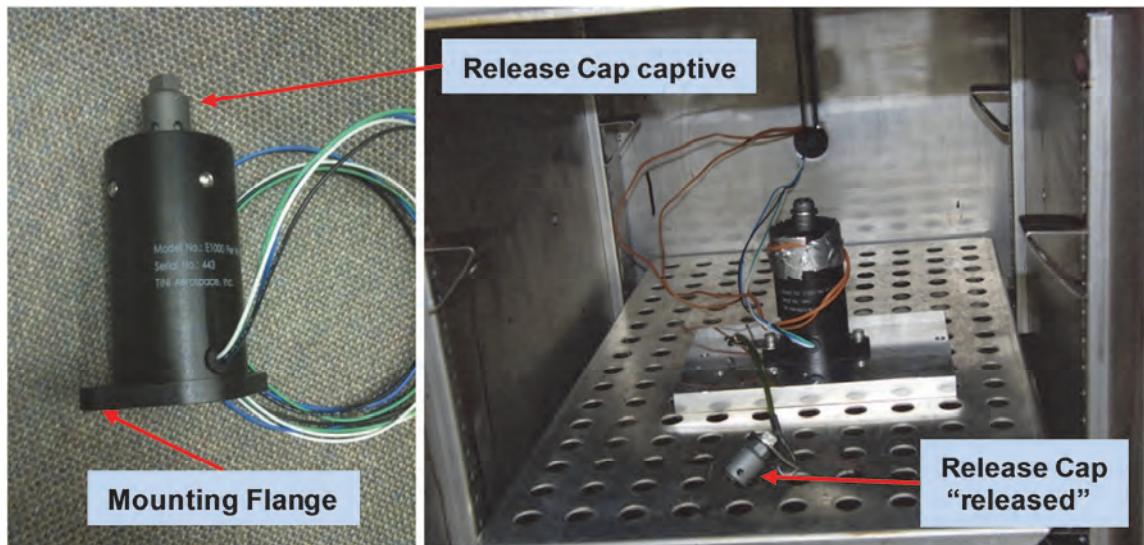


Figure 12. The ERM-1000 release restraint device shown on the left with the release cap captive, locked to the ERM. The figure on the right shows the ERM during component thermal testing with the release cap ejected after actuation.

The stock version of the ERM was modified slightly to work with the TIRS structure and electronics. The mounting flange, usually at the base of the device on the opposite end from the released cap, was moved to the same end as the released cap. This mechanical modification had heritage from other programs and was deemed low risk. Electrically, a 10-ohm in-line resistor was added to the heater circuit to better match our source current.

The ERM device is mounted to the instrument structure, and protrudes through the instrument radiator. The releasable cap attaches to the earth shield though a spring-loaded, bolt-catcher type compliant retraction interface, called the Coupler Retraction Mechanism, shown in Figure 13. This ensures that the cap clears the ERM completely upon release, and that the cap does not protrude beyond the interior surface of the earth shield, as this would slightly degrade the radiative performance of the shield. The mechanical contact between the structure and the earth shield at the lock down/release point is a matched radius cup and ball. This interface constrains all translations but is compliant to all rotations. To avoid the possibility of cold welding at this interface, dissimilar materials were used. The radiator side ball is aluminum 6061T6 with a type III hard anodized finish. The cone is titanium 6Al4V with a Tiodize® type II (Teflon® impregnated) finish. The ball and cup both have a large clearance hole through them that the ERM releasable cap and bolt catcher extend through. The cup and cone effectively isolate the ERM from earth shield moment and shear loads at the release point, allowing it to be loaded in pure tension.

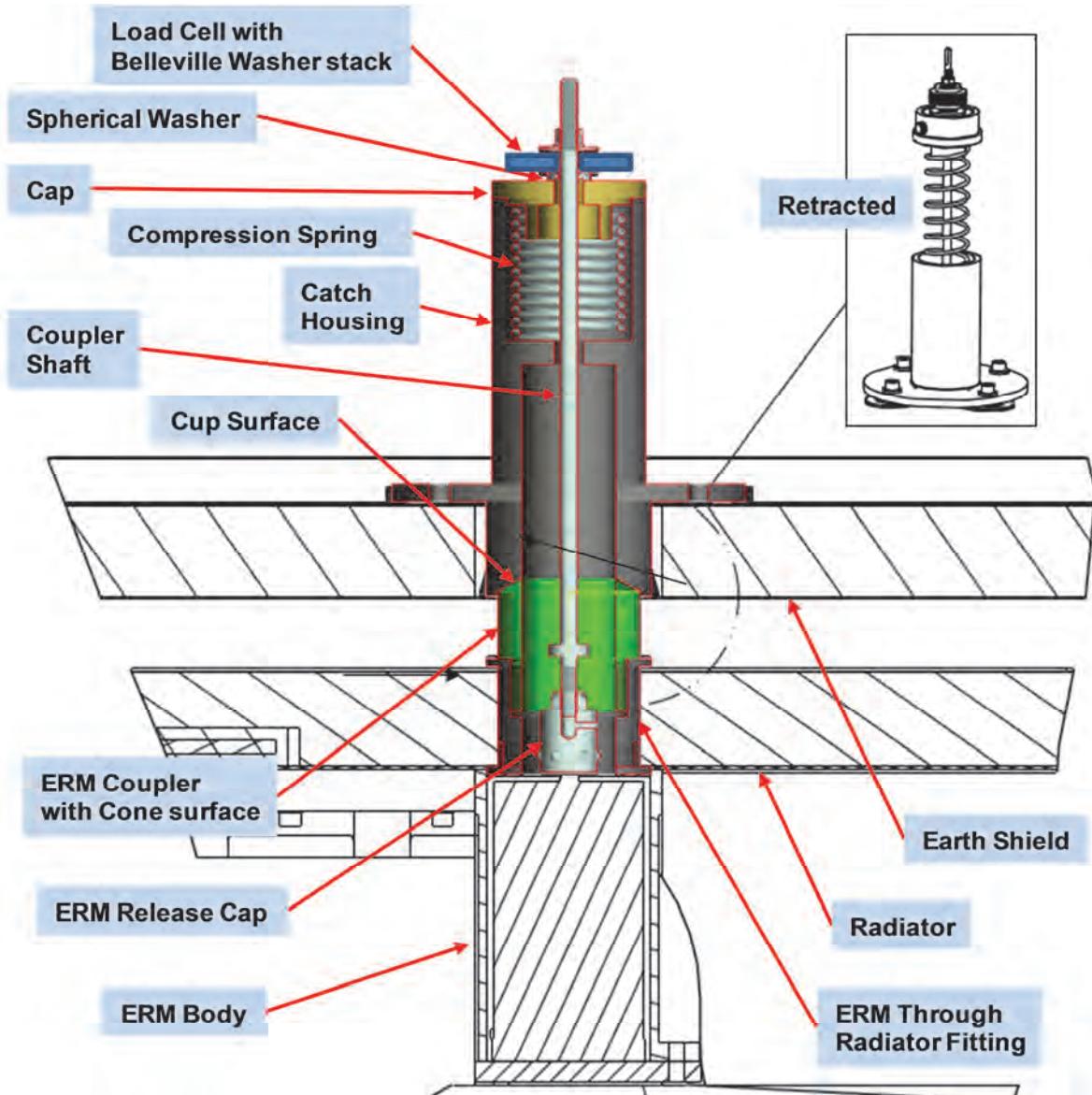


Figure 13. A section view through the ERM and Coupler Retraction Mechanism. The inset figure on the upper right shows the deployed configuration: The compression spring is fully expanded with the ERM release cap pulled into the catch housing.

A kick-off load was introduced into the stowed earth shield by bending it slightly. This was done by increasing the deflection at the restraint point, effectively pulling in at the center of the panel, reacting it against the snubbers and hinges. Due to this preloading, the panel was “bowed-in” when stowed. This bowing provided a kick-off load when the panel sprang back upon release, and obviated the need for dedicated kick-off springs.

Performance Testing Results

The ESDM underwent several deployment tests, with the velocity through most of the range varying between 2 and 5 degrees per second. The ESDM was deployed under ambient conditions, and in vacuum at room temperature and at -5°C. The thermal vacuum test is shown in Figure 14. Following acoustic and vibration tests, it was deployed again. All tests were successful and the results are shown in Figure 15. As is expected, the deployment time increased at cold temperature as the damper viscosity

increased. The analytical predictions were too fast by about a factor of 2 due to incorrect assumptions about the drag caused by the unfolding wings, which turned out to be much higher than predicted.

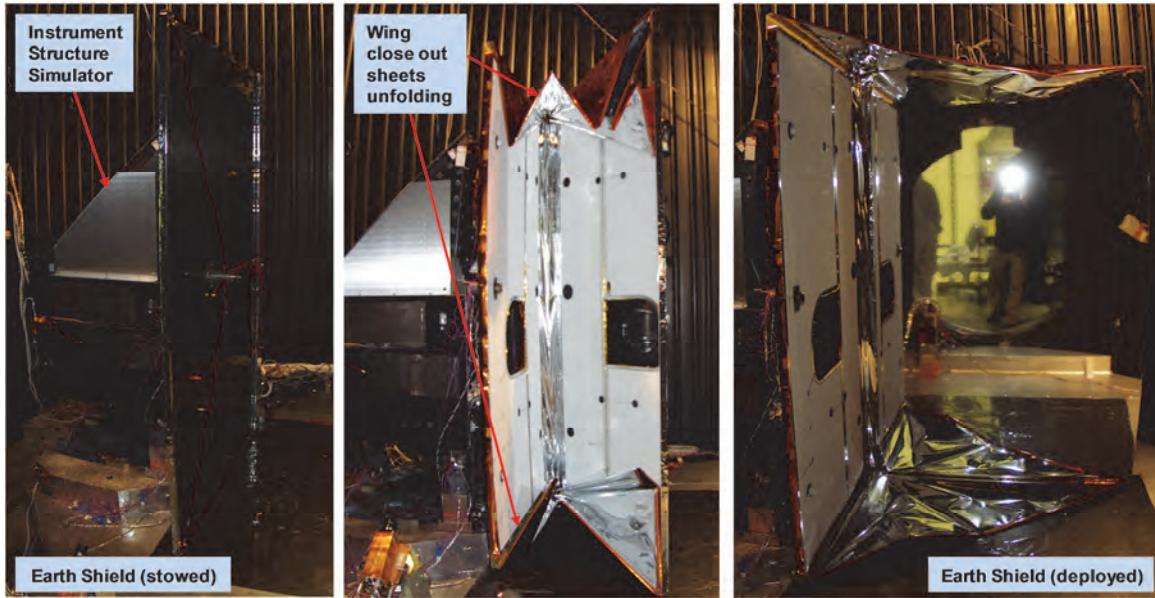


Figure 14. The Earth Shield and ESDM shown deploying within the thermal vacuum chamber after the successful cold vacuum deployment test. The drag torque from the wing close out sheets proved to be variable and made estimation difficult. Note the reflection of the chamber door and photographer's camera flash on the inner surface of the deployed earth shield in the right figure.

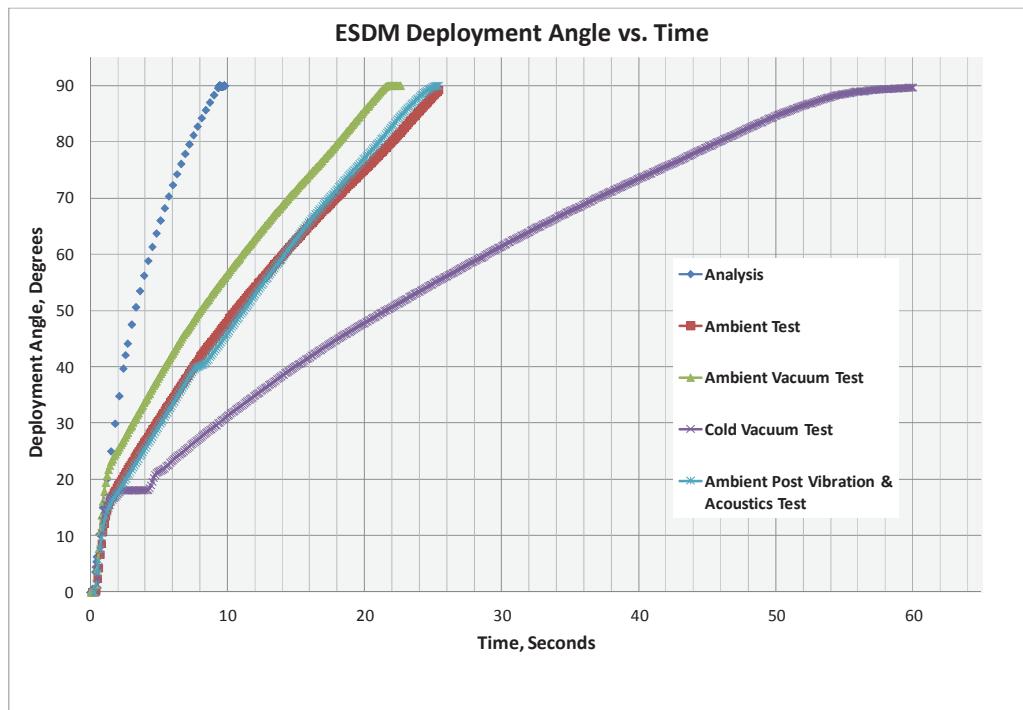


Figure 15. ESDM deployment analysis and test data. The ambient analytical prediction is the blue dots on the left, the ambient test data is the green, blue, and red traces, and the purple trace is the cold vacuum deployment data. Some of the non-linear behavior of the damper is shown in the purple (cold vacuum) test trace near $t = 3$ seconds. Also, the variable drag from the wings unfolding is shown on the blue (post environmental test) trace near $t = 8$ seconds.

Earth Shield Deployment Mechanism Development Issues

Use of a heritage design allowed the ESDM to change very little between the system requirements review and the critical design review, which was extremely beneficial due to the compressed schedule. The ESDM did not have any major developmental issues, but several notable minor ones.

A 4 factor of safety is there for a reason

The foldable mylar wing close out sheets made analysis difficult. Estimates made of the drag torque produced by the wings during the design phase were too low and assumed it was constant; i.e., not a function of deployment angle. The flight wings ended up much heavier than predicted. The wings drag torque varied with deployment angle, and did not vary consistently, but hysteretically. However, the high torque margin allowed the design to absorb the increased torque without modification.

Lesson Learned: High torque margins are extremely desireable in deployable mechanisms. The high factor of safety (usually = 4) used for non-conservative forces/torques in the design of the mechanism allowed for unpredicted behaviors to be compensated for.

Not everything is in the included documentation

The ERM device would self-release if manually reset while the unit was still cold. This occurred immediately after the successful cold vacuum test, when the unit was being reset. Fearing a defective ERM, we immediately contacted the vendor, and prepared to do an in-depth failure examination. The vendor stated that it is perfectly normal for an ERM to inadvertently release if reset at cold temperatures, and that there should be nothing wrong with the ERM. This was not mentioned in the documentation.

Lesson Learned: Communication with vendors is vital at all levels, down to the smallest component. Timely contact with the ERM vendor saved the team the effort of pursuing a failure review, and identifying alternative release/restraint devices.

Test harnesses may interfere with deployments

The ESDM performed as designed and experienced only a single failure during development testing. This failure was not due to the ESDM itself, but to test instrumentation. During the cold temperature deployment test, an accelerometer popped off of the strongback; harness running from the accelerometer to the chamber wall snagged on the strongback and prevented it from deploying the full 90 degrees. The ESDM deployed nominally after reattachment of the accelerometer, and the offending harness was rerouted so as to not interfere with the deployment even if the accelerometer popped off a second time.

Lesson Learned: Assume test components such as accelerometers and thermal sensors will fall off during environmental testing. Contingency harness control measures should be implemented such that when the sensors unintentionally fall off, they, along with their associated harness, will not interfere with instrument or mechanism operations. Examples of these measures could be harness safety lines and/or additional harness tie down points. Adequate test harness length should be available to accommodate these features if this is considered early enough in the test program.

Cryo-Cooler Launch Lock Mechanism

Even with internal compensation, reciprocating elements within the TIRS cryo-cooler were known to generate jitter. Throughout the TIRS instrument development, this jitter was specified to be below a threshold where it would interfere with instrument operations. A few months after the critical design review, the as-built TIRS cryo-cooler was shown to have significantly higher jitter than was specified. This jitter needed to be suppressed. Passive vibration isolators were implemented between the cryo-cooler and the instrument structure, but these isolators did not have adequate stiffness to support launch loads. A launch lock would be needed. Luckily, a single extra pyro channel remained unused in the instrument control electronics, and could be utilized. It was available as a pyro-activated aperture door mechanism was removed from the design after the preliminary design review, but the electronics to run it were left in

place. The CCLL would use this channel. Several flight spare ERM release/restraint devices were on hand as ESDM spares. These would be used as the schedule precluded obtaining other release devices, and the available control electronics were designed to actuate this particular device. Spare ESDM potentiometers were also available, and one was used as a sensor to verify the state (locked, unlocked, or somewhere in between) of the launch lock. The driving requirements for the CCLL are listed in Table 3.

Table 3. CCLL Driving Requirements

Requirement	Value
Keel Dimensions	17.24 x 19.48 x 8.50 inch (438 x 495 x 216 mm)
Keel Mass	90 lbm (40.9 kg)
Allowable Keel Deflection	< 0.015 inch (0.4 mm)
Stowed Frequency	≥ 60 Hz
Cold Operational Temperature	-40°C
Uncompensated Momentum	≤ 25 Nms
Uncompensated Torque	≤ 158 Nm

The cryo-cooler is mounted to an aluminum Keel plate which houses the compressors, expander, and cold heads. This Keel is suspended beneath the instrument -X panel, near the focal plane array (FPA). The first stage is coupled to the telescope 170K cold shields, and the second stage cold head is coupled to the 43K FPA. Both stages utilize flexible conductive link heat straps to provide a thermal conduction path that would not transmit jitter loads from the cryo-cooler to the FPA or shields. Circleflex™ damping flexures were used to provide passive vibration isolation between the keel and the instrument structure. Use of these flexures reduced the cryo-cooler frequency to levels which would damage the cryo-cooler at launch. The Keel Assembly is shown in Figure 16.

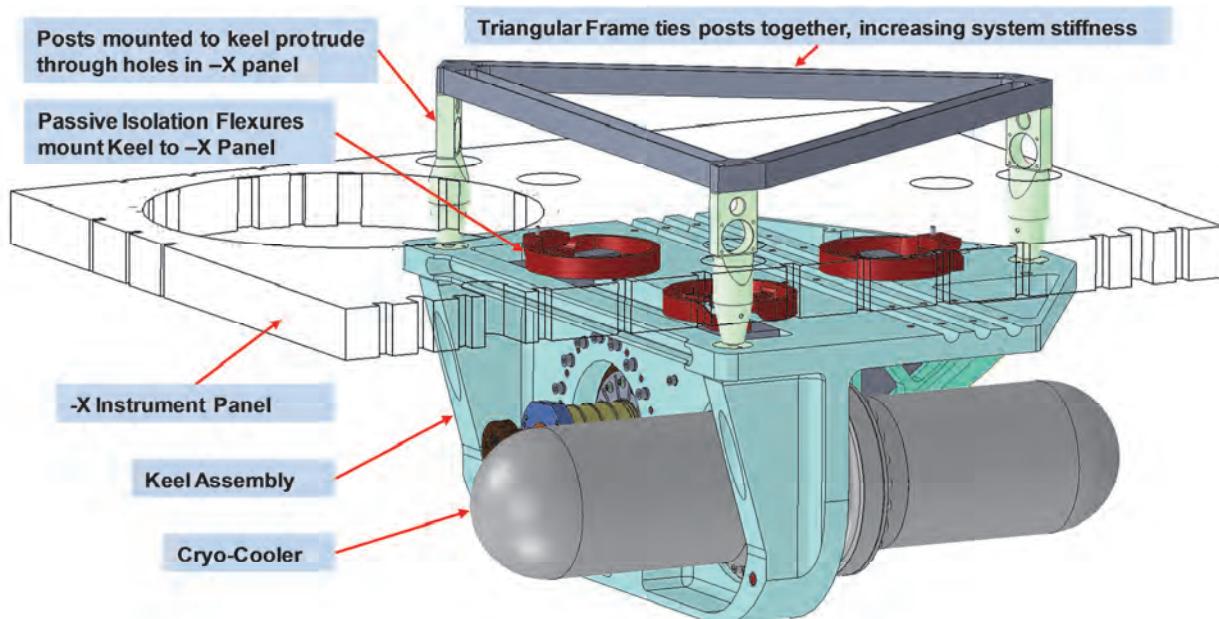


Figure 16. The Keel Assembly, as modified with CCLL interfaces is shown. The 3 posts were added to provide accessible interfaces for a launch lock mechanism mounted on the opposite (interior) side of the -X instrument panel. The triangular frame was added later to increase overall stiffness.

The only available volume available for the launch lock was within the instrument, opposite the externally mounted keel. Posts would have to extend from the keel through clearance holes (that would have to be cut) in the -X instrument panel. The lock hardware would restrain these legs.

To properly launch lock the cryocooler, it must be constrained in all 6 degrees of freedom. Only a single ERM-type release device could be used; hence the system could only be constrained at a single point. It was also desirable for the ERM to be mounted on the instrument exterior to facilitate easy access for manual resetting. Additionally, the cryo-cooler could never displace by more than 0.015" (0.38 mm) due to close clearances between the flexible conductive links and the FPA cold shield. Calculations showed that the flexures would displace the keel by no more than 0.010" (0.25 mm) when gravity was removed, or as the gravity vector changed when the instrument was rotated. The engaged launch lock carried the launch loads of the cryo-cooler keel, and when disengaged, allowed the keel to float on the passive isolator flexures.

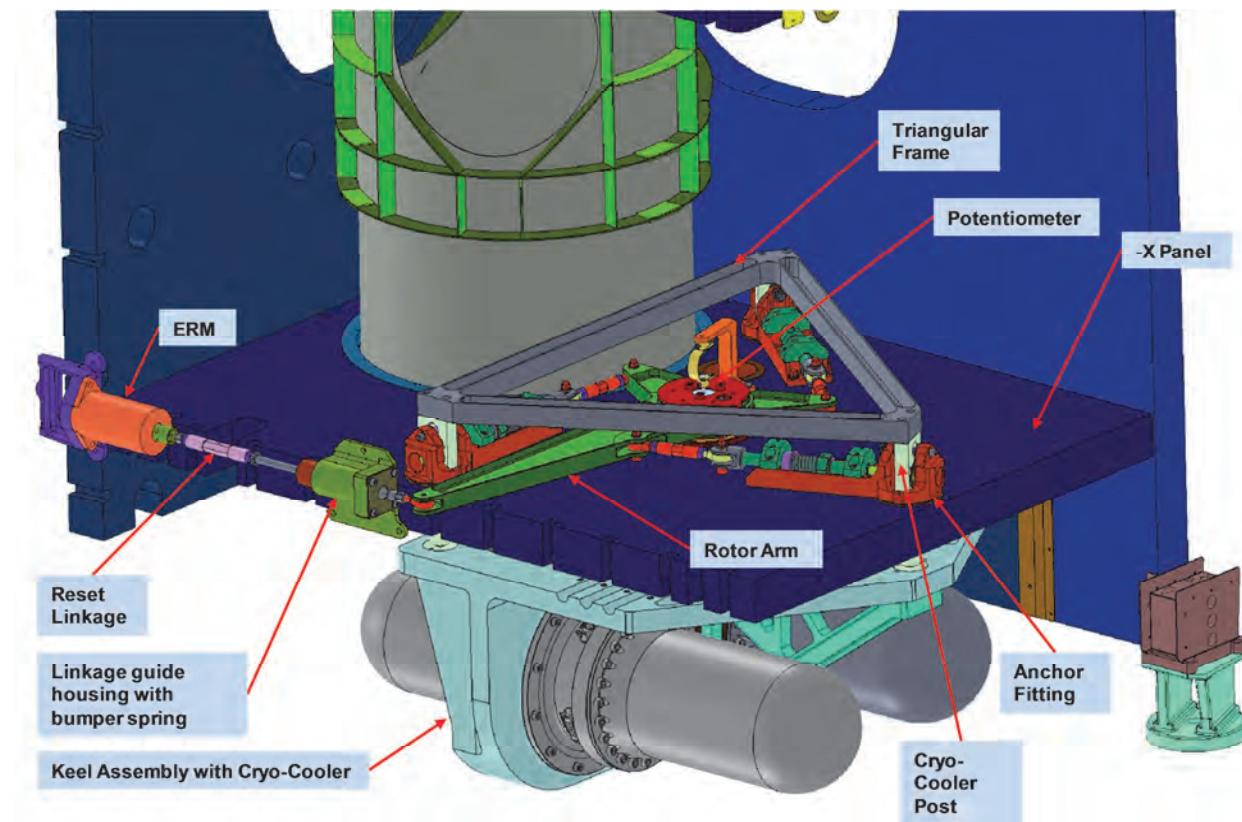


Figure 17. The CPLL Assembly, as shown with the instrument -Y and -Z panels removed. Note that the Rotor Arm protrudes through the -Y panel, and the ERM and Linkage Guide Housing are mounted on the exterior side of the -Y panel. A spare ESDM potentiometer is used to verify rotor arm position and indicate proper deployment. It is mounted to the -X panel underneath the rotation axis of the rotor arm, and is tied to the rotor arm using a compliant coupling similar to the one used on the ESDM.

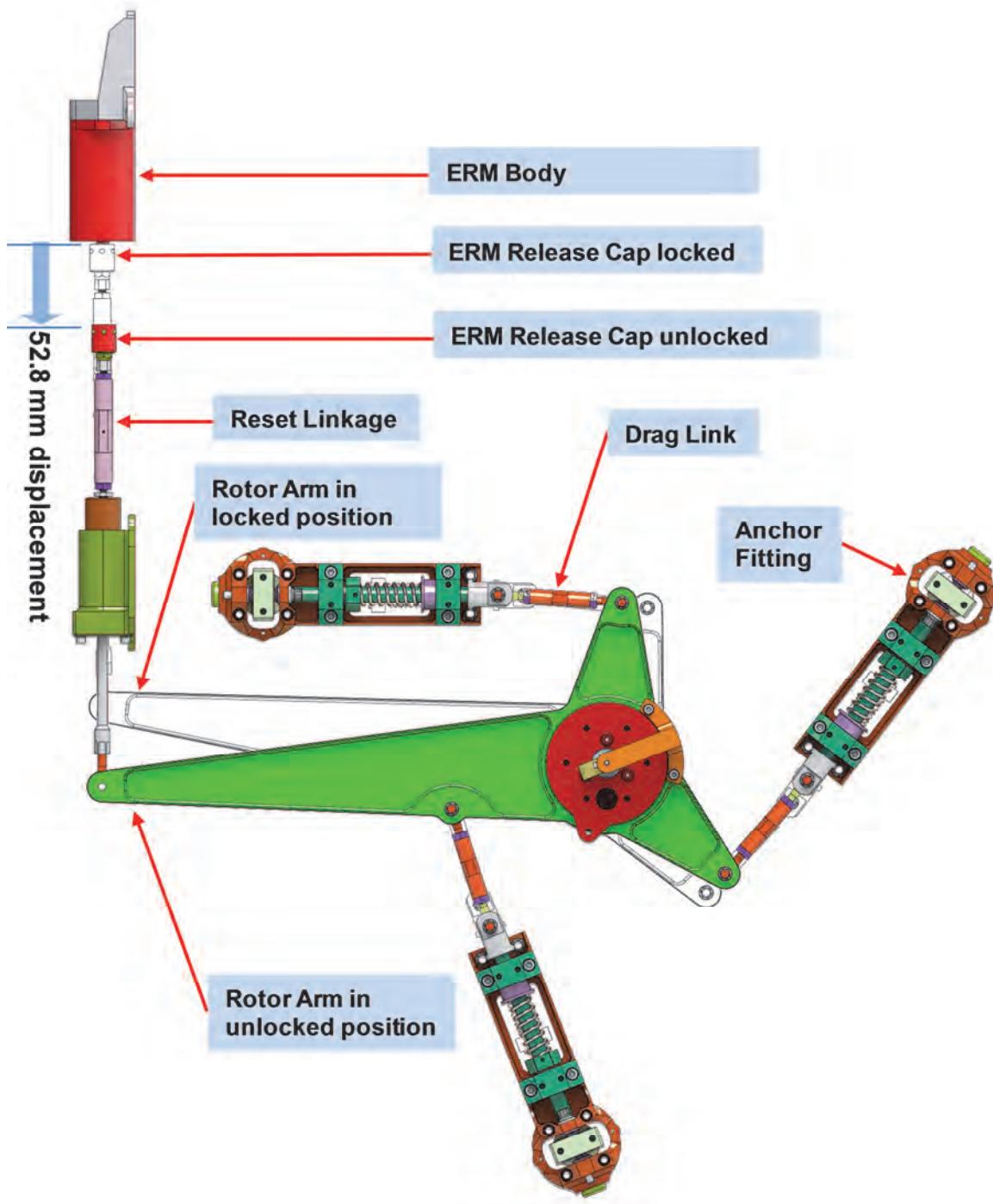


Figure 18. The overall architecture of the CCLL is shown above. The solid colored components show the launch lock in the unlocked position, with the ERM Cap released from the ERM body. The wireframe shows the position of the launch lock in the locked position, with the ERM Release Cap locked to the ERM body. The Rotor Arm rotates ~9.5 degrees between the locked and unlocked positions. Commercial grade tie rod end hardware was used in all of the linkages.

Pin Pusher Actuators

Several concepts were traded, with a 3-point constraint architecture selected. This used 3 drive pins on the instrument going into three holes on the cryo-cooler keel structure posts. The dimensional clearance between the pins and the holes is only 0.002 inch (0.05 mm). Each point constrained 2 translations and 2 rotations, providing a 2-2-2 degree of freedom kinematic lock. To release the launch lock, the pins were pushed through the holes by spring pistons. To facilitate resetting, the pins were not completely removed from the holes, and the holes were given a toroidal profile. The drive pins were stepped down so that a thicker diameter matched the toroidal hole diameter, and a thinner diameter provided adequate free clearance. The pins were pushed the distance required to remove the larger diameter pin length from the toroidal bushing hole engagement diameter to a seating hole in the anchor fitting. Each restraint point had a pin pushing, compression-type spring, as shown in Figure 19. Each drive pin was tied to a central rotor disk via a drag link. As the pins are pushed out of the engagement bushings, the rotor disk rotated approximately 9.5 degrees, as shown in Figure 18. If the rotor disk is not allowed to rotate, the pins are held in place and the springs are compressed. If the disk is free to rotate the springs are free to expand and push out the drive pins. The disk also couples the motion of all of the pin pullers together; if any single spring fails, the rotor disk rotation, powered by the surviving springs, will pull the pin with the failed spring.

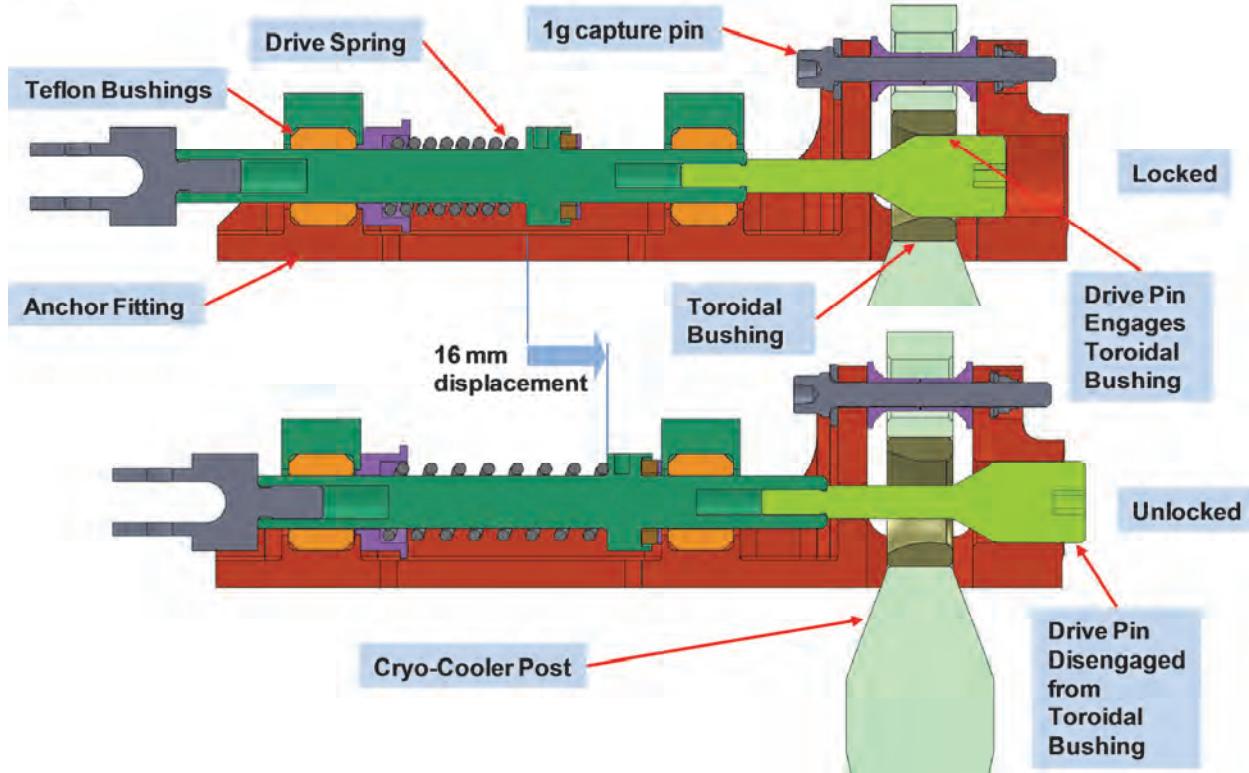


Figure 19. The spring-powered, pin pusher actuator shown locked (stowed) in the upper figure, and unlocked in the lower figure. The ERM restraint device prevents the compressed drive spring from pushing the the green Drive Pin out of the Toroidal Bushing. When the ERM releases the central rotor, the drive spring is free to expand and pushes the Drive Pin out of the Toroidal Bushing and into a guide hole in the anchor fitting. To reset the actuator, the the Drive Pin is manually pulled back through the Toroidal Bushing (via the Reset Linkage and the Rotor Arm) and connected to the reset ERM.

The titanium Anchor Flittings and Toroidal Bushings had a Tiodize® type II (Teflon® impregnated) finish. The Drive Pins are made of aluminum bronze, CDA 63020 per AMS 4590B. A light film of Braycote

Micronic 602EF grease was applied to the Drive Pin, and to the sliding surfaces in the anchor housings and the toroidal bushings.

Release/Restraint Device

The ERM restraint device prevents the rotor disk from rotating. When fired, the ERM releases the disk, the pins retract, and the cryo-cooler unlocks. The ERM is not coupled directly to the rotor disk. An extension arm runs from the rotor disk through a clearance slot in the instrument -Y panel. A tie rod runs from the extension arm to the ERM mount. This allows the ERM to be mounted on the instrument exterior, facilitating reset access. A potentiometer is used to indicate rotor position, providing a positive indication of the locked or unlocked state. The ESDM potentiometer was used, as spares were immediately available. Telemetry lines to support this sensor were also available in the control electronics.

Cryo-Cooler Launch Lock Mechanism Development Issues

To reduce risk and expedite schedule, a functional breadboard unit was fabricated quickly to validate the overall architecture, and the flight unit and an engineering test unit were developed in parallel. The developmental intention was to qualify the design in parallel with the flight fabrication. There was no schedule available to environmentally qualify a unit and then fabricate the flight unit serially. It had to be done in parallel. The ETU unit was built onto a flight-like composite panel for environmental testing. The flight unit was built up directly onto the flight structure and was qualified at the instrument level. The ETU and flight units were identical.

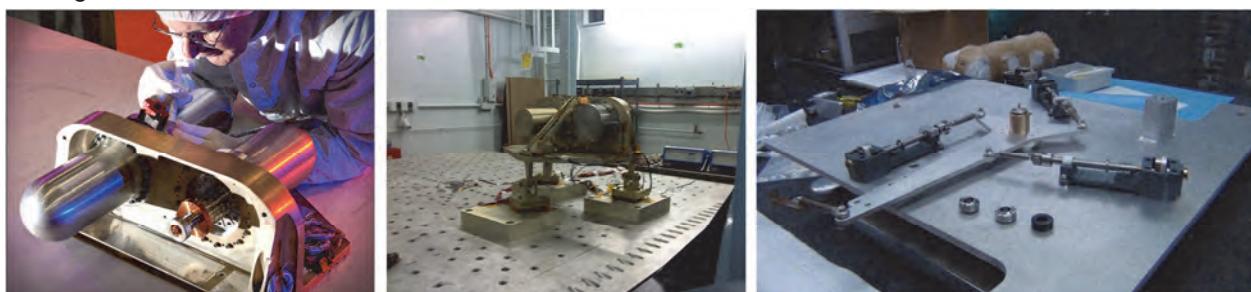


Figure 20. In the left figure, the flight Cryo-Cooler is shown in development at the vendor, mounted within the flight Keel structure. Vibration testing of the ETU Keel Assembly (with Cryo-Cooler mass simulators) to verify post stiffness is shown in the center figure. The CPLL functional breadboard unit is shown in the right figure.

It became evident during the initial development and analysis of the mechanism that 60-Hz stiffness was going to be a very difficult requirement to meet, with initial concepts predicted to be ~42 Hz. Several design changes were implemented, including optimizing the Drive Pin/Toroidal Bushing clearance and the addition of the Triangular Frame, which raised the system stiffness to meet and finally exceed the requirement. The CPLL first mode frequency was measured at 65 Hz.

Upon actuation, the CPLL produces a peak torque of 99 N-m (877 lb-in), and an angular momentum of 12.4 Nms (110 in-lb-s), within the limits specified in Table 3.

The CPLL ETU successfully passed qualification testing in September 2011 and the flight unit has been installed into the TIRS instrument. Many issues were encountered and ultimately solved in this unique mechanism.

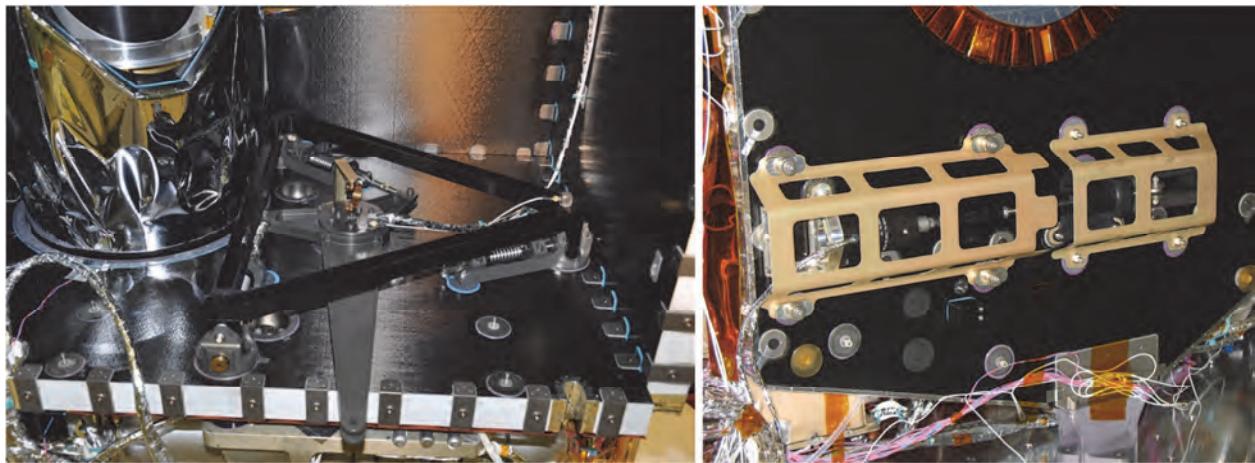


Figure 21. The CCLL is shown during installation into the TIRS instrument, with the -Y panel removed. The left figure shows the rotor arm, anchor fittings, and prominent triangular frame. The Cryo-Cooler legs were integrated into the CCLL before the keel, and attached to it later. The drive springs are visible in the anchor fittings just beneath the triangular frame. The right figure shows the instrument with the -Y panel replaced, with the ERM mounted on the right and the rotor arm coming through the panel on left side, with the two joined by a linkage. The gold colored frames that partially obscure the ERM hardware are box enclosures that will keep thermal blanketing clear of the moving parts, while allowing access for manual ERM resetting.

Use of commercial grade mechanical components for space flight

Due to the compressed schedule, procuring flight quality tie rod ends and/or spherical bearings was impossible. The only option was to fly commercial industrial components. Traceability paperwork to verify material type and quality was generally not available, or was not sufficiently trustworthy for mission assurance. To reduce risk, many extra components were procured, and used not as spares, but for testing. Components were proof tested to measure yield and ultimate tensile strength, and chemically analyzed to verify material type, finish, and surface hardness. Parts that were selected from the lot for flight were static-load tested to qualification load levels before use. The commercial components used in the CCLL successfully passed mechanism component level and instrument level testing.

Lesson Learned: Generally available, commercial industrial hardware may be qualified for spaceflight use if a comprehensive set of tests to verify base material type, coatings, finish, yield and ultimate strength are carried out. The hardware should be purchased in lots and many identical units tested to determine unit-to-unit statistical differences and aid in flight part selection from the lot.

Unpredicted behavior during vibration testing

During vibration testing it was found that the frequency of the system would increase as full level input was approached. This occurred in the lateral directions only. The shifts in frequency for the Z lateral axes are shown in the Figure 22. The shift that was seen during testing in the Y-Axis was not as significant as the one seen for the Z-Axis. The Y-Axis shift was 10 Hz from -18 dB to Full Level. The shift for the Z-Axis was 31 Hz from -18 dB to Full Level. The predicted frequency was higher than the 65 Hz measured during testing, but that was for an idealized system, and did not take into account a number of factors that could be attributed to the difference.

Z Axis Vibration Response Overlay for Cryocooler Mount

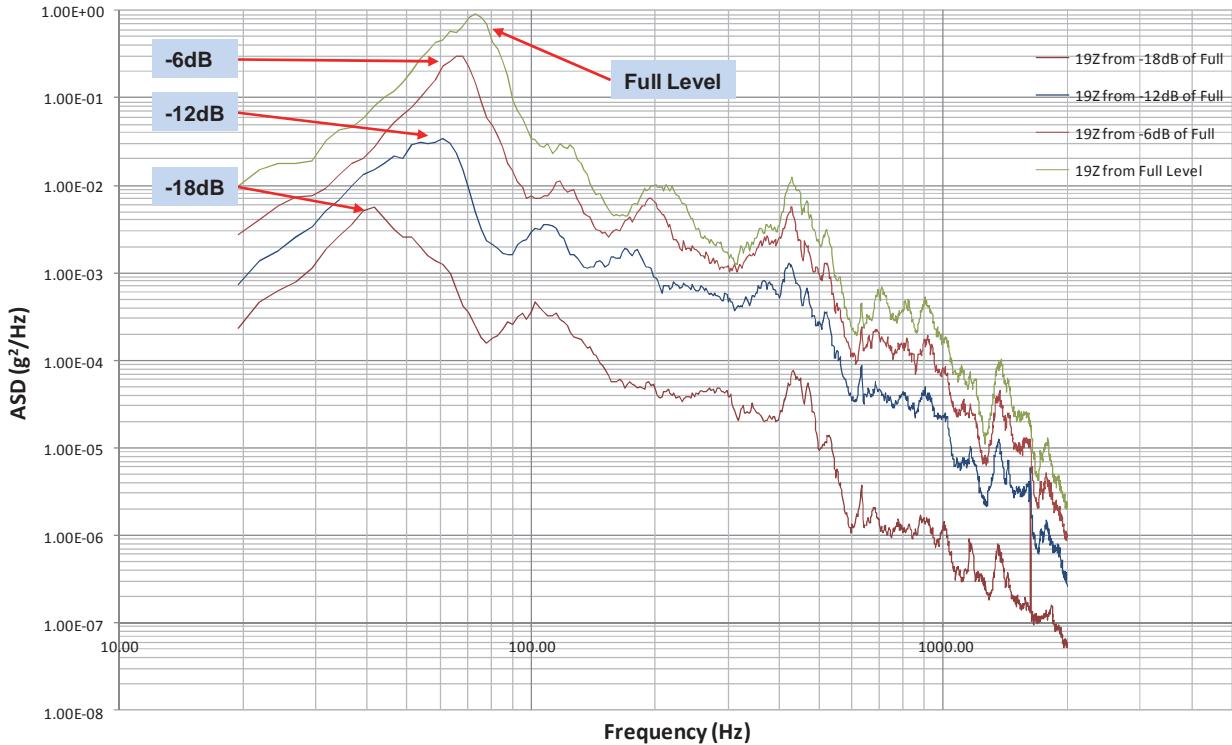


Figure 22. The frequency of the stowed CCLL was shown to increase as the test level was increased to full level. Note how the first mode frequency peaks shift the right (increase) as the test level increases from -18 dB to full level. This behavior was not predicted, and occurred in the 2 lateral (ZY mechanism plane) axis. It did not occur in the axial (X, thrust) axis.

The shift was a result of the gap clearance around the Drive Pin to Toroidal Bushing interface. The gap was necessary to ensure that the mechanism would operate reliably at cold temperatures and was misalignment tolerant. As more energy was input into the system the gap would close, and the system would become stiffer. This characteristic made predicting the behavior of the system difficult, but established that smaller clearances made the system stiffer.

Lesson Learned: Mechanisms which utilize sliding interfaces are difficult to model accurately, and will generally be less stiff than predicted. The measured system frequency will increase as test loads increase to full levels. This is due to sliding clearances being reduced in proportion to input level during vibration tests where the lines of action of the sliding device are close to the test axis. This was not seen when the test axis was perpendicular to the mechanism lines of action.

Conclusions

The SSM, ESDM, and CCLL span a broad range of mechanisms types; from microradian precision mirror positioning to coarse deployment of the large earth shield. Due to the compressed schedule, it was not possible to fully develop engineering test unit mechanisms before the flight mechanisms. A protoflight approach had to be utilized to save time, and even then some prudent development processes, such as the encoder electronics signal integrity analysis, and the SSM bake out, were sacrificed. Higher levels of risk had to be accepted to meet the delivery schedule. We were able to mitigate the consequences resulting from the analytical and contamination control omissions, and the heritage justification to forego critical analysis was proven false. The building of a simple breadboard SSM mechanism, which verified

the performance of the architecture to instrument management, had as much "political" value as technical value.

Whereas heritage arguments hurt the SSM development, the ESDM benefitted strongly from heritage. It required little more than cosmetic changes from the heritage LRO design; its development proceeded comparatively painlessly compared to the SSM, yet some lessons were learned, and classic lessons reinforced. The relative simplicity of the mechanism allowed for adequate analysis to be undertaken, and many developmental performance tests to be done. The vendor-supplied components, such as bearings, potentiometers, and dampers, were known early and hence procured early, with adequate time for characterization testing and bake out. A dedicated breadboard was (correctly) not needed, as the TIRS flight design was a derated version of the original LRO design. This was the classic, proper heritage application case; the new mechanism was as close to "build-to-print" identical to the heritage mechanism as was reasonably possible.

The CCLL was just the opposite of the ESDM; There were no heritage mechanisms that would meet its requirements. The 6-month development schedule, and a fixed set of available interfaces, drove the team to a non-traditional approach that was difficult to analyze, but relatively easy to test. Here the early breadboard was absolutely essential to verify function, measure forces, and test critical sliding clearances. Methods were developed to lot-qualify commercial grade mechanical hardware (with little or dubious traceability paperwork) for flight use (albeit at higher risk), as flight-quality components were impossible to procure in the available time.

The TIRS mechanisms development was undertaken knowing that a higher level of risk had to be assumed in order to minimize the development time. Many weeks were lost and the instrument schedule re-arranged several times to accommodate delayed mechanism deliveries due to the consequences of this decision. Ultimately, the difficulties were overcome, the mechanisms were integrated into the instrument, and have functioned flawlessly throughout instrument environmental testing.

Acknowledgements

The authors would like to sincerely thank the many individuals whom, through their Herculean efforts during this rapid development, were key to the success of the TIRS mechanisms. They are: Melissa Edgerton, Alissa Mitchell, and Monica Zuray, Mechanisms Engineers. Edwin Lee, Randy Frazier, and Scott Weedon, Mechanical Designers. David Maidt, Thermal Analyst. Scott Hoeksema and Milagros Silverio, Contract Oversight. Tommy Emmett, Co-op Student. Andy Wohl, Mechanisms Integration & Test, Gordon Bowers, Technician. We would also like to especially thank Dr. Michael Dube, and Anh Tran for their assistance in bearing lubrication and analysis, and John Sudey for his expertise in jitter control.

References

1. Dennis Reuter, Cathy Richardson, James Irons, Rick Allen, Martha Anderson, Jason Budinoff, Gordon Casto, Craig Coltharp, Paul Finneran, Betsy Forsbacka, Taylor Hale, Tom Jennings, Murzy Jhabvala, Allen Lunsford, Greg Magnuson, Rick Mills, Tony Morse, Veronica Otero, Scott Rohrbach, Ramsey Smith, Terry Sullivan, Zelalem Tesfaye, Kurtis Thome, Glenn Unger, Paul Whitehouse "The Thermal Infrared Sensor on the Landsat Data Continuity Mission." Geoscience and Remote Sensing Symposium (IGARSS) 2010 IEEE International, Honolulu, Hawaii
2. Budinoff, Jason G., R. Barclay, K. Bergandy, A. Matuszeski, J. Schepis, "Development of The Scene Select Mechanism for the Thermal Infrared Sensor Instrument." Proc. 14th European Space Mechanisms & Tribology Symposium – ESMATS 2011, Constance, Germany (ESA SP-698, September 2011)
3. Capon, Thomas, "Design of a Digital Control System for Positioning a Scene Select Mechanism Professional Intern Program Level II Project" NASA GSFC Code 544, July 2011

Resolution for Fretting Wear Contamination on Cryogenic Mechanism

Charles S. Clark*

Abstract

The Near infrared camera (NIRCam) instrument for NASA is one of four science instruments to be installed into the Integrated Science Instrument Module of the James Webb Space Telescope (JWST) which is intended to conduct scientific observations over a five year mission. The NIRCam instrument incorporates multiple mechanisms that perform specific tasks as part of the observatory ground testing, instrument commissioning, and on-orbit science and diagnostics—all of which must operate between 293 and 37 K and be tested to typical launch and space environment standards.

Two of these mechanisms, the pupil imaging lens assembly (PIL) and filter wheel assembly (FWA), use common bearing mounts designed for operation at ambient and cryo temperatures. Modifications to the existing bearing mounts were developed to address fretting damage and associated contamination between the bearing race inner diameter and fixed shaft interface. Comparative proto-flight level vibration testing of four (4) new design configurations was performed alongside a control configuration similar to the original design. To ensure the trial tests simulate worst case environments, the setup went through the equivalent of five 3-axis vibration tests, one single cryo cycle, and a post cryo-cycle vibe test. The final vibe test was run in a 5% relative humidity environment as requested by the customer to reflect latest thinking of the actual JWST launch environment. This paper presents details of the investigation, re-design trades, and trial testing that demonstrated that a titanium shaft with a diamond-like-coating along with a Nitronic-60 sleeve was the preferred configuration of the bearing mount design for both the FWA and PIL units.

Introduction

The near infrared camera (NIRCam) is one of five instruments aboard the James Webb Space Telescope (JWST) observatory which will be conducting deep space scientific observations from the second Lagrangian point of the Sun-Earth orbit at a passively cooled temperature of 37 K. The NIRCam instrument will process the light from the JWST 6.5-meter primary mirror at wavelengths of 0.6 to 5.0 microns. The NIRCam instrument is designed with two optical benches constructed of beryllium that are mirror copies of each other as shown in Figure 1. Each of the two NIRCam optical benches is configured with optical elements that divide the science beam into a shortwave and longwave path. The filter wheel assembly (FWA) and the pupil imaging lens assembly (PIL) are two different types of mechanisms being developed for the NIRCam instrument to support on-orbit calibration of the JWST observatory as well as conduct mission scientific observations. There are four FWAs and two PIL assemblies installed on the NIRCam instrument, with two FWAs and one PIL located on each optical bench. As shown in Figure 1, one FWA is installed on the longwave path, and one FWA and one PIL are on the shortwave path.

* Lockheed Martin Space Systems Company - Advanced Technology Center, Palo Alto, CA

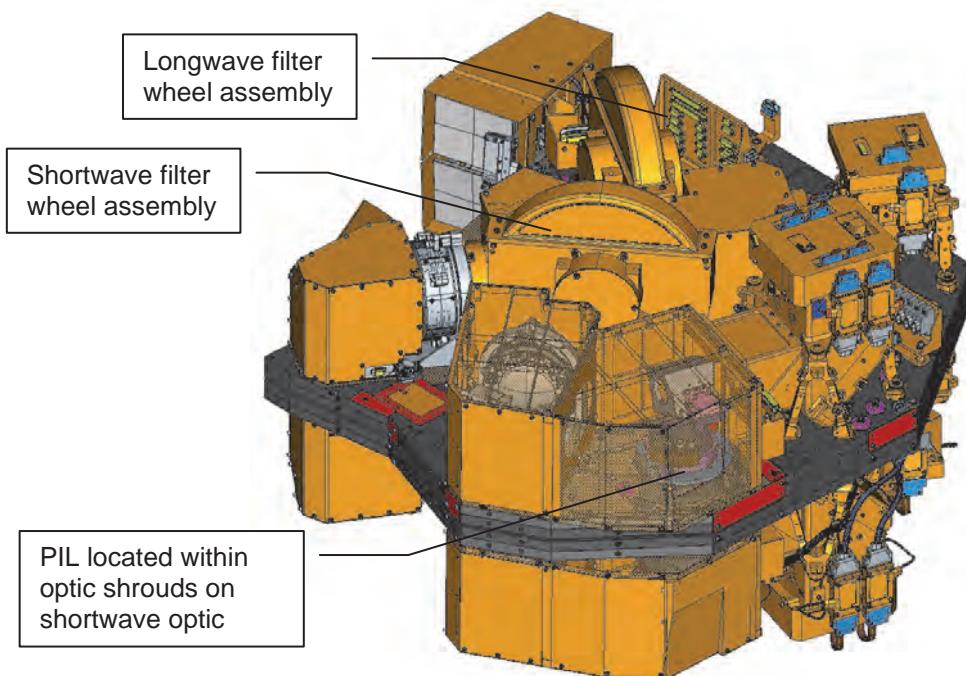


Figure 1. The locations of two filter wheel assemblies and the one pupil imaging lens assembly are shown on the module A (top) beryllium optical bench. Stray light shrouds appear transparent in the figure to show the PIL located within.

The FWA is designed to insert specific optical elements into the NIRCam optical beam. Each FWA unit consists of two independently driven wheels that each hold 12 optical elements and is required to insert each optic element into a target position with a repeatability of ± 75 microns. Each FWA unit is configured with primary mirror wave-front sensing elements, optical calibration sources, and numerous optical filters dependent upon which longwave or shortwave path the FWA resides. An illustration of the FWA is shown in Figure 2. The primary function of the PIL assembly is to deploy a set of optics into the beam path. Once inserted, the NIRCam instrument focus is changed to image the 18-segment, 6.5-meter diameter, primary mirror instead of deep space. To achieve this function, the PIL must deploy its optics into the specified point in the beam path with a repeatability of 0.016 degree. The PIL assembly is shown in). **Figure 3.**

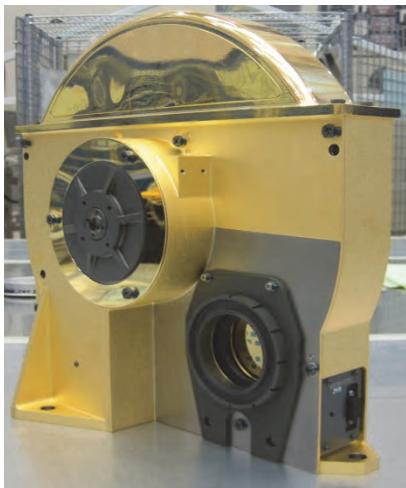


Figure 2. The filter wheel assembly (FWA). **Figure 3.** The pupil imaging lens assembly (PIL).

The FWA and PIL, along with all NIRCam components, are designed to support many demanding requirements. The units must operate after being subjected to the stresses of launch loads and in the vacuum of space. These units are also required to have a minimum first mode frequency of 100 Hz, operate with a maximum power input of 0.6 mW, and all actuators must have appropriate torque margins. While these requirements are not unusual for space flight mechanisms, both the FWA and PIL mechanisms are required to operate at 37 K to allow imaging at the near infrared spectrum. Furthermore, the FWA and PIL are not allowed to generate debris larger than 300 microns over their lifespan to ensure minimal image degradation through contamination. The PIL was given a unique requirement that specified the mechanism shall include a fail-safe system that, given a set of reasonable failure conditions while in the deployed state, the PIL optic would be able remove itself from blocking the science beam. Previous papers [1], [2], and [3], are available for more information about the FWA and PIL mechanism mission requirements and original design.

The FWA and PIL are both rotating mechanisms that share common motor and bearing mount designs. The bearing and related bearing mount design ensures low friction rotation at ambient and cryogenic temperatures. The original designs for both mechanisms integrated a fixed titanium shaft, 440C cryo and space-rated bearings, and 455 CRES rotors. Due to different materials and the large operational temperature excursion, a flex bearing mount was chosen as illustrated in **Figure 4**. For operation at cryogenic temperatures, a Teflon film bearing lubrication is employed through a transfer process from a Teflon and fiberglass composite ball-bearing cage to the balls and races of the bearing. With the back-to-back bearing configuration, the bearing preload is set by clamping the inner race of the bearing. This bearing preload is critical to ensuring smooth running, low-friction rotation. Selecting a spring with a spring-force just higher than the bearing pre-load, and applying the spring force through a close tolerance slip-fit bearing sleeve, one ensures the bearings have constant pre-load but allows for slight changes from differential coefficients of thermal expansion and possible Teflon lubrication buildup.

While this design works well in quiescent environments, the forces induced during launch would exceed the capability of the spring system alone. Two features were added to the flex mount design to achieve the needed stiffness through launch. First, a hard-stop was added to the sleeve that only allows 75 microns of slip. The second feature is a cryo-release tube that effectively locks out the spring during the ambient launch temperatures but shrinks away at cryo temperatures, allowing the spring to pre-load the bearing. Through prototype and qualification testing, this design was proven to meet two-time-life testing with the required low friction rotation.

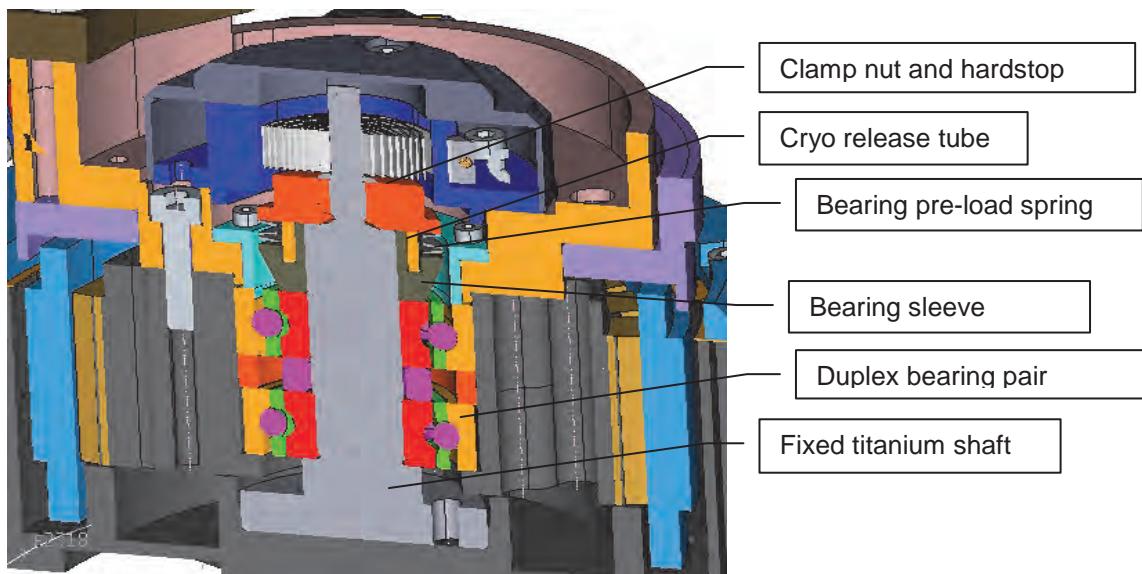


Figure 4. The spring clamped bearing mount design for the pupil imaging lens assembly (PIL).

Finding the Problem

Testing of the FWA prototype, and the FWA and PIL qualification units successfully demonstrated all performance requirements, but a planned disassembly of the PIL revealed an unforeseen problem in the bearing mount. The PIL qualification unit was fully assembled and performance tested at ambient temperatures and then subsequently subjected to proto-flight random and sinusoidal vibration testing. Because of the unique optic configuration of the PIL, the first vibration test of the system was performed with a surrogate PIL optic installed. After successfully completing this initial vibration test, the PIL was partially disassembled to swap out the surrogate optic with the actual optic. At this point, contamination was found at the base of the PIL shaft as shown in Figure 5.

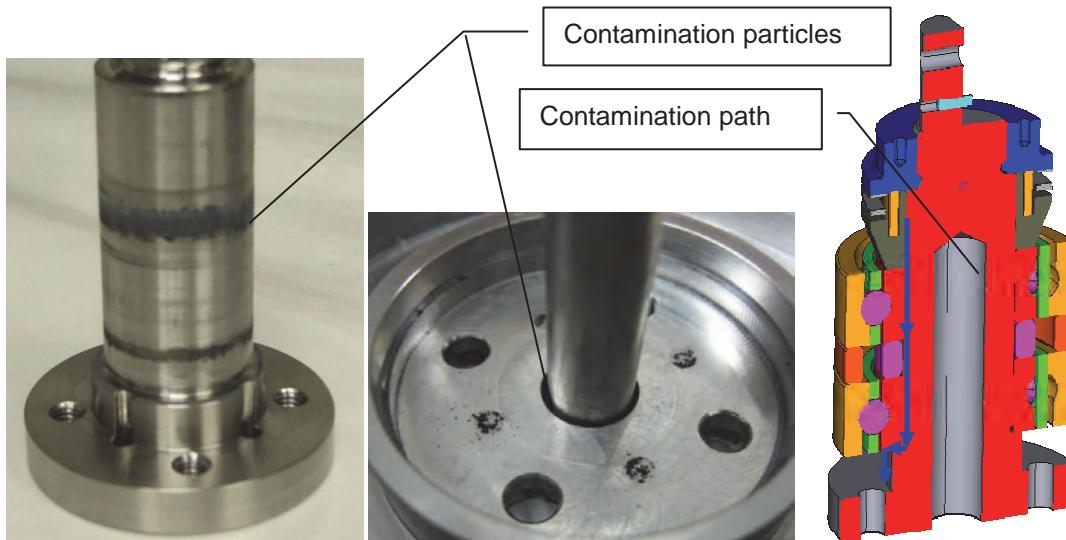


Figure 5. Contamination found in the PIL qualification unit after vibration testing, and a diagram of the PIL bearing mount illustrating the suspected contamination path.

Investigation into the powdery contamination found in the PIL qualification unit initially focused on the bearing sleeve which showed evidence that some of the anodic coating was worn away, but the investigation was quickly expanded to look at the entire bearing assembly. Magnified optical inspection and scanning electron microscope (SEM) analysis of the sleeve showed evidence of wear with debris in the form of conglomerate particles. This type of conglomerate particle debris which is made up of many sub-micron sized particles is characteristic of fretting wear¹. The wear debris found on the sleeve contained mostly titanium from the shaft and sleeve base material as well as silicon and oxygen from the anodic coating. However, it seemed unlikely that all the debris could come from the wear areas between the sleeve and shaft. Analysis of debris from other areas at the base of the PIL shaft showed the same conglomerate particles, but these particles consisted of titanium and iron, but did not contain silicon and oxygen. The iron was most likely from wear of the bearing. Titanium is a fretting-wear sensitive material, and it became clear that the microscopic motion of the flexure bearing mount during vibration testing resulted in the wear-generated particulate contamination seen on the PIL qualification unit. Since a similar bearing mount was used in the FWA design, the FWA qualification unit was disassembled to inspect for possible fretting wear.

After disassembling the FWA qualification unit, it became evident that the assembly suffered from the same fretting wear issue. Much of the bearing-to-shaft interface surfaces were covered with similar wear

¹ Fretting wear is a type of adhesive wear that will occur when contacting surfaces are undergoing small, oscillatory, tangential displacements. The relative sliding motion causes localized adhesion and disruption of the surface generating fine particulates which then oxide and become imbedded back into the surface causing further abrasion damage.

particulates as seen on the PIL design. However, nodular buildup of fretting wear particles had collected in relief areas of the design as shown in **Figure 6**. These 0.127-mm (0.005-inch) diameter nodules had the consistency of dry powder but would easily smear when touched or dissolve into a paste with isopropyl alcohol. The material composition, as determined from a scanning electron microscope analysis, was the same as what was seen in the PIL. Due to the stringent cleanliness requirement for these mechanisms and the optics that surrounded them on the NIRCam bench, this contamination from fretting wear of the flexure bearing mount was unacceptable. The next step was to resolve the issue.

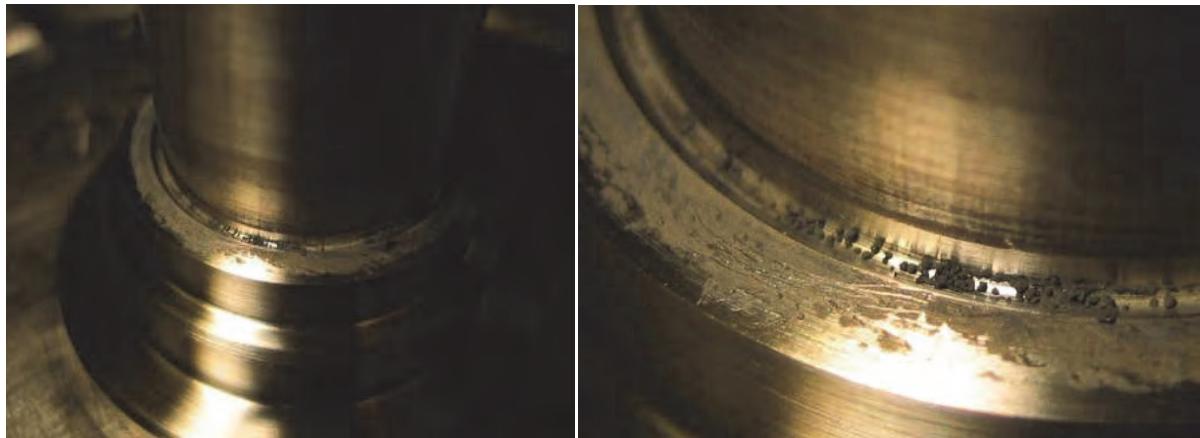


Figure 6. Similar fretting wear found in FWA qualification unit bearing shaft. The 0.127-mm (0.005-inch) nodules collected from the bearing relief consisted of nanometer-sized particles of titanium from the shaft and iron from the bearing and had the consistency of dry powder that smeared when touched.

Fretting Wear Resolution Trade Studies

The fretting wear contamination was clearly unacceptable, but what course of action could be taken that would ensure no contamination of the nearby optics, no performance degradation of the different functionalities of the FWA and PIL mechanisms, and not result in significant delays to the program? The team considered a number of possible solutions including using a conventional hard-clamp bearing mount, trying to contain the contamination, fabricating the shaft from a less fret-wear sensitive material, adding different wear resistant coatings to the shaft, as well as combinations of these ideas. The team was uncomfortable with a hard-clamped bearing design for two main reasons. First, the team was already considering changing the material of the bearing flexure clamp. Secondly, the test history of the current design had met all other performance requirements, and a hard-clamped bearing mount design would likely require a new set of qualification testing. Therefore, the design team focused on changes to materials and coatings and possible containment.

There is a wealth of knowledge related to wear-resistance coatings and materials for many industrial applications as well as many aerospace applications. However, the knowledge base dwindles significantly for wear-resistant materials and coatings for applications at cryogenic temperatures that must operate in a vacuum and also survive launch vibrations in a dry air environment. By investigating known heritage materials and coatings used for near-ambient temperature space applications and more recent coating technology innovations that show promise, a selection of four candidate solutions were chosen. It was clear that test data at cryogenic temperatures for the selection was all but non-existent, and even the ambient test data did not provide wear performance related to the FWA and PIL fretting wear issue. The team quickly determined that a test was the best method to discern the best solution for the problem.

Down Selection Testing for Best Fretting Wear Performance

The team devised a test for the worst case design configuration; the design that induced the most stress on the bearings. The FWA bearing design supported the higher mass spread out over large wheels and required the most stiffness to keep the dynamic deflections to a minimum. It was impractical, however, to build four filter wheel assemblies. Therefore, the team developed a surrogate design that would replicate the FWA bearing mount design to the exact dimensions and tolerances. The FWA design consisted of two independently driven optic wheel assemblies mounted on a common fixed shaft. Each optic wheel assembly was configured with the same flexible bearing mount and incorporated the same duplex bearing pair as used on the PIL, but with a thicker set of bearing spacers as seen in **Figure 7**.

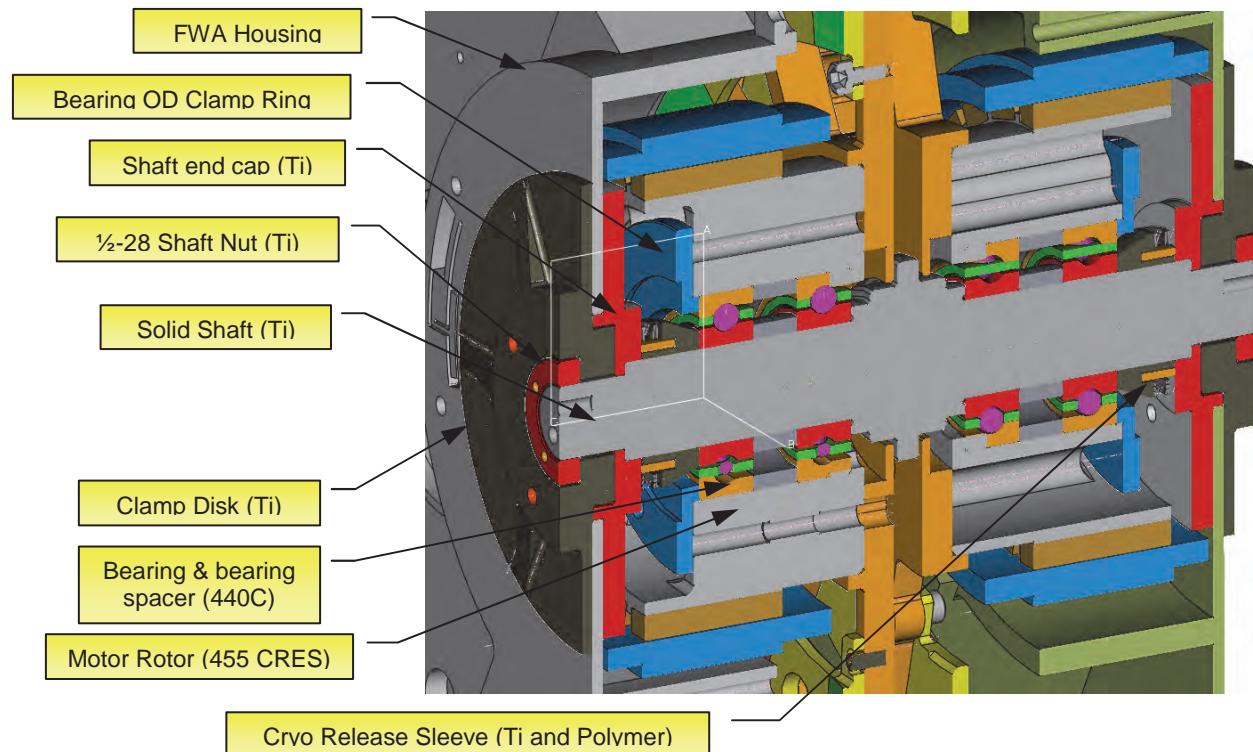


Figure 7. FWA dual wheel bearing and motor mount configuration on solid titanium shaft.

The test configuration replicated only half of the FWA design and included a surrogate wheel of the same mass that induced the same bearing forces and moment of inertia. The test configuration also replicated many of the other parts to exact dimensions and tolerances. The difference of each of the four test configurations was the unique change that presented possible solution to the fretting wear issue. Because the hardened 440C steel of the bearing was already very resistant to fretting, no changes to the bearings were incorporated. The test configurations focused only on changes to the titanium shaft and anodic coated titanium bearing sleeve. Three coatings and two material changes were chosen as candidate solutions for the test.

The coatings were chosen for their wear resistance and adherence properties on titanium down to cryogenic temperatures. The coatings selected were titanium-nitride (TiN), ion-plated gold (Au), and an amorphous carbon-based tungsten-carbon/carbide (WCC). The Au and TiN coatings have been used successfully as wear-resistance coatings at near ambient aerospace applications and have demonstrated good adherence to titanium. Despite having no direct aerospace heritage, the excellent wear and adherence data demonstrated by the WCC coating warranted a spot on the candidate list.

The design team was very hesitant to change materials due to the differential CTE issues, but the wear resistant properties of Nitronic-60² and MP35N³ were hard to ignore. A previous aerospace application demonstrated the wear characteristics of an MP35N shaft and a Nitronic-60 sleeve, and the FWA solid shaft design could benefit from the higher strength of the MP35N. So for the fret wear test configuration, all sleeves were to be made of Nitronic-60, and one shaft was to be made from MP35N. However, because of the differential CTE issue, and the lack of direct CTE measurements of this material down to 35 K, samples of each of these materials were tested with the results shown in Figure 8.

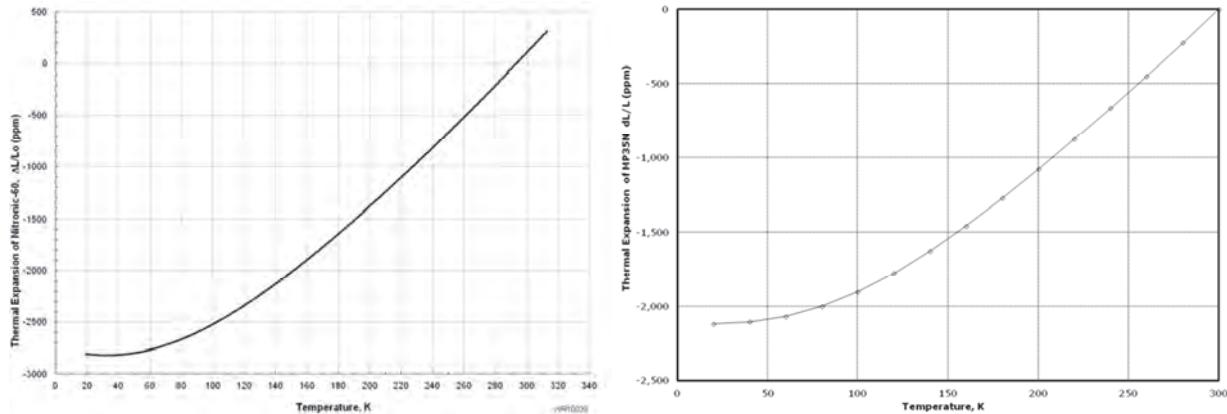


Figure 8. Measurements of thermal expansion down to 35 K for both Nitronic-60 and MP35N. The $\Delta L/L$ of Nitronic-60 at 35 K is 0.28% and 0.21% for MP35N.

Although each unique candidate solution was representative of the original design, the team judged that there were enough differences in the test that a control configuration was needed. Therefore, a fifth configuration was added to include the original, un-coated titanium shaft and anodic coated sleeve. After completing the assembly of each of the configurations, each was mounted onto a common vibration block that was to be used to subject all units to the required three-axis vibration test. A thorough analysis of the five-wheel test block, as shown in Figure 9, was performed to confirm block input values would induce representative loads into the system.

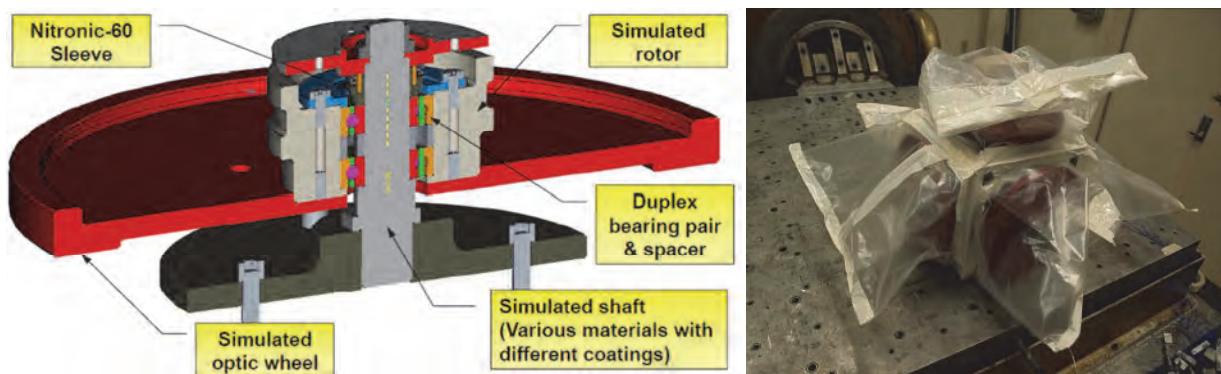


Figure 9. Diagram of test configuration and picture of the five test configurations mounted to a vibration block and sealed for contamination prevention.

² Nitronic-60 is an austenitic stainless steel alloy known for its wear and galling resistance and is used in many high temperature and corrosion resistant applications.

³ MP35N is a nickel, cobalt, chromium, and molybdenum, allow which has a inherent high strength, outstanding corrosion resistance, and excellent cryogenic properties.

In preparation for testing the candidate solutions, the team recognized that the fret wear contamination was observed after only one 3-axis vibration test, but the FWA and PIL flight units will undergo four vibration tests during ground preparations and then launch. Additionally, the flight units will be subjected to a number of cryogenic test cycles in between the various vibration tests. Furthermore, the JWST review team volunteered that the launch capsule may be purged with dry nitrogen through ascent, and it is documented that WCC coating friction levels increase and TiN coatings friction levels decreases in low humidity environments. With all these factors in mind, the team developed a test plan that would subject the candidate solutions to all representative atmospheric and vibration conditions and be subsequently dis-assembled to determine which configuration produced minimum fretting wear contamination.

Test Results

The test configuration was subjected to the equivalent of five 3-axis vibration tests, a cryo test, and one final vibration test with all units purged to less than 5% relative humidity. The data review from the set of five 3-axis vibration tests yielded no anomalies with first mode frequencies at 200 Hz, maximums of a little over 30 Gs rms, and only small variations from predictions. Additionally, signature run comparisons throughout the test showed modest variations in amplitude and no changes in frequency. The tests were deemed successful, and before progressing to the cryo testing, the assemblies were disassembled for inspection of the bearing mounts.

The control configuration with a titanium shaft and anodic coated titanium sleeve showed similar fretting wear debris as before, shown in Figure 10. The ion-gold coated titanium shaft with Nitronic-60 sleeve also fared poorly due to apparent coating failure and fretting wear debris as shown in Figure 11. The TiN coated titanium shaft showed improved fret wear performance, but a nominal amount of fret wear debris was still found on this configuration as shown in Figure 12. The WCC-coated titanium shaft, however, showed no indication of coating wear, and very little fret wear debris as shown in Figure 13. Finally, the MP35N shaft showed very small amounts of wear and little wear debris. After initial inspection, the WCC-coated titanium shaft showed the best performance.

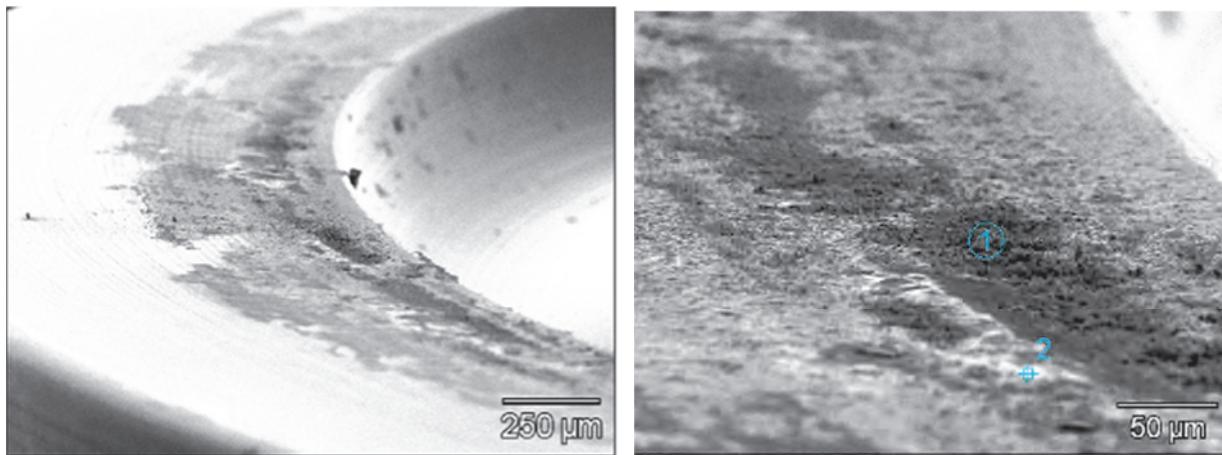


Figure 10. Scanning electron microscope (SEM) analysis of the titanium shaft and anodic-coated titanium sleeve. Titanium and iron debris (1 & 2), and conglomeration of fine particles are characteristic of the fret wear seen before on original design.

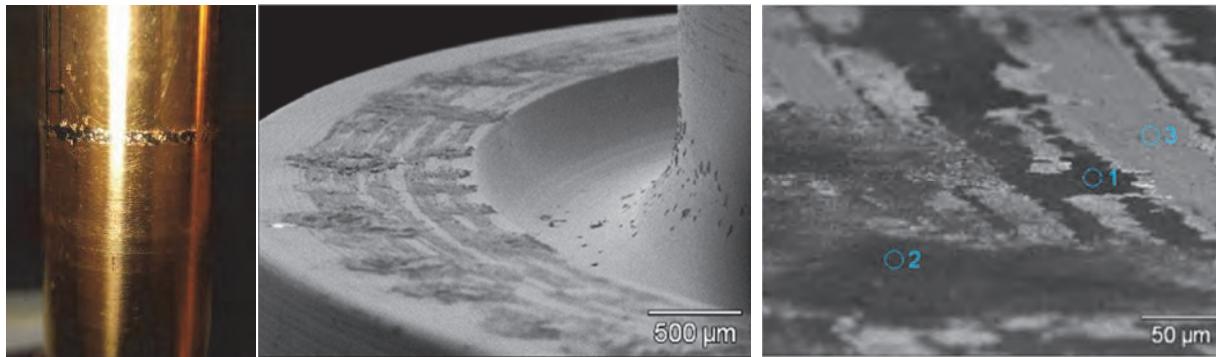


Figure 11. SEM analysis of ion-plated gold titanium shaft and Nitronic-60 sleeve. The photo shows the titanium shaft with gold coating failure. The SEM micrographs showing bare Ti surface (1), iron debris (2), and ion gold plating and Ti debris (3).

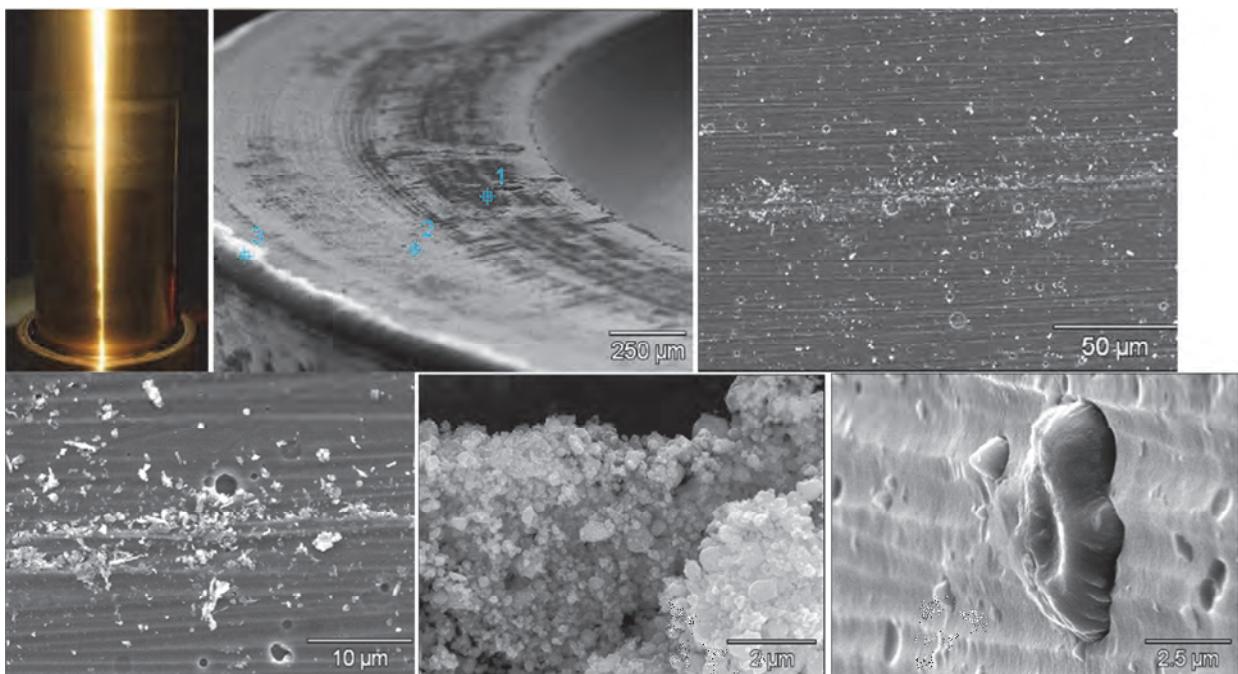


Figure 12. Photo and SEM analysis of TiN-coated titanium shaft and Nitronic-60 sleeve. The TiN-coated titanium shaft showed only small amounts of wear. The SEM analysis indicates iron, Ti, and TiN debris (1 & 2), and TiN plating on the shaft bearing seat (3). The small particulates observed on the shaft consisted of conglomerates of sub-micron sized iron and TiN particles typical of fret wear. The last micrograph shows an example of the numerous voids and protrusions prevalent in TiN coatings.

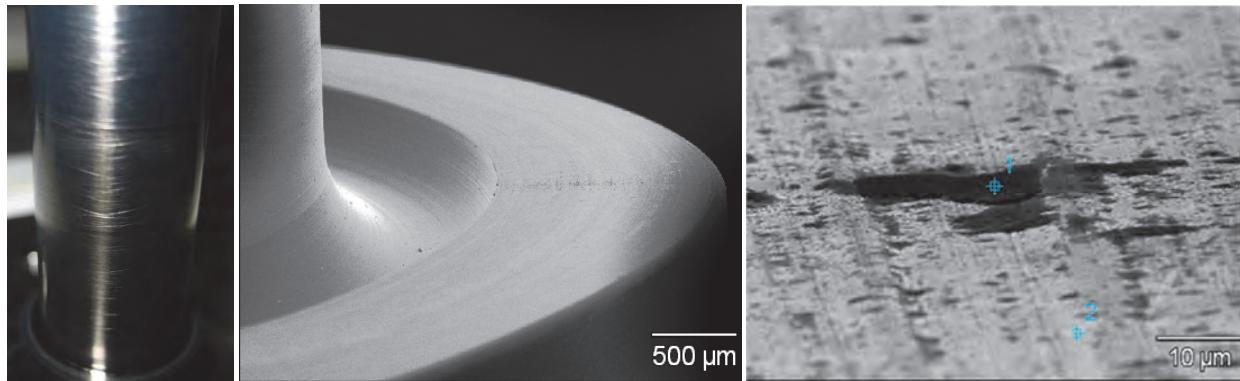


Figure 13. SEM analysis of the WCC-coated shaft and Nitronic-60 sleeve. The WCC-coated titanium shaft showed no wear marks on the shaft surface. Only small amounts of tungsten and iron debris were found on the shaft bearing seat.

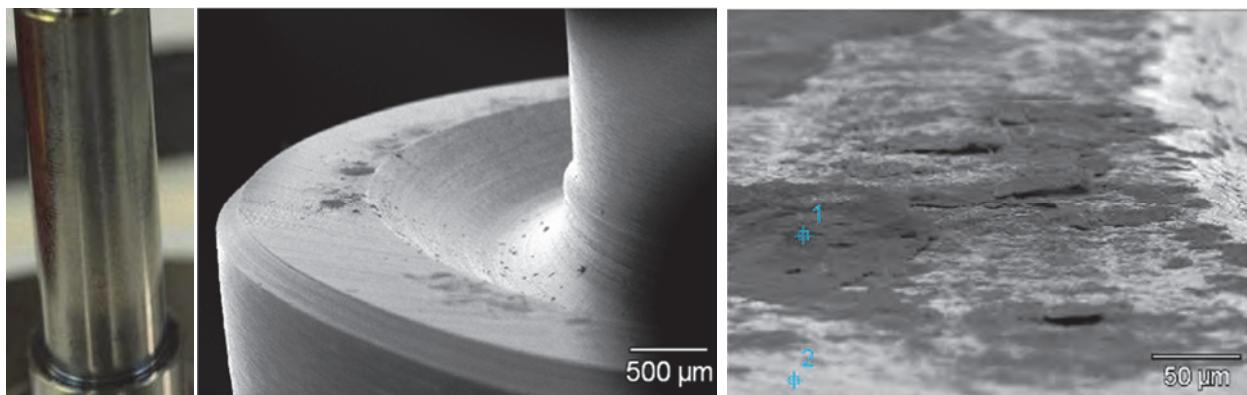
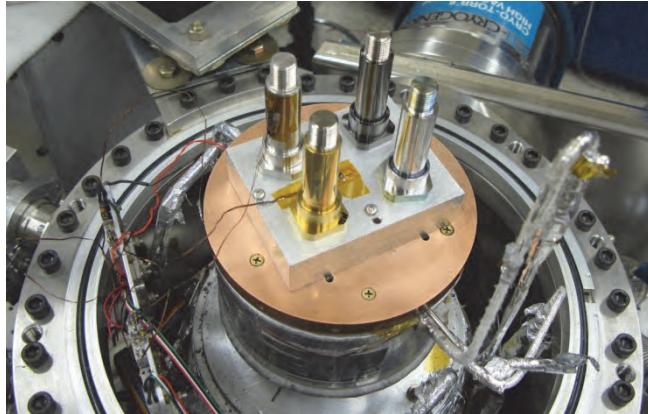


Figure 14. SEM analysis of the MP35N shaft and Nitronic-60 sleeve. The MP35N shaft surface showed wear only at the microscopic level, and very little wear debris. The debris consisted predominately of iron with some cobalt alloy constituents.

The next test was to subject the different shafts to cryogenic temperatures. Of the four initial candidate shafts, only three were placed in a cryogenic chamber and brought down to 35 K at a maximum of 40 K per hour as shown in Figure 15. The ion-plated gold shaft was not advanced due to poor performance. After returning them to ambient conditions, the shafts were reviewed under visual magnification as well as SEM analysis. The results of the inspection after cryo yielded no adhesion anomalies, and the shafts were re-installed into their respective surrogate FWA configuration for the last vibration test.



**Figure 15. Cryogenic test fixture with candidate shafts mounted to cold head (shrouds removed).
The gold shaft was replaced with a spare titanium shaft for temperature instrumentation.**

The last test for the candidate configurations was a shortened version of the previous three-axis vibration test but in dry air. During this vibration test, the assemblies were only subjected to one random and one sine vibration test per axis. However, these vibration tests required that each configuration be plumbed to dry air to ensure the tests were conducted in less than 5% RH dry air. This was stipulated by the customer to address the possibility that the JWST observatory would be launched in dry air conditions combined with the fact that the friction coefficient of WCC coatings increases in dry environments. As shown in Figure 16, each configuration was plumbed with independently controlled dry air input and monitored with independent humidity meters. As a side note, the MP35N configuration was eliminated from the test due to the higher density (i.e., weight) of this material. After this vibration test was completed, the units were disassembled and inspected.



Figure 16. Second vibration test of the TiN-coated, WCC-coated, and bare (control) titanium shaft configurations. Note the dry air input as well as the humidity meters for each configuration.

Conclusion

After finding contamination in the bearing mounts of the FWA and PIL assemblies through testing, the team was able to identify the root cause and modify the design to resolve the issue. Fretting wear between the titanium shaft and bearings and sleeve was found to be the source of the contamination. The team selected a set of candidate designs that could be implemented to minimize the fretting issue after conducting a study of possible remedies. Due to limited cryogenic data on the candidate solutions, a series of random vibration tests on a simulated wheel assembly were run to verify the improved fretting

wear performance at 35 K. The original configuration was included in the tests for a control comparison. A clear winner was found in the WCC-coated titanium shaft with Nitronic-60 sleeve and original 440C bearings, as shown in Figure 17. The cobalt alloy (MP35N) configuration also showed little wear and only small amounts of debris, but it did not perform as well as the WCC-coated shaft. It also had the disadvantage of a differential CTE and higher density. The titanium-nitride coated titanium shaft showed more wear than the WCC-coated shaft and more debris was observed with this configuration. The micro-pits and protrusions were also a detractor for this configuration. Lastly, the ion-plated gold configuration showed the poorest performance with significant adhesion problems and large amounts of wear debris. The hard WCC-coating proved to be the best solution to minimize the risk of wear contamination for this application.

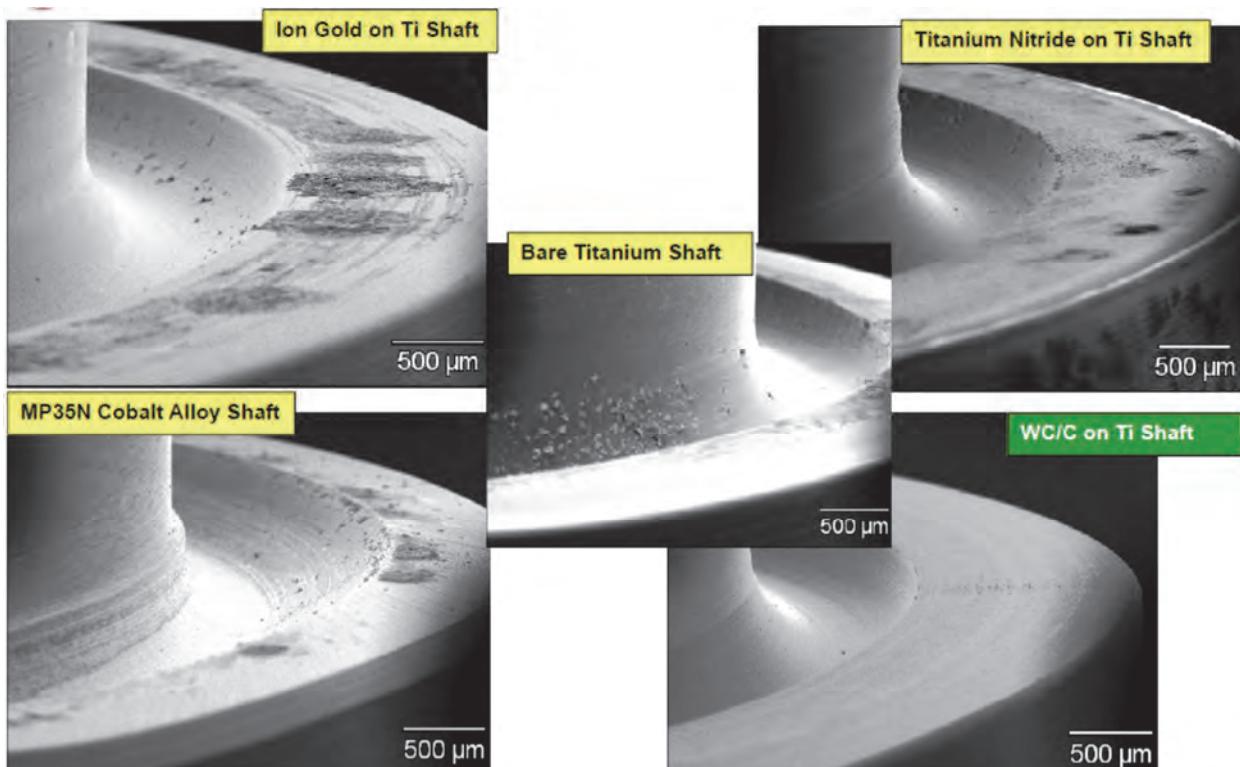


Figure 17. Four candidate configurations showing relative fret wear performance. The WCC-coated titanium shaft demonstrated the least susceptibility to fretting wear.

References

1. Clark, Charles S., "Redesign and Test of Cryogenic Mechanism for Improved Stiffness", Proc. SPIE Paper 8150-19 (August 2011).
2. Clark, Charles S., "NIRCam Pupil Imaging Lens Actuator Assembly", Proc. SPIE Paper 7439C-46 (August 2009).
3. Sean McCully, "Experimental Development Tests of a Cryogenic Filter Wheel Assembly for the NIRCam Instrument and James Webb Space Telescope", Proc. Aerospace Mechanisms Symposium (May 2006).

Design and Manufacturing Considerations for Shockproof and Corrosion-Immune Superelastic Nickel-Titanium Bearings for a Space Station Application

Christopher DellaCorte* and Walter A. Wozniak*

Abstract

An intermetallic nickel-titanium alloy, 60NiTi (60wt%Ni, 40wt%Ti), is a promising tribological material for space mechanisms. 60NiTi offers a broad combination of physical properties that make it unique among bearing materials. 60NiTi is hard, electrically conductive, highly corrosion resistant, readily machined prior to final heat treatment, easily lubricated and is non-magnetic. It also falls within the class of superelastic alloys and can elastically endure large strains (beyond 5%) making it highly resistant to excessive and unexpected (shock) loads. Key material properties and characteristics such as elastic modulus, tensile fracture sensitivity and residual stress behavior, however, differ from conventional alloys such as steel and this significantly affects bearing design and manufacturing. In this paper, the preliminary design and manufacture of ball bearings made from 60NiTi are considered for a highly corrosive, lightly loaded, low speed bearing application found inside the International Space Station's water recycling system. The information presented is expected to help guide more widespread commercialization of this new technology into space mechanism and other applications.

Introduction

Recent research on binary nickel-titanium (Ni-Ti) alloys has identified them as promising candidates for bearings and mechanical components [1]. The nickel-rich alloy, 60NiTi in particular, exhibits a remarkable combination of properties and characteristics relevant to rolling element bearings for space mechanism applications. For instance, 60NiTi is hard, electrically conductive, highly corrosion resistant, readily machined prior to final heat treatment, easily lubricated and is non-magnetic [2,3]. 60NiTi is also in the family of superelastic alloys and can elastically endure large strains (beyond 5%) making it highly resistant to shock loads. Table I lists many of these properties as they are currently known alongside the conventional shape memory alloy 55NiTi and more traditional bearing materials. As an emerging material, some of these published properties are estimated or preliminary.

Table I – Representative Thermophysical and Mechanical Properties of Bearing Materials

Property	60NiTi	55NiTi	440C	Si ₃ N ₄	M-50
Density	6.7 g/cc	6.5 g/cc	7.7 g/cc	3.2 g/cc	8.0 g/cc
Hardness	56-62 Rc	35-40 Rc	58-62 Rc	1300-1500 Hv	60-65 Rc
Thermal Cond. W/m·°K	18	9	24	33	~36
Thermal Expansion	~10x10 ⁻⁶ /°C	~10x10 ⁻⁶ /°C	10x10 ⁻⁶ /°C	2.6x10 ⁻⁶ /°C	~11x10 ⁻⁶ /°C
Magnetic	Non	Non	Magnetic	Non	Magnetic
Corrosion Resistance	Excellent	Excellent	Marginal	Excellent	Poor
Tensile/Flexural Strength	~1000 MPa	~900 MPa	1900 MPa	600-1200 MPa (Bend Strength)	2500 MPa
Young's Modulus	~114 GPa	~100 GPa	200 GPa	310 GPa	210 GPa

* NASA Glenn Research Center, Cleveland, OH

Proceedings of the 41st Aerospace Mechanisms Symposium, NASA Jet Propulsion Laboratory, May 16-18, 2012

Poisson's Ratio	.34	.34	.30	.27	.30
Fracture Toughness	TBD	TBD	22 MPa/ \sqrt{m}	5-7 MPa/ \sqrt{m}	20-23 MPa/ \sqrt{m}
Max. Use Temp	~400°C	~400°C	~400°C	~1100°C	~400°C
Elect. Resistivity	$\sim 80 \times 10^{-6}$ Ω-cm	$\sim 80 \times 10^{-6}$ Ω-cm	$\sim 36 \times 10^{-6}$ Ω-cm	Insulator	$\sim 60 \times 10^{-6}$ Ω-cm

TBD means "to be determined"

Shock loading is a significant design challenge for space mechanisms. On orbit bearing loads, in the absence of gravity tend to be very low but the severe launch vibration environment can lead to bearing damage through the Brinell effect in which hard rolling elements dent more vulnerable races [4]. For applications that demand long life and ultra smooth operation, such Brinell damage can be catastrophic. In such cases, great care is taken using vibration isolation features and tie-down systems to avoid the problem. These add weight and complexity. At times, load capacity design margins are increased for bearings and this leads to increased mass and power consumption. Clearly, the development of more resilient bearings is an advantage for aerospace bearings and mechanisms.

Recent investigations into the hardness and Brinell damage sensitivity of 60NiTi show a potential pathway to engineer ball bearings that are highly resistant to indentation damage [1]. In preliminary indentation tests either Si₃N₄ or 60NiTi balls (12.5mm diameter) were pressed into flat plates made from 60NiTi and the bearing alloys 440C, M50 and Stellite 6B. Initial experiments were carried out at light loads that were increased on subsequent trials. In this manner, both the classic Brinell Hardness Number (BHN) and the threshold load to achieve the first observable dent were obtained. The data, tabulated in Table II, shows that 60NiTi provides significantly more static load capacity (higher threshold load) than the other materials tested.

Table II. Hertz contact stresses and contact diameter at the threshold load for various plate and indenter material combinations.

Plate	Indenter	Threshold load, kgf (lbs)	Peak Stress, GPa (ksi)	Contact Dia., mm (in)	Avg. Stress, GPa (ksi)
Stellite 6B	Si ₃ N ₄	10 (22)	2.06 (299)	0.30 (0.012)	1.37 (199)
440 C	Si ₃ N ₄	51 (112)	3.48 (504)	0.52 (0.021)	2.32 (336)
M50	Si ₃ N ₄	150 (331)	5.09 (738)	0.74 (0.029)	3.39 (491)
60NiTi	Si ₃ N ₄	552 (1214)*	5.56 (806)	1.36 (0.054)	3.71 (537)
Stellite 6B	60NiTi	15 (33)	1.56 (226)	0.42 (0.017)	1.04 (151)
440 C	60NiTi	150 (331)	3.33 (483)	0.92 (0.036)	2.22 (322)
M50	60NiTi	501 (1102)	5.02 (728)	1.37 (0.054)	3.35 (486)
60NiTi	60NiTi	1512 (3327)	5.90 (856)	2.19 (0.086)	3.94 (571)

*Using 1.2 μ m (50 μ in) dent depth fatigue criterion. Threshold load is ~360kgf (~800 lb) using more stringent 0.5 μ m (20 μ in) dent depth criterion for quiet running bearing.

The reasons for this behavior are complex and discussed in detail in Reference 1 but briefly, the large elastic deformation range of 60NiTi combined with its high hardness and relatively low elastic modulus result in an increased contact area, reduced peak and average stresses and enhanced static load capacity. Given these somewhat unexpected results and capabilities, the next logical steps are to design and fabricate bearings from 60NiTi for evaluation.

Bearing design and manufacturing is a field that is mature and well developed for steels and, in the case of rolling elements (balls and rollers), silicon nitride ceramics. 60NiTi is a superelastic material in the class of intermetallics (neither a metal nor ceramic with respect to atomic bonding) and has key physical properties and attributes that differ from the traditional bearing materials. Among the relevant differences are a relatively low elastic modulus, limited tensile ductility (a tendency for brittle failure in tension), and a

requirement for a rapid quench during heat treatment which leads to significant residual stresses. These three key differences along with other second order attributes affect bearing design and manufacturing processes.

The following sections describe the general design and manufacturing process for 60NiTi bearings by considering a specific space mechanism bearing application; the Distillation Assembly (DA) centrifuge that is part of the ISS Environmental Control System (ECLSS) on the International Space Station (ISS). The ball bearings used in this application operate in a highly corrosive environment at low speed under very low average loads thus fatigue is not a great concern. However, the bearings must endure high launch loads without damage. Based upon preliminary data, 60NiTi appears to be a viable candidate bearing material. This paper lays out the design process and the results of pathfinder manufacturing investigations to develop a more generalized methodology for incorporating superelastic materials into space mechanisms.

Materials and Procedures

Bearing grade 60NiTi is manufactured via a proprietary high-temperature powder metallurgy (PM) process roughly similar to that described in the literature [5]. Pre-alloyed 60NiTi powder is hot iso-static pressed (HIPed) into various shapes and sizes depending upon the desired end product. To make 60NiTi balls, the powder is HIPed into rough, spherical ball blanks that were then ground, polished and lapped. Because the PM process yields ball blanks that have isotropic mechanical properties high quality (Grade 5) bearing balls can be readily produced. The finished 60NiTi ball specimens, shown in the photograph in Figure 1, are bright and shiny in appearance and resemble conventional polished steel balls.



Figure 1. 60NiTi Grade 5 test balls.

To make other shapes such as bearing races and mechanical and thermo-physical property measurement specimens, 60NiTi rods and ingots were first made using the same PM process. Figure 2 shows such specimens produced by the PM process.



Figure 2. 60NiTi ingots and blanks produced by PM process.

Once the ingots and other shapes are produced, a series of steps that include wire electrode discharge machining (EDM), conventional machining using carbide tools and grinding are employed. A multi-step thermal process (heat treatment) generally occurs after rough machining to near final dimensions but before final grinding and polishing in the case of balls and bearing raceways. For parts that are not dimensionally critical, simple wear plates for example, final grinding after heat treatment may be unnecessary.

A typical heat treatment includes solution treating at 1000°C in vacuum or inert gas atmosphere followed by a rapid quench in water. The solution treating dissolves precipitate phases like Ni_4Ti_3 and Ni_3Ti forming the preferable NiTi phase. Rapid quenching locks in the dominant NiTi phase and discourages the formation of the other phases that can lead to brittleness and low hardness. Details regarding the processing and resulting properties are the subject of ongoing research and are partially described elsewhere [6]. Using the generalized processes described above, specimens are being fabricated to enable rolling contact fatigue stress limits, bend strength, Charpy impact toughness, compressive strength and thermal properties such as thermal expansion, thermal conductivity and thermal diffusivity. This data will be available in the future but initial bearing design can proceed using information available and estimated.

Design and Manufacturing Considerations

A baseline bearing can be designed using the preliminary and estimated 60NiTi materials properties. This design can then be reviewed and analyzed for its general appropriateness the DA bearing application. Using the preliminary design, a manufacturing method must be then developed and tested. Since key structural properties of 60NiTi differ from bearing steel (notably the elastic modulus is low and high machining forces are needed for material removal), the manufacturing process and tooling may differ from the norm. If the manufacturing investigation identifies design deficiencies it can be revised in an iterative manner. Further, as additional material properties are obtained, such as rolling contact fatigue stress limits, the design can be revisited. The following sections expand upon the preliminary design analysis and a pathfinder manufacturing trial.

Results and Discussion

The DA bearing application currently under consideration is characterized as highly corrosive and mechanically benign. The bearings are nominally 50-mm bore deep groove ball bearings operating at low speed (a few hundred rpm) under very modest axial preload. In space, there is virtually no imposed radial load. Table III gives the representative baseline bearing conditions.

**Table III - Representative Application Bearing Parameters
And Operating Conditions**

Parameter	Value or Condition
Outer Diameter, OD	~80 mm
Inner Diameter, ID	~50 mm
Width, W	~16 mm
Ball Size, D	~9 mm
Ball Material	Si_3N_4
Race Material	Cobalt Alloy
Cage	Snap fit, polymer
Lubricant	Lithium based grease
Ball-Race Stress Limit	~2 MPa
Ball-Race Mean Stress	~1 MPa
Axial Preload	~200 N
Radial Load (terrestrial)	~100 N/bearing
Speed	100-300 rpm
Environment	Warm, highly acidic aqueous solution
Ambient Pressure	Slight vacuum

When reviewing the data and parameters in Table III it becomes clear that the environmental stresses on the bearings, namely the warm and highly acidic environment, far outpace the modest mechanical loads and stresses. In fact, during early system development, the originally specified martensitic stainless steel bearings (440C) experienced unacceptable surface corrosion. Following bench top corrosion studies in a simulated environment, the steel bearings were replaced with the cobalt race- Si_3N_4 ball hybrid bearing design as a baseline.

Figure 3a shows a photograph of the DA assembly during ground tests. This device is essentially a rotating drum evaporator that utilizes a belt drive to provide a low pressure, warm internal chamber that boils wastewater on the ISS. The steam coming off of the drum section is collected and condensed and is then further treated before re-use. Further details of this system can be found in the literature [7-9]. In cross section (Figure 3b shows a representative design), the subject rotor system is a simple configuration of two shielded ball bearings that are lightly spring preloaded and operate in the warm, moist and acidic environment.

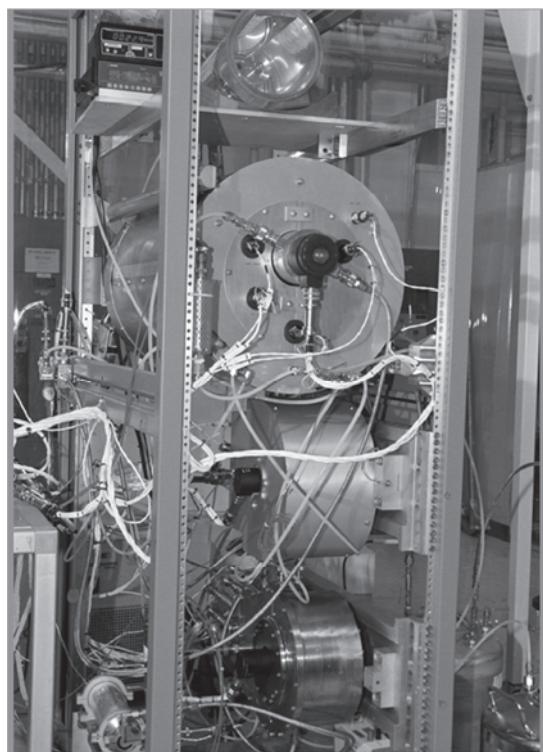


Figure 3a. ISS Distillation Assembly in ground tests.

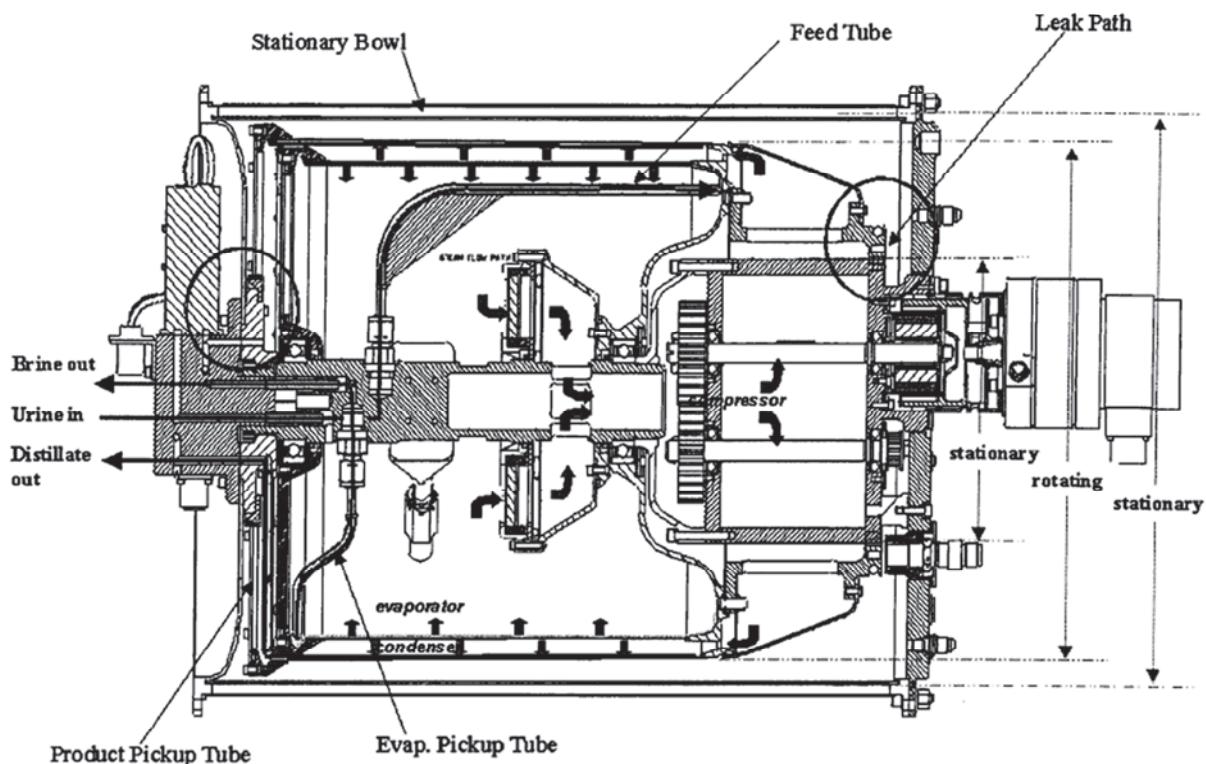


Figure 3b. Representative ISS Distillation Assembly cross-section taken from reference 9.

Figure 4 shows a photograph of the centrifuge bearings after removal from service. The bearings are a straight ball bearing design and utilize a cobalt alloy for the races and silicon nitride for the balls to achieve maximum corrosion resistance.



Figure 4. ISS Distillation Assembly centrifuge bearings.

The performance of the current DA bearings has not been completely satisfactory. The very first system launched suffered from raceway damage that occurred during bearing assembly and installation. Though this damage did not result in system failure, long life could not be assured. The second system launched was returned to earth after a short period of use for repair of an unrelated system component. During a routine bearing inspection significant race wear was observed. Figure 5 shows a photograph of the surface of a worn inner race in which the ball has created a pronounced wear track.

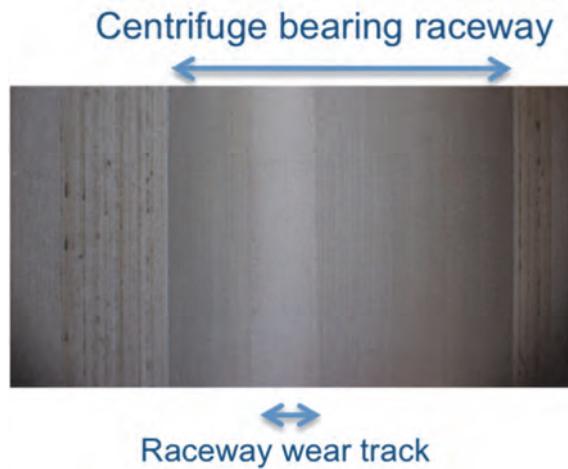


Figure 5. Photograph of an ISS Distillation Assembly centrifuge bearing showing wear track following operation on orbit.

The wear was attributed to the lack of hardness of the cobalt-based races compared to the ceramic balls. The bearings still functioned, but again, long-life was not assured. It is these shortcomings of the current bearing race materials that provide the impetus to consider 60NiTi. Among the first material selection criteria to be assessed is corrosion resistance to the process fluid.

A variety of candidate bearing alloys including steel, 60NiTi and the baseline cobalt alloy were evaluated for corrosion resistance. In this test, ball sized specimens were immersed in a warm and highly acidic aqueous solution that simulates the application. The specimens were weighed before and after exposure for times up to one week and the immersion fluid was analyzed to determine its metal ion content as a means to assess corrosion behavior of the alloys. Table IV shows a summary of the results.

Table IV - Corrosion Mass Loss for Balls (12.7-mm dia.) Soaked in simulated DA solution (115 hr, 65°C, pH 1.0)	
M50 Tool Steel	27,600µg
Cobalt Alloy	389µg
60NiTi	224µg

Not surprisingly, the corrosion resistance of 60NiTi is excellent. Unlike stainless steels, nickel and cobalt alloys do not rely upon the formation of chrome rich passivation layers for their corrosion resistance. Rather, such alloys employ intrinsically corrosion resistant constituents in their chemistry. For Ni-Ti alloys, such as 60NiTi, both nickel and titanium are regarded as highly immune to aqueous acidic corrosion thus the corrosion resistance for the alloy is to be expected. For corroboration, the current cobalt alloy bearing races have not shown any evidence of corrosion problems even after months of service. Since the 60NiTi fares better, in terms of corrosion, than the current cobalt alloy is it justifiable to expect the superelastic bearings will not suffer corrosion. In terms of mechanical properties, however, deeper consideration is warranted.

The bulk hardness of 60NiTi (table I) ranges from Rc 58 to Rc 63 depending upon the heat treatment employed and the dimensions and geometry of the specimen. This is comparable to traditional bearing steels and much harder than the baseline cobalt alloy race material. Rolling and sliding wear tests of 60NiTi under dry and grease lubricated conditions yield tribological behavior comparable to that for hardened bearing steels like 440C [2, 3]. For these reasons, the wear observed in the current bearings is not expected for bearings made from the much harder 60NiTi. 60NiTi, however, has a much lower elastic modulus than both traditional steels and the cobalt alloy. This could affect bearing operation.

The elastic modulus for 60NiTi closely resembles titanium and is less than half that of steel and superalloys (Table I). Thus under load, one expects to encounter deformations and deflections that are approximately twice the level of comparable steel or superalloy components. For mechanical systems in which rigidity and position control is paramount, such a change in elastic behavior can be a design challenge. In a bearing, the radial and axial stiffness are direct functions of the material elastic modulus and thus shaft deflections, for a given load, will increase when going to a superelastic bearing design. At the ball-race contact within a bearing, the lower modulus results in larger hertz contact areas and commensurately lower stresses. Recently reported analyses of 60NiTi roller bearings suggest that comparing all steel to all 60NiTi cases can be complex [10]. The reduced modulus of 60NiTi can be viewed as a higher compliance. Under load in a full bearing system, every rolling element deforms to a higher degree than a steel roller and thus shares the bearing load more readily with its neighboring rolling elements. This effectively reduces the load on each rolling element and may actually increase the ultimate load capacity beyond that estimated from the static load capacity data contained in Table II.

From a design perspective, larger contact areas, lower stresses and higher deflections arising from the use of low modulus materials implies that a careful and thorough detailed design review must be undertaken for all highly loaded bearing applications especially those in which precise orbit control and positioning is vital. For the DA bearing application, the loads are very low and the positioning (bearing stiffness) requirements are minimal. The only continuous loads on the bearings arise from spring preload washers and modest fluid motion-dynamic unbalance forces during normal rotation (relatively low speed of 200 rpm). For completeness, a cursory design stress and stiffness review was done and it concluded that from a mechanical perspective, for this application, the elastic modulus of the bearing race material is

not a critical parameter as long as the static load capacity exceeds that of the baseline superalloy and it does (Table II).

Based upon the results from the mechanical loads and stresses review and the preliminary corrosion studies, it appears that a 60NiTi bearing utilizing the very same geometry and dimensions as the cobalt-hybrid baseline design is a good initial baseline design to consider for manufacturability. Before a manufacturing pathfinder trial can begin, a computer-generated model of the target bearing was developed. This model helps the manufacturing engineer visualize the bearing geometry and devise a manufacturing plan. The bearing model is shown in Figure 6.

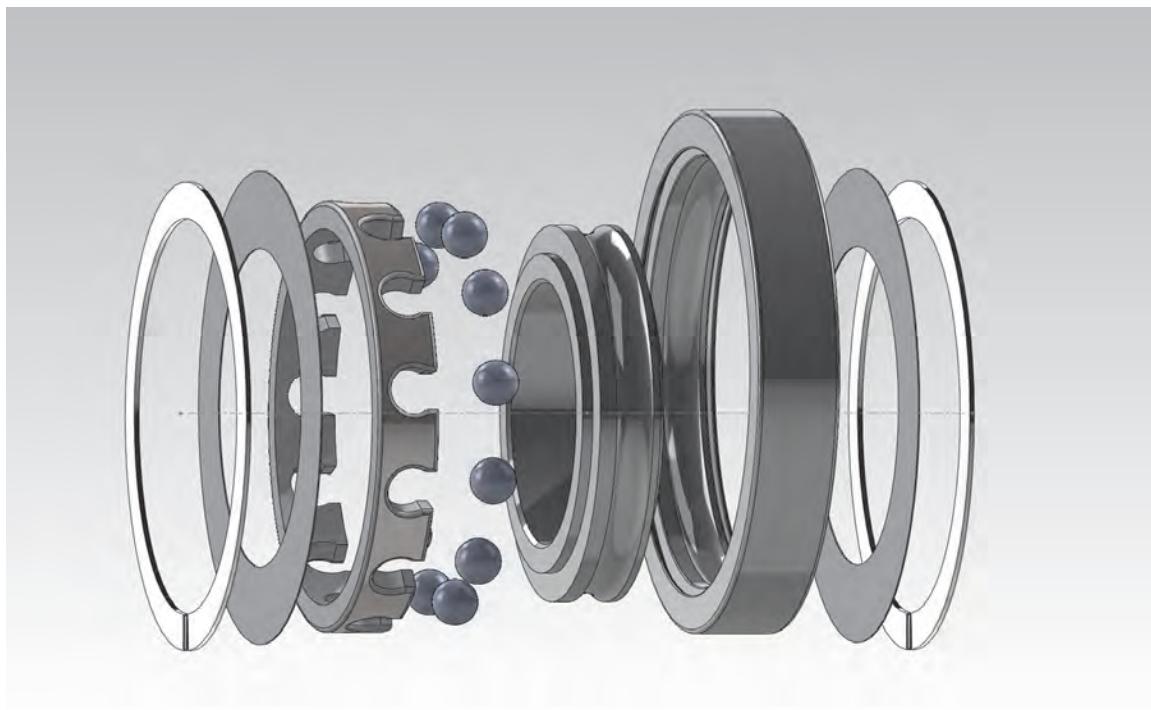


Figure 6. Computer model of DA bearing.

The manufacture of 60NiTi balls is a fully commercialized process and many standard ball sizes are available. The steps needed to make precise raceways from 60NiTi to a desired geometry are not yet fully developed. Decades of experience with various steels has resulted in numerous rules-of-thumb (ROT) for their manufacture. Preferred annealing, rough machining, hard turning, heat treatment, grinding, polishing, acidic surface passivation, normalizing and other processes for steels are well understood and accepted by the manufacturing community. For 60NiTi these ROT's remain undefined. The following paragraphs attempt to layout an acceptable, by not necessarily an optimal, processing path driven by 60NiTi's several unique properties and characteristics, namely its low elastic modulus, resistance to metal cutting and deformation (i.e., low ductility), and its intrinsically brittle tensile behavior.

The basic manufacturing steps employed to go from ingots to finished bearings are as follows: rough machining to near final shape and size using a combination of wire electro discharge machining (EDM) and carbide tool based machining, heat treating to develop high hardness, finish grinding and polishing. Because 60NiTi exhibits limited ductility and is susceptible to brittle tensile behavior, heavy machining operations such as drilling, high removal turning and milling should be avoided. Instead, we have successfully employed a combination of plunge and wire EDM to generate simple blanks from larger ingots and these are then rough machined to near final shape using more conventional machining methods. Figure 7 shows a slice of 60NiTi made by wire EDM and subsequently cut into cylindrical (donut

shaped) race blanks. The ingot, made by powder metallurgy has a rind and center core of steel with 60NiTi filling the annular space. This is part of the PM process and enables more efficient use of the relatively high cost 60NiTi materials.

60NiTi Slice from Ingot



EDM drill and cut donut shaped race blanks

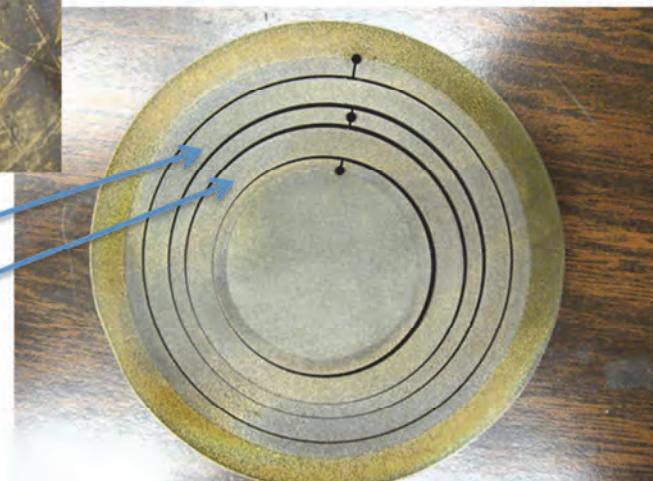


Figure 7. 60NiTi race blanks cut from ingot using EDM processes.

The resulting ring blanks are then shaped into race rings using properly shaped carbide tooling through a plunge turning operation. With this operation, the ring inside diameter is first turned or ground to ensure it is uniform and close to finish dimension (within ~0.01 mm). The ring is then mounted on an expanding type mandrel and care is taken to avoid excessive clamping forces. Because the elastic modulus is half that of steel, excessive clamping force on the inside diameter can result in considerable stretching of the ID leading to unpredictable dimensions after turned race is removed from the mandrel. Once mounted, the OD is plunge turned using a carbide tool previously shaped to match the desired race ring profile. In our tests, we used wire EDM to manufacture the plunge tool from a standard carbide lathe bit. Figure 8 shows the process for turning an inner race ring prior to the heat treatment step.

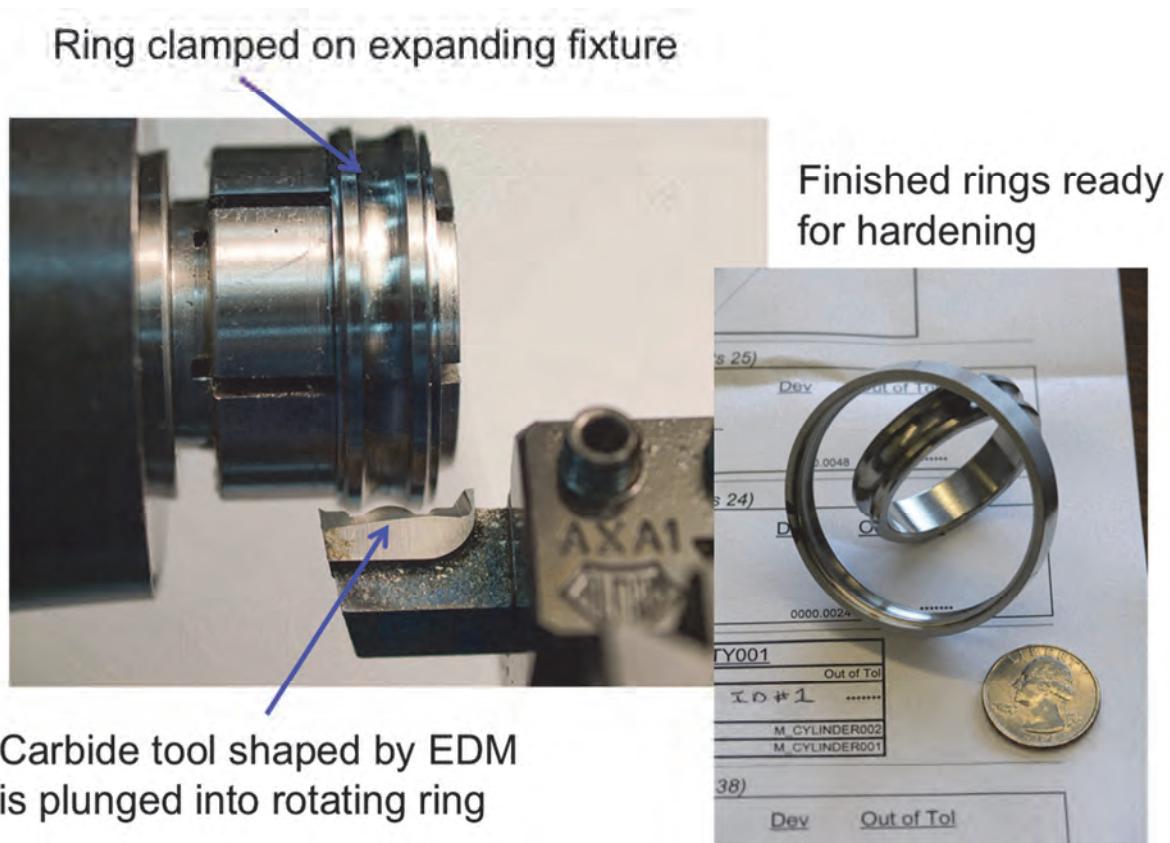
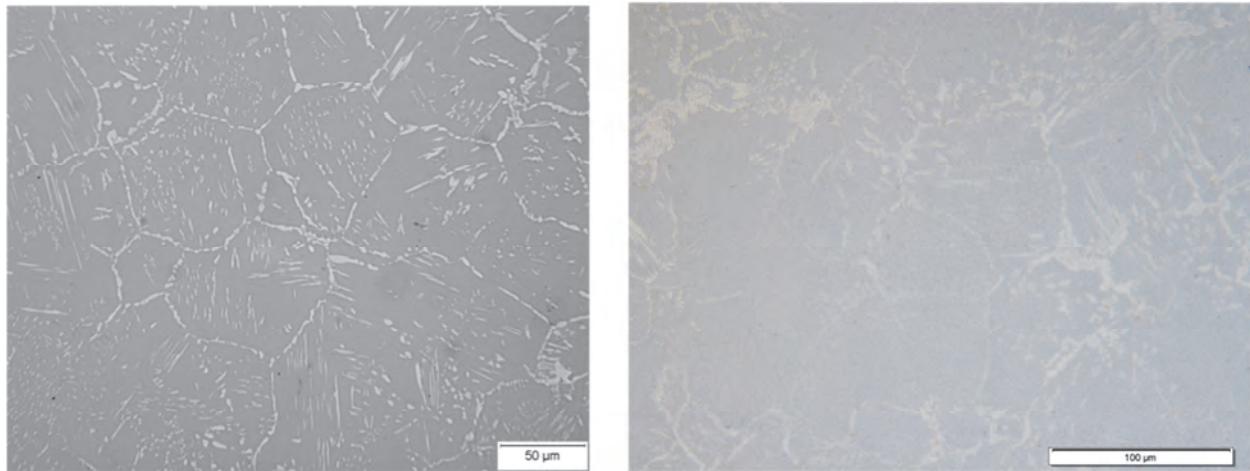


Figure 8. Plunge turning of 60NiTi race rings using a carbide tool profiled to match the desired race geometry using wire EDM.

The final steps include heat treatment and finish grinding and lapping. The heat treatment has been described in detail in reference 6 and briefly includes a solution treatment at 1000°C followed by a rapid water quenching. A vacuum or inert atmosphere is used to prevent excessive surface oxidation. Figure 9 shows the microstructure of 60NiTi prior to and after heat treatment. The heat treatment dissolves undesirable higher order phases resulting in a largely homogenous NiTi phase structure with hardness in the range of 58 to 63 on the Rockwell C scale.



As-received 60NiTi (lighter phase is Ni_3Ti).

Heat-treated 60NiTi.

Figure 9. Microstructure of 60NiTi before (left) and after heat treatment (right).

After heat treatment, standard industry grinding and polishing are employed to yield a finished bearing. Care must be taken to avoid excessive tensile stresses during bearing assembly. Unlike steel that can endure high tensile deformation without fracture, 60NiTi is brittle in tension and outer races, in particular, can break during bearing assembly when hoop stresses are high. To overcome this problem, either separable bearing designs or the use of differential inner ring cooling and outer ring heating are recommended. Beyond that, no other special considerations are needed. The bearings behave and perform as one expects based upon the geometry and lubricant selected. Future efforts to fully characterize the rolling contact fatigue stress-life relationships and gain a better understanding of the tensile strength and toughness behavior of 60 NiTi are planned to guide more mechanically demanding bearing applications.

Summary Remarks

60NiTi offers a viable path towards rolling element bearings that have exemplary corrosion and wear resistance. Though sensitive to brittle fracture in tension, research suggests that extreme static load capacity and resilience imparted by its superelastic behavior is possible. The reduced elastic modulus, compared to steel, may impact highly loaded bearing internal geometry but for the DA bearing application being considered, a direct 60NiTi replacement is reasonable. Lastly, manufacturing research underway suggests that with proper care, modern manufacturing methods are capable of producing high precision ball bearings from 60NiTi.

Acknowledgements

The authors wish to acknowledge the support of the NASA Engineering and Safety Center (NESC) and the NASA Fundamental Aeronautics Program (Subsonic Rotary Wing Project). Their continued funding and technical and programmatic guidance has contributed greatly to bringing this new technology from the lab and closer to commercialization.

References

1. C. DellaCorte, R.D. Noebe, M.K. Stanford, and S.A. Padula: "Resilient and Corrosion-Proof Rolling Element Bearings Made From Superelastic Ni-Ti Alloys for Aerospace Mechanism Applications," NASA TM-2011-217105, September 2012.
2. C. DellaCorte, S. V. Pepper, R. D. Noebe, D.R. Hull, and G. Glennon: "Intermetallic Nickel-Titanium Alloys for Oil-Lubrication Bearing Applications," NASA TM-2009-215646, March 2009.
3. S. V. Pepper, C. DellaCorte, R. D. Noebe, D.R. Hull, and G. Glennon: "Nitinol 60 as a Material for Spacecraft Triboelements," ESMATS 13 Conference, Vienna, Austria, September 2009.
4. A. Palmgen: "Ball and Roller Bearing Engineering, Chapter 8, "Bearing Failures," pages 217-225, 3rd Edition, SKF Industries, Philadelphia, PA, 1959.
5. M.D. McNeese, D.C. Lagoudas, and T.C. Pollock: "Processing of TiNi from Elemental Powders by Hot Isostatic Pressing," Materials Science and Engineering, A280 (2000), pages 334-348.
6. M.K. Stanford, F. Thomas, and C. DellaCorte: "Processing issues for Preliminary Melts of the Intermetallic Compound 60-NiTiNOL," NASA TM-2011-2xxxx, August 2011.
7. D.L. Carter: "Status of the Regenerative ECLSS Water Recovery System," SAE 2009-01-2352, 39th International Conference on Environmental Systems, July 12-16, Savannah, GA, 2009.
8. C.D. Wingard: "Compatibility Testing of Polymeric Materials for the Urine Processor Assembly (UPA) of International Space Station (ISS)," NASA report 20030106448-2003127090, NASA Marshall Space Flight Center, Huntsville, AL, 2003.
9. D.W. Holder and C.F. Hutchens: "Development Status of the International Space Station Urine Processor Assembly," SAE 2003-01-2690, 33rd International Conference on Environmental Systems, July 7-10, Vancouver British Columbia, 2003.
10. T.L. Krantz: "On Calculation Methods and Results for Straight Cylindrical Roller Bearing Deflection, Stiffness and Stress," Proceedings of the ASME 2011 International Design Engineering Technical Conferences & Computers and Information in Engineering Conference IDETC/CIE 2011, August 29-31, 2011, Washington, D.C., paper number DET2011-47930.

Wear of Steel and Ti6Al4V Rollers in Vacuum

Timothy Krantz^{*} and Iqbal Shareef^{**}

Abstract

This investigation was prompted by results of a qualification test of a mechanism to be used for the James Webb Space Telescope. Post-test inspections of the qualification test article revealed some loose wear debris and wear of the steel rollers and the mating Ti6Al4V surfaces. An engineering assessment of the design and observations from the tested qualification unit suggested that roller misalignment was a controlling factor. The wear phenomena were investigated using dedicated laboratory experiments. Tests were done using a vacuum roller rig for a range of roller misalignment angles. The wear in these tests was mainly adhesive wear. The measured wear rates were highly correlated to the misalignment angle. For all tests with some roller misalignment, the steel rollers lost mass while the titanium rollers gained mass indicating strong adhesion of the steel with the titanium alloy. Inspection of the rollers revealed that the adhesive wear was a two-way process as titanium alloy was found on the steel rollers and vice versa. The qualification test unit made use of 440F steel rollers in the annealed condition. Both annealed 440F steel rollers and hardened 440C rollers were tested in the vacuum roller rig to investigate possibility to reduce wear rates and the risk of loose debris formation. The 440F and 440C rollers had differing wear behaviors with significantly lesser wear rates for the 440C. For the test condition of zero roller misalignment, the adhesive wear rates were very low, but still some loose debris was formed.

Introduction

This investigation was prompted by results of a qualification test of a mechanism to be used for the James Webb Space Telescope. The mechanism is used to move a magnet for certain operations of the telescope's near infrared spectrometer (NIRSpec) instrument. The motion of the magnet is guided by a set of preloaded steel rollers in contact with anodized Ti6Al4V. The qualification testing was accomplished in a cold vacuum chamber to match as closely as possible the extreme deep space environment. Post-test inspections of the qualification test article revealed some wear of the steel rollers and mating Ti6Al4V surfaces, and some loose debris was found. The NASA Engineering Safety Center (NESC) is investigating the potential risk of the wear and debris toward hindering the full capability of the NIRSpec instrument. This article will discuss the NESC investigation of the wear phenomena including dedicated laboratory experiments.

Qualification Testing Article and Testing Results.

The mechanism of interest is a translator assembly that features a set of 11 rollers to guide the motion of a magnet (Fig. 1). The translation of the magnet is used to affect the positions of micro-shutters. A motor and linkages provide the motive force. The translator assembly undergoes oscillatory motion in a straight line. The translating distance is approximately 200 mm on each stroke (total of 400 mm of travel during back and forth motion) and translation time in one direction during qualification testing was 10.5 seconds. The qualification test included 96,000 of such forward and return excursions.

The translator assembly motion is guided by a set of eleven rollers. The in-plane guide is provided by a set of four rollers (two of these rollers are visible to the far right side of Fig. 1). These four rollers contact both sides of a guide rail defining the direction of motion. The out-of-plane position and motion is guided by a set of seven rollers. Three rollers are in contact with a base plate defining one plane and four rollers are in contact with a cover defining a second parallel plane. The roller preloads are set by a shimming

^{*} Glenn Research Center, Cleveland, OH

^{**} Bradley University, Peoria, IL

procedure to a nominal normal load of about 18 N. The roller is a cylinder with diameter of 21.2 mm. The roller profile is a crown radius with a flat feature in the center of the crown. Assuming line contact across the flat feature, the Hertz contact maximum pressure is about 240 MPa. The rollers are made from 440F steel (a free machining variant of 440C). The roller material was in the annealed condition and passivated. A pair of deep groove ball bearings supports each roller. The fastener securing the roller bearings to the axle is a locking style bolt assembled in a manner allowing for a small amount of axial play. The rollers are in contact with Ti6Al4V that had been stress relieved and anodized.

After completion of the qualification test, wear was visible on the rollers of the translator assembly and on the mating surfaces. Fig. 2 shows the condition of a qualification test roller. Some loose particulate debris was also found, which was collected and analyzed [1-2]. The worn surfaces and wear debris provide evidence that the wear process was primarily adhesive wear. In total it appears that the steel has transferred to the mating Ti6Al4V surfaces. The loose wear debris included both the steel and titanium alloy materials. The severity of wear was not the same on all rollers.

From observations of the wear patterns and wear debris of the qualification unit, study of the literature, and engineering assessment of the kinematic configuration, manufacturing tolerances, and roller mounting details, the roller alignment seemed likely to be a key variable influencing the wear rate. To better understand the wear phenomena and to explore possible mitigation strategies, a set of laboratory roller tests were conducted in vacuum. The next sections will discuss the testing apparatus, specimens, procedures, and the corresponding results.

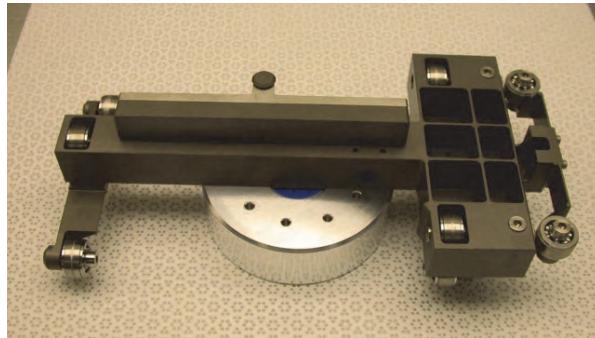


Figure 1 – Translator assembly [1].

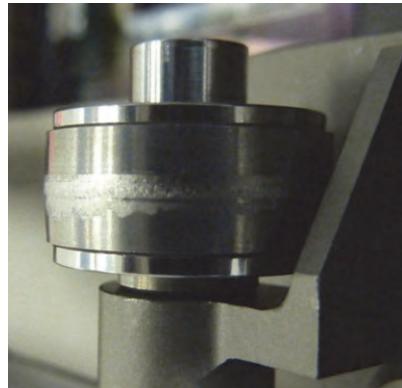


Figure 2. Condition of roller after completion of qualification test [2].

Laboratory Test Apparatus, Specimens, and Procedure

Test Apparatus for Roller Pairs

Testing was done using the NASA Glenn Research Center Vacuum Roller Rig (Figure 3). The rig allows for application and measurement of a load pressing the rollers together while having a purposely misaligned and adjustable shaft angle. The rig is depicted in schematic form in Figure 4. A drive motor provides motion to the driving roller. A magnetic-particle brake attached to the output shaft imposes torque on the driven roller. The rig can be operated with the brake not energized. For such a condition the torque transmitted through the roller pair is the drag torque of the output shaft (drag of the seals and support bearings). The normal load pressing the rollers together is provided by an air cylinder. The cylinder acts through a gimbal point to rotate the plate that mounts the driving shaft and drive motor. The rotation of the drive motor plate displaces the driving roller toward the driven roller shaft in an arc motion. The pressure to the cylinder, and thereby the load between the contacting rollers, is adjusted by a hand-operated valve (open-loop control). A turbomolecular pump assisted by a scroll pump provides vacuum in the test chamber. The typical condition in the test chamber is a pressure of about 3×10^{-7} Torr. The most

prevalent remaining constituent in the chamber during testing is water vapor as determined by residual gas analyzer [3]. Figure 5 provides a simplified schematic of the test rollers labeled with some of the nomenclature used herein.

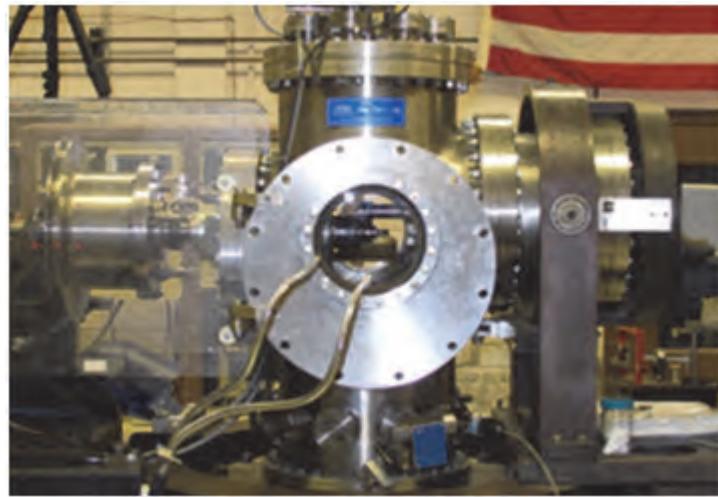


Figure 3 – Vacuum roller rig.

A set of sensors on the test apparatus monitors the test conditions. The outputs of the analog sensors were digitized and stored via a data acquisition system at a rate of up to 0.66 hertz. Each of the sensors will be described in turn.

The misalignment of the driving roller shaft and driven roller shaft is depicted in an exaggerated manner in Figure 4(b). The misalignment is measured via a linear variable differential transformer (LVDT). The transducer housing is attached to the bedplate, and the translating, spring-loaded transducer tip contacts against a mechanical stop on the turntable. To establish the aligned condition, special tooling blocks were machined to locate the roller-mounting surfaces of the two shafts as parallel. With the shafts aligned by the tooling blocks, the transducer circuit balance was adjusted to provide an output of zero. The precision of this method for aligning the shafts was limited by the dimensions of the roller mounting surfaces used as the reference planes. From analysis of the test rig drawing tolerances and geometry, the alignment procedure using the tooling blocks to define the zero-degree position has a precision within 0.08 degrees. Rotation of the turntable from the aligned position moves the LVDT sensor. The angular displacement of the turntable was determined by mounting a laser light source on the moving shaft at the roller mounting location and directing the light onto a paper placed at a known radial distance from the center of the turntable. The movement of the laser light was marked on the paper and distance between the points measured and used to relate the sensor output to the angular motion of the turntable.

The torque on the output shaft is monitored by a strain-gage type torquemeter of 22 N-m (200 in-lb) torque capacity. Calibration was done in place using deadweights acting on a torque arm of known length attached at the test roller position and reacting the output shaft to ground.

The load pressing the rollers together is termed herein the “normal load” (Figure 5). The normal load is applied via an air-pressure actuated piston. The air piston acts through a load cell against the drive motor plate that is gimbal-mounted relative to the test chamber (Figure 4(a)). In this way the air piston moves the roller on the input shaft in an arc motion toward the test roller. The arc motion of the input shaft table is measured by an LVDT. Once the rollers are in contact, additional force commanded to the air piston increases the normal load between the test rollers. Careful calibration processes allow calculating the normal load on the test roller based on the sensor outputs from the load cell and the LVDT that measures the input shaft position.

When rollers operate in a misaligned condition a force will develop in the direction of the shaft axis [4-7]. In such a condition points on the two rollers in intimate contact and within a “stick” zone of the contact patch are constrained to move in unison. If the points were not in contact the kinematic constraints would provide a slightly different path of motion. The difference in the actual path of motion and that defined by the motion if the points were not in contact gives rise to surface strains and a resultant axial force. A sensor to measure this force is labeled as the “axial force” sensor in Figure 4. The axial force sensor is co-located on the output shaft with the torquemeter sensor. The configuration of the rig did not allow for direct deadweight calibration in place. To calibrate the sensor in place, the following procedure was used. First, a load cell was calibrated via deadweights and then was placed on the free end of the output shaft to act as a reference load cell. A threaded jackscrew acted against the reference load cell and a hard stop in the vacuum chamber. Adjusting the jackscrew length allowed for changing the force imparted on both the reference load cell and the rig’s axial load cell and to the machine frame. In this manner the same force was applied to both load cells, and the reference cell output was used to calibrate the axial load cell sensor in place.

The preceding two paragraphs describe the sensors (and sensor calibrations) to determine two mutually perpendicular forces acting on the driven test roller. A force also acts along a third axis. This is the force directed tangential to the roller diameter and is termed here as the “tangential” force. The tangential force on the input shaft roller acts through a gimbal point (Figure 4(b)). The rotational motion about the gimbal point is restrained by a mechanical link to the turntable structure. A load cell is used to sense the force in said mechanical link to the turntable structure. This sensor was calibrated in place by using a pulley-cable system and dead weights to relate the tangential force applied at the test roller position to the sensor output. During testing, this sensor is also affected by spin moments [4-5] that can develop in roller contacts. The data from the tangential force sensor was recorded for possible future use, but such data were not of immediate interest and are not reported herein.

Shaft speeds and total number of shaft revolutions were measured using encoders on each shaft. The encoder pulses were counted and recorded via a digital pulse counter. The encoder pulses were also monitored by a frequency converter to provide a convenient shaft speed display to the test operator. The encoders provide 6,000 pulses for each shaft revolution.

Test roller conditions were photographed at regular intervals through a viewport. The images were captured digitally using a single-lens reflex camera with a 150 mm micro lens and a 12 million effective pixel image sensor. A debris pan was used to capture debris created from the roller pairs. A video camera recorded the condition of a portion of the debris pan. In spite of several attempts to adjust video camera setting and lighting, the video images failed to capture all that could be observed by eye through the viewport.

Test Specimens

The test specimens used for this research had a nominal geometry of 35.6 mm outer diameter and a 12.7 mm width. The apparatus requires that at least one roller has a crowned profile to avoid edge loading. The roller on the drive motor (input) shaft was provided a crown radius of 200 mm and was made from steel. The roller on the lower (output) shaft had a flat profile and was made from Ti6Al4V alloy.

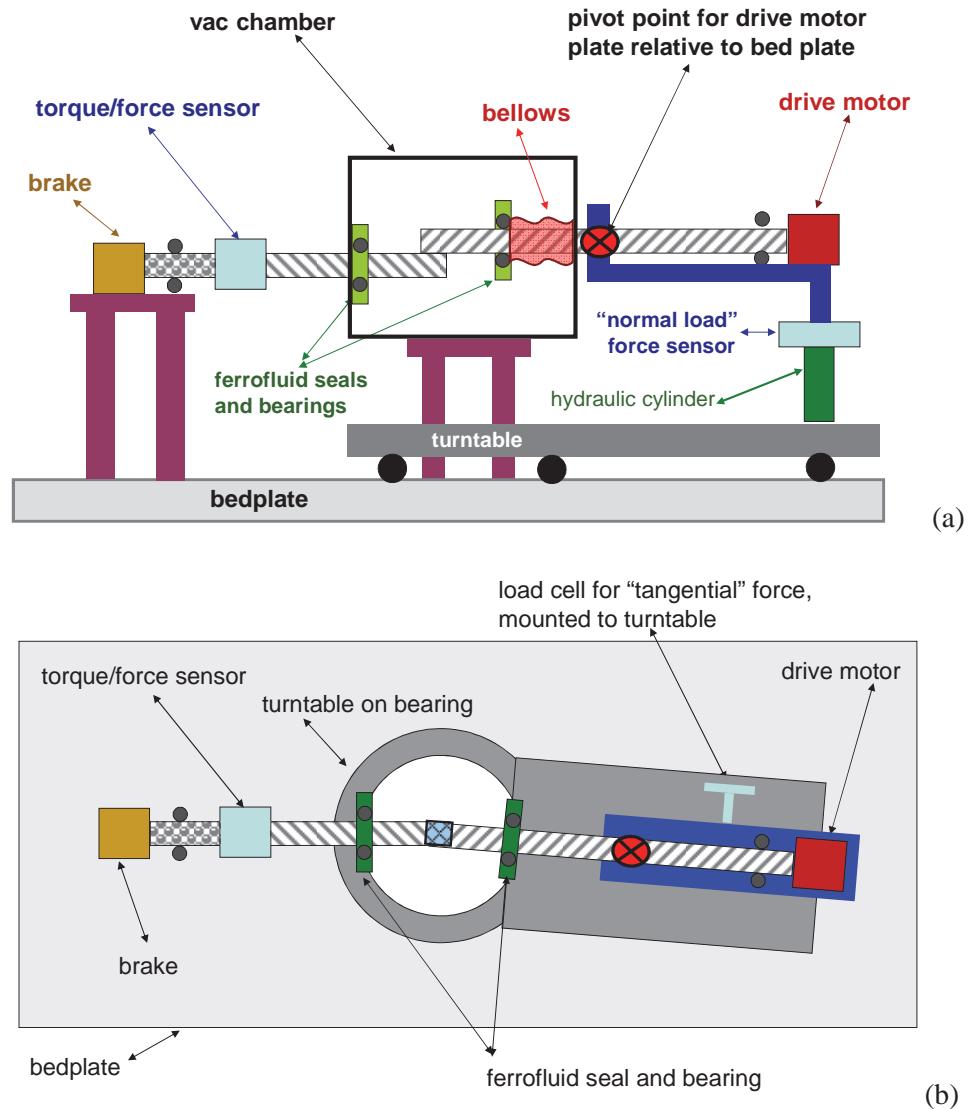


Figure 4 – Schematic views of the vacuum roller rig. (a) Schematic, side view.
(b) Schematic, overhead view with shaft misalignment depicted and exaggerated.

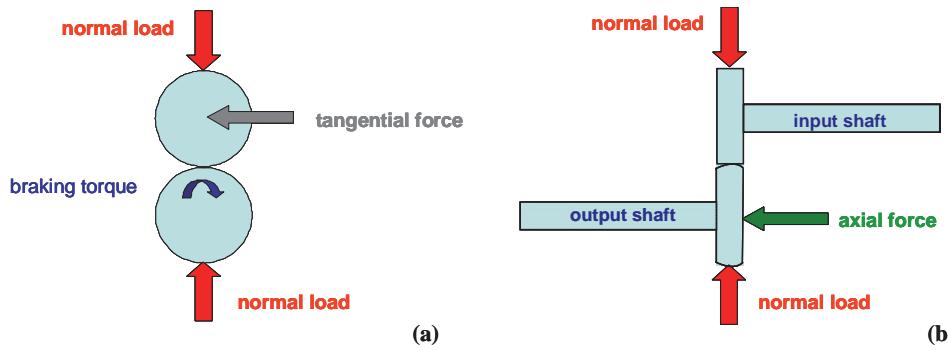


Figure 5 – Simplified schematic view including some of the important sensed data.
(a) Schematic, front view. (b) Schematic, side view.

The material condition, manufacturing details, and surface roughness can all influence the wear behavior. The details of the roller conditions are given in Table I and additional details follow. The qualification test unit has rollers made from 440F steel in the annealed condition and the working surface specified to have a roughness of 0.4 μm maximum. The qualification test rollers were passivated per ASTM A-380-06. The 440F alloy is similar to 440C but includes the introduction of either selenium and/or additional sulfur to alter the machining characteristics relative to 440C. From x-ray photoelectron spectroscopy both the qualification test unit rollers and the 440F laboratory test rollers were found to have selenium as a constituent. The surface hardness of a 440F laboratory test roller was measured as 24 RC. Laboratory test rollers were made intending to enhance resistance to adhesive wear and to reduce debris generation. These rollers were made from 440C, hardened to RC 58, and provided a fine ground surface. Roughness of the test rollers was documented by stylus profilometer inspections. Typical roughness profiles in the rolling direction are provided in Fig. 6. The roughness data of Fig. 6 were prepared filtering the data using 0.8 millimeter cutoff and 300:1 bandwidth ISO standard filter. The roughness of the 440F rollers (0.15 micrometer Ra) was significantly larger than the roughness of the 440C rollers (0.07 micrometer Ra).

The test rollers that mated with the 440 series rollers were made of Ti6Al4V. The Ti6Al4V rolling surfaces of the qualification unit were observed to have distinctive machining marks, and so the laboratory Ti6Al4V rollers were made using a turning operation as the resulting surface texture of the test rollers were judged similar to the surfaces of the qualification unit. The rollers were stress relieved per AMS 2801 after machining. The roller hardness was RC 35. Some of the Ti6Al4V rollers were anodized per Tifin 200 matching the qualification unit treatment. A typical roughness profile for the Ti6Al4V rollers after anodizing is provided in Fig. 6. The typical roughness average value was 0.44 micrometer Ra. Some testing was done with Ti6Al4V rollers that were not anodized to make project progress previous to the completion of the anodize process.

Procedure to Install Test Rollers

Test specimens were cleaned and installed using careful procedures to provide clean test surfaces. The test rollers were cleaned just prior to installation into the rig using de-ionized water and 0.05 micron alumina powder. After appropriate hand scrubbing, the cleaning powder was rinsed with deionizer water making sure that the entire roller surface wetted uniformly to confirm complete cleaning of surface oils. The water was removed from the roller using dried pressurized nitrogen. Test rollers and mounting hardware were handled only with gloved hands and clean tools to complete installation into the test apparatus.

Procedure for Testing Rollers

The first step for testing after installation of the test rollers was to immediately isolate the testing chamber and provide a vacuum, using the scroll roughing pump, to approximately 50×10^{-3} Torr chamber pressure. This isolation step was done even if test scheduling required some delay between the time of installation of rollers and the time for testing to minimize exposure of the cleaned surfaces to any contaminants that might be present in the atmosphere. Prior to testing the turbomolecular pump was used to bring the testing chamber to approximately 3×10^{-7} Torr.

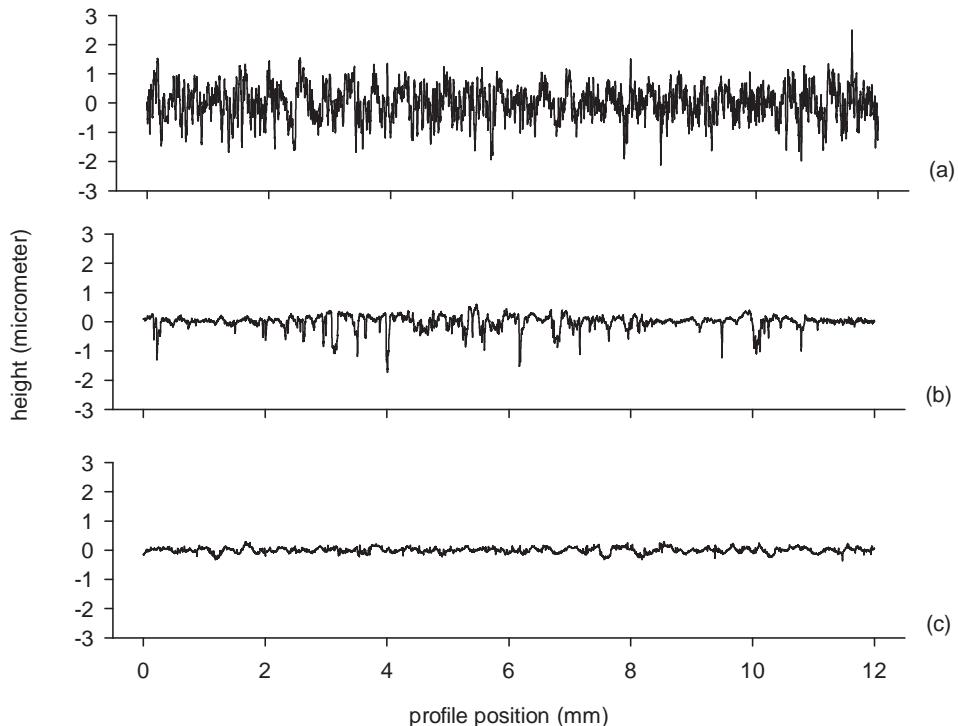


Figure 6 – Typical surface roughness of test rollers, profile traces obtained using a 2-micrometer radius tip conisphere stylus tracing in the direction of rolling.
(a) Ti6Al4V roller. (b) 440F roller. (c) 440C rollers.

Contact analyses were completed to select roller normal loads, speeds, and alignment angle and to relate those choices to the operating conditions of the qualification test unit rollers. The contact conditions for the qualification test were studied assuming that the contact pressure distribution was affected by the moment produced by the axial load caused by misalignment. To estimate this effect, it was assumed that the ratio of axial load to normal load was 0.6 and such load produced an overturning moment by acting through the ball bearing center. It was also assumed that the supporting structure provided 90 percent of the reaction to the overturning moment while the pressure distribution provided 10 percent of the reaction. The pressure distribution for such a loading condition while accounting for the roller profile having a crown but modified with a flat section was calculated using the method of Vijayakar [9-10]. The contact condition for a perfectly aligned roller having zero axial force was also solved. The predicted contact pressure distributions are provided in Fig. 7. The misalignment of the roller axis will cause a shift of the pressure from the central flat section onto the crowned region, and a maximum contact pressure of about 450 MPa occurs near the transition from flat to crown geometry. Because of test rig limitations, the laboratory test conditions could not match these conditions exactly. The laboratory testing was done at maximum contact pressure of about 770 MPa. The laboratory tests were used to study trends and fundamental qualitative wear behavior.

The test rig speed was selected using the idea that the “contact time” of the test unit and laboratory rollers should be matched. Here the “contact time” is the time required for a point on the roller to pass through the Hertz contact region. The contact time on the qualification test unit for condition of misaligned rollers was 0.015 second. To match this condition the test rig was operated at 1.6 rad/s (15 rpm) for the majority of laboratory testing.

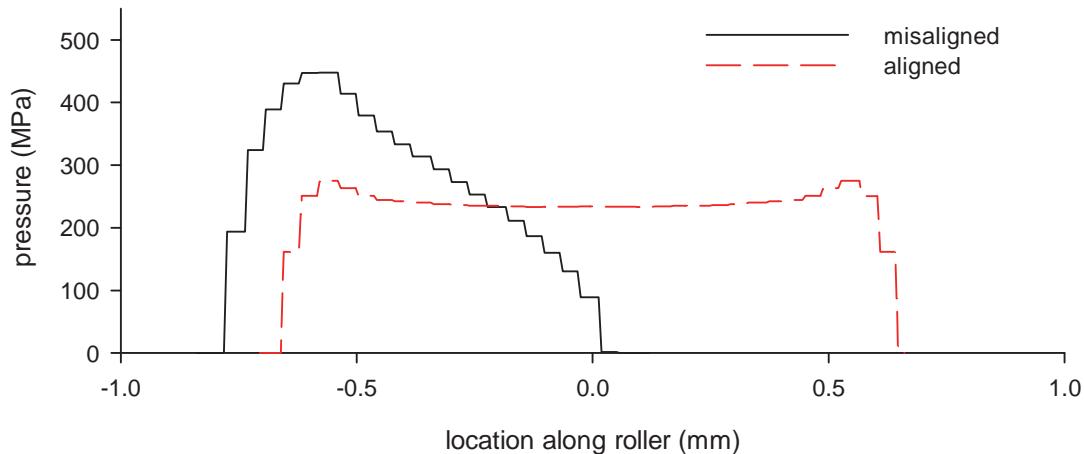


Figure 7 – Contact pressures on qualification test unit roller for cases of misaligned and aligned rollers. The pressures shown are at the midpoint of the Hertz contact in the direction of rolling.

The lab apparatus can be operated with the misalignment angle at a maximum value of about 1.5 degrees. The influence of the misalignment angle on the contact conditions depends on overall system stiffness and the contact dimensions. The sliding distance in such a condition can be approximately quantified as proportional to the product of the misalignment angle and the length of the contact patch in the rolling direction. Using this concept the misalignment angle of the lab test apparatus times a factor of 1.7 provides the approximate simulated misalignment angle of the qualification test unit. The lab test was conducted for misalignment angles up to 1.5 degrees that would simulate a misalignment angle of about 2.5 degrees for the qualification unit.

A summary of the test conditions is provided in Table 1. The tests are listed sequentially in the order of testing. In general one would prefer to have a randomly chosen testing order, but in this work roller availability dictated the testing sequence. In some cases the same roller pair was tested at more than one misalignment angle. In those cases the angles were tested sequencing from smallest to largest.

Post-test documentation of the rollers included recording of the mass of each roller, profilometry, and photographs. Some rollers were inspected via scanning electron microscope. Debris was collected. In some cases the debris was swept from the debris tray, collected to a glass vial, and total mass of debris determined. In some cases debris was collected using a square piece of tacky material that could be placed onto the tray and lifted to collect the debris. The collected debris could then be subjected to automated analysis of debris particle counts and sizes. At completion of one test there was no debris readily visible on the brass-hued debris tray, but a swiping of the tray with a cotton-gloved finger revealed debris. The glove fingertip was saved to retain the debris. For later tests a dark grey anodized plate was used for the debris tray. The darker and matte-finished plate allowed to more easily see the small particles.

Test Results

Roller wear.

Photographs of the test rollers were recorded through a view port during test operations at regular intervals. Figure 8 provides a set of photographs documenting the progression of wear during tests with test ID 3, 4 and 8 (test ID per Table 1). These photos show the difference in wear resulting from material condition. The first two rows of Figure 8 can be used to compare and contrast the wear when using annealed 440F rollers (first row) to the wear when using hardened 440C (second row). In these photos the upper roller is the one made from steel alloy and the lower roller is the titanium alloy. The steel rollers took on a relatively uniform appearance of wear while the titanium rollers had patches of irregular appearance. The wear rate can be qualitatively judged by the width of the wear track of the upper roller

that, when new, had a circular crown. As this roller loses material the wear track widens. The worn 440C roller appears slightly smoother than the 440F roller suggesting that steel wear debris would in general be smaller for the case of 440C compared to 440F. Recall that the 440F is alloyed to be “free machining” and to thereby produce chips more easily and of greater length during machining. The last row of Figure 8 shows dramatically reduced wear when the rollers are exactly aligned (final row of Figure 8). Even after significantly longer running time the aligned rollers appear almost like the running-in condition (first few hundred cycles) of the misaligned rollers. Still, for the aligned condition one can notice in the very center of the wear track a narrow band that exhibits adhesive wear.

Table 1. Summary of Test Conditions

test #	roller pair	test ID	upper roller		lower roller		test conditions	
			material	outer surface condition	material	outer surface condition	speed (rpm)	misalignment angle (deg)
1	1	1	440C	bare	Ti6Al4V	bare	15	-1.4
2	2	2	440F	bare	Ti6Al4V	bare	15	-1.4
3	3	3	440F	bare	Ti6Al4V	anodized	15	-1.4
4	4	4	440F	bare	Ti6Al4V	anodized	15	0.0
5	5	5	440F	passivated	Ti6Al4V	anodized	9	-1.4
6	6	6	440F	passivated	Ti6Al4V	anodized	15	-0.4
7	7	7	440F	passivated	Ti6Al4V	anodized	15	-0.9
8	8	8(a)	440F	passivated	Ti6Al4V	anodized	15	0.0
9	8	8(b)	440F	passivated	Ti6Al4V	anodized	15	-0.1
10	8	8(c)	440F	passivated	Ti6Al4V	anodized	15	-0.2
11	8	8(d)	440F	passivated	Ti6Al4V	anodized	15	-0.3
12	8	8(e)	440F	passivated	Ti6Al4V	anodized	15	-0.7
13	9	9	440C	bare	Ti6Al4V	anodized	15	-1.5
14	10	10	440C	bare	Ti6Al4V	anodized	15	-1.4
15	11	11	440C	passivated	Ti6Al4V	anodized	15	-0.9

To study the wear, rollers were inspected using a scanning electron microscope (SEM). By using x-ray photoelectron spectroscopy the constituents of particular regions of the rollers could be investigated. In all cases, two-way transfer of material was observed. That is, titanium alloy substrate was found on the 440 steel rollers and steel alloy was found adhered to the titanium alloy rollers. An example from inspection of the titanium alloy roller from test ID 3 of Table 1 is provided in Figure 9. An overall view of a region near the center of the wear track is given in Fig 9(a), and also noted are regions where spectroscopy was assessed. The bright regions noted as #1 and #2 in Fig. 9(a) produced the respective spectra of Fig. 9(b-c). Here in the spectra of Fig. 11(b-c) we note the clear presence of iron, chromium, and alloying elements of the 440 steel. Region #2 had a brighter appearance suggesting a more complete coverage of the substrate, and the spectrum for region #2, Fig. 9(c), has a very strong peak correlating to iron. The darker region noted as numeral 3 in Fig. 9(a) produced the spectrum of Fig. 9(d). Here the titanium is still exposed, we observe peaks correlating to titanium and aluminum, and peaks correlating to iron and chromium are not present. The spectrum for the region marked with the numeral 4 in Fig. 9(a) is not shown here but was consistent with that of Fig. 9(d). These trends were true for all of many samples inspected. In all cases the worn regions included regions of the base material still exposed and also contained adhered material from the mating roller. As will be noted, in net, mass was lost for the 440 steel rollers. However, in all cases Ti6Al4V material was found on the tested steel rollers via SEM spectroscopy.

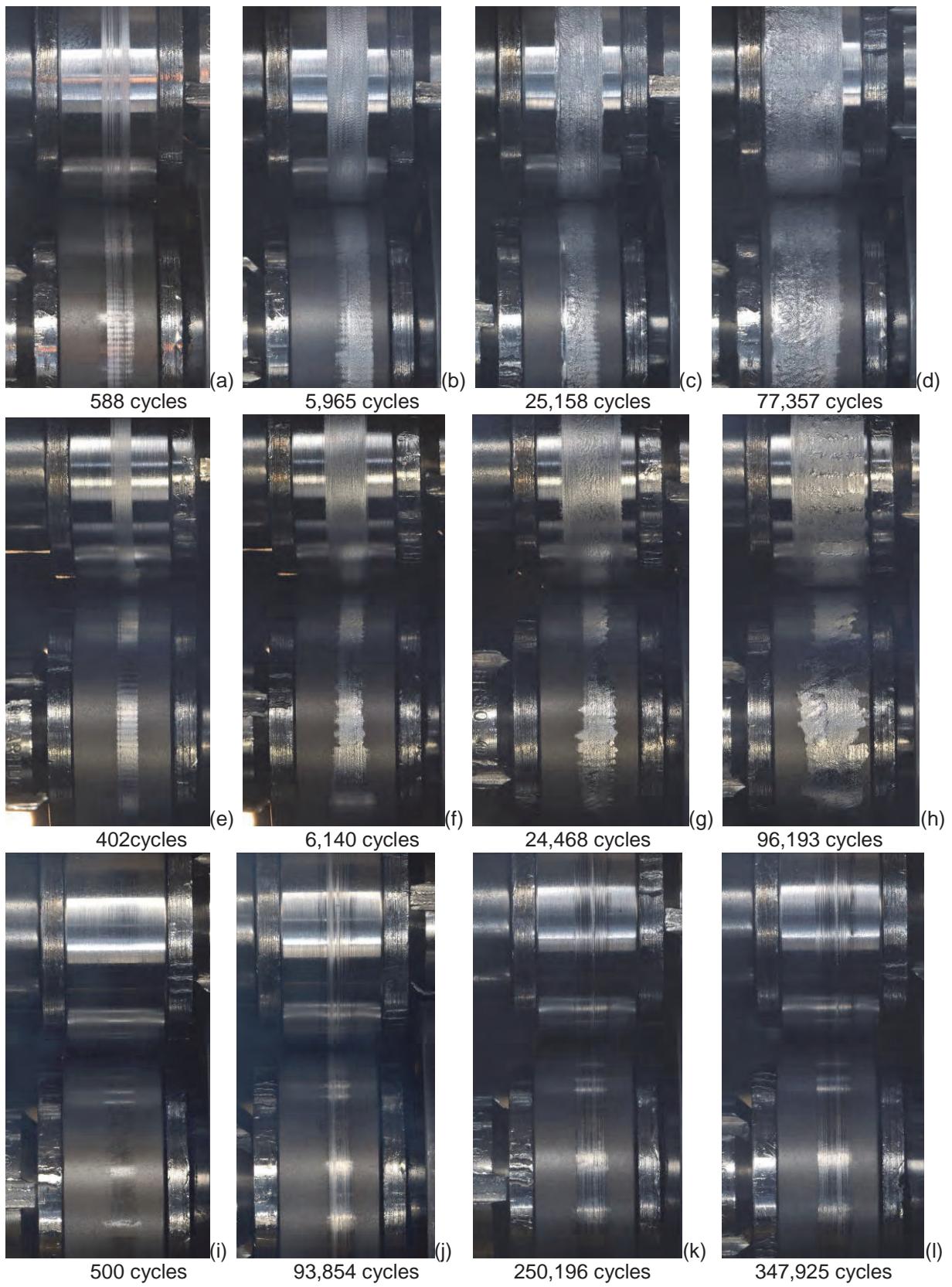


Figure 8 - Progression of wear during 3 tests. The cycle count is denoted below each photo.
(a-d) 440F at 1.4° misalignment. (e-h) 440C at 1.5° misalignment. (i-l) 440F at 0.0° misalignment.

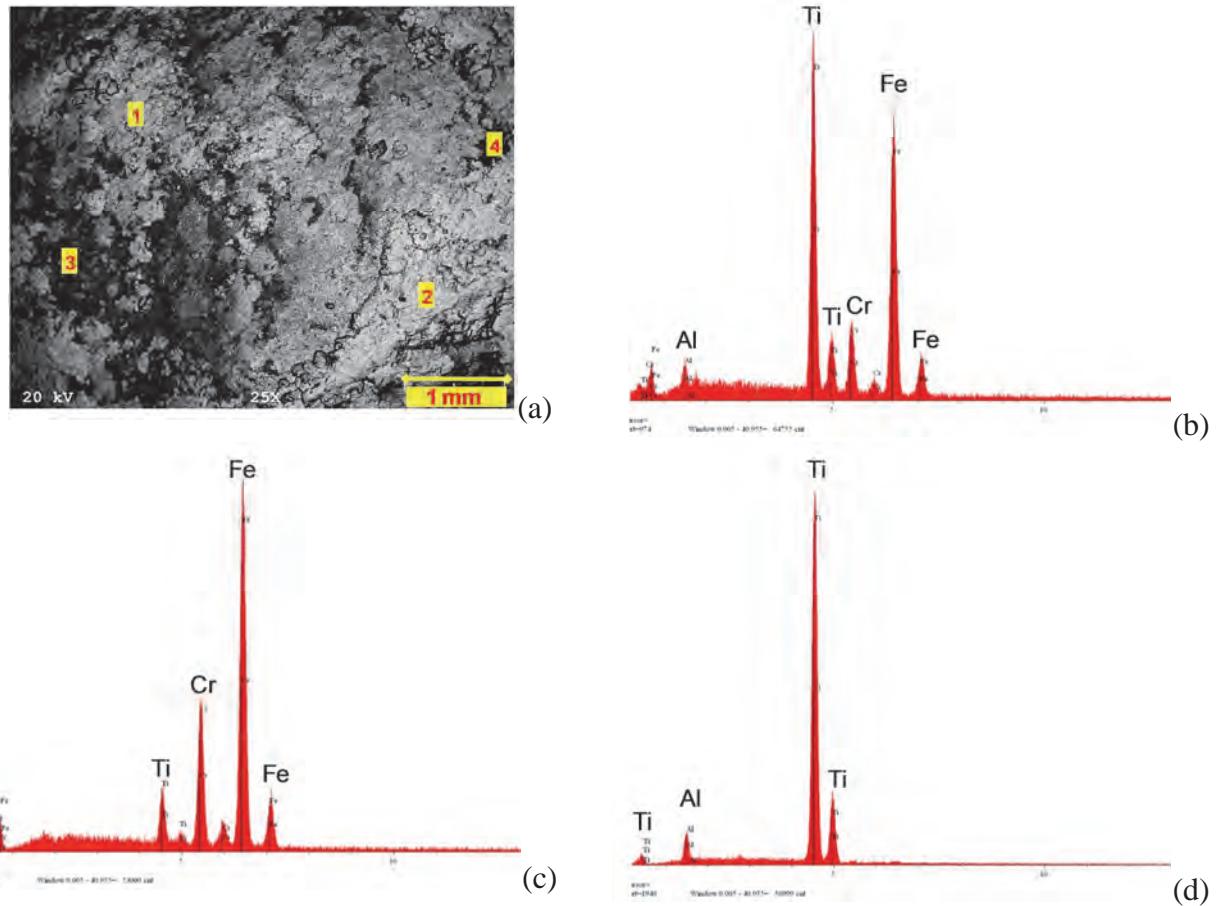


Figure 9 – Scanning electron inspections of the wear track on the titanium test roller for test #3.
(a) SEM image. **(b)** Spectrum for region noted as 1 in 9(a). **(c)** Spectrum for region noted as 2 in Fig. 9(a). **(d)** Spectrum for region noted as 3 in Fig. 9(a).

The roller masses were determined using a scale with digital readout to 0.0001 gram. Masses of the rollers were measured after cleaning and just before installation in the test rig. The roller masses were also measured just after removal from the test chamber. The change in mass at the end of the test quantifies the net transfer of material by adhesive wear. The sum of the mass change for the two rollers provides a calculated value of debris lost from the roller pair. Because of practical test considerations, the test durations were not the same for each test. To provide a method for direct quantitative comparison, the change in mass was divided by the total number of revolutions of the input shaft (that is the total number of contact stress passes) to quantify the wear rate. The mass change data and calculated wear rates are summarized in Table 2.

Often wear is modeled as proportional to the sliding distance. In these roller tests, to a first order effect the sliding distance is proportional to the misalignment angle. The rate of mass change was plotted as a function of misalignment angle (Fig. 10). Note that in the net, the steel rollers lost mass while the titanium alloy rollers gained mass. We also note that the 440F material had a higher rate of wear compared to the 440C in all cases. Rabinowicz [8] has noted that the experimental evidence for wear rate being proportional to sliding distance (as often assumed true) is mixed. He states that usually the relationship is not perfectly obeyed but the proportional relationship represents experimental data “reasonably well”. This observation matches the behavior from this investigation in that the misalignment angle (and thereby the sliding distance) correlates to the wear rate, but the linear relationship is not exact. Not only the wear rate but also the wear behavior differed for tests with 440F steel vs. 440C steel. Adhesive wear tends to progress toward an “equilibrium surface” [8] meaning the surface roughness changes with running, and

the wear process can either roughen or smoothen the surfaces depending on the materials and starting conditions. The equilibrium surfaces for the tests with 440F vs. 440C differed as depicted in Fig. 11. Tests with the 440C material resulted in smoother running surfaces (Fig 11(b)), and the photos suggest that the particle size of wear debris is likely smaller, in general, for the case of 440C. The Ti6Al4V rollers when mated with the 440F steel tended to gain material by adhesive wear in a more uniform fashion, that is, the coverage of the surface was more significant and uniform in appearance. It is possible that the hardened 440C behavior differed from that of the annealed 440F not only because of the change of the elastic limit but also because of an alteration of the metallurgical structure and alteration of the adhesion compatibility with the Ti6Al4V [8].

Table 2 – Summary of Roller Wear Test Results

		test duration	mass change; Ti6Al4V	mass change; 440 steel	calculated mass liberated	calculated rate of mass liberated
test #	test ID	revolutions of input shaft	grams	grams	milligrams	micrograms per cycle
1	1	26,080	0.0049	-0.0054	0.500	0.019
2	2	60,228	0.0981	-0.1258	27.700	0.460
3	3	77,326	0.1350	-0.2072	72.200	0.934
4	4	347,925	-0.0006	-0.0052	5.800	0.017
5	5	55,411	0.0817	-0.1052	23.500	0.424
6	6	60,850	0.0151	-0.0210	5.900	0.097
7	7	124,900	0.1314	-0.1664	35.000	0.280
8	8(a)	93,027	-0.0005	-0.0038	4.300	0.046
9	8(b)	24,001	0.0012	-0.0012	0.000	0.000
10	8(c)	24,000	0.0017	-0.0018	0.100	0.004
11	8(d)	24,095	0.0025	-0.0027	0.200	0.008
12	8(e)	93,117	0.0464	-0.0501	3.700	0.040
13	9	96,193	0.0682	-0.0698	1.600	0.017
14	10	41,055	0.0200	-0.0210	1.000	0.024
15	11	90,004	0.0672	-0.0688	1.600	0.018

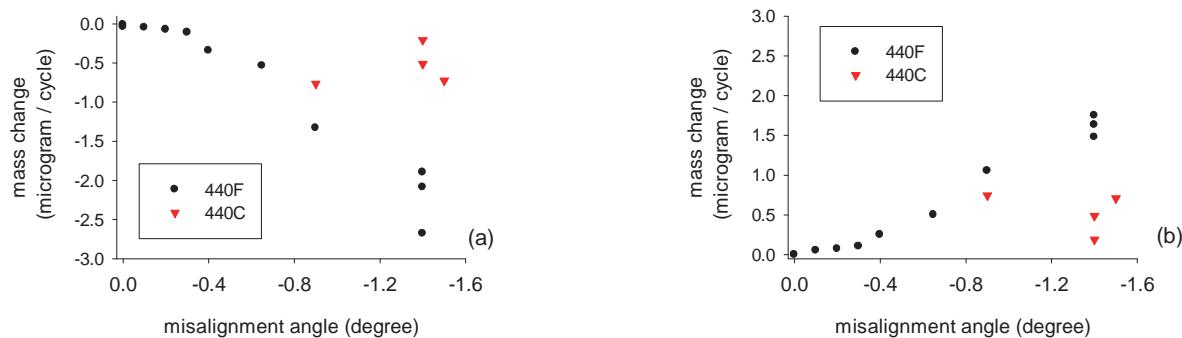


Figure 10 – Change of mass per cycle (shaft revolution) as a function of misalignment angle. (a) Mass loss of 440 steel rollers. (b) Mass increase of Ti6Al4V rollers, symbols denoting the mating material.

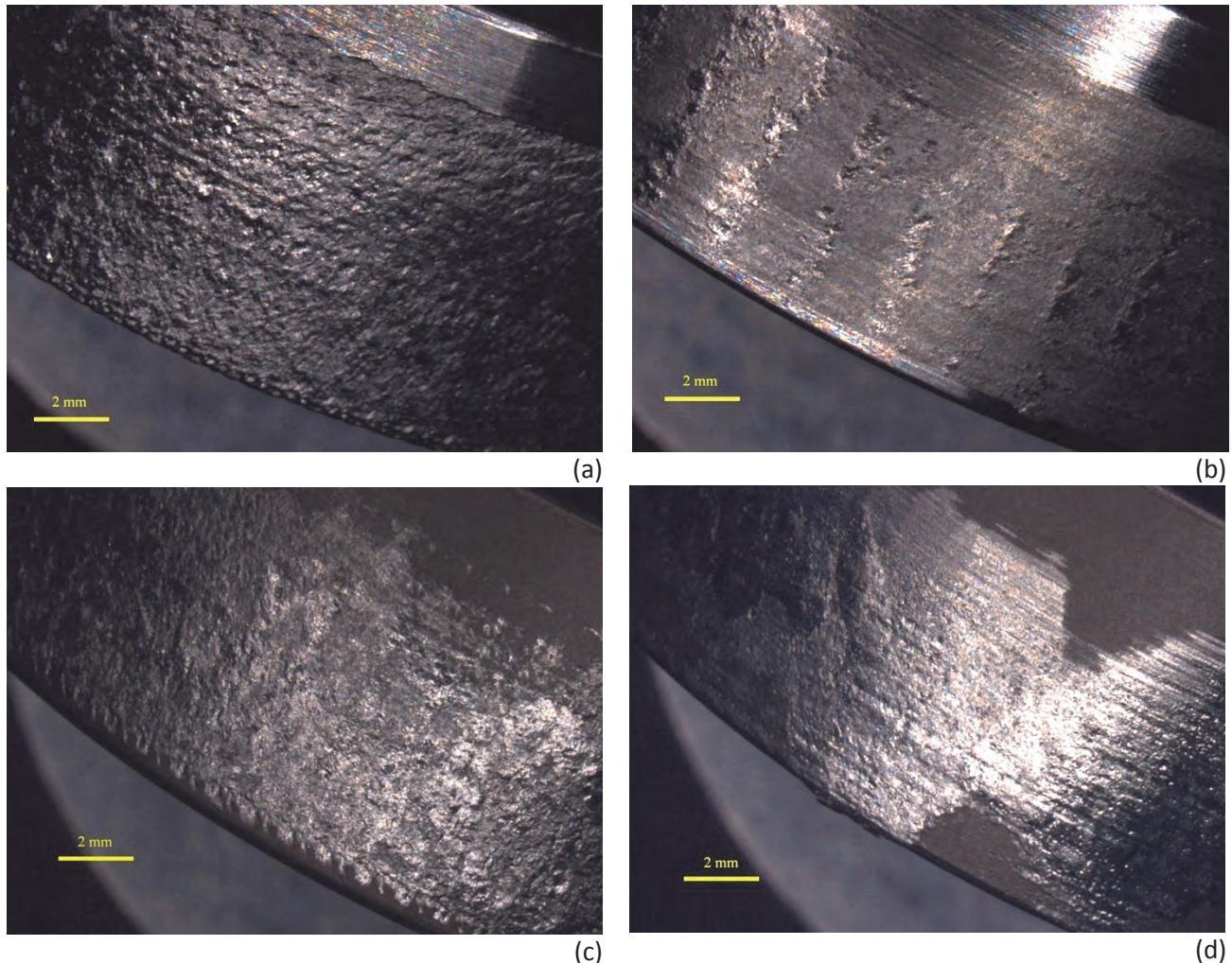


Figure 11 – Condition of rollers at end of test showing differing behavior of 440F vs. 440C.
(a) 440F, test ID 5. (b) 440C, test ID 9. (c) Ti6Al4V test ID 5. (d) Ti6Al4V, test ID 9. The test ID numbers refer to Table 1.

Wear debris.

During testing of the qualification test unit, some loose debris was formed. The scope of the NESC assessment included consideration of mission risk from the loose debris. The laboratory testing revealed aspects of the loose debris as follows. From Table 2, note that loose debris was generated at rates on the order of 0.5 micrograms per cycle for large roller misalignment. The wear rates were greatly reduced for the case of zero roller misalignment. However, the adhesive wear was not completely eliminated with aligned rollers, and some debris was formed. Figure 12 (a-b) provides images of the largest sized particles collected from the two tests operated with zero roller misalignment. Figure 12 (c) is a typical example of the large number and widely distributed debris that occurred for extensive run time and the largest misalignment angles tested. A portion of the debris pan was not within direct line of sight of the rollers, but that region still contained significant numbers of particles.

Summary

Laboratory testing of 440 steel rollers in contact with Ti6Al4V in vacuum was completed to study the wear behavior and to quantify wear rates. The tests also assessed the influence of material condition and roller misalignment. The wear rate was found to be roughly proportional to the roller misalignment angle. The rate of loose particle mass created was on the order of 0.5 micrograms per cycle. The adhesive wear was

a two-way phenomenon with titanium alloy material found adhered to the steel and vice versa. Loose particles with linear dimensions on the order of 200 micrometer were created even for the condition of zero roller misalignment. For large misalignment angles, large numbers of loose particles could be created, and debris was found in locations that were not within a direct line of sight. The wear behavior differed for the case of 440F and 440C steel rollers. With the 440C rollers, the adhesive wear rate was reduced, and the final surface textures of the 440C rollers were smoother than the 440F rollers.

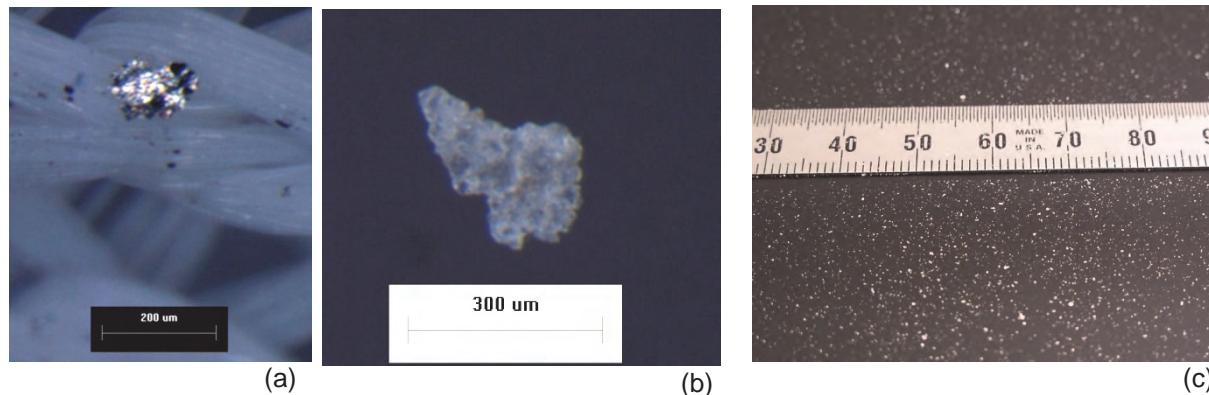


Figure 12 - Examples of loose particle debris. (a) Test ID 4 with zero roller misalignment. (b) Test ID 8(a) with zero roller misalignment. (c) Test ID 5, rollers misalignment -1.4 degrees. The test ID numbers refer to Table 1.

Acknowledgements

This research was supported by the NASA Engineering Safety Center. The experimental work was done with assistance from Mr. Richard Manco, Sierra Lobo Inc. Dr. Iqbal Shareef's contributions were supported by the NASA GRC Summer Faculty Fellowship Program.

References

1. McClendon, M., "NIRSpec MSS Magnet Actuator Life Test Unit Wear Particle Evaluation", obtained by Krantz, T., May 16, 2011
2. Authors unstated, "Micro Shutter Subsystem (MSS) Qualification Unit Test Report", JWST-RPT-013819, Rev. A, June 2010.
3. Pepper, S., "Research Note-Characterization of the Test Environment of JWST Roller Wear Evaluation at NASA-GRC", Aug. 1, 2011.
4. Johnson, K.L., **Contact Mechanics**, Cambridge University Press, 1985.
5. Kalker, J.J., "Rolling contact phenomena: linear elasticity", Rolling Contact Phenomena CISM Courses and Lectures, Issue 411, Springer-Verlag, 2000.
6. McGinness, H., "Lateral forces induced by a misaligned roller", DSN Progress Report 42-45, March and April 1978, Jet Propulsion Laboratory, Pasadena, CA, 1978.
7. Krantz, T., DellaCorte, C., Dube, M., "Experimental Investigation of Forces Produced by Misaligned Steel Rollers", proceedings of the 40th Aerospace Mechanisms Symposium, NASA/CP-2010-216272, also NASA/TM-2010-216741, 2010.
8. Rabinowicz, E., **Friction and Wear of Materials**, 2nd edition, Wiley-Interscience, 1995.
9. Vijayakar, S., "A combined surface integral and finite element solution for a three-dimensional contact problem", International J. of Numerical Methods for Engineering, vol. 31, 1991.
10. Vijayakar, S. "Multi-body Dynamic Contact Analysis Tool for Transmission Design – SBIR Phase II Final Report", Army Research Laboratory ARL-CR-487, 2003.

Angular Runout Test Setup for High-Precision Ball Bearings

Scott W. Miller*, Jonathan P. Wood* and Stuart Loewenthal*

Abstract

Ball bearing runout error is generally a limiting factor for the precision of pointing systems and astronomical instruments. A test setup was developed to optically measure the angular runout of a series of off-the-shelf duplex angular contact bearing pairs each having the same cross-section, but different ABEC ratings and manufacturers. A total of 6 bearing sets ranging from ABEC 3 to ABEC 7 were tested. The repeatable, synchronous runout generally improved with higher ABEC quality bearings as expected, although occasionally significant variation were observed with bearings of the same ABEC ratings. Less significant differences were observed for non-repeatable runout as a function of ABEC quality rating. A major finding is that strictly relying strictly on ABEC rating may be insufficient for applications where bearing runout plays an important role.

Introduction

When developing precision pointing systems and astronomical instruments supported by ball bearings, angular runout is often a key factor affecting pointing accuracy, stability, and overall performance. Line-of-sight pointing accuracy on precision pointing platforms are adversely affected by bearing runout since irregular encoder code disk motion can seriously degrade readout accuracy. Pointing mirrors are also vulnerable to bearing wobble particularly non-repeatable angular runout which cannot be easily calibrated out. Estimating angular runout based on bearing catalog individual race radial worst case tolerance will generally lead to a significant over prediction of the angular runout of the bearing assembly. In the case of a duplex bearing pairs, matching up the bearing high spots as marked on precision bearing races will essentially cancel most of the angular runout of the bearing. This will happen at the expense of enhancing radial runout motion. However, radial centerline motion is less of an issue for most optical systems that are more affected by angular pointing errors. The American Bearing Manufacturer's Association (ABMA) standards do not provide any requirements for the runout of an assembled bearing pair, but instead specify maximum raceway to mounting feature runouts for each bearing race. This will generally not predict the runout of the assembled bearing pair, thus data showing assembled bearing runouts for different Annular Bearing Engineering Committee (ABEC) ratings is not readily available to the designer.

Machine tool spindle bearing runout and disk drive spindle bearing errors are well known limiting factors for their capabilities. Standards for determining the quality of precision spindles have been available for some time. [1]. Eric Marsh and his colleagues at Pennsylvania State University have been prolific contributors to this field of precision metrology [2] [5].

Disk drive spindle runout is traditionally characterized by using two or more non-contacting proximity probes referencing the hub of the spindle, e.g. see [3]. However the runout includes spindle hub machining eccentricities and surface finish errors that must be subtracted out in order to arrive at the bearing contribution. Precision pins or spheres can be fixed at the end of the spindle to avoid minimizing machining geometric errors, but this is not always possible with many spindle designs and the eccentricity of the target to the bearing spin axis is still present.

In the approach reported herein the bearing spin axis angular errors are measured optically and the geometric accuracy of the hub is not a concern. The test setup shown in Figure 1 optically measures the

* Lockheed Martin Space Systems Company, Palo Alto, CA

angular axis of rotation errors of an assembled, preloaded, duplex bearing pair. The test setup was originally developed to determine whether ABEC 3 bearings would have sufficiently low angular runout to be used in a prototype precision pointing gimbal.

This paper will present measured angular runout data for preloaded ball bearing pairs of a unique diameter and cross section, but three separate ABEC ratings. The goal of this testing is to provide a correlation between assembled bearing runout and ABEC rating. This data will be presented in several forms, including repeatable or synchronous runout as well as non-repeatable or asynchronous runout. [1-3]

Of particular interest to the authors are the repeatability of the angular runout errors and frequency content in terms of mechanical harmonics. The data presented will be useful for estimating angular runout during the design process and the test setup presented allows for bearing-level screening and selection based on minimizing angular runout in bearing applications.

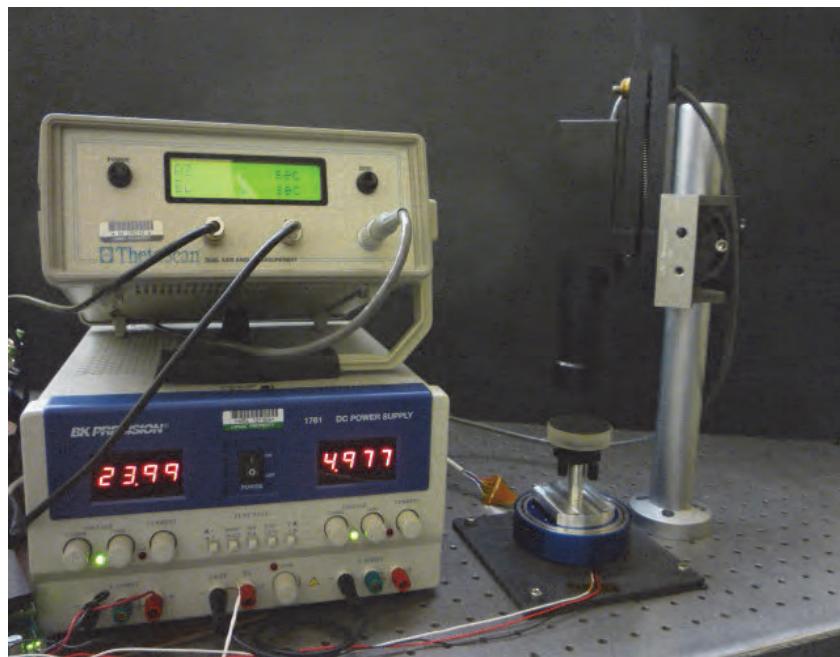


Figure 1. Test Setup Overview

Test Fixture Overview

Each bearing tested was of the same diameter and cross section, so that a single fixture could be used for all testing. The test fixture consists of an aluminum housing and shaft, an integral, direct drive brushless DC motor, and an encoder for motor control purposes. The outer housing is mounted to the bench with the rotation axis parallel to gravity. Figure 2 shows both a photograph and schematic of the test fixture. The features of the housing and shaft that contact the bearing races were diamond turned in order to obtain appropriately precision bearing fits. The diameter tolerancing method is $\pm 5 \mu\text{m}$ (0.0002 in) from the basic diameter, which permits a line-to-line contact under maximum material conditions. A benign thermal soak allows installation or removal of the bearings without applying excessive force. A mirror with a micrometer adjustable tip-tilt stage is mounted to the shaft. Bearing angular runout is measured using an electronic autocollimator.

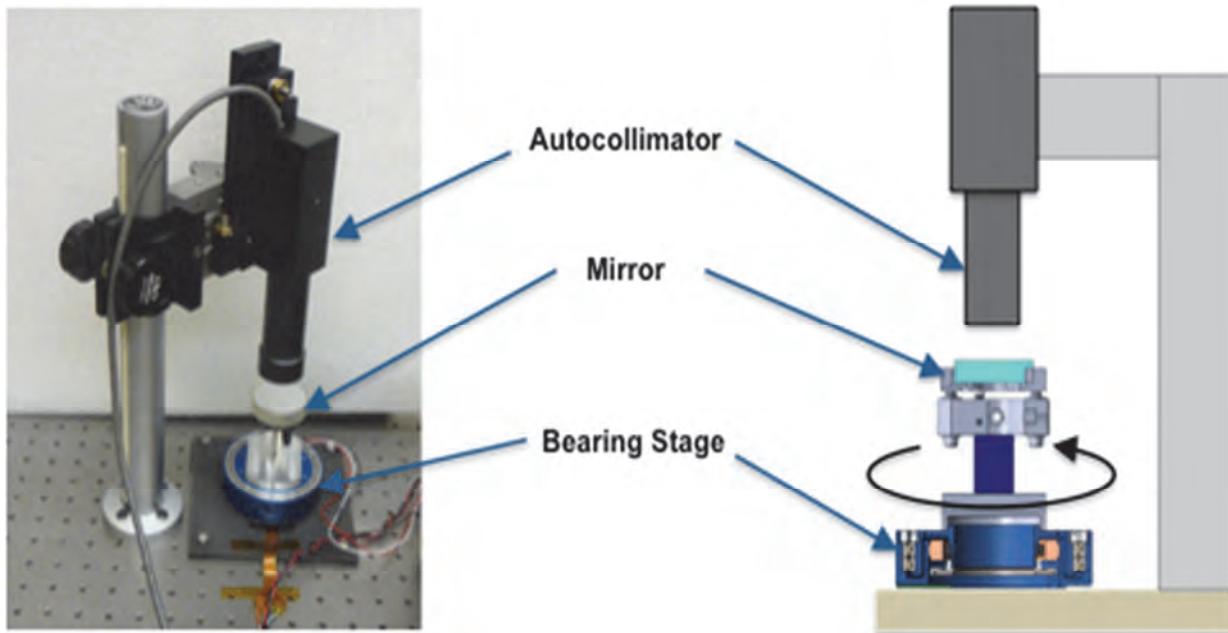


Figure 2. Test Setup Description

The test setup procedure begins with aligning the mirror roughly perpendicular to the bearing axis (see Figure 3). The autocollimator launches a reference beam, which reflects off the mirror and returns to a detector. When perfectly aligned, the reflected beam follows the same path as the reference beam upon return and has no angular difference between beams. However, introducing an angular displacement between the bearing axis and mirror normal or shaft axis will cause the reflected beam to sweep a conical path during shaft rotation, which will project a circular profile on the autocollimator detector. The nominally aligned case and an angular perturbation case are depicted in Figure 3. Recognize that if the bearing set were geometrically perfect then the trace recorded by the autocollimator would remain circular. The deviation from this perfect circle is therefore a direct measure of the bearing angular error.

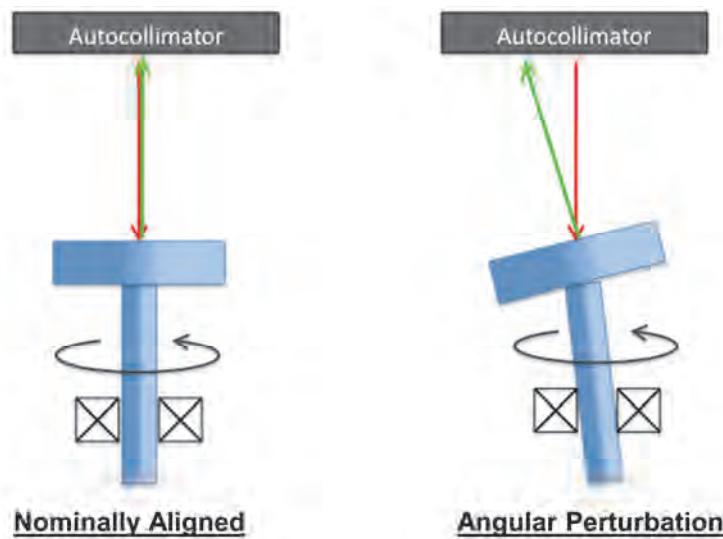


Figure 3. Measurement Method Overview

The degree of mirror tilt is somewhat arbitrary and does not affect the accuracy of the readings. This degree of mirror tilt is measured by the autocollimator and provides the scale factor for the bearing measurements. Also it was determined that if mirror tilt was too small, bearing wobble would cause crossover patterns of the reflected beam, such as a "figure eight" pattern. Therefore, the mirror to bearing axis alignment was intentionally perturbed for all testing cases to trace a nominal 500-microradian diameter path, as a seen by the autocollimator detector. Note that the effect of this approach was to introduce a calibrated, constant tilt of the mirror normal axis relative to the bearing axis.

Each test consisted of ten clockwise revolutions, followed by ten counter-clockwise revolutions. All tests were performed using a constant, low-speed rotation rate of 4.28 RPM (14 seconds per revolution), taking approximately five minutes to complete the full 20 revolutions. Note that the particular motor control speed was selected in order to determine slow-speed, or kinematical, bearing behavior, neglecting the dynamic effects.[4] The autocollimator azimuth and elevation signals were sampled by the data acquisition system at 250 Hz.

Bearing Summary

A total of six unique bearings were tested from three separate vendors. Although the same diameter, cross section and duplex arrangement were used throughout, each configuration had a unique retainer. ABEC ratings include 3, 5 & 7. Also, note that SN6 had a single outer race for the duplex set. The complete bearing summary table is shown in Table 1.

Table 1. Test Bearing Summary

Serial Number	ABEC	OD		Cross Section		Vendor	Ball Dia		Ball	Retainer	Type
		(in)	(mm)	(in)	(mm)		(in)	(mm)			
1	3	3.0	76.2	0.25	6.35	A	0.125	3.175	52	Nylon	DB
2	3	3.0	76.2	0.25	6.35	A	0.125	3.175	52	Nylon	DB
3	3	3.0	76.2	0.25	6.35	A	0.125	3.175	52	Nylon	DB
4	7	3.0	76.2	0.25	6.35	B	0.125	3.175	52	Brass	DB
5	7	3.0	76.2	0.25	6.35	B	0.125	3.175	52	Brass	DB
6	5	3.0	76.2	0.25	6.35	C	0.125	3.175	60	Teflon Toroid	DB (1-Piece Outer Race)

Test Results

The type of results presented can be described as kinematic or quasi-static since they are done at a relatively low rotation rate. This is to avoid structural resonances in the system so that the measurements can be directly related to bearing behavior. Measured bearing wobble was processed using several methods. The primary method for evaluating synchronous and asynchronous runout was obtained from the elevation versus azimuth plots. A cursory, qualitative analysis compares the acquired test data trace to the perfect circle at 500-microradian diameter, which we will refer to as the "reference diameter". Several performance aspects should be noted. First, the deviation from the average test data and the reference diameter is defined as "Synchronous Error". It is synchronous in that it repeats itself every revolution. Second is the portion of the error that does not repeat itself, forming a radial hash band about the average test data. This is defined as the "Asynchronous Error". These two definitions are illustrated in Figure 4. Finally, hysteresis is observed during cycle reversal, which is most evident in SN5 and SN6 traces. All six traces are shown in Figures 5 to 10, labeled sequentially from SN1 through SN6.

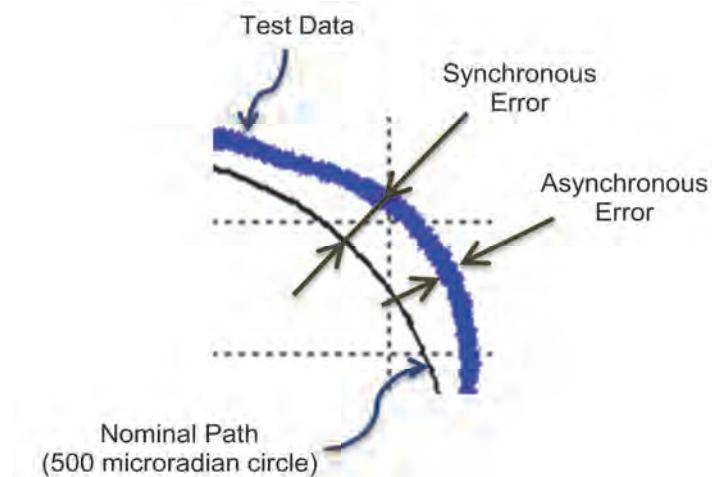
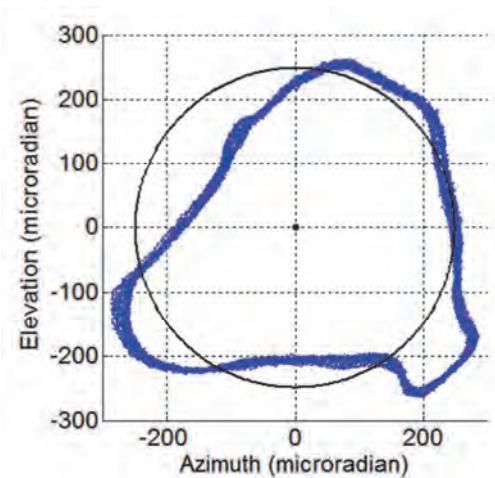
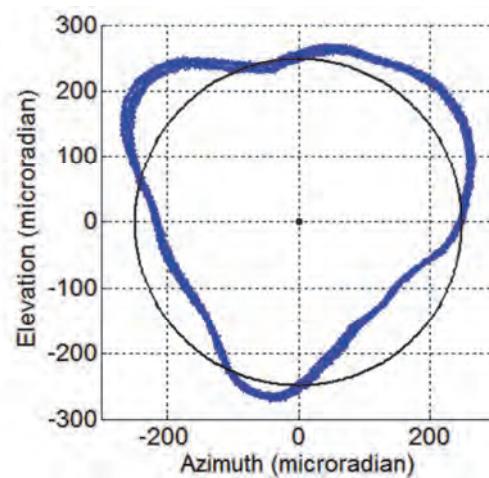


Figure 4. Error Nomenclature



**Figure 5. Elevation vs. Azimuth Test Data
SN 1 (ABEC 3)**



**Figure 6. Elevation vs. Azimuth Test Data
SN 2 (ABEC 3)**

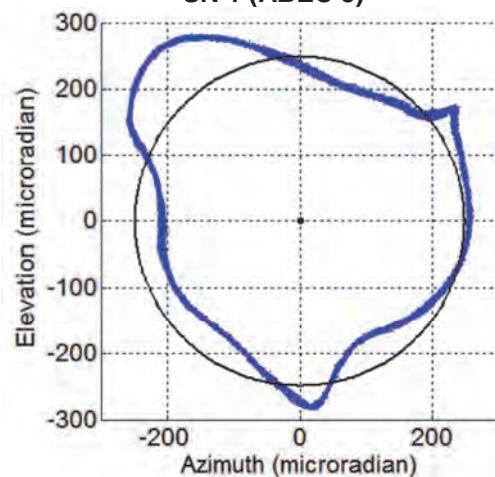


Figure 7. Elevation vs. Azimuth Test Data

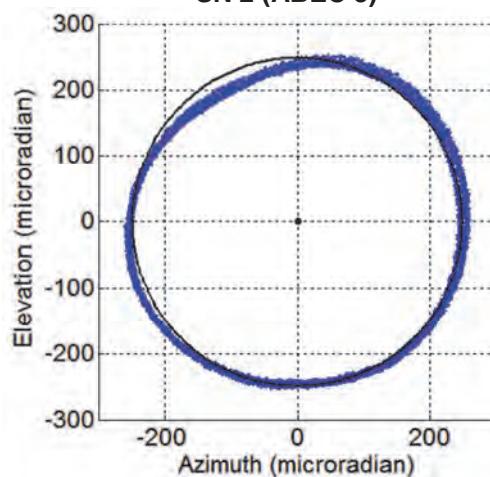
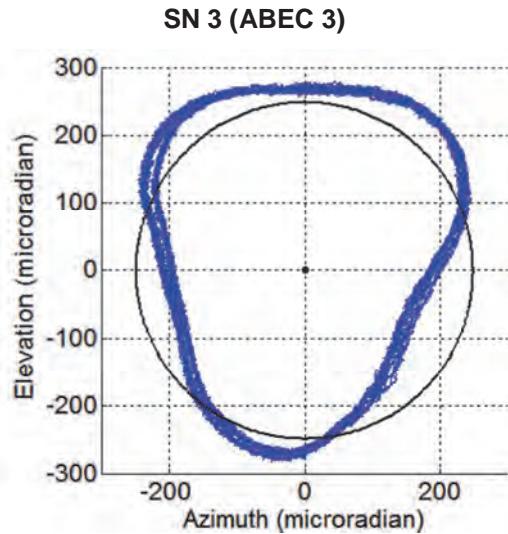
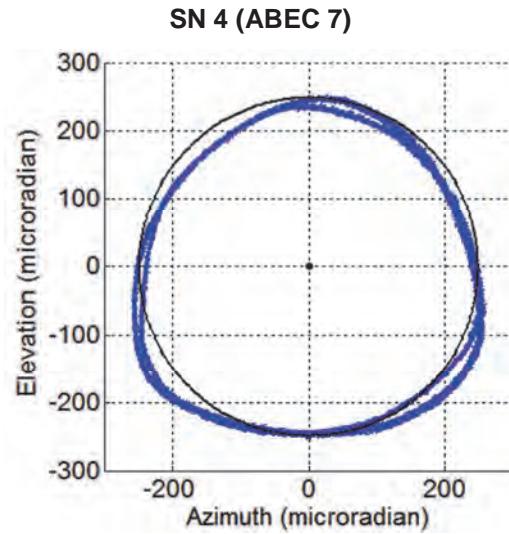


Figure 8. Elevation vs. Azimuth Test Data



**Figure 9. Elevation vs. Azimuth Test Data
SN 5 (ABEC 7)**



**Figure 10. Elevation vs. Azimuth Test Data
SN 6 (ABEC 5, Super-Duplex)**

Data Processing

It was conservatively assumed that the radial runouts of the two bearings in the duplex pair act in opposite directions, using worst-case runout data from the ABMA standard. These predicted angular runouts are shown in Table 2. A summary of the actual runouts measured from each bearing pair is shown in Table 3. Each bearing pair significantly out-performed the expected angular runout based on this calculation method, most likely due to the fact that the bearings were installed in the test fixture with the high spot markings on each race aligned. The data presented shows that even the ABEC 3 bearings tested offer a very low level of asynchronous angular runout. It is important to emphasize that the angular runout estimation method presented in table is by no means an established approach. In fact, the data from this testing show that this estimation approach provides excessive conservatism and that the best way to determine angular runout is to perform testing on the bearings to be used. The angular runout performance of a given bearing set will depend on workmanship factors, including machining tolerances and ball size matching, but the results presented are also indicative of the order of magnitude one can expect with different ABEC rated bearings of the size range presented.

Table 2. Predicted Angular Runouts Using Different Methods

	Predicted Angular Runouts Using Different Methods								Angular Runout Summation Method	Angular Runout RSS Method
	Pitch Diameter		Bearing Width		Radial Runout Inner		Radial Runout Outer			
	(in)	(mm)	(in)	(mm)	(in)	(μm)	(in)	(μm)	(microradian)	(microradian)
ABEC 3	3.25	82.6	0.25	6.35	0.00040	10	0.0006	15	4000	2884
ABEC 5	3.25	82.6	0.25	6.35	0.00020	5.1	0.0004	10	2400	1789
ABEC 7	3.25	82.6	0.25	6.35	0.00015	3.8	0.0002	5.1	1400	1000

Table 3. Measured Angular Runouts

SN	ABEC	Synchronous Error Amplitude (microradian)	Asynchronous Error Amplitude (microradian)	Synchronous Error RMS (microradian)	Asynchronous Error RMS (microradian)
SN 1	3	116	13.0	52	3.0
SN 2	3	74	11.4	38	2.6
SN 3	3	90	8.4	38	2.0
SN 4	7	30	11.0	22	2.8
SN 5	7	88	12.6	36	3.0
SN 6	5	28	12.0	18	2.6

As shown in Table 3 & Figure 11, one of the ABEC 7 bearings exhibited unusually high angular runout. This ABEC 7 bearing actually had higher angular runout than some of the ABEC 3 bearings. Of course the angular runout measured for this bearing does not necessarily mean that the bearing would be rejectable per the ABMA raceway groove runout requirements. It does however, demonstrate the variation that can be seen from bearing to bearing, even at higher ABEC ratings. Interestingly, the one ABEC 5 sample outperformed both ABEC 7 samples in terms of angular runout. However, the SN 6 ABEC 5 bearing had a one piece outer race which assured that the radial runout high point of the bearing set was perfectly matched eliminating any deleterious scissoring action. The inconsistency of angular runout performance serves to illustrate the importance of “cherry picking” of bearings for high-precision applications. If “cherry picking” is performed on a sample of bearings, it is important to mark the relative clocking between both adjacent inner and adjacent outer races respectively within a given duplex pair, as the race-to-race clocking can influence the angular runout performance. The cherry-picking approach may also be used to screen for linear runouts and drag torque properties. In this case, only one relative clocking between corresponding races was tested. However, it is conceivable that relative clocking could play an influential role in the angular runout performance, such that re-clocking of the inner or outer races relative to each other could increase or decrease the measured angular runout, depending on the relative orientation of the high spots between the two races.

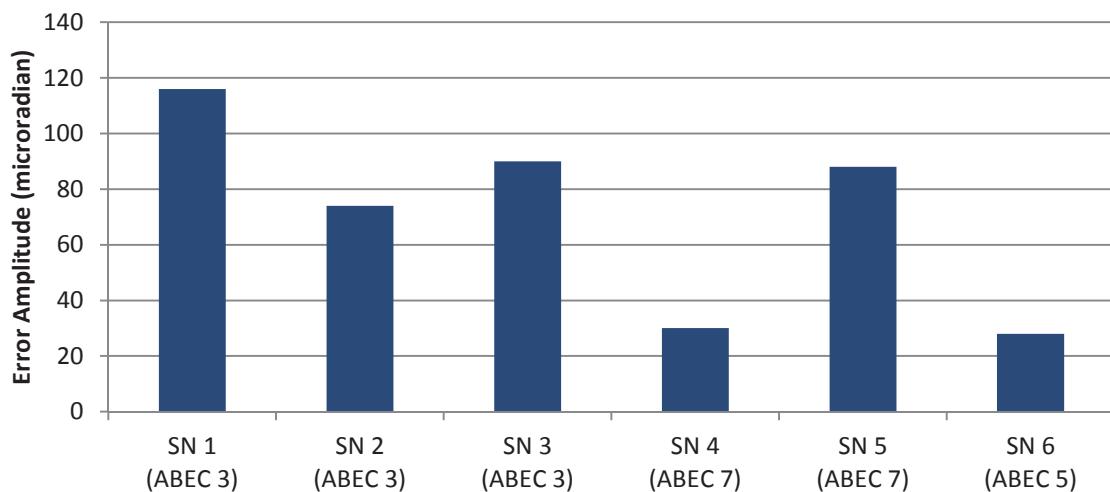


Figure 11. Maximum Synchronous Error Data

As shown in Figure 12, the asynchronous error was very low, and was nearly the same magnitude for each bearing pair, regardless of ABEC rating. The asynchronous error is most likely a manifestation of the ball accuracy (sphericity) and ball-to-ball diameter matching. The later in conjunction with raceway geometry errors dictates preload variations as the balls orbit the bearing. This is one example where the performance of the bearing pair is workmanship dependant and could vary greatly from one manufacturer to another, or even lot to lot. The repeatability of the test setup is another factor. Figure 19 shows the Asynchronous error versus angle plot for SN3.

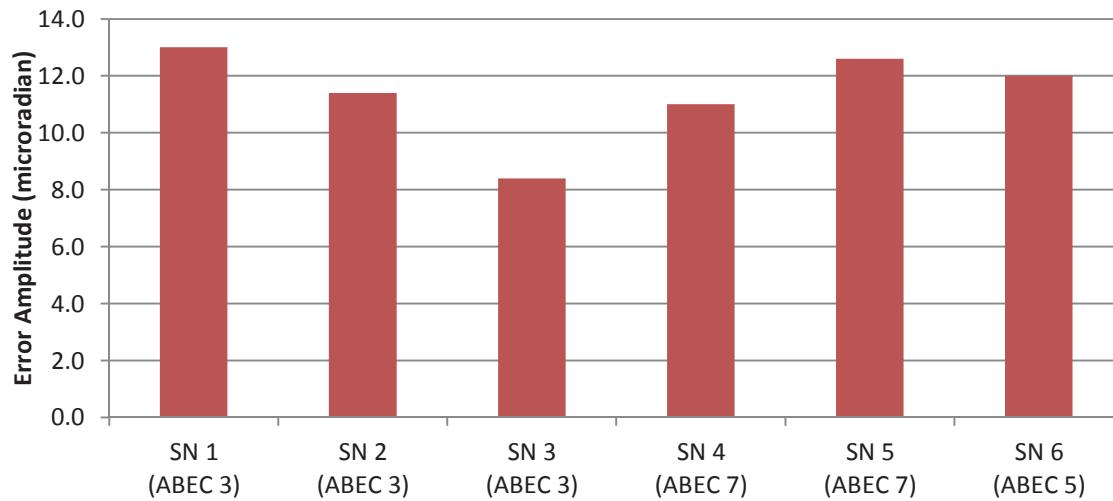
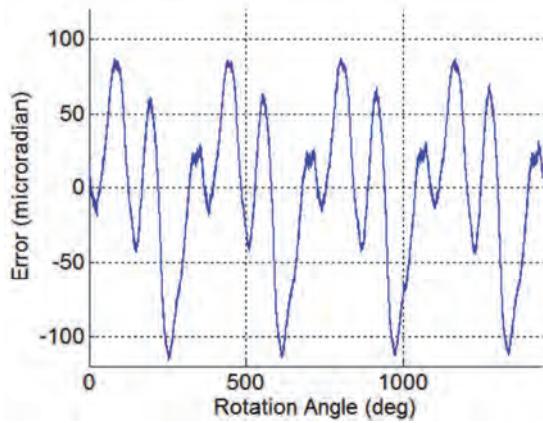
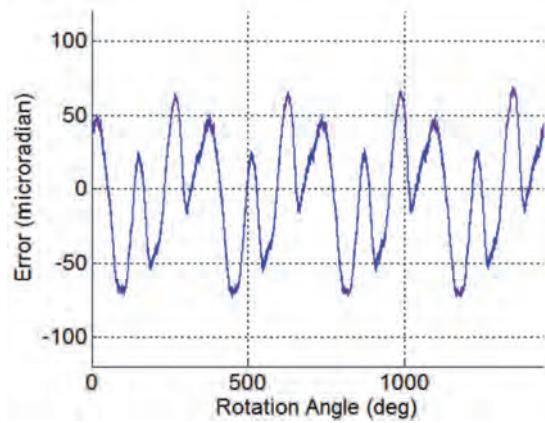


Figure 12. Maximum Asynchronous Error Data



**Figure 13. Synchronous Error Versus Angle
SN 1 (ABEC 3)**



**Figure 14. Synchronous Error Versus Angle
SN 2 (ABEC 3)**

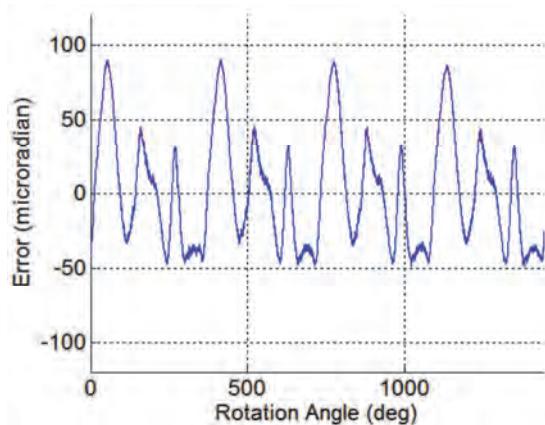


Figure 15. Synchronous Error Versus Angle
SN 3 (ABEC 3)

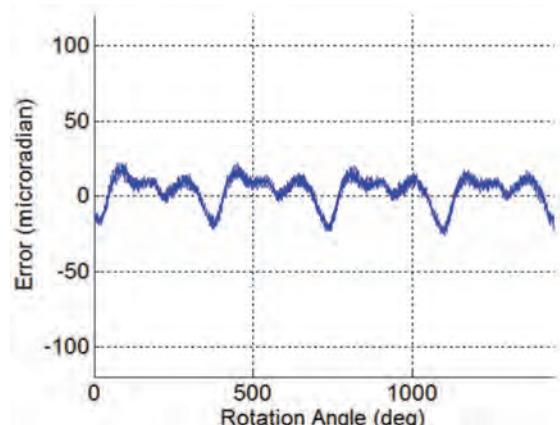


Figure 16. Synchronous Error Versus Angle
SN 4 (ABEC 7)

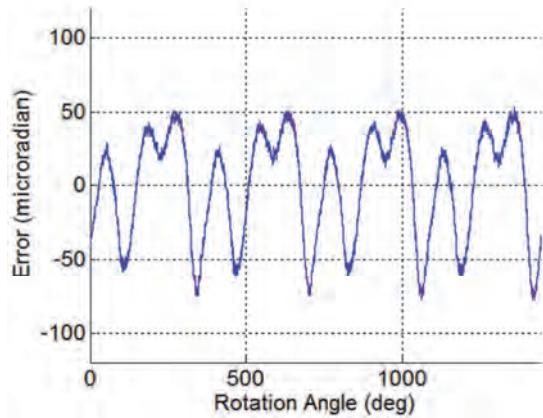


Figure 17. Synchronous Error Versus Angle
SN 5 (ABEC 7)

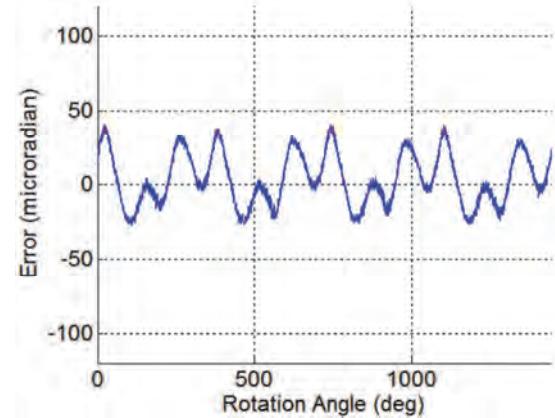


Figure 18. Synchronous Error Versus Angle
SN 6 (ABEC 5)

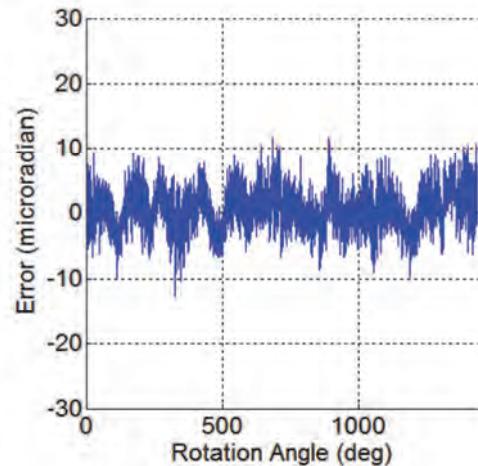
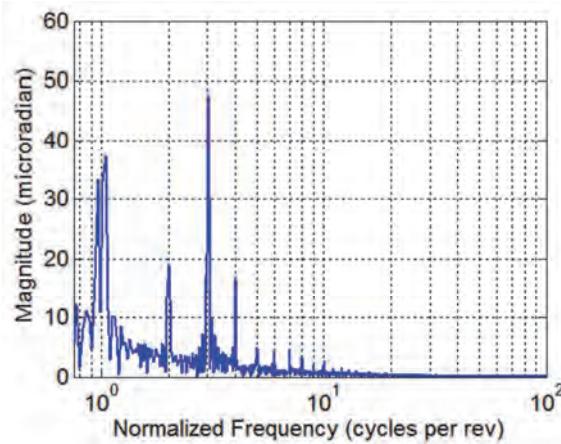


Figure 19. Asynchronous Error Versus Angle

SN 1 (ABEC 3)

A Fast Fourier Transform (FFT) analysis of the data reveals dominate spikes at 1, 2, 3, and 4 cycles per revolution. The largest and most consistent spikes occur at 3 cycles per revolution. The ball pass frequency and ball spin frequency for the bearings tested are all above 10 cycles per revolution. The large spikes at 2, 3, and 4 cycles per revolution and absence of any significant spikes above 10 cycles per revolution indicate that the angular runout of the bearings is dominated by race machining tolerances rather than ball out-of-roundness. Typically, when bearing raceways are machined, a tri-lobing of the race is the largest source of machining error. This is consistent with the dominance of the 3 cycles per revolution FFT spikes.



**Figure 20. Magnitude vs. Cycles Per Rev
SN 1 (ABEC 3)**

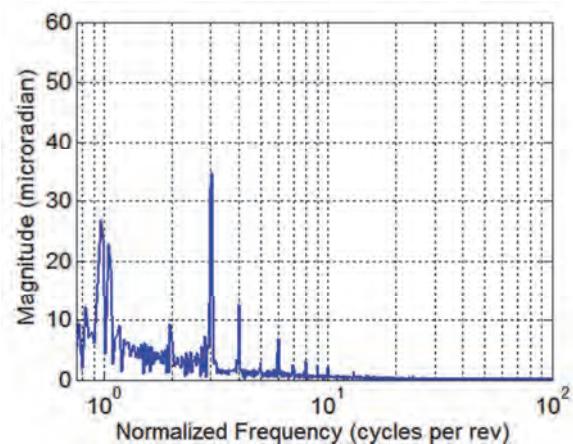


**Figure 21. Magnitude vs. Cycles Per Rev
SN 2 (ABEC 3)**

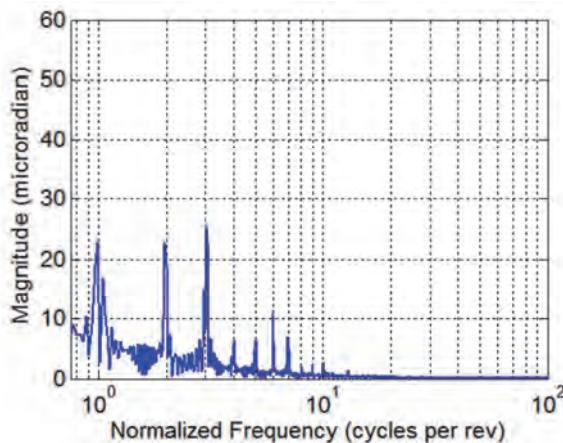


**Figure 22. Magnitude vs. Cycles Per Rev
SN 3 (ABEC 3)**

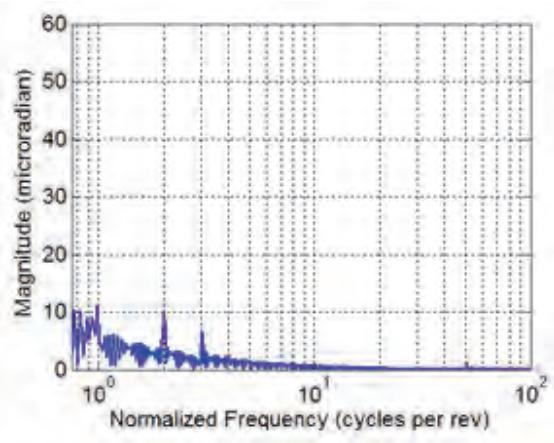


**Figure 23. Magnitude vs. Cycles Per Rev
SN 4 (ABEC 7)**

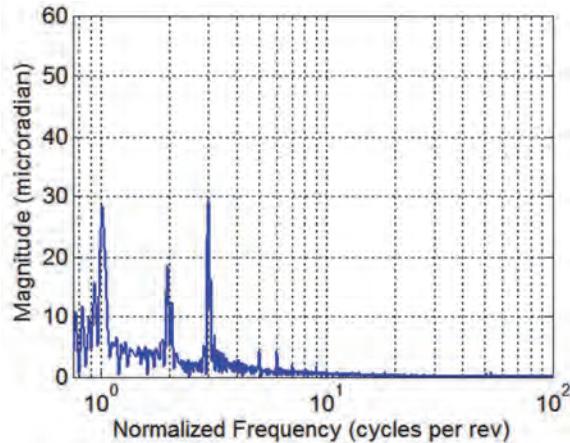


**Figure 24. Magnitude vs. Cycles Per Rev
SN 5 (ABEC 7)**

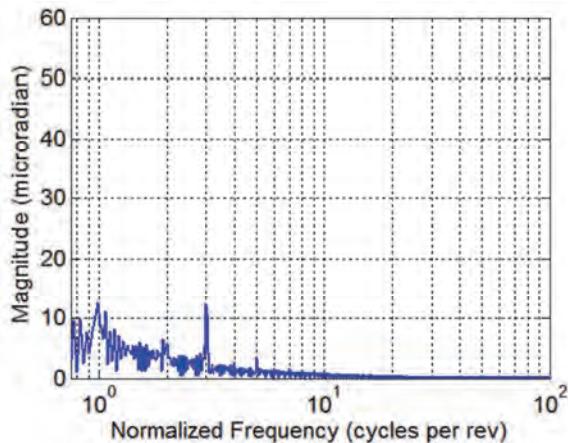


**Figure 25. Magnitude vs. Cycles Per Rev
SN 6 (ABEC 5)**

Lessons Learned

An economical bearing fixture was initially fabricated using standard lathe tolerances, in order to determine if exotic feature grinding was necessary. After processing the initial test data, it was determined that the fixture diametral clearance to bearing race was excessive, which was made evident by a cycle-to-cycle trace precession and large asynchronous error. The error trace precession reversed directions, corresponding to the bearing rotation direction. It was concluded that the economical fixture did not provide adequate relative concentricity control between the duplex pair races. The second bearing fixture, which is the one presented in this paper, had decreased the asynchronous error substantially over the economical fixture and proved that bearing mount tolerances have a large influence over the shaft runout performance to levels similar to the bearings themselves. It can be concluded that it is imperative that bearing mount features be precision machined and ground even when using ABEC 3 bearings and especially for slim section angular contact pairs.

Test results showing relatively low asynchronous error of all three ABEC 3 bearings came as a pleasant surprise. Testing additional quantities beyond those presented is, of course, desirable for statistical data processing. From a design standpoint, the data gathered from this testing may allow much more economical ABEC 3 bearings to be used, while still meeting the same design requirements that based on the predicted angular runout, would have required ABEC 7 bearings. This serves to illustrate the development testing benefits, which lead to the relaxation of requirements and ultimately cost savings. Although designing for the worst-case predicted angular runout would have resulted in a conservative design, it would have unnecessarily driven the design to excessively tight tolerances and excessively expensive bearings.

Conclusions

Three ABEC qualities were measured for synchronous and asynchronous runouts. Although bearings with a higher ABEC rating did correlate with lower measured synchronous runout, it was also observed that asynchronous runout was relatively consistent, independent of the ABEC rating. Also bearings had significantly lower angular runout than estimated using ABMA individual race tolerances. This confirms that such analytical estimates are not a viable substitute for actual runout measurements of the assembled bearing set. Finally, in the case of ABEC 7 bearings, the behavior of two bearings acquired at the same time, from the same vendor and to the same part number did not show consistent performance. For this reason, it is recommended that for critical applications, all bearings be tested prior to assembly and that appropriate spares are procured, if the application demands superior performance consistency.

Acknowledgements

The authors would like to thank their Lockheed Martin colleagues, including Kyle Brookes for his role in the design of the bearing test fixture and for the technical review provided by Dr. Jean-Noel Aubrun and Dr. Ken Lorell.

References

1. ISO-230-7, "Geometric accuracy of axes of rotation" and ASME B89.3.4-1985, "Axes of Rotation, Methods for Specifying and Testing."
2. Marsh Eric and Grejda, Robert "Experiences with the Master Axis Method for Measuring Spindle Error Motions, Precision Engineering 24 (2000) 50–57
3. "Bearing Runout Measurements" Agilent Technologies, Applications Note 243-7.
4. Harris, Tedric A. and Kotzalas, Michael N. "Advanced Concepts of Bearing Technology" CRC Press, 5th edition (2007), p182.
5. Weiss, Jeffrey R. "Rolling Element Bearing Metrology" *Penn State University Thesis, May 2005*.

LightSail-1 Solar Sail Design and Qualification

Chris Biddy* and Tomas Svitek*

Abstract

LightSail-1, a project of The Planetary Society, is a Solar Sail Demonstration mission built on the CubeSat platform. Stellar Exploration Inc. designed, built and fully qualified the Solar Sail module for LightSail-1 which includes a boom deployer mechanism that stows a total boom length of 16 meters (4×4 meter booms) which are used to deploy a 32-m^2 sail membrane in a 2U package. This design utilizes the rigid TRAC boom developed by AFRL (Air Force Research Laboratory) for deploying and tensioning the membrane that makes up the sail. In order to maximize the size of the solar sail, the boom deployer took on a unique shape to maximize packaging efficiency and achieve an 80:1 deployed to pre-deployed ratio. This paper will discuss the design challenges, unique design features as well system verification for LightSail-1.

Introduction

LightSail-1 is a project of The Planetary Society and is privately funded by members of the organization (Figure 1). The Planetary Society has been a proponent of solar sails for many years and the LightSail program is dedicated to advancing solar sail technology.

The main objective of LightSail-1 is to demonstrate the viability of solar sails by demonstrating a positive change in orbit energy, the ability to manage the orbit energy, and to control the spacecraft under solar sail power. These objectives will be achieved by developing and demonstrating key technologies such as sail deployment and sail material management during flight as well as the control of the spacecraft's attitude.

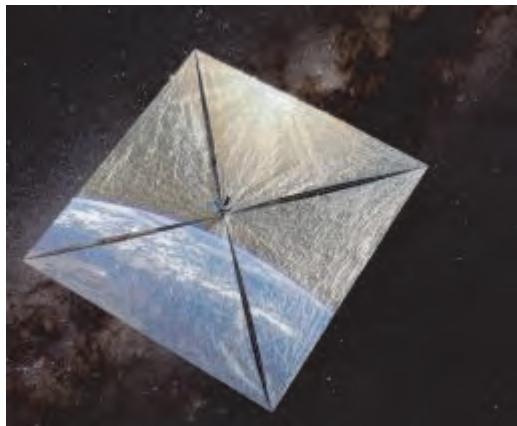


Figure 1. Artist rendering of LightSail-1 (The Planetary Society).

LightSail-1 follows work done for The Planetary Society on another program called COSMOS-1 which was also a solar sail demonstration mission. Unfortunately COSMOS-1 failed to reach orbit due to launch vehicle failure. COSMOS-1 was ~ 100 kg and had a total sail area of $\sim 600\text{ m}^2$. This gives COSMOS-1 a solar sail characteristic acceleration (a common metric for evaluating solar sail performance) of 0.047 mm/s^2 .

* Stellar Exploration, San Luis Obispo, CA

LightSail-1 Program Requirements

The main requirements and corresponding selected implementation for LightSail-1 are summarized in Table 1. Many of these requirements were derived from COSMOS-1.

Table 1. LightSail-1 requirements.

Requirement	Selected Implementation
Low Cost	CubeSat Platform
Greater Performance than COSMOS-1	3U CubeSat (maximum mass = 5 kg) requires 32 m ² sail
Demonstrate Orbit Energy Change	2 On-board 3 axis accelerometers and optical tracking
Demonstrate Thrust Control	Requires ADCS with 90° Slew Maneuver
Image the Sail during/after deployment	2 On-board Aerospace Corporation Cameras

Based on the customer requirements and associated trades it was decided to build LightSail-1 on a 3U CubeSat platform with a 32-m² square solar sail achieving a solar sail characteristic acceleration of 0.050 mm/s².

LightSail-1 Configuration

The overall spacecraft was divided into three sections that include the avionics section, sail module, and payload section. The avionics section is ~1U and houses the avionics board, the sensor interface board, a transceiver, eight Lithium Polymer batteries and battery control boards, three torque rods, a momentum bias wheel, three single axis MEMS gyros, and a three-axis MEMS accelerometer. The sail module is ~1.5U and includes the sail storage cavity, and boom deployer. The payload section is ~0.5U and contains the deployer spindle drive motor and gear train, a three-axis MEMS accelerometer, a deployable monopole antenna, a deployable panel burn wire mechanism, and a storage compartment for two Aerospace Corporation built cameras mounted to the ends of the deployable panels.

Design Challenges

The following is a list of design challenges to the development of the sail module for LightSail-1.

- How to package the sail and booms in the allowable volume
- How to manage boom strain energy while stowed and during deployment
- How to control the sail deployment
- How to constrain sail material and booms prior to deployment (including during launch)
- How to manage sail material during deployment

It was determined early in the design phase that controlled deployment of the sail would be achieved by driving the deployer spindle that the booms are attached to with a brushless DC motor. Because the booms have a large stored strain energy when fully stowed, a method of constraining the booms while the motor was not energized was required to avoid auto-deployment of the booms. It was decided that this could be achieved by implementing a worm drive that could not be back driven in the gear-train. The worm drive provided the required gear reduction from the motor to the spindle as well as eliminated the need for an additional mechanism to constrain the booms during launch. In order to keep the sail material contained in the sail storage structure the deployable solar cell panels closed over the sail storage module constraining the sail material in place.

Detailed Design

The boom chosen for LightSail-1 is the TRAC boom developed by AFRL because of its packaging efficiency and specific stiffness. These booms were used in NanoSail-D and successfully flown on NanoSail-D2 last year. The TRAC boom consists of two Elgiloy metal strips each formed into a c-shaped curve and laser welded together back-to-back forming an inverted v-shape. The TRAC boom is shown in Figure 2.

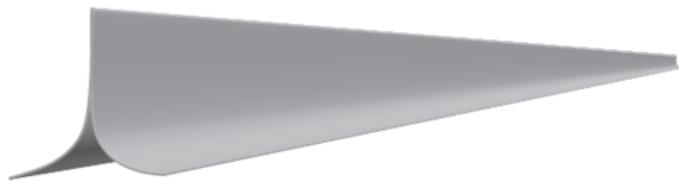


Figure 2. TRAC boom.

The TRAC boom collapses and is then rolled around a drum so it can be stored in an annular space. The TRAC boom has a self-deploying feature due to the stored strain energy in the boom while collapsed and rolled around the drum. This collapsible and rollable feature of the TRAC boom allows it to be stored in a very compact fashion. Due to the constraint imposed on the individual metal strips by the weld bead, the minimum bend radius is driven by the maximum strain of the material.

The sail storage section consists of a section with a wedge shaped cavity cut on each of the four faces. Also included is a hole passed through the center of the section for the routing of the wire harness to connect the avionics board in the top of the spacecraft to the sensors and deployer motor housed in the payload section. This configuration was driven somewhat by the requirement to have P-POD interface rails at least 75% of the overall length of the spacecraft (Figure 3).

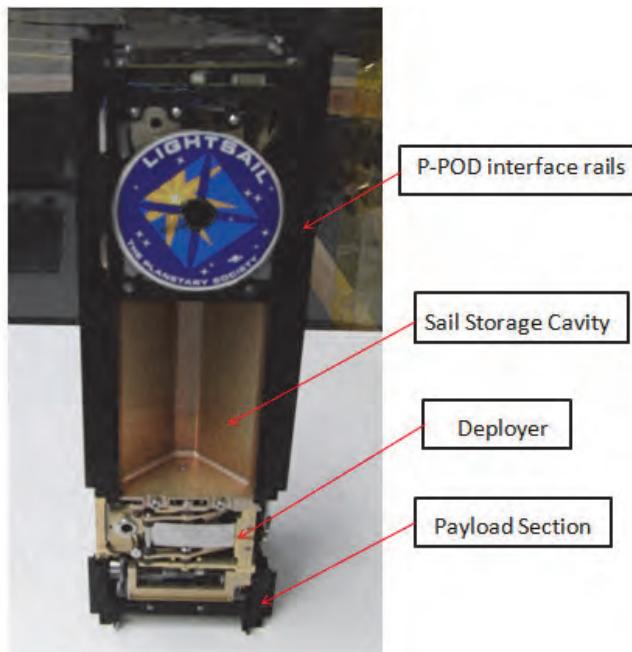


Figure 3. LightSail-1 layout.

The sail folding concept consisted of z-folding the sail in two directions while varying the fold widths from the center to the outside tips to take a wedge shaped cross-section matching the sail storage cavity (Figure 4).

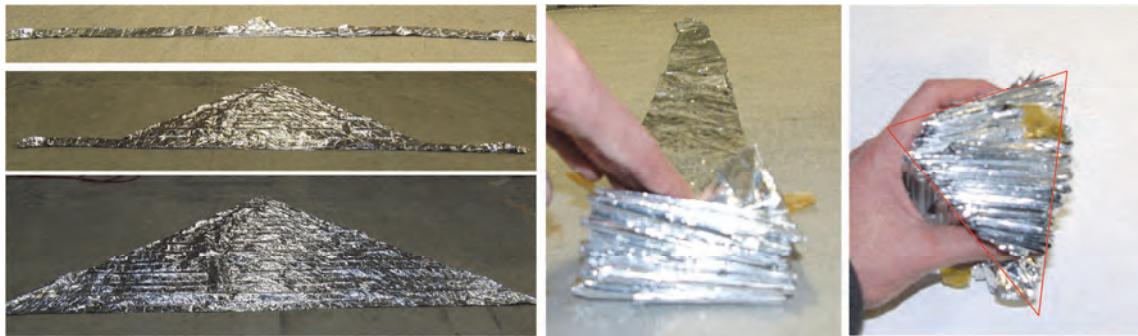


Figure 4. Sail Folding Procedure.

Prototype sails were built to empirically determine the magnitude of the fold height and width tolerances that were required, (and reasonable from a manufacturing standpoint) for the proper fitment into the sail storage cavity.

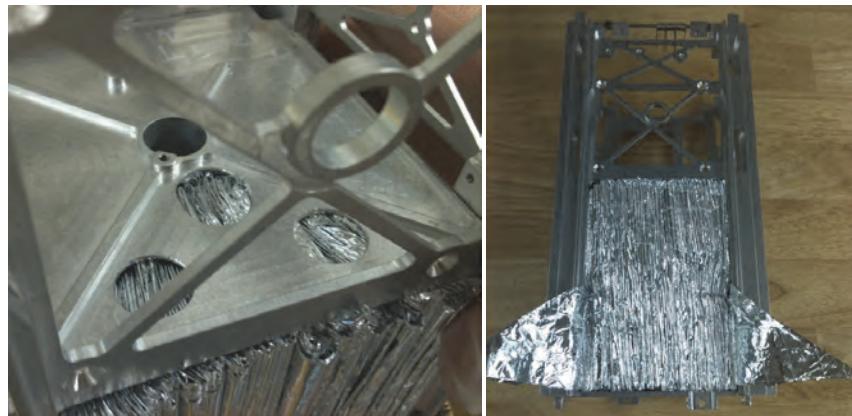


Figure 5. Sail test-fit in engineering structure.

The design of the sail was such that it had a slight interference fit in the sail storage cavity for sail management purposes during deployment. The idea being that each fold would be pulled out of the sail storage cavity one by one as the booms were deployed while the rest of the folded sail material was held in place. This would insure that the sail material would not billow from the cavity and potentially tangle around a deploying boom or get caught in the deployer and fail to deploy properly (Figure 6).

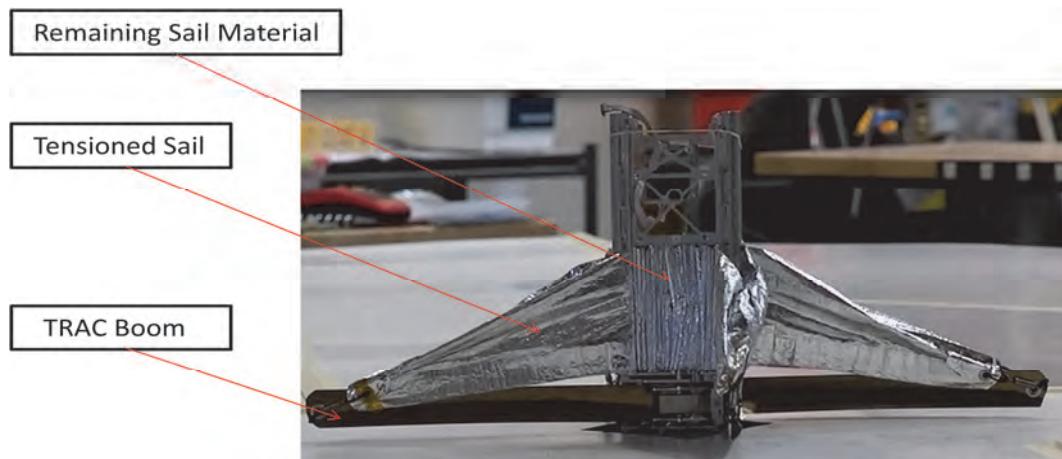


Figure 6. Sail behavior during deployment.

The sail-to-boom connection is made using metal grommets in the sails and booms with split rings and extension springs in series as shown in Figure 7. The extension springs are required to maintain an appropriate tension in the sail during thermal cycling.

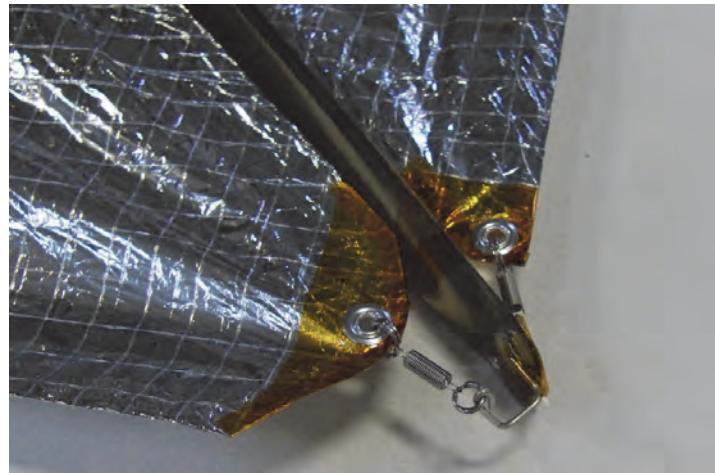


Figure 7. Sail to Boom connection feature.

Deployer Design

The deployer has four main functions: (1) Provide an attachment point to the boom to react all deployment loads (2) Protect the booms from yield due to strain (3) Store the 4m TRAC booms within the CubeSat allowable cross-section, (4) Provide smooth unrestrained deployment of the TRAC booms and Sail material.

The deployer is made up of a simply supported spindle mounted between two plates that the booms are attached to. The booms are clamped to the spindle and held with two stainless steel #4-40 bolts. This feature provides the attachment point for the booms and takes all the boom reaction loads. The spindle and clamp are machined with a flare at the bottom so as to not completely pinch the booms while mounted to the spindle. This increases the area moment of inertia of the boom over the pinched configuration providing a better boom root condition. The spindle flanges constrain and protect the booms from contacting any non-moving surfaces during deployment. The spindle with flanges and clamps are shown in Figure 8.

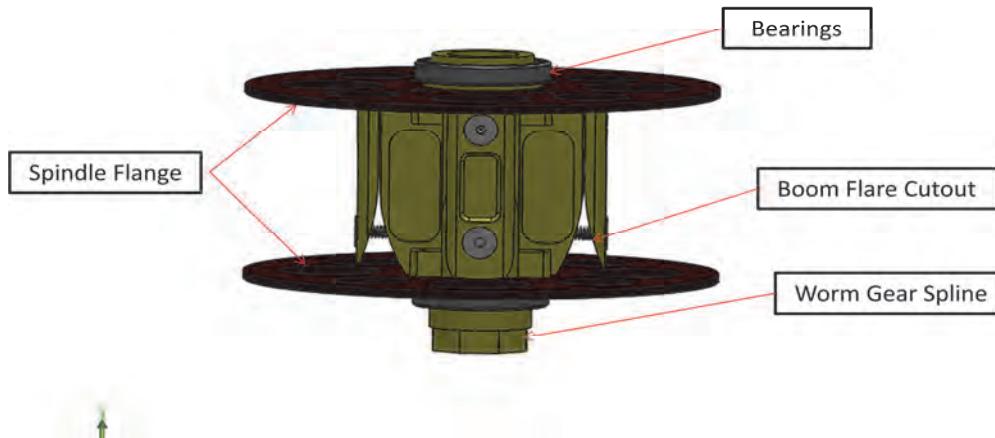


Figure 8. Spindle with boom clamps and flanges.

The rest of the deployer assembly contains four Tensioner Assemblies that are arranged between the two plates 90° from each other as well as multiple Delrin rollers mounted near the four corners, and four flexure clamp assemblies mounted adjacent to the Delrin Boom Exit Guides. These components are shown in Figure 9.

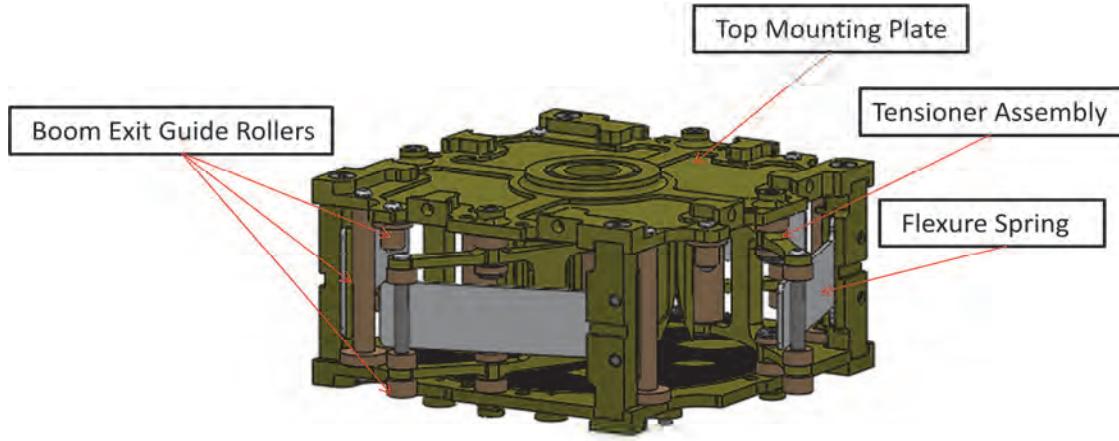


Figure 9. The deployer assembly with booms not shown.

As mentioned above, the booms require the application of a normal force to first collapse the boom into its pinched configuration and then to force the boom to roll around the drum. This is accomplished with the tensioner which uses the reaction force of a deflected cantilever flat spring against the flexure contact pin. The force on the flexure contact pin produces a moment on the tensioner body which pivots around two shoulder screws with Delrin bushings. This moment is reacted at the Boom Roller causing a normal force against the boom wrap. The flexure spring passes through the space between the shoulder screws and contacts the contact pin mounted in the tensioner. Standoff rollers are used to isolate the boom wrap from the metal tensioner body and shoulder screw heads. The tensioner assembly is shown in Figure 10.

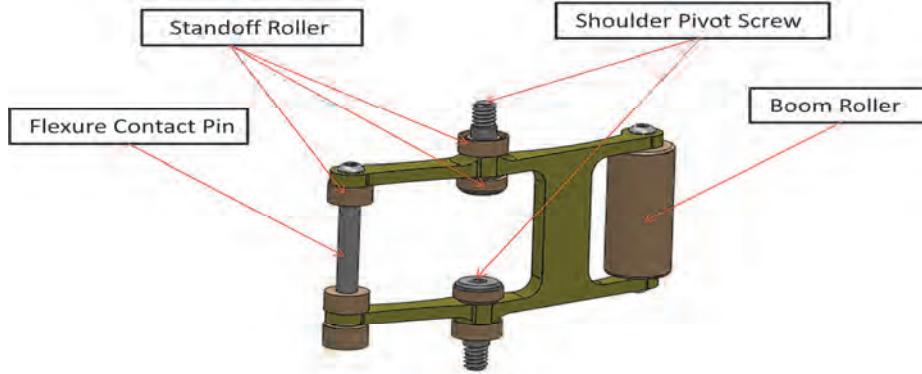


Figure 10. Tensioner Assembly.

Figure 11 shows a top view of the deployer in the fully deployed configuration with the top plate and spindle flange transparent, and the booms not shown for clarity. This fully deployed configuration refers to the state when the booms are just beginning to be rolled around the spindle to be stowed, or at the end of deployment.

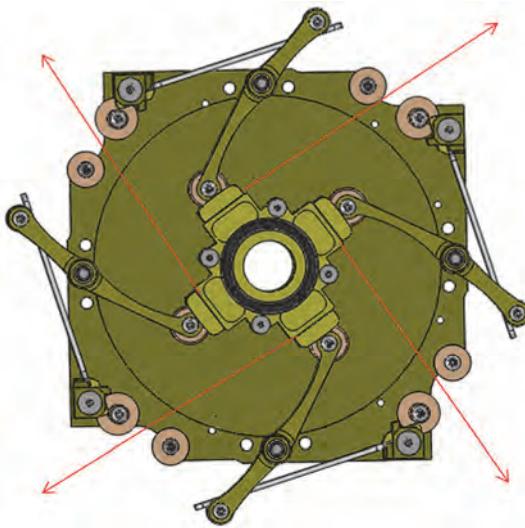


Figure 11. Tensioner orientation at full boom deployment with the flexure springs in the relaxed state (red arrows indicate the path of the booms).

As the booms are wound around the spindle, the increasing outside diameter of the boom wrap pushes the contact roller on the tensioner outward increasing the deflection of the flexure spring. As the boom wrap thickness reaches its maximum outside diameter and the flexure spring reaches its maximum deflection, the tensioner assembly is stowed within the CubeSat allowable cross-section as shown in Figure 12.

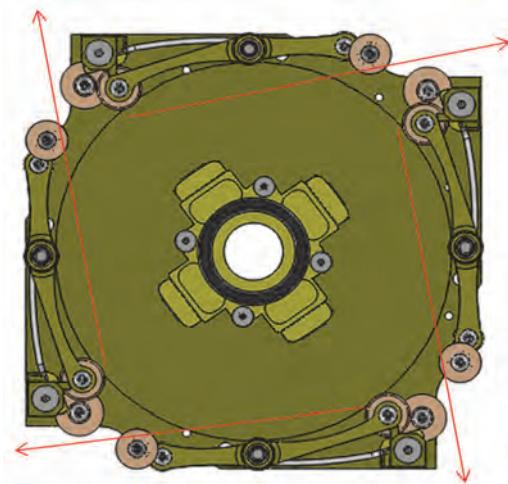


Figure 12. Tensioner orientation for stowed booms with flexure spring at maximum deflection (red arrows indicate the path of the booms).

The “rocker-arm” configuration of the tensioner allows for very compact packaging by taking up area around the boom wrap and not protruding past the allowable CubeSat cross-sectional area while in the stowed configuration. The deployer and elegant design of the TRAC boom resulted in a deployed to pre-deployed ratio of 80:1 since the packaged cross-section is $0.1 \text{ m} \times 0.1 \text{ m}$ and the deployed boom length, tip to tip, is 8 m.

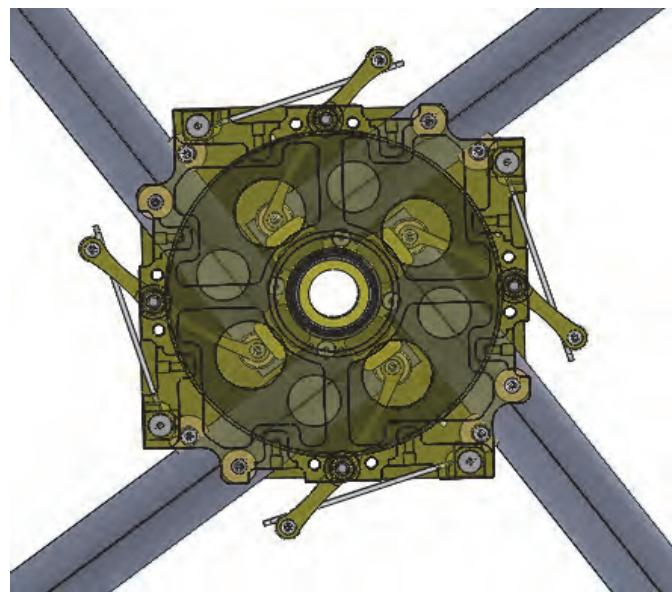


Figure 13. Deployer with top plate and flanges transparent to show booms in fully deployed configuration.

Development testing of the boom deployer assembly consisted of measuring the drive motor current required to deploy the booms while varying parameters within the deployer including the flexure spring rate, and coefficient of friction between adjacent boom wraps. This testing revealed a strong correlation between the required motor drive current required to deploy the booms and (1) the coefficient of friction between the adjacent boom wraps, and (2) the flexure spring thickness. It was discovered that a large coefficient of friction was desired between adjacent boom wraps because a higher axial force could be transferred from the drive motor through the boom wrap to the deployed length of the boom. Since the sails had a slight interference fit with the sail storage cavity a small axial force was imparted on the booms in order to pull the sail material out of the cavity and unfold it. Initially this axial force would cause ballooning of the boom wrap inside of the deployer. This ballooning was controlled with a higher spring rate on the flexure spring which exerted a larger normal force on the boom wrap keeping it contained. This was critical for achieving reliable deployment of the sail.

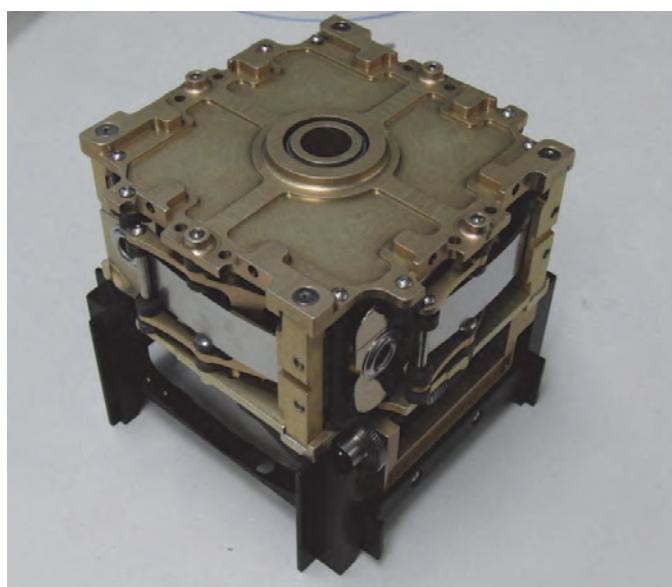


Figure 14. Flight deployer and payload assembly in fully stowed configuration.

Figure 14 shows the deployer and payload section in the flight configuration with the booms fully stowed. Figure 15 shows the spacecraft fully assembled (with engineering deployable solar cell panels).

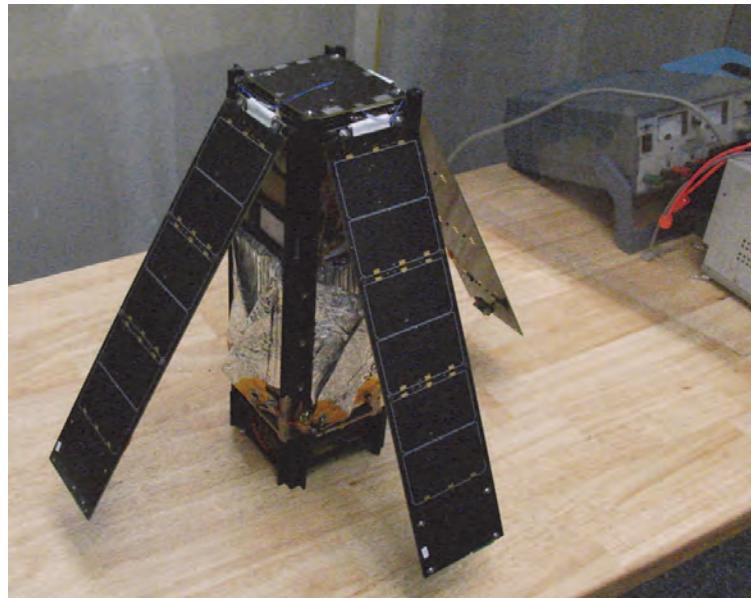


Figure 15. LightSail-1 fully assembled.

System Validation

System validation consisted of full-scale sail deployment tests before and after random vibration testing, and TVAC testing while monitoring the drive motor current as the performance metric. Cold full-scale sail deployment tests while monitoring motor drive current were conducted as well to verify cold deployment performance. In order to conduct sail deployment tests a method of off-loading was required to simulate a zero-g environment. This was accomplished by building a deployment table to support the weight of the booms and sail during testing. The table is shown in Figure 16 and features removable panels in order to access the spacecraft while the sail and/or booms are deployed.

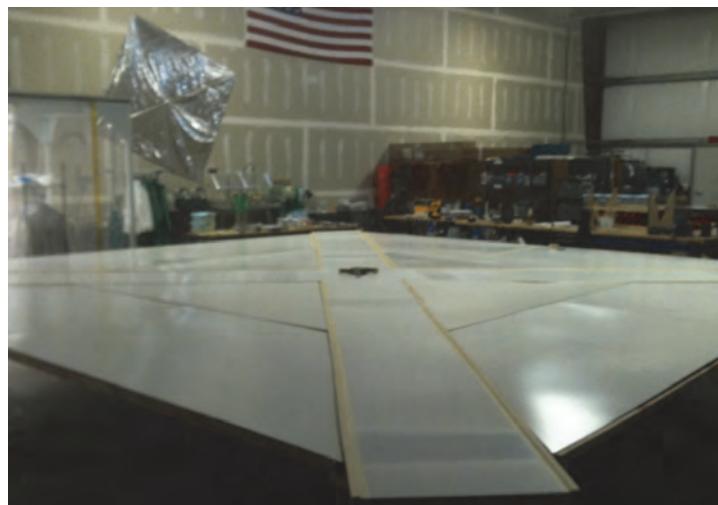


Figure 16. Sail deployment table.

Random Vibration Testing

Random Vibration tests were conducted to validate the structural design of the spacecraft and also to validate the deployer mechanism design. The random vibration test would also be used to validate the worm drive locking feature. Figure 17 shows LightSail-1 on the vibration table at Cal Poly.

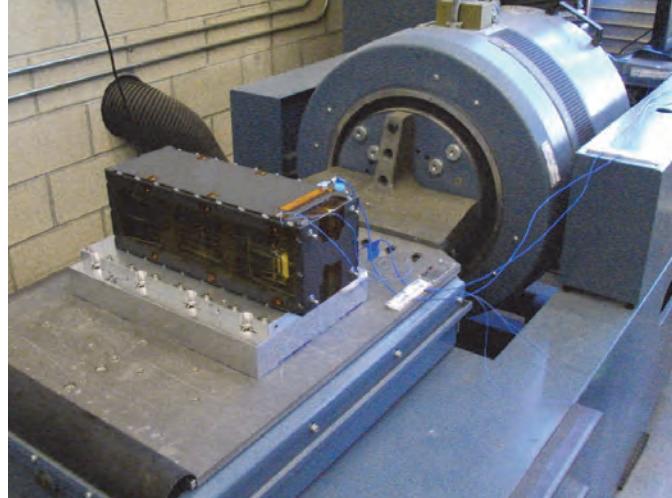


Figure 17. LightSail-1 during random vibration testing at Cal Poly.

The structure and worm drive locking feature performed well. The worm drive locking feature was verified by observing that the spindle orientation had not changed after random vibration testing by lining up reference marks on the spindle and deployer top plate before random vibration testing. If the reference marks lined up after random vibration testing it confirmed that the spindle was held fixed by the worm drive, which is what occurred.

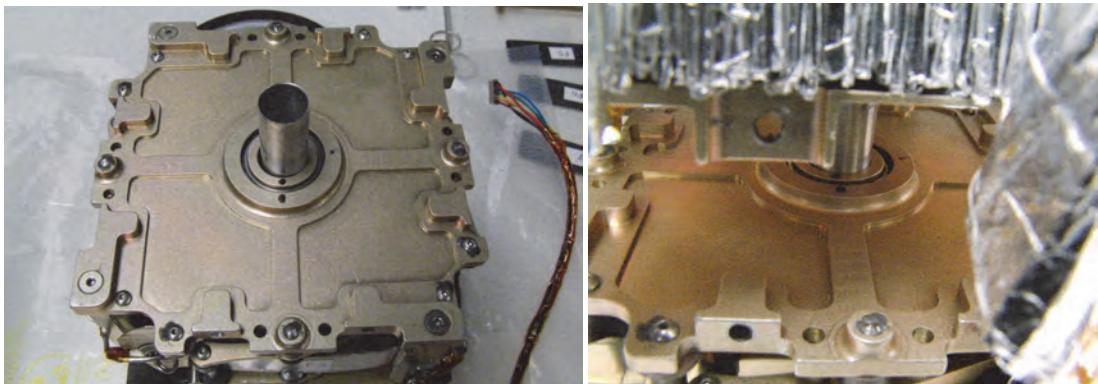


Figure 18. Spindle reference marks before (left) and after (right) random vibration testing.

While the structure performed well and the worm drive locking feature was validated, it was observed that the booms were pulled inside the deployer ~10 mm during the random vibration test. It was determined that the boom wrap was allowed to balloon slightly due to some compliance in the flexure spring/tensioner assembly. This was solved by packaging the booms in such a way that the tensioner was completely bottomed out against a hard stop while the boom wrap was pulled tight. Additionally, a pin was added to the tip of each boom to act as a hard stop to not allow the boom to retract into the deployer.

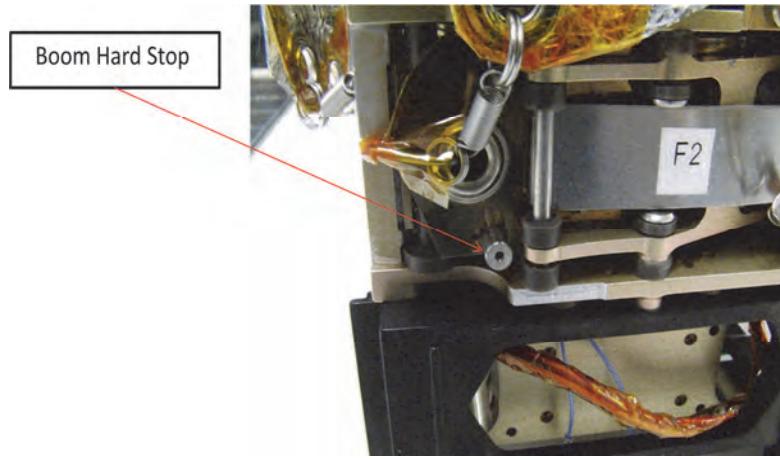


Figure 19. Boom hard stop.

Following the implementation of the above mentioned solutions the random vibration test was repeated to validate the design with full scale sail deployment tests conducted before and after random vibration testing. The deployment tests were successful with no significant difference in the motor drive current between the two deployment tests.

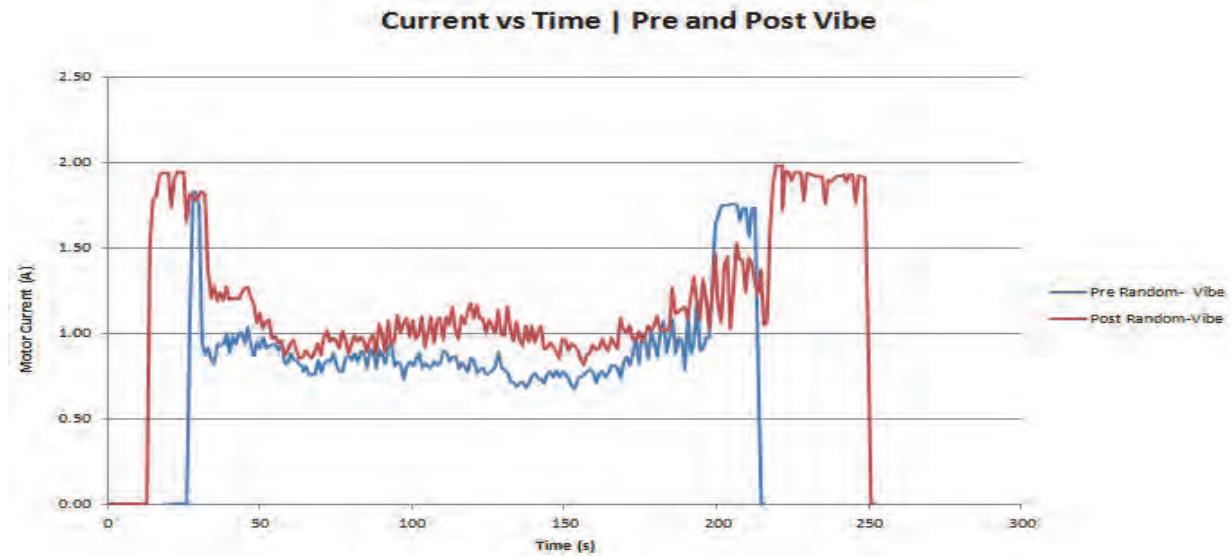


Figure 20. Drive motor current plot for Pre and Post Random Vibration deployment tests.

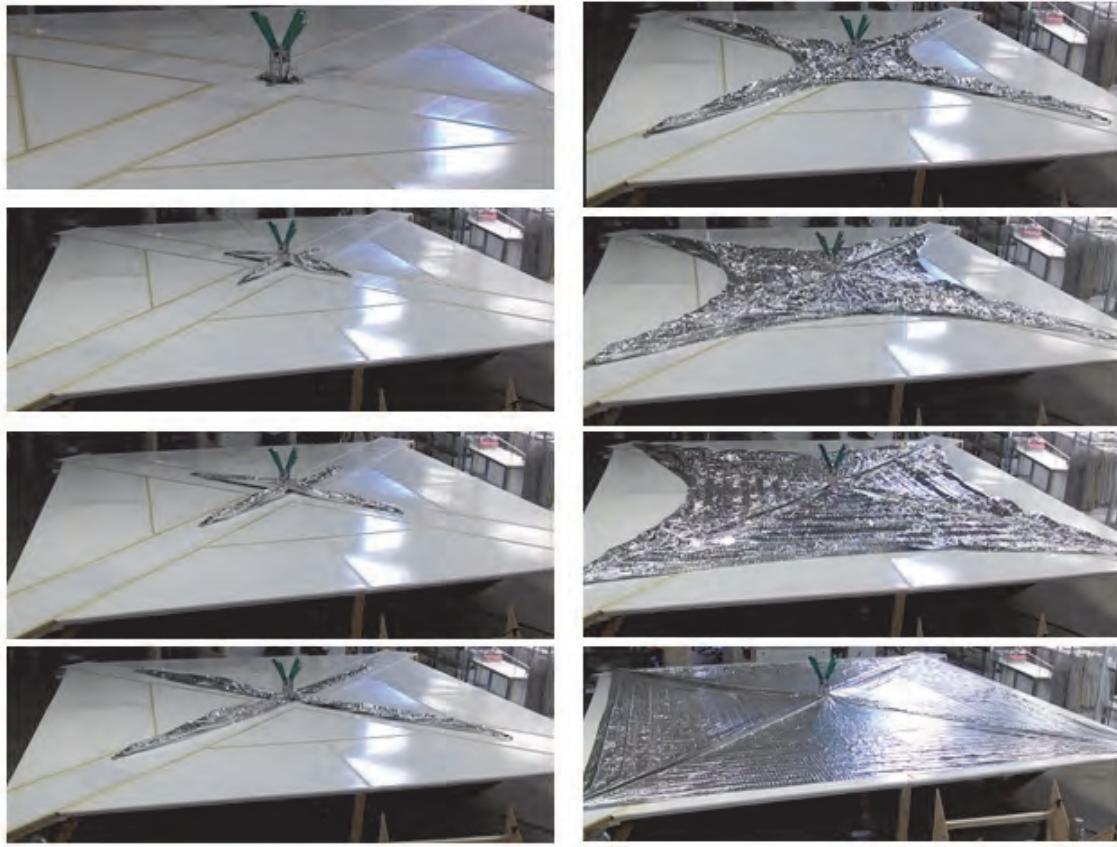


Figure 21. Sail deployment test.

Cold Deployment Testing

Cold deployment testing consisted of cooling only the deployer and booms to a prescribed temperature and then deploying only the booms while monitoring the drive motor current and comparing that with the current required to deploy the booms at room temperature. It was decided to focus on the deployer mechanism and booms, without the sail, because the sail behavior was not expected to change significantly over the temperature range being tested and because of the difficulty controlling moisture in a laboratory environment (without a vacuum chamber). The moisture in the system needed to be carefully controlled since the cold testing was conducted below freezing and the introduction of ice in the system could limit the performance of the deployer. The cold testing was performed by flowing cold nitrogen vapor into a container housing the deployer with small cutouts for the booms to pass through until the deployer assembly reached the appropriate temperature after which the booms were deployed. The drive motor current was monitored during cold deployment testing for comparison with room temperature deployment data. The deployer was qualified down to -6°C where it was well within the allowable motor current margin.

Many full-scale deployment tests have been conducted on the engineering model hardware for development. Full-scale "acceptance" deployment tests will be conducted on the flight hardware including before and after random vibe and TVAC. As of this writing the flight unit TVAC test has not been completed. These flight hardware tests are held to a minimum because of degradation of the sail material during re-folding of the sail after deployment testing. However up to 6 deployment tests on a set of sails is reasonable without significant degradation.

Conclusion

The result of work done on the LightSail-1 program is a fully qualified 32-m² solar sail packaged in a ~1.5U volume with a mass <3 kg (4.6 kg total spacecraft mass). The boom deployer assembly has a deployed to post deployed ratio of 80:1. It is planned to launch LightSail-1 by the end of 2012.

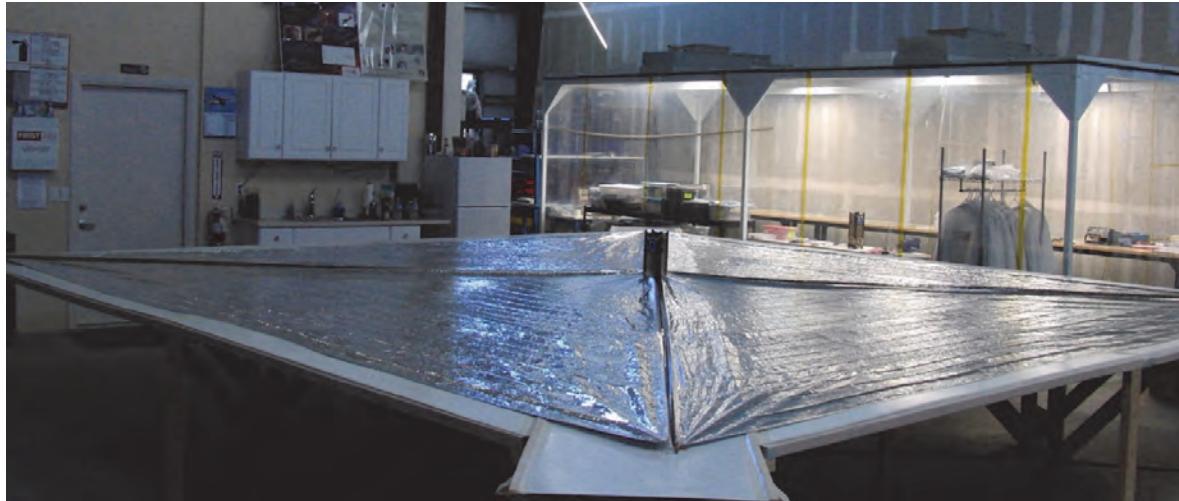


Figure 22. LightSail-1 fully deployed in the lab at Stellar Exploration.

Acknowledgments

The authors would like to thank The Planetary Society and its members for sponsoring LightSail-1, Louis Friedman and Jim Cantrell for hiring Stellar Exploration as the sail module developer and spacecraft integrator, and Bill Nye (The Planetary Society's Executive Director) for his continued support of the LightSail program. The authors would also like to thank Jeremy Banik of AFRL for his guidance and support during the development of LightSail-1.

References:

- Anderson, J.L. (11/29/11). NASA. NASA's NanoSail-D 'Sails' Home -- Mission Complete. Retrieved January 3, 2012, from http://www.nasa.gov/mission_pages/smallssats/11-148.html
- McInnes, C. R. (1999). Solar Sailing Technology Dynamics and Mission Applications. Chichester, U.K: Praxis Publishing.
- Montgomery, Edward E., Adams, Charles L. (2008, April). NanoSail-D. CubeSat Developers Workshop, San Luis Obispo, CA.
- The Planetary Society. Projects: LightSail-Solar Sailing. Retrieved January 3, 2012, from http://www.planetary.org/programs/projects/solar_sailing/lightsail1.html

A Novel Release Mechanism Employing the Principle of Differential Coefficients of Thermal Expansion

Clint Apland*, David Persons*, David Weir*, and Michael Marley*

Abstract

APL has developed a novel miniaturized release mechanism that can be used in CubeSats, NanoSats and miniature space-borne science instruments. This miniature device is inexpensive, reusable, power-efficient, and doesn't consume any flight parts. The principle of operation for the release mechanism is to use two parts that have complementary coefficients of thermal expansion (CTE). Requirements, key challenges, performance results and lessons learned are presented. Results from a total of 37 test actuitations of the design under various environmental conditions demonstrated a robust device that performed reliably in a flight-like environment.

Introduction

While in the process of developing the first 3U CubeSats designed and built at APL, the authors became convinced they needed a unique release mechanism for use in restraining and releasing the CubeSat's four solar array panels. Driven by power and volume limitations, the actuator developed in this original work is inexpensive, has a single moving part, generates no shock, uses little power, is re-settable, and does not consume any flight parts in its operation. In the process of qualifying the release mechanism, we revised the design twice to improve the performance, ease of operation and installation of the device, and to reduce the cost of producing the devices.

The CTE Release Actuator (CTERA) has successfully completed functional testing in vacuum, self-actuation testing and static load testing. It was tested under three power profiles representing those expected during flight. It has been tested in an actuator only configuration, as well as with a deployable structure representing a possible mission use.

The principle of operation for the release mechanism uses two parts that have complementary coefficients of thermal expansion (CTE). The material with a low CTE is inserted into a hole in the material with the high CTE after the high CTE material is heated. Once the high CTE part cools, the low CTE part is trapped due to an interference fit between the two parts. The interference is sized for the retaining force desired from the actuator. The low CTE part, called the plug, is fastened to the part or assembly to be separated from the space vehicle. When the high CTE part, called the cup, is re-heated, the low CTE part is freed, just as a bolt would be freed from a separation nut.

Key challenges for the design included analysis to set the machining tolerances required, choice of the mechanical surface properties of the two interfacing parts, finding low cost heaters with high watt-density that operate at low voltage, and testing various power profiles to minimize the power drawn by the device. A MathCAD design tool was developed for initial sizing of the interference fit, and later, using a test-verified release coefficient, to predict the release temperature under the influence of the kick-off spring.

* Johns Hopkins University Applied Physics Laboratory, Laurel, MD

Requirements

As the packaging layout of the reference mission progressed, these key requirements for the design of this tiny actuator became evident:

- Tiny envelope of less than 9.83 cm^3 (0.6 in^3) – the device needed to fit into an approximately $2.54 \times 2.54 \times 1.524 \text{ cm}$ ($1'' \times 1'' \times 0.6''$) envelope.
- Low power availability - Since power for the CubeSat reference mission was at a premium, we needed to minimize the amount of power drawn by the actuator. The conductive heat loss between the cup and the plug, as well as the cup and the spacecraft, was a priority.
- Low upper temperature limit – The avionics on the reference mission didn't have the capability to sense the temperature of the actuator; therefore we needed to use a set time for resistor power cutoff. This limitation forced the design to release at a much lower operating temperature in order to reduce the risk of damaging the resistor heating source.
- A relatively large holding capacity for the actuator's size – the load requirement with test factor of 1.5 was 143 N (32.25 lb).
- A tension-only boundary condition – due to the short distance from the hinge, a spherical ball boundary condition was needed, with no room for a spherical bearing.
- Low shock – The CubeSat specification prohibits pyrotechnic devices. APL also chose to minimize shock generated by the chosen release mechanism to protect CubeSat avionics and mechanisms. The CTERA produces negligible shock.
- Easily resettable – The device used in the APL CubeSat needed to be easy to reset. Removing the device from the SV for re-set would cause unacceptable delays in the I&T process.
- Use of non-magnetic materials throughout the mechanism.

Trade Study Results

We conducted a quick electrical characteristic comparison, shown in Table 1, between the CTE actuator and commercial devices, with a particular focus on the energy required to actuate them. The table shows five release actuators and their electrical characteristics. We did not attempt to differentiate mechanical characteristics, since only one other device in the table fits the size constraints to which the CTE actuator was designed.

Table 1 - Device Trade Study

Device	Current (A)	Voltage (V)	Power (W)	Resistance (Ω), Total	Δtime (s)	Energy (W-s)	% Battery Energy
Device #1 (SMA)	1.00	9.00	9.0	9	35	315	0.20%
Device #2 (SMA)	5.36	7.50	40.2	1.4	0.032	1	0.0008%
Device # 3 (Paraffin Initiated Actuator)	0.36	28.08	10.1	78	150	1516	0.94%
Device #4 (SMA)	3.50	14.70	51.5	4.2	0.035	2	0.0011%
APL CTE Actuator	2.60	7.28	18.9	2.8	17.8	337	0.21%

Device # 1 can be used in applications similar to those for which the CTE Actuator can be employed. This device has lots of heritage, produces almost no shock, and is a highly reliable device in APLs experience. Its nominal power performance is slightly better than that of the actuator. This device must be removed from the space vehicle (SV) or instrument to be re-set and it consumes notched bolts with each actuation. This particular model would need to have a custom heater resistance to be used on a CubeSat, since the 9-ohm resistive heater wouldn't dissipate enough power to actuate the device at minimum voltage (6V). This device, unless non-recurring engineering was expended to re-size it, simply would not fit in the volume allotted in the APL CubeSat.

Device #2 is another shape memory alloy device. This device uses a shape memory alloy to actuate a ball detent mechanism which releases a deployable item. Its load capacity is far beyond what is needed for many CubeSats or small instruments. It uses very little power and has an almost instantaneous actuation. It's also much larger and more massive than could be used in this APL CubeSat. It draws far more current than a CubeSat could supply without dedicated capacitor banks. While it produces much less shock than a pyrotechnic device, it still produces shock, which must be evaluated in the design process.

Device #3 uses a resistive heater that heats paraffin wax. When the wax is heated, it expands. The actuators are designed to produce linear motion with a defined output force. They are compact, highly reliable, and insensitive to contamination. They require a companion mechanism to affect the release of a deployable device. They consume much more energy than any other device compared.

Device #4 uses shape memory alloy wires to rotate a cam which allows a four segment nut to separate and release a bolt. They have a much higher load capacity than is needed for the reference application. They use very little energy and are near-instantaneous actuators. They are much larger and massive than could be used in this APL CubeSat. They draw much more current than is available in a CubeSat.

Prior to conducting the trade study, we eliminated pyrotechnic actuators from consideration, because the CubeSat specification forbids their use. We also considered two other custom designs, one that operated by cutting ‘fishing line’ and the other that operated by vaporizing a Ni-Chrome wire. Enough work was completed on each design to determine that for the particular combination of available volume, power and holding force of this application, the designs were overly complex and difficult to manufacture and assemble. We conducted creep testing on available polymer lines compatible with a low power line cutter, and concluded that the lines’ creep would result in loss of preload in the restraint, causing gapping and unacceptably high loads during flight. We also had contamination concerns arising related to melting plastic and its possible re-solidification on solar array cells or optical surfaces. While promising, given a different situation, these ideas were eventually shelved for this application.

Design Function & Development

The **first generation device** (Figure 1) used parts without any surface coatings and used a single 30-W thick film power resistor as the heater element. It served as a proof-of-concept, but was not suitable for flight use. The outer cup was fabricated from 6061-T6 aluminum, the inner plug from 6AL4V titanium. The machining tolerances for the cup (high CTE) and plug (low CTE) parts were critical, since the interference fit between the two was just $15 \mu\text{m}$ ($0.0006"$), nominal OD to ID. Because of this, we machined the parts to a diametrical tolerance of $3.81 \mu\text{m}$ ($\pm 0.00015"$). A simple tension-only test stand was used for testing the single first generation prototype. The first generation actuator consisted of an un-plated aluminum body fabricated on a manually operated lathe, and single 30-W 3Ω thick film resistor, an interface plate with fiberglass thermal insulators, and an un-plated titanium plug.

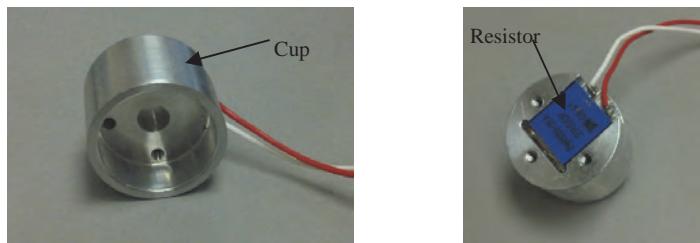


Figure 1 – First generation device with a bare aluminum body and a single 30-W resistor

The **second generation device** featured redundant heaters, a kick-off spring and a vent hole, and is depicted in Figure 2. The heaters have a temperature limit of roughly 135°C at our highest operating current, and the operating range of the actuator needed to be well below this temperature during operation. Our reference mission didn't have the capability to sense the temperature of the actuator (this

was a self-imposed limitation implemented early in the program and will be reversed in future CubeSats); therefore we needed to design for a much lower operating temperature to reduce the risk of damaging the resistors. We therefore chose to limit the operating temperature to 115°C. In practice, actuation temperatures rarely reach 115°C, but setting the actuators for flight gets much easier as the temperature increases. The aluminum cup is thermally isolated from the host structure with G-10 isolators to minimize heat loss and the overall power needed to actuate the device. We are exploring the idea of coating the flight actuators with low emissivity coatings to reduce power required for actuation by limiting heat loss due to thermal radiation.

The aluminum parts are plated with a hard coat anodize treatment, but the titanium parts were left bare. The device acted as its own tell-tale separation indicator. When the plug is fully seated in the cup, it contacts the kick-off spring, which is electrically connected to the cup. A circuit is completed from the CubeSat input-output card through the CTERA and its titanium plug, through the solar array substrate, back over the solar array hinge line, into the CubeSat harness into the IO card. When the plug is released, continuity is broken, indicating separation. We verified the concept through several cycles of operation on the tension-only test-stand. The design required great care to re-set. The single-piece plug needs to be precisely aligned with the cup, inserted in as short a time as possible to reduce plug heating. This second-generation design also required fighting against a 44.5-N (10-lb) kickoff spring force during insertion. We ended up galling the surface of the plugs in our efforts to accomplish this. The second generation device functioned unreliably in flight-like use with a solar array wing. The flight-like wing, with its hinge line parallel to the gravity vector, imposed side loads upon the release mechanism that the test stand did not.

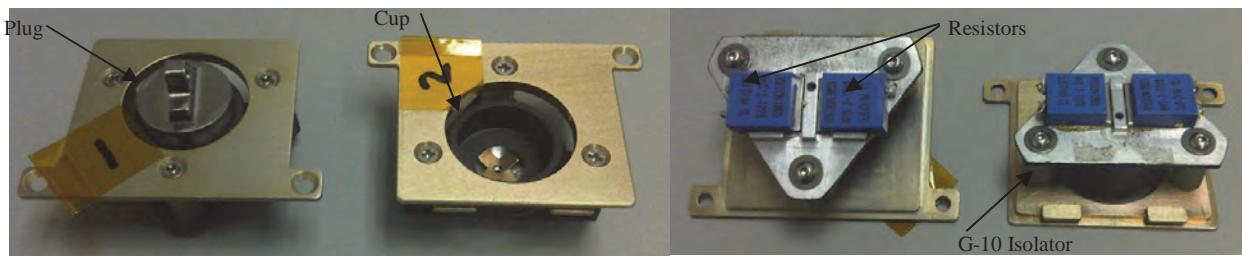


Figure 2 – Underside (left) and top side (right of the second generation device)

The **third generation device** featured a lower mass high CTE part, a reduced length interface between the two materials, and less heat transfer between the high CTE and low CTE parts, and surface treatments on both of the mating parts. Elimination of the kickoff spring preload during the precision mate of the high and low CTE parts made the mechanism much easier to re-set. Redesign of the solar array fitting accommodated the range of motion constraints imposed by the flight solar array wing by using a custom ‘near-spherical bearing’ featuring a pin and dual conical hole. The new interface to the reference mission solar array wing allows more alignment adjustability between the wing and the actuator. This tolerance eliminates racking and binding during wing deployment. Figure 3 depicts the third generation actuator body and plug and the assembly of pin, lower interface bracket and plug cap. The space-saving pin and dual cone features provide ‘near spherical bearing’ behavior in much less volume. To minimize galling and cold welding the aluminum and titanium parts under a sustained 6.9 mPa (1000 psi) interface pressure, surface finishes were critical. Two versions were fabricated, featuring different combinations of surface treatments on the high and low CTE materials. Some limited functional testing was used to determine which surface treatment combination would be used for the final design. Metrics were part wear, the change in temperature required to achieve separation, and the electrical energy expended to achieve separation. We selected hard coat anodize for the aluminum parts, and Tiodize, Type 2 for the titanium parts. Reduction of the contact area between plug and cup significantly reduced the amount of energy required for the actuator to function. Additionally, the annular interface area between the bottom of the plug and the cup was reduced by the addition of 8 radial ridges, which dramatically reduce the amount of heat transfer between the cup and the plug. Reducing energy absorbed by the plug reduces the amount of delta-T required to separate the plug from the cup. Because of the solar array deployed

geometry, the hinge causes each of the panels to deploy 90 deg and to twist 45 deg in an axis normal to the initial deployment axis.

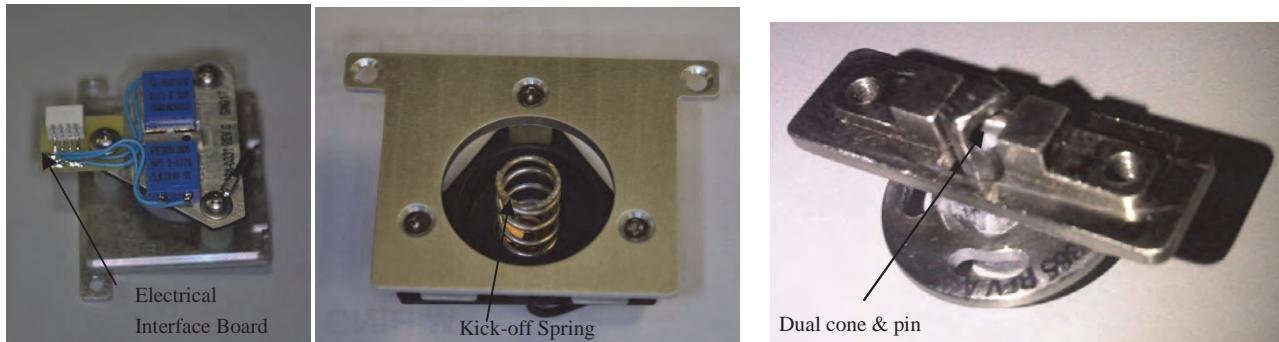


Figure 3 – Third generation actuator showing interconnect PC board, tell-tale harness, kickoff spring and retainer, and upper interface assembly with “near spherical bearing”

Because of this and because of the small radius the plug travels during deployment, the second-generation actuator had the tendency to bind during deployment. The reduction of the cylindrical interface area between the cup and plug reduced the likelihood of binding due to any lateral load or misalignment during actuator release. Binding was also reduced by changes to the lead in angles on the outer diameters of the cup and plug. The taper on the inner diameter of the plug reduces the probability of the cup hanging on the kick-off spring during deployment. The change to a two-piece plug, consisting of an annular plug with a cap allows insertion of the plug without compressing the kick-off spring. This eliminates the possibility of binding and galling while setting the actuator for flight, greatly facilitating reassembly. Figure 4 shows some of the features of the third generation actuator.

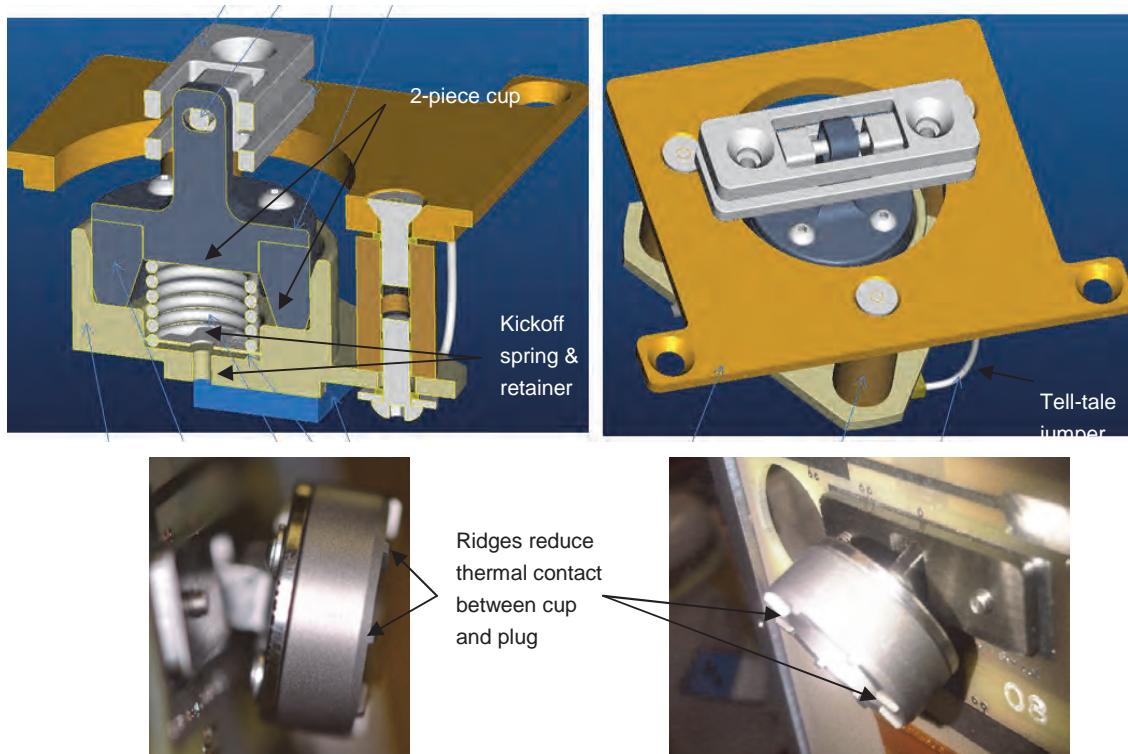


Figure 4 – Four views of the third generation device.

Testing Results & Data Analysis for Each Generation

First Generation

The primary intention of the first round of testing was to verify our assumptions about the electrical and thermal aspects of the concept. The device would eventually reach the temperature we calculated was required for separation (approximately a 70°C delta), but we learned that a single 30-W device was insufficient in both power handling capacity and output power. The power output was considered insufficient because it took several minutes for the device to change temperature. We theorized that more power input would reduce the delta-T of the low CTE plug part, as increasing the temperature of the high CTE part faster would provide less time for heat transfer to the low CTE part. This would, in turn, require a lower delta-T in the high CTE part to achieve separation. This was proven later in modifications implemented in the third generation device. We consulted with electrical component engineers who helped us pick parts using appropriate levels of part de-rating. Before this, we failed a few resistors by running them above their current-temperature curves. Using appropriate de-rating guidelines, we increased the resistance to 5.6 Ω, doubled the number of resistors, and switched from 30-W parts to 50-W parts. After the initial thermal and electrical tests were complete, we verified that concept would work, as we were able to expand the aluminum part to the point that we were able to assemble the unit. When we performed the first simulated actuation by removing the plug from the actuator at ambient pressure, we realized we had forgotten a vent hole in the actuator body. We also learned that we couldn't make the parts on a manually operated lathe. We needed a CNC lathe to achieve the required tolerances for consistent device operation. The first generation test rig is depicted in Figure 5.

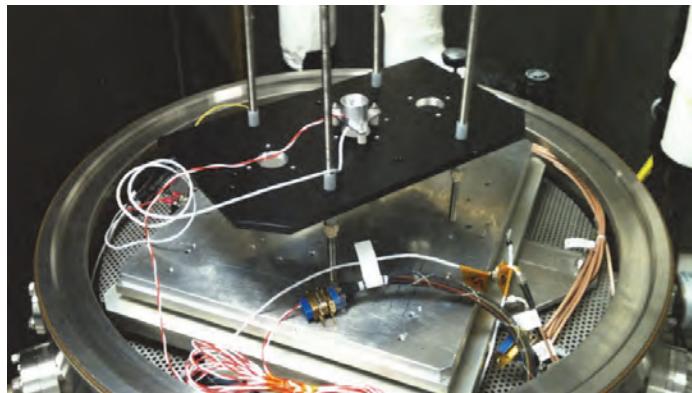


Figure 5 - First generation device shown in a bell jar type vacuum chamber. Striped wires are power, white wires are temperature sensors.

Second Generation

The second generation of the actuator was subjected to the tests listed below. Static load testing was conducted prior to functional testing on the actuator, and a load of 334 N (75 lb) was maintained for 15 minutes. Following static load testing, we performed several separations at ambient conditions with 2 A of current. As expected, it took a long time to separate (236 sec). The delta-T to separate was low, 66°C, which we think can be attributed to the virgin state of the actuator (blemishes accrue with uncoated parts). Initial functional testing at vacuum was then successfully completed (separations 4 and 5). Lastly, 12 separations were conducted in vacuum under flight conditions, with the results summarized in Table 2.

Run 15 was a scrub. Power was cut off before the full actuation occurred. Note 4 indicates a smooth plug insertion. Note 5 indicates a rough plug insertion. Nine of the twelve separations can be considered to be in family with the majority of the sample population. There were three separations that were out of family. We think these three separations took longer because the insertion of the plug into the cup for these runs was rougher. The rough insertions likely were due to a misalignment of the parts. As the number of cycles increased, we noted some wear marks forming on the uncoated titanium part, indicating that some galling took place, primarily during insertions, but during ejection, as well.

Table 2- Test data from second generation actuator.

Test #	Vacuum (Torr)	Current (A)	Voltage (V)	Power (W)	Tamb (°C)	Trel (°C)	ΔT (°C)	Δtime (s)	ΔT/Δt	Energy (W-s)	% Batt Energy	Note
4	2.50E-01	2.00	5.60	11.2	19.1	94.0	74.9	147	0.51	1646	1.02%	5
11	2.50E-02	2.16	6.05	13.1	23.6	94.0	70.4	100	0.70	1306	0.81%	4
17	2.50E-02	2.16	6.05	13.1	23.6	93.6	72.0	100	0.72	1320	0.82%	4
12	2.50E-02	2.16	6.05	13.1	21.1	104.0	82.9	123	0.67	1607	1.00%	5
18	2.50E-02	2.16	6.05	13.1	19.3	91.0	71.7	115	0.62	1502	0.93%	4
5	2.50E-01	2.58	7.22	18.6	24.0	87.8	63.8	70	0.91	1305	0.81%	4
6	2.50E-02	2.60	7.28	18.9	18.5	92.0	73.5	68	1.08	1287	0.80%	5
7	2.50E-02	2.60	7.28	18.9	18.9	89.2	70.3	66	1.07	1249	0.77%	4
8	2.10E-02	2.60	7.28	18.9	19.5	100.3	80.8	69	1.17	1306	0.81%	5
9	2.10E-02	2.60	7.28	18.9	20.0	90.2	70.2	62	1.13	1174	0.73%	4
10	2.50E-02	2.60	7.28	18.9	23.5	91.0	67.5	61	1.11	1155	0.72%	4
13	2.50E-02	3.02	8.46	25.5	18.9	88.7	69.8	46	1.52	1175	0.73%	5
14	2.30E-02	3.02	8.46	25.5	19.9	80.2	60.3	39	1.55	996	0.62%	4
16	2.50E-02	3.02	8.46	25.5	23.8	80.6	56.8	38	1.49	970	0.60%	4
	Not a "standard" power case.											
	Low power case											
	Nominal Power Case											
	High Power Case											
	Outlier											

We performed a preliminary analysis of only the separations performed in vacuum. A B-basis time to separate was calculated for the whole data set, and each of the three battery state of charge cases. The B-basis time to separate was calculated as follows: $T_{2\sigma} = \text{Mean} + (2 * \sigma)$ where $T_{2\sigma}$ is the 2 sigma time to separate, **Mean** is the arithmetic mean of the times to separate, and σ is the standard deviation between the times to separate. Table 3 lists the data for the four cases analyzed (all vacuum separations, nominal power, high power, low power).

Table 3 - Second generation statistical results.

Data Set	Mean Time to Separate	Standard Deviation	2-sigma time to separate
All vacuum	78.86	33.04	144.94
Nominal (2.6A)	65.2	3.56	72.33
Low (2.16A)	109.5	11.45	132.39
High (3.06A)	41	4.36	49.717

The lessons learned from the 2nd generation testing were:

- This version of the actuator was too difficult to set for flight. The operator was required to precisely align the plug in the cup and then to insert it into the cup with enough force to overcome the preload spring. Having to push the plug into the cup with force makes the actuator too susceptible to galling.
- Performance degrades over time because of galling produced during resetting operations. Both high pressure surfaces needed to be hard coated.
- The actuator was susceptible to racking when coupled with the reference mission solar array engineering model.

- The amount of energy required for release needed to be further minimized for the 3rd generation design.
- The tell-tale function of the actuator was determined to be reliable through all testing.
- Installation of the plug is critical to the consistent operation of the actuator. We determined to make insertion easier and more repeatable by a redesign that eliminated the preload spring force during insertion.
- Use the highest possible insertion temperature during assembly.

Third Generation

The first 4 units fabricated were fabricated to select which actuator coatings should be employed for follow-on use of the actuators fabricated for flight. Actuator SN002 featured Chemical Conversion Coating (MIL-C-5541, Class 3) coating on the aluminum cup part and Tiodize, Type II (AMS-2488, Type 2) on the titanium plug part. For SN002 (Engineering Model), we conducted 7 separations, and then we retired the unit.

Actuator SN004 featured Hard Coat Anodize (MIL-A-8625, Type 3) on the aluminum cup part and Tiodize, Type II (AMS-2488, Type 2) on the titanium plug part. We conducted 6 separations, the self-actuation test, the static load test, and 2 more actuations. The third generation tests used an engineering model CubeSat solar array to represent the correct boundary conditions for the device. Figure 6 depicts the solar array wing and test fixture. The SN004 actuator had much better performance, and its tolerances and coating combination were selected for the final design.

We characterized performance of the SN004 actuator in the following sequence:

- A single functional test at ambient conditions to verify workmanship (test 4.1). Time and delta-T were recorded for all functional tests.
- Two separations in vacuum at nominal power (tests 4.2 and 4.3).
- A separation in vacuum at high power (4.5).
- A separation in vacuum at low power (4.6).
- A self-actuation test to determine the maximum temperature the actuator can be exposed to without spontaneously actuating (4.7). Temperature at separation was recorded.
- A static load test to verify that the actuator can withstand launch loads. Time and load were recorded (4.8).
- Two separations in vacuum at nominal power to verify that the device was not affected by the static loads test (4.9 and 4.10).

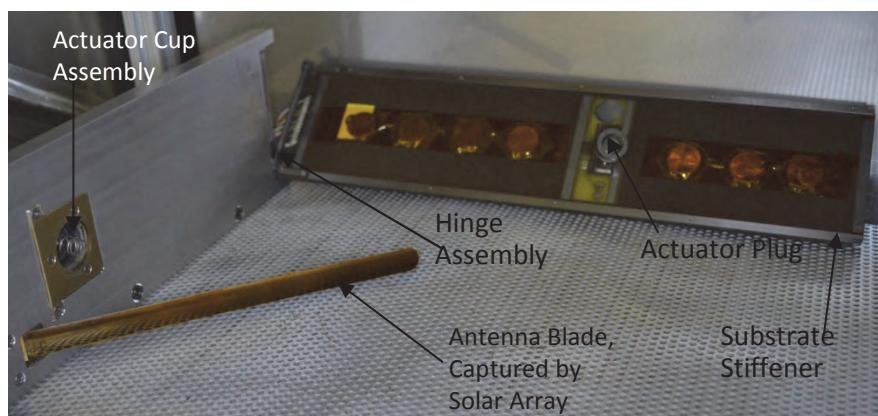


Figure 6 – The solar array wing and test fixture duplicated the boundary conditions for flight actuator testing.

The test at ambient conditions verified that workmanship was acceptable. The two tests at ambient temperature in vacuum showed the expected reduction in delta-T and time to separate. These results also showed (despite the small number of tests) a tight data grouping, showing that the device is repeatable. The tests at 3 A and 2.16 A showed that, as expected, the time to separate is inversely proportional to input current, when the tests are run at the same initial temperature. Somewhat surprisingly, the delta-T for the 2.16 A case was lower than those of the 2.6-A cases. Figure 7 shows the test stand inside the vacuum chamber.

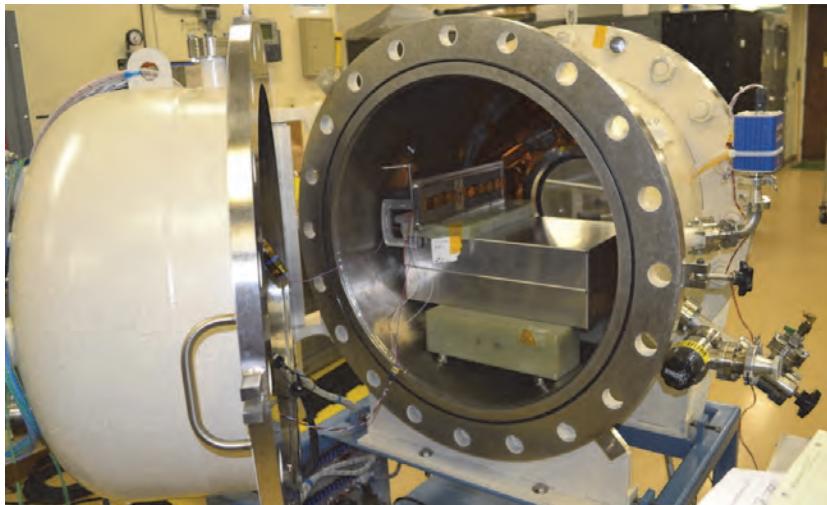


Figure 7 – Test stand, actuator and CTERA shown in vacuum chamber.

Following the tests at 2.16 A and 3 A, we conducted the self-actuation test. The purpose of the self-actuation test was to determine the temperature at which the actuator would release a deployable structure while unpowered. The actuator was required to reach a temperature higher than 50°C before self-actuating to demonstrate a 10°C temperature margin. The ambient pressure temperature cycling chamber was set to ramp temperature at a rate of 1°C per minute, starting at room temperature, which was approximately 19°C. We monitored the tell-tale circuit until the device actuated at 65.9°C. The highest predicted temperature for the CubeSat prior to solar array deployments is 40°C, which gives a margin of 25.9°C on self-actuation.

Following the self-actuation test, we conducted a static loads test. The purpose of the static load testing was to determine if the selected coatings and tolerances of the serial number 004 actuator can withstand launch loads after 7 separations. Note that the interference fit for the actuator tested, SN 004, is significantly smaller than those of the flight devices (SN 011-018). Since holding capability is a function of the interference fit, the flight actuators are able to react more load than the SN 004 device. The fixture used for static load testing is depicted in Figure 8. Tension on the actuator was increased in $\frac{1}{4}$ load increments and held for at least 30 seconds until the final load of 160 N (36 lb) was reached. Load was maintained at or above 156 N (35 lb) for 5 minutes. Following the static loads test, the CTERA was cycled two more times at ambient temperature and nominal power in vacuum (tests 4.9 and 4.10). Results from these two tests indicated that the electrical and thermal performance of the device wasn't affected by the static loads test. Results from tests 4.2, 4.3, 4.9 and 4.10 are tightly grouped. The raw data from the tests are presented in Table 4

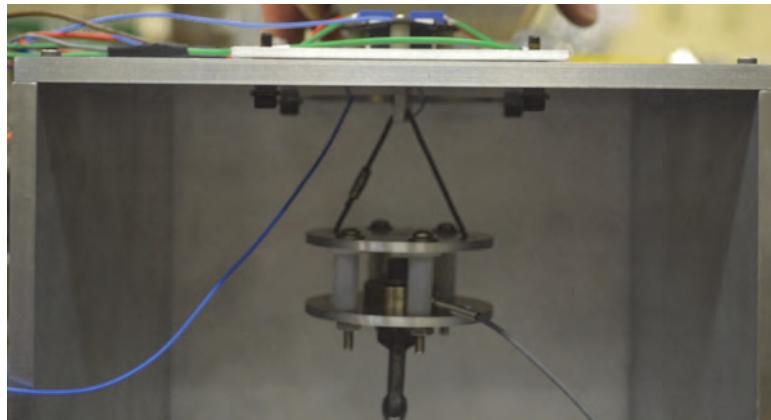


Figure 8 – The CTERA withstood 1.5 times the maximum expected flight load for 5 minutes.

Table 4 - Non-flight third generation actuator data, SN 004.

Test #	Vacuum (Tori)	Current (A)	Voltage (V)	Power (W)	Tamb (°C)	Trel (°C)	ΔT (°C)	Δtime (s)	ΔT/Δt Energy (W-s)	% Batt Energy	Interference Fit	Note
4.1	ATM	2.60	7.28	18.9	19.5	71	51.5	33	1.56	625	0.39%	0.0003
4.2	2.50E-02	2.60	7.28	18.9	18.7	45.0	26.3	18.5	1.42	350	0.22%	0.0003
4.3	2.50E-02	2.60	7.28	18.9	18.5	44.0	25.5	18	1.42	341	0.21%	0.0003
4.9	2.50E-02	2.60	7.28	18.9	18.4	47.8	29.4	17	1.73	322	0.20%	0.0003 1
4.10	2.50E-02	2.60	7.28	18.9	18.5	46.0	27.5	17.5	1.57	331	0.21%	0.0003 1
4.5	2.50E-02	3.02	8.46	25.5	18.5	39.8	21.3	12	1.78	306	0.19%	0.0003
4.6	2.50E-02	2.16	6.05	13.1	18.8	42.2	23.4	26	0.90	340	0.21%	0.0003
4.4	7.55E+02	2.60	7.28	18.9	UN K	UN K	UN K	UN K	UN K	UNK	0.0003	2
4.7	7.55E+02	0.00	0.00	0.0	18.9	65.9	47.0	NA	NA	NA	0.0003	3
4.8	7.55E+02	0.00	0.00	0.0	19.0	NA	NA	NA	NA	NA	0.0003	4
1	After static load test.											
2	Actuated while adjusting current delivered to the resistor. At ambient. No data recorded.											
3	Will not self actuate until ~66°C. SV will not go above 40°C. Adequate margin.											
4	Static Load Test. Requirement (with test factor 1.5) was 143.5N (32.25#). Held above 157N (35.3#) for 5 minutes.											

When the results from SN 004, with AMS-2488, Type 2 coating for titanium and hard coat anodize coating for the aluminum were compared to those for SN 002, with the same titanium finish and chemical conversion coating (MIL-C-5541, Class 3) of the aluminum, the SN 004 device was the clear winner.

SN 002 was tested first, and we concluded testing after the first 7 cycles because the data were poorly grouped, the performance of the device was perceptibly deteriorating, and we observed increasing damage to the interfacing surfaces of the aluminum and titanium parts. SN 002 raw data are not presented due to space restrictions.

Once the final design was selected, we fabricated eight flight units and conducted the following tests in the following order to validate the design. The flight mechanisms (SN 011 through 018) underwent the following testing to further validate the design and workmanship, and the raw data from these tests are presented in Table 5:

- At least one separation at nominal current at ambient temperature in vacuum (for SN 011-018, green shaded portion of the table)
- A single separation at minimum current at -20°C in vacuum (for SN 011-018, light blue shaded area of the table)
- Random vibration test on the Serial Number 001 3U CubeSat in the NASA NLAS CubeSat dispenser (SN 011-014)A single separation in vacuum after soak at 11°C and transient to -1°C on the Serial Number 2 3U CubeSat (mechanism SN 015-018)

Table 5- Data taken from third generation flight devices (SN011-018)

Test #	Vacuum (Torr)	Current (A)	Voltage (V)	Power (W)	Tamb (°C)	Trel (°C)	ΔT (°C)	Δtime (s)	ΔT/Δt	Energy (N·s)	% Batt Energy	Interference Fit	Note
11.2	2.50E-02	2.60	7.28	18.9	21.8	81.3	59.5	46	1.29	870	0.54%	0.00055	
11.3	2.50E-02	2.60	7.28	18.9	21.0	77.7	56.7	48	1.18	909	0.56%	0.00055	
11.5	2.50E-02	2.60	7.28	18.9	19.6	86.9	67.3	45	1.50	852	0.53%	0.00055	
12.1	2.50E-02	2.60	7.28	18.9	21.0	85.0	64.0	53	1.21	1003	0.62%	0.0007	
13.1	2.50E-02	2.60	7.28	18.9	21.2	95.7	74.5	70	1.06	1325	0.82%	0.0007	
14.1	2.50E-02	2.60	7.28	18.9	21.0	79.0	58.0	50	1.16	946	0.59%	0.00045	
15.1	2.50E-02	2.60	7.28	18.9	21.4	79.6	58.2	55	1.06	1041	0.65%	0.00065	
15.2	1.40E-03	2.60	7.28	18.9	18.8	87.4	68.6	52	1.32	984	0.61%	0.00065	
16.1	2.50E-02	2.60	7.28	18.9	20.0	94.2	74.2	59	1.26	1117	0.69%	0.0007	
17.1	2.50E-02	2.60	7.28	18.9	20.5	91.8	71.3	58	1.23	1098	0.68%	0.0006	
18.1	2.50E-02	2.60	7.28	18.9	20.8	87.6	66.8	58	1.15	1098	0.68%	0.00065	
11.4	1.50E-05	2.16	6.05	13.1	-20	73.0	93.0	120	0.78	1568	0.97%	0.00055	
12.2	1.30E-06	2.16	6.05	13.1	-19.9	87.9	107.8	127	0.85	1659	1.03%	0.0007	
13.2	6.00E-06	2.16	6.05	13.1	-20	98.8	118.8	140	0.85	1829	1.13%	0.0007	
14.2	5.50E-06	2.16	6.05	13.1	-20.1	58.1	78.2	129	0.61	1685	1.04%	0.00045	
15.2	1.70E-06	2.16	6.05	13.1	-20.1	78.5	98.6	130	0.76	1698	1.05%	0.00065	
17.2	9.80E-06	2.16	6.05	13.1	-20	94.0	114.0	140	0.81	1829	1.13%	0.0006	
18.2	3.40E-06	2.16	6.05	13.1	-20			133		1737	1.08%	0.00065	
16.2	8.50E-07	2.16	6.05	13.1	-20.3			122		1594	0.99%	0.0007	
15.3	6.00E-06	2.19	8.06	17.6	-1.0	82.0	81.0	71	1.14	1252	0.78%	0.00065	
16.3	6.00E-06	2.16	8.00	17.3	-1.0	80.0	87.0	72	1.21	1243	0.77%	0.0007	
17.3	6.00E-06	2.17	7.92	17.2	-1.0	96.0	89.0	78	1.14	1342	0.83%	0.0006	
18.3	6.00E-06	2.14	7.90	16.9	-1.0	92.0	91.0	79	1.15	1335	0.83%	0.00065	
11.6	ATM	2.26	6.33	14.3	50			57		814	0.50%	0.00055	
12.3	ATM	2.26	6.33	14.3	50			63		900	0.56%	0.0007	
13.3	ATM	2.29	6.40	14.6	50			84		1228	0.76%	0.0007	5
14.3	ATM	2.23	6.25	14.0	50			59		824	0.51%	0.00045	
5	Automated shutdown failed because of a harness fabrication error. Manual shutdown was delayed.												

We performed a basic analysis of the raw data from the **flight device (SN 011-018)** separations at ambient, cold vacuum (-20°C), thermal balance and thermal cycling cases. From these data, we determined the mean, standard deviation and two-sigma data, for time to separate, delta-T, and power required to separate.

The two-sigma time to separate is calculated as follows: $T_{2\sigma} = \text{Mean} + (2 * \sigma)$ where $T_{2\sigma}$ is the 2 sigma time to separate, **Mean** is the arithmetic mean of the times to separate, and σ is the standard deviation between the times to separate.

We recommended to our team that 2 sigma durations be programmed to assure that timed separations are successful. Table 6 lists the data for the four cases analyzed (2.6 A at ambient temperature in vacuum, 2.16 A at -20°C in vacuum, ~2.15 A during thermal balance testing at 0°C, ~2.25 A during thermal cycling in ambient pressure at 50°C).

Table 6 – Rudimentary statistical analysis of CTERA temperature, time and energy data

Vacuum, 2.6A, 20°C			
	mean	std dev	X + 2σ
Time	54.0	7.2	68.4
dT	65.4	6.6	78.5
Energy	1022.1	136.0	1294.1

Vacuum, Thermal Balance, 2.15A, 0°C			
	mean	std dev	X + 2σ
Time	75.0	4.1	83.2
dT	87.0	4.32	95.6
Energy	1292.8	52.8	1398.4

Vacuum 2.16 A, -20°C			
	mean	std dev	X + 2σ
Time	130.1	7.4	144.9
dT	101.7	15.0	131.6
Energy	1699.9	96.6	1893.1

Ambient, Thermal Cyclling, 2.25A, 50°C			
	mean	std dev	X + 2σ
Time	65.8	12.4	90.6
dT			
Energy	941.6	194.8	1331.2

We had already confirmed that actuation in vacuum reduces the energy required to actuate (see the difference between test 4.1 and tests 4.2-4.10). Looking further at the data, we noticed a correlation between input power and time to separate, and a correlation between initial temperature and time to separate. The following several figures pictorially represent relationships between initial temperature, delta-T, time, power level, and the different interference fits of the various actuators. The left chart of Figure 9 shows that release time is directly related to the energy expended, as one would expect. It also shows a correlation between the power applied to the device, illustrated here by various current levels, and time to release. The faster energy is applied to the device (more power), the less time and energy it takes to operate. The right chart of Figure 9 shows the relationship between release delta-T and power. As power increases, release delta-T decreases. It appears as the power applied to the high CTE part is increased, its rate of expansion is higher and less heat is applied to the low CTE part. Since less heat is applied to the low CTE part, it expands less and more slowly, resulting in a lower delta-T before the parts separate.

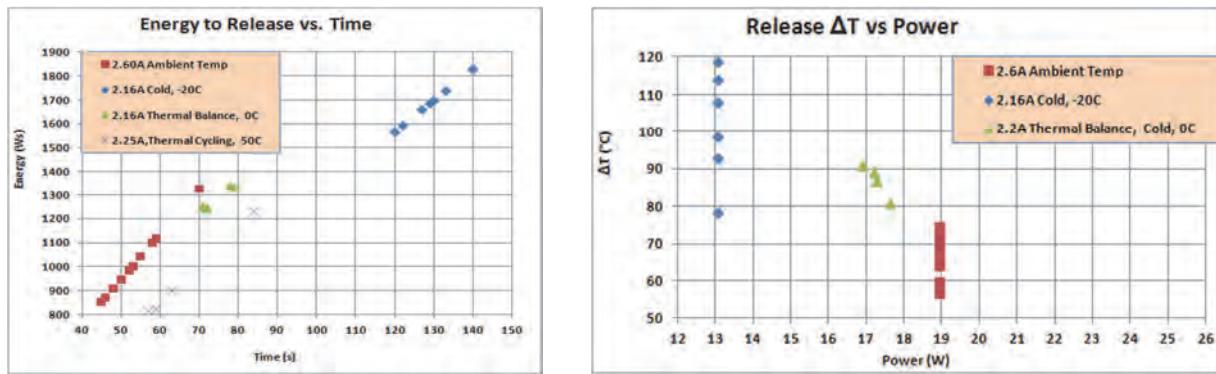


Figure 9 – Strong relationships between energy, delta-T, and time to separate

The left chart of Figure 10 shows the effect the interference fit has upon the delta-T required for the parts to separate. As the analytical model suggests, the looser fit requires less delta-T for the parts to separate. The right chart of Figure 10 shows the effect the interference fit has upon the energy required to separate. The high CTE part doesn't need to expand as much to free the low CTE part, which takes less energy. Additionally, when the interface pressure between the two parts is lower, less conductive heat transfer results between the two parts, so less energy is wasted heating the low CTE part. We initially expected less scatter in these charts, but realized static friction effects cause scatter (torque vs. preload tests exhibit this scatter, for example), and that minute surface imperfections have an appreciable affect on results, since the interface pressures are quite high in this design. These two charts also show two other relationships. The first, which we already discussed, is between input power and the time, energy, and delta-T required for separation. The second, discussed in the following paragraph, is the relationship between the initial temperature and the time, energy and delta-T required for separation.

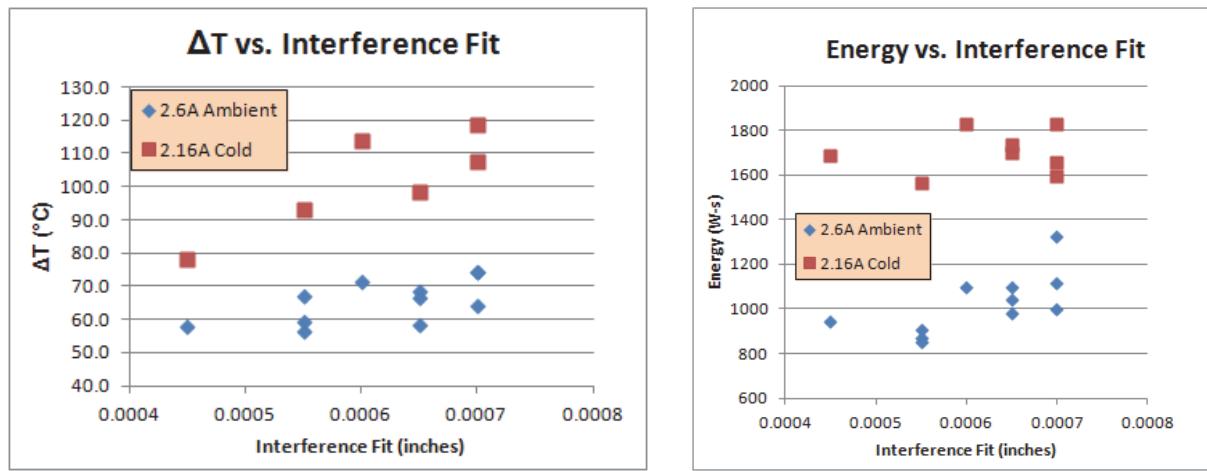


Figure 10 – Relationships between interference fit, delta-T and energy required to separate

The left chart of Figure 11 shows the relationship between the initial temperature and the energy required to separate. The right chart of Figure 11 shows the relationship between actuation delta-T and the initial temperature. Since the parts were manufactured at 20°C, they will have a tighter interference fit with a lower initial temperature and will have a looser interference fit as they have a higher initial temperature.

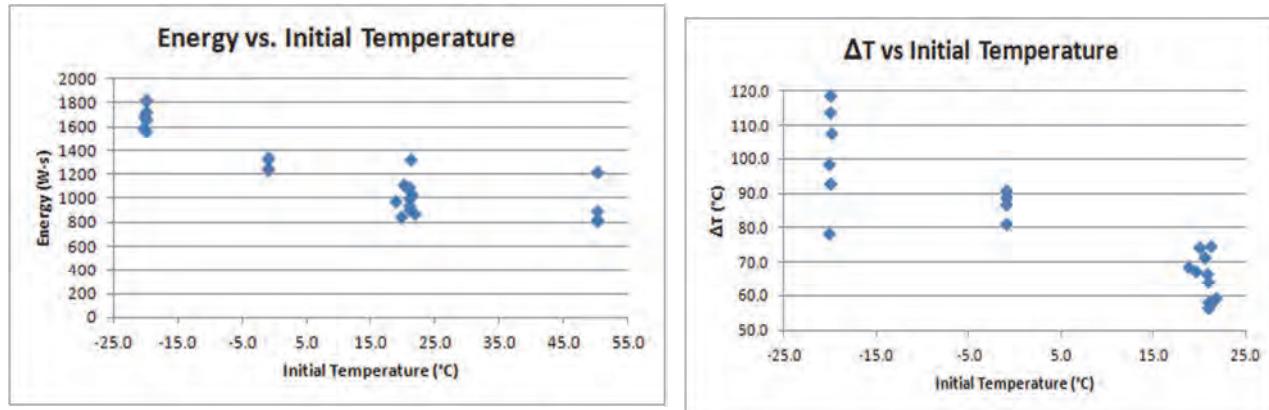


Figure 11 – Relationships between initial temperature, and energy to actuate

Testing of the flight parts has thus far confirmed the following:

- A single CTERA has been shown to not degrade in performance over 10 cycles. We intend to perform further life testing when given the opportunity.

- Despite variability in interference fits from device to device, actuation data are tightly grouped and can be used, when factored, for timed separation commands when the bus is at room temperature in vacuum.
- The tell-tale function of the actuators was determined to be reliable through the vibration testing and subsequent thermal cycling testing they underwent.
- Tell-tale reliability is not affected by vibration or thermal cycling.
- Operating condition effects:
 - The effect of supplied current on total energy and “on-time” is significant.
 - The effect of initial temperature on actuation times is also significant.
 - Since the “on-time” can vary wildly with initial temperature and supplied current, these devices should not be used open loop to avoid damaging the heaters. We recommend either: implement tell-tale reading circuits, as APL’s CubeSat did, or implement temperature sensors with each actuator and shut the devices off when the devices reach the maximum allowable temperature, or code in a two dimensional look-up table in the flight software, which sets “on-time” as a function of battery state of charge (resulting in current delivered to the device) and initial temperature.

Lessons Learned

- Don’t skimp on Ground Support Equipment (GSE) and test equipment. Test GSE are just as important as the flight hardware:
 - It would have been immediately obvious that the first (and second) generation devices were incompatible with the CubeSat solar array deployment motion if we had tested with a flight-like wing mechanism from the beginning. Representing boundary conditions correctly would have saved one design iteration.
 - Pay attention to data acquisition. We lost some data due to shortcuts in setting up the data acquisition system. We also would have been able to capture more data (such as temperature vs time curves) with a more advanced data acquisition system.
 - We could have saved money and time by testing more than one device at a time with more elaborate GSE
 - Enlist subject matter experts initially. We could have eliminated one design revision if we had known of electrical parts de-rating guidelines and selected the right resistors in the beginning.
- Incremental development is cost effective. By making really cheap parts, testing a little and learning a lot, fabricating a slightly more elaborate second generation device, testing a little and learning a lot more, we were still able to develop and test the flight device in a short, inexpensive effort.
- Manufacturing methods are critical to the success of a mechanism design; it wouldn’t have cost much more to fabricate the first generation parts on the newer generation CNC lathe, rather than the manually operated lathe.

Conclusion

A compact device for releasing deployable structures has been developed exploiting differential coefficients of thermal expansion of two dissimilar materials. The resultant device is economical, miniature, simple in concept and execution, uses little power, produces negligible shock, is easily resettable, and is able to restrain a relatively large load, considering its size. Through a total of 37 test actuations, the third generation design demonstrated a robust device that performed reliably in a flight-like environment. This device is applicable to small deployable devices on instruments, CubeSats and Nanosatellites, and has the capability to be used as an initiation device for mechanisms used on conventional spacecraft and larger instruments. Future work will focus on alternate materials, such as invar, which has a very low CTE, and manufacturing processes, as well as integration into larger load capacity mechanisms.

A Nichrome Burn Wire Release Mechanism for CubeSats

Adam Thurn^{*}, Steve Huynh^{*}, Steve Koss^{*}, Paul Oppenheimer^{*}, Sam Butcher^{*},
Jordan Schlater^{**} and Peter Hagan[†]

Abstract

The nichrome burn wire release mechanism uses a nichrome burn wire which when activated heats up and cuts through a Vectran tie down cable allowing the deployable on the satellite to actuate. The release mechanism was designed from scratch with the goals to make it small, inexpensive, simple, reliable and easy to use by anyone including student-run University CubeSat projects. The release mechanism, shown in Figure 1, utilizes a two saddle design with compression springs to apply a spring stroke and force to the nichrome wire to thermally cut through the Vectran cable when heated. Through a test program and using a design of experiments (DOE) approach it was determined that the applied current to the nichrome wire and the diameter of the nichrome wire were the key parameters governing successful performance. To activate the nichrome wire a constant current of 1.60 ± 0.05 amps is applied to ensure a successful and reliable cut. The tight tolerance constant current source is necessary in order to reliably: 1.) thermally cut the cable and 2.) prevent overheating failure of the nichrome wire to allow the mechanism to be reusable for many actuations without replacing the nichrome filament. The tight tolerances on the current prevent failure of the nichrome wire from overheating under too much current in a vacuum while also providing adequate thermal margin to cut through the Vectran tie down cable in air which requires more current than in vacuum. The burn wire release mechanism has been tested in air at room temperature and in vacuum at temperatures as low as -50°C and as high as 70°C on two different Vectran cable thicknesses. The release mechanism has shown to have cut times ranging from 2.4 to 7.2 seconds under these operating conditions. The burn wire release mechanism has 400 firings in component and system level testing without a single failure. The mechanism has been qualified for flight on the TEPCE (Tether Electrodynamic Propulsion CubeSat Experiment) program to release two carpenter tape deployments and a stacer and tether deployment system.

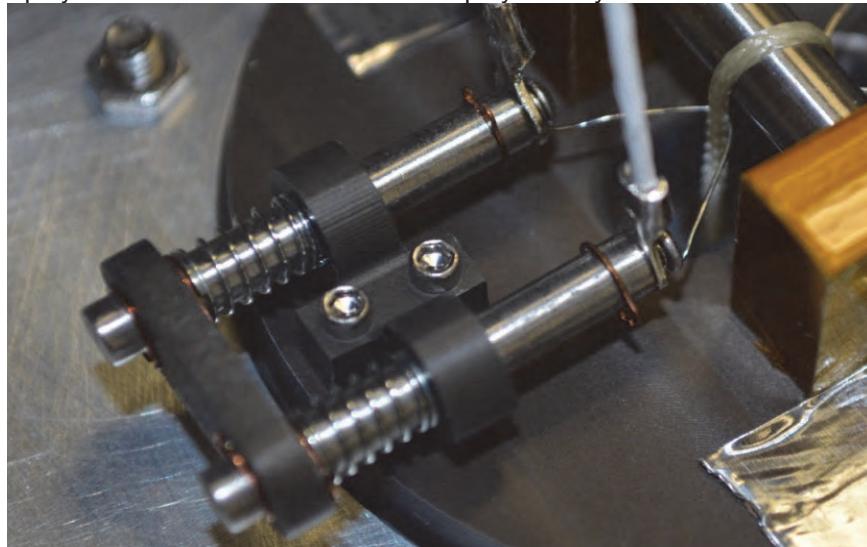


Figure 1. Assembled burn wire release mechanism

^{*} Naval Research Laboratory, Washington DC

^{**} NRL Co-op Student from the University of Cincinnati, Cincinnati, OH

[†] NRL Co-op Student from Northeastern University, Boston, MA

Introduction

CubeSats have grown into a class of satellites which are rapidly introducing new, inexpensive technologies in space. This ever increasing complexity and functionality in a small package brings rise to numerous mechanisms and deployables necessary in order to meet mission requirements. Release mechanisms often add significant development cost to a satellite program and in the world of small satellites, such as CubeSats, the need for simple, reliable, and inexpensive release devices can be critical to the success of the program. The ability for a single mechanism to accomplish many of these releases is a desirable trait among CubeSat users. Whether the mechanism be used to release antennas, solar arrays, deployable doors, etc.; an inexpensive, simple and reliable release mechanism would help to further promote the class of small satellites throughout the community. Since there are currently no standard commercialized CubeSat class release devices on the market, one was developed at the Naval Research Laboratory (NRL) via internal fellowship funding, since these programs are never funded sufficiently to develop one with program funding.

A spring-loaded nichrome burn wire solution was selected because it: 1.) could be actuated with standard CubeSat bus power and fairly simple, low cost electronics, 2.) was simple enough that University students could build and use it, and 3.) was inexpensive enough that CubeSat funding levels could afford it. With few moving parts, simply machined components and the majority of the hardware able to be purchased through low cost commercial suppliers such as McMaster-Carr, the nichrome burn wire release mechanism would allow CubeSat programs, including Universities, to keep down cost and complexity and ensure a high level of reliability for the release mechanisms needed for successful satellite operation.

Design

The release mechanism, utilizes a compression spring system in order to apply a force and a stroke to the nichrome burn wire. When a constant current is applied to the nichrome wire, it will thermally cut through a Vectran tie down cable allowing it to release the deployable it had secured. The nichrome wire used on the mechanism is 30 AWG type Chromel C with an allowable free length ranging from 10.0 (0.4") to 32 millimeters (1.25"). The free length of the nichrome wire is configured into a V shape with the apex in the V being the primary area for cutting through the tie down cable (See Figure 1). The nichrome wire free length range is determined by the minimum length which will avoid problems with heat sinking the nichrome wire to the rest of the mechanism. At a free length of at least 10 mm the apex in the V of the nichrome wire will be sufficiently far enough away from the mechanism heat sinks to avoid heat loss and ensure a successful cut. The maximum length of the nichrome wire is limited by the free length which causes the wire to lose structural stability when heated. At a free length greater than 32 mm the apex of the nichrome wire when heated becomes very hot and the resulting loss in tensile strength can cause necking of the wire which would impact further use of the nichrome wire. Using this free length range the resistance of the nichrome wire as measured from the screw head to screw head of the release mechanism is in the range of 0.4 to 0.9 Ω . When selecting the free length of the nichrome wire it is critical that the release mechanism has ample spring stroke to cut through the Vectran cable with the allowable deflection of the Vectran cable. Particularly in vacuum where convective heating cannot be taken advantage of, the nichrome wire must completely stroke through the Vectran cable in order to ensure a successful release. If the spring stroke on the wire is lost before the entire cable is cut then it is possible for the nichrome wire to remain stuck in the Vectran cable without severing it enough to have a successful cut. Therefore the tension on the Vectran cable must be enough that it does not allow for large, sagging bends in the cable which would allow for the springs on the mechanism to lose their preload and cutting stroke.

The compression springs are held between two saddles which are positioned on a pair of stainless steel dowel pins using retaining rings. The saddles are machined from 6061 aluminum which has been hard anodized to prevent electrical shorting (See Figure 1). The dowel pins have a tapped hole on their upper end where a #0-80 button head screw threads into. The head of the #0-80 screw attaches the nichrome

wire to a ring terminal which is connected to two flying leads and provides the electrical connection to the release mechanism. The nichrome wire is secured between the ring terminal and the underside of the head of the #0-80 screw (See Figure 2). The ring terminals which can be purchased cheaply with tin plating will need to be stripped by a plating manufacturer for a small cost, approximately \$1 per ring terminal. The #0-80 screw is secured into the tapped hole of the dowel pin using 3M Scotch-Weld™ 2216 B/A on the threads of the screw to prevent the screw from backing out and losing the secure connection of the nichrome wire. Figure 3 shows CAD models of the nichrome burn wire release mechanism in the deployed and stowed states.

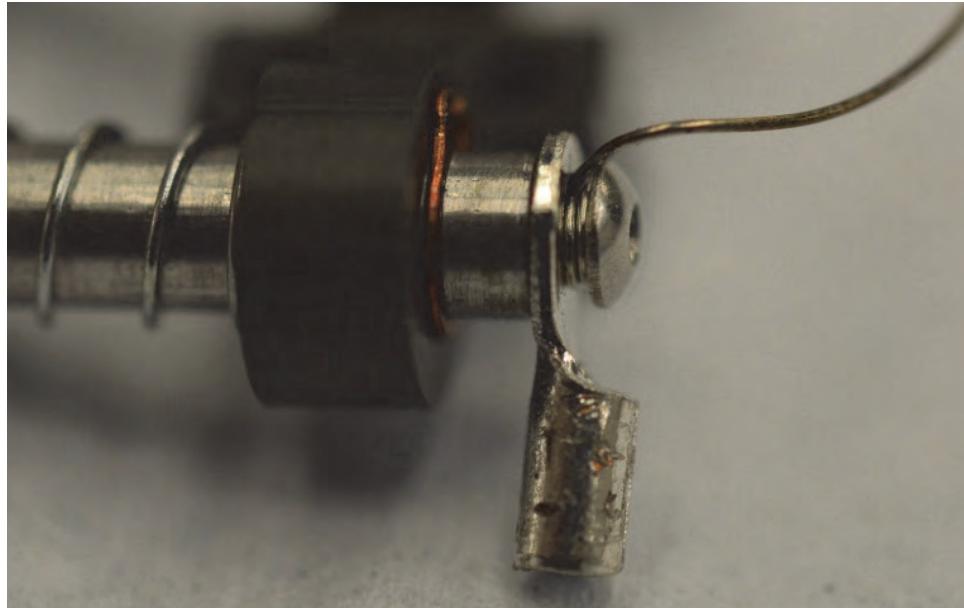


Figure 2. Nichrome wire secured between the button head screw and ring terminal

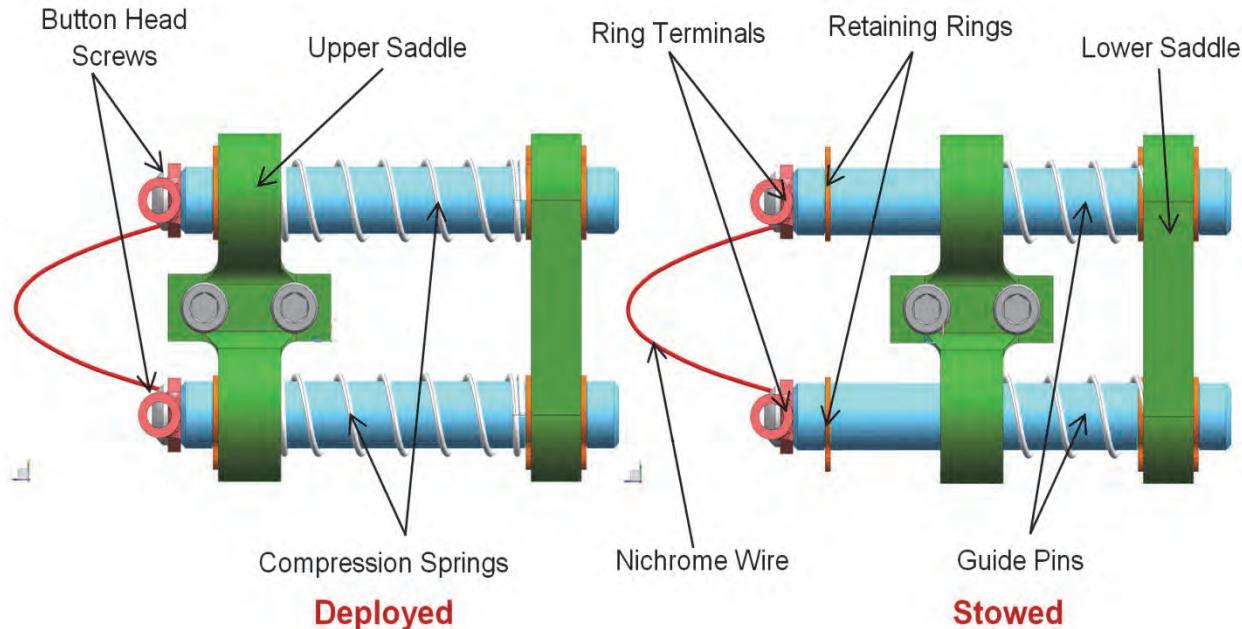


Figure 3. Nichrome burn wire release mechanisms in the deployed and stowed configurations.

The mechanism was designed to thermally cut through two different deniers of Vectran cable. Both Vectran cables were 12 strand tubular braids with either 200 or 400 denier strands and were

manufactured without an oil finish for low outgassing. The 200 denier Vectran cable has a tensile breaking strength of 300 N and the 400 denier Vectran has a tensile breaking strength of 600 N. Vectran cable was selected as the primary tie down cable due to its low creep over time, its relative strength to other materials, and its resistance against self-abrasion.

The entire burn wire release mechanism once assembled has dimensions of approximately 32-mm (1.25") long by 16.5-mm (0.65") wide by 11.5-mm (0.45") tall. Figure 4 shows two, redundant burn wire release mechanisms stowed on the TEPCE tether deployment system. Due to the small size, assembly and workmanship, inspection is best done with the aid of magnification such as a stereo microscope.

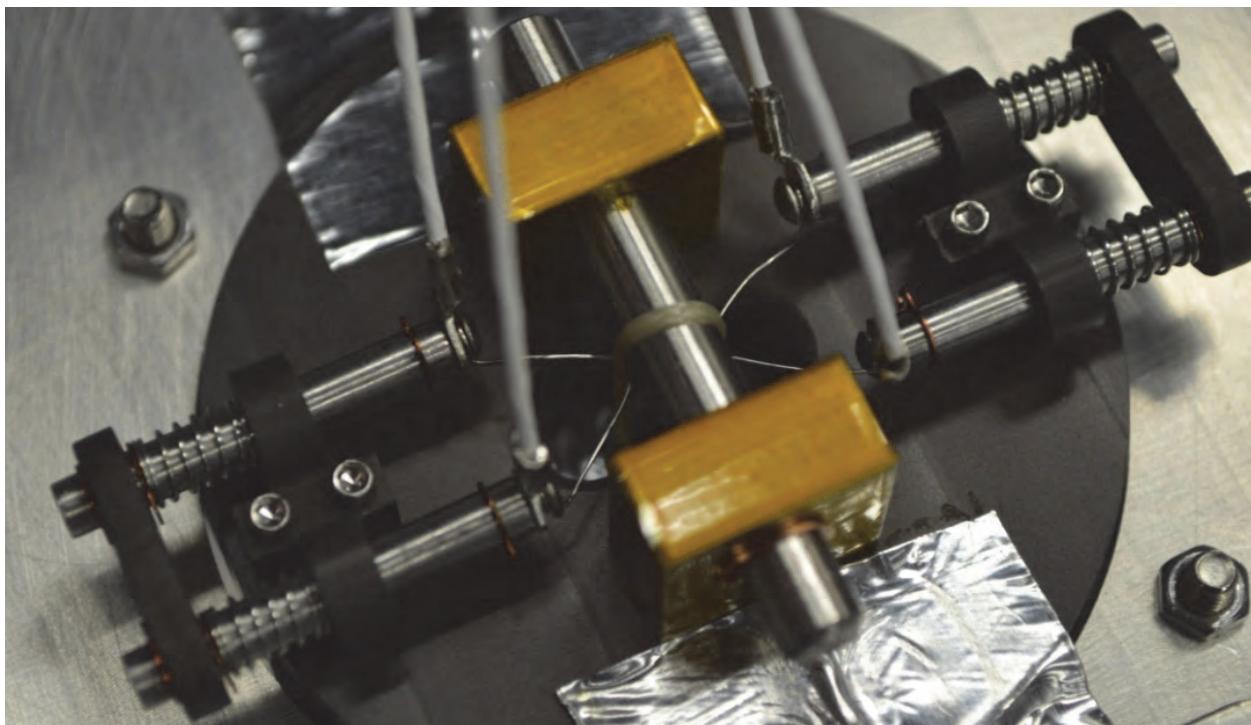


Figure 4. Release mechanisms on Vectran tie down cable for TEPCE tether deployment system

Testing

The goals established for a generic CubeSat class release mechanism were: 1.) to be simple enough to replicate the build and assembly by all CubeSat users (including Universities), 2.) be inexpensive, 3.) reliably release in a few seconds but rugged enough to survive for a 30 second timer for each actuation, 4.) have a design life at least 50 actuations, 5.) work at the same power draw in both air and vacuum and 6.) fit into as small a volume as possible. A burn wire based release device was selected based on a trade study between numerous miniature actuators including bolt releases, pin pullers, and linear and rotary actuators. Then the parameters associated with the burn wire, the compression springs and the tie down cable were investigated. Since a large number of parameters needed to be tested in order to find the optimal design of a nichrome wire system, a design of experiments (DOE) approach was taken in order to test multivariable changes in the minimum number of experiments. The parameters chosen to test were the nichrome spring stroke and force applied, the nichrome wire diameter, the free length of the nichrome wire and its corresponding resistance, the tie down cable, the tension on the tie down cable, the current supplied to the nichrome wire, the number of actuations (life) for each nichrome wire, the performance in air and vacuum and the effect of the environmental temperature. Additionally, minimizing the cut time of the Vectran tie down cable was a goal. Using the JMP Statistical Discovery software a DOE test matrix was designed and tests were conducted and important factors in the design were determined.

Through the DOE analysis in JMP, it was found that the most important factor for successful cut times in both air and vacuum was the supplied current to the nichrome wire. As long as the compression springs supplied spring stroke all the way through the Vectran tie down cable and the nichrome wire had enough current to thermally cut through the tie down cable then the release mechanism would successfully release. The diameter of the nichrome wire was then based on that which provided a large enough electrical current margin to reliably release in air balanced against not failing in vacuum due to overheating the nichrome wire. An electrical circuit was designed to supply a constant current to the nichrome wire independent of the resistance of the wire and the voltage available from the spacecraft. As long as the minimum required power (0.9 W) was available from the spacecraft then the electrical circuit would supply a constant current to the nichrome wire.

It was found that the 30 AWG nichrome wire provided an acceptable margin relative to overheating in vacuum versus failing to thermally cut in air. Since the design envelope for the two failure modes was not large, the constant current source was kept to tight tolerances. The minimum amount of current needed to reliably cut through the tie down cable in air (worst case) was 1.40 amps. The supplied current to the nichrome wire that would cause a failure due to overheating in vacuum (worst case) was 1.90 Amps. Therefore a constant current requirement of 1.60 ± 0.05 amps was selected to provide margin on either side of the failure modes and was used to design the electrical circuit. This allowed the mechanism to successfully operate in both air and in vacuum without having to change any circuitry or software. It is critical to note that the critical operating window – in vacuum/space where it must work – is larger than the worst case window that includes operation in air for ground testability. Additionally, in all tests to date where the nichrome wire has been overheated to failure, it has first cut through the Vectran cable for a successful release prior to the nichrome wire failing such that this has not actually resulted in a failure to deploy but rather ended the reusable life of the nichrome wire filament. This shows that the nichrome burn wire release mechanism has a much larger margin to work successfully in vacuum where it counts. The schematic for the constant current circuit design used on the nichrome burn wire release mechanism is given in Figure 5.

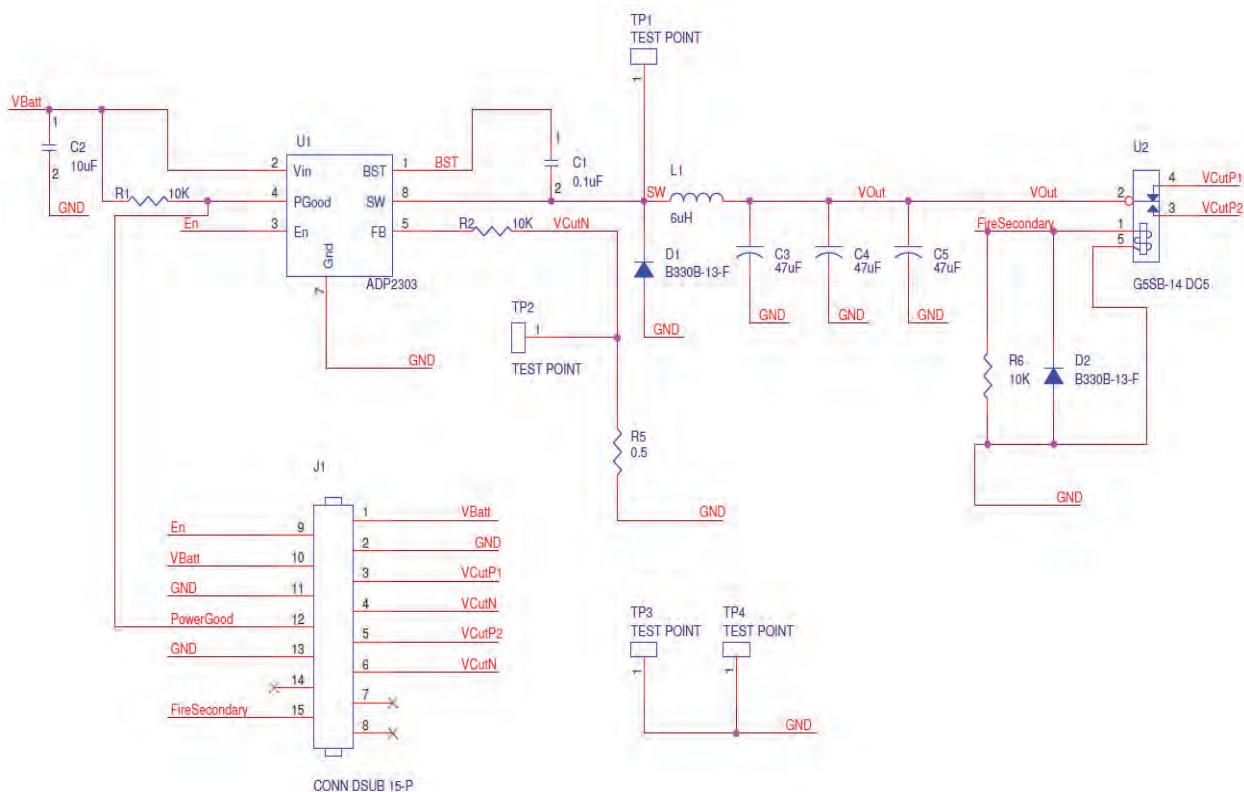


Figure 5. Schematic for the constant current circuit design.

Results

The design and optimization of the burn wire release mechanism revolved primarily around understanding the performance of the nichrome wire. The failure current of the nichrome wire under only the tension of its own weight was first investigated and the results for the 30 AWG nichrome wire is given in Table 1. This data shows that the upper bound of the nichrome wire failure current is established at 1.90 amps.

Table 1. Failure currents of the 30 AWG nichrome wire under only the tension of its own weight.

Nichrome Wire Resistive Length (mm/in)	Resistance (Ω) – as measured from screw to screw	Failure Current (amps)	Failure Time (sec)
13 / 0.50	0.8	2.15	7
19 / 0.75	1.1	2.05	7
25 / 1.0	1.5	1.95	7
32 / 1.25	1.3	1.95	9
38 / 1.50	1.5	1.9	10
45 / 1.75	1.6	1.95	14
51 / 2.0	1.8	1.9	20
57 / 2.25	2	1.9	17
64 / 2.5	2.1	1.975	30
70 / 2.75	2.2	1.975	19
76 / 3	2.2	1.975	13
83 / 3.25	2.4	1.9	15
89 / 3.5	2.6	1.9	19
Avg. Failure Current		1.960	

Using the tight tolerance constant current circuit, 419 successful tests of the release mechanisms have been conducted without a failure. Of the 419 tests, 242 were conducted in air at room temperature and 177 were conducted in vacuum at various temperatures. Tests were also conducted to intentionally overheat the nichrome wire and cause it to fail but even in these cases; the nichrome wire always first cut through the tie down cable ensuring a successful release and then the nichrome wire would fail after the successful cut from overheating. Figure 6 shows test data taken for the air and vacuum operation of the burn wire release mechanisms cutting through 200 and 400 denier Vectran cables.

Time to Cut Thru Vectran as a Function of Supplied Current to the Nichrome Wire

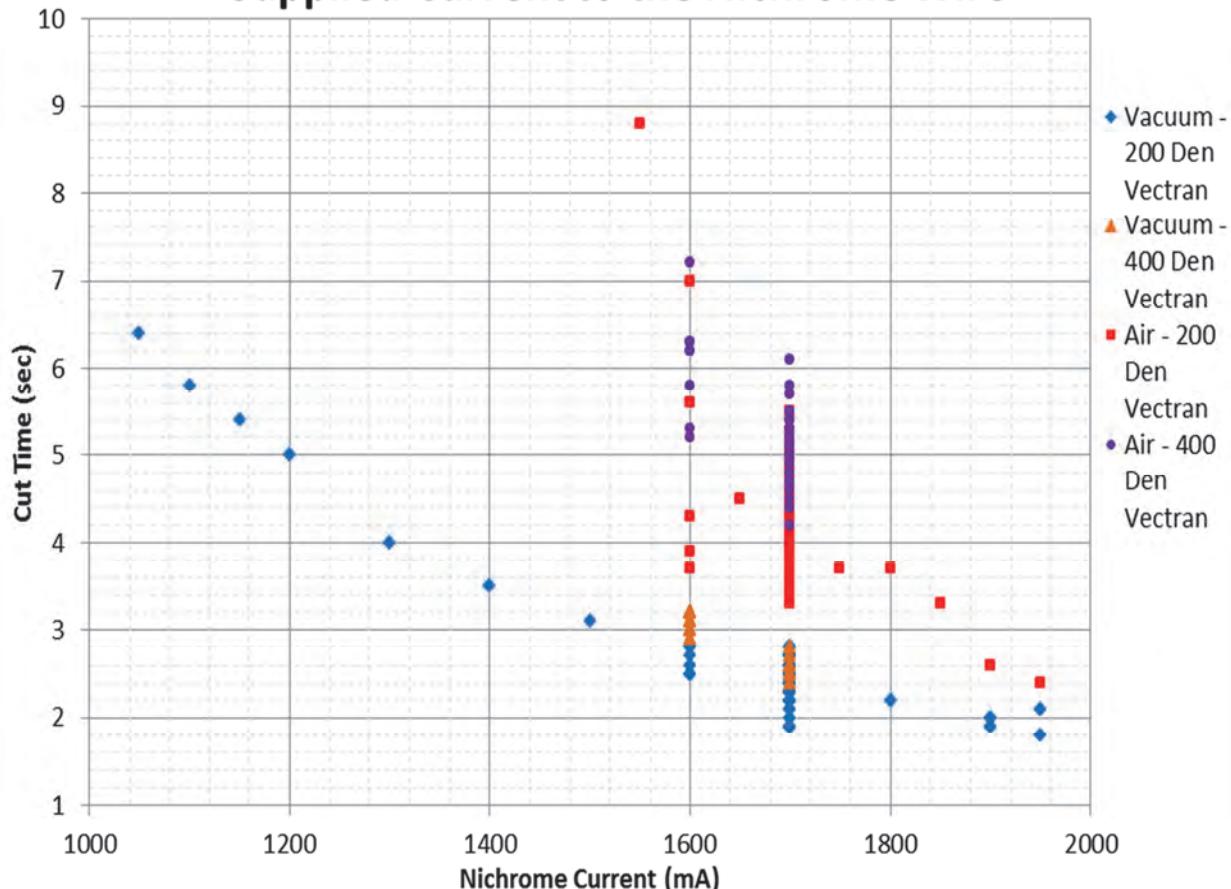


Figure 6. Release mechanism deployment times for varying currents of both Vectran cables in air and vacuum environments.

Using the constant current circuit which supplied the nichrome wire with 1.60 amps with a 30 second powered timer, the cut times for the burn wire release device in air and vacuum and using both Vectran cables ranged from 2.4 to 7.2 seconds. For the critical operating window in vacuum this gives approximately a 10X margin on the cut time versus the 30 second powered timer limit. Table 2 gives a summary of the average cut times for the operating conditions.

Table 2. Average cut times of the burn release mechanisms.

	Average Cut Time (sec)
200 Denier Vectran in Air	5.3
200 Denier Vectran in Vacuum	2.6
400 Denier Vectran in Air	6.2
400 Denier Vectran in Vacuum	3

The burn wire release device was also tested down to -50°C and up to 70°C without any noticeable effect on the performance. This is likely due to the nichrome wire heating up to over 750°C and having negligible thermal mass, such that the difference in initial temperature has a negligible effect. It was also

demonstrated that when using the tight tolerance constant current circuit the burn wire release mechanism can be actuated at least 50 times without having to change out the nichrome wire. Many of the burn wire release mechanisms were used past the 50 actuations, up to 80 actuations, and still performed nominally Figure 7 shows the release mechanism immediately following a successful cut through the Vectran cable in vacuum with the nichrome wire still glowing hot.

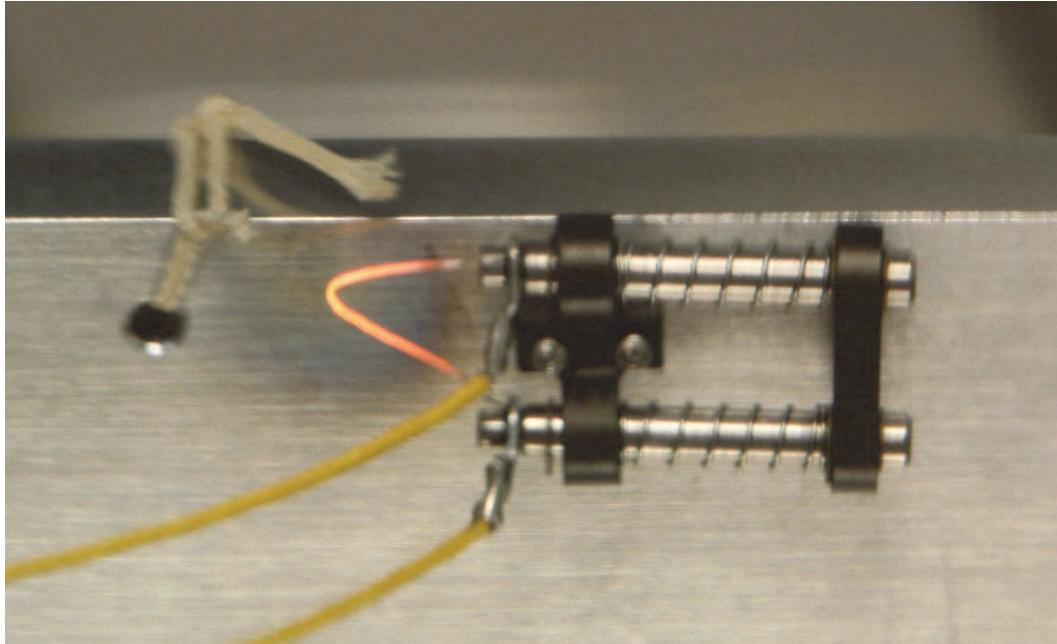


Figure 7. Burn wire release mechanism immediately following a successful cut through Vectran cable.

To be useful to all CubeSat users, including Universities the burn wire release mechanism needed to be simple to manufacture and assemble and to be cost effective. For the NRL TEPCE CubeSat program headed by NRL, the cost for all hardware associated with building 10 of the burn wire release mechanisms was \$1600 making the cost per mechanism \$160. This cost included having a local machine shop manufacture both the upper and lower saddles and the dowel pins. However, a student with reasonably proficient machining skills could make the mechanism components themselves and eliminate all but the anodizing costs which could drop the price for 10 mechanisms to approximately \$200. Table 3 gives a price breakdown of the hardware associated with machining and building up the burn wire release mechanisms for use on a small satellite.

The nichrome wire release device has been through component level testing in different configurations ranging from carpenter tape deployments to a stacer and tether deployment to the deployment of 3U solar array panels on a CubeSat. The release device has also undergone system level testing on the TEPCE CubeSat program.

Table 3. Cost breakdown for burn wire release mechanisms.

Part Description	Material	Secondary Processing	Quantity	Total Cost
Upper Saddle	Aluminum 6061	Hard Anodize	10	\$849.00
Lower Saddle	Aluminum 6061	Hard Anodize	10	\$200.00
Dowel Pin	18-8 Stainless	None	20	\$430.00
Compression Springs (CI013DE03M from Lee Spring)	302 Stainless Steel	None	100	\$101.00
1/8" External Snap Rings (McMaster-Carr)	Beryllium Copper	None	100	\$12.50
#0 Stud Ring Terminals (McMaster-Carr and Stripping Manufacturer)	Copper	Tin Stripping	100	\$45.30
#0 Fasteners (McMaster-Carr)	18-8 Stainless Steel	None	100	\$5.68
0.0100" Diameter Nichrome Wire	Nickel Chromium	None	1/8 lb.	\$18.65
			Total Cost for 10 Mechanisms	\$1,662.13
			Cost per Mechanism	\$166.21

Cautions and Areas for Potential Improvement

A drawback to the burn wire release mechanism is that the successful operation of it relies largely on the workmanship and assembly of the mechanism in its intended application. A loss of spring preload is possible if the Vectran tie down cable is not tensioned properly. Additionally, the available play and stiffness of the electrical wiring for the flying leads or and improperly securing the nichrome wire under the screw head can all lead to potential failures of the burn wire release mechanism to successfully cut through the Vectran tie down cable. Therefore it is critical that throughout the assembly and installation of the burn wire release mechanism that careful attention is given to these areas of concern and risk of failure is mitigated. Properly tensioning the Vectran tie down cable, ensuring an appropriate free length of nichrome wire and proper placement of the burn wire release mechanism will help to avoid the threat of the springs losing preload. Conducting pull tests of the nichrome wire and verifying the connection under a stereo microscope after securing it between the ring terminals and the screw head will verify that the nichrome wire connection is reliable and the possibility of the nichrome wire coming unattached can be avoided. When installing the release mechanism it is vital to verify that ample play is given for the electrical wiring of the flying leads to the mechanism and that snag hazards of the wiring are avoided. If the electrical wiring does become snagged or runs out of available room to move, the small force associated with the burn wire release mechanism will likely not be sufficient to compensate for a snag and the release mechanism would fail to cut through the tie down cable.

Improvements could be made to the burn wire release mechanism to lower the reliance on workmanship and add confidence and reliability to the mechanism. To minimize the risk of the flying leads being a snag hazard, one could investigate adding a jumper wire to the mechanism with a connection pad that would have all of the moving wires contained to the mechanism itself and then the electrical leads could be mounted to the stationary portion of the mechanism. This would mandate a design change to the saddles and add slight complexity to the release mechanism but would help to alleviate the risk of failed release due to the electrical wiring to the mechanism. Another improvement could be a new way to mechanically connect the nichrome wire to the release mechanism instead of using the preload and clamping force of

the screw to hold the nichrome wire. While properly securing the nichrome wire and verification of this connection has proven successful in testing to date, the concern still exists that the nichrome wire could slip out from under the screw head and increase the nichrome wire free length which would in turn allow the compression springs to relax and spring preload could be lost.

Conclusions

The burn wire release mechanism was designed in order to be used by a broad range of small satellite users in a manner that was simple, reliable, and inexpensive. Using a nichrome burn wire design the release device is capable of cutting through various tie down cable materials and providing successful satellite mechanism deployments. The burn wire release mechanism specifications were chosen in order to be user friendly in both air and vacuum environments and to give the user the ability to implement a release mechanism which has been previously tested and will work in a number of applications.

Drawings and assembly procedures have been produced in order to allow any small satellite user to conveniently reproduce the nichrome burn wire release mechanism for their specific application. The nichrome burn wire release mechanism will hopefully allow for a more universal release mechanism which can be reliably used in a wide array of applications for CubeSat and other small satellite users. By giving the engineer a mechanism which has proven reliability, the hope is that the cost and complexity of smaller satellite programs can be kept at a minimum.

References

1. Vectran Technical Data Brochure. Kuraray America, Inc. Vectran Division. 2008
2. General Considerations for the Processing of Vectran Yarns. Kuraray America, Inc. Vectran Division. 2007
3. Fette, R.B., M.F Sovinski. Vectran Fiber Time-Dependent Behavior and Additional Static Loading Properties. NASA/TM-2001-212773. December 2004
4. ASTM B344-01. Standard Specification for Drawn or Rolled Nickel-Chromium and Nickel-Chromium-Iron Alloys for Electrical Heating Elements. American Society for Testing and Materials. August 2010.
5. JMP 9 Statistical Discovery software. SAS. 2010

Antenna Deployment Mechanism for the Cubesat Xatcobeo. Lessons, Evolution and Final Design

José Antonio Vilán Vilán*, Miguel López Estévez* and Fernando Aguado Agelet*

Abstract

This paper aims to explain the whole development process that has been undertaken over the past few years including the problems encountered and the solutions adopted in what was to become the final design of an antenna deployment system for the Xatcobeo picosatellite. This mechanism was first presented at the 40th Aerospace Mechanism Symposia. At that time, we presented an evolved version of our antenna deployment mechanism, with many conclusions and lesson learned. However, only now can we present the final version of this mechanism with all the development problems, solutions and conclusions reached as well as the lessons learned over 3 years of work.

Introduction

In the paper published for the 40th AMS we explained the mechanism's general operation. This included how the antenna retention system, the burning system, and the opening detection all worked. Although, in general terms, none of these features has been changed to any great extent, they are all different in some way from what we described then. This is due to the many problems we came across and the way their solutions have led to changes in all the device's parts.

Modifications

This article will analyze in detail all the changes the design has undergone throughout the development period. Namely:

- The dimensions of some of the parts on the main piece (sub-chassis)
- The sub-chassis design
- New attachments
- The materials used
- The retention wire burning circuit. Two resistance types
- Retention wire tying
- Power Voltage
- Thermo-vacuum test

Also, totally new features will be explained that have been developed since the first article, such as:

- Electrical interface
- Mechanical interface
- Design of the RBF. PEM nut
- New part for resistance support
- Thermal interface between the sub-chassis, the new support part, the resistance and the shielding panel
- Calculations for avoiding the appearance of ESD following ECSS standards
- Compliance with the standard for outgassing values
- Final integration process and envelopes. Problems with dimensions and assembly.
- Modification of the margin with the enveloping film
- Qualification Tests

* University of Vigo, Vigo, Spain

Mechanism Background

This deployment mechanism is based on one main part, called the sub-chassis, which is designed to be built from a polymer using fast prototyping. All the elements needed for the mechanism's operation are installed onto this piece. This includes the antenna enveloping film, the burning resistance, and the opening detection switch. The sub-chassis can itself be installed in the shielding panel on one side of the Cubesat, which means that everything is easily inserted in a modular way.

Operation is very simple. The retention film is attached to the sub-chassis and allows the antennas to be folded and retained against the edge of the sub-chassis. Once the assembly is closed, a nylon wire passes through both the film and the antennas, and it is this that keeps everything folded away until the time for burning. At that moment, the burning resistance will cut the retention wire and the antennas will be deployed, leaving the retention film joined to the sub-chassis unable to detach itself.

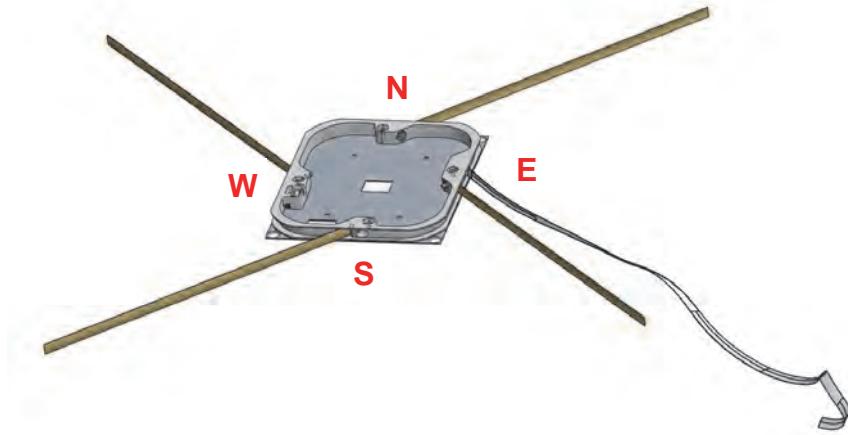


Figure 1. Final Deployment Mechanism

General view of the Mechanism

General operation is, as mentioned above, basically the same as before. The main difference lies in the fact that the enveloping film, instead of being fixed to the sub-chassis together with one of the antennas with which it was in direct contact, is now attached independently onto the sub-chassis. This way avoids problems related to the noise that could be produced on the antenna, but which requires a new nut and bolt to be included.

Furthermore, the enveloping film attachment moves from point S on the sub-chassis to point E. This is due to the fact that if it were attached at point S, the end of the antenna attached at point E would end beyond the retention point. The pressure from the retention wire would thus lead to this unpressed end opening towards the outside in such a way that it would exceed the limit given by the available envelope. In compensation, the film is roughly 80 mm longer. It needs to be perforated twice for the retention wire to pass through, which means its capacity for retention is much greater precisely because it passes twice over the retention point and none of the antenna's parts are left with no pressure against the sub-chassis.

Sub-chassis

The sub-chassis, as stated above is the cornerstone of this mechanism. Its special features allow it to be extremely light and act as the piece that enables the installation of all the other mechanism elements. This means it is of vital importance for endowing the assembly with modularity and simplicity.

Material and Manufacture

One of the main changes in this piece involves the material chosen to make it. In the previous article we had chosen polyamide 6 as the material and Selective Laser Sintering as the manufacturing method. During the development of this piece research into the properties of various polyamides led us to opt for polyamide 12 with fiberglass reinforcement. There were several reasons for this:

- The first reason is that PA12 is lighter than PA6 by about 10%, and absorbs less water. This was a step in the right direction which was to reduce the weight of the whole assembly as much as possible.
- The second is that the prototypes manufactured using SLS on PA12 with Fiberglass reinforcement were more precise than those made from PA6 with Fiberglass. This favored the correlation between the CAD model and the actual model. Bearing in mind that the attachment of the various parts onto the sub-chassis was based on a tight fit, it was very important to suitably meet this correlation. Moreover, this was also a way of improving repeated similarity between the different prototypes that were commissioned.

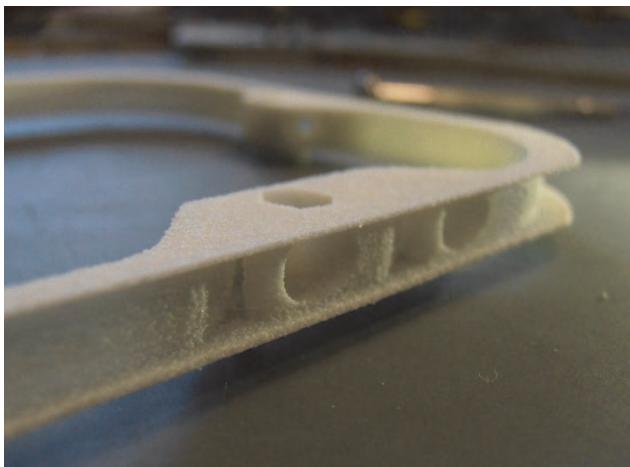


Figure 2. Sub-chassis detail. E point

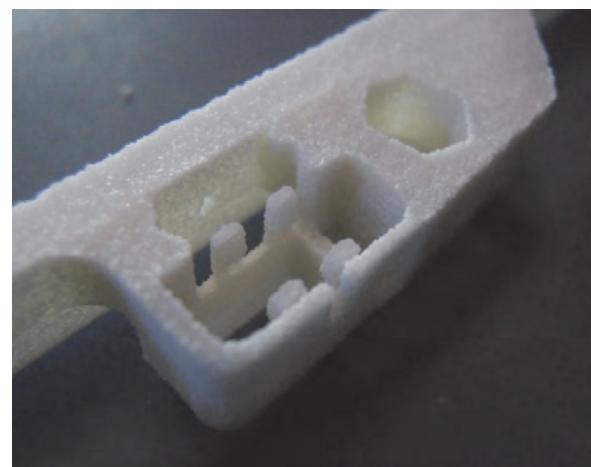


Figure 3. Burning receptacle. W point

Design and Dimensions

The changes made in the sub-chassis were aimed at solving problems arising during the development stage. Below we outline both the problems and the solutions in the design:

- Burning receptacle (resistance, switch, wire, tying system, increase of material in the area in order to insulate the resistance as much as possible and make the parts that are heat sensitive as massive as possible).
- New attachment for the film (equilibrium of the part, improvement in retention)
- Modification of the tabs (longer at the corners and narrower)
- The piece was reduced in width from 6.5 mm to 6.3 mm

Retention and Burning System

The previously published version of the system for burning and cutting the retention wire explained that a 0.125-W 9- Ω resistance had been chosen. The parameters used for dimensioning this resistance were early ones and the voltage for the power was later modified to 3.3 V. Once this value was accepted as the one which would produce the burn, a re-dimensioning of the resistance was begun to maintain the dimensions and nominal value of the power, i.e., the sought after resistance would be 0.125 W.

Test

In order to select the correct resistance from those available commercially, thermo-vacuum and room-temperature tests were carried out. The thermo-vacuum tests were redesigned until pressures even lower than those used earlier were achieved; a new vacuum pump was installed; the vacuum chamber and the

electrical connections were modified. This was all with the intention of achieving lower pressures, gaining greater control of temperature and eliminating losses in the vacuum chamber electrical connectors.

To reach the desired low temperatures, liquid nitrogen was used. To apply the liquid nitrogen indirectly, a system was designed comprising a bath of the liquid in a container within the vacuum chamber into which an oval-shaped piece of copper was dipped. While the lower part of the copper was submerged in the nitrogen, the upper part had the deployment mechanism bolted to it. The copper acted as a thermal conductor and the device's temperature was quickly reduced. Finally, a probe was installed in contact with the sub-chassis, as this is the part with the lowest heat conductivity and therefore the one that would be the slowest at changing temperature. The probe would thus provide the most reliable temperature reading for the parts that have a thermal balance inside the assembly. This is the atmosphere in which the device was enclosed and connected up in order to be fed power for the deployment to take place.

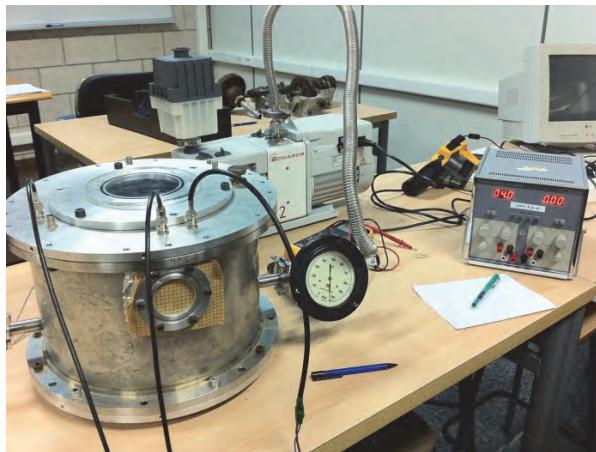


Figure 4. Thermo-vacuum chamber

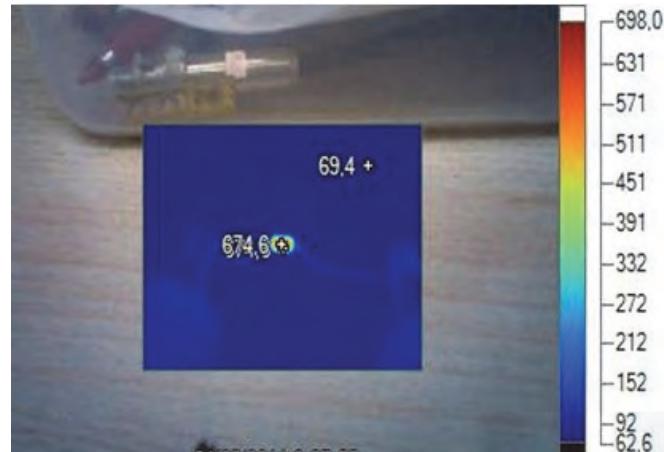


Figure 5. Thermal image of the resistance (°F)

Besides this device, various tests were carried out on the wire burning at room temperature using a thermal camera for observation. With the combined results from thermal-vacuum and room-temperature tests, in which the same potential was burned and the same resistance used, the temperature value was found that the resistance must reach at room temperature in order to burn the retention wire in the thermal-vacuum atmosphere. This temperature is directly linked to an electrical power value needed, and it is thus simpler to select a resistance from commercially available values.

Thanks to these tests we detected that the resistances, on being subjected to much greater powers than the nominal ones, underwent deterioration and variation in their properties when the current was passed through them. This was helpful when determining the point at which the resistance was capable of burning the wire in the coldest environment and not destroy itself at room temperature. For this, the deterioration was related to the variation in the current flow by maintaining the power voltage constant over time. This fact can only be due to the variation in the resistance value over time due to the deterioration through overload. The graph in Figure 6 shows the results from observation of the resistance in a thermal-vacuum test at 3.3 V over more than a minute of burning, with two seconds of stop before the opening of the antennas



Figure 6. Monitored intensity during burning thermo-vacuum test

Change of direction. New Burning Voltage

Once the resistance was dimensioned to burn at 3.3 V, at a specific value of $5.6\ \Omega$, changes were made to the project from outside our design process. The voltage supply was changed from being a set figure to one somewhere in the interval between 4 and 5 V. This not only caused a delay and meant the work done so far could not be applied in the Xatcobeo project, but it also posed a new problem for the task of guaranteeing correct resistance operation, which did not now have a fixed voltage value but instead had a rather wide range of values.

The challenge set by the new resistance values lay in guaranteeing that the selected resistance would burn the wire at the coldest temperature and with the lowest voltage (now 4 V), while at the same time ensuring that the resistance would not be destroyed at the highest voltage (5 V) and at the highest temperature, i.e., room temperature. Furthermore, the limitations still existed of using commercial values and consuming the least power possible.

One possible consideration was to select a resistance of 0.25 W, as it would then be possible to dissipate more power and, in theory, have more room for manoeuvre. Thus, two sub-chassis were designed independently, each one adapted to each resistance type. However, when the burning tests were carried out, it was observed that, the 0.25-W resistance was much more easily destroyed than the 0.125 W one contrary to what we had first thought. This meant this options had to be totally discarded and the tests became more centered on finding a suitable resistance at 0.125 W.



Figure 7. Burning thermo-vacuum test

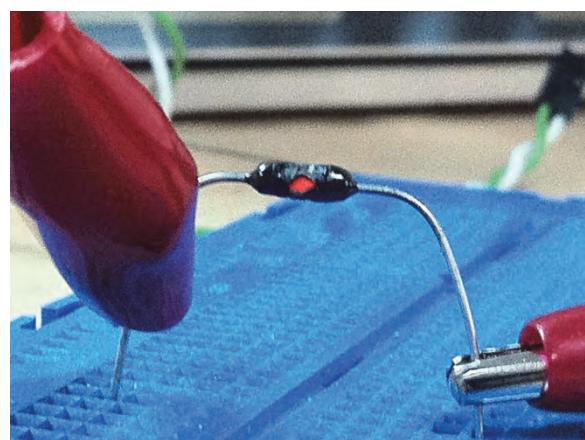


Figure 8. Destroying a 0.125W resistance

Thermo-vacuum tests were carried out at -100°C using several resistance values to determine the wire burning. The burning tests consisted of a three-minute continual burn in order to check both that no damage was caused to the resistance and also the burning time at 4 V and 5 V. Observation was also made of the current variation produced by the deterioration of the resistance. In this way all possible effects were checked and operation was guaranteed in the face of much higher time values than the real

ones for the burning cycle, which were set at 20 seconds by these tests and which double the burning time in the worst possible conditions.

Furthermore, numerous tests were carried out of the burning in a vacuum, at room temperature, and at the highest voltage in the range, in order to guarantee that the worst conditions for thermal dissipation, the highest temperature and the maximum power value did not destroy or serious damage the resistance. Burning was also for a continuous three-minute period, and some tests were even carried out at up to 15 minutes non-stop without destroying the resistance, although there was some relatively major deterioration after this time.

All the testing and dimensioning work led to a resistance of 6.8Ω and 0.125 W being selected, thanks to which burning was produced in 2-3 seconds at room temperature and 6-9 seconds at -70°C .

Retention system. Remodelling

In the 2010 article we described the retention system as a film joined to the sub-chassis and sharing an attachment point with one of the antennas, namely antenna S. The material chosen was a polyvinyl acetate, which had the optimum mechanical properties but not the best electrical ones as its surface resistivity was too high and so posed an ESD risk.

This was one of the main problems, along with the one mentioned above concerning the attachment of the film to antenna S, which had one serious inconvenience in that the antenna attached at point E is not completely pressed against the sub-chassis as it finishes its run along the side several centimetres beyond the burning receptacle, where the retention knot is tied. The local pressure applied by the knot deformed the antenna and made its end cross over the limit of the envelope allowed on the deployment device and go beyond the Cubesat rail.

There was a third problem linked directly to the film attachment. This time with the antenna's shared attachment. The radio-communication and IT engineering group discovered that the film, on being in direct contact with the antenna and unearthing, would introduce a great deal of noise into the signal, which meant measures had to be taken and changes made.

To solve the first of these problems we decided a change of material was needed. So we began to look for a polymer that would keep the lightness but also guarantee suitable antenna insulation, be dissipative, and, furthermore, have mechanical and thermal properties that were similar to the excellent ones of the polyvinyl acetate.

We chose a commercially available polymeric film and carried out thermo-vacuum deployment tests with it. The results were excellent, for, despite being thinner than the acetate, it complied with the mechanical needs for correct antenna retention operation.

In order to ensure correct surface resistivity, and even though we knew the material was catalogued as being anti-ESD, we decided to make the calculation needed to demonstrate that, in effect, the chosen film met the electrical requirements. We decided to use document ECSS as a reference, which states that in the worst case it should bear an electric potential of 100V between extreme and basis. Also the current density through the film should not exceed 10 nA/cm^2 in order to avoid ESD risk.

Independent attachment of the enveloping film

The independent attachment of the retention film is one of the greatest changes the sub-chassis underwent due to the above. For this there was a possibility of creating a new fixing point in any free area of the sub-chassis. Many options were considered, such as locating the attachment point in the free area just below the burning receptacle on the sub-chassis corners or on a prolongation of one of the antenna attachments.

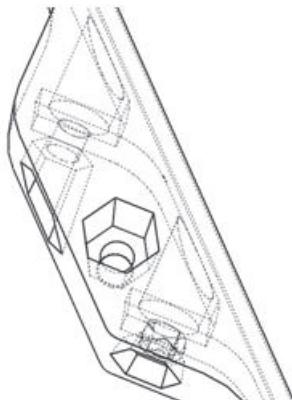


Figure 9. Independent fixation

We finally chose the last option which included a shift of the attachment point from antenna S to E. This led to improved antenna E retention and to the sub-chassis' center of gravity moving towards the geometric center of the piece because a practically perfect anti-symmetric piece was attained by this change.

Retention wire and mechanical interface with the Switch

In the mechanism presented in 2010, the detection switch was used to know the state of the antennas after each period of supply to the burning resistance. This meant that the retention wire pressed the switch tab and thus indicated that the antennas were folded. The loss of tension allowed the switch tab to lift and indicate that the antennas were open when the wire was cut.

Mechanically, the wire had to go through (in order, from the outside of the sub-chassis ring towards its inside) the enveloping film, and the antennas, the sub-chassis' outer wall, and pass over the resistance, close the switch, pass through the inner wall of the receptacle and be tied in a hole located a few millimetres away from the line of the wire.

A problem arose in the hole through which the wire had to pass in the internal wall of the burning receptacle. In some of the tests the tab was not able to open as a result of the trajectory curve that the retention wire had to follow. In order to solve this, the hole had to be designed above its previous position, although this compromised both the wall's integrity and the ease of tying as it made it difficult to achieve the tension needed to keep the antennas tied up.

This was achieved by introducing a second hole and tie attachment in such a way that the wire was tied between the two holes with no possibility for it to turn either before or after the burning. This detail increased the tension attained when tying and security, and also improved the wire's behavior in our search for perfect switch operation.



Figure 10. Burning receptacle

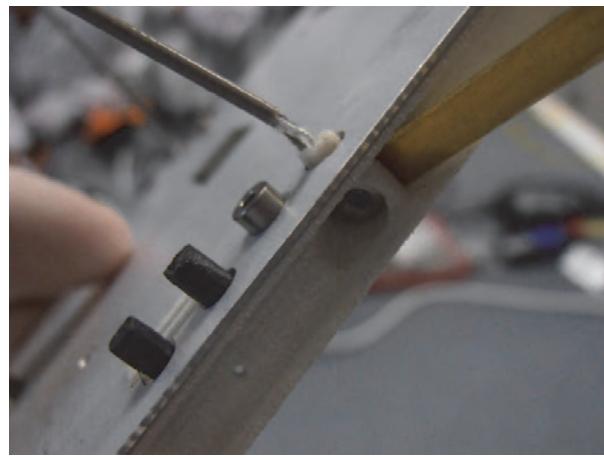


Figure 11. Detail of the interface between resistance support, sub-chassis and shielding

Resistance support piece

After many trials burning the retention wire, and bearing in mind that the order of events made it possible to produce successive burns in the case that the switch did not open after the burn, it was decided to test successive burns carried out on the same resistance, the same sub-chassis, and with the same assembly.

The result was that the resistance withstood all the successive burns perfectly well, without too much deterioration and without putting the retention wire's burning capability at risk. However, the heating up of the conductors in the resistance itself, together with the force applied by the tightened wire in contact with the resistance, produced a process similar to hot wire cutting on the part of the sub-chassis used for holding the resistance in the correct position.

This was a risk when several successive burns were needed to burn the retention wire. That is why a part was designed to substitute that part of the sub-chassis. This part holds the resistance in an unchanging position regardless of how many burns are used.

A material was sought that could withstand high temperatures of around 300°C, would comply with values for outgassing, and would, in addition, present no ESD problems, i.e., one that was electro-dissipative without being conductive. The resistance could then be supported directly by it. The solution is a technical polymer made of PEEK, graphite and carbon fiber, which is also machinable and can thus be easily manufactured.

Finally the sub-chassis was redesigned to make this piece fit the lower part, where it is inserted, in such a way that the sub-chassis attachment itself was used for this piece. In this way we avoided adhesives or new mechanical joints and kept the assembly light. It also avoided the inclusion of new elements in the burning receptacle area, which was already congested.

Outgassing and ESD

All the compounds making up the device must be selected so that the outgassing values do not exceed 1% in the TML and 0.1% in the CVCM. These values are demanded by the ECSS standard.

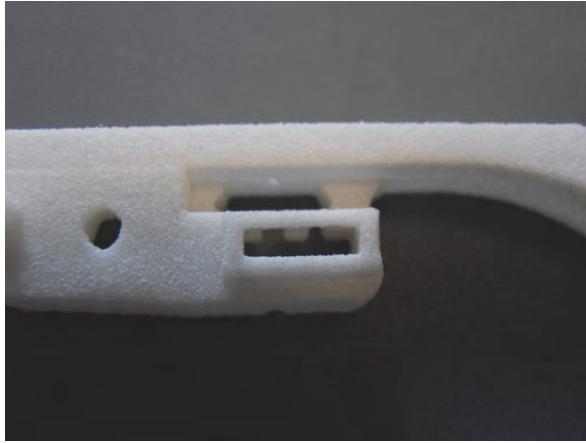


Figure 12. Sub-chassis

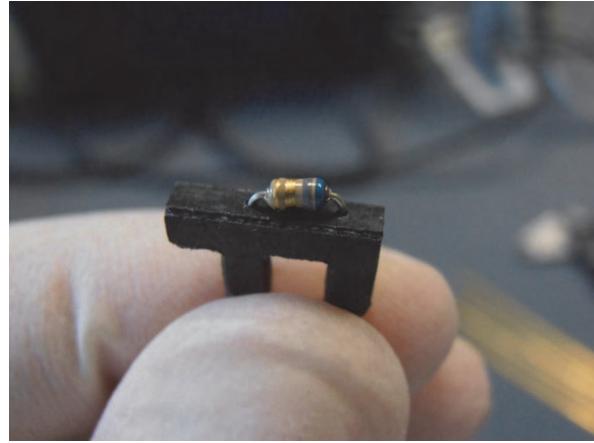


Figure 13. Resistance support

This is not a problem when working with metals, as no conventional metals have appreciable outgassing values, which means that there is no problem when working with aluminum, steel or titanium. However, when polymers are used it becomes more complicated to comply with the outgassing values demanded by the standard. It is often impossible in practice for the suppliers of finished parts to give outgassing values as they are parameters for very specific applications.

As this is considered to be a low-cost research project, we do not work with suppliers from the aerospace industry as they are far too expensive. Which means that obtaining the outgassing values for the polymers we work with has been complicated. We have already analysed the case of the polyamide, which, due to it containing fiberglass and being manufactured using laser sintering, has values below the limits according to the ESTEC/544 (QM/3958) reference test from 2004.

PEEK with Graphite and Carbon Fiber is an extremely expensive product, which in our case does not have major repercussions on the project given that the piece we use is very small. Here are the outgassing values for this compound:

Total Mass Loss (TML) [%]	0.16	ESA, ESA PSS-01-702
Collected Volatile Condensable Material (CVCM) [%]	0.00	ESA, ESA PSS-01-702

As for the dissipative film, it can be seen to be a conflictive element for several reasons, but above all because of the ESD risk. Regardless of this, it also had to comply with the outgassing parameters. Below are the values.

Total Mass Loss (TML) [%]	0.32	ASTM E-595
Collected Volatile Condensable Material (CVCM) [%]	0.00	ASTM E-595

The other elements on the device are metals such as Ti6Al4V for the mechanical attachment, or aluminum for the shielding, which do not cause problems with regards outgassing.

ESD

Much has been said about the way in which the device retains the folded antennas by using a polymeric enveloping film, and also about the sub-chassis structure that acts as the support for all the device's elements. Both share the same feature of being made out of polymeric materials, which not only reduces weight but also acts as electrical insulation at the same time.

Initially, this feature seems to be nothing but advantageous, but when the space environment is analysed it can be seen that there are several serious drawbacks, some of which we have already mentioned. These include steep temperature gradients, expansion forces, heat build-ups due to the lack of convection in heat transmission equations, and, in addition to others not mentioned here, the risk of electrostatic discharges (ESDs) appearing due to the high doses of ionized plasma that exist in the space environment.

After analysing the needs and requirements set out in the ECSS-E-ST-20-06C standard, we selected a commercially available electro-dissipative film. This is Polyethylene terephthalate (PET) sheeting with an aluminized face with anti-corrosive primer.

We decided to check whether this material was apt for our specific application. ESA experts in ESD were consulted and by combining their advice with the standards we made a series of calculations that show the material to be completely valid for the working environment it will have in space, even in the worst case.

The first hurdle is the unit in which surface resistivity is and the calculation of the electro-dissipative film's total resistance. The characteristics film gives a value of $6.81 \text{ e}10 \Omega/\text{Square}$, which is the unit used to differentiate resistances of surface resistivities.

First, we had to calculate the film's total resistance:

$$R = \frac{\rho \cdot l}{w \cdot t}$$

Where ρ is the surface resistivity, l the length of the strip, w its width and t its thickness.

$$R = \frac{6.81 \text{ e}10 \cdot 500}{4,5 \cdot 0,0508}$$

$$R = 1,4895 \text{ e}14 \Omega$$

As mentioned, the standard gives a current density limit of $J = 10 \text{ nA/cm}^2$ and, in order to avoid electrostatic discharges in inverse voltage gradients (e.g. between a dielectric and a conductor at a greater negative potential), a maximum potential difference (V) is established between dielectric and adjacent conductor exposed to the vacuum of +100 V. Furthermore, when A is the area exposed in cm^2 , we know that:

$$R = \frac{V}{J \cdot A}$$

$$R = \frac{100}{1 \text{ e} - 8 \cdot 50 \cdot 4,5} = 4,44 \text{ e} + 08 \Omega$$

That is, for our case:

$$R \geq 4,44 \text{ e} + 08 \Omega$$

If we reverse this reasoning and take R as data to calculate the current density resulting from using the resistance:

$$J = \frac{V}{R \cdot A} = \frac{100}{1,4895 \text{ e} + 14 \cdot 50 \cdot 4,5} = 2,98385 \text{ e} - 14 \text{ A/cm}^2 \ll 1 \text{ e} - 8 \text{ A/cm}^2$$

According to what is established in the standard, this value cannot exceed $1\text{e}-8 \text{ A/cm}^2$ (28 ECSS-E-ST-20-06C page 28). Thus we demonstrated that the material is fit for purpose in space, as it easily meets the requirements of the standard.

Mechanical, Electrical and Thermal Interfaces

Before describing the final design and its features, we would like to explain all the interfaces found on the device as we believe it is important to know about them in order to understand the characteristics of the design.

This project is characterised by the number of factors that must be taken into account during the design and dimensioning tasks. The wish to make a system with such strict requirements and objectives, one which is also totally modular and independent from the structure itself, means that there are numerous conditioning factors caused by local conflicts between the various elements in the assembly. We have decided to call these conflicts “interfaces”, of which there are three kinds:

- Mechanical Interfaces. These are all the relationships, contacts, and dependences of the distinct parts in the device that are mechanical in nature.
 - The most obvious ones are those generated between the deployment device and the shielding onto which it is installed, and that between the shielding and the frame. The latter is the simplest and consists of 4 countersunk M3 drill holes, whereas the former is the most complex of all the faces of the Xatcobeo, the reasons for which are given below:
 - Attachment of the sub-chassis. There are 4 holes through which the bolts should pass to attach the sub-chassis to the shielding. These are M2 pass through holes.
 - Antenna connection. One of the most conflictive points on the assembly and easily the one that took up the most design, verification and redesign time during the whole project.
 - At this point is the mechanical interface between the sub-chassis and the shielding, formed by 4 holes through which a part of the polymeric piece can pass towards the inside of the satellite.
 - There is a further mechanical interface between the connection cable and the holding bolt for the antenna, which had to be taken into account so that the traction from bolt tightening did not break the connection wire.
 - Between the connection cable and the insulation protruding from the sub-chassis. This protruding piece is designed to fit the coaxial's inner insulation and thus eliminate mechanical stresses on the connection wire.
 - Between the cable's coaxial mesh and the joint between sub-chassis and shielding. This interface gave the integration problems described later.
 - Finally, there is a less noticeable interface made up by the sub-chassis and its parts that protrude towards the internal face of the satellite and the structure frame.
 - There are other mechanical interfaces that do not directly involve the deployment device but which take place in the shielding, such as the microHDMI connection and the RBF bolt.
- The following mechanical interface is made up of the antennas and the shielding and that generated in the joint attachment of the antenna and polymeric enveloping film.
 - It is formed by the antenna itself, the bolt that enables attachment and the sub-chassis, with the antenna connection wire in the middle.
- The interface between the polymeric film and the antennas. These can be divided into two, as follows:
 - Whilst the antennas are folded

- Once the antennas have been deployed and the film is attached to the assembly and has free movement. Another reason for avoiding ESD and earthing it, should it make contact and discharge towards an antenna.
- Mechanical interface between the resistance and the sub-chassis. The resistance must remain in a set position during the burning time, which means there is contact between both elements. This interface, furthermore, is designed so that its characteristics stop the resistance from becoming detached after burning, even if the power cables were to become loose for any reason.
- Switch and sub-chassis. This is another of the interfaces that caused the most headaches throughout the project. It is very important that the switch be installed at the exact point it was designed for, because in this way the trajectory of the retention wire is correct and its aperture is guaranteed together with correct deployment measurement. There have been many modifications based on the results from tests and flight prototypes.
- Nylon wire. The nylon wire is another of the more complicated interfaces as it is in contact with the enveloping film, the antennas, the outside of the sub-chassis, the resistance, the switch, the inside of the sub-chassis and, finally, with the sub-chassis again, when it goes through the tying holes.
- Interface between the polymeric support piece for the resistance, the sub-chassis and the shielding. This piece should leave the resistance in the correct place and fit tightly in order to avoid vibrations or shifts of position.
- Attachments. The use of different materials to make the device's parts means that expansion gradients can appear at the areas where there are mechanical conflicts between materials depending on the temperature changes produced during orbit. This takes on greater importance at the attachment points on the sub-chassis for the antennas, where there is contact between Polyamide 12 with fiberglass and the Titanium, Aluminium and Vanadium Alloy. Some play is needed in order to avoid polymer fault.
- Electrical Interfaces. All the electrical relationships between elements in the device are given in this section:
 - Burning resistance. The design must guarantee electrical separation between the power cables to the resistance and the metallic mass of the satellite that serves as its electrical mass. At the same time the electrical connection must be guaranteed between the resistance conductors and the power cables to the antenna board. In this case by soldering.
 - Switch. In the same way as for the resistance, the switch connections must be electrically insulated to ensure perfect measurement. As with the resistance, the connection must be guaranteed with the measurement cables in the switch. Soldering is also the solution here.
 - Antennas. It is clearly necessary to insulate the antennas from any electrical contact that may exist. This is a point had also previously been studied and included in the design of the sub-chassis itself, as can be seen in the tabs.
 - Connection of antennas and metallic mass. The bolt must keep the connection wire for each antenna in contact in order to ensure perfect data transmission. At the same time, the metallic mesh of the coaxial cable for antenna connection must be kept between the shielding and the sub-chassis, i.e., earthed at all times.
 - The dissipative layer of the sub-chassis and the shielding. To avoid ESD in the sub-chassis, it was decided to use dissipative paint on it and earth it in contact with the shielding by direct contact between the covering and the shielding.
- Thermal Interface. This interface is somewhat complicated given that in one small area 4 different materials are in contact, each with distinct conductivities, distinct fusion points and distinct responsibilities in the device; these are the resistance, the sub-chassis, the shielding and a piece that acts as the resistance support and is the sub-chassis' protection against high

temperatures, not from the resistance but from the conductors located on both sides of it. Further details will be given in the section dealing with the burning resistance.

Integration of the Remove Before Flight

For the Remove Before Flight assembly, we had to bear in mind the great precision that had to be attained in the trigger position and, therefore, in the way this was guided towards the interior switch. It was decided that the best way to guide the trigger was by means of a threaded hole, and for the trigger to be a 16-mm long M2.5 bolt, as it had to close the switch at this distance until the RBF was removed.

In order to guide the bolt conveniently, one option was to use a single nut because the shielding is too thin for a hole to be threaded. However, the option to attach a nut using some kind of adhesive posed the problem of not being able to achieve suitable precision and of the bolt being likely to deviate with respect to the switch.

To solve this problem we resorted to a type of self-clinching nut called a PEM nut, which consists of a mechanical joint that uses pressure to embed itself thanks to the geometry of the nut itself. We designed an installation method which meant there could be no over pressure, and therefore no deformation of the shielding, using a simple installation tool for the nut and a small manual hydraulic press.

To check whether the nut would hold up after installation, several tests were carried out on a shielding that was identical to that for the flight. These consisted of severe mistreatment by means of heavy blows that destroyed the shielding. However, the PEM nut remained unmoved by all the knocks and accelerations that were produced. Finally, it is worth pointing out that in the vibration test (which was more professional and better monitored) that formed part of the Qualification tests, the PEM nut behaved perfectly and as expected.

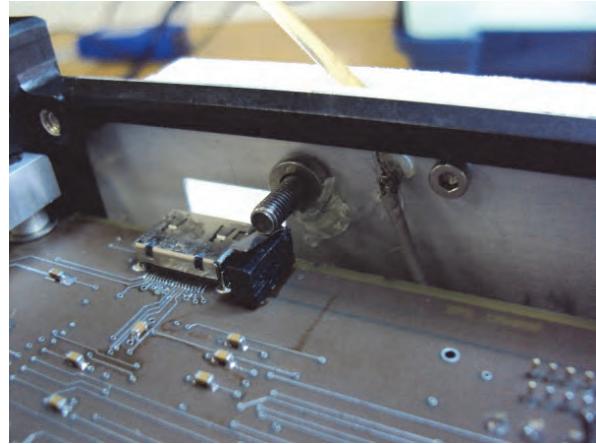


Figure 14. PEM nut for guiding the RBF

Integration and Qualification

During the assembly tests for the mechanism, there were never any problems arising regarding the integration of the mechanism; nor were there any problems stemming from the mechanical interfaces. These tests had been carried out with a shielding that was identical to the one for flight, and the coaxial meshes of the connection cables for the antennas had been frayed to improve the coupling between cable, sub-chassis and shielding. However, the flight connection cables had been made in such a way that the coaxial mesh was compact, cylindrical and soldered. This led to the coupling between these three elements being highly unsatisfactory.

It must be said that the design had a margin of 0.2 mm with regards to the limit for the envelope given in the Cubesat standard, set at 6.5mm. However, the pressure generated when the sub-chassis attachment bolts were tightened on the rolled up coaxial meshes produced a bending moment located at each of the four attachment points. This deformed the piece elastically to the point where the corners of the sub-chassis exceeded the available envelope dimensions by several millimetres.

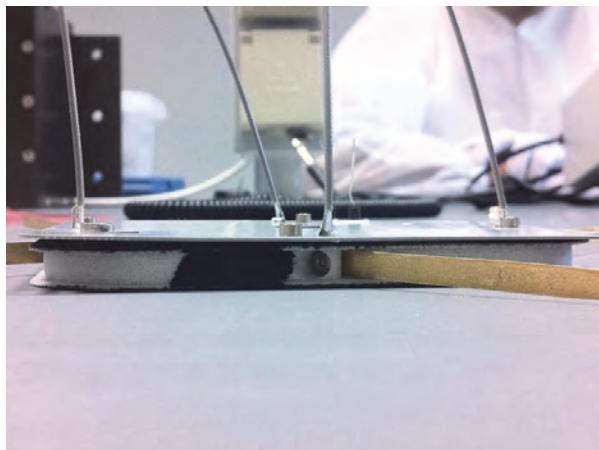


Figure 15. Integration problem with the coax

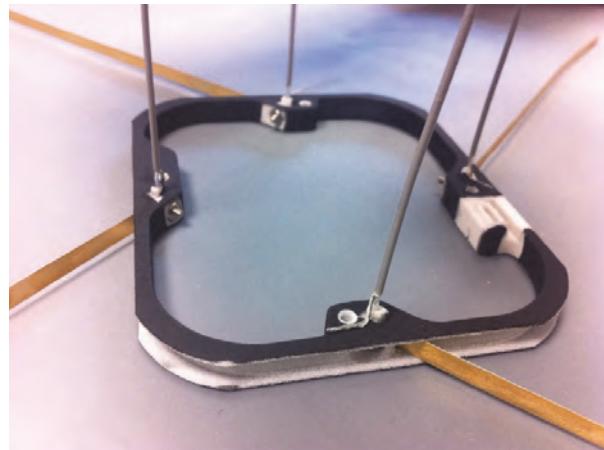


Figure 16. Coated Sub-chassis during the integration process

To solve this integration problem two measures were taken to avoid protrusion of the envelope.

- It was decided to look at the way in which the coaxial meshes were integrate, that is, we undid the rolling and the soldering and frayed them all. The aim was to increase the contact surface (and therefore reduce local pressure) and reduce the thickness of the mesh, as both factors were producing the excess in dimensions.
- The sub-chassis had been designed at the limits of its possibilities, but thanks to the results of the material chosen and the manufacturing method turning out to be better than expected, we decided to reduce the thickness of the upper tab on the sub-chassis by 0.15 mm and the lower one by 0.05 mm, which gave us 0.2mm of additional margin.

Both these actions combined resulted in the mechanism comfortable complying with the standard set for the film and all the measurement taken showed that the mechanism entered with a margin of at least 0.1 mm at any point on the design inside the envelope dimensions laid down.

Qualification Tests

The final step for the project was to carry out qualification tests on the satellite. We will focus here on those to do with the antenna deployment mechanism. These are the thermal-vacuum test and the vibration test.

Both tests were undertaken at the INTA facilities (Madrid) and had support from many members of the Xatcobeo project and INTA staff. The first was a complete simulation of the heat process during launch and orbit initiation, and a real-time simulation of orbital periods. During this test there was deployment of a duplicate of the antenna deployment mechanism, given that the main one was assembled on Xatcobeo. The results from the deployment were more than satisfactory.

With regards the vibration test, this was carried out at room temperature with a TEST-POD MkII, following a random profile as given in the reference document used as a guide in the tests. This reached up to 28g of acceleration. The test results were satisfactory as all the components in the deployment mechanism withstood the test with no shifts in their positions, no breaks, and no need to fine tune any part of the design. In short, there were no setbacks from the vibration test, which was the most ambitious one from the outset.

Conclusions

After almost three years of development, we have achieved a design that fulfils all the standards involved in the project. At the same time we have attained extreme lightness and great simplicity in operation and assembly. A great deal of the design's success lies in the use of polymers and the way their characteristics have been applied correctly after a process of testing, modification and verification.

Many of the problems and drawback found in the project have also stemmed from the use of these materials, and their use is an engineering risk when the aim is the search for extreme lightness. But thanks to this risk, a mechanism weighing in at only 13g has been completely validated even when faced with the most demanding tests.

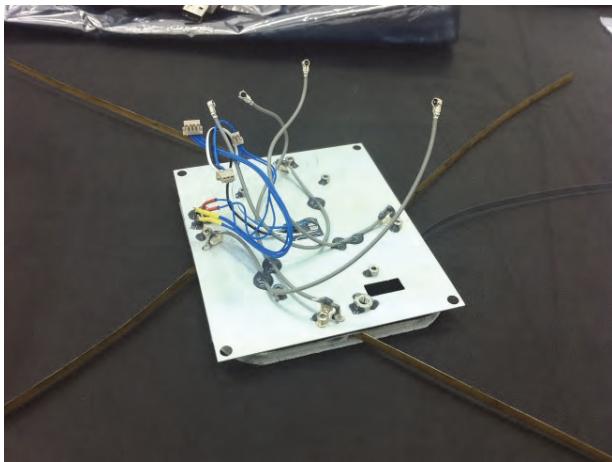


Figure 17. Rear side with the antennas deployed

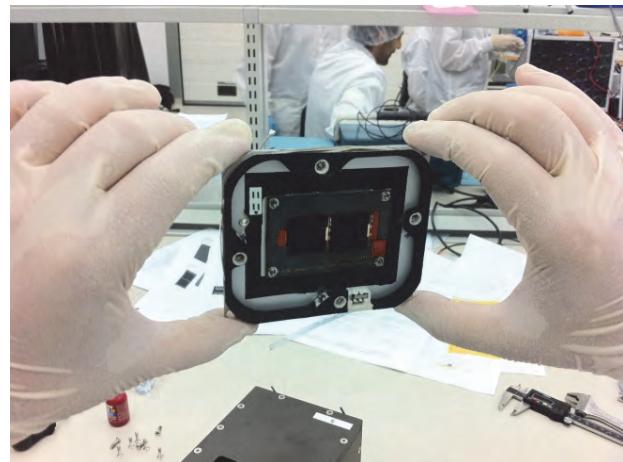


Figure 18. Front side with the antennas folded

We believe that the design process has sought validity within the characteristics decided upon for this mechanism in the face of all the important factors. Also the testing process has been exhaustive. The results have shown that the durability and reliability of not only the retention system but also the burning and detection system are all proven and guaranteed. The definitive test will soon take place when Xatcobeo is placed in orbit in the VEGA inaugural flight. However we are confident of the results shown by the mechanism in testing and of the reliability that the design has shown on the ground.

Given all that has been described in this and the previous article, we believe that using a combination of polymeric materials as a base and fast prototyping as a manufacturing method provides major advantages. These include the speed of the design process, the lightness of the assembly and the reduced cost of the project, and makes it possible to obtain feedback from flight parts at a reduced cost. It is also possible to overcome drawbacks stemming principally from the need for a direct correlation between the computer model and the manufactured item.

The final conclusion, as stated above, will be seen on launch. However, the results obtained so far show future possibilities for this combination of material and manufacture, for the response has been highly satisfactory.

References

1. Encinas Plaza, J.M., Vilán Vilán, J.A., Aguado Agelet, F., Barandiarán Mancheño, J., López Estévez, M., Martínez Fernández, C., Sarmiento Ares, F. "Xatcobeo: Small Mechanisms for CubeSat Satellites – Antenna and Solar Array Deployment" *Proceedings of the 40th Aerospace Mechanisms Symposium*, (2010), 415-430.

REPORT DOCUMENTATION PAGE					Form Approved OMB No. 0704-0188
<p>The public reporting burden for this collection of information is estimated to average 1 hour per response, including the time for reviewing instructions, searching existing data sources, gathering and maintaining the data needed, and completing and reviewing the collection of information. Send comments regarding this burden estimate or any other aspect of this collection of information, including suggestions for reducing this burden, to Department of Defense, Washington Headquarters Services, Directorate for Information Operations and Reports (0704-0188), 1215 Jefferson Davis Highway, Suite 1204, Arlington, VA 22202-4302. Respondents should be aware that notwithstanding any other provision of law, no person shall be subject to any penalty for failing to comply with a collection of information if it does not display a currently valid OMB control number.</p>					
PLEASE DO NOT RETURN YOUR FORM TO THE ABOVE ADDRESS.					
1. REPORT DATE (DD-MM-YYYY) May 2012		2. REPORT TYPE Conference Publication			3. DATES COVERED (From - To) May 16-18, 2012
4. TITLE AND SUBTITLE 41st Aerospace Mechanisms Symposium			5a. CONTRACT NUMBER NAS7-03001		
			5b. GRANT NUMBER		
			5c. PROGRAM ELEMENT NUMBER		
6. AUTHOR(S) Edward A. Boesiger			5d. PROJECT NUMBER		
			5e. TASK NUMBER		
			5f. WORK UNIT NUMBER		
7. PERFORMING ORGANIZATION NAME(S) AND ADDRESS(ES) Jet Propulsion Laboratory California Institute of Technology 4800 Oak Grove Drive Pasadena, CA 91009			8. PERFORMING ORGANIZATION REPORT NUMBER		
9. SPONSORING/MONITORING AGENCY NAME(S) AND ADDRESS(ES) National Aeronautics and Space Administration Washington, DC 20546-0001			10. SPONSORING/MONITOR'S ACRONYM(S)		
			11. SPONSORING/MONITORING REPORT NUMBER NASA/CP-2012-217653		
12. DISTRIBUTION/AVAILABILITY STATEMENT Unclassified—Unlimited					
Subject Category					
Availability: NASA CASI (301) 621-0390		Distribution: Nonstandard			
13. SUPPLEMENTARY NOTES					
14. ABSTRACT The proceedings of the 41 st Aerospace Mechanisms Symposium are reported. JPL hosted the conference, which was held in Pasadena Hilton, Pasadena, California on May 16-18, 2012. Lockheed Martin Space Systems cosponsored the symposium. Technology areas covered include gimbals and positioning mechanisms, components such as hinges and motors, CubeSats, tribology, and Mars Science Laboratory mechanisms.					
15. SUBJECT TERMS Spacecraft components; gimbals and positioning mechanisms, components such as hinges and motors, CubeSats, tribology, and Mars Science Laboratory mechanisms.					
16. SECURITY CLASSIFICATION OF: a. REPORT U b. ABSTRACT U c. THIS PAGE U			17. LIMITATION OF ABSTRACT UU	18. NUMBER OF PAGES 520	19a. NAME OF RESPONSIBLE PERSON STI Help Desk at help@sti.nasa.gov 19b. TELEPHONE NUMBER (Include area code) (301) 621-0390